August 1998 • NREL/CP-570-25315-Vol. 2

CONF-980440--Vol.2

Proceedings of the 1998 U.S. DOE Hydrogen Program Review

April 28-30,1998 Alexandria, Virginia

Volume II

Sponsored by the
Office of Solar Thermal, Biomass
Power and Hydrogen Technologies
U.S. Department of Energy

National Renewable Energy Laboratory
1617 Cole Boulevard
Golden, Colorado 80401-3393
A national laboratory of the U.S. Department of Energy
Operated by Midwest Research Institute
for the U.S. Department of Energy
Under Contract No. DE-AC36-83CH10093

DISCLAIMER

DISCLAIMER

Portions of this document may be illegible in electronic image products. Images are produced from the best available original document.

NREL/CP-570-25315

Proceedings of the 1998 U.S. DOE Hydrogen Program Review

April 28-30,1998 Alexandria, Virginia

Volume II

Sponsored by the
Office of Solar Thermal, Biomass
Power and Hydrogen Technologies
U.S. Department of Energy

National Renewable Energy Laboratory
1617 Cole Boulevard
Golden, Colorado 80401-3393
A national laboratory of the U.S. Department of Energy
Operated by Midwest Research Institute
for the U.S. Department of Energy
Under Contract No. DE-AC36-83CH10093

Prepared under Task No. HY811010

August 1998

TABLE OF CONTENTS

Volume I

Biological Systems

Electrochemical Systems

Process and Systems Analysis

Volume II

Storage and Separation Systems

Thermal Systems

Transportation Systems

HYDROGEN STORAGE DEVELOPMENT

G. J. Thomas and S. E. Guthrie
Sandia National Laboratories
Livermore, CA 94550

Abstract

A summary of the hydride development efforts for the current program year (FY98) are presented here. The Mg-Al-Zn alloy system was studied at low Zn levels (2 – 4 wt%) and midrange Al contents (40 – 60 wt%). Higher plateau pressures were found with Al and Zn alloying in Mg and, furthermore, it was found that the hydrogen desorption kinetics were significantly improved with small additions of Zn. Results are also shown here for a detailed study of the low temperature properties of Mg_2NiH_4, and a comparison made between conventional melt cast alloy and our vapor process material.

Background and Approach

The purpose of the work described in this report is to demonstrate improved hydrogen storage materials and systems. The project uses an integrated approach which includes materials development for improved performance as well as engineering efforts to optimize storage systems. Our lightweight hydride alloy development has been focused on Mg alloys [1-3]; however, recent promising results on a catalyzed allanate material [4] have prompted us to study this system as well, and it is anticipated that we will pursue these types of materials as part of our hydride development activities in the future. Engineering efforts this year have been limited by operating budget to cost, size and weight analyses applicable to a specific fixed site application [5].

Our approach in the Mg-based hydrides is to study bulk alloy additions which increase equilibrium overpressure, in combination with stable surface alloy modifications and particle size control to improve kinetic properties. These efforts attempt to build on the considerable previous work in this area, but examines specific alloy systems in greater detail and with attention to known phase properties and structures. Hydride pressure-composition-temperature measurements are correlated with detailed microstructural analyses in these studies. Different material synthesis methods are used, including melt-cast, rapid solidification and mechanical alloying. We have also compared performance in a Mg-Ni alloy prepared by our vapor process [1] to material prepared by these conventional techniques.

In our hydride bed engineering studies, we consider heat and fluid flow within beds as well as considering system integration. The work attempts to improve performance and reduce fabrication costs through modeling and experimental measurements, using our extensive knowledge of material behavior in hydrogen environments.

There are three main objectives to this work:

1. Develop improved light weight, low cost hydrides for energy applications.
2. Develop improved and innovative hydride bed designs.
3. Demonstrate and evaluate hydrogen storage systems.

The project is broadly organized into two tasks - hydride development and storage system engineering. Additional projects this year include a Phase 1 study with International Fuel Cells, Inc. on a PEM fuel cell-hydride application, IEA experimental collaborations on hydride development, a comprehensive hydride data base and a safety analysis of hydrogen use in underground mines (this study is scheduled to begin July 1, 1998). This report will describe recent work on hydride material development.

Past Results

Earlier pressure-composition-temperature (PCT) measurements were performed on a series of Mg-Al-Zn alloys. This work was motivated by our observations that adding Zn to Mg and Mg alloys resulted in improved kinetic and equilibrium properties . A systematic survey was implemented to more fully explore the effects of added Zn in Mg-Al alloys. Two sets of melt-cast alloys were prepared and initial measurements were performed. These measurements have been essentially completed this year and will be described in the next section.

Addressing manufacturing issues, a process for bed immobilization was tested. This process consists of the injection of inert microporous carbon material into the void space of packed hydride material to prevent mass transport as the particles fracture and during

hydrogen cycling. Microscopic examination and experimental measurements demonstrated successful immobilization with less than 1 % added to the bed weight. This is far less than the normal filtering and internal packaging weight and greatly reduces the assembly complexity of typcial bed designs. Limited cycle tests did not show any evidence for a loss in capacity from hydrocarbon production.

A novel vapor process was previously reported for the fabrication of Mg_2Ni with improved properties. To better understand these improvements, a study was initiated as part of the IEA Hydrogen Agreement to provide more analytical capability through task sharing and collaboration. In this program we provided detailed PCT and kinetic measurements on vapor process Mg_2Ni and commerical melt cast Mg_2Ni. Experiments were also performed to compare the low and high temperature hydride phases. This work has been completed this year and is described below.

Mg-Al-Zn Alloy Development

PCT measurements and electron microscopy characterizations were made on various compositions of Mg-Al-Zn to survey the low Zn (2-4 at %), mid range Al and Mg (40-60 at%) region of the phase diagram. Most of the alloys under study were from melt-cast ingots; however, it was found that Zn could easily be added to existing Mg-Al alloys by mechanical mixing. The high vapor pressure of Zn resulted in uniform doping of the material at 300° C.

Zinc is believed to occupy substitutional sites on the Al sublattice in these alloys, that is:

$$Mg_xAl_y > Mg_x(Al,Zn)_y$$

Referring to Figure 1, essentially two levels of equilibrium plateau pressures at 300°C may be followed across the Al+Zn axis. The lower level of plateau pressures are those of Mg-Al alloys without Zn. These generally required a temperature of 300° C or higher to allow completion of the measurements because of relatively slow desorption kinetics. By comparing these values to the Mg point on the ordinate, the addition of Al can be seen generally to increase the plateau pressure. The higher level of plateau pressures are those with Zn added to the Mg and Al. Although not shown, the Zn-containing materials had superior kinetic properties and could be characterized down to 200°C. As indicated by the symbols for the equilibrium phases in this alloy system (at the higher Al + Zn contents), each point can be correlated to distinct phases of both the binary Mg-Al and the ternary phase diagrams. Thus, the points suggest improvements in known, stable phases. However, the most promising results occur in the region associated with the R phase. In this region, Al+Zn compositional swings of only a few percent result in differently coordinated phases. This region has been difficult to survey using

conventional fabrication methods due to the propensity of the melt to precipitate the ordered γ and β phases during cooling. This leads to the correct average concentration, but imbalances the local concentration away from the the R phase region. This behavior is seen in figure 2 where the results of microscopic analysis are compared to the average concentration on the phase diagram for a representative sample following PCT measurements at 300° C.

We have found that a more effective approach is to start with Mg-Al alloys and introduce the Zn by a vapor process similar to that used in the formation of Mg_2Ni. This can be observed in figure 3 where gas atomized single phase powders of a Mg-Al alloy has been heated under hydrogen in the presence of Zn particles. Note the lack of microstructural variation. Condensation of the Zn on the Mg-Al particles and subsequent solid state diffusion results in complete homogenization of the alloy. This was also found to occur for other Mg-Al compositions. We believe we now have sufficient knowledge to fabricate a single phase alloy at the highest plateau pressure in this series. Currently, we are determining the optimum Zn concentration for best performance and lowest weight.

Low Temperature Studies of Mg2Ni

It is generally accepted that an ordered phase transformation from a cubic to a monoclinic structure occurs at 210-230° C in Mg_2Ni. We have found that this transformation is coincident with greatly diminished hydrogen kinetics. In TEM studies by Noreus [6] and verified by us (N. Yang), it was also observed that the occurrence of a microtwin deformation microstructure correlated with whether the hydride phase was formed above or below the transition temperature. The microtwins were present in hydrides formed above the transition temperature and were stable under observation.

In collaboration with D. Noreus, Univ. of Stockholm, as part of our IEA activities, we have compared PCT measurements at low temperatures of these two structures using two different starting materials – traditional melt-cast samples of Mg_2Ni and those formed by our vapor process. In figures 4 and 5, two sets of isotherms are shown with PCT measurements at 200°C (473K) and 180°C (453K). Within each plot frame can be recognized two sets of data for the vapor process (VP) material and the melt-cast (M) material. In addition, the hydride phase for each of these starting materials were formed - either at 300°C (HT) or at 180°C (LT). As mentioned earlier, microtwins were present in the HT hydride, but not in the LT hydride. At 200° C, we can see that no differences in the plateau pressures can be attributed to the hydride formation temperature, but that there are differences due to the fabrication processes. At 180°C, we see measurable differences in plateau pressures that can be attributed to the hydride formation temperature in both alloy lots. The lower plateau pressure in the microtwinned hydride is consistent with the more stable structure produced when the material relaxes by

forming the defects. The opposite is true in the unstable hydride without microtwins. Interestingly, the change in plateau pressure does not correlate directly with the cubic-monoclinic transition temperature, but rather occurs at a lower temperature. The difference in free energy between the two microstructures can be estimated from the plateau pressures to be 0.85 kJ/mole and appear to nucleate in the region 180-200°C.

Note in all cases that the vapor process material, which does not have a Mg impurity phase, has a higher equilibrium pressure than the commercial alloy. Our analyses have shown the vapor process alloy to be single phase, and hydrogen capacity measurements indicates that full capacity varies only ~5% in a temperature range from 180-300°C. We attribute the lower plateau pressures in the conventional alloy (M) to the presence of the Mg impurity phase. Differences in the plateau pressures are shown in the van't Hoff plots of Figures 6 and 7. In Figure 6, the data from the melt-cast alloys can be seen to be consistently below the solid line at temperatures lower than 300°C. The solid line represents an extrapolation of earlier Reilly-Wiswall data and its slope reflects an activation energy of 65KJ/mole. The melt-cast data indicates a slightly more stable hydride (68.6 KJ/mole) at lower tempratures. Little variations were found about the transition temperature. In the plot shown in Figure 7, the vapor process data can be seen to agree with the Reilly-Wiswall data down to temperatures as low as 150°C. Deviations in the plateau pressures do occur in this material above the transition temperature, indicating another effect. However, the microtwinning effect (HT-LT) in both materials can be seen to be much less than differences between the two starting alloys.

The detailed understanding we have achieved of the behavior of Mg_2NiH_4 at low temperatures (180-250°C) may help in identifying the role that relaxation microstructures have hydride stability and hydrogen kinetics of other magnesium alloy hydrides.

References

1. S.E. Guthrie, G.J. Thomas, D. Noreus and E. Ronnebro
   Properties of Mg2NiH4 at 450-570 K
   Conference Proceedings Materials Research Society (MRS) 1998 Spring Meeting, San Francisco, CA April 1998

2. S.E. Guthrie and G.J.Thomas
   A Novel Process for Fabricating Mg_2Ni
   presented at the Society for Advanced Material Processing and Engineering (SAMPE), Anaheim, CA, June 1998
   accepted for publication in the meeting proceedings

3. S.E. Guthrie and G.J. Thomas
   The Properties of Mg_2Ni Formed by a Vapor Phase Process
   IEA Task 12 Annual Report

4. B. Bogdanovic and M. Schwickardi
   Ti-doped alkali metal aluminum hydrides as potential novel reversible hydrogen storage materials.
   J. Alloys and Compounds, V. 253 (1997) p.1

5. G. J. Thomas
   Hydride Bed Design Considerations for a Fuel Cell Application
   Phase 1 Study Report

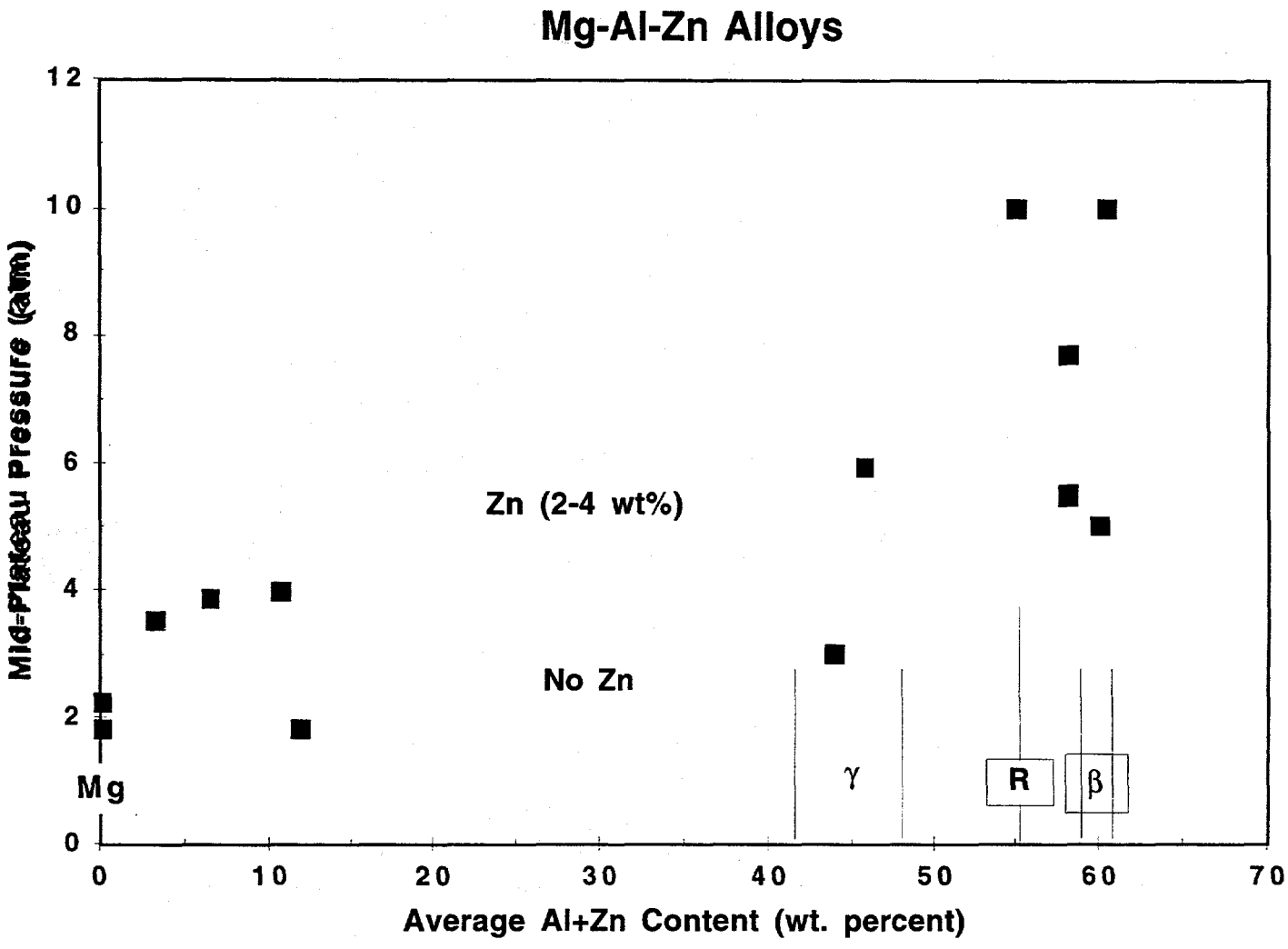

Figure 1. The equilibrium hydrogen pressure measured at the midpoint of the plateau are shown for the different Mg-Al-Zn alloy compositions. As stated in the text, Zn is believed to substitutionally occupy Al sites. All of the lower pressure data were found in alloys without Zn. Only 2 to 4 wt% Zn increased plateau pressures significantly and also increased hydrogen desorption kinetics.

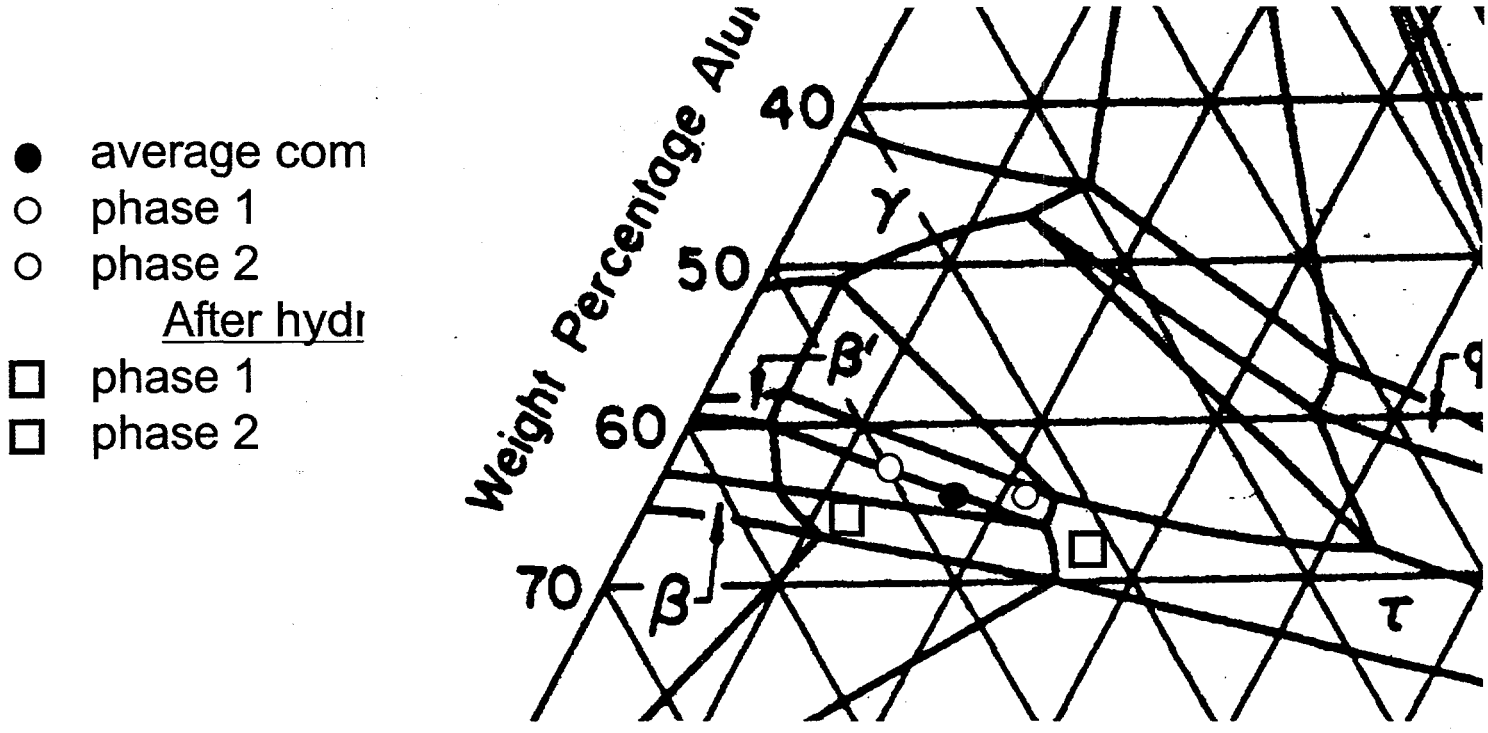

Figure 2. A section of the Mg-Al-Zn phase diagram is shown. The horizontal lines correspond to Mg weight percentage, while the diagonal lines parallel to the Al axis correspond to Zn weight percentage. The black circle indicates the average concentration of the starting material. Compositional analysis shows two phases present, with concentrations indicated by the open circles. After hydride measurements were completed, the compositions of the two phases had changed to the values indicated by the open squares.

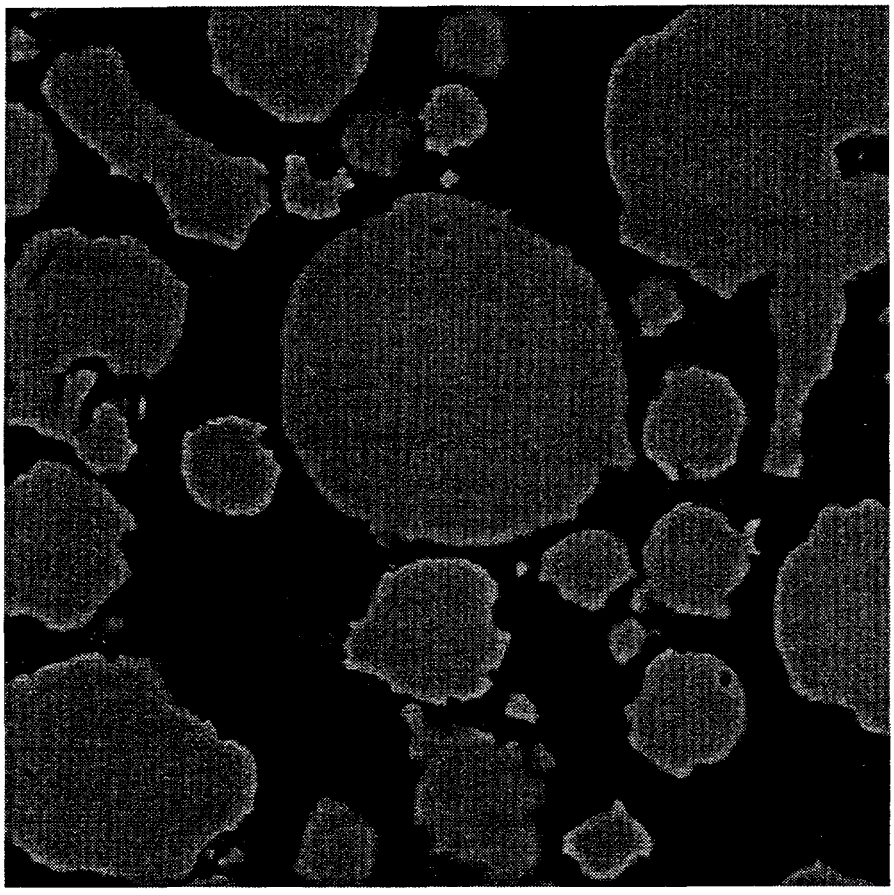

Figure 3. Backscattered electron image of a polished cross-section of a Mg-Al-Zn alloy following hydride measurements. The starting material was a gas atomized powder of Mg-Al which was mechanically mixed with Zn particles. No excess Zn is evident and quantitative analysis of the elemental compositions within the powder particles are consistent with the initial quantity of added Zn. The lack of contrast variations within the particles indicates that the composition is very uniform and that no other phases are present.

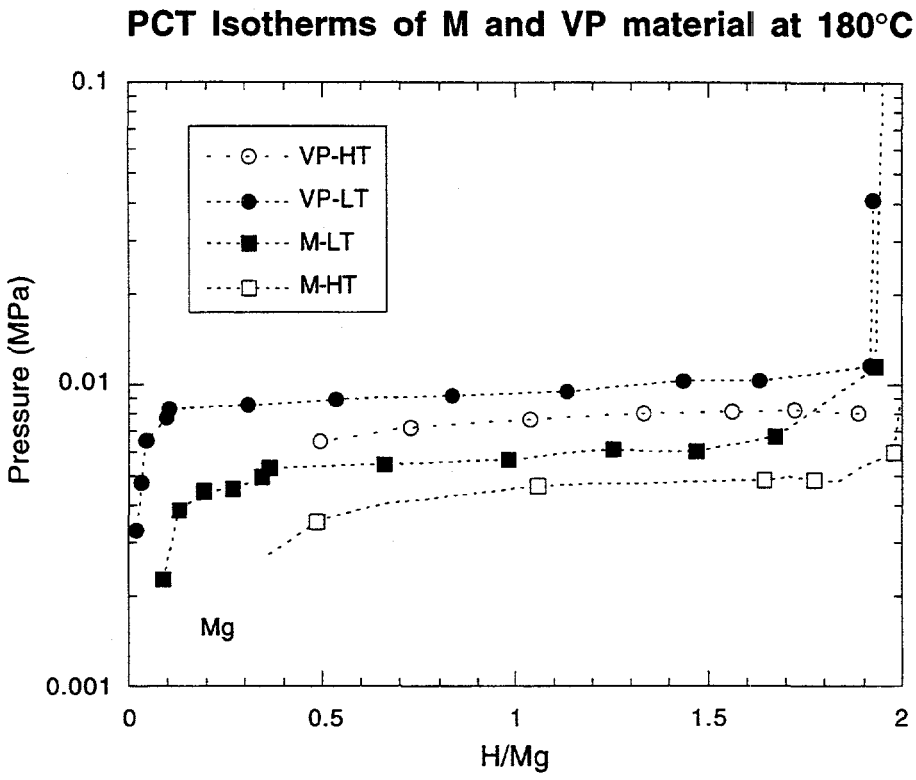

Figure 4. Isotherms at 180°C reveal plateau differences between the LT and HT conditions. In both materials (melt and VP), the lower hydride formation temperature lead to a higher plateau.

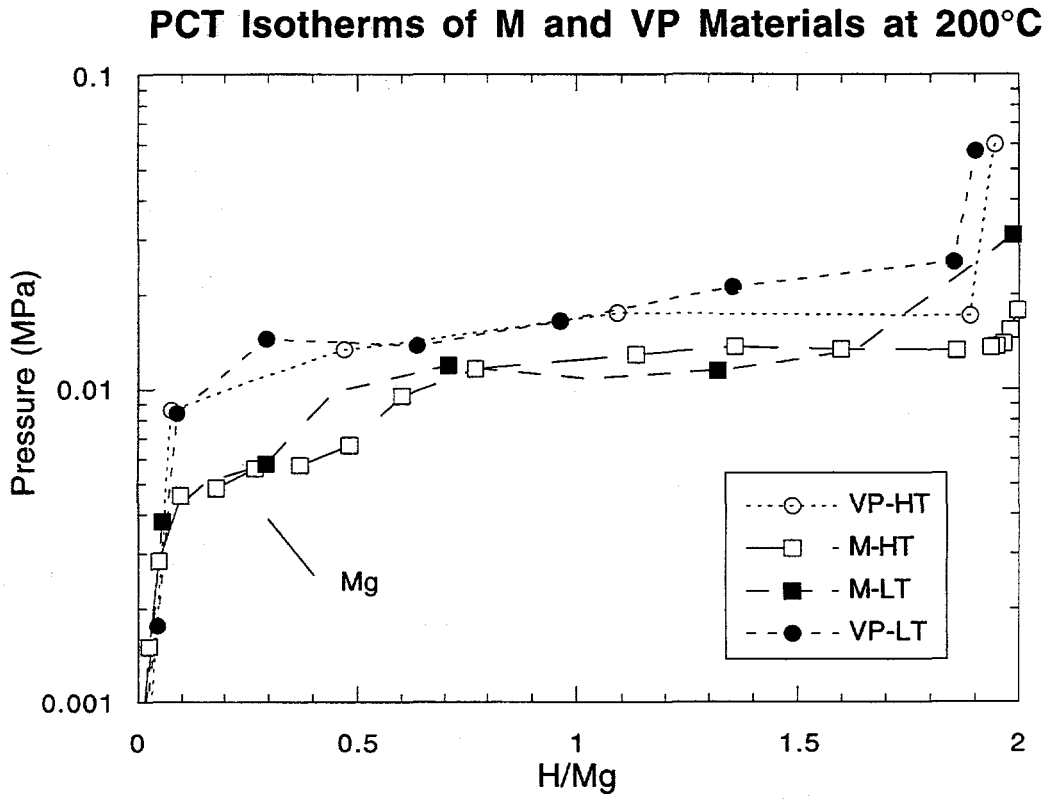

Figure 5. Isotherms at 200°C relect little differences between hydride plateau values suggesting that the microtwin effect vanishes by 200°C for both materials.

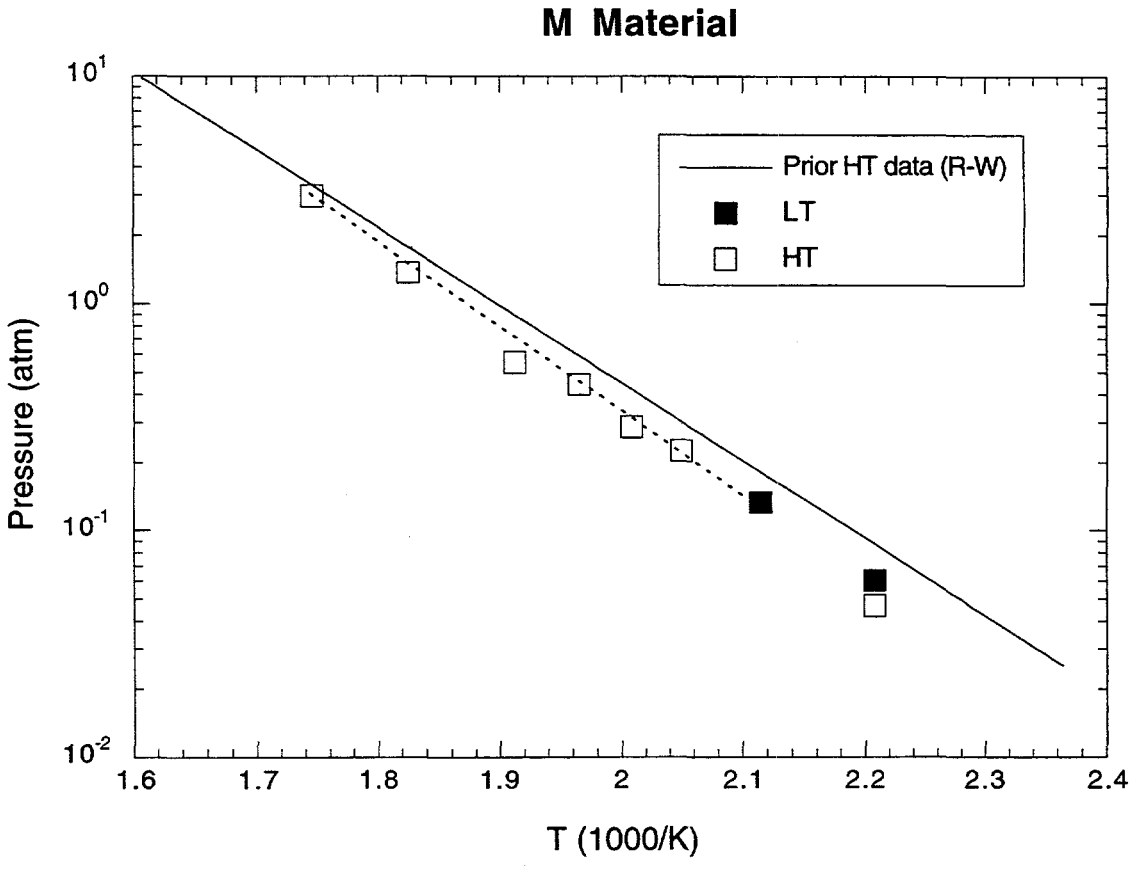

Figure 6. Vant Hoff plot of melt alloy deviatied from a composite data set of HT and VP results. LT measurements were only made at 180°C and 200°C.

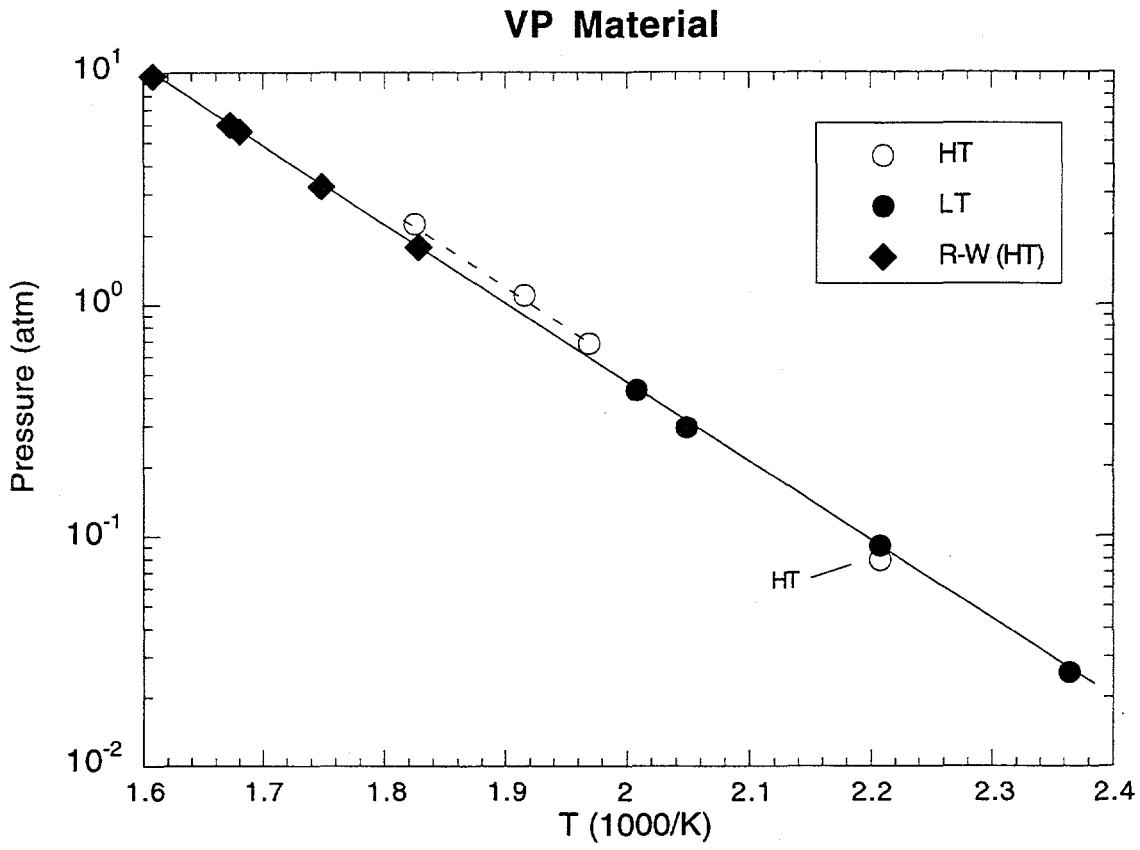

Figure 7. Vant hoff plot of VP alloys suggests that the LT sample preparation leads to a relationship consistent with high temperature Reilly-Wiswall (HT) results. HT conditions may imply (dashed line) a cross-over at or about 200°C given the consistently higher values of the VP-HT at higher temperatures.

IMPROVED MG-BASED ALLOYS FOR HYDROGEN STORAGE

Krishna Sapru, Lu Ming N.T. Stetson, J. Evans
Energy Conversion Devices, Inc
1675 West Maple Road
Troy, MI 48084

Abstract

The overall objective of this on-going work is to develop low temperature alloys capable of reversibly storing at least 3 wt.% hydrogen since, allowing greater than for 2 wt.% at the system level which is required by most applications. Surface modification of Mg can be used to improve its H-sorption kinetics We show here that the same Mg-transition metal-based multi-component alloy when prepared by melt-spinning results in a more homogeneous materials with a higher plateau pressure as compared to preparing the material by mechanical grinding. We have also shown that mechanically alloyed $Mg_{50}Al_{45}Zn_5$ results in a sample having a higher plateau pressure. This work was done under a cost-shared USDOE contract #DE-FC36-96GO10145.

Introduction

Because metal hydrides offer many advantages such as safety, long life, and high volumetric energy density, they are a very attractive means for hydrogen storage for PEM fuel cells and for other applications such as internal combustion engines. This is especially true for small vehicles and for portable power. H-Storage of >2 weight percent at the system level is required to meet both gravimetric energy density and system cost targets. Therefore, the development and commercialization of high capacity, low cost Metal Hydride Storage Systems (MHSS's) will enable the broad-based commercialization of metal hydride technology.

Technical Discussions

Technical Goals

Our goal is to develop commercially viable metal hydrides capable of storing greater than 3 wt.% hydrogen, that will result in a system storage capacity of >2wt.%. For this, we need to develop an alloy having greater than 3 wt.% H-Storage capacity, capable of delivering H_2 at the requirements for the PEM fuel cell, namely

- greater than 1 atm. Pressure
- desorption below 150°C

Additional requirements:

- Cost and availability of raw materials
- Ease of large scale manufacturing
- Long cycle life
- Resistance to poisoning of impurities in hydrogen gas

Technical Challenge

The greatest challenge in developing Mg-based, high capacity, low temperature alloys is to affect the thermodynamic properties of Mg. A key reason for this challenge is the limited number of elements with which Mg forms solid solutions and its low miscibility with most transition metal elements.

Past Results

We have previously shown [1,2,3] that in the process of making multi-component Mg-transition metal-based alloys for the storage of hydrogen using a high energy mechanical alloying process:

- Addition of graphitic C and heptane improves alloy yield and H-sorption kinetics.

- Increase in grinding speed significantly improves the diffusion of transition metal (TM) elements into Mg particles, produces smaller particles, and results in improved kinetics.

- For a fixed alloy composition, processing parameters affect alloy properties.

- Addition of several TM elements improve kinetics without appreciable change in H-storage capacity. There is also a small decrease in the value of ΔH.

Current Year Accomplishments

Surface Modification

A series of experiments were done to study the effect of surface modifiers on the kinetics of clean, mechanically ground Mg. Alloying was done for 6 hours at 930 rpm. For the surface modification experiments, catalytic materials were added during the last 30 minutes of grinding (except in the case of Ni, where three different grinding duration's were tried). The modifiers included elements such as Fe, Co, Ni, Mn, Cu, Mo and Pd, and pre-alloyed fine powders such as Mg_2Ni, Ni-Mo. **Figure 1** shows the effect of surface modification of some of these modifiers on the desorption kinetics of Mg. We see that while Mg_2Ni had the most significant affect on the kinetics of the alloy, 30 minutes of grinding with NiMo has the same effect as 90 minutes of Ni grinding. **Figure 2** shows the difference in SEM's between 30 min. Ni modification and 30 min. Mg_2Ni modification. Mg_2Ni modification results in homogeneous incorporation of catalyst throughout the sample.

Bulk Modification and Effect of Process

Modification with Transition Metal Elements

Bulk modification affects both kinetics and thermodynamic properties. We have shown that the modification of Mg-Ni-Mo-C by the incorporation of additional elements (Cu, Si, Fe, Mn) results in improved kinetics and a slight improvement in the PCT plateau pressure. The same multi-component material was prepared by melt spinning (MS). The ribbons as shown in **figure 3b** from the melt-spinning are very brittle. In contrast to the sample prepared by mechanical alloying (MA), the melt spun sample (MS) was very homogeneous. From **figure 4** we see that while the dehydriding kinetics of the as-prepared sample was not as good as the MA prepared sample, by using the results from surface modification, this problem was overcome. Curves 2 and 2a in **figure 4** are for MA sample and curve 1 is for the MS sample. Curve 3 represents the kinetics of the MS sample having a surface coating of Mg_2Ni.

Figure 5 shows the 300°C desorption isotherms of several Mg-transition metal-based alloys, including the material made by melt spinning (with and without a surface modifier coating). It can be seen that the MS sample results in a higher plateau pressure, indicating additional alloying or interactions between Mg and the modifier elements.

Modification with Low-Weight Elements (Al, Zn, C)

Several samples of Mg-Al-Zn were prepared by MA process. **Figures 6, 7** and **8** show the dehydriding kinetics, XRD's and P-C isotherms respectively, for this alloy. The slower desorption kinetics as compared to the Mg-Ni-Cu-Mn-Fe-Si-C sample (also shown here for comparison) is probably due to the absence of a transition metal element catalyst. The XRD pattern indicates the formation of certain Mg-Al(Zn) compounds during the alloying process. The PCT data shows that the plateau pressure of the Mg-Al-Zn alloy is significantly higher than for Mg-TM alloy (also included in this figure for comparison). The important point to note is the absence of a MgH_2 region. This Mg-Al-Zn system is presently not optimized.

Cycling Study

Some samples were subjected to cycling between vacuum and 200psia at 300°C. The hydrogen gas used is 99.9995% pure. **Figures 9** and **10** show that after 500 absorption/desorption cycles while there is some degradation in kinetics, there is not much loss in H-storage capacity. Tests are ongoing.

Acknowledgements

We thank the U. S. Department of Energy for providing partial funding under contract #DE-FC36-96GO10145.

References

1. K. Sapru, L. Ming, J. Evans and N. Stetson, 1997. "Develop Improved Metal Hydride Technology for the Storage of Hydrogen" in Proceedings of the 1997 U.S. DOE Hydrogen Program Review, Herndon, Virginia, pp255-276.

2. K. Sapru, L. Ming, J. Evans and N. Stetson, 1998. "Disordered Mg-Based Alloys for Hydrogen Storage" in Proceedings of the 1998 U.S. NHA Annual Meeting, Herndon, Virginia, in print.

3. K. Sapru, L. Ming, J. Evans and N. Stetson, 1998, "Effect of Processing Parameters on Mg-Based Hydrogen Storage Materials Prepared by Mechanical Alloying", 12th World Hydrogen Energy Meeting, Argentina, to be published.

Figures

Figure 1 Desorption Kinetics at 300°C
Figure 2 SEMs of Mg with Surface Modification: a) Ni; b) Mg_2Ni
Figure 3a SEM of MA Material
Figure 3b SEM of MS Ribbons
Figure 4 Desorption Kinetics at 300°C
Figure 5 Desorption P-C-T Curves at 300°C

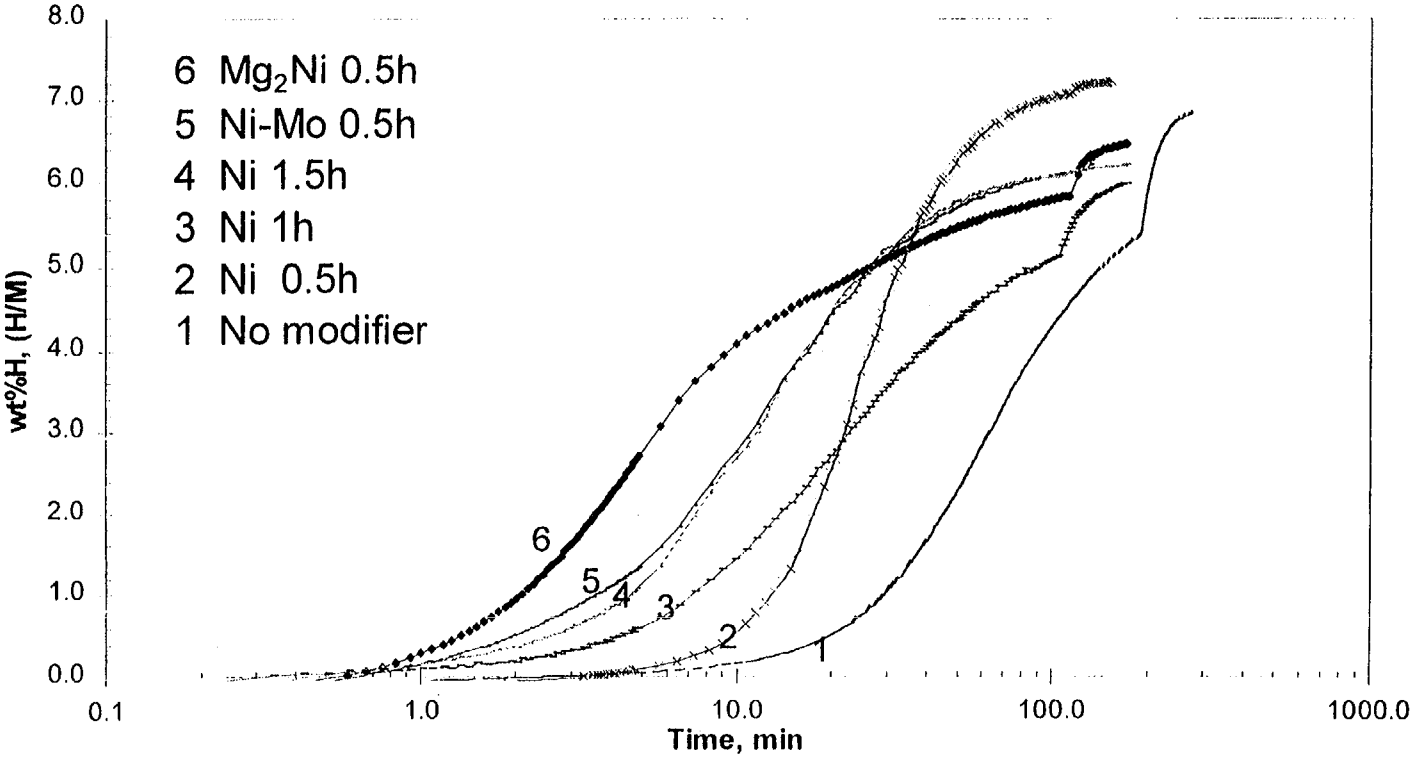

Figure 1 Desorption Kinetics at 300°C

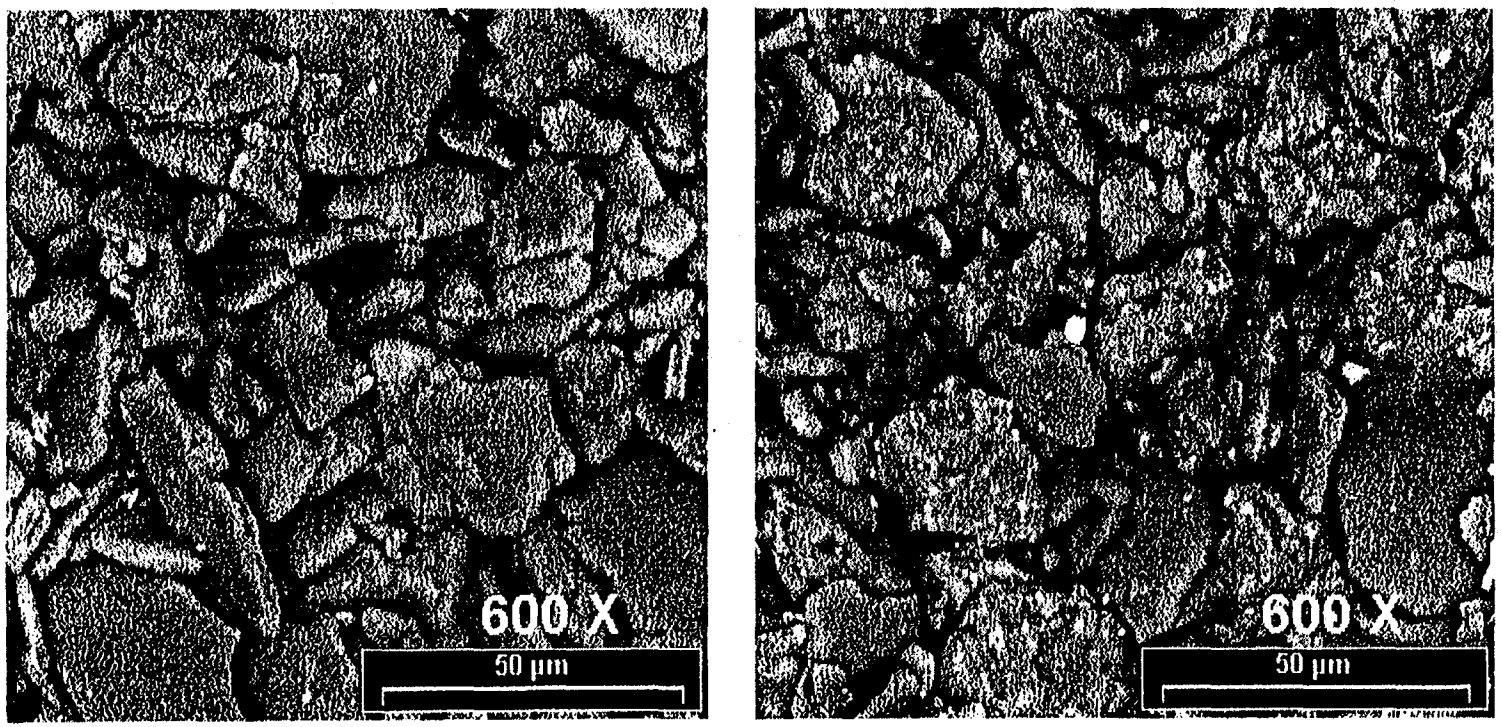

a) b)

Figure 2 SEMs of Mg with Surface Modification: a) Ni; b) Mg_2Ni

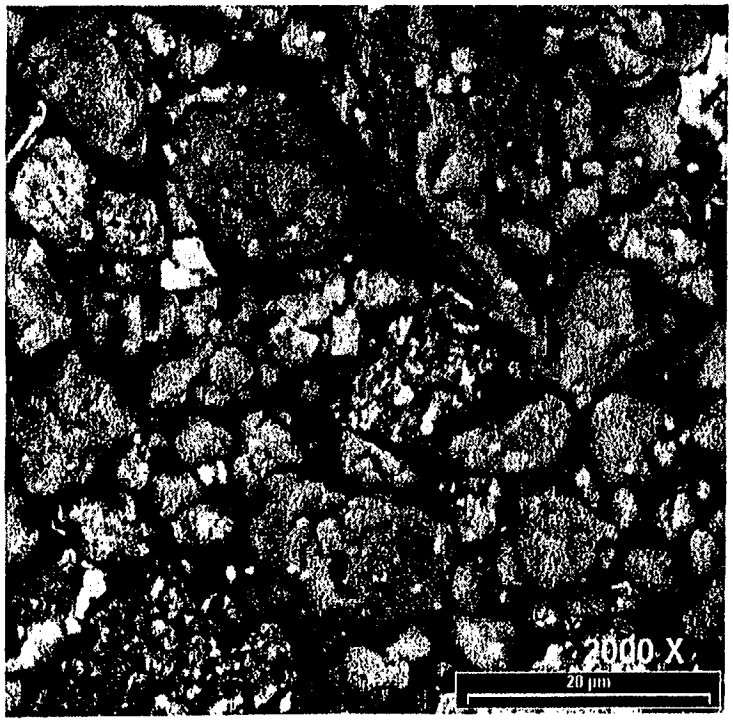

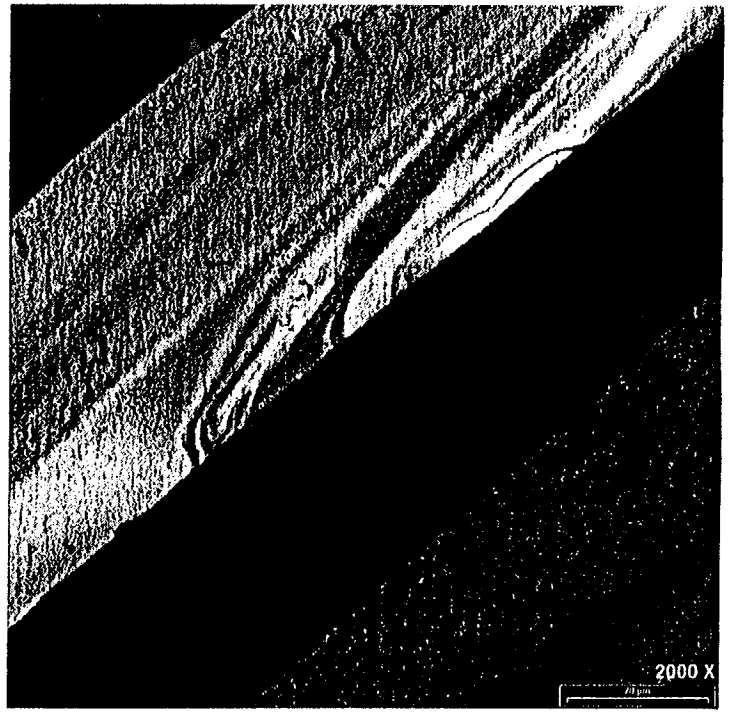

Figure 3 a) SEM of MA Material

b) SEM of MS Ribbons

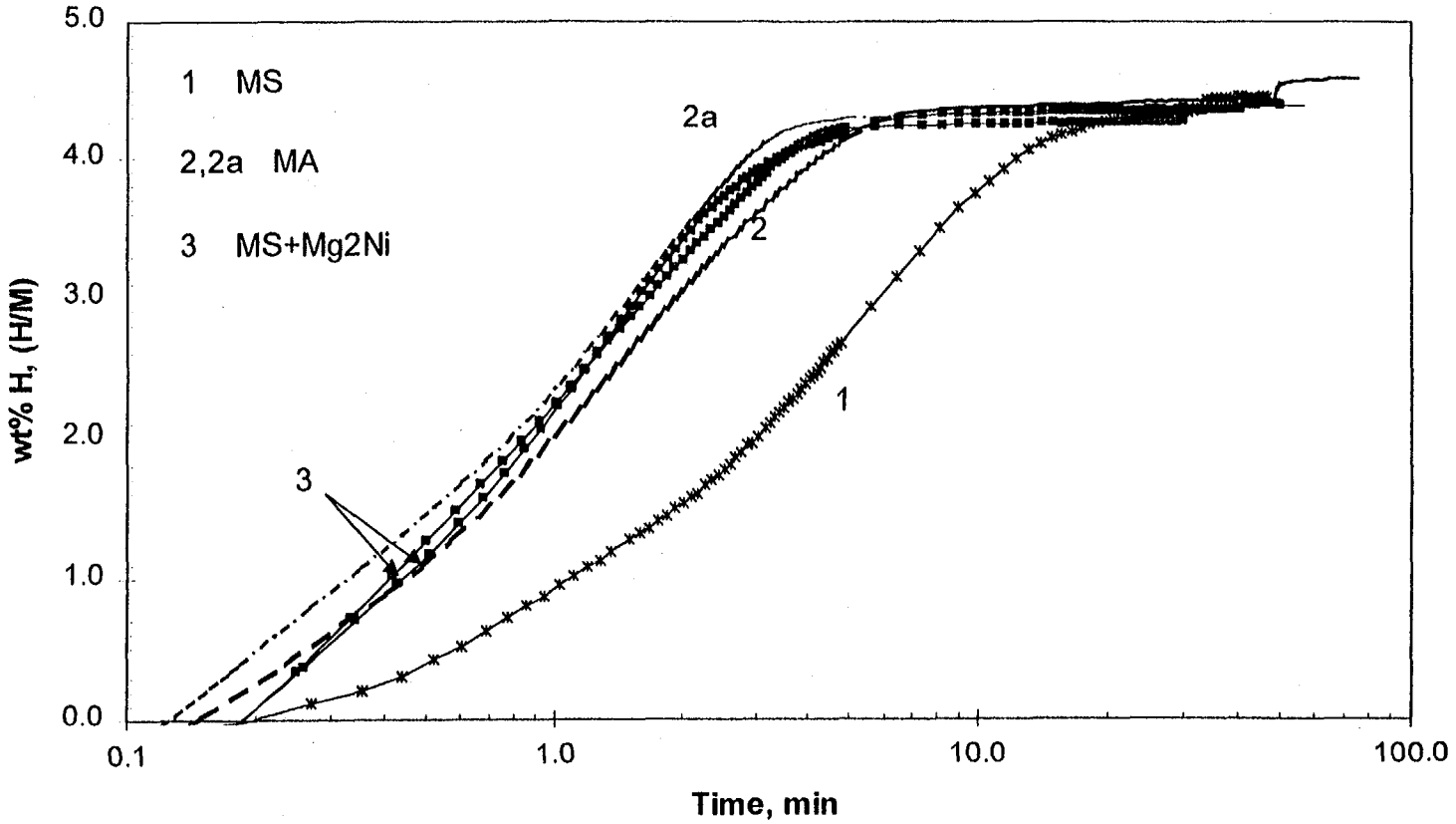

Figure 4 Desorption Kinetics at 300°C

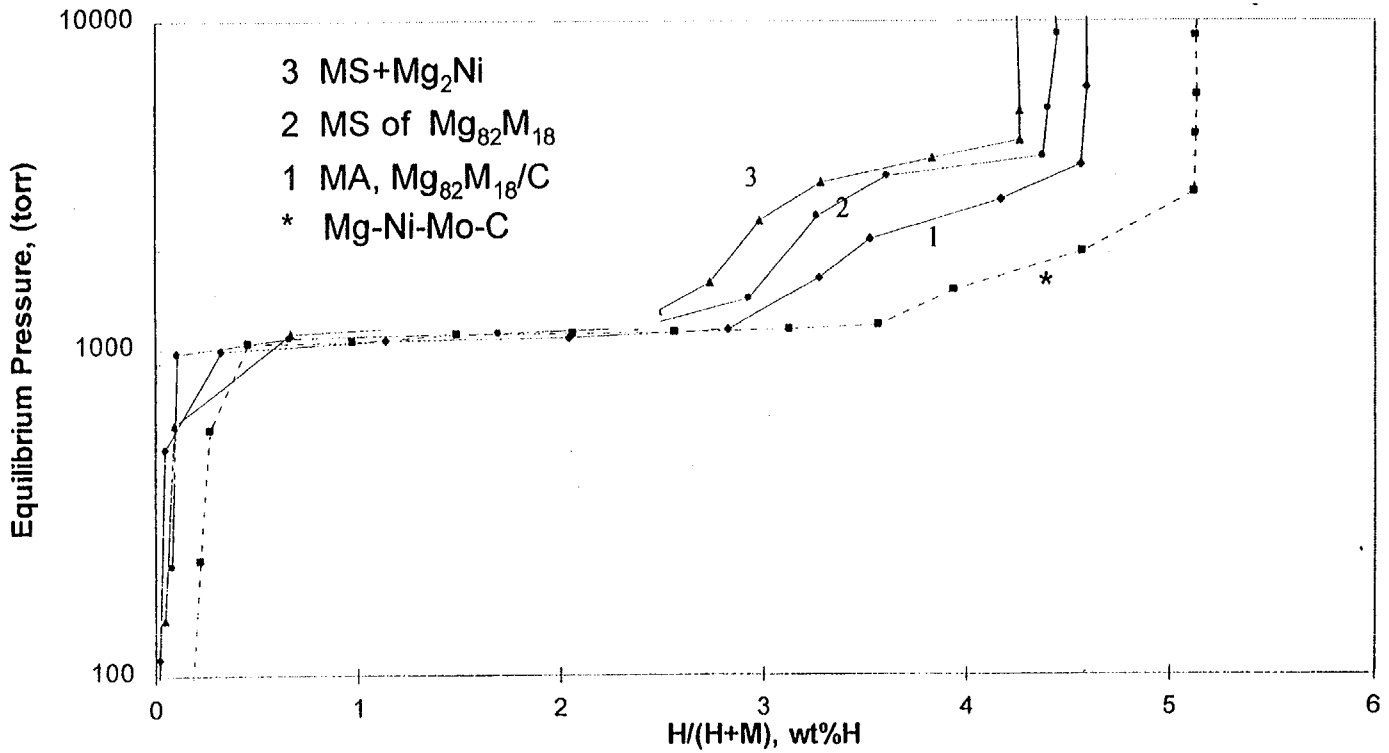

Figure 5 Desorption P-C Isotherms at 300°C

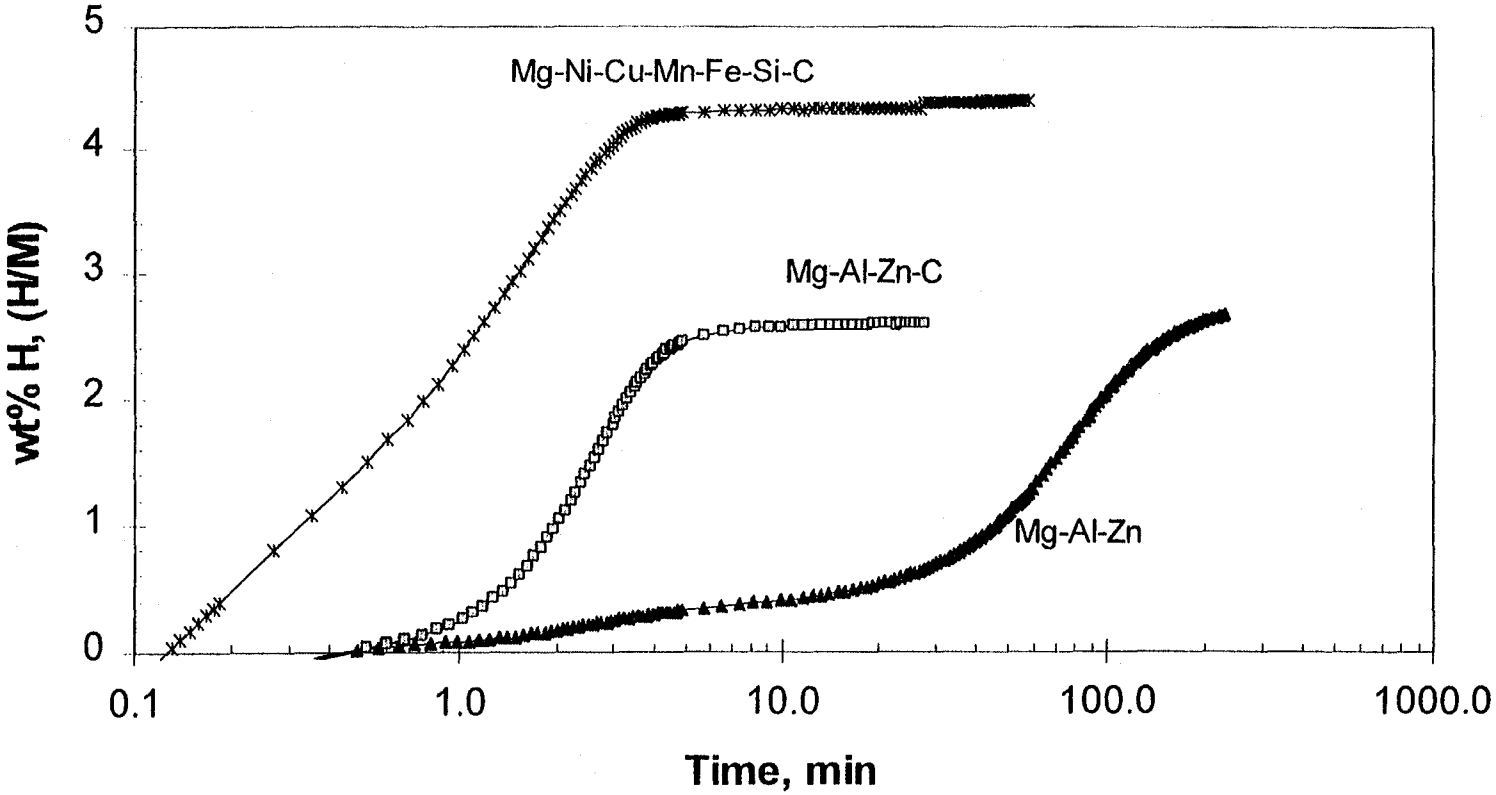

Figure 6 Desorption Kinetics at 300°C

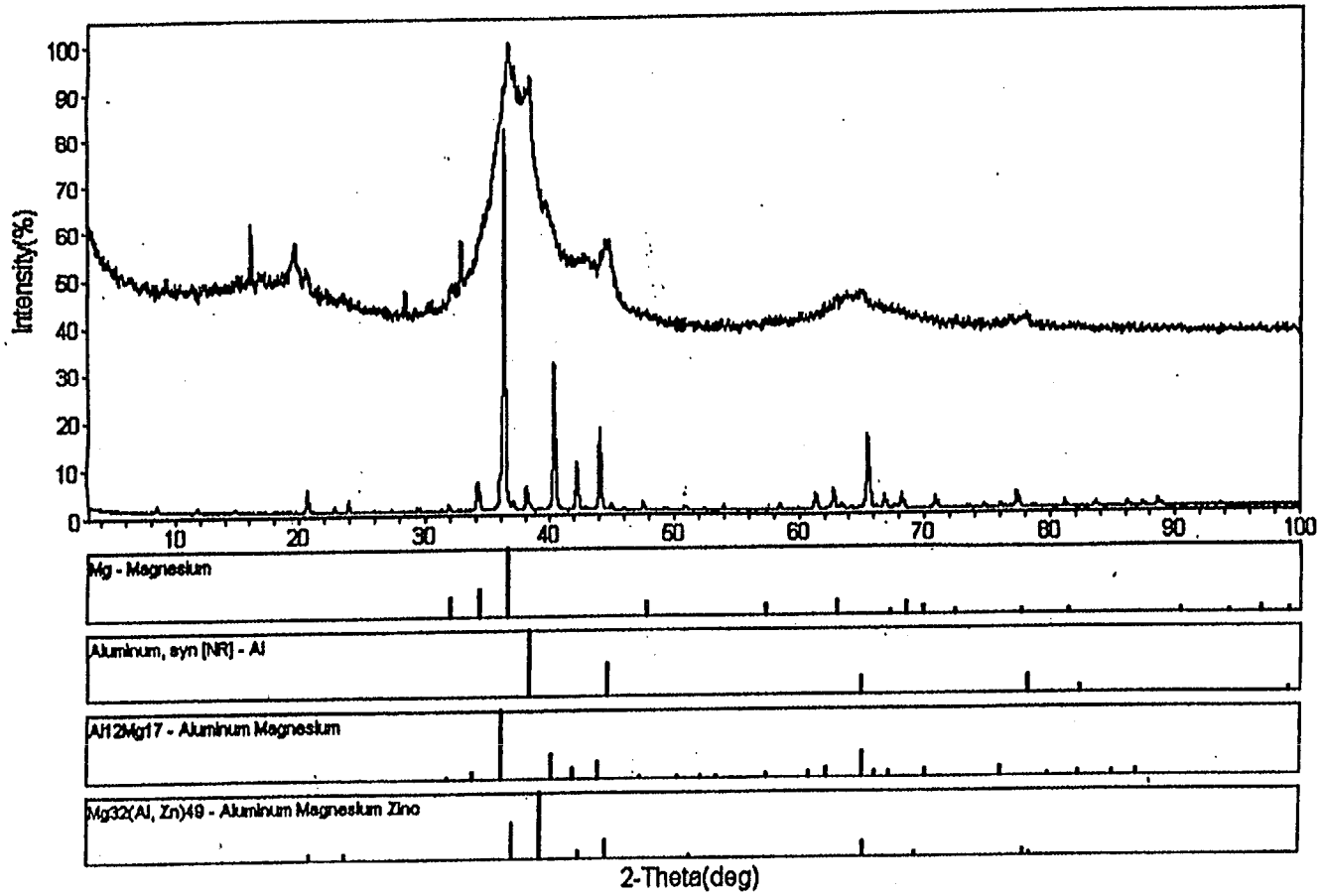

Figure 7 XRD of Mg-Al-Zn/C Prepared by MA

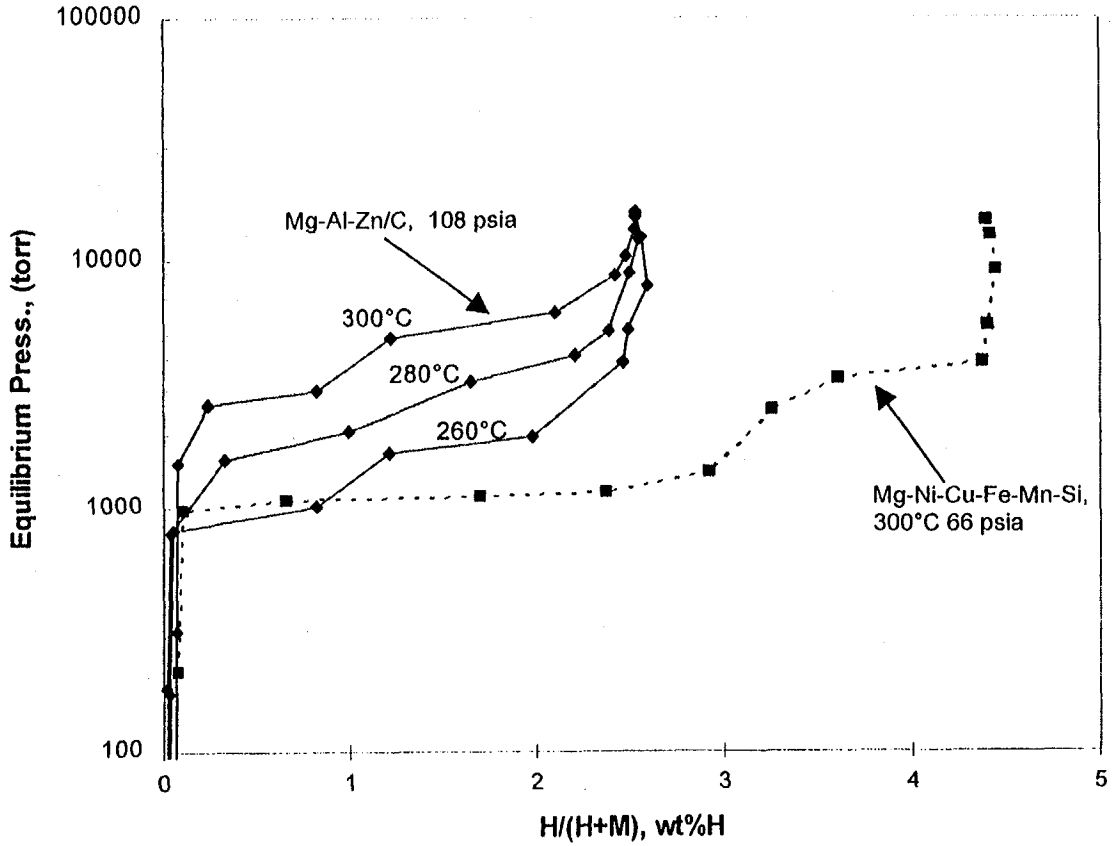

Figure 8 Desorption P-C-T Curves for Mg-Al-Zn/C by MA

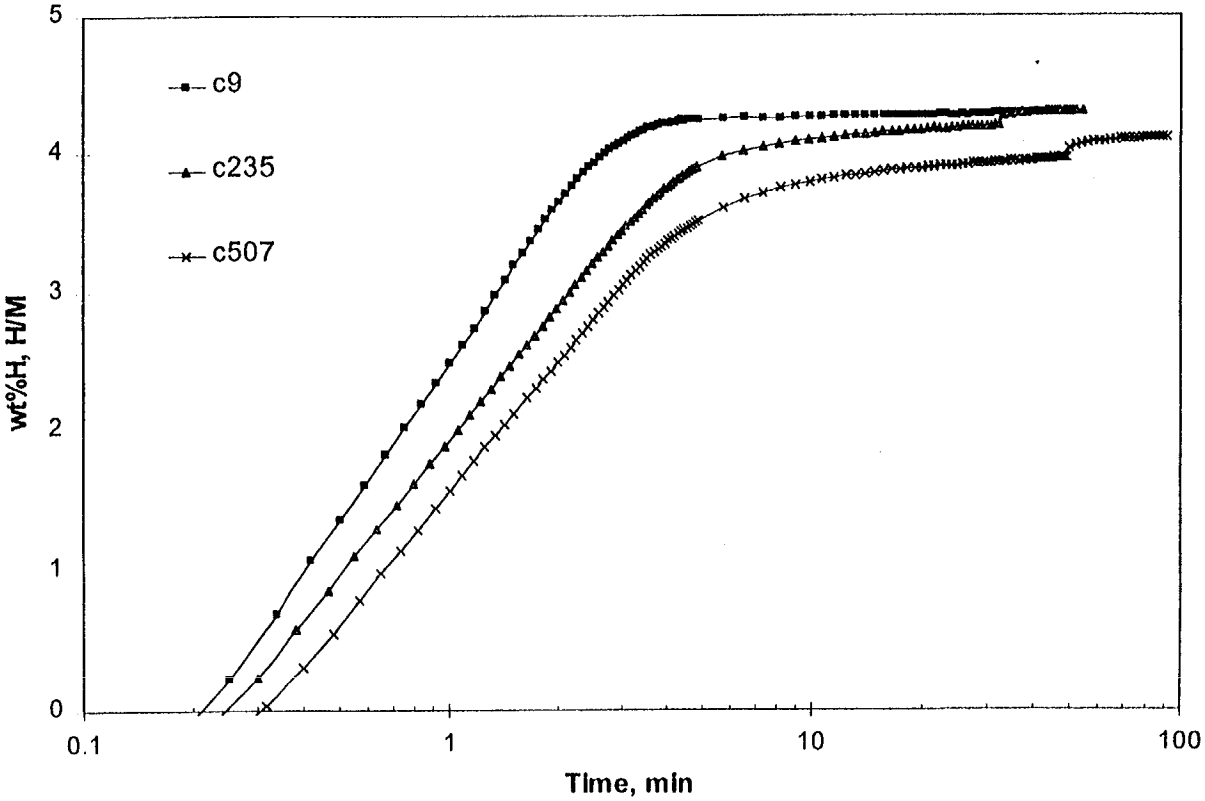

Figure 9 Desorption Kinetics at 300°C

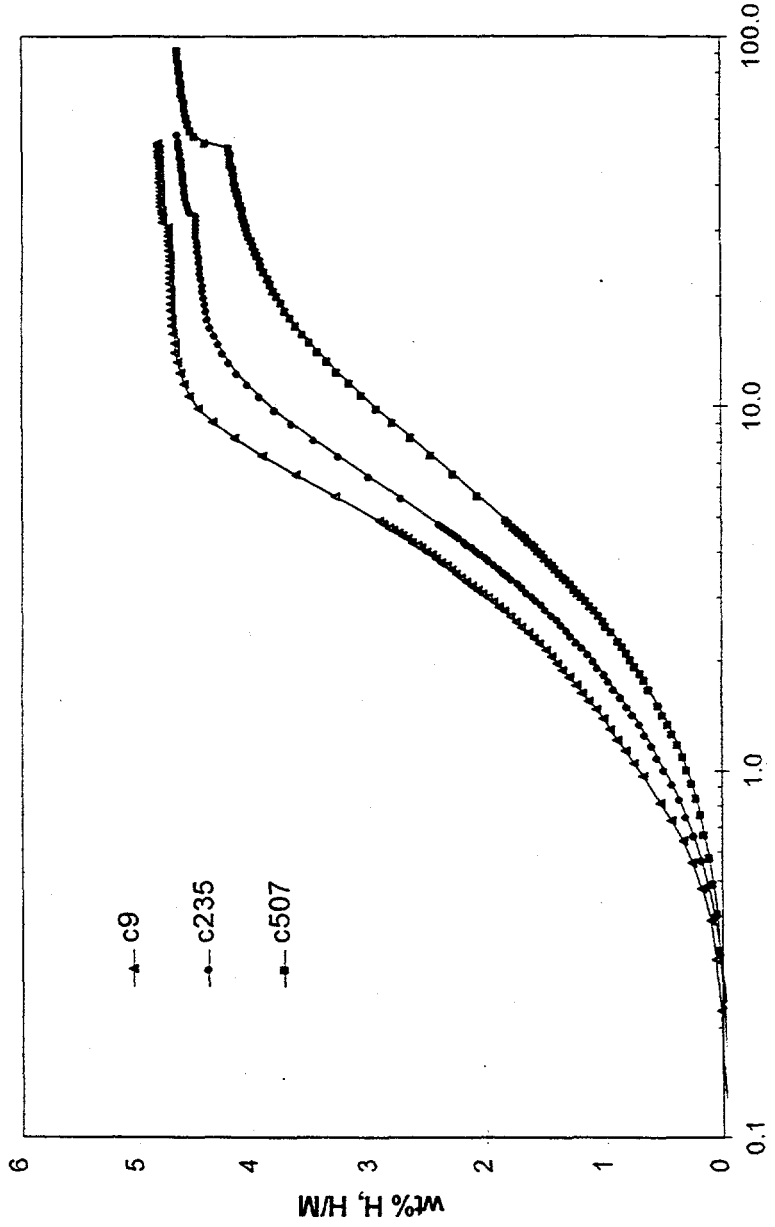

Figure 10 Desorption Kinetics at 300°C

HYDROGEN STORAGE VIA POLYHYDRIDE COMPLEXES

Craig M. Jensen and Ragaiy A. Zidan
Department of Chemistry and Hawaii Natural Energy Institute
University of Hawaii
Honolulu, HI 96822

Abstract

The reversible dehydrogenation of $NaAlH_4$ is catalyzed in toluene slurries of the $NaAlH_4$ containing the pincer complex, $IrH_4\{C_6H_3\text{-}2,6\text{-}(CH_2PBu^t_2)_2\}$. The rates of the pincer complex catalyzed dehydrogenation are about five times greater those previously found for $NaAlH_4$ that was doped with titanium through a wet chemistry method. Homogenization of $NaAlH_4$ with 2 mole % $Ti(OBu^n)_4$ under an atmosphere of argon produces a novel titanium containing material. TPD measurements show that the dehydrogenation of this material occurs about 30 °C lower than that previously found for "wet" titanium doped $NaAlH_4$. In further contrast to "wet doped" $NaAlH_4$, the dehydrogenation kinetics and hydrogen capacity of the novel material are undiminished over several dehydriding/ hydriding cycles. Rehydrogenation of the titanium doped material occurs readily at 170 °C under 150 atm of hydrogen. TPD measurements show that about 80% of the original hydrogen content (4.2 wt %) can be restored under these conditions.

Introduction

For decades, hydrogen has been targeted as the utopian fuel of the future due to its abundance and environmental friendliness. A major difficulty in the utilization of hydrogen as a fuel is the problem of onboard hydrogen storage. High pressure and cryogenic hydrogen storage systems are impractical for vehicular applications due to safety concerns and volumetric constraints. This has prompted an extensive effort to develop solid hydrogen storage systems for vehicular application. Metallic hydrides (Sandrock et al.

1992; Sandrock 1995), activated charcoal (Carpetis and Peshka, 1980; Agarwal et al., 1987) and carbon nanotubules (Dillon et al., 1997) have been investigated as hydrogen carriers. Unfortunately, despite decades of extensive effort, especially in the area of metallic hydrides, no material has been found which as has the combination of a high gravimeteric hydrogen density, adequate hydrogen dissociation energetics, and low cost required for commercial vehicular application (Suda and Sandrock, 1994).

The dehydrogenation of $NaAlH_4$ is known to occur by a multistep process involving the reactions seen in equations 1 and 2 (Dymova, 1975). This process is thermodynamically

$$3\ NaAlH_4 \text{ ----------> } Na_3AlH_6 + 2\ Al + 3\ H_2 \qquad (1)$$

$$Na_3AlH_6 \text{ ----------> } 3\ NaH + Al + 3/2\ H_2 \qquad (2)$$

favorable at moderate temperatures. However, it is characterized by very slow kinetics (Dymova, 1975) and reversibility only under severe conditions (Dymova, 1974). Thus despite favorable thermodynamics and a high available hydrogen weight percentage, $NaAlH_4$ has generally been precluded from consideration as a potential hydrogen storage material and there has been very little effort to develop this material as a hydrogen carrier. This thinking has been changed recently by Bogdanovic and Schwickardi. Their pioneering study demonstrated that upon doping with selected titanium compounds, the dehydrogenation of anionic aluminum hydrides could be kinetically enhanced and rendered reversible under moderate conditions (Bogdanovic and Schwickardi, 1997). These findings represent a breakthrough in the application of this class of hydrides to hydrogen storage. However, further kinetic enhancement of the dehydriding and rehydriding processes are required to produce a material which is suitable for practical vehicular applications. Also the hydrogen capacity of Bogdanovic's material diminished upon extended cycling. It is therefore necessary to find improved catalysts of increased stability.

We are developing $NaAlH_4$ based hydrogen storage materials which contain catalytic additives. The polyhydride complex, $IrH_4\{C_6H_3\text{-}2,6\text{-}(CH_2PBu^t_2)_2\}$ was found to be an unusually robust and active catalysts for the reversible dehydrogenation of cycloalkanes to arenes (Gupta et al, 1997). This suggested that it might act as a catalyst for the reversible dehydrogenation of $NaAlH_4$. We have also explored the effect of variation in the method of the introduction of titanium to this host material.

Results

Pincer Complex Catalyzed Dehydrogenation of $NaAlH_4$.

The pincer polyhydride complex, $IrH_4\{C_6H_3\text{-}2,6\text{-}(CH_2PBu^t_2)_2\}$ examined as a catalyst for the dehydrogenation of $NaAlH_4$. As seen in Figure 1, hydrogen is evolved from toluene slurries of the $NaAlH_4$ containing the pincer catalyst at rates about five times greater those found $NaAlH_4$ which was doped with an equimolar amount of titanium through the method of Bogdanovic (Bogdanovic and Schwickardi,, 1997).

Preparation of the Novel Titanium Containing Material.

Freshly recrystallized $NaAlH_4$ was added to prescribed amounts of $Ti(OBu^n)_4$ under an atmosphere of argon. The originally colorless mixture was homogenated using a mortar and pestle until it become red-violet. The resulting paste was visually very distinct from the brown powders obtained through Bogdanovic's procedure for producing titanium doped

materials. Elemental analysis showed that only trace amounts of carbon are present in this material.

We examined the dehydrogenation of this novel material in the solid state. Clearly the material produced by this method exhibits catalytic effects which are an order of magnitude improved over the materials originally prepared by Bogdanovic or those containing the polyhydride catalyst.

Thermal programmed (TPD) measurements.

TPD measurements were made on samples of undoped $NaAlH_4$ (**1**); $NaAlH_4$ which was doped with titanium through the Bogdanovic method (**2**); and $NaAlH_4$ which was doped with titanium through the method described above. Excellent agreement was found among samples of 2 and 3 which were prepared independently. The data obtained for **2** is also consistent with the finding of Bogdanovic. The TPD measurement of samples of the three different materials are plotted in Figure 2. While the catalytic effect of titanium is evident for both **2** and **3**, the temperature of dehydrogenation of **3** is seen to be 30 °C lower than that of **2**.

A priori, it seemed possible that the differences observed in the dehydriding behavior of **2** and **3** were simply due to variation in the level of titanium loading in the two materials. In order to probe this possibility, independent TPD measurements were made on samples of **2** and **3** which were prepared using 1.0, 2.0, and 4.0 mol % $Ti(OBu^n)_4$ respectively. As seen in Figure 3 variation in the amount of $Ti(OBu^n)_4$ used in the preparation showed little effect on the dehydrogenation temperature. However, increasing the titanium content of the material does show the expected gravimetric effect of lowering the H/M wt %. These results indicate that only a fraction amount of titanium introduced into the materials is catalytically active. Furthermore, there is clearly a significantly larger amount of catalytically active titanium in **2** than **3**. However, we can not say at this point why the dry doping method is more effective than the wet doping method for the generation of the active titanium sites. It is possible that the action of wet doping method is restricted to the surface of the hydride while the dry doping method introduces active titanium sites in the bulk. Thus our homogenization technique may be crudely equivalent to ball milling of the material.

Cycling Studies

Since the reversibility is a requirement for most applications, the behavior of rehydrogenated samples were investigated. In an initial set of experiments, samples were rehydrided under 1600 psi of hydrogen pressure at 200 °C. Under these conditions, only about 40% of the hydrogen in the original material is replaced at the moderate hydrogen pressure. TPD measurements were then made on the rehydrided samples. Figure 4 shows the percentage of hydrogen desorbed from the samples as a function of temperature, considering the desorbed hydrogen at the first cycle to be 100%. The uptake is clearly less than found in the original sample showing that only partial hydrogenation could be obtained under this conditions. The second dehydriding cycle of **3** occurs at nearly the same temperature observed for the first. This sharply contrasts the dehydriding behavior of **2** for which dehydriding occurs at a significantly higher temperature, closer to that of **1**, in the second cycle.

In a second set of experiments, samples were rehydrided at 150 atm and 170 °C. As seen in Figure 5, TPD measurements show that about 80% of the original hydrogen content (4.2 wt %) of **2** and **3** can be restored under these conditions. However, unlike the Bogdanovic

material, **2**, for which the capacity drops to 3.8 wt % on the second cycle, no loss of hydrogen capacity was observed for our novel material, **3** through the 5 dehydrogenation/rehydrogenation cycles. Also TPD studies show that the dehydrogenation temperature of **2** drifts back toward that of **1** on cycling. A 10 °C rise in is observed for second cycle alone. The dehydrogenation temperature of **3**, on the other hand, remains constant through the first 5 cycles.

Conclusion

The polyhydride pincer complex and titanium doping have been observed to catalyze the dehydrogenation kinetics of $NaAlH_4$. The greatest catalytic effect was observed for $NaAlH_4$ in which titanium was induced through a solid state method. These results demonstrate the catalytic effect of titanium dopants first reported by Bogdanovic was only a starting point and that further improvement of the kinetics of the reversible dehydriding of $NaAlH_4$ is possible. Furthermore, we have shown that it is possible to introduce catalysts into $NaAlH_4$ such that enhanced dehydrogenation kinetics and the attainable hydrogen capacity are undiminished over several dehydriding/ hydriding cycles.

Future Work

The material will be monitored through 100 dehydrogenation/rehydrogenation cycles in order to determine its long term stability. The equilibrium hydrogen pressures and other thermodynamic parameters will be determined from PCT curves obtained at 100 °C above. The kinetics of the dehydrogenation at these temperatures will also be determined with more precision that our preliminary data allows. We will continue to modify the hydride system and study the dehydriding kinetics of the resulting materials.

References

Agarwal, R.K., J.S. Noh, J.A. Schwarz, and R. Davini, 1987. *Carbon* 25:219.

Bogdanovic, B. and M. Schwickardi, 1997. *J. Alloys and Compounds* , 1-9:253.

Carpetis, C. and W. Peshka, 1980. *Int. J. Hydrogen Energy* , 5: 539.

Dillon, A.C., K.M. Jones, T.A. Bekkedahl, C.H. Kiang, D.S. Bethune and M.J. Heben, 1997. *Nature* , 386:377.

Dymova, T.N., Y.M. Dergachev, V.A. Sokolov, and N.A. Grechanaya, 1975. *Dokl. Akad. Nauk USSR*, 224:591.

Dymova, T.N., N.G. Eliseeva, S.I. Bakum, and Y.M. Dergachev, 1974. *Dokl. Akad. Nauk USSR*, 215:1369.

Gupta, M., C. Hagen, W. C. Kaska, R. E. Cramer, and C. M. Jensen, 1997. *J. Am. Chem. Soc.*, 119:840.

Sandrock, G., S. Suda, and L. Schlapbach, 1992. *Topics in Appl. Phys.*, 67:197.

Sandrock, G. 1995. *Application of Hydrides* in *Hydrogen Energy Systems* (ed Yurum), 253-280. Netherlands: Kluwer Academic Publishers.

Suda, S. and G. Sandrock, 1994. *Z. Phys. Chem.*, 183:149.

FIGURE CAPTIONS

Figure 1. Dehyrogenation of $NaAlH_4$ at 120 °C.

Figure 2. Thermal programmed desorption (2 °C min^{-1}) of hydrogen from undoped, wet titanium doped, and dry titanium doped $NaAlH_4$.

Figure 3. Thermal programmed desorption (2 °C min^{-1}) of hydrogen from samples of dry titanium doped $NaAlH_4$ prepared from 1, 2, and 4 (0.5x, x, and 2x) mol % $Ti(OBu^n)_4$.

Figure 4. Thermal programmed desorption (2 °C min^{-1}) of hydrogen from dry titanium doped $NaAlH_4$ following one dehydrogenation/rehydrogenation cycle. 100 % corresponds to the amount of hydrogen released in the first dehydrogenation.

Figure 5. Thermal programmed desorption (2 °C min^{-1}) of hydrogen from dry and wet titanium doped $NaAlH_4$ after 3 cycles of dehydrogenation/rehydrogenation.

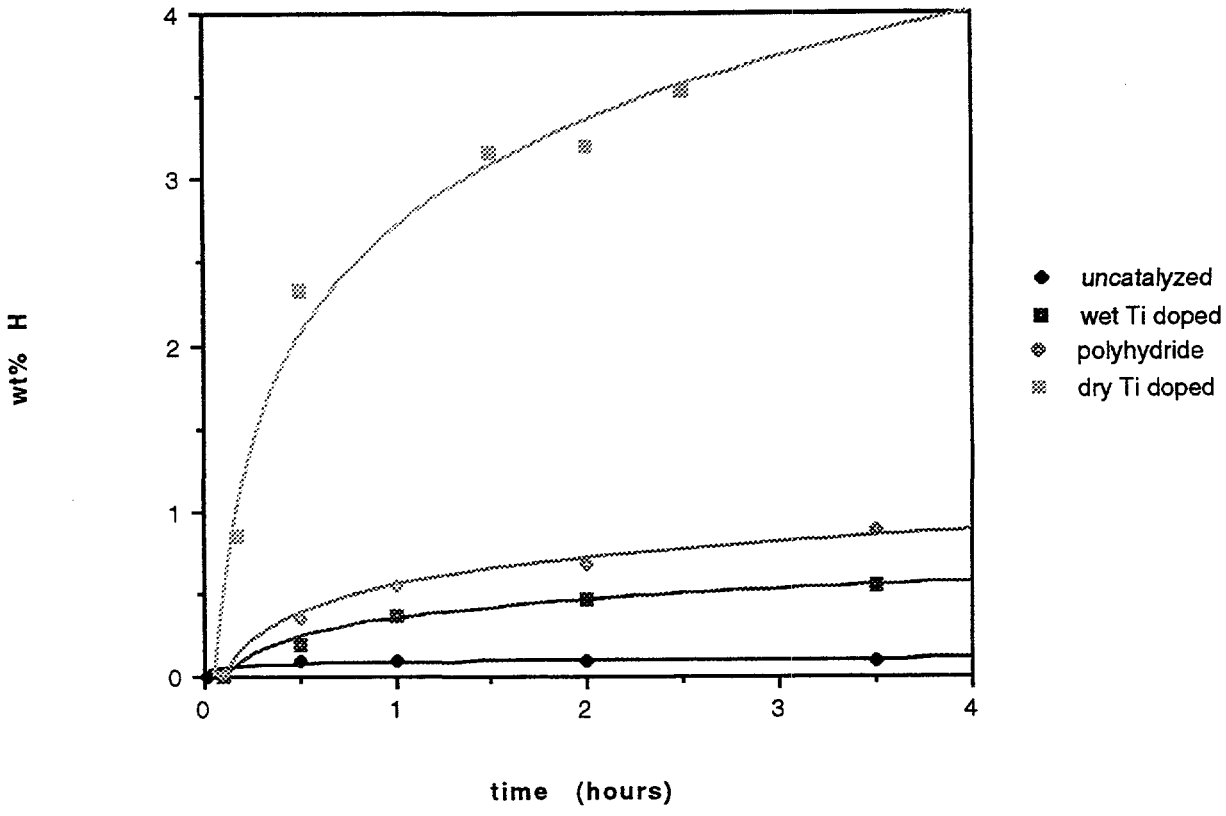
wt% H
time (hours)
0
1
2
3
4
uncatalyzed
wet Ti doped
polyhydride
dry Ti doped

Figure 1

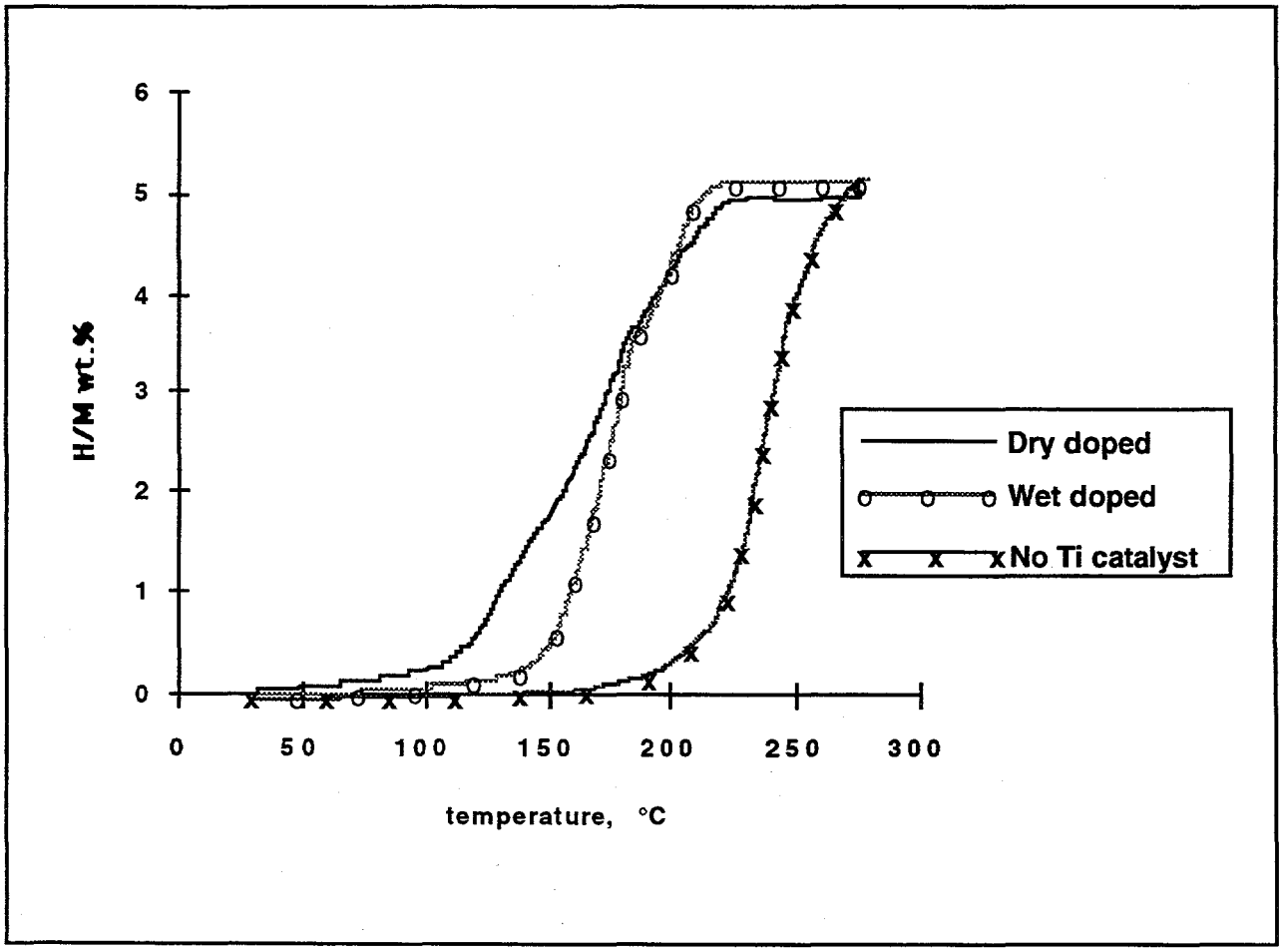
6
5
4
3
2
1
0
H/M wt.%
0
50
100
150
200
250
300
temperature, °C
Dry doped
Wet doped
No Ti catalyst

Figure 2

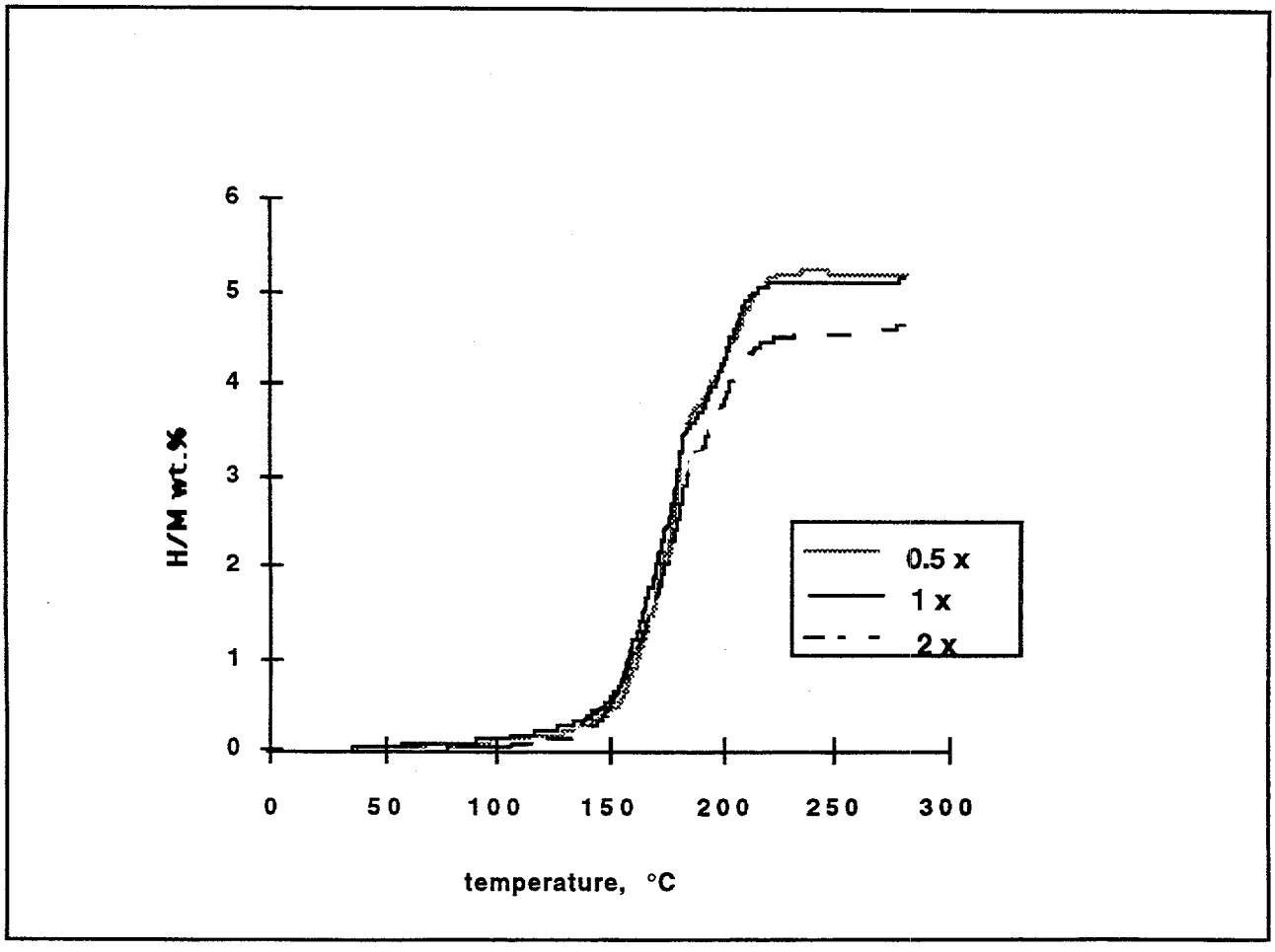

Figure 3

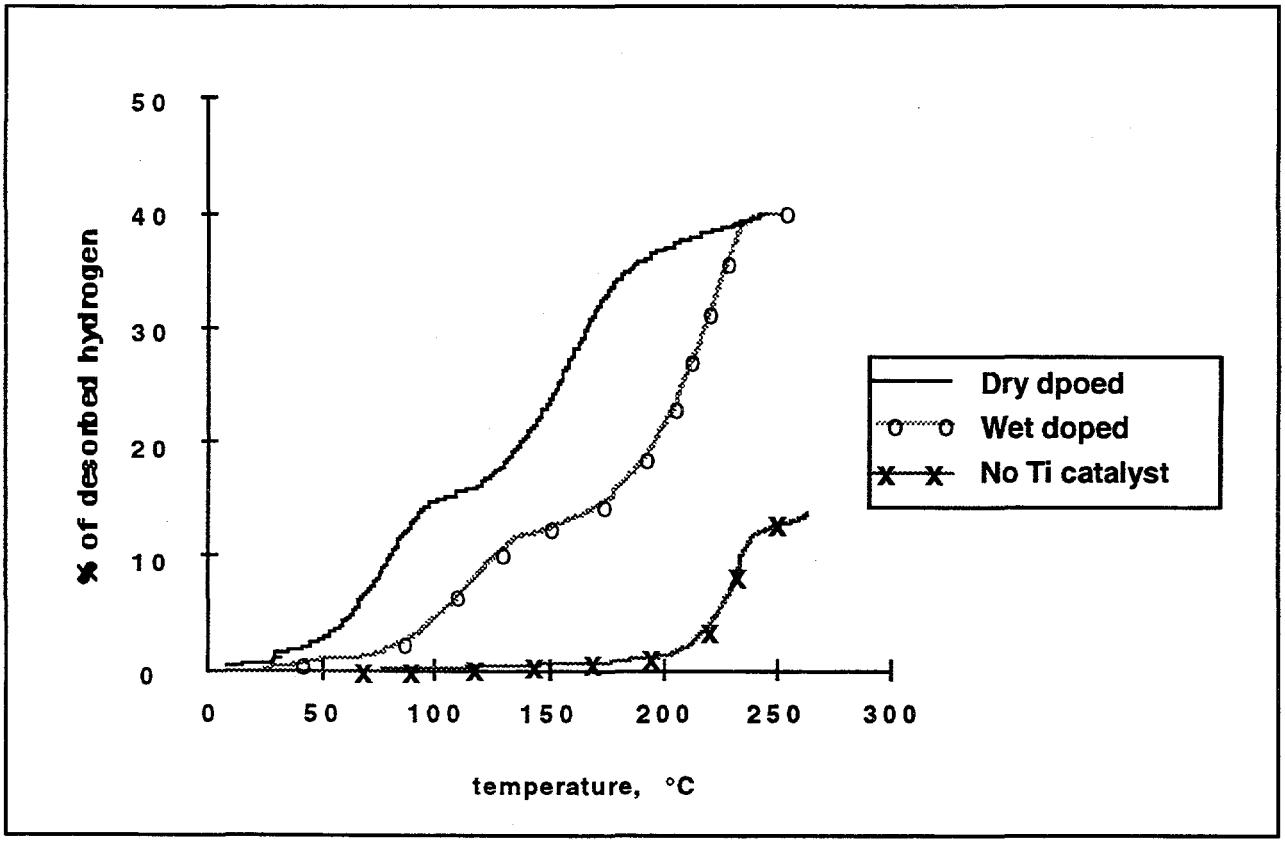
50
40
30
20
10
0
% of desorbed hydrogen
0
50
100
150
200
250
300
temperature, °C
Dry dpoed
Wet doped
No Ti catalyst

Figure 4

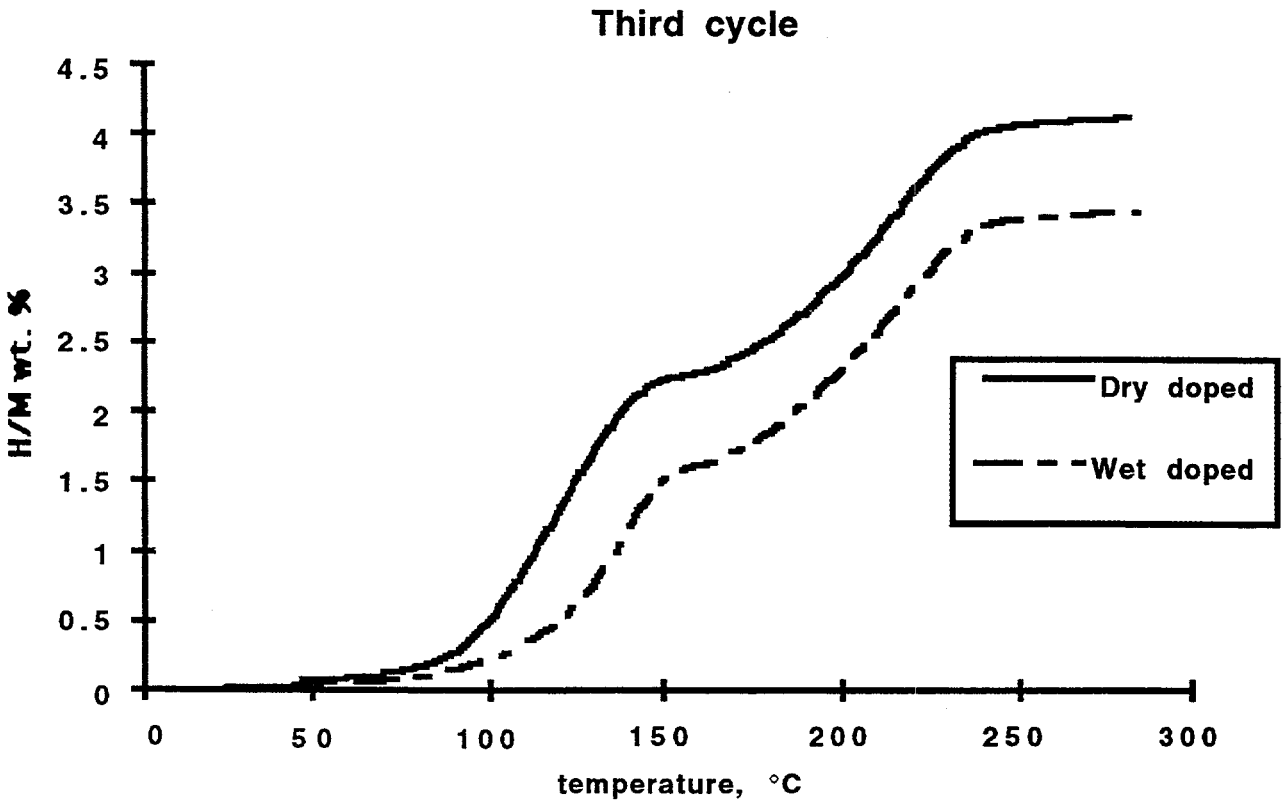
Third cycle
4.5
4
3.5
3
2.5
2
1.5
1
0.5
0
H/M wt. %
0
50
100
150
200
250
300
temperature, °C
Dry doped
Wet doped

Figure 5

HYDROGEN STORAGE IN FULLERENES AND IN AN ORGANIC HYDRIDE

J. C. Wang, R. W. Murphy, and F. C. Chen
Energy Division
Oak Ridge National Laboratory
Oak Ridge, Tennessee

and

R. O. Loutfy, E. Veksler, and W. Li
Materials & Electrochemical Research Corp.
Tucson, Arizona

Abstract

While we have demonstrated the importance and usefulness of thermal management to the hydrogen storage in fullerenes, our recent effort has concentrated on materials improvement and physical model development. In this paper, we report the results of this effort as follows: (1) Liquid phase hydrogenation of fullerenes indicated that more than 6 wt% capacity can be obtained at 180 °C, 350-400 psi; (2) Dehydrogenation of fullerene hydrides below 225 °C was demonstrated using an Ir-based P-C-P pincer complex catalyst; (3) Cyclic hydrogenation and dehydrogenation tests of an organic hydride at 7 wt% capacity were conducted at 180-260 °C; and (4) Physical models developed for fullerenes were determined to be applicable to this organic hydride (with much smaller activation energies).

Introduction

The overall objective of our project is to investigate thermal management technologies for various hydrogen storage options. For a given option (e.g., the fullerene option) this is accomplished through (1) development of an understanding of the relevant storage mechanisms and (2) incorporation of the understanding into simulations that can be used to facilitate material enhancement and to optimize storage capabilities. As demonstrated in our previous heat generation/conduction simulations, the characteristics of a hydrogen storage device using fullerenes can be significantly controlled by the heating and cooling rates in the device (Murphy *et al.* 1997, Wang *et al.* 1996). This is because the thermal activation mechanisms involved

exhibit a very strong temperature dependence [see, for example, Eq. (1) below]. While we have demonstrated the importance and usefulness of thermal management to the hydrogen storage in fullerenes, our recent effort has concentrated on materials improvement and physical model development. This paper summarize the results of this effort.

Fullerenes such as C_{60} can absorb large amounts of hydrogen (e.g., 7.7 wt% of hydrogen in $C_{60}H_{60}$) if suitable pressure and temperature are applied. Previous experimental results obtained at Materials Research & Electrochemical (MER) Corporation demonstrated that greater than 6 wt% of hydrogen can be stored in C_{60} and C_{60}/C_{70} mixed fullerenes (Murphy *et al.* 1997, Wang *et al.* 1996). The absorbed hydrogen can be released if the fullerene hydrides are suitably heated. Both the hydrogenation and dehydrogenation processes can be reasonably characterized by thermal activation mechanisms. For example, the rate of hydrogen release from a fullerene hydride sample can be represented by the Arrhenius form

$$Rate = A\frac{c}{c_{max}} e^{-\frac{E}{kT}} , \qquad (1)$$

where c is the concentration of hydrogen in the fullerene, c_{max} its maximum value, E the activation energy, and A the pre-exponential factor related to the attempt frequency of the hydrogen "atoms" to escape from the fullerene. A has the same units as *Rate* and the dimensionless factor c/c_{max} represents the trend that at a given time, the hydrogen escape rate is proportional to the amount of hydrogen present in the sample. The activation energy for dehydrogenation (160 kJ/mole) was estimated to be approximately 60 kJ/mole greater than that for hydrogenation. The difference was interpreted as the heat of hydrogenation for fullerenes. This interpretation was found to be consistent with the results of subsequent combustion calorimetry measurements (Murphy *et al.* 1997).

Although fullerenes are capable of storing hydrogen, there remains the challenge of bringing the hydrogenation/dehydrogenation conditions (e.g., pressure and temperature used) to practical ranges. Material improvements were made by experimenting with various catalysts including Ni, Pt, Ru, and mechanically alloyed Mg and Ni powder. The idea was based on the expectation that the catalysts would lower the potential barrier in the thermal activation mechanisms so that the needed temperature (around 400 °C according to our earlier work) could be reduced. Tests conducted for fullerenes in the solid phase, however, showed only limited success. To make the catalysts function more effectively, we have been experimenting with methods of improving their contact with the fullerenes. One method tried was to use a solvent as a bridge between the catalysts and the dissolved fullerene molecules. The current status of our effort of using solvents to improve the hydrogenation and dehydrogenation of fullernes is presented in this paper.

In addition to the development for the fullerene option, an organic hydride was found to have a good potential for hydrogen storage. For proprietary reasons, we represent the hydrogen storage process for this material in the following form:

$$OrgHydr1 + Hydrogen \rightleftharpoons OrgHydr2 , \qquad (2)$$

where *OrgHydr1* and *OrgHydr2* are abbreviations for organic hydride 1 and 2, respectively. Multi-cycle tests involving the hydrogenation and dehydrogenation of these organic hydrides showed that up to 7 wt% of hydrogen can be stored and released. Preliminary results for this hydrogen storage system are presented in this paper.

Liquid-Phase Hydrogenation

To perform hydrogenation of fullerenes in the liquid phase, a pressure-concentration-temperature vessel was designed at MER which allows dehydrogenation without moving the samples. A fullerene sample in a solvent (25 - 30 ml) plus catalyst was placed in the vessel, and the system was flushed with hydrogen and evacuated. Hydrogen gas was then introduced into the vessel at a specified starting pressure and the vessel heated to a pre-set temperature. After maintaining the temperature for a given duration, the hydrogen uptake by the sample in weight percent was determined from pressure changes recorded during the experiment. The temperature was measured by a thermocouple placed on the top of the reaction chamber.

The test results indicated that more than 6 wt% of hydrogen can be absorbed by fullerenes at 180 °C under 350-400 psi. No significant dehydrogenation occurred at this temperature, suggesting that the dehydrogenation temperature is higher than that for hydrogenation. This is qualitatively consistent with our conceptual model developed for the solid-phase hydrogenation/dehydrogenation of fullerenes: the activation energy for dehydrogenation is greater than that for hydrogenation (Murphy *et al.* 1997, Wang *et al.* 1996).

The experiment just described was performed to explore the feasibility of liquid-phase hydrogenation of fullerenes. The main conclusion from this experiment is that the presence of the solvent and catalyst enables the hydrogenation to take place at a much lower pressure and temperature in the liquid-phase than in the solid-phase. The solvent together with the catalyst can be considered as a "homogeneous catalyst."

The separation of the solvent from the fullerene hydride in a hydrogen storage device is believed to be relatively simple and should pose no problem in practice. A possible conceptual design of the storage device is to use the solvent during hydrogenation, and separate and store it away after the hydrogenation is completed.

In order to gain some kinetic information on the hydrogenation of fullerenes using a solvent and catalyst, a series of experiments was designed and performed as follows:

(1) Hydrogenation of samples was carried out under a 500 psi (34 atm) hydrogen pressure at 100, 120, 150, 180, and 200 °C; and
(2) For each temperature, the hydrogenation time of 30 min was used.

By keeping the hydrogenation time short, the amounts of hydrogen absorbed at different temperatures reveal kinetic information about the process. The hydrogen absorption results are listed in Table 1 and an Arrhenius plot of these data is shown in Fig. 1. As can be seen from the figure, two activation energies are identifiable: 4.3 and 22 kJ/mole at low (<3.5 wt % H_2) and

high (>3.5 wt % H_2) hydrogen concentrations, respectively. These activation energies are much smaller than the earlier estimate for the solid-phase hydrogenation, 100 kJ/mole. The break in the Arrhenius plot shown in Fig. 1 implies that during the liquid-phase hydrogenation of fullerenes, two different processes control the reaction rate. The process with higher activation energy dominates only when the temperature becomes high enough.

Table 1. Hydrogen absorbed in fullerene during 30 min of liquid-phase hydrogenation.[a]

Temperature (°C)	Hydrogen Absorbed (x in $C_{60}H_x$)
100	21.4
120	23.0
150	25.2
180	38.2
200	48.8

[a]Under a hydrogen pressure of 500 psi (34 atm)

A possible interpretation of the break in the Arrhenius plot is given below: After C_{60} molecules absorbing some hydrogen with the lower activation energy (4.3 kJ/mole), $C_{60}H_x$ molecules become insoluble and precipitate as solid particles. The inner part of a precipitated particle can absorb additional hydrogen only when hydrogen "atoms" reach them by diffusion under concentration gradient. If this interpretation is correct, then the higher activation energy of 22 kJ/mole may be associated with the diffusion of hydrogen atoms among the $C_{60}H_x$ molecules. Further experiments are needed to verify this interpretation. No similar break in the Arrhenius plot has been observed in the solid-phase hydrogenation experiments. This may be due to the fact that the activation energy for hydrogenation in that case is much higher (100 kJ/mole) and, at the hydrogenation temperatures, diffusion is too fast to be a controlling factor for hydrogenation.

Dehydrogenation Experiment using Iridium-Based Catalyst

Gupta *et al.* (1996, 1997) recently reported that a number of alkanes and cycloalkanes can be successfully dehydrogenated using Ir-based complexes. The process is believed to proceed through an initial oxidative addition of the alkane C-H bond to the metal, followed by further liberation of molecular hydrogen. Through a cooperation with Professor Craig Jensen, an Ir-based compound (dihydro irridium bisphosphine complex) was purchased from the University of Hawaii and used in preliminary experiments on the dehydrogenation of fullerene hydrides. To avoid contamination by moisture, 375 mg of fullerene hydride (containing about 4.5 wt% of hydrogen) was mixed with 125 mg of Ir-based P-C-P pincer catalyst in a glovebox. The mixture,

together with 5 g of naphthalene, was placed in a dehydrogenation chamber . The chamber was closed, removed from the glovebox, connected to the experimental setup, wrapped with heating tapes, and insulated . After evacuation of the lines, the system was heated, and the pressure and temperature in the chamber monitored for the duration of the experiment. The recorded pressure and temperature as functions of time are plotted in Fig. 2.

At the end of the heating period, the system was allowed to cool down to the room temperature overnight and the final pressure reading at room temperature then taken. The overall pressure versus temperature graph is shown in Fig. 3. Also plotted in the figure is the vapor pressure of naphthalene as a function of temperature obtained by curve fitting experimental dat (Boublik *et al.* 1984). As indicated in the figure, the activation energy for naphthalene evaporation is estimated (from an Arrhenius plot) to be about 50 kJ/mole.

At temperatures above 170 °C, the total pressure shown in Fig. 3 is less than the vapor pressure of naphthalene alone. We believe this was because that some of the lines connected to the chamber were at a lower temperature than that measured in the chamber and condensation at those places probably reduced the naphthalene vapor pressure in the system. In any case, from the initial and final pressures (at room temperature), it was estimated that about 23% of the total hydrogen stored in the fullerene became hydrogen gas in the chamber at the end.

The dehydrogenation result described above is preliminary and additional experiments need to be performed when more catalyst becomes available. Nevertheless, this result is very encouraging and has important implications. As mentioned earlier, our previous solid phase dehydrogenation of fullerenes required a temperature of approximately 400 °C. A dehydrogenation temperature near 225 °C (as can be seen from Fig. 3) suggests a substantial reduction of the activation energy for dehydrogenation. This result and the small activation energies for hydrogenation reported in the liquid phase hydrogenation section (see Fig. 1) demonstrate the possibility that, when a suitable catalyst is used in the presence of a solvent, the potential barrier in the thermal activation mechanisms can be significantly reduced.

Hydrogen Storage in an Organic Hydride

As described by Eq. (2), hydrogen may be absorbed by one organic hydride to form another organic hydride. If the process is reversible, the system may be used for hydrogen storage applications. The organic hydride system reported here is capable of storing more than 7 wt% of hydrogen with a gravimetric capacity of more than 60 kg/m^3. Multi-cycle tests have been performed on the system. The following is a report of our preliminary results.

Figure 4 shows the hydrogenation result under 8-10 atm (120-150 psi) of hydrogen pressure at 180 °C. During the experiment, the hydrogen flow rate was controlled in order to slow down the reaction. Hence, kinetic information cannot be reliably extracted from this result. However, compared to the results listed in Table 1, the hydrogenation pressure and temperature for this organic hydride system are even lower than those needed for the liquid phase hydrogenation of fullerenes.

The stored hydrogen can be released by heating the organic hydride samples. The release rate depends on the catalyst used. A set of dehydrogenation curves at various temperatures is shown in Fig. 5. For this set of experimental results, the total amount of hydrogen stored in each sample before dehydrogenation was 28.9 liters. As can be seen from the slopes of the curves, the hydrogen release rate increases with temperature, a trend which is consistent with the thermal activation mechanisms.

An Arrhenius plot was obtained (Fig. 6) using the release rates estimated near t=100 min. The activation energy for dehydrogenation was estimated to be about 84 kJ/mole. This value is much smaller than the corresponding value for fullerene hydrides which was estimated to be 160 kJ/mole. Overall, the hydrogen storage mechanisms in the organic hydrides and in the fullerene hydrides discussed in this paper are very similar. A schematic comparison of the thermal activation mechanisms for the two systems is provided in Fig. 7. The question mark in the figure indicates that a corresponding estimate of the activation for hydrogenation is not yet available for the organic hydrides.

Summary of Current Status

From the results reported above, the current status of our project is summarized as follows:

- Liquid phase hydrogenation of fullerenes showed that more than 6 wt% of hydrogen can be absorbed by fullerenes at 180 °C under a pressure of 350-400 psi;
- Dehydrogenation of fullerene hydrides below 225 °C using an Ir-based P-C-P pincer complex catalyst has been demonstrated;
- Evidence that the activation energies for hydrogen storage in fullerenes can be significantly lowered has been accumulated;
- Multi-cycle test involving the hydrogenation/dehydrogenation of an organic hydride at 7 wt% capacity has been demonstrated at 180-260 °C ; and
- The results of data analysis indicated that the physical models developed for fullerenes are also applicable to the organic hydride (with much smaller activation energies).

Plans for Future Work

Future work will address both fullerene and other carbon-based hydrogen storage options. A substantial portion of the methodology developed and the experience gained for hydrogen storage in fullerenes is applicable to this wider family of materials. Future work is planned as follows:

- Continue to experiment with various catalysts to improve the hydrogen storage performance of fullerenes;
- Continue to experiment with liquid phase hydrogenation/dehydrogenation of fullerenes including the use of liquid catalysts with low vapor pressures;
- Expand the database for the organic hydride hydrogenation/dehydrogenation option;
- Interpret all new information, refine current models, determine the most attractive carbon-based options, and perform thermal management simulations as needed;

- Continue to cooperate with others (such as Univ. of Hawaii and NIST) to improve and/or characterize material properties; and
- Participate in the Annex 12 International Energy Agency cooperative project.

Acknowledgment

Work performed at ORNL was sponsored by the U. S. Department of Energy under contract No. DE-AC05-96OR22464 with Lockheed Martin Energy Research Corporation. The authors wish to thank R. O. Johnson and J. W. Terry for their critical reading of the manuscript.

References

Boublik, T, V. Fried, and E. Hala 1984. *The Vapour Pressures of Pure Substances.* Amsterdam: Elsevier.

Gupta, M, C. Hagen, R. J. Flesher, W. C. Kaska, and C. M. Jensen 1996. "A Highly Active Alkane Dehydrogenation Catalyst: Stabilization of Dihydrido Rhodium and Iridium Complexes by a P-C-P Pincer Ligand." Chem. Commun. (17): 2083-2084.

Gupta, M, C. Hagen, W. C. Kaska, R. E. Cramer, and C. M. Jensen 1997. "Catalytic Dehydrogenation of Cycloalkanes to Arenes by a Dihydrido Iridim P-C-P Pincer Complex." J. Am. Chem. Soc. 119: 840-841.

Murphy, R. W., J. C. Wang, F. C. Chen, R. O. Loutfy, and X. Lu 1996. "Thermal Management for Fullerene-Based Hydrogen Storage." In *Proceedings of the 1997 U.S. DOE Hydrogen Program Review*, 315–331. Herndon, VA: May 21–23, U.S. Department of Energy.

Wang, J. C., F. C. Chen, and R. W. Murphy 1996. "Thermal Management Technology for Hydrogen Storage: Fullerene Option." In *Proceedings of the 1996 U.S. DOE Hydrogen Program Review*, Vol II, 819-29. Miami, FL: May 1–2, U.S. Department of Energy.

Figure Captions

Fig. 1. Arrhenius plot using the liquid-phase hydrogenation data listed in Table 1.

Fig. 2. Pressure and temperature graphs for the dehydrogenation of a fullerene hydride sample in naphthalene.

Fig. 3. Dehydrogenation curve of a fullerene hydride sample in naphthalene.

Fig. 4. Hydrogenation curve of OrgHydr1 at 180 °C under 8-10 atm.

Fig. 5. Dehydrogenation of OrgHydr2 at various temperatures.

Fig. 6. Arrhenius plot for the dehydrogenation or OrgHydr2 showing the activation energy.

Fig. 7. Comparison of conceptual models for hydrogen storage in OrgHyd1 (solid line) and fullerenes (dashed line).

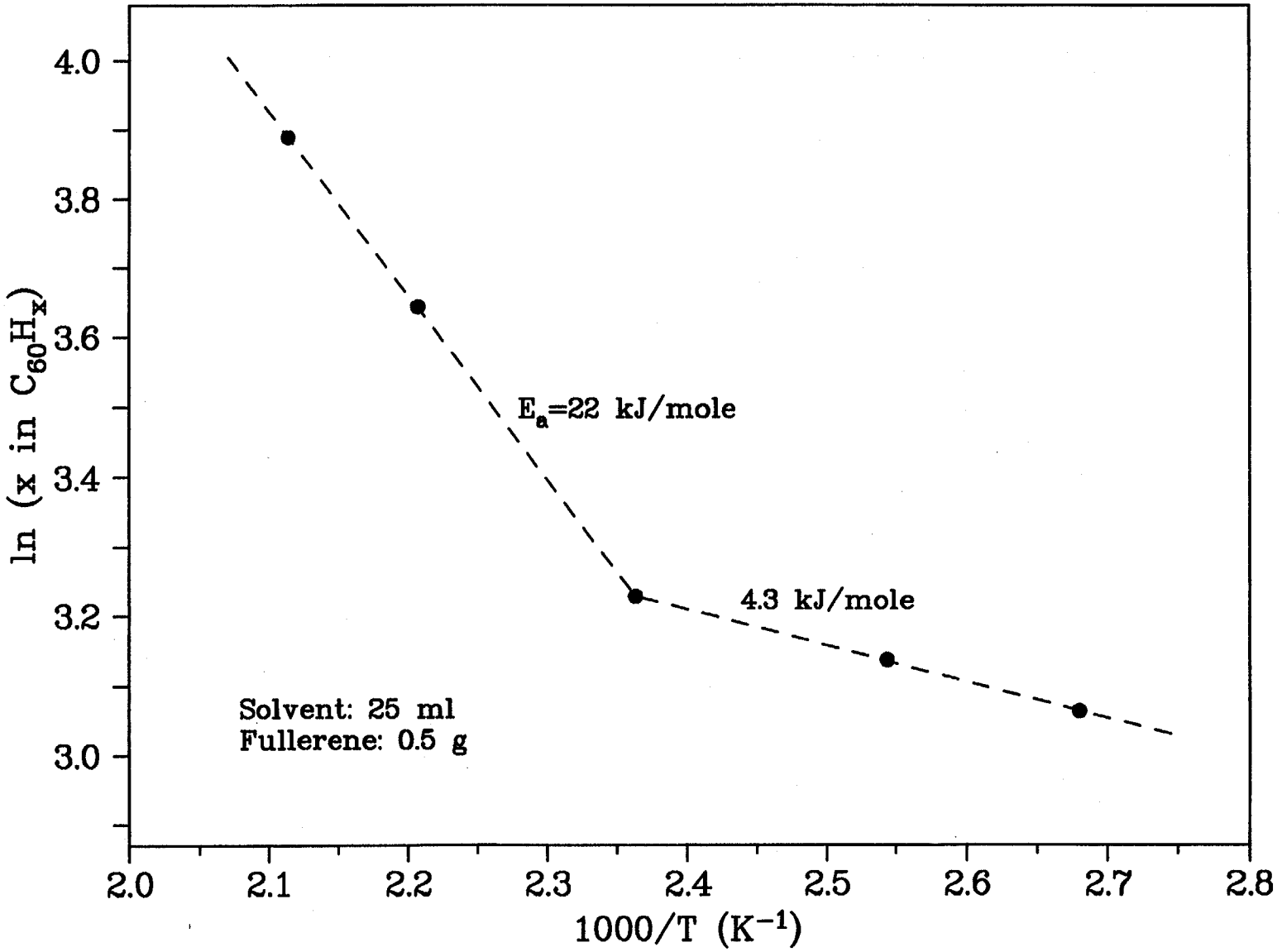
4.0
3.8
3.6
3.4
3.2
3.0
ln (x in $C_{60}H_x$)
E_a=22 kJ/mole
4.3 kJ/mole
Solvent: 25 ml
Fullerene: 0.5 g
2.0
2.1
2.2
2.3
2.4
2.5
2.6
2.7
2.8
1000/T (K^{-1})

Figure 1

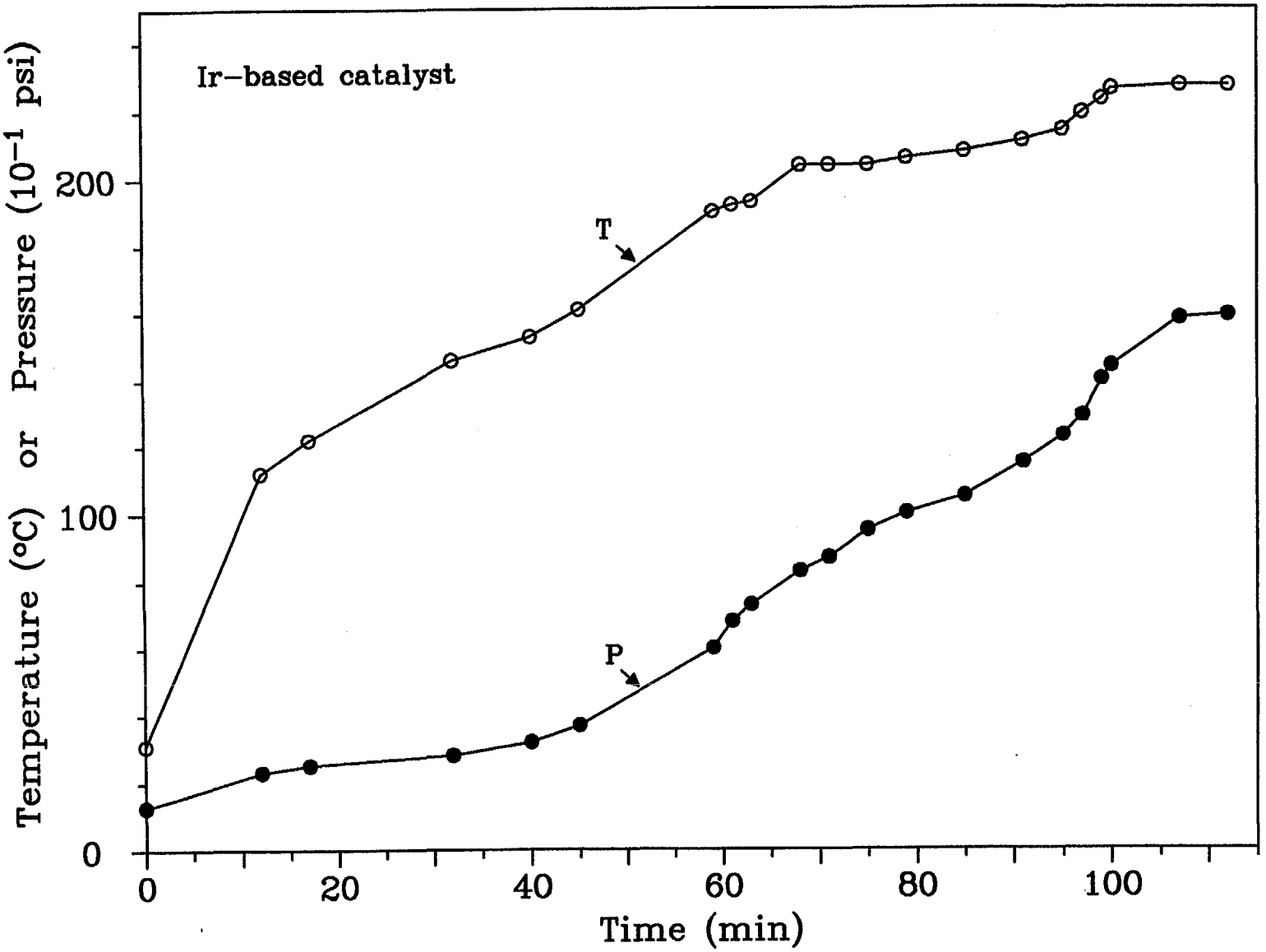
Ir–based catalyst
T
P
Temperature (°C) or Pressure (10^{-1} psi)
Time (min)
0
100
200
0
20
40
60
80
100

Figure 2

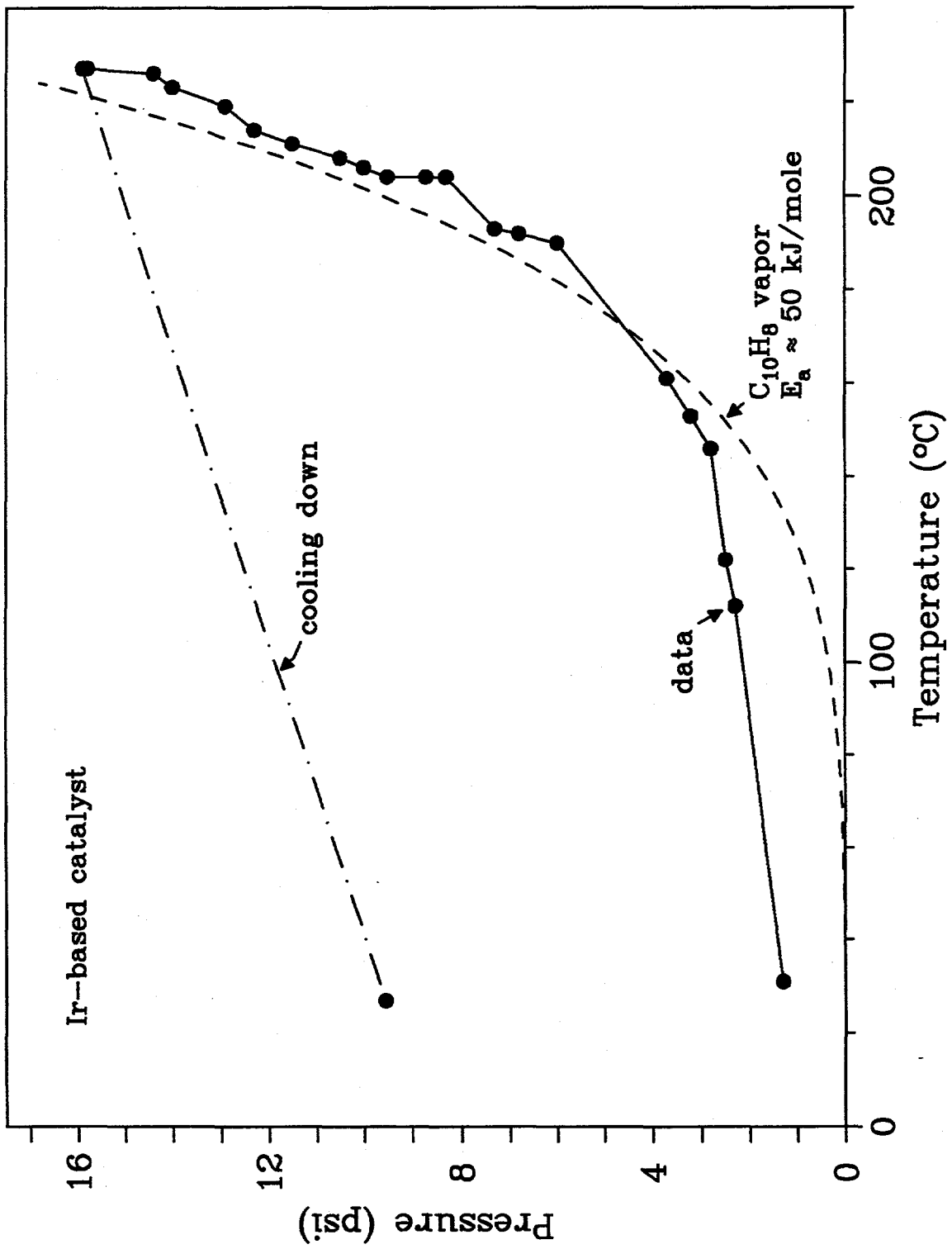
Pressure (psi)
16
12
8
4
0
0
100
200
Temperature (°C)
Ir-based catalyst
cooling down
data
$C_{10}H_8$ vapor
$E_a \approx 50$ kJ/mole

Figure 3

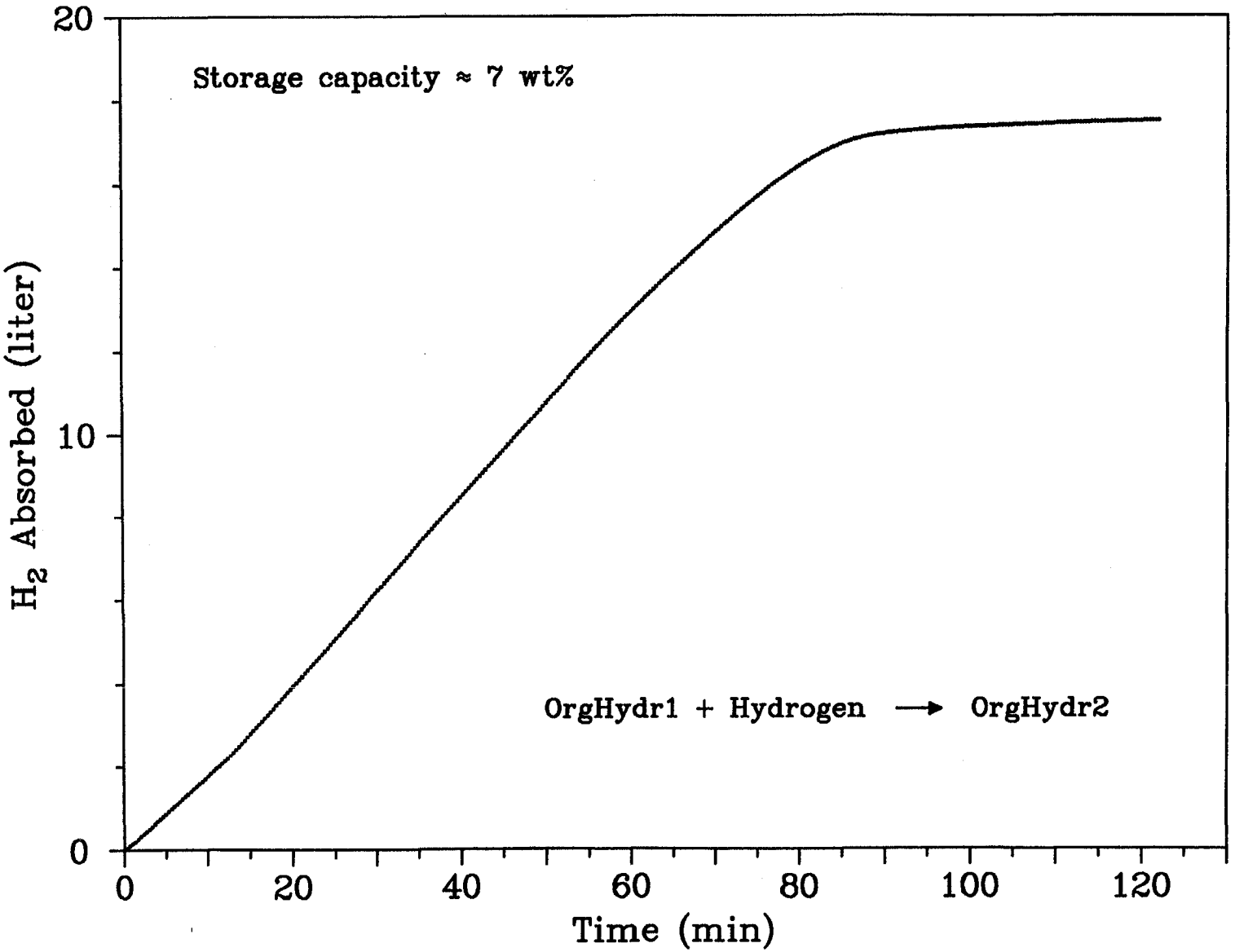
Storage capacity ≈ 7 wt%
OrgHydr1 + Hydrogen → OrgHydr2
H2 Absorbed (liter)
Time (min)
0
10
20
0
20
40
60
80
100
120

Figure 4

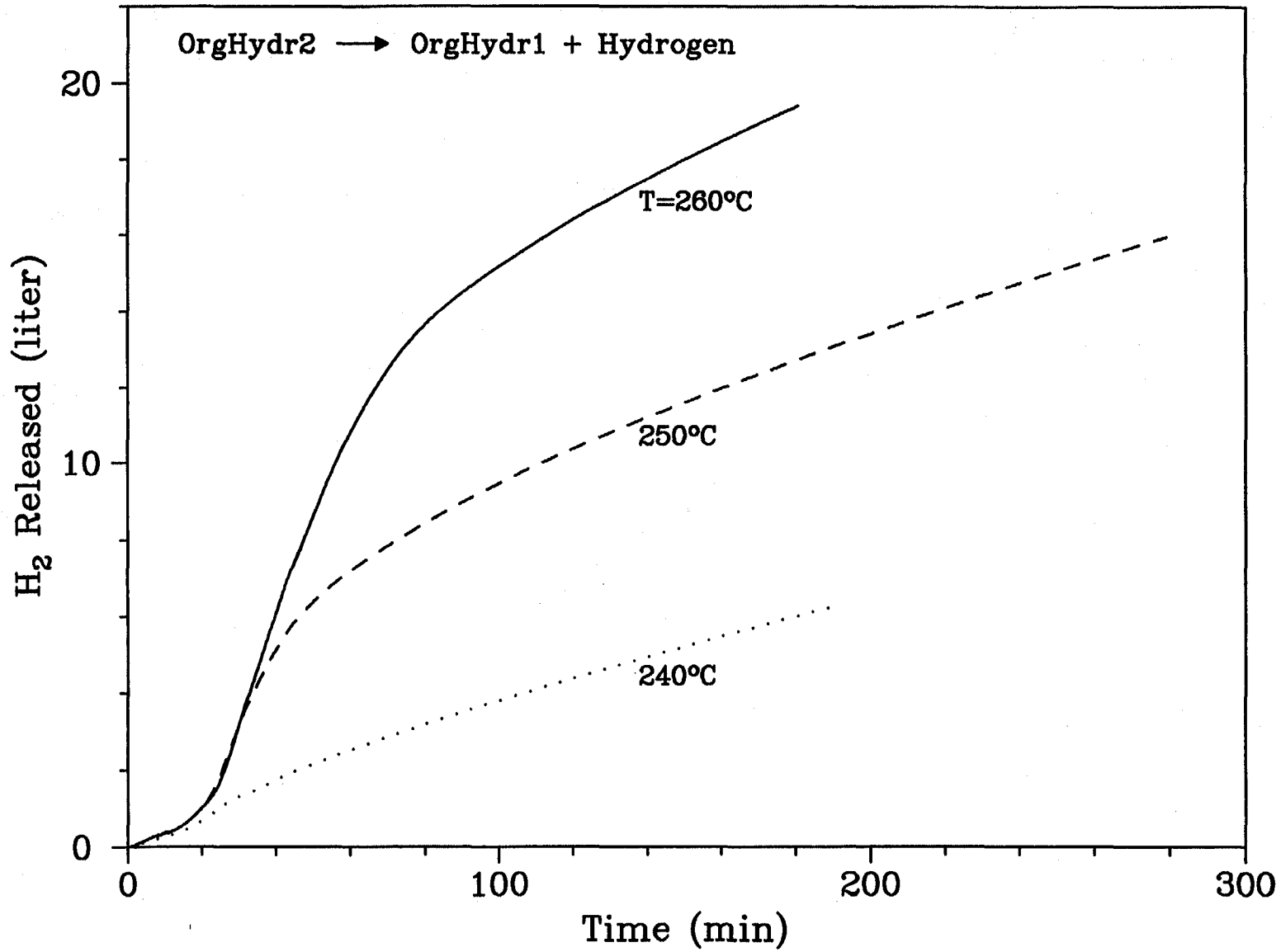
OrgHydr2 ⟶ OrgHydr1 + Hydrogen
T=260°C
250°C
240°C
H_2 Released (liter)
Time (min)
0
10
20
0
100
200
300

Figure 5

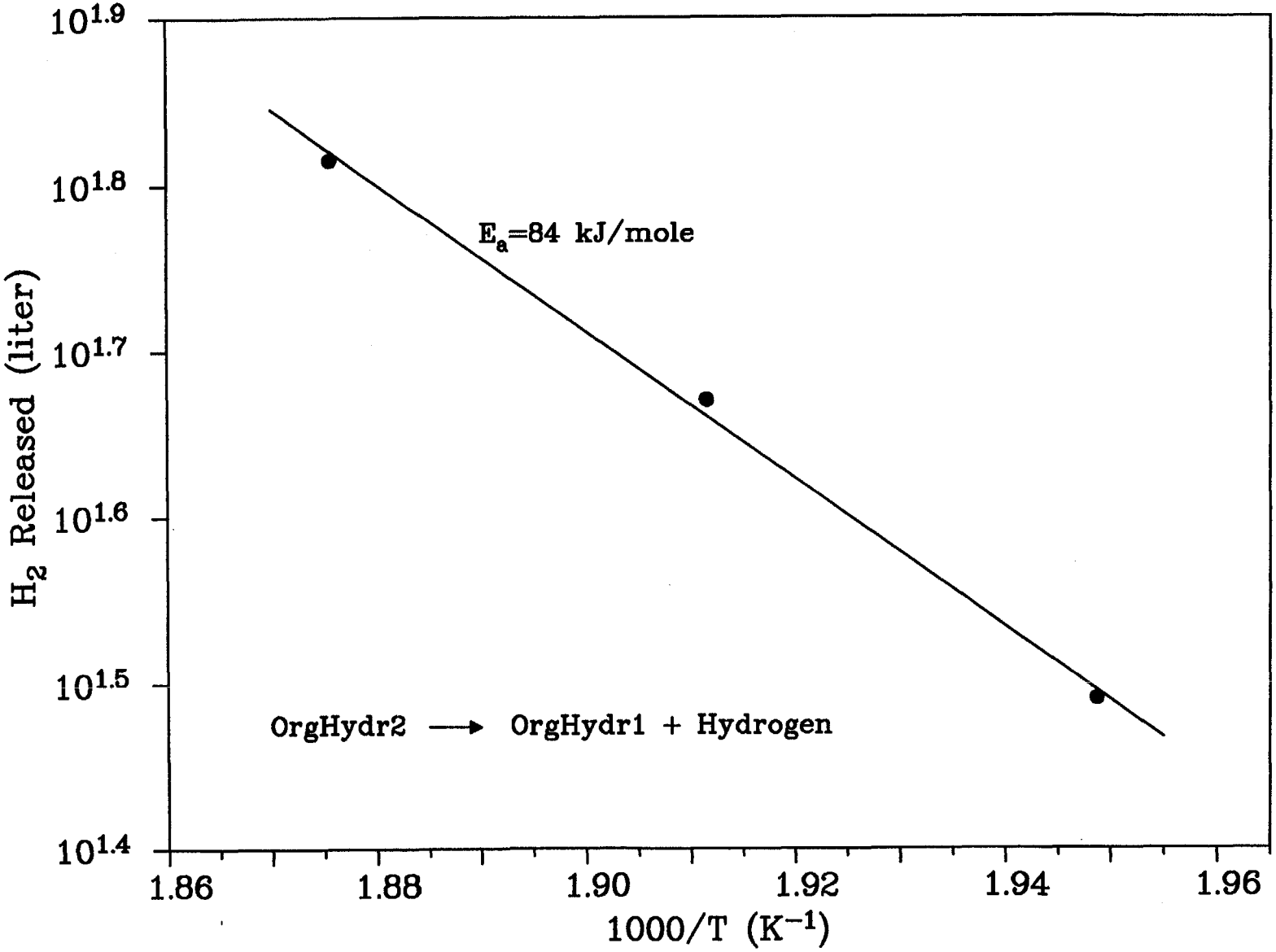
$10^{1.9}$
$10^{1.8}$
$10^{1.7}$
$10^{1.6}$
$10^{1.5}$
$10^{1.4}$
H_2 Released (liter)
E_a=84 kJ/mole
OrgHydr2 ⟶ OrgHydr1 + Hydrogen
1.86
1.88
1.90
1.92
1.94
1.96
1000/T (K^{-1})

Figure 6

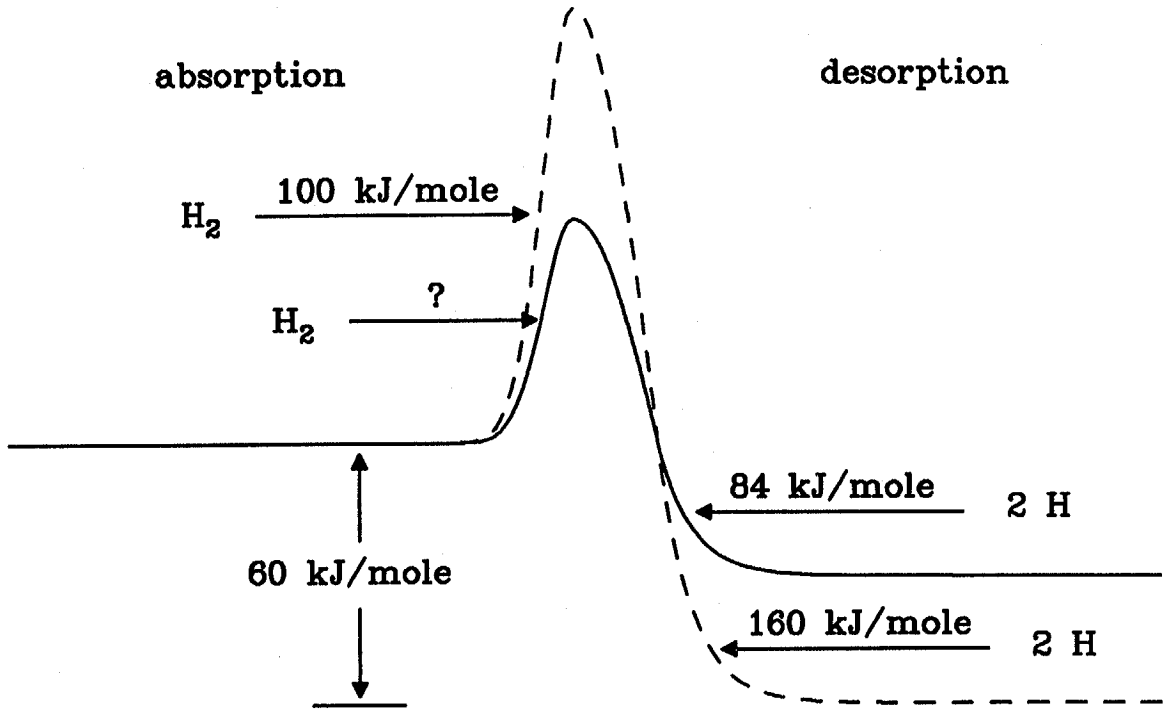
absorption
desorption
H_2
100 kJ/mole
H_2
?
84 kJ/mole
2 H
60 kJ/mole
160 kJ/mole
2 H

Figure 7

HYDROGEN TRANSMISSION/STORAGE WITH A METAL HYDRIDE/ORGANIC SLURRY

Ronald W. Breault, Jon Rolfe, and Andrew M^{c}Claine
Thermo Power Corporation
45 First Avenue
Waltham, MA 02254-9046

Abstract

Hydrogen has immense potential as an efficient and environmentally-friendly energy carrier of the future. It can be used directly by fuel cells to produce electricity very efficiently (> 50%) and with zero emissions. Ultra-low emissions are also achievable when hydrogen is combusted with air to power an engine or to provide process heat, since the only pollutant produced, NO_X, is then more easily controlled. To realize this potential, however, cost effective methods for producing, transporting, and storing hydrogen must be developed.

Thermo Power Corporation has developed a new approach for the production, transmission, and storage of hydrogen. In this approach, a chemical hydride slurry is used as the hydrogen carrier and storage media. The slurry protects the hydride from unanticipated contact with moisture in the air and makes the hydride pumpable. At the point of storage and use, a chemical hydride/water reaction is used to produce high-purity hydrogen. An essential feature of this approach is the recovery and recycle of the spent hydride at centralized processing plants, resulting in an overall low cost for hydrogen. This approach has two clear benefits: it greatly improves energy transmission and storage characteristics of hydrogen as a fuel, and it produces the hydrogen carrier efficiently and economically from a low cost carbon source.

Our preliminary economic analysis of the process indicates that hydrogen can be produced for $3.85 per million Btu based on a carbon cost of $1.42 per million Btu and a plant sized to serve a million cars per day. This compares to current costs of approximately $9.00 per million Btu to produce hydrogen from $3.00 per million Btu natural gas, and $25 per million Btu to produce hydrogen by electrolysis from $0.05 per Kwh electricity. The present standard for production of hydrogen from renewable energy is photovoltaic-electrolysis at $100 to $150 per million Btu.

Introduction

The overall objective is to investigate the technical feasibility and economic viability of the chemical hydride (CaH_2 or LiH) organic slurry approach for transmission and storage of hydrogen with analysis and laboratory-scale experiments, and to demonstrate the critical steps in the process with bench-scale equipment. Specific questions which have been addressed in work to date include:

- What is the formulation and physical properties of slurries that meet the energy density criteria?
- What are the organics which can be used to form the slurry?
- What are the conditions required for hydrogen generation?
- What are the properties of the slurry after hydrogen generation?
- What is the projected efficiency and cost of hydrogen production?

Background

Hydrogen (H_2) has been suggested as the energy carrier of the future. It is not a native source of energy, but rather serves as the medium through which a primary energy source can be transmitted and utilized to fulfill our energy needs. Hydrogen has a number of advantages:

- It can be made from renewable energy sources such as biomass, solar, and hydroelectric.
- In combustion, water is the main product, with zero to low emissions when used as a combustion heat source.
- It can be directly used in fuel cells for high efficiency, zero emission electric power generation.
- H_2 is a widely-used chemical raw material for chemical synthesis.

At present, H_2 is used industrially primarily as a chemical synthesis raw material. It is generally produced on-site by steam-reforming of methane. The primary problems restricting widespread use of H_2 as an energy carrier are its:

- Very high cost compared to fossil fuels.
- Poor gas pipeline transmission characteristics relative to natural gas.
- Poor energy storage characteristics.
- Supply from native energy sources.

The concept under development addresses a new approach which greatly improves the energy transmission and storage characteristics of H_2 as a fuel for industrial and transportation applications. Further, a method of producing the H_2 carrier from a low cost carbon source such as biomass, both economically and with high energy efficiency, is described.

Application of Metal Hydride/Water Reaction for Hydrogen Storage and Transmission

The way in which the metal hydride/water reaction would be used in a closed loop system for the storage and transmission of hydrogen is illustrated in Figure 1. The process consists of the following major steps:

1. Slurrying the metal hydride with a liquid carrier and transporting it to the point(s) of use.
2. Generating hydrogen on demand from the metal hydride/liquid carrier slurry at the point of use by adding water and then transporting the resulting metal hydroxide/liquid slurry back to the hydride recycle plant.
3. Drying, separating, and recycling the metal hydroxide to the metal hydride at the centralized recycle plant and returning the liquid carrier for reuse.

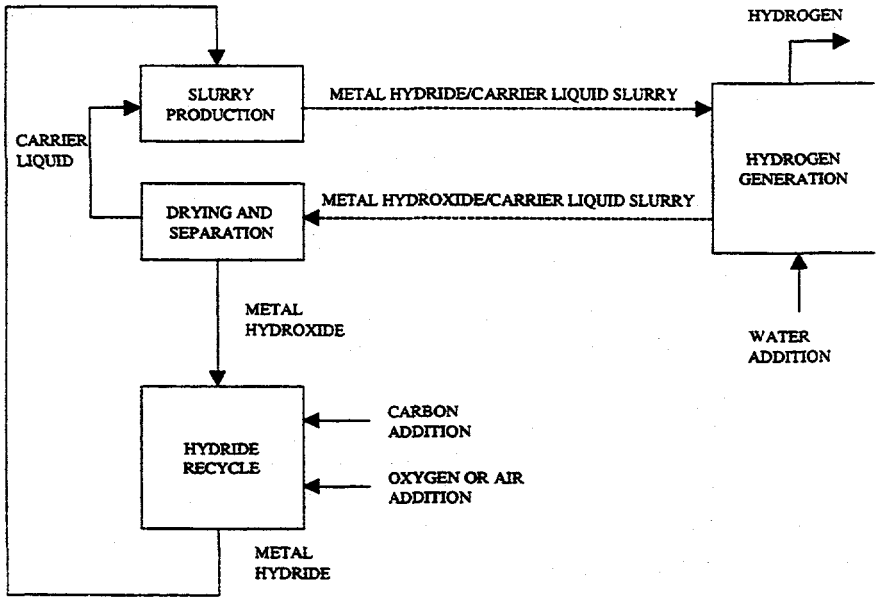

Figure 1. Simplified Process Diagram for Hydrogen Transmission/Storage With a Metal Hydride

Metal Hydride/Water Reactions and Hydrogen Storage Characteristics

A variety of metal hydrides react with water at ambient temperature to produce high purity hydrogen. Examples of reactions are:

$$CaH_2 + 2H_2O \rightarrow Ca(OH)_2 + 2H_2 \uparrow$$
$$LiH + H_2O \rightarrow LiOH + H_2 \uparrow$$
$$LiBH_4 + 4H_2O \rightarrow LiOH + H_3BO_3 + 4H_2 \uparrow$$
$$NaBH_4 + 4H_2O \rightarrow NaOH + H_3BO_3 + 4H_2 \uparrow$$

The hydrogen generation capability of these hydrides when reacted with water is outstanding. For example, the volume of H_2 (STP) produced by complete hydrolysis of 1 kg (2.2 lb) of lithium hydride is 2800 liters (99 ft^3) and by 1 kg (2.2 lb) of lithium borohydride is 4100 liters (145 ft^3).

In Table 1, the energy density of these hydrides when reacted with water is presented and compared to gasoline, as well as the storage of H_2 as a liquid, gas, and a reversible hydride. The energy densities of the reactive hydrides are given on the basis of the initial hydride mass. The energy densities of the hydride/water reaction are respectable when compared to gasoline or methanol, with $LiBH_4$ having the highest energy densities on both a mass and volume basis. The heat of reaction must be removed during the H_2 generation.

Comparing the chemical hydrides of Table 1 with the volumetric and gravimetric energy density goals results in Table 2.

The comparison is based on the energy densities of the initial hydride as a 50% slurry and the mass and volume of the storage container assuming a 20% void in the container when the hydride is completely spent. The LiH, $LiBH_4$, and $NaBH_4$ hydrides exceed the volumetric energy density goal by moderate factors (1.09 to 1.64). LiH and $LiBH_4$ exceed the gravimetric energy density goal by moderate factors (1.03 to 1.41), with CaH_2 slightly lower than the goal. It should be noted that energy density is not the only criterion which needs to be compared. Other factors such as cost and ease of handling must also be considered.

In summary, several hydride/water reactions exceed the performance goals of the solicitation for both the volumetric and gravimetric energy densities. An additional feature is the ability to generate H_2 on demand and to control the rate of reaction by regulating the rate of water addition to the hydride bed. If desired, H_2 can also be generated at a high pressure for direct use in pressurized fuel cells without compression.

Table 1. Comparison of Metal Hydrides to Other Hydrogen Storage Methods and Gasoline

Hydride	H_2 Volume Per Mass Hydride (STP ft^3/lb)	Energy Density		Water Reaction Enthalpy per HHV	Fraction Hydrolysis H_2 (lb H_2 per lb Hydride)	Hydride Density (gm/cm^3)
		HHV/Mass, Btu/lb	HHV/Bulk Volume (Btu/gallon)			
Ca H_2[1]	17.1	5,850	92,800	0.396	0.0958	1.90
Li H(1)	45.2	15,500	99,600	0.388	0.254	0.77
Li B H4(1)	65.9	22,600	124,500	0.212	0.370	0.66
Na B H4(1)	38.0	13,000	116,700	0.157	0.213	1.074
Fe Ti H(1.6)(2)	2.7	935	42,900	0.122(4)	0.0153	5.5
Liquid Hydrogen[3]	—	61,100	35,650	—	—	0.07
Gaseous Hydrogen (5000 psia, 300 K)	—	61,100	15,574	—	—	0.03058
Gasoline	—	20,600	130,000	—	—	—

[1] Reaction with Water
[2] Dissociation by Heating
[3] Liquid Fuel
[4] Based on Dissociation Energy

Table 2. Comparison of the Volumetric and Gravimetric Energy Densities

Component	Volumetric Energy Density (Btu/gallon)	Average Gravimetric Energy Density (Btu/lb)
Goal	106,367	6,138
CaH_2	61,065	2,552
LiH	147,632	6,295
$LiBH_4$	174,366	8,655
$NaBH_4$	116,255	5,326

Program Activity Discussion

The program goal is to investigate the technical feasibility and economic viability of the chemical hydride (CaH_2 or LiH) organic slurry approach for transmission and storage of hydrogen through a research program which consists of technical and economic analyses and laboratory-scale and bench-scale experiments.

The initial program was structured to gain a more detailed understanding of the technical and economic aspects of the overall process, and of key elements for each of the three critical steps in the process: metal hydroxide to metal hydride conversion, metal hydride/organic slurry formation and pumping, and hydrogen generation from the slurry by addition of water.

In the next phase, we will demonstrate the critical steps in the process with bench-scale equipment and perform a more in-depth technical and economic evaluation of the process. Successful completion of this work will provide the technical basis and economic justification for proceeding to the next logical step in the development, a pilot-scale plant.

This approach has been chosen as the most logical and cost-effective way to advance the state-of-the-art of this promising technology past the conceptual stage. Advancing this technology to a stage where a sufficient technology base has been developed will establish the technical and economic feasibility of the concept with a level of confidence that warrants the further development and ultimate implementation of the technology.

System Component and Processing Selection

A preliminary analysis of the chemical hydride slurry approach for storing hydrogen was performed. An initial selection of mineral oil, decane, and dodecane for the initial slurry liquid was made. The organic material required for the slurry must not react with the chemical hydride. It must provide a coating for the hydride particles to protect them from atmospheric moisture in the event that the hydride comes in contact with the atmosphere. It must be useable in the normal temperature range of operation, 20°C to 150°C, and it must be removable from the spent slurry so that the spent slurry can be regenerated without consuming the organic material. Mineral oils and alkanes meet these requirements.

The final issue in the choice of the organic carrier component of the slurry is the volatility of the organic. One means of removing the organic from the spent slurry will be to boil it off the slurry. It must not be so volatile that it becomes an air pollution problem. Mineral oil, which is a mixture of several alkanes, is another alternative organic material for the slurry. It is frequently used in the production of sodium hydride and lithium hydride to protect the hydride from contact with the atmosphere. Mineral oils come in various viscosities ranging from near that of water to quite viscous.

We decided to begin the experimental slurry evaluations using light mineral oil rather than the more refined decane. The plan will be to separate the mineral oil from the spent slurry with a centrifuge.

Metal Hydride/Organic Slurry

Discussion of Slurry Setup

Currently, simple tests have been completed and observations have been made based on the ASTM descriptions of sedimentation characteristics. Size classification sieves have been obtained for the optimization stages of the slurry development. A ball mill, with its associated alumina jars and media, has been obtained for size reduction of the candidate hydrides. A small laboratory centrifuge has been obtained for accelerated age stability tests, and the appropriate disposable sedimentation tubes have been obtained. Cup-type viscometers have been purchased to allow standard centistoke values of the slurries to be determined. A shaker table is being used to evaluate the potential for milling of the hydride during transportation and movement and the subsequent effect of particle attrition on the slurry properties.

Discussion of Chemical Stability of the Organic Medium

Infrared Absorption Spectrophotometry is performed on the organic compound as supplied, and then on a sample which has been subjected to the heat and pressure of the hydrogen generation process. In the reaction of light metal hydrides and water, strong bases result. The purpose of this test is to detect gross molecular changes in the organic medium. As the preferred slurry system becomes better defined, GC/MS will be performed on the preferred organic medium after one or more reaction cycles. Figure 2 displays a typical result from the infra-red spectroscopic analysis.

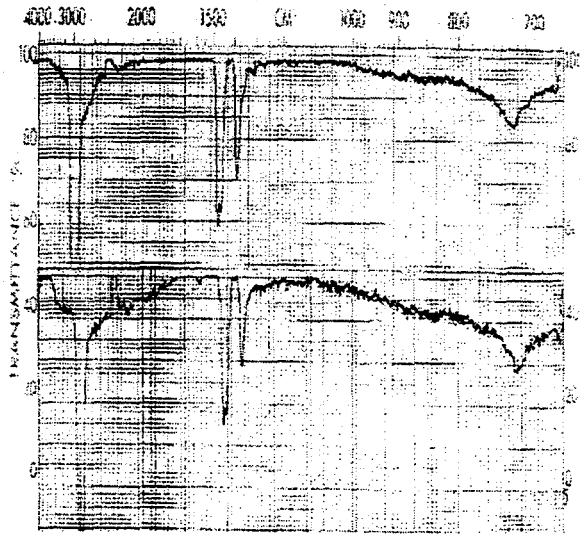

Figure 2. Example of Infrared Spectroscopic Analysis Results for a Test Using Sodium Hydride and Light Mineral Oil

Discussion of Hydride Slurry Results

Slurries have been prepared of sodium hydride, lithium hydride, sodium borohydride, and calcium hydride.

Least practical appear to be the slurries made from sodium borohydride. While the materials are relatively safe to handle and have a favorable hydrogen content, their complete hydrolysis requires the presence of an acid. Regeneration of these compounds is potentially problematic. Unlike the single light metal hydrides, the exhausted material consists of borates and boric acid.

The most promising hydrides appear to be calcium hydride and lithium hydride. In the former case, the end product is harmless slaked lime, consisting of calcium hydroxides and its hydrates. We have shown that hydrolysis is limited to relatively safe pressures (c.a. 300 psig), and because of the formation of compounds of low solubility, does proceed to completion without requiring additives or other reactants, delivering >80% of the theoretical hydrogen yield. This is an important safety consideration, as it is desired that the waste product be completely exhausted and nonreactive.

From the consideration of energy density per weight of hydride, lithium hydride is superior. Both hydrides are practical to regenerate.

Sodium hydride has a base-limited hydrolysis reaction. When the pH of the system reaches approximately 13.6, the hydrolysis reaction stalls. One method by which this problem can be addressed is by the addition of aluminum metal to the slurry. The resulting aluminate reaction with the base forces the hydrolysis reaction to completion by consuming the base, forming an inert aluminate end product. The formation of the aluminate also releases still more hydrogen, splitting oxygen from the hydroxide. Regeneration issues regarding aluminates will need to be investigated if this method is to be further explored.

For the slurries to be useable in practical systems, they must be relatively safe to handle, have an attractive energy density, and be stable in storage. Further refinement of the dispersant system with a surfactant could depress viscosity enough to allow higher hydride concentrations with attendant increased hydrogen content per weight. For our purposes, the slurries should consist of at least 50% hydride. The upper limit of hydride loading is determined by the viscosity of the slurry. At loadings greater than this amount, viscosity and shear rise abruptly. Surfactants such as silicone-terminated alkyls can collapse these systems, resulting in hydride loadings of at least 60%, while still producing easily-pumped formulations. The slurries presently prepared from calcium and lithium hydrides by ball milling with alumina media have particle sizes between 5 and 10 microns. Good physical stabilities have been achieved by the use of polymeric dispersants which sterically stabilize the hydride/mineral oil system. Polymeric dispersants allow the use of higher molecular weight lyophiles than do conventional alkyl terminated systems, which are generally limited to 12-carbon chains. With the use of polymeric dispersants, the slurries are stable and do not present the sedimentation or settling difficulties of the initial slurry formulations. More than twenty minutes are required in a clinical centrifuge at 5,125 X G for sedimentation to begin with the current slurries. The slurries of calcium and lithium hydrides, at

50% hydride content, are pourable liquids with the consistency of heavy cream or paint. Their measured viscosities are 20 seconds with a #4 Zahn cup (approximately 210 cPs).

The following photomicrograph, Figure 3, taken at 1,000X in polarized light, shows a calcium hydride slurry made by the above method.

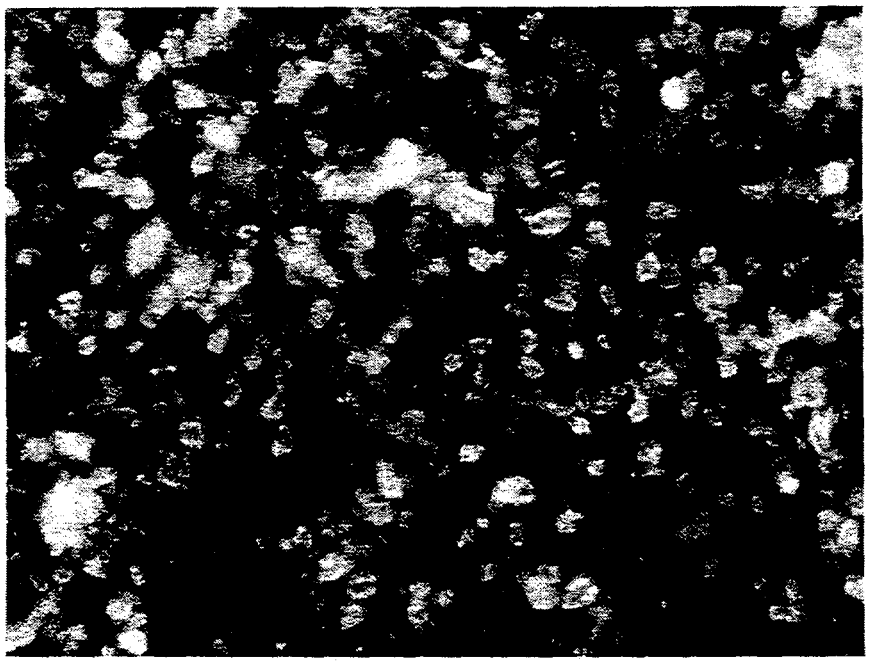

Figure 3. Photomicrograph (1000X) of Calcium Hydride Slurry

Hydrogen Generation

Tables 3 and 4 display various characteristics of the chemical hydrides of interest. Calcium hydride and lithium hydride offer an attractive option for the metal hydride/slurry program and have been selected for the initial evaluation of the metal hydride/slurry storage. Other hydrides which should eventually be investigated are Lithium-boro-hydride, Lithium-alumino-hydride, Sodium-boro-hydride, and Sodium-alumino-hydride. From Table 4, one can see that LiH offers the opportunity to provide 0.25 g of hydrogen per gram of hydride. This is very attractive when compared to the 1.5% to 6% of the more traditional metal hydrides. $LiBH_4$ and $LiAlH_4$ offer even greater storage capacity.

Table 3. Physical Characteristics of Light Metal Hydrides

		Temperature		Density
		Melting	Decomp	g/ml
Calcium Hydride	CaH_2	816 (in H_2)	600	1.9
Lithium Hydride	LiH	680		0.82
Sodium Hydride	NaH	800	800	0.92
Sodium Hydride 60% in oil	NaH			
Sodium Aluminum Hydride	$NaAlH_4$	178		1.28
Sodium BoroHydride	$NaBH_4$	500	400	1.074
Lithium Aluminum Hydride	$LiAlH_4$		125	0.917
Lithium BoroHydride	$LiBH_4$	278	275	0.666

Table 4. Hydrogen Storage Capabilities of Chemical and Absorption Hydrides

	Moles H_2 Released per Mole Hydride	Mass per Mole H_2 Released	Mass H_2 Released per Mass Hydride	Reactions
Mg	1	24.31	0.083	$Mg + 2H_2O = Mg(OH)_2 + H_2$
LiH	1	7.95	0.254	$LiH + H_2O = LiOH + H_2$
NaH	1	24.00	0.084	$NaH + H_2O = NaOH + H_2$
CaH_2	2	21.05	0.096	$CaH_2 + 2H_2O = Ca(OH)_2 + 2H_2$
MgH_2	1	26.33	0.077	$MgH_2 = Mg + H_2$
$LiBH_4$	4	5.45	0.370	$LiBH_4 + 4H_2O = LiOH + H_3BO_3 + 4H_2$
$NaBH_4$	4	9.46	0.213	$NaBH_4 + 4H_2O = NaOH + H_3BO_3 + 4H_2$
$LiAlH_4$	5	7.59	0.266	$2LiAlH_4 + 2H_2O = 2LiH + 2H_2O + 2Al + 3H_2 = 2LiOH + 2Al + 5H_2$
$NaAlH_4$	5	10.80	0.187	$2NaAlH_4 + 2H_2O = 2NaH + 2H_2O + 2Al + 3H_2 = 2NaOH + 2Al + 5H_2$
$FeTiH_{1.6}$	0.8	131.70	0.015	
$LaNi_5H_{6.7}$	3.35	131.11	0.015	
Mg_2TiH_6	3	34.19	0.059	
$MgTi_2H_6$	3	42.05	0.048	

Slurries of lithium hydride and calcium hydride were contacted with water to measure the hydrogen release rates. Figure 4 displays the reaction of half a mole of lithium hydride with one mole of water.

The reaction rates can be calculated from the pressure rise and temperature data collected during the hydrogen generation testing. These rates are derived from the data by calculating the number of moles of gas required to produce the pressures measured within the closed volume. From this value, the number of moles of argon used to drive the water into the autoclave is subtracted as well as the number of moles of water vapor calculated from the measured temperature of the hydride/water mixture. Figure 5 displays a typical hydrogen generation curve for lithium hydride and water.

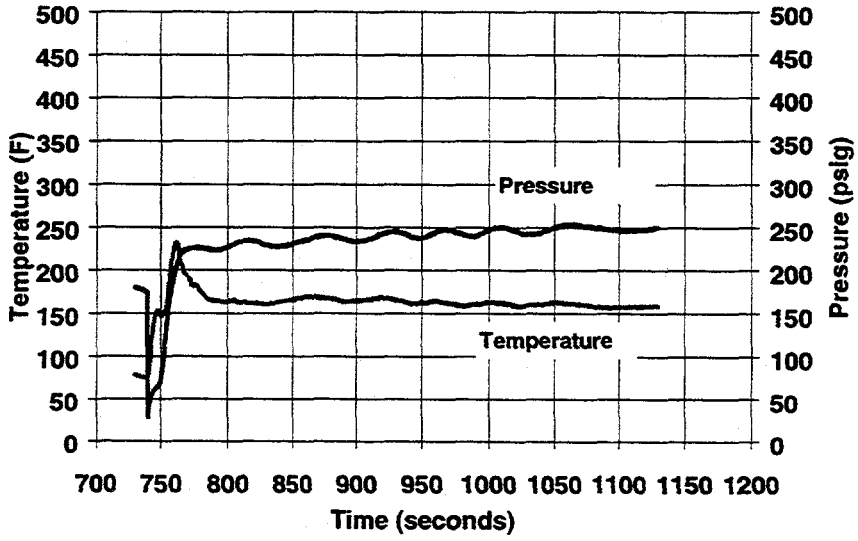

Figure 4. 40% Lithium Hydride Slurry with Mineral Oil - 0.5 mole LiH, 1.0 mole H_2O

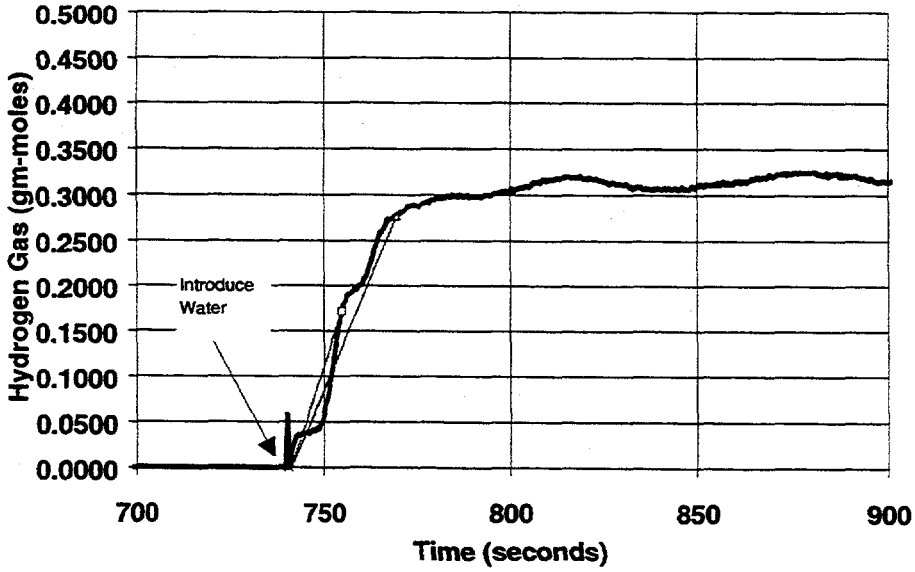

Figure 5. Lithium Hydride in 50% Slurry with Light Mineral Oil

The rates range from 0.0015 to 0.0165 gmole/s depending on the hydride, oil fraction, water stoichiometry, and mixing rate. No attempt has been made to assess the impact each of these properties have on the rate. In general:

- The calcium hydride was observed to be considerably slower than the sodium hydride and the lithium hydride.
- The greatest consistency was achieved with the calcium hydride.
- The sodium hydride with aluminum was observed to be the fastest reacting hydride, but the results of the two tests performed vary dramatically.

The conclusion from these tests is that the reaction rates are sufficiently rapid to be of interest in a hydrogen generation system. Further testing needs to be performed to determine the effect of the particle size, the water availability, the pressure of the reaction, and the temperature of the reaction. These characteristics will be needed to define the design of a demonstration reactor.

Preliminary Design and Economics

Preliminary Design of Hydroxide Regeneration System

A preliminary design of the hydroxide to hydride regeneration system has been conducted to identify process stream conditions and to allow the major equipment components to be sized such that a capital equipment cost could be developed. The system is shown in Figure 6. The analysis has been conducted for both lithium hydroxide and calcium hydroxide regeneration.

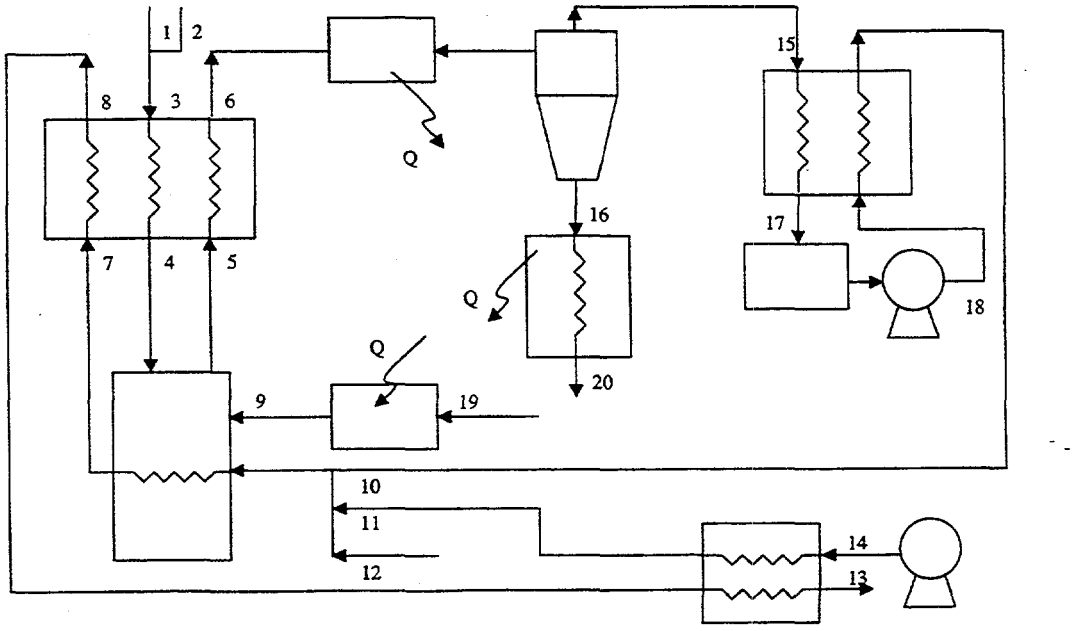

Figure 6. Hydroxide Regeneration System

The material and energy balances for the two metals were conducted for a plant supplying hydrogen to 250,000 cars.

Plant size- Service 250,000 cars

- 6.4 billion Btu/hr
- 13 tons H_2/hr
- 1876 MW_t
- 1/3 size of First FCC unit
- 1/25 size of Today's FCC units

The results are shown in Tables 5a,b,c for lithium. Lithium hydroxide is combined with carbon for the reduction and fuel, streams 1, 2a and 2b, to form stream 3 and is fed to the top of an indirect vertical heat exchanger which preheats the incoming reactants while cooling the stream containing the lithium hydroxide, streams 5 and 6. The possibility for removing heat from the indirect fired process heater is also provided, streams 7 and 8.

The hot preheated and partially reacted reactants, stream 4, enter the reduction reactor in which they are heated indirectly to the reaction temperature by combustion of the recycled carbon monoxide, stream 10, and additional fuel, stream 12, with preheated air, stream 11. The possibility of adding direct heat to the reactor is accomplished by adding oxygen to the reduction reactor by stream 9. The products of reduction leave the reduction reactor through stream 5. Within the reactant preheater, the lithium hydride is formed through the non-equilibrium kinetics as the mixture of lithium, hydrogen and carbon monoxide is cooled. Additional heat is taken out of the product stream for the generation of electrical energy which is added back into the reduction reactor to reduce the additional fuel.

The product, lithium hydride, is separated form the carbon monoxide in the hot cyclone, stream 16. This is further cooled to produce additional power which is also added to the reduction reactor. The hot carbon monoxide, stream 15, is passed through a self recuperator to get a cold stream of CO which could have a barrier filter installed to remove all the lithium hydride and a blower to circulate the CO, stream 18. This stream is reheated with the incoming CO and fed into the indirect process heater as discussed above.

The hot combustion products leaving the solids preheater, stream 8, are used to preheat the combustion air and produce power which is fed back into the reduction reactor.

The energy efficiency of the hydrogen storage is obtained by dividing the heat of combustion of the hydrogen in the metal hydride by the heat of combustion of the carbon used for the reduction and the additional fuel. The results are:

- Lithium - 52.1%
- Calcium - 22.9%

Table 5a. State Points - Lithium Hydroxide to Hydride Regeneration

Stream		1	2a	2b	2	3	4	5	6
Name		Hydroxide feed	Carbon for heat	Carbon for metal reduction	Carbon Feed	Hydroxide and Carbon Feed	Preheated Hydroxide and Carbon	Reduction Reactor Output	Lithium Hydride Condenser Offgas
Pressure	Bar	1	1	1	1	1	1	1	1
Temperature	K	298	298	298	298	298	1650	1850	950
Mass Flow Rate	kg/hr	139,601	0	70,022	70,022	209,623	209,623	209,623	209,623
Component Mass Flows	kg/hr								
metal gas								40,452	
metal (l)									
metal (s)									
metal hydride (s)	46,329								46,329
metal hydroxide (s)		139,601				139,601			
metal oxide (s)							87,089		
H2O									
H2O(l)									
C			0	70,022	70,022	70,022	35,011		
CO2									
CO							81,647	163,294	163,294
H2							5,876	5,876	0
O2								0	
N2									
Hydrocarbon feed									
Organic removed prior	30,577								
Total Enthalpy	kJ/hr	-2.827E+09	0.000E+00	0.000E+00	0.000E+00	-2.827E+09	-1.393E+09	9.092E+08	-7.881E+08

Table 5b. State Points - Lithium Hydroxide to Hydride Regeneration

Stream		7	8	9	10	11	12	13	14
Name		Combustor Exhaust	Exhaust Exchanger outlet	Preheated Oxygen for Direct Heating	Preheated CO	Preheated Combustion Air	Additional Fuel	Stack Gases	Combustion Air
Pressure	Bar	1	1	1	1	1	1	1	1
Temperature	K	2000	2000	298	800	1800	298	400	298
Mass Flow Rate	kg/hr	328,775	328,775	0	163,294	151,008	14,473	328,775	648,079
Component Mass Flows	kg/hr								
metal gas									
metal (l)									
metal (s)									
metal hydride (s)	46,329								
metal hydroxide (s)									
metal oxide (s)									
H2O		32,505	32,505					32,505	
H2O(l)									
C									
CO2		296,270	296,270					296,270	
CO					163,294				
H2					0				
O2		0	0	0		151,008		0	151,008
N2		0	0					0	497,071
Hydrocarbon feed							14,473		
Organic removed prior	30,577								
Total Enthalpy	kJ/hr	-2.313E+09	-2.313E+09	0.000E+00	-5.473E+08	2.950E+08	-6.755E+07	-3.034E+09	0.000E+00

Table 5c. State Points - Lithium Hydroxide to Hydride Regeneration

Stream		15	16	17	18	19	20
Name		Separator CO product	Hot Hydride	CO Cooler Product	CO Pressurized	Oxygen In	Cold Hydride Product
Pressure	Bar	1	1	1	1	1	1
Temperature	K	950	950	400	400	298	355
Mass Flow Rate	kg/hr	163,294	46,329	163,294	163,294	0	46,329
Component Mass Flows	kg/hr						
metal gas							
metal (l)							
metal (s)							
metal hydride (s)	46,329		46,329				46,329
metal hydroxide (s)							
metal oxide (s)							
H2O							
H2O(l)							
C							
CO2							
CO		163,294		163,294	163,294		
H2		0		0	0		
O2						0	
N2							
Hydrocarbon feed							
Organic removed prior	30,577						
Total Enthalpy	kJ/hr	-5.183E+08	-2.698E+08	-6.247E+08	-6.247E+08	0.000E+00	-5.059E+08

Economics of the Approach

The preliminary economics for the process are obtained by first developing a capital cost for the process equipment and then estimating the operating cost to define the needed sales price of the metal hydride for the required after tax return on the investment.

The capital equipment costs for the process are shown in Table 6 for the lithium process. These estimates, as well as the operating cost estimates, were obtained using standard chemical engineering practice. The operating cost assumptions are shown below:

- Carbon — Variable, \$0.67 to 1.67/10^6 Btu
- Fuel — \$2.5/10^6 Btu
- Labor
  - -Operators — 25 at \$35,000/yr
  - -Supervision & Clerical — 15% of Operators
- Maintenance & Repairs — 5% of Capital
- Overhead — 50% of Total Labor and Maintenance
- Local Tax — 2% of Capital
- Insurance — 1% of Capital
- G&A — 25% of Overhead
- Federal and State Tax — 38% of Net Profit

Table 6. Capital Cost - Lithium Hydride Regeneration

		Total cost
1	Furnace Cost, base 70m3	9,236,116
2	Solids preheater, 70 m3	9,236,116
3	Condensor, base 100MW	-
4	Hydride Reactor, Base 35m3	720,417
5	Blower, H2 from sep.base, 75m3/s	270,254
6	Steam Turbine Generator	25,693,663
7	Cent Slurry sep.	189,413
8	Hydride cooler, base 70 m3	9,236,116
9	Heat Exch/recuperator, base 20e9J/s	2,814,328
10	Hydrocarbon Decomp, base 100MW	-
	Sum, Total Cost	57,396,424

The manufacturing cost summary is presented in Table 7 for lithium.

Table 7. Manufacturing Cost Summary - Lithium Hydride Regeneration

Plant Size	No. cars per day served	2,000,000		
Physical Plant Capital Cost($)				
	Fixed Capital	199,865,957		
	Initial charge LiOH	32,759,101		
	Working Capital	19,986,596		
	Total Capital	252,611,653		
Direct Cost				
	carbon cost, $/lb			0.02
	carbon cost, $/yr		212,955,679	
	Fuel cost, $/lb			0.0575
	Fuel cost, $/yr.		126,549,051	
	Op. Labor, $/yr.		875,000	
	# Staff	25		
	Annual Salary	35,000		
	Sup&Clerical, $/yr.		131,250	
	Maint&Repairs, $/yr.		9,993,298	
	Total Direct, $/yr.		350,504,278	
(Indirect Op. Exp)				
	Overhead, $/yr.		5,499,774	
	Taxes, $/yr.		3,997,319	
	Insur, $/yr.		1,998,660	
	Total Indirect Cost, $/yr.		11,495,753	
Total Mfg Exp			362,000,030	
	Depreciation, $/yr.		19,986,596	
	G&A, $/yr.		1,374,943	
	Distrib&Sales, $/yr.		0	
	R&D, $/yr.		0	0
Total Genl Expenses, $/yr.			1,374,943	
Total Expenses, $/yr.			363,374,974	
Revenue From Sales Hydride, $/yr.			505,650,462	0.0708
Total Revenues, $/yr.			505,650,462	
Net Annual Profit, $/yr.			142,275,488	
Income Taxes, $/yr.			46,469,779	
Net Annual Prof after Taxes, $/yr.			95,805,709	
After-Tax Rate of Ret (%)		37.93		
$/10^6 btu		4.57		

The sensitivity of the cost of the hydride and the rate of return as a function plant size and carbon cost is shown in Figures 7 and 8 for lithium and 9 and 10 for calcium. In Figure 7, the cost of hydrogen is plotted versus the plant size for four values of the cost of carbon. For a 250,000 car-per-day plant, the cost of hydrogen is on the order of $3.61 per million Btu at a carbon cost of one cent per pound and a fixed return on the investment of 15 percent. In Figure 8, the effect of plant size and carbon cost for a fixed hydrogen cost on the rate of return is shown. In this case, if the hydrogen can be sold for a value of $4.57 per million Btu, the return to the investors can range from 15 to 65 percent depending on plant size and carbon price. The same trends are seen for calcium.

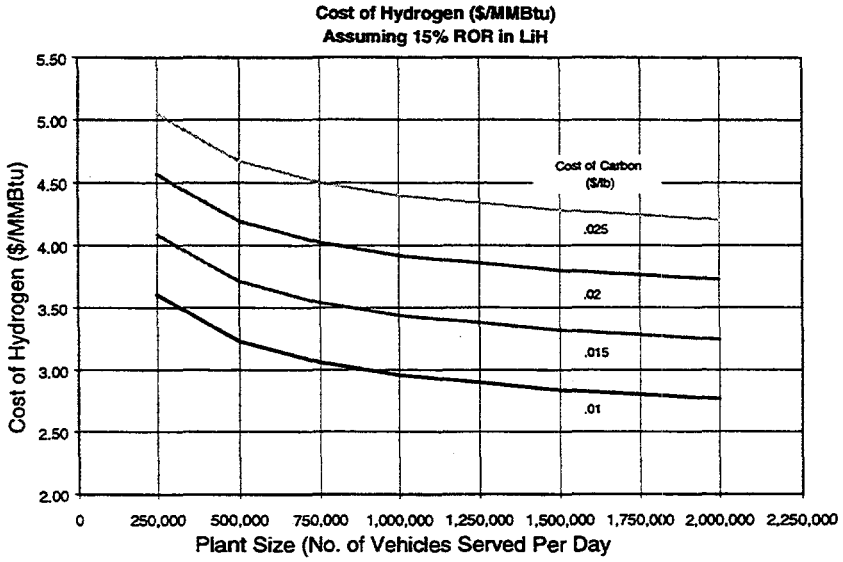

Figure 7. Sensitivity of Hydrogen Cost to Carbon Cost and Plant Size for Lithium Hydride

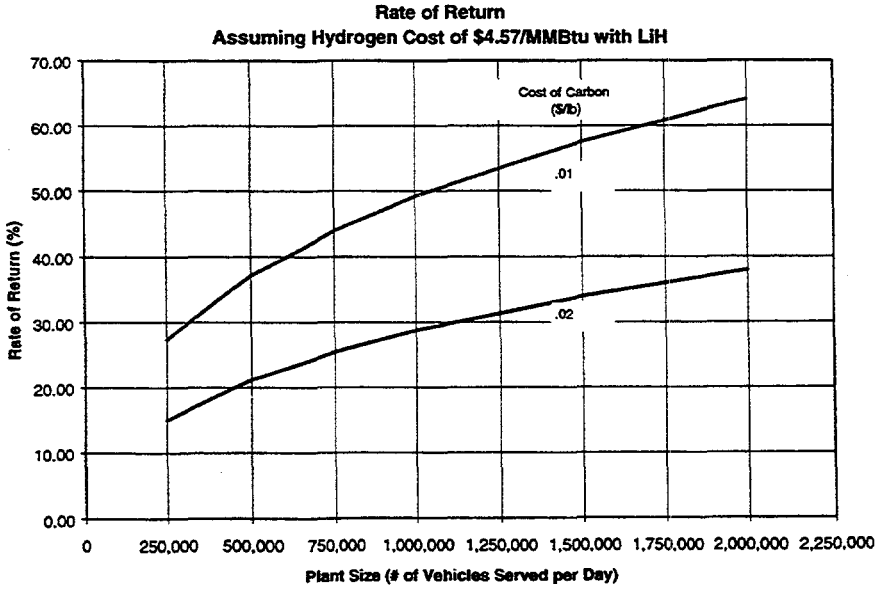

Figure 8. Sensitivity of Rate of Return to Carbon Cost and Plant Size for Lithium Hydride

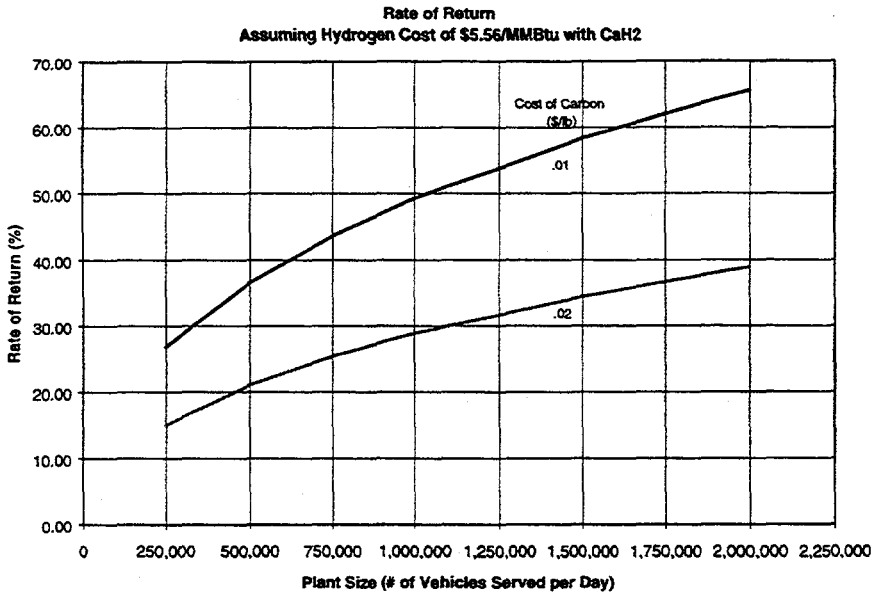

Figure 9. Sensitivity of Rate of Return to Carbon Cost and Plant Size for Calcium Hydride

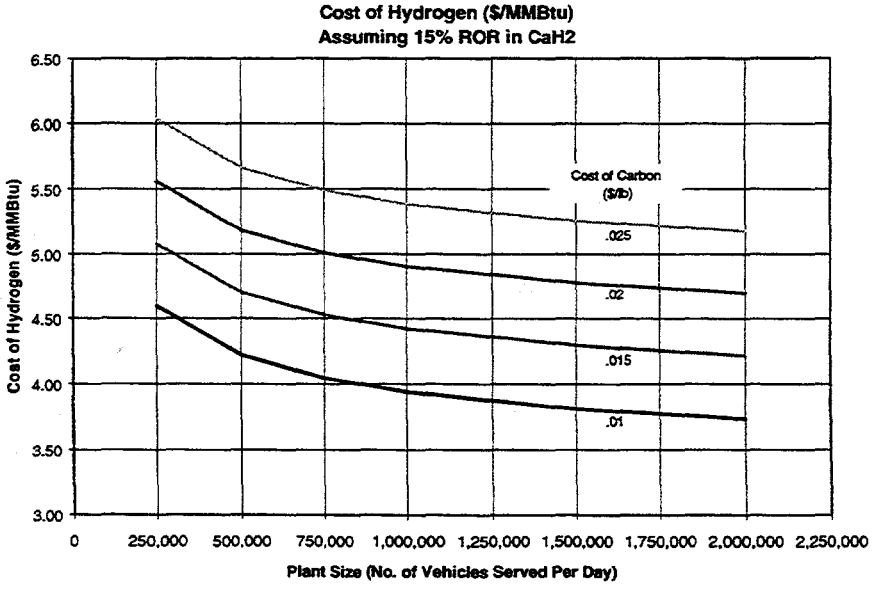

Figure 10. Sensitivity of Rate of Return to Carbon Cost and Plant Size for Calcium Hydride

Summary and Follow On Activities

The results of the work to date are:

- Best Organic - Light Mineral Oil
- Best Hydrides -LiH & CaH_2
- +95% Hydrogen Release/Recovery
- Reaction rate controllable
- pH/Pressure Control
- Stable slurry
- Polymeric dispersants sterically stabilize the suspension
- Cost of Hydrogen $2.75 to $6.00 per 10^6 Btu

The follow on activities are:

- Conduct laboratory-scale experiments of the chemical hydroxide to chemical hydride conversion process.
- Update analysis of the complete cycle.
- Development of final process specifications and plans for bench-scale demonstrations of the components.
- Demonstrate the bench-scale recycle experiment and the slurry production and pumping experiment.

References

[1] "Plans For A U.S. Renewable Hydrogen Program," Block, D. and Melody I., Florida Solar Energy Center, Proceedings of 10th World Hydrogen Energy Conference, Cocoa Beach, FL, June 20-24, 1994.

[2] Ulrich, "A Guide To Chemical Engineering Process Design And Economics", John Wiley & Sons, 1984.

SIMULTANEOUS PURIFICATION AND STORAGE OF HYDROGEN

Scott Hynek, Ware Fuller, Robert Weber and Eric Carlson
Arthur D. Little, Inc.
Cambridge, MA 02140

Abstract

Specially coated magnesium particles have been shown to selectively absorb hydrogen from a hydrogen-rich gas stream such as reformate. These coated magnesium particles can store the absorbed hydrogen as required and subsequently deliver pure hydrogen, just as uncoated magnesium particles can. These coated magnesium particles could be used in a device that accepts a steady stream of reformate, as from a methane reformer, stores the selectively absorbed hydrogen indefinitely, and delivers purified hydrogen on demand.

Unfortunately, this coating (magnesium nitride) has been shown to degrade over a period of several weeks, so that the magnesium within evidences progressively lower storage capacity. We are investigating two other coatings, one of which might be applicable to hydridable metals other than magnesium, to replace magnesium nitride.

Introduction

There are several practical methods of storing pure hydrogen. Storing it by hydriding a metal is one of these methods. However, no known metal can hydride and dehydride for long when exposed to hydrogen contaminated by impurities. If the impurities are present in significant concentrations, as they are in reformate, no known metal can hydride and dehydride at all.

Likewise, there are several ways of separating hydrogen from hydrogen-rich gas mixtures like reformate. Passing it through a hydrogen-permselective membrane is one

of those ways. However, hydrogen-permselective membranes are quite expensive. The thickness of these membrane is determined by a compromise: both performance and cost favor thin membranes, whereas the ability to withstand high pressure drops and the ability to use substrates with practical pore sizes both favor thick membranes.

If a particle of hydridable metal could be coated with a thin hydrogen-permselective membrane, there would be two major benefits:

1. The coated particles could accept hydrogen directly from reformate, yet could subsequently discharge pure hydrogen.

2. The membrane could be inexpensive, because a very thin membrane would suffice; a very thin membrane can be adequately supported by a solid, yet hydrogen-absorptive, metal particle.

The goal of this effort is to identify, prepare and demonstrate by testing, that magnesium powder coated with a suitable hydrogen-permselective layer will hydride/dehydride in the presence of reformate. Magnesium powder thusly coated could be termed 'reformate-tolerant magnesium' or RTM.

Why magnesium? Because magnesium hydride has the highest weight percentage hydrogen of any practical metal hydride, and because magnesium is relatively inexpensive. Another good reason is that we have already demonstrated for DOE a highly efficient means for stationary storage of hydrogen using nickel-coated magnesium powder (NCMP) and a phase change material.

Discussion

We have identified two practical uses for such reformate-tolerant magnesium:

Hydrogen Fueling Stations - A reformer-based hydrogen fueling station must include a purification device such as a pressure swing adsorber (PSA) to separate the hydrogen from the H_2O, CO_2, CO and N_2 in the reformate, plus a separate device to store the hydrogen pending demand for refueling. A single bed of reformate-tolerant magnesium powder could perform both the separation (purification) and the storage functions.

Fuel Cell Vehicles - Fuel cell vehicles utilizing on-board reformers would benefit greatly from the ability to store some of the reformate for use during startup. However, compressed gas storage of reformate is impractical, requiring both a multistage compressor and a high pressure storage cylinder. A single, small bed of reformate-tolerant magnesium powder could store enough hydrogen to run the fuel cell while the fuel processor is warming up. It could also be used to supply additional, pure, hydrogen to meet peak loads.

A suitable coating system for magnesium particles should possess the following five characteristics:

1. *Hydrogen Permselectivity* - It must pass hydrogen, but it must not pass any other species with which the magnesium might react.

2. *Chemical Inertia* - It must not itself react with the other species, lest it lose its hydrogen-permselectivity.

3. *Kinetics* - It should catalyze the dissociation of hydrogen molecules, so that the hydriding reaction kinetics are enhanced.

4. *Cost* - The coating should be inexpensive.

5. *Durability* - The coating must remain attached to the magnesium.

We recognized that a single coating might not possess all of these characteristics. We thus refer to a 'coating system,' which might consist of multiple coatings.

The major problem is that most coatings are not inert to the other species present in reformate, at least not at the temperatures (>300°C) at which magnesium hydrides/dehydrides.

Past Results

This project began with the thermal integration of nickel coated magnesium powder (NCMP) with a phase change material (PCM). This was to achieve high efficiency hydrogen storage. The mass of the NCMP and the PCM, plus the mass of the heat exchanger in which both were located, rendered this technique applicable only to stationary storage of hydrogen.

The NCMP was located on the tube side of a shell-and-tube heat exchanger, and the PCM on the shell side. As the NCMP hydrided, the heat of the hydriding reaction melted the PCM. As the NCMP dehydrided, the heat of fusion from the solidifying PCM provided the heat of the dehydriding reaction.

The primary reason for the nickel coating was to catalyze the dissociation of the H_2 molecules, so that atomic hydrogen could enter into the hydriding reaction. Nickel is also less active than magnesium, but not inactive enough to serve as a hydrogen-permselective coating.

Recent Results

Our preliminary results indicate that a coating that possesses the above characteristics may be achievable.

1. We have established that magnesium particles can easily be coated with magnesium nitride by means of chemical vapor deposition (CVD) in a fluidized bed reactor.

2. We have established that these magnesium nitride coatings do not seriously degrade the ability of the magnesium particles to hydride and dehydride in the presence of pure hydrogen.

3. We have established that these coated magnesium particles can repeatedly hydride and dehydride in the presence of a mixture of hydrogen, steam, and carbon dioxide.

4. Unfortunately, we have also established that the magnesium nitride coating does not remain hydrogen-permselective for more than several weeks.

We measured the ability of coated magnesium particles to hydride and dehydride using a closed, heated volume in which is contained the magnesium particles (with or without coatings) and a gas (either pure hydrogen or a mixture of hydrogen and other species). Our technique consists of the following steps:

1. Allow the particles and the hydrogen in the gas to reach equilibrium at 300°C ,

2. Vent some of the gas until the hydrogen partial pressure equals the hydrogen/magnesium hydride equilibrium pressure at 300°C (1.45 atm),

3. Allow the particles and the hydrogen in the gas to reach equilibrium at 350°C,

4. Allow the particles and the hydrogen in the gas to reach equilibrium at 300°C ,

Steps 3 and 4 are repeated as long as desired.

In the search for alternative coatings, we recognized that not all of the five criteria listed above are truly necessary.

- Dissociation of hydrogen molecules can be accomplished by other means, such as by mixing the coated particles with nickel powder.

- Almost any coating, if thin enough, is inexpensive (witness the use of very thin coatings of precious metals in automotive catalytic converters).

- Most coatings, if thin enough, are effectively hydrogen-permselective. This is because extremely thin coatings have imperfections, such as gap or cracks. The smallest of these cracks can pass only hydrogen. Any cracks large enough to pass other species will fill up with magnesium oxide, but this does not affect those cracks small enough to pass only hydrogen.

Therefore, perhaps we really only need a coating that

1. does not react with other species present in reformate, and

2. remains attached to the magnesium.

This theory appeared to be substantiated by the initial success of our thin coating of magnesium nitride. However, it turned out that Mg_3N_2 did, in time, react with other species present in reformate.

During the past year, we greatly improved the coated particle testing apparatus. No longer is it necessary to coat and test the particles in the same reactor. Now it is possible to coat particles in the original reactor, and to test six separate samples of coated particles simultaneously in six separate test sections, shown below.

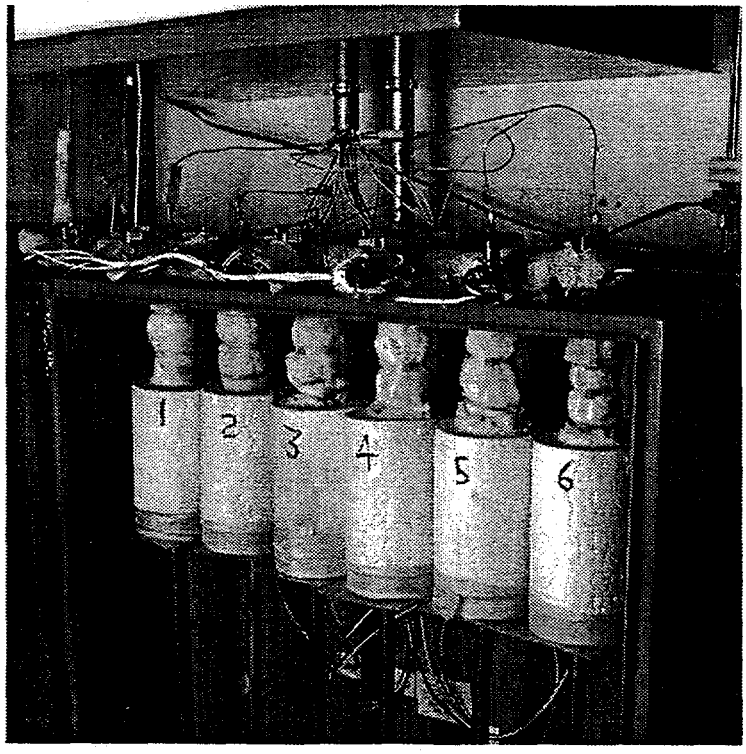

Each of these test sections has its own electric heater, controlled by its own programmable controller. The temperatures and pressures within all six test sections are monitored by thermocouples and pressure transducers, all connected to a datalogger, shown below.

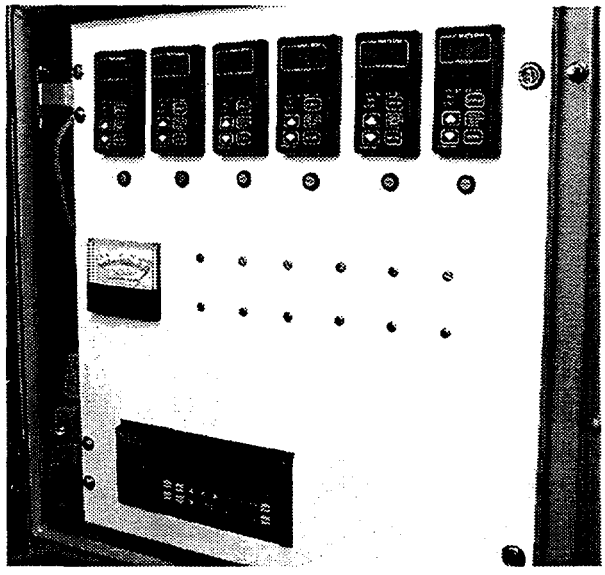

It is possible to retrieve the data from that datalogger remotely, using a pair of modems.

We used this improved facility to determine the sensitivity of NCMP to CO_2, H_2O and CO, individually and simultaneously. This showed that NCMP is inert to neither CO_2, H_2O nor CO.

Interestingly, NCMP can recover from exposure to a fixed amount of CO, as shown below

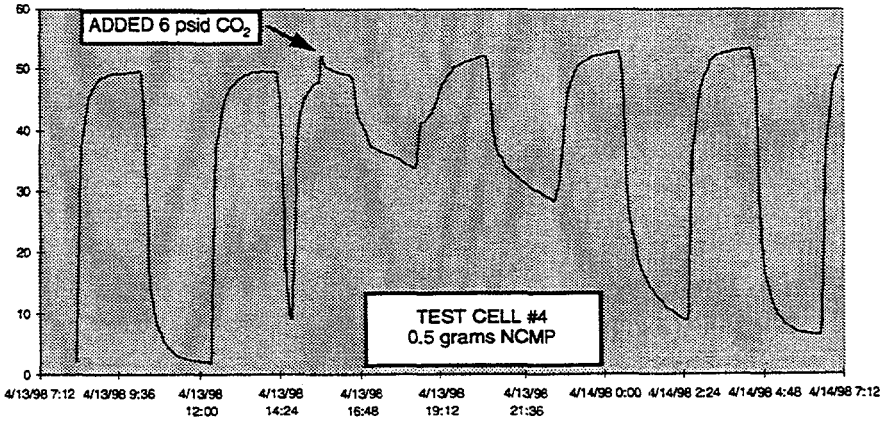

It can also recover from exposure to a fixed amount of CO_2, as shown below

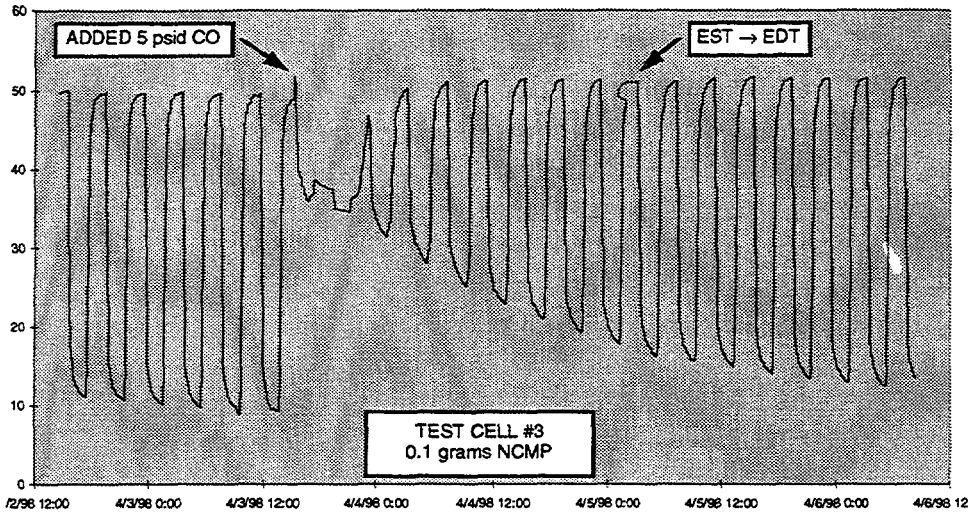

However, neither of these results should be taken to suggest that NCMP could withstand exposure to a continued supply of either CO or CO_2, as it would be if exposed to a reformate stream.

Future Work

We have identified two new potential coatings for magnesium, and plan to evaluate them. One of these coatings is a salt of magnesium, so it presumably would be firmly attached to the magnesium powder. The other of these coatings would appear to have all of the other required attributes.

We have embarked on a literature search to investigate the fabricability and the thermochemical stability of the first of these coatings.

We have also contracted to have a sample of the second coating prepared, so that we can test its ability to hydride/dehydride. We will first test this coated powder in pure hydrogen, and then in mixtures of H_2, CO, CO_2 and H_2O.

We also plan to investigate means by which the instability of Mg_3N_2 might be accommodated. For example, how realistic might it be to re-coat the particles periodically? Or, might NH_3 in reformate prevent decomposition of Mg_3N_2?

HYDROGEN STORAGE IN INSULATED PRESSURE VESSELS

S. M. Aceves and O. Garcia-Villazana
Lawrence Livermore National Laboratory
7000 East Ave., L-641
Livermore, CA 94551, USA
saceves@llnl.gov

Abstract

Insulated pressure vessels are cryogenic-capable pressure vessels that can be fueled with liquid hydrogen (LH_2) or ambient-temperature compressed hydrogen (CH_2). Insulated pressure vessels offer the advantages of liquid hydrogen tanks (low weight and volume), with reduced disadvantages (lower energy requirement for hydrogen liquefaction and reduced evaporative losses).

This paper shows an evaluation of the applicability of the insulated pressure vessels for light-duty vehicles. The paper shows an evaluation of evaporative losses and insulation requirements and a description of the current analysis and experimental plans for testing insulated pressure vessels. The results show significant advantages to the use of insulated pressure vessels for light-duty vehicles.

Introduction

Probably the most significant hurdle for hydrogen vehicles is storing sufficient hydrogen onboard. Hydrogen storage choices can determine the refueling time, cost, and infrastructure requirements, as well as indirectly influence energy efficiency, vehicle fuel economy, performance, and utility. There are at least three viable technologies for storing hydrogen fuel on cars. These are: compressed hydrogen gas (CH_2), metal hydride adsorption, and cryogenic liquid hydrogen (LH_2), but each has significant disadvantages.

Storage of 5 kg of hydrogen (equivalent to 19 liters; 5 gallons of gasoline) is considered necessary for a general-purpose vehicle, since it provides a 320 km (200 mile) range in a 17 km/liter (40

mpg) conventional car; or a 640 km (400 mile) range in a 34 km/liter (80 mpg) hybrid vehicle or fuel cell vehicle. Storing this hydrogen as CH_2 requires a volume so big that it is difficult to package in light-duty vehicles (Pentastar Electronics 1997), and it certainly cannot be used in trucks. The external volume for a pressure vessel storing 5 kg of hydrogen at 24.8 MPa (3600 psi) is 320 liters (85 gal). Hydrides are heavy (300 kg for 5 kg of hydrogen [Michel 1996]), resulting in a substantial reduction in vehicle fuel economy and performance.

Low-pressure LH_2 storage is light and compact, and has received significant attention due to its advantages for packaging (Braess 1996). Significant recent developments have resulted in improved safety (Pehr 1996a, 1996b) and fueling infrastructure (Hettinger 1996). Disadvantages of low-pressure LH_2 storage are: the substantial amount of electricity required for liquefying the hydrogen (Peschka 1992); the evaporation losses that occur during fueling low-pressure LH_2 tanks (Wetzel 1996); and the evaporation losses that occur during long periods of inactivity, due to heat transfer from the environment.

An alternative is to store hydrogen in an insulated pressure vessel that has the capacity to operate at LH_2 temperature (20 K), and at high pressure (24.8 MPa; 3600 psi). This vessel has the flexibility of accepting LH_2 or CH_2 as a fuel. Filling the vessel with ambient-temperature CH_2 reduces the amount of hydrogen stored (and therefore the vehicle range) to about a third of its value with LH_2.

The fueling flexibility of the insulated pressure vessels results in significant advantages. Insulated pressure vessels have similar or better packaging characteristics than a liquid hydrogen tank (low weight and volume), with reduced energy consumption for liquefaction. Energy requirements for hydrogen liquefaction are lower than for liquid hydrogen tanks because a car with an insulated pressure vessel can use, but does not require, cryogenic hydrogen fuel. A hybrid or fuel cell vehicle (34 km/l, 80 mpg) could be refueled with ambient-temperature CH_2 at 24.8 MPa (3600 psi) and still achieve a 200 km range, suitable for the majority of trips. The additional energy, costs, and technological effort for cryogenic refueling need only be undertaken (and paid for) when the additional range is required for longer trips. With an insulated pressure vessel, vehicles can refuel most of the time with ambient-temperature hydrogen, using less energy, and most likely at lower ultimate cost than LH_2, but with the capability of having 3 times the range of room temperature storage systems.

Insulated pressure vessels also have much reduced evaporative losses compared to LH_2 tanks. These results are based on a thermodynamic analysis of the vessels, and are the subject of the next section of this paper.

From an engineering and economic perspective, insulated pressure vessels strike a versatile balance between the cost and bulk of ambient-temperature CH_2 storage, and the energy efficiency, thermal insulation and evaporative losses of LH_2 storage.

Thermodynamic Analysis

This section describes a thermodynamic model of a pressure vessel, with the purpose of calculating evaporative losses. The following assumptions are used in the analysis:

1. Kinetic and potential energy of the hydrogen flowing out of the vessel are neglected.
2. Thermal conductivity of the vessel insulation is considered to be independent of internal and external temperature.
3. Gaseous hydrogen is preferentially extracted from the vessels. LH_2 is only extracted when the amount of gaseous hydrogen is not enough to satisfy the driving requirements.
4. Temperature and pressure are uniform within the vessel. This assumption has recently been verified for small vessels of the size required for light-duty vehicles (Bunger 1996).

5. No conversion between the para and ortho phases of hydrogen is considered. This assumption is used because vessel temperature changes little during most operating conditions, so that the equilibrium concentration of each phase remains fairly constant. In addition to this, the para-ortho conversion is slow, with a transition time of the order of a few days (Mathis 1976), so that in most cases, hydrogen does not stay in the vehicle vessel long enough for any significant conversion to occur.
   The first law of thermodynamics written for a pressure vessel is (VanWylen 1978):

$$M\frac{du}{dt} + M_v\frac{d(c_{p,v}T)}{dt} = Q - \left(\frac{p}{\rho}\right)\dot{m} \qquad (1)$$

The two terms in the left-hand side of Equation (1) are the rates of change of the internal energies of the hydrogen and the vessel. Heat transfer into the vessel (Q in the equation) is positive and tends to increase the temperature of the vessel. However, the last term in the right hand side of Equation (1) represents a cooling effect on the vessel, when mass is extracted ($\dot{m}>0$). Considering that the density of hydrogen is very low, this term is often significant. The last term in Equation (1) is commonly known as the flow work, since it is the work that the hydrogen stored in the vessel has to do to push out the hydrogen being extracted.

Equation (1) is solved for a low-pressure LH_2 storage and for the insulated pressure vessel. The equation is solved iteratively with a computer program which includes subroutines for calculating hydrogen properties. The required property values are obtained from McCarty (McCarty 1975). The specific heat of the vessel materials, $c_{p,v}$ is obtained as a function of temperature from correlations given in the literature (Scott 1967).

Vessel Characteristics

This paper considers three vessels, described as follows:
1. A conventional, low-pressure LH_2 tank with a multilayer vacuum superinsulation (MLVSI) and 0.5 MPa maximum operating pressure.
2. An insulated pressure vessel (24.8 MPa maximum operating pressure) with MLVSI fueled with LH_2.
3. An insulated pressure vessel with microsphere insulation (aluminized microspheres within a vacuum) fueled with LH_2.

Vessel properties are listed in Table 1. Two insulating materials (MLVSI and microspheres) are used in the analysis to study the effect of insulation level on hydrogen losses. No low-pressure LH_2 tank with microsphere insulation is studied in this paper, because low-pressure LH_2 tanks are very sensitive to heat transfer from the environment. According to Bunger and Owren (Bunger 1996), LH_2 poses requirements that are beyond the thermal performance of current vacuum powder insulation.

All vessels are designed to store 5 kg of hydrogen. The weight of the vessels, accessories, insulation, and external cover are calculated from data given by (James 1996). The vessels are assumed to have a cylindrical shape with hemispherical ends, and the length of the cylindrical segment is assumed to be equal to the diameter. Insulation properties are obtained from (Bunger 1996), which lists ranges of measured conductivity. Worst-case (highest) conductivity values are selected from these ranges.

Table I. Characteristics of the Hydrogen Vessels Being Analyzed.

	liquid Tank 1	insulated Vessel 2	pressure vessels Vessel 3
Mass of hydrogen stored, kg	5	5	5
Total weight, kg	21	30	30
Internal volume, liters	85	95	95
External volume, liters	112	144	144
Internal diameter, m	0.39	0.42	0.42
Internal surface area, m^2	0.98	1.1	1.1
Aluminum mass within insulation, kg	9	10	10
Carbon mass within insulation, kg	0	10	10
Design pressure, MPa (psi)	0.5 (70)	24.8 (3600)	24.8 (3600)
Performance factor[1], m (10^6in)	-	33000 (1.3)	33000 (1.3)
Safety factor	-	2.25	2.25
Insulating material	MLVSI[2]	MLVSI[2]	microsphere
Thermal conductivity of insulator, W/mK	0.0001	0.0001	0.0004
Insulation thickness, m	0.02	0.02	0.02
Heat transfer through accessories, W	0.5	0.5	0.5

[1] defined as burst pressure*volume/weight.
[2] MLVSI = multilayer vacuum superinsulation

The heat transfer rate, Q, has two components: heat transfer through the insulation, and parasitic heat transfer. Heat transfer through the insulation is assumed proportional to the temperature difference between the environment and the hydrogen inside the vessel. Parasitic heat transfer takes into account heat transfer through accessories, connecting lines, etc., and is assumed constant and equal to 0.5 W for a 2 cm insulation thickness.

This paper considers the application of hydrogen vessels to two vehicles: a hydrogen vehicle with a 17 km/liter (40 mpg) gasoline-equivalent fuel economy (Aceves 1996); and a high efficiency hybrid or fuel cell car with a 34 km/l (80 mpg) gasoline equivalent fuel economy (Smith 1995). The results can be easily scaled for application to vehicles with any other fuel economy.

Results

Figure 1 shows hydrogen losses during operation. The figure assumes that the vessels are filled to full capacity (5 kg), and then the vehicles are driven a fixed distance every day. The figure shows total cumulative evaporative hydrogen losses out of a full tank as a function of the daily driving distance. The figure includes information for 17 km/l and 34 km/l cars respectively in the lower and upper x-axes. The figure shows that a low-pressure LH_2 tank loses hydrogen even when driven 50 km per day in a 17 km/l car (100 km in a 34 km/l car). Losses from a low-pressure LH_2 tank grow rapidly as the daily driving distance drops. Insulated pressure vessels lose hydrogen only for very short daily driving distances. Even a microsphere-insulated vessel does not lose any hydrogen when driven 10 km/day or more (20 km/day in the 34 km/l car). Since most people drive considerably more than this distance, no losses are expected under normal operating conditions.

Figure 2 shows losses for a parked vehicle. The figure shows cumulative hydrogen losses as a function of the number of days that the vehicle remains idle. The most unfavorable condition is assumed: the vehicles are parked immediately after fueling. The low-pressure LH_2 tank has 2 days of dormancy (2 days without fuel loss) before any hydrogen has to be vented. After this, losses increase quickly, and practically all of the hydrogen is lost after 15 days. This may represent a significant inconvenience to a driver, who may be unable to operate the vehicle after a

long period of parking. Insulated pressure vessels have a much longer dormancy (up to 16 days). Total losses for the insulated pressure vessel with MLVSI is only 1 kg after 1 month of parking. In addition to this, insulated pressure vessels retain about a third of their total capacity even when they reach thermal equilibrium with the environment after a very long idle time, due to their high pressure capacity, therefore guaranteeing that the vehicle never runs out of fuel during a long idle period.

Figures 1 and 2 show a comparison in thermal performance for insulated pressure vessels and LH_2 tanks with equal insulation thickness (2 cm). Another important aspect of the comparison consists of determining the required insulation thickness for a LH_2 tank to have the same thermal performance as an insulated pressure vessel. This is illustrated in Figure 3. Figure 3 shows the effect of changing the insulation thickness on the thermal performance of an LH_2 tank. The figure shows the dormancy (number of days before any fuel loss occurs in a parked vehicle), and the minimum daily driving distance required for obtaining zero fuel losses, both as a function of the insulation thickness. The analysis assumes that the heat transfer through accessories is inversely proportional to the insulation thickness, so that it drops from the base-case value of 0.5 W for a thickness of 2 cm to 0.05 W at 20 cm thickness. The figure shows two diamond-shaped symbols, which indicate the corresponding dormancy (16 days, from Figure 2) and the daily driving distance for no losses (3 km/day, from Figure 1), for an insulated pressure vessel with 2 cm of MLVSI. The figure shows that, to achieve the same thermal performance as the insulated pressure vessel, an LH_2 tank requires either 13 or 20 cm of MLVSI. An insulation thickness of 13 cm is required to obtain the same period of parking without losses, and 20 cm are necessary to obtain the same minimum daily driving distance for no losses.

The big insulation requirements for LH_2 tanks with the same thermal performance as insulated pressure vessels have a major effect on external volume. Figure 4 shows internal and external volume for the insulated pressure vessel and LH_2 tank with 2 cm of MLVSI, and for LH_2 tanks with the same dormancy, and the same daily driving distance for no losses. It is clear that the vessels with equal thermal performance as the insulated pressure vessels are impractical due to their large volume. As a conclusion it can be said that insulated pressure vessels are a substantially more compact storage technology than LH_2 tanks, when vessels with equal thermal performance are compared.

Experimental Testing and Stress Analysis of Insulated Pressure Vessels

The analysis presented in this paper has assumed that insulated pressure vessels can be built to withstand the thermal stresses introduced when an initially warm vessel is filled with LH_2. It is desirable to use commercially-available aluminum-lined, fiber-wrapped pressure vessels to avoid the cost of custom-made vessels, even though commercially-available pressure vessels are not designed for low-temperature operation. While the applicability of these vessels for LH_2 storage in vehicles has not been demonstrated, an experiment has been carried out (Morris 1986) in which carbon fiber-aluminum and kevlar-aluminum vessels were cycled over a limited number of cycles (17) at LH_2 temperature. The vessels were burst-tested after cycling. The results of the experiment showed that there was no performance loss (no reduction in safety factor) due to cycling. This experiment indicates that it may be possible to use commercially-available fiber-wrapped aluminum vessels for operation at LH_2 temperature and high pressure. However, additional cyclic testing is necessary, because a vehicle requires many more than 17 fueling cycles.

To accomplish the required testing, an experimental setup has been built inside a high-pressure cell. A schematic is shown in Figure 5. The plan consists of running the vessels through 1000 high-pressure cycles and 100 low-temperature cycles. The cycles are alternated, running 10 pressure cycles followed by a temperature cycle, and repeating this sequence 100 times. Liquid nitrogen will be used for low-temperature cycling, and gaseous helium for high-pressure cycling.

This test is expected to replicate what would happen to these vessels during operation in a hydrogen-fueled car.

Cyclic testing of the pressure vessels is being complemented with a finite element analysis, which will help to determine the causes of any potential damage to the vessel during low-temperature operation. Finite element analysis is currently under progress. A mesh has been built, and a thermal analysis of the pressure vessel has been conducted. Figure 6 shows results for the early stages of the vessel filling process. The figure shows the lower part of the vessel, along with the mesh used in the simulation. Only a section of the vessel is analyzed, since it is axisymmetric. The conditions for the analysis are: the initial temperature is 300 K, the exterior of the pressure vessel is well insulated, and the interior of the vessel is being filled with liquid nitrogen. The liquid nitrogen level increases at a constant rate, and it is assumed that the vessel is full in 15 minutes. Figure 6 shows the level of liquid nitrogen with an arrow. The figure shows that the aluminum cools down very quickly due to its high thermal conductivity, while the composite material remains almost at ambient temperature. This condition is certain to introduce stresses in the vessel. These stresses will be calculated in the next stage of the analysis, when the thermal model is linked to a stress analysis model.

Validation of the finite element analysis will be done by applying strain gages and temperature sensors to the vessel. Cycled vessels will then be analyzed with non-destructive evaluation techniques, and finally they will be burst-tested, to evaluate any reduction in safety factor due to cycling.

Additional work in progress includes the design of an insulation. This is shown in Figure 7, which indicates that an outer jacket will be built around the vessel. This is necessary for keeping a vacuum space, required for obtaining a good thermal insulation with multilayer insulation (MLVSI). As a part of the insulation design, a pressure vessel outgassing experiment is currently being conducted. This is necessary, because an excessive outgassing rate from the pressure vessel material (fiber and epoxi) may result in a loss of vacuum, considerably reducing the performance of the insulation. The insulation design includes access for instrumentation for pressure, temperature, level and strain, as well as safety devices to avoid a catastrophic failure in case the hydrogen leaks into the vacuum space.

The instrumented and insulated vessel will be cycled with liquid hydrogen to test the instrumentation and insulation performance. A schematic of the experimental setup is shown in Figure 8. Testing will be conducted outdoors at a high-explosives facility to avoid the risk of an explosion that may occur as a result of hydrogen venting.

Conclusions

This paper shows that insulated pressure vessels have good packaging characteristics and thermal performance compared to LH_2 tanks, and also a potential for reduced need for liquid hydrogen. For these reasons, they are considered to be a good alternative for hydrogen storage. The most important results can be summarized as follows:

1. Insulated pressure vessels do not lose any hydrogen for daily driving distances of more than 10 km/day for a 17 km/l energy equivalent fuel economy. Since almost all cars are driven for longer distances, most cars would never lose any hydrogen.
2. Losses during long periods of parking are small. Due to their high pressure capacity, these vessels retain about a third of its full charge even after a very long period of inactivity, so that the owner would not risk running out of fuel.
3. Insulation of an LH_2 tank has to be between 6.5 and 10 times thicker than for an insulated pressure vessel to achieve equal thermal performance. Considering the large volume occupied by such a thick insulation layer, insulated pressure vessels are a more compact storage technology than LH_2 tanks, for equal thermal performance.

4. Previous testing has determined the potential of low-temperature operation of commercially-available aluminum-lined wrapped vessels for a limited number of cycles. Further testing will extend the number of cycles to the values required for a light-duty vehicle. Additional analysis and testing will help in determining the safety and applicability of insulated pressure vessels for hydrogen storage in light-duty vehicles.

Nomenclature

$c_{p,v}$	specific heat of the vessel enclosed within the insulation
$\dot{m}$	mass flow rate of hydrogen extracted from the vessel
M	total mass of hydrogen stored in the vessel
M_v	mass of the vessel enclosed within the insulation
p	pressure
Q	heat transfer rate from the environment into the vessel
t	time
T	temperature
u	specific internal energy of hydrogen
ρ	density of the hydrogen leaving the vessel

Acknowledgments

Work performed under the auspices of the U.S. Department of Energy by Lawrence Livermore National Laboratory under Contract W-7405-ENG-48.

References

Aceves, S.M., and Smith, J.R., 1996, "Lean-Burn Hydrogen Spark-Ignited Engines: The Mechanical Equivalent to the Fuel Cell," In "Alternative Fuels, Volume 3," Proceedings of the 18th Annual Fall Technical Conference of the ASME Internal Combustion Engine Division, Fairborn, OH, October 1996, pp. 23-31.

Braess, H.H., and Strobl, W., 1996, "Hydrogen as a Fuel for Road Transport of the Future: Possibilities and Prerequisites," Proceedings of the 11th World Hydrogen Energy Conference, Stuttgart, Germany.

Bunger, U., and Owren, G., 1996, "Development Potentials for Small Mobile Storage Tanks with Vacuum Powder Insulations," Proceedings of the 11th World Hydrogen Energy Conference, Stuttgart, Germany, pp. 1043-1052.

Hettinger, W. Michel, F., Ott, P., and Theissen, F., 1996, "Refueling Equipment for Liquid Hydrogen Vehicles," Proceedings of the 11th World Hydrogen Energy Conference, Stuttgart, Germany, pp. 1135-1143.

James, B.D., Baum, G.N., Lomax, F.D., Thomas, C.E., Kuhn, I.F., 1996, "Comparison of Onboard Hydrogen Storage for Fuel Cell Vehicles," Directed Technologies Report DE-AC02-94CE50389, prepared for Ford Motor Company.

Mathis, D.A., 1976, "Hydrogen Technology for Energy," Noyes Data Corporation, Park Ridge, NJ.

McCarty, R.D., 1975,"Hydrogen: Its Technology and Implications, Hydrogen Properties, Volume III," CRC Press, Cleveland, Ohio.

Michel, F., Fieseler, H., Meyer, G., and Theissen, F., 1996, "Onboard Equipment for Liquid Hydrogen Vehicles," Proceedings of the 11th World Hydrogen Energy Conference, Stuttgart, Germany, pp. 1063-1077.

Morris, E.E., Segimoto, M., and Lynn, V., 1986, "Lighter Weight Fiber/Metal Pressure Vessels Using Carbon Overwrap," AIAA-86-1504, Proceedings of the AIAA/ASME/SAE/ASEE 22nd Joint Propulsion Conference, June 16-18, Huntsville, Alabama.

Pehr, K., 1996a, "Experimental Examinations on the Worst Case Behavior of LH_2/LNG Tanks for Passenger Cars," Proceedings of the 11th World Hydrogen Energy Conference, Stuttgart, Germany.

Pehr, K., 1996b, "Aspects of Safety and Acceptance of LH_2 Tank Systems in Passenger Cars," International Journal of Hydrogen Energy, Vol. 21, pp. 387-395.

Pentastar Electronics, 1997, "Direct-Hydrogen-Fueled Proton-Exchange-Membrane Fuel Cell System for Transportation Applications, Conceptual Design Report," Report DOE/CE/50390-9, prepared for U.S. Department of Energy, Office of Transportation Technologies, under contract DE-AC02-94CE50390.

Peschka, W., 1992, "Liquid Hydrogen, Fuel of the Future," Springer-Verlag, Vienna, Austria.

Scott, R.B., 1967, "Cryogenic Engineering," D. Van Nostrand Company, Inc. Princeton, NJ.

Smith, J.R., Aceves, S.M., and Van Blarigan, P., 1995, "Series Hybrid Vehicles and Optimized Hydrogen Engine Design," SAE Paper 951955, SAE Transactions, Journal of Fuels and Lubricants, Vol. 104, pp. 816-827.

VanWylen, G.J., and Sonntag, R.E., 1978, "Fundamentals of Classical Thermodynamics," John Wiley and Sons, New York, NY.

Wetzel, F.J., 1996, "Handling of Liquid Hydrogen at Filling Stations," Proceedings of the 11th World Hydrogen Energy Conference, Stuttgart, Germany, pp. 1123-1134.

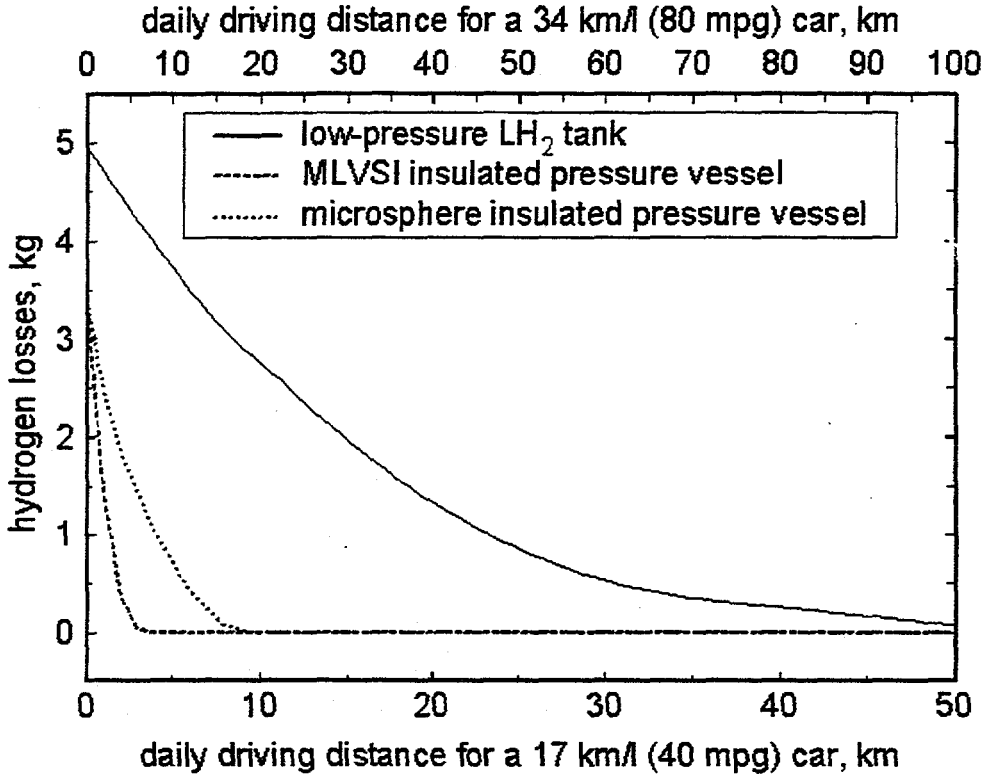

Figure 1. Cumulative hydrogen losses in kg as a function of daily driving distance, for vehicles with 17 km/liter (40 mpg); or 34 km/l (80 mpg) fuel economy, for the three vessels being analyzed in this paper.

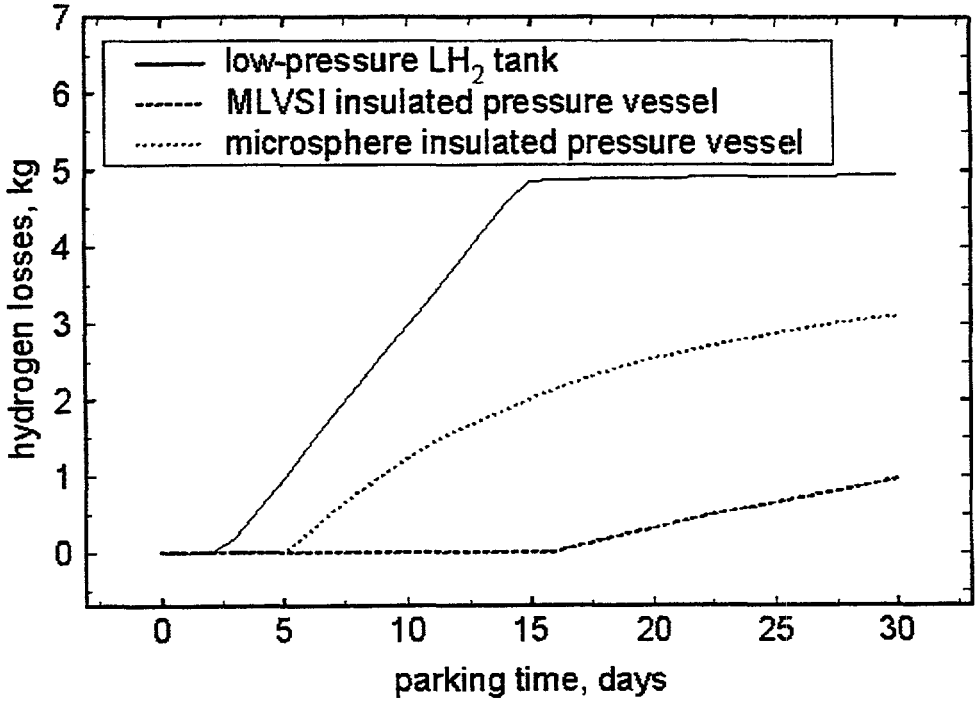

Figure 2. Cumulative hydrogen losses in kg as a function of the number of days that the vehicle remains idle, for the three vessels being analyzed in this paper, assuming that the vessels are initially full.

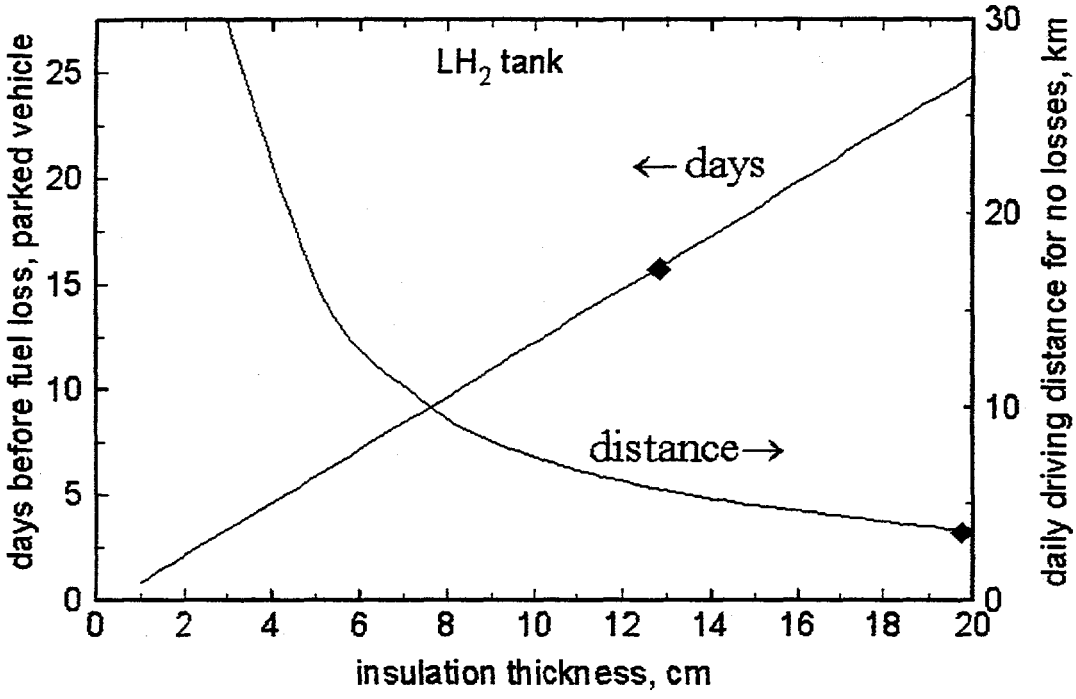

Figure 3. Dormancy and daily driving distance required for obtaining zero fuel losses, as a function of the insulation thickness, for a LH_2 tank.

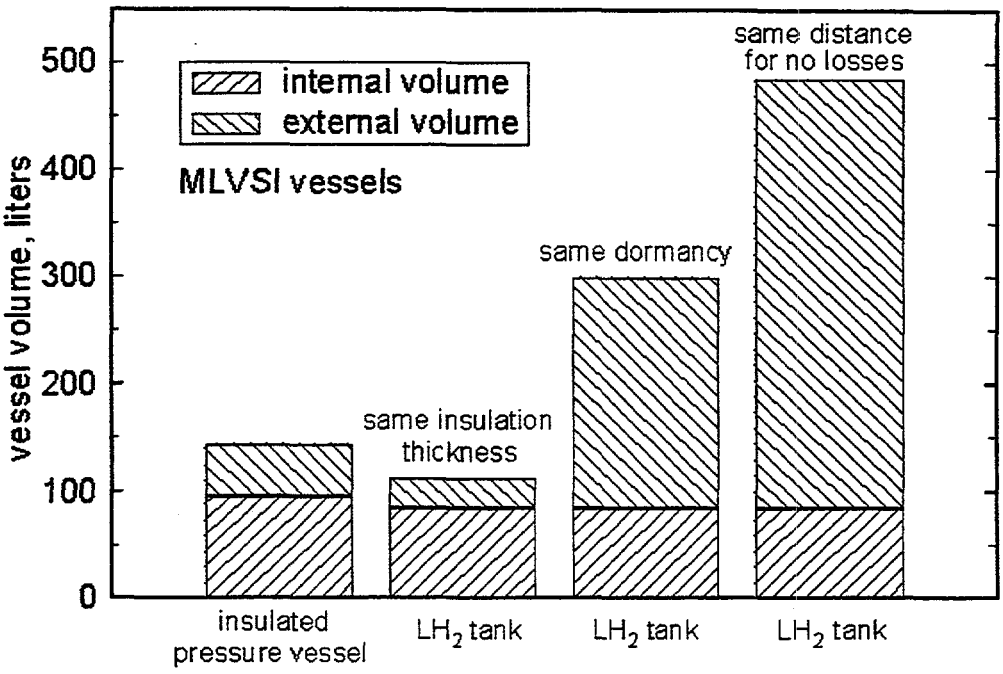

Figure 4. Internal and external volume for the base-case insulated pressure vessel and LH_2 tank, and for LH_2 tanks with same dormancy, and the same daily driving distance for no losses.

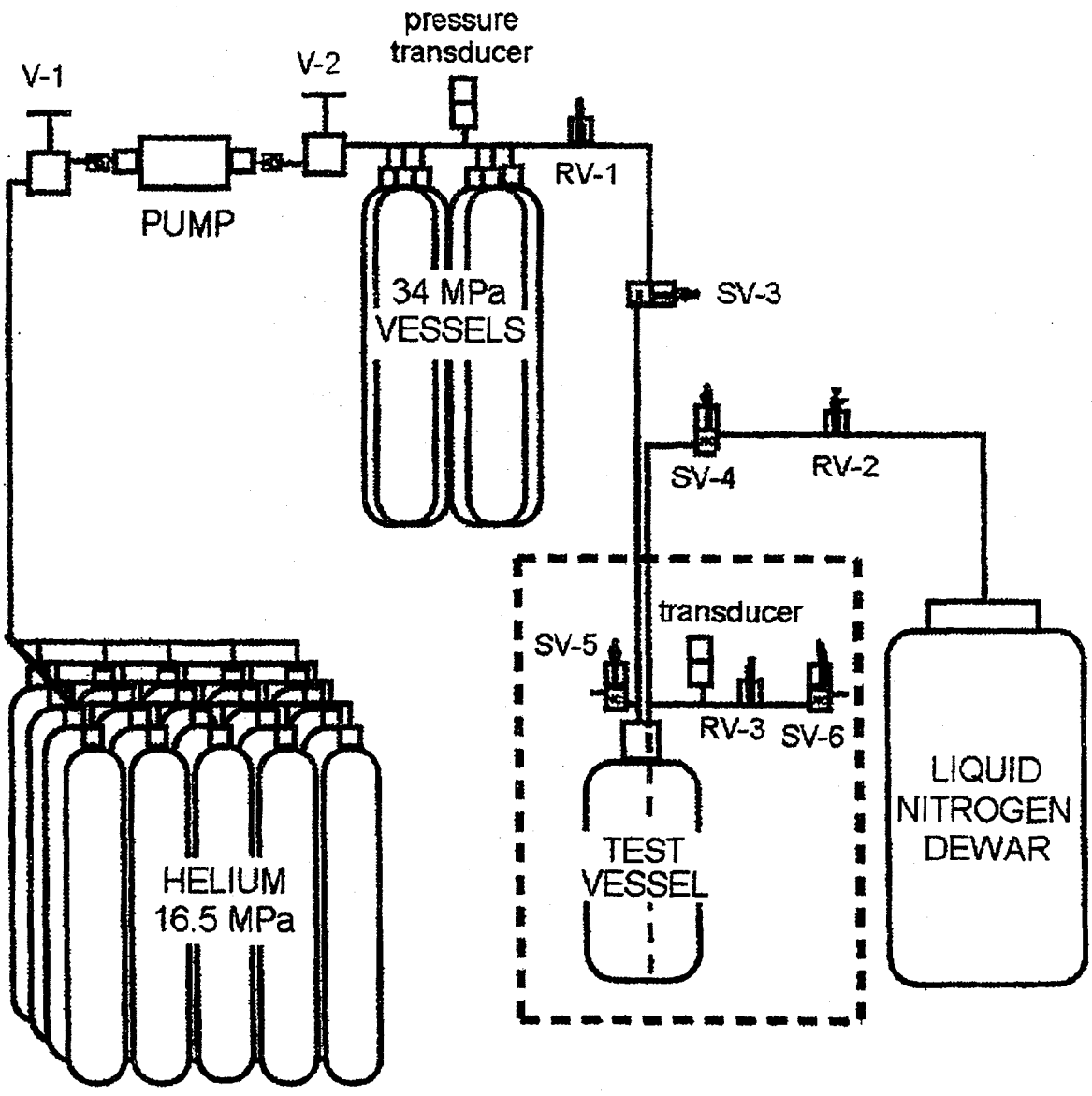

Figure 5. Schematic of the experimental setup for temperature and pressure cycling of a pressure vessel.

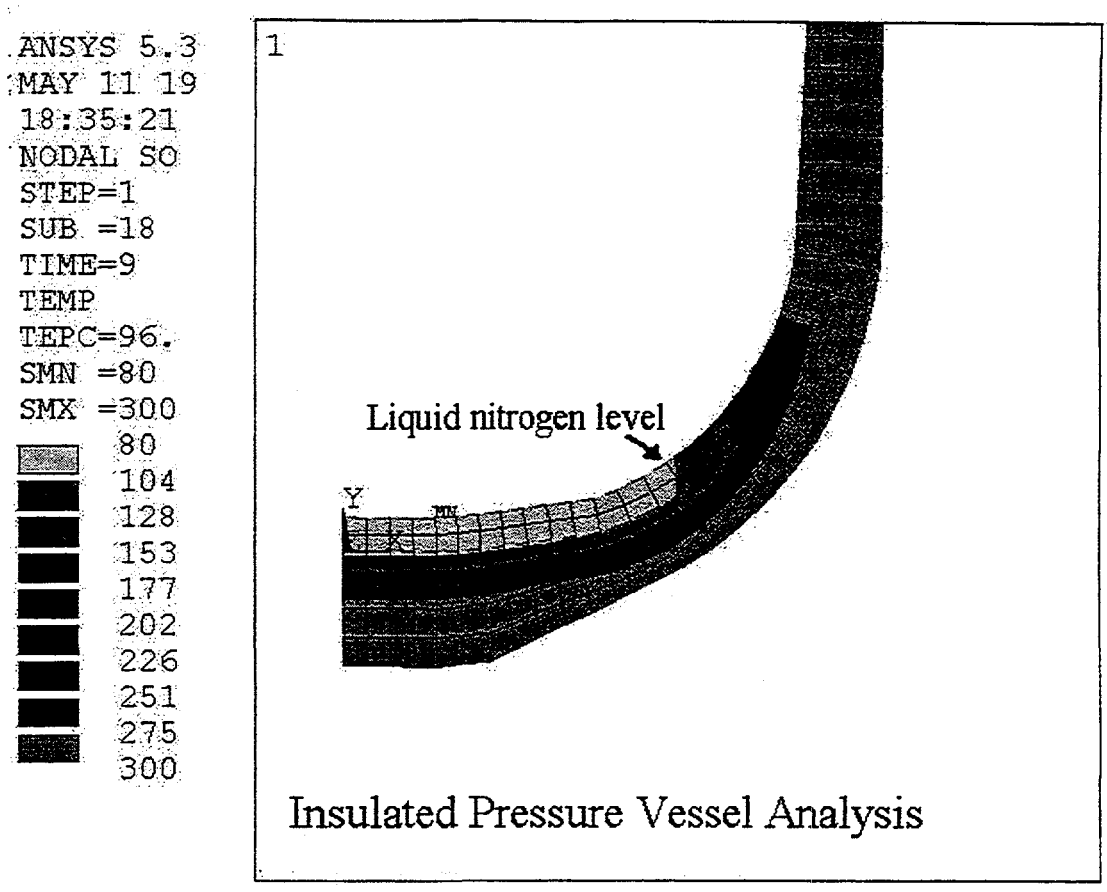

Figure 6. Finite element analysis mesh and temperature distribution during the early stage of the filling process. The figure shows the lower part of the vessel, along with the mesh used in the simulation. Only half of the vessel is analyzed, due to symmetry.

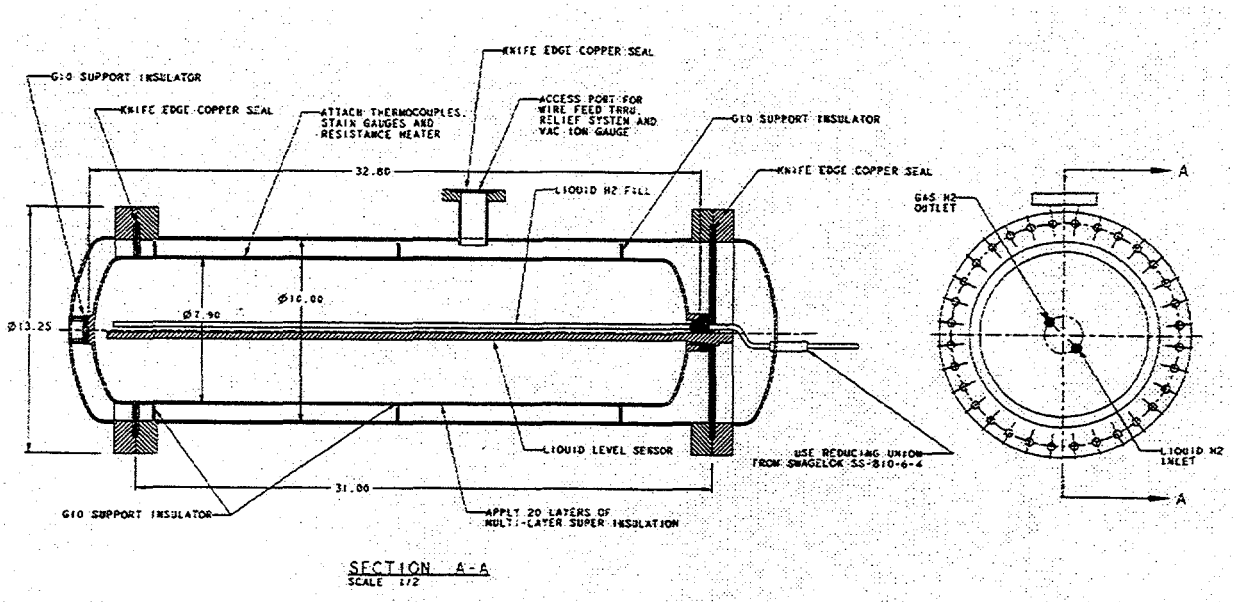

Figure 7. Insulation design for pressure vessel. The figure shows a vacuum space, for obtaining high thermal performance from the multilayer insulation, and instrumentation for pressure, temperature, level and strain.

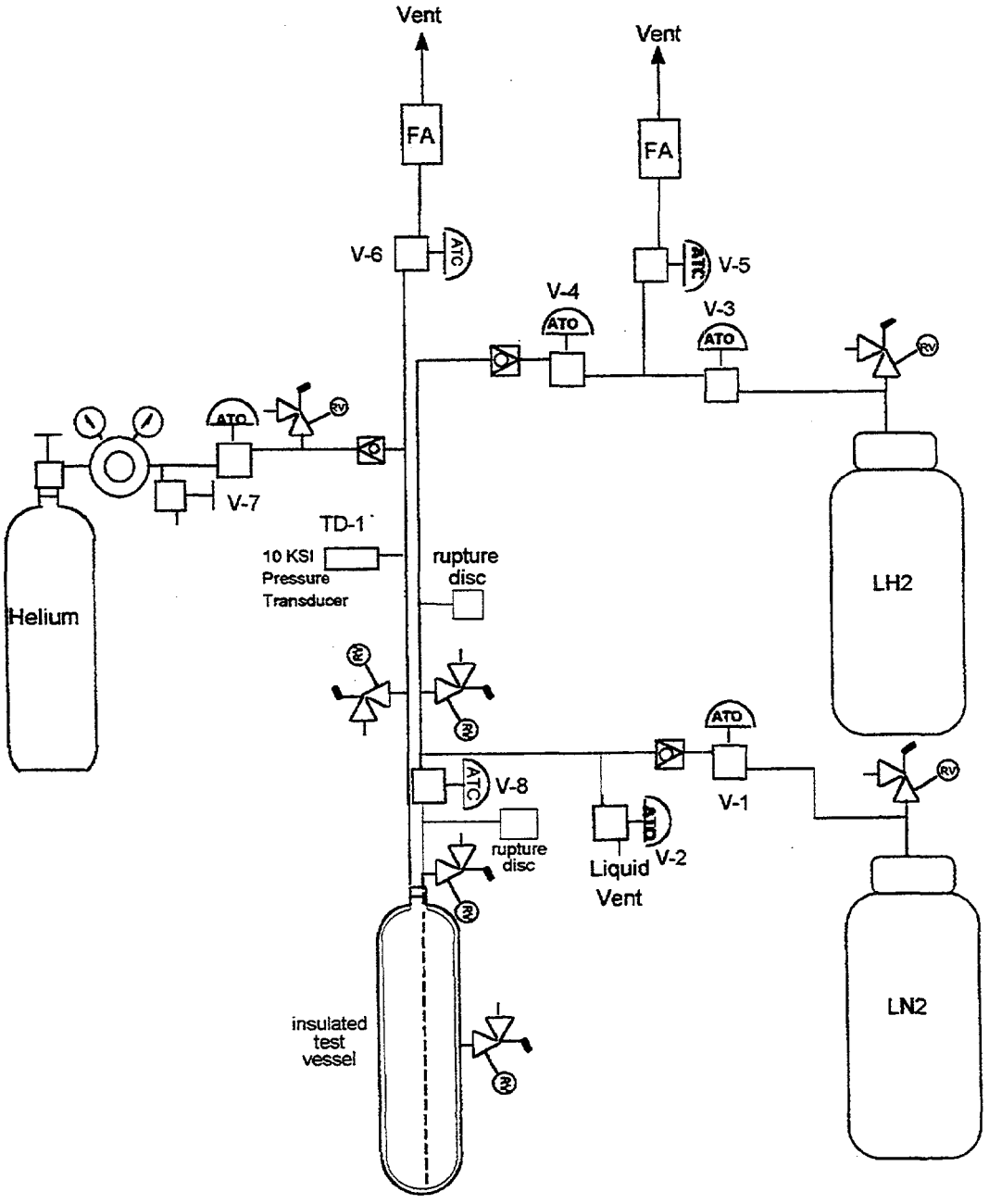

Figure 8. Schematic of the experimental setup for liquid hydrogen cycling of the instrumented and insulated pressure vessel.

SEPARATION MEMBRANE DEVELOPMENT

Myung W. Lee
Savannah River Technology Center
Savannah River Site
Aiken, SC 29808

Abstract

A ceramic membrane has been developed to separate hydrogen from other gases. The method used is a sol-gel process. A thin layer of dense ceramic material is coated on a coarse ceramic filter substrate. The pore size distribution in the thin layer is controlled by a densification of the coating materials by heat treatment. The membrane has been tested by permeation measurement of the hydrogen and other gases. Selectivity of the membrane has been achieved to separate hydrogen from carbon monoxide. The permeation rate of hydrogen through the ceramic membrane was about 20 times larger than Pd-Ag membrane.

Background

Billions of standard cubic feet of hydrogen are consumed every day by the refinery industry alone. Demand for hydrogen is continue growing in recent years. In the hydrogen recovery and production, separation of hydrogen from other gases is important part of process. PSA is main separation method. Metal alloys or composite metal membrane have been used for hydrogen purification. Metal is sensitive to poisonous gases. Ceramic membrane, inert to poisonous gas, is desirable.

The sol-gel encapsulated metal hydrides, developed at Savannah River Technology Center have solved the problem of decrepitation of metal hydride particle. The pore size of the sol-gel coating can be tailored to discriminate between H_2 (2.89A) and CO (3.76A) on the basis

of molecular size in much the same manner that silica membranes have been shown to have the ability to separate hydrogen and nitrogen.

Overall Approach

Overall objective is to develop and demonstrate a thin dense glass coating on a coarse ceramic substrate which allow hydrogen to easily permeate through but no other gases. The process of the glass coating is formed by the sol-gel process. The pore size of the thin dense layer are controlled by a heat treatment which densify the coating.

Filter Fabrications

Sol-Gel Formulations

The sol-gel technique has been well published in the literature (ref . 1-9). The technique stars with the hydrolysis of an organo-metallic compound. The hydrolyzed compound is polymerized via water and alcohol condensations and dried by removing water and the solvent. An acid or base is used to catalyze the polymerization reaction. The heat treatment following the drying step is used to further modify the final product. The reactions involved are generally as follows:

Organo-metallic Compound:

M-(OR)4

Hydrolysis:

(OR)4-M-OR + H2O = (OR)3-M-OH + ROH

Water Condensation:

(OR)3-M-OH + (OR)3-M-OH = (OR)3-M-O-M-(OR)3 + H2O

Alcohol Condensation:

(OR)3-M-OH + (OR)3-M-OR = (OR)3-M-O-M-(OR)3 + ROH

where M is metal such as Si, Al, or Ti and R for an alkyl group (-CxH2x+1) in most case -C2H5 or -CH3.

The first solution is formed by mixing one part ethanol into 2 part tetraethyl orthosilicate (TEOS). The second solution is formed by mixing 2~5 part of ethanol to one part of water. Acidity of second solution is adjusted by adding HCl until the PH is in the range of 1 to 2.5. The second solution is added to the first solution while stirring continuously to for sol. The sol is then covered and allowed to age for 2~24 hours which allows the sol, initially a water-like consistency to become viscous. This viscous sol is used to make thin coating.

Sol-gel filter Formation

The viscous sol is coated on a course substrate (silica or alumina). Next step is the drying to evaporate water and alcohol formed by a polymerization. The filter then allowed to gel completely for few days. The drying can be done either by evaporation at room temperature or in a ventilated oven at elevated temperature.

Heat Treatment

The dried sample can be heat treated under vacuum to vary the pore size. While the sample in under the vacuum, its temperature is raised to a target value and maintained for 2 hours. The target temperature used are 200, 300. 400, and 600C. Further treatments are done by a microwave oven. Heat treatment densify the coating.

Experimental Results

Performance Testing

The performance of the sample has been tested by measuring the permeation rate of hydrogen through filter. The pressurized hydrogen gas is allowed to flow through the filter to a constant lower pressure. The flow rate are determined. The results are compared with the flow rate of typical Pd-Ag membrane in Figure 1. At low pressure range, sample tested was about 20 time larger permeation rate than typical Pd-Ag membrane.

Conclusion

Hydrogen filter are produced by a sol-gel process. Preliminary test shows promising results. Improvement on defect free, large filter is in progress.

References

1. Keizer,K., Leenaars,A., and Burggraaf, A., *Inorganic, porous membranes: Preparation, Structure and Potential applications*, in Ceramics in Advanced Energy Technologies, Krockel, merz, and Van der Biest, Editors, 1982, D. Reidel Publishing Co., Boston
2. Gillot, J., *The developing use of inorganic membrane: a historical perspective in inorganic Membrane: Synthesis, Characteristics, and Applications*, Bhave, Editor, 1991, Van Nortrand Reinhold, New York
3. Yoldas, B.E., *Alumina sol preparation from alkoxides*, American Ceramic Soc. Bull., 1975, **54**, 285
4. Okubo, T., Haruata, K., Kusakabe, K., and Morooka, S., *Preparation of a sol-gel derived thin membrane on a porous ceramic hollow fiber by the filtration technique*, J. Mebr. Sci., 1991, **59(1)**, 73-80
5. Scherer, G.W., *Recent progress in drying of gels*, J. Non-Cryst. Solids, 1992, **147**, 363-374
6. Atkinson, A. and Guppy, R., *Mechanical stability of sol-gel films*, J. Mat. Sci. 1991, **26**, 3869-3873
7. Garino, T.J., *The cracking of sol-gel films during drying*, in Material Research Society Symposium, 1990, Pittsburgh, Material Research Society, 497-502
8. Clasen, R., *Preparation and Sintering of high-density green bodies to high purity silica glass*, J. Non-Cryst. Solids, 1987, **89**, 335-34
9. Schmidt, H., Rinn, G., Nass, R., and Sporn, D., Film preparation by inorganic-organic sol-gel synthesis, Mat.Res. Soc. Symp. Prc., 1988, **121**, 734-757

Figure 1 Permeability for Hydrogen

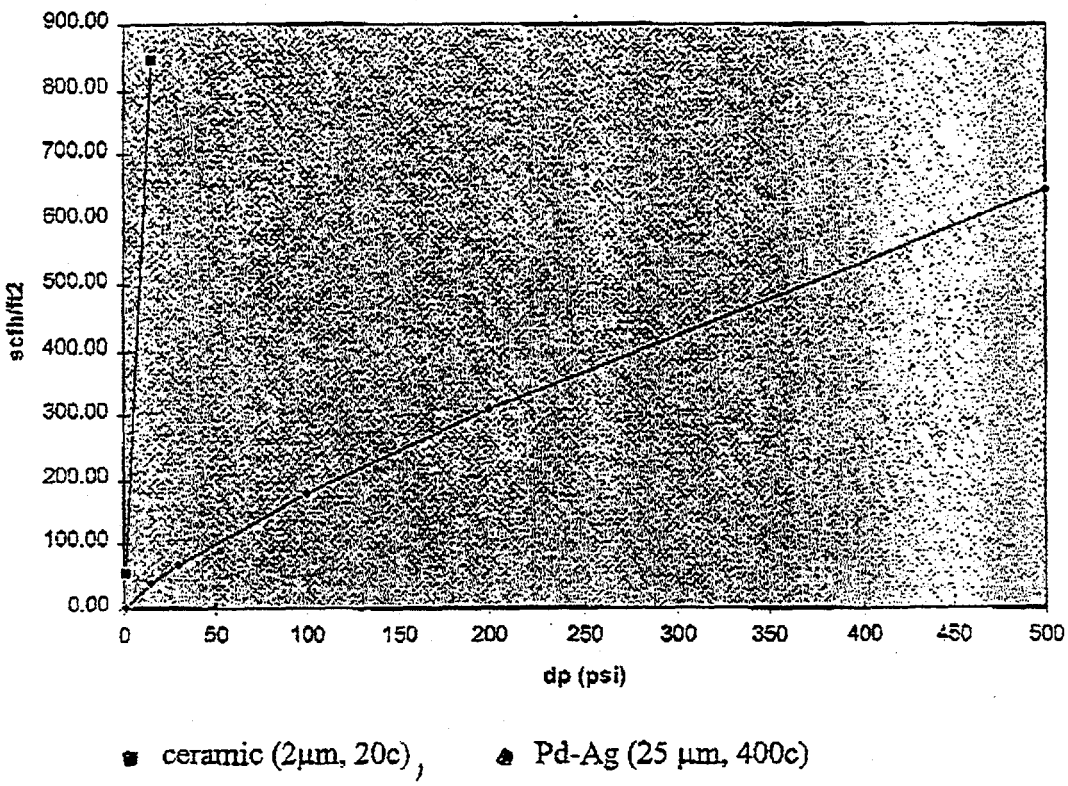

Figure 1 Permeability for Hydrogen

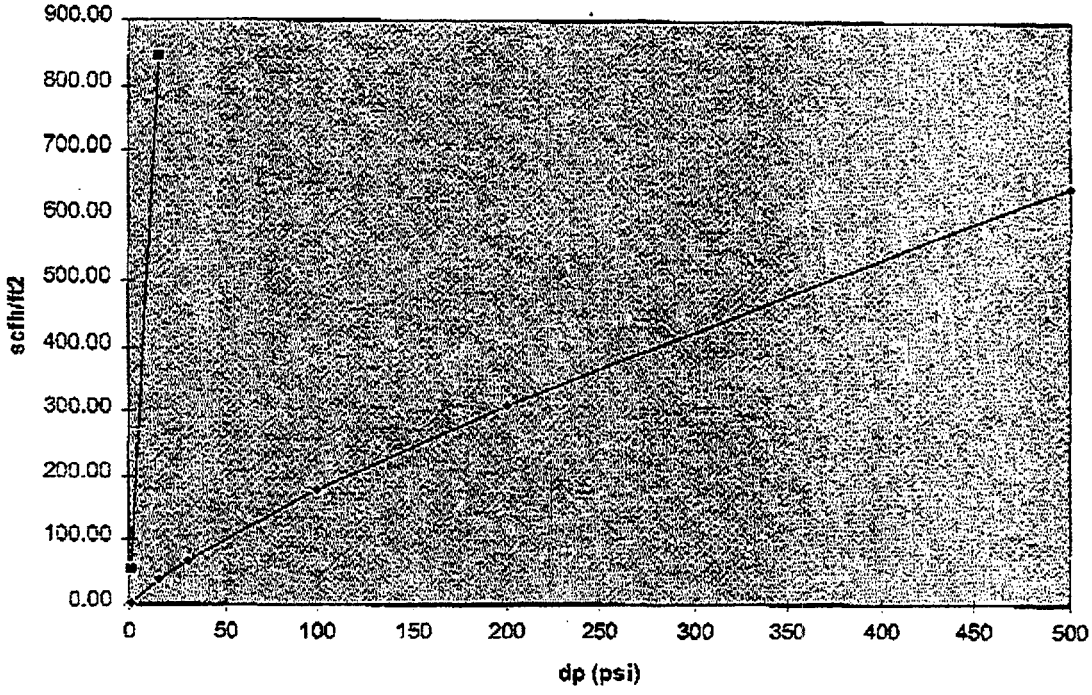

■ ceramic (2μm, 20c), ▲ Pd-Ag (25 μm, 400c)

HYDROGEN STORAGE IN GRAPHITE NANOFIBERS

C. Park, C. D. Tan, R. Hidalgo, R. T. K. Baker and N. M. Rodriguez
Chemistry Department, Hurtig Hall,
Northeastern University,
Boston, MA 02115

Abstract

Graphite nanofibers (GNF) are a type of material that is produced by the decomposition of carbon containing gases over metal catalyst particles at temperatures around 600°C. These molecularly engineered structures consist of graphene sheets perfectly arranged in a parallel, perpendicular or at angle orientation with respect to the fiber axis. The most important feature of the material is that only edges are exposed. Such an arrangement imparts the material with unique properties for gas adsorption because the evenly separated layers constitute the most ordered set of nanopores that can accommodate an adsorbate in the most efficient manner. In addition, the non-rigid pore walls can also expand so as to accommodate hydrogen in a multilayer conformation. Of the many varieties of structures that can be produced we have discovered that when gram quantities of a selected number of GNF are exposed to hydrogen at pressures of ~2,000 psi, they are capable of adsorbing and storing up to 40 wt % of hydrogen. It is believed that a strong interaction is established between hydrogen and the delocalized p-electrons present in the graphite layers and therefore a new type of chemistry is occurring within these confined structures.

Introduction

The ever growing demand for energy, as well as the increase in environmental concerns, are exerting pressure for the development of cleaner fuels and more efficient engines. The conventional internal combustion engine currently used in most automobiles produces an array of

pollutants including, particulate materials, nitrogen oxides, sulfur oxides, hydrocarbons and carbon monoxide as well as large amounts of carbon dioxide. Although reduction of toxic emissions has been achieved to some degree by the use of the catalytic converter unit, this approach puts great demands on supported noble metal systems, which are required to operate with maximum efficiency over extreme temperature ranges (Taylor 1984).

It has been predicted that oil reserves will peak in about 15 years and therefore, in order to sustain the energy demand it is necessary to find new fuels and more efficient processes. A new technology that is becoming the subject of increasing research effort, is that of fuel cells. In this method, direct conversion from chemical into electrical energy is realized, and consequently, the efficiency of the process is enhanced by almost a factor of three over that of the conventional internal combustion engine, where most of the energy is wasted as heat. Hydrogen and oxygen are the essential reactants for the PEM fuel cells that are being developed for electric vehicles (Appleby 1989, Kordesch 1995). A number of factors contribute to the choice of hydrogen as a fuel, not least being the fact that it is one of the most abundant elements found in nature and during its reaction with oxygen the only product is water. Unfortunately, due to the lack of a suitable storage system and a combination of both volume and weight limitations, the driving range of electric vehicles is restricted to about 100 miles. This is one of the shortcomings that has prevented this very promising technology from reaching the commercial arena.

Currently, four methods are being considered for hydrogen storage in commercial applications; pressurized gas storage, liquefied hydrogen, selected metal hydrides and refrigerated super-activated carbon. Pressurized gas offers the advantage of being simple, however, in mobile applications the large volume coupled with the small capacity (8.7 wt. % at 5,000 psi and 7.6 wt. % at 10,000 psi) will limit its practicality. Liquefied hydrogen is expensive since it requires constant refrigeration and loss of the gas by evaporation is inevitable. While the latter two approaches may offer benefits over the other technologies with regard to safety aspects, they do however, have their own set of associated drawbacks. Metal hydrides are heavy, expensive, release heat during the hydrogen absorption process (Lynch 1991) and require the use of about one third of the stored energy during the release of the hydrogen fuel.

Because of their extremely high surface area, active carbons constitute without any doubt the preferred adsorbent in many processes (Noh 1987, Mattson 1971, Puri, 1970, Wigmans 1986). Carbon molecular sieves have been known for several decades (Walker 1966, Koresh 1980, Koresh 1981, Kappor,1989, Walker 1990, Cabrera 1993, Hynek 1997) and present an alternative choice for many commercial gas separation processes. These structures are produced from a variety of carbonaceous solids of different origins, including active carbons, cokes, and chars. Activated carbons possess a wide pore size distribution, where the fraction of micro- and nanopores is rather small. While these materials are very effective for the adsorption of a variety of molecules, one has to consider that the interaction between the adsorbent and the adsorbate is only of a physical nature, and as a consequence, the retention of gases is only achieved at extremely low temperatures. The use of activated carbons for gas storage at high temperatures has been found to be ineffective since the solid takes up storage volume without appearing to add any substantial benefits to the overall capacity.

In more recent years there has been a growing interest in the effects of confinement and the influence of the walls of the solid on the gas adsorption process. Indeed, theoretical studies carried out by Gubbins (Cracknell 1995, Rhykerd 1975, Balbuena 1993) using modern statistical mechanic fluids theory indicate that when fluids are restricted within narrow pores, their behavior does not conform to that predicted by classical thermodynamic methods. Non local density functional theory method calculations and molecular simulations have been employed to determine the optimum pore size of carbons for gas adsorption and it was concluded that the ideal system consisted of slit pores bounded by parallel single layers of graphite (Cracknell 1995). One of the reasons for this requirement is that in such a configuration, the solid will exhibit the highest ratio of nanopore volume to total volume and as a consequence void space will be eliminated.

In addition, since adsorption of gas molecules on the wall of the pore can cause profound perturbations in the system it is perhaps this aspect that might allow retention of the adsorbate at higher temperatures and at low pressures. It is well known that certain solids, particularly metals, chemisorb gases at room temperature and indeed, this property is routinely used to determine the metal surface area in supported catalyst systems (Anderson 1975). In contrast to physical adsorption, chemisorption requires energy in order to release the adsorbed molecules.

Graphite, is a layered solid in which the various planes are bonded by van der Waals forces where the minimum distance possible between the carbon layers for single crystal graphite is 0.335 nm. In this crystalline structure delocalized π-electrons form a cloud above and below the basal plane and it is this arrangement that imparts a certain degree of metallic character to the solid that results in a relatively high electrical conductivity across each carbon layer. The interlayer spacing in graphitic materials is a property dependent on a number of parameters including, the nature and the thermal history of the precursor, and can vary between 0.335 and 0.342 nm, which by appropriate intercalation procedures can be expanded up to values of 0.9 nm (Dresselhaus 1993, Dresselhaus 1981). Unfortunately, in its conventional form of flat sheets, graphite has an extremely low surface area (~ 0.5 m^2/g) resulting from the very small number of edges that are exposed and this aspect has tended to limit its usefulness as a practical selective adsorption agent for small diameter molecules due to diffusion restrictions.

Graphite nanofibers, GNF, are a novel material that has been developed in our laboratory from the metal catalyzed decomposition of certain hydrocarbons (Baker 1987, Kim 1991). These structures possess a cross-sectional area that varies between 5 to 100 nm and have lengths ranging from 5 to 100 mm (Rodriguez 1993). High-resolution transmission electron microscopy studies have revealed that the nanofibers consist of extremely well-ordered graphite platelets (Rodriguez 1995), which are oriented in various directions with respect to the fiber axis. The arrangement of the graphene layers can be tailored to a desired geometry by choice of the correct catalyst system and reaction conditions, and it is therefore possible to generate structures where the layers are stacked in a "ribbon", "herring-bone", or "perpendicular" orientation with respect to the direction of the fiber axis.

Experimental

Synthesis and Characterization of Graphite Nanofibers

GNF were prepared from the decomposition of ethylene, carbon monoxide and hydrogen mixtures over selected metal powders at temperatures between 500 and 700°C as described in previous publications (Baker 1987, Kim 1991). The solids were demineralized by immersing them in a mineral acid solution for a period of a week, washed and dried before testing. GNF were examined by high resolution transmission electron microscopy, temperature programmed oxidation, X-ray diffraction and nitrogen adsorption techniques.

Hydrogen Adsorption/Desorption

Hydrogen adsorption experiments were performed in a custom built unit that consists of two stainless steel vessels. The sample vessel, which is 100 cm^3 in volume is connected to the hydrogen reservoir vessel via a high pressure bellows valve. GNF are loaded in the sample container and the entire system evacuated in an oil free environment for about 5 hours at 150°C. The connecting valve is then closed and the sample cooled to room temperature for several hours. Hydrogen is permitted to enter the reservoir vessel and the pressure allowed to reach thermal equilibrium over a two hour period. The connecting valve is then opened and hydrogen immediately gains access to the sample and undergoes adsorption at room temperature. Blank experiments to determine the various parameters involved during gas expansion were conducted in the absence of GNF and also in the presence of other solids. Approximately 1 gram of GNF was placed in the adsorption unit and allowed to react with hydrogen at 1800 psi at room temperature for a several hours. Changes in pressure were carefully monitored as a function of time. Following adsorption hydrogen was allowed to exit the system and the volume carefully measured by displacement of water. Throughout these processes the adsorption unit was continuously monitored with a high sensitivity H_2 detector to ensure a complete absence of leaks in the system.

Results and Discussion

TEM examinations of the carbon deposited during the catalytic formation of GNF indicated that under the conditions described above, nanofibers were the only product of the reaction, with no other forms of carbon being present. A high resolution transmission micrograph of the typical appearance of the nanofibers is presented in Figure 1, where the graphene layers that are separated at a distance of ~ 0.34 nm can be observed. A schematic rendition illustrating the arrangement of graphite platelets within the structure is shown in Figure 2a.

When samples of catalytically grown GNF were placed in the adsorption unit, hydrogen uptake to unprecedented levels was obtained. Certain types of graphite nanofibers were found to be capable of adsorbing and storing extremely high quantities of hydrogen at room temperatures in amounts that were over an order of magnitude higher than those found with conventional materials such as metal hydrides (Chambers 1998). Figure 3 shows two typical isotherms for the adsorption of the hydrogen over a sample of GNF. Following the first adsorption, hydrogen was

released from the specimen and a second adsorption was carried out. Based on the pressure drop of the second uptake it is estimated that this sample of GNF adsorbs over 40 wt % of hydrogen.

The extraordinary hydrogen adsorption behavior exhibited by GNF is believed to be due to the unique structure of this molecularly designed solid. The material consists of graphite platelets possessing a small cross-sectional area, which is estimated to be on average 20 nm, combined with an abundance of exposed edges. In addition, since hydrogen possesses a kinetic diameter of 0.289 nm, a value slightly smaller than that of the interlayer spacing in graphite nanofibers, 0.342 nm as measured by X-ray diffraction, adsorption occurs due to the gas being able to readily gain access to the inner regions of the solid (Figure 2b). Another aspect of significance in this regard is that the solid consists entirely of non-rigid wall nanopores that extend across the nanofiber.

Following adsorption we found that a significant amount of hydrogen was still retained within the structure and the presence of this stored gas caused the lattice to expand as determined by X-ray diffraction. The interaction of hydrogen with graphite surfaces has been investigated using various techniques including neutron scattering (Nielsen 1980). It has been concluded that a commensurate $\sqrt{3} \times \sqrt{3}$ structure is achieved at low coverage and an incommensurate layer is observed at monolayer coverage. Following the formation of a second monolayer, a lattice parameter of 0.35 nm is observed. This value is smaller than the measured bulk hexagonal closed packed of 0.376 nm, which suggests that the presence of graphite causes hydrogen to adopt an unusually highly packed structure, thus accounting for the high storage levels measured in the current experiments.

Changes in the Structure of GNF Following Hydrogen Desorption

Pore size distribution and X-ray diffraction studies have indicated that following hydrogen adsorption experiments, the solid undergoes tangible structural perturbations. Figures 4a - 4c illustrate the changes in the pore size distribution of a GNF sample prior to exposure to a high pressure of hydrogen (4a), immediately following adsorption/desorption experiments (4b) and after 8 days (4c). X-ray diffraction experiments were conducted on a sample preceding the hydrogen treatment and ensuing desorption (Figures 5). It can be observed that hydrogen induces an expansion of the lattice from 3.40Å (prior to adsorption) to 3.47 following a decrease in the pressure. The structure seems to revert to the original value after a few hours.

We interpret these changes according to the notion that as hydrogen enters the graphene layers, a concomitant expansion of the lattice takes place to accommodate the gas molecules. Furthermore, we believe that following desorption, sufficient hydrogen still remains within the structure so as to generate a structure where the layers are separated to a greater extent than encountered in the initial state, (prior to hydrogen adsorption experiments) and that the residual amount is bound in a relatively strong form within the nanofiber structure being slowly released over a period of time. This process is consistent with the finding that both the pore size distribution and X-ray diffraction patterns gradually relax back to their initial state. Clearly, if the desire is to release all the hydrogen in a single burst then we must explore the potential of utilizing additional procedures to enhance this step. While raising the temperature is one option, other more sophisticated methods that can be operated at room temperature will be explored.

Future Studies

Given the extraordinary performance of GNF towards hydrogen storage, coupled with the extreme sensitivity of the material to the presence of impurities, we intend to continue our research in order to optimize the parameters associated with both adsorption and desorption phenomena. The objectives for the second part of the project are as follows:

- To scale up the production (100 grams) quantities of GNF that possesses the optimum hydrogen adsorption properties
- To examine the impact of controlled gasification treatments (activation) of GNF on the hydrogen storage capacity
- To investigate the effect of interlayer expansion of GNF via selected intercalation methods on the hydrogen adsorption/desorption characteristics
- Independent testing has been conducted by scientists in our laboratory and we plan to invite other organizations to conduct testing in our facilities following our protocol.

Acknowledgments

Financial support for this work was provided by the United States Department of Energy, Grant number DE-FC36-97GO10235

References

Anderson, J. R. 1975. In "Structure of Metallic Catalysts" Academic Press, New York, .

Appleby A. J. and Foulkes, F. R. 1989. Fuel Cell Handbook, Van Nostrand.

Baker R. T. K. and Rodriguez, N. M. 1987. U.S. Patent 5,149,584.

Balbuena, P. B. and Gubbins, K. E. 1993. Langmuir, 8 1801

Cabrera, A. L. Zehner J. E., Coe, C. G., Gaffney, T. R., Farris, T. S. and Armor, J. N., 1993. Carbon 31, 969 .

Chambers, A. Park, C. Baker R. T. K. and Rodriguez, N. M. 1998. J. Phys. Chem. in press.

Cracknell, R. F. Gubbins, K. E. Maddox M. and Nicholson, 1995. D. Accounts of Chemical Research, 28, 281

Dresselhaus, M. S. and Dresselhaus, 1981. G. Adv. Phys. 30, 139 .

Dresselhaus, M. S. Dresselhaus, G. Suguhara, K. Spain, I. L. andGoldberg, H. A. "Graphite Fibers and Filaments", Springer-Verlag, Berlin, 1993.

Hynek, S, Fuller, W. and Bentley, J. 1997. Int. J. Hydrogen Energy, 22, 601

Kapoor, A., and Yang, R. T., 1989. Chem. Eng. Sci. 44, 1723 .

Kim, M. S. , Rodriguez N. M.and Baker, R. T. K. 1991. .J. Catal. 131, 60

Kordesch K. V. and Simader, G. R. 1995. Chem. Rev. 95, 191

Koresh, J., and Soffer, A., 1980. J. C. S. Faraday 1, 76, 2457, 2472 .

Koresh, J., and Soffer, A., 1981. J. C. S. Faraday 1, 77, 3005 .

Lynch, F. E. 1991. J. Less Common Metals 172, 943 .

Mattson J. S. and Mark, Jr., H. B. 1971. "Activated Carbons" Dekker, New York. .

Nielsen M. 1980. "Phase Transitions in Surface Films" edited by J.G. Dash and J. Ruvalds. Plenum Press, NY

Noh, J. S. Agarwal R. K. and Schwarz, J. A. 1987. Int. J. Hydrogen Energy, 12, 693 .

Puri, B. R. 1970. .in "Chemistry and Physics of Carbon" P. L. Walker, Jr., Ed., Dekker, New York, 6, 191

Rhykerd, C., Tan Z.L., Pozzhar A. and Gubbins, K. E. J. 1991. Chem. Soc. Faraday Trans, 87 2011

Rodriguez, N. M. 1993, J. Mater. Res. 8, 3233 .

Rodriguez, N. M. Chambers A. and Baker, R. T. K. 1995. Langmuir 11, 3862 .

Taylor, K. C. 1984. in Automobile Catalytic Converters, Springer-Verlag, New York, p. 120 .

Walker P. L., Jr., 1990. Carbon 28, 261 .

Walker, P. L., Jr., Austin, L. G., and Nandi, S. P., 1966. in "Chemistry and Physics of Carbon", P. L. Walker, Jr., ed., Vol. 2, p. 257, Marcel Dekker, New York .

Wigmans, T. 1986. "Carbon and Coal Gasification" J. L. Figueiredo and J. A. Moulijn, Eds., NATO ASI Series No.105, Martinus Nijhoff Publ. Dordrecht, p. 559 .

Figure Captions

Figure 1. High resolution electron micrograph of a graphite nanofiber, showing the graphite platelets in a parallel arrangement.

Figure 2. (a) Schematic representation of the structure of graphite nanofiber; (b) enlarged section showing details of the hydrogen adsorption process.

Figure 3. Change in hydrogen pressure as a function of time in the presence of 1.1285 g of GNF H-200 at room temperature.

Figure 4. Pores size distribution of an H-500 GNF: (a) before hydrogen adsorption; (b) immediately following adsorption/desorption; and (c) 8 days after hydrogen treatment.

Figure 5. X-ray diffraction patterns of a GNF H-200 sample (a) prior to hydrogen adsorption; (b) immediately following adsorption/desorption; (c) 24 hours after hydrogen treatment, and (d) 48 hours following hydrogen treatment.

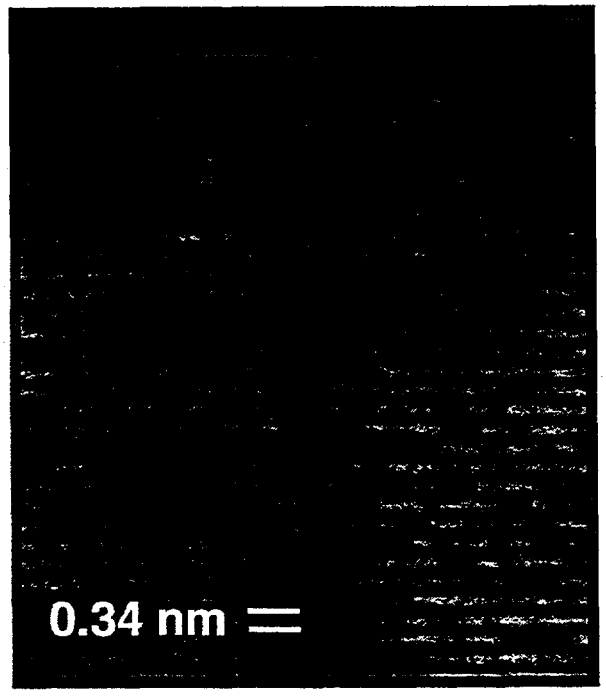

Figure 1

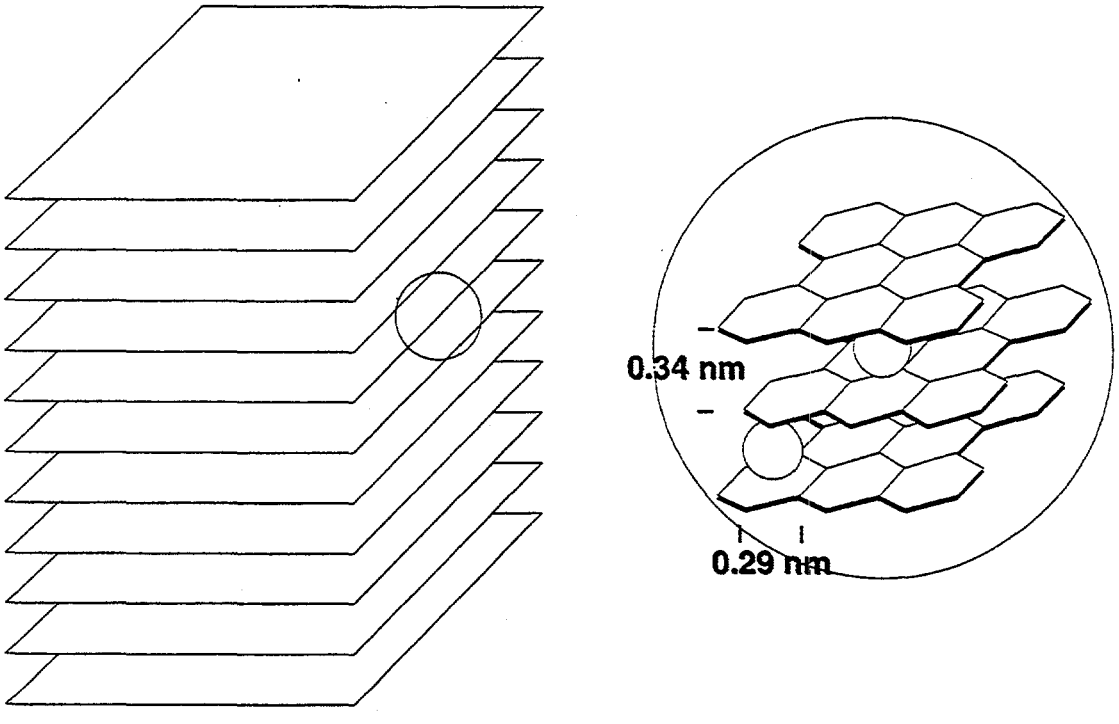

Figure 2

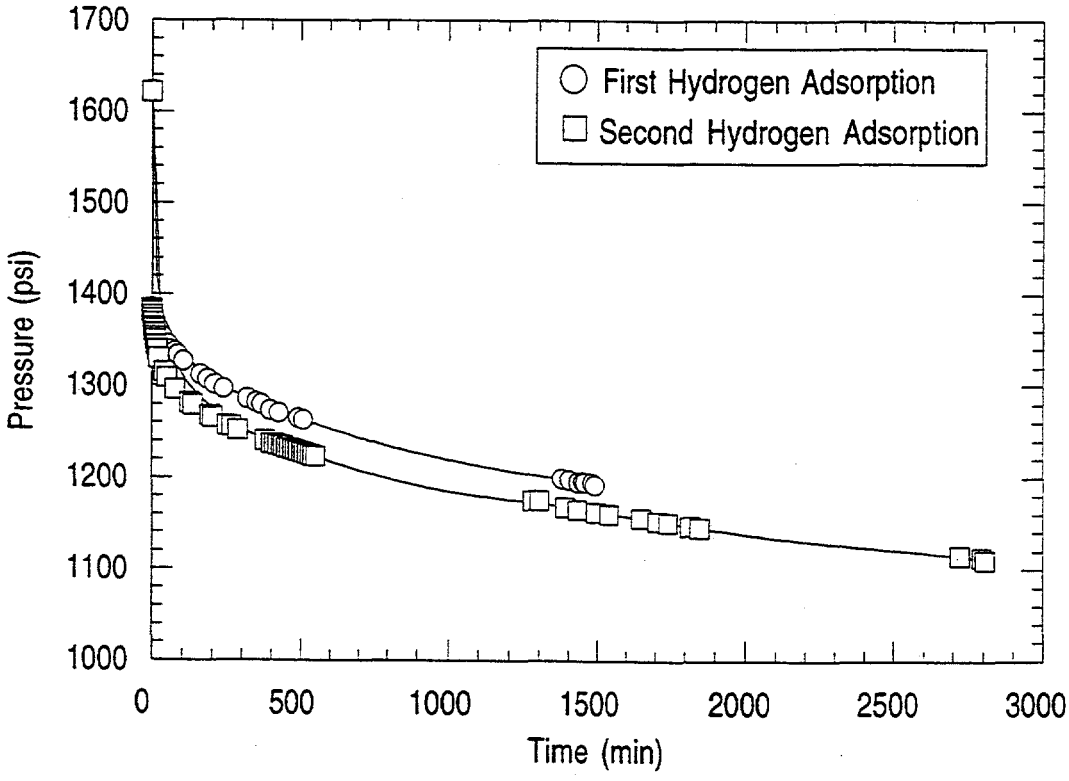
First Hydrogen Adsorption
Second Hydrogen Adsorption
Pressure (psi)
1700
1600
1500
1400
1300
1200
1100
1000
0
500
1000
1500
2000
2500
3000
Time (min)

Figure 3

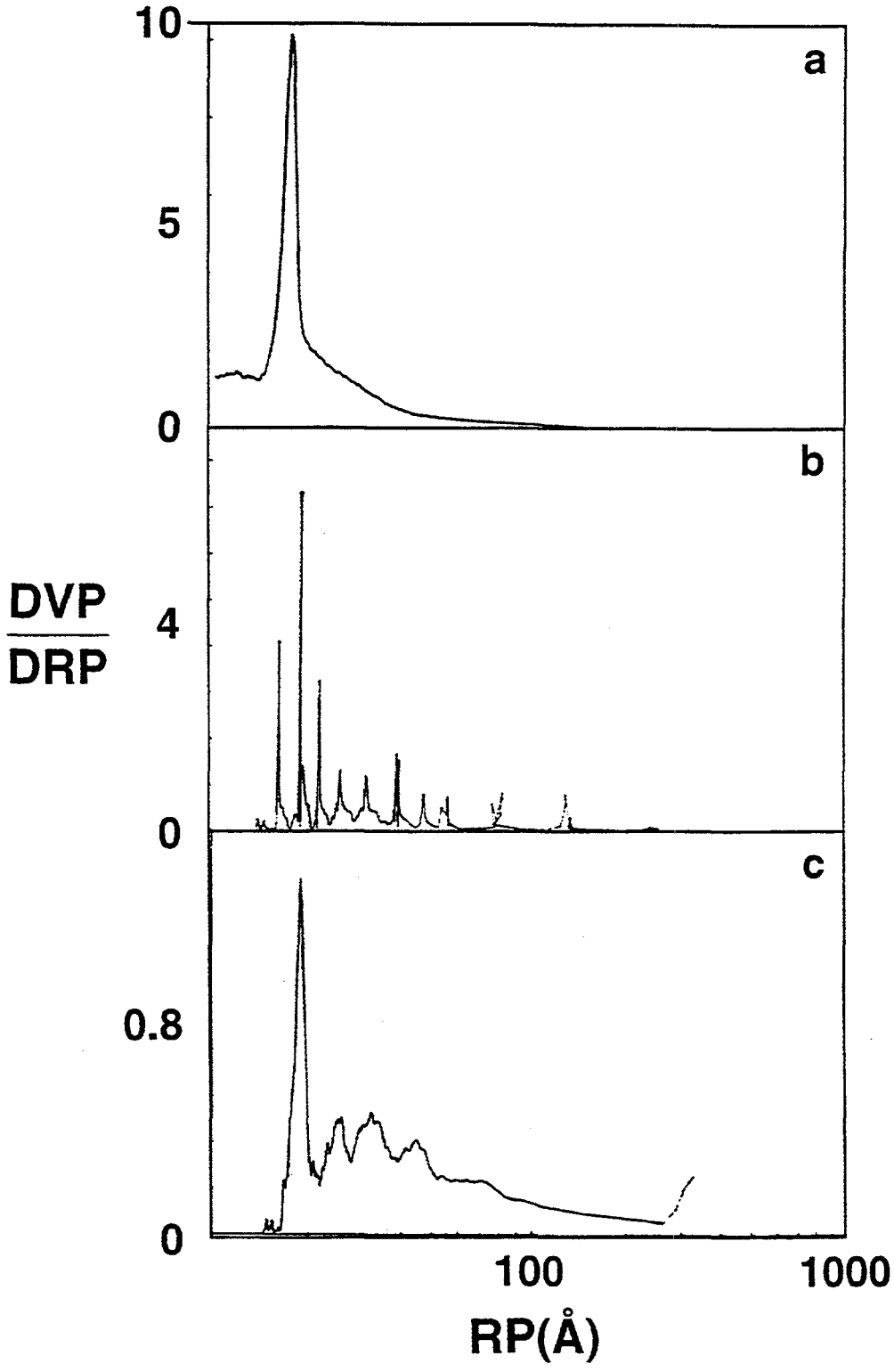

Figure 4

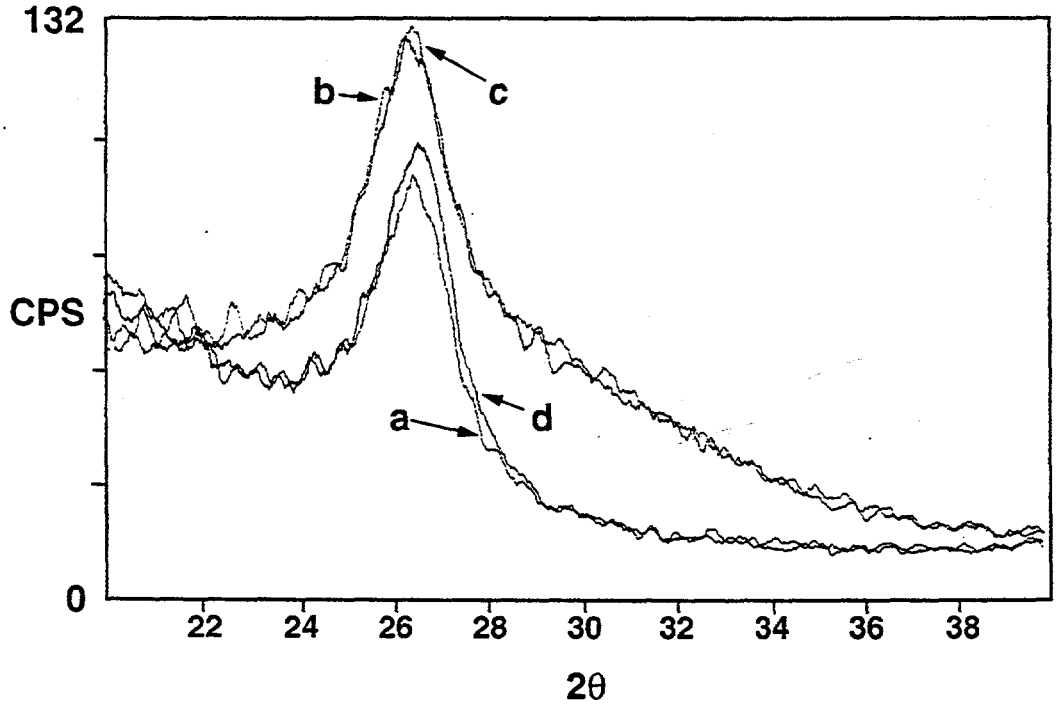

Figure 5

CARBON NANOTUBE MATERIALS FOR HYDROGEN STORAGE

A.C. Dillon, P.A. Parilla, K.M. Jones, G. Riker, and M.J. Heben
National Renewable Energy Laboratory
Golden, CO 80401-3393

Abstract

Carbon single-wall nanotubes (SWNTs) are essentially elongated pores of molecular dimensions and are capable of adsorbing hydrogen at relatively high temperatures and low pressures. This behavior is unique to these materials and indicates that SWNTs are the ideal building block for constructing safe, efficient, and high energy density adsorbents for hydrogen storage applications. In past work we developed methods for preparing and opening SWNTs, discovered the unique adsorption properties of these new materials, confirmed that hydrogen is stabilized by physical rather than chemical interactions, measured the strength of interaction to be ~ 5 times higher than for adsorption on planar graphite, and performed infrared absorption spectroscopy to determine the chemical nature of the surface terminations before, during, and after oxidation. This year we have made significant advances in synthesis and characterization of SWNT materials so that we can now prepare gram quantities of high-purity SWNT samples and measure and control the diameter distribution of the tubes by varying key parameters during synthesis. We have also developed methods which purify nanotubes and cut nanotubes into shorter segments. These capabilities provide a means for opening the (10,10) tubes which were unreactive to the oxidation methods that successfully opened (9,9) tubes, and offer a path towards organizing nanotube segments to enable high volumetric hydrogen storage densities. We also performed temperature programmed desorption spectroscopy on high purity carbon nanotube material obtained from our collaborator Prof. Patrick Bernier and finished construction of a high precision Seivert's apparatus which will allow the hydrogen pressure- temperature-composition phase diagrams to be evaluated for SWNT materials.

Statement of the Problem / Relevance of the Work

Background

With the 1990 Clean Air Act and the 1992 Energy Policy Act, the United States recognized the need for a long term transition strategy to cleaner transportation fuels [1]. This realization comes while the U.S. continues to increase petroleum imports beyond 50% of total oil consumption, with nearly 50% of the total oil consumed being used in the transportation sector [2]. Because of the potential for tremendous adverse environmental, economic, and national security impacts, fossil fuels must be replaced with pollution-free fuels derived from renewable resources. Hydrogen is an ideal candidate as it is available from domestic renewable resources and usable without pollution. It could, therefore, provide the long-term solution to the problems created by the Nation's dependence on fossil fuel.

Interest in hydrogen as a fuel has grown dramatically since 1990, and many advances in hydrogen production and utilization technologies have been made. However, hydrogen storage technology must be significantly advanced in performance and cost effectiveness if the U.S. is to establish a hydrogen based transportation system. As described in the U.S. DOE Hydrogen Program Plan for FY 1993 - FY 1997, compact and lightweight hydrogen storage systems for transportation do not presently exist.

Hydrogen provides more energy than either gasoline or natural gas on a weight basis. It is only when the weight, volume, and round-trip energy costs of the entire fuel storage system and charging/discharging cycle is considered that hydrogen's drawbacks become apparent. New approaches enabling more compact, lightweight, and energy efficient hydrogen storage are required in order for the wide-spread use of hydrogen powered vehicles to become a reality.

Research and development geared towards implementation of a national hydrogen energy economy has many indirect economic benefits. With almost 600 million vehicles in the world in 1992 - double the number in 1973 - the conflict between energy requirements, power generation, and environmental concerns is felt on a world-wide basis [3]. Thus, in addition to providing domestic energy alternatives, investment in hydrogen energy research will result in opportunities for U.S. technologies in over-seas markets.

Currently Available Hydrogen Storage Technologies

Hydrogen can be made available on-board vehicles in containers of compressed or liquefied H_2, in metal hydrides, or by gas-on-solid adsorption. Hydrogen can also be generated on-board by reaction or decomposition of a hydrogen containing molecular species [4]. Although each method possesses desirable characteristics, no approach satisfies all of the efficiency, size, weight, cost and safety requirements for transportation or utility use. The D.O.E. energy density goals for vehicular hydrogen storage call for systems with 6.5 wt % H_2 and 62 kg H_2/m^3 to provide a 350 mile range in a fuel cell powered vehicle. This requirement amounts to the storage of ~2.9 kg of H_2 in the weight and volume occupied by a conventional gasoline tank. These storage density goals will only be met with significant advances in the capabilities of hydrogen storage technologies.

Gas-on-solid adsorption is an inherently safe and potentially high energy density hydrogen storage method which should be more energy efficient than either chemical or metal hydrides, and compressed gas storage. Consequently, the hydrogen storage properties of high-surface-area "activated" carbons have been extensively studied [5-7]. However, activated carbons are

ineffective in hydrogen storage systems because only a small fraction of the pores in the typically wide pore-size distribution are small enough to interact strongly with gas phase hydrogen molecules.

Technical Approach and Summary of Past Work

The gas adsorption performance of a porous solid is maximized when all pores are not larger than a few molecular diameters [8]. Under these conditions the potential fields from the walls of the so-called micropores overlap to produce a stronger interaction than would be possible for adsorption on a semi-infinite plane. At sufficiently low temperatures, where the escaping tendency of the gas is much less than the adsorption potential, the entire micropore may be filled with a condensed adsorbate phase. For the case of hydrogen, with a van der Waals diameter of 2.89 Å [9] pores would be required to be smaller than ~40 Å to access this nanocapillary filling regime. Sufficiently small pores would exhibit an adsorption potential strong enough to localize H_2 at relatively high temperatures. Ideally, the entire porous volume of an adsorbent would be of the microporous variety, and the volume and mass of the adsorbent skeleton would be the minimum necessary to develop the adsorption potential and provide sufficient thermal conductivity for management of heat fluxes associated with adsorption and desorption.

We have been working on the idea that aligned and self-assembled single wall carbon nanotubes could serve as ideal hydrogen adsorbents since 1993. The concept was motivated by theoretical calculations which suggested [10] that adsorption forces for polarizable molecules within SWNTs would be stronger than for adsorption on ordinary graphite. Thus, high H_2 storage capacities could be achieved at relatively high temperatures and low pressures as compared to adsorption on activated carbons.

In the Proceedings of the 1994 Hydrogen Program Review, we presented microbalance data which demonstrated gravimetric hydrogen storage densities of up to 8.4 wt% at 82 K and 570 torr on samples containing carbon nanotubes. This substantial uptake at low hydrogen pressures demonstrated the strong interaction between hydrogen and these materials, consistent with higher heats of adsorption than can be found with activated carbons.

In the 1995 Hydrogen Program Review Proceedings, we presented the results of our temperature programmed desorption (TPD) studies which showed significant H_2 adsorption near room temperatures. The adsorption energies on nanotube materials were estimated to be a factor of 2-3 times higher than the maximum that has been observed for hydrogen adsorption on conventional activated carbons. To our knowledge, these are the first results which demonstrate the existence of stable adsorbed hydrogen *on any type of carbon at temperatures in excess of 285 K*. We also analyzed the nanotube production yields versus rod translation rate in the electric arc.

In 1996 we performed a detailed comparative investigation of the hydrogen adsorption properties of SWNT materials, activated carbon, and exfoliated graphite. We also determined that the cobalt nanoparticles present in the arc-generated soots do not play a role in the observed hydrogen uptake. We determined the amount of hydrogen which is stable at near room temperatures on a SWNT basis is ~ 10 wt%, and found that an initial heating in vacuum is essential for producing high temperature hydrogen adsorption. Further experiments suggested that SWNTs are selectively opened by oxidation during this heating, and that H_2O is more selective in oxidation than O_2 due to hydrogen termination of dangling bonds at the edges of opened nanotubes. Purposeful oxidation in H_2O resulted in hydrogen storage capacities which were improved by more than a factor of three. We also correlated the measured nanotube densities produced by specific synthesis rod translation rates during arc-discharge with hydrogen storage capacities determined by TPD. Finally, we utilized NREL's High Flux Solar Furnace to form nanotubes by a new and potentially less expensive route for the first time.

In 1997 we confirmed that H_2 is stabilized by purely physical - rather than chemical - binding. The desorption of hydrogen was found to fit 1st order desorption kinetics as expected for physisorbed H_2, and the activation energy for desorption was measured to be 19.6 kJ/mol. This value is approximately five times higher than the value expected for desorption of H_2 from planar graphite and demonstrates that SWNT soots can provide very stable environments for H_2 binding. We also employed diffuse reflectance Fourier transform infrared (DRFTIR) spectroscopy to determine the concentrations and identities of chemisorbed species bound to the carbon surface as a function of temperature, and determined that "self-oxidation" allows high-temperature adsorption of hydrogen to occur in (9,9) SWNT materials. We also began synthesizing SWNT materials in much higher yield than is currently possible with arc-discharge by using a laser vaporization process, and determined that the (10,10) tubes predominantly made by this method could not be activated towards high-temperature H_2 physisorption by the same oxidative methods that were found to be effective for tubes produced by arc-discharge.

This year we have made significant advances in synthesis and characterization of SWNT materials so that we can now prepare gram quantities of high-purity SWNT samples and measure and control the diameter distribution of the tubes by varying key parameters during synthesis. We have also developed methods which purify nanotubes and cut nanotubes into shorter segments. These capabilities provide a means for opening the (10,10) tubes which were unreactive to the oxidation methods that successfully opened (9,9) tubes, and offer a path towards organizing nanotube segments to enable high volumetric hydrogen storage densities. We also performed temperature programmed desorption spectroscopy on high purity carbon nanotube material obtained from our collaborator Prof. Patrick Bernier, and finished construction of a high precision Seivert's apparatus which will allow the hydrogen pressure- temperature-composition phase diagrams to be evaluated for SWNT materials.

Experimental

Pulsed and Continuous Wave Laser Synthesis of SWNTs

Powdered graphite (particle size 4μ) doped with 0.6 atomic % each of Co and Ni powder (particle size 1 μ) was uniformly combined with polyethylene glycol, M_n ~ 3400, (PEG) in a 50 wt% ratio. Four grams of the final mixture was pressed in a 1 inch dye with a Carver hydraulic press at 10,000 pounds for 3 min. The targets thus obtained were slowly heated in argon between 200-1000 °C over 8 hrs. and maintained at 1000 C for an additional 4 hrs. Above ~400 C the PEG was observed to completely evolve. The resulting porous cobalt-nickel/graphite targets had expanded ~ 25% and had a density of ~0.3 g/cm^2. Targets with 30 and 40 wt % PEG as well as dense targets containing only the cobalt-nickel/graphite mixture were also fabricated.

During the syntheses, the targets were supported with a tantalum holder in a 1 1/2 inch quartz tube which could be enclosed by a circular single-zone furnace. Prior to laser irradiation the quartz tube was purge-cycled three times between 1 and 750 Torr Ar over 20 min. while the target was baked with an infrared lamp. During the experiments the chamber pressure was maintained at 500 Torr with Ar flowing at 50 sccm. A Control Q-switched Nd:Yag (1064 nm) laser beam was directed at normal incidence by a scanning mirror and focused to ~ 0.86 mm^2. The beam was rastered in a rectangular pattern at frequencies of 0.01 and 1 Hz in the x and y directions, respectively. The laser power could be easily monitored at various points in the experiments with a Scientech AC50HD calorimeter head.

Targets prepared with 50% PEG were shown to be the most efficient for the room temperature production of SWNTs. The following detailed analysis was thus performed using only these highly porous targets. Pulsed laser experiments were conducted at pulse repetition rates

of 3, 6, 10 and 24 kHz. The operating characteristics of the laser are such that the pulse frequency, pulse width, and energy per pulse are all interdependent. Table 1 lists the corresponding values for these experiments as well as the calculated peak power and measured average power. Continuous wave (c.w.) experiments with average powers corresponding to the respective average powers of the pulsed runs and a maximum average power experiment of 30 W were also performed. The laser radiation exposures were 30 min. However, in each of the experiments the appearance of cones or spires on the target surface led to a dramatic drop-off in the target etch rate consistent with previous laser sputtering reports of HOPG[11]. For all of the laser runs, carbon soot was collected on the quartz tube directly above the target holder. For the c.w. and both the 24 and the 25.5 kHz pulsed experiments a "web"-like material spanned the tube walls directly behind the target holder. Following each experiment, the soot and web components were collected separately for TEM analysis.

Pulse Frequency (kHz)	Pulse Width (nsec)	Energy Density per Pulse (J/cm2)	Peak Power (kW)	Average Power (W)
3	~175	0.62	~30	16
6	~250	0.39	~13	20
10	~300	0.28	~8	24
24	~575	0.12	~2	25.5

Table 1: Pulsed laser operating characteristics of the Nd-Yag laser for the experiments. Pulse widths and peak power are estimates based on manufacturer's specifications.

A Molectron MY35 Nd:Yag laser was used to produce large quantities of material. The pulse width and repetition rate were held constant for most of these synthesis runs at values of ~100 ns and 10 Hz, respectively. When Q-switching was employed the pulse width was compressed to ~ 10 ns. A maximum energy of approximately 850 mJ/ pulse could be obtained. The laser light was focused to a spot that ranged in size from 1-10 mm^2, and rastered on the target in the same manner as reported above. Dense targets were fabricated from powdered graphite (particle size 4μ) doped with 0.6 atomic % each of Co and Ni powder (particle size 1 μ) by pressing four grams of the mixture with a Carver hydraulic press at 10,000 pounds for 3 min. in a 1 inch dye. Porous targets were ablated, rather than vaporized, at these high energy densities and were only cursorily investigated. The target temperature could be controlled from room temperature to 1200 °C with a three-zone clam-shell furnace. The pressure and flow rate of the inert ambient could be independently controlled. Most runs were performed at 500 Torr in the presence of a 100 sccm flow of Ar gas.

Purification of Laser-generated SWNTs

Approximately 0.1g of laser-generated SWNT material was refluxed in 28 ml of 2.6 M nitric acid for 25 hrs. at 120° C. Upon cooling the solution was filtered with a 0.2μ Anotec alumina filter. The collected material consisted of a black carbon paste and was resuspended in 56 ml of 2.6 M HNO_3 and sonicated for 1 hr. This new solution was again filtered, and the precipitate was rinsed with d.i. water and allowed to dry. The final collected carbon material had a paper-like consistency. Following both filtrations the nitric acid filtrate was brown in color.

Cutting of Laser-generated SWNTs

Approximately 50 mg of the laser-generated SWNT material was sonicated for 24 hrs in the following solutions: concentrated H_2SO_4, HCl, Aqua Regia (4:1 HCl:HNO_3), 3:1 H_2SO_4:HNO_3, 5:18:1 HCl:H_2SO_4:HNO_3, and 5% Bromine and Iodine in methanol. The solutions were filtered

with 0.2μ Anotec alumina filters. In each case a black carbon past-like material was collected for TEM analysis.

Transmission Electron Microscopy (TEM)

Samples were prepared for TEM by suspending 0.2 mg in 10 ml of acetone. The solutions were sonicated for 5 min., and 6 drops were placed on Ted Pella Ultra-thin Carbon Type-A 400 mesh grids. TEM images were obtained on a Phillips CM-30 TEM/STEM operating at 200 kV with a 50 μm objective aperture for improved contrast. The images were recorded on a 1024 x 1024 CCD camera

For the quantitation of SWNT contents in the laser-generated materials three grids of each sample were prepared. Three images of each grid were then taken at random different spots on the grid with a magnification of 17k for a total of nine images of each sample. An additional high resolution image displaying the lattice patterns of the individual SWNTs was taken at a magnification of 160k. The two-dimensional spatial areas of the cobalt particles, amorphous carbon / nano-crystalline graphite and SWNTs observed in the TEM images were obtained using the NIH Image graphical analysis software package. Measurements of SWNT, amorphous carbon / nanocrystalline graphite and cobalt particle densities were then quantified as a statistical average of the nine images of each sample.

For the cutting and purification studies each sample was surveyed for ~45 minutes, and ~ 5 images were recorded between 4.4k and 160k to ensure a true representation of the material.

Raman Spectroscopy

Raman spectra were obtained from pure samples of collected carbon soots. The Raman backscattering was excited using 50 mW of the 488 nm wavelength of an Ar ion laser. The scattered light was analyzed in a Jobin Yvon 270M spectrometer with a 1200 groves/nm grating equipped with a liquid-nitrogen cooled Spectrum One CCD and a holographic notch filter. A Nikon 55 mm camera lens was employed to focus the beam on the sample to a spot approximately 0.25 mm^2. Light polarized both perpendicular and parallel to the scattering plane was collected. Spectra were recorded with the laser at normal incident to the sample and with an integration time of 10-30 min. A resolution of ~ 0.6 nm (2-6 cm^{-1}) was measured with the 546.07 nm line of an Oriel Hg(Ar) spectral calibration lamp.

Temperature Programmed Desorption

Details of the ultra high vacuum (UHV) chamber employed for the TPD studies have been reported previously. Briefly, the sample is mounted at the bottom of a liquid nitrogen cooled cryostat, and a mass spectrometer provides for line-of-site detection of desorbing species. An ion gauge and capacitance manometer are employed to monitor pressure. Gas exposure is controlled with a variable conductance leak valve. Isolation gate valves separate the sample compartment during high-pressure gas exposures.

Carbon samples weighing ~1 mg were placed in a packet formed from 25 μm thick platinum foil. Pin holes in the foil enabled gas diffusion into and out of the packet. The packet could be cooled to ~90 K by the liquid nitrogen cryostat, and resistively heated with a programmable power supply. The sample temperature was measured with a thin thermocouple spot-welded to the platinum packet. The samples were heated in vacuum at 1 K/s to 970 K prior to TPD studies. Hydrogen (99.999% purity) exposures between 300-600 Torr at room temperature were employed to elucidate the H_2 adsorption properties of the samples. The samples were cooled to ~ 130 K prior to the evacuation of the hydrogen gas.

Results and Discussion

Optimization of Laser Synthesis of SWNTs

Pulsed and continuous wave laser light was directed on porous cobalt-nickel / graphite targets at room temperature and the generation of SWNTs was examined. In all of the laser experiments the condensed carbon material took the form of either a rubbery soot or a very fine web-like material. Both types of materials were collected and analyzed with TEM. These materials were composed of various fractions of amorphous carbon / nano-crystalline graphite, cobalt/nickel nano-particles and single-wall carbon nanotubes. No multi-walled carbon nanotubes or large graphitic fragments were observed. Within any given experiment, the web portion of the collected material had a much higher SWNT density than that of the soot. The web component was not observed for experiments in which SWNTs were found only in low yields in the soot. The fraction of cobalt/nickel nano-particles remained essentially constant at ~ 15% in both the web and soot materials in all of the experiments. The quantity of SWNTs produced relative to the amount of amorphous carbon or nano-crystalline graphite varied dramatically with the character of the target and laser operating parameters.

Room temperature c.w. (30 W) laser production of SWNTs was shown to be most efficient for porous targets. Dense targets, prepared without any binder, did not result in the production of SWNTs for either pulsed experiments between 3-25.5 kHz or c.w. experiments between 16-30 W. Previous studies indicated that SWNT laser-vaporization yields increased with increasing target temperature up to 1200 °C[12]. However, a target temperature of 1000 °C did not increase the SWNT production yield in comparison to room temperature, 30 W c.w. runs.

Figure 1 displays SWNT densities in a) collected web and b) collected soot components for both laser techniques with irradiation of 50% porous targets. The c.w. experiments were performed at the average power which was measured for each of the pulsed experiments. Figure 1 demonstrates that for both c.w. and pulsed operation a linear increase in the fraction of SWNTs is observed for increasing average laser power. Note that no web component of material was visible in the chamber for the slower pulsed runs of 3 and 6 kHz (0.62 and 0.39 J/cm2),. In fact, no SWNTs were observed for the 3 kHz (16 W) experiment, and the soot material collected for the 6 kHz (20 W) experiment contained only ~4% SWNTs.

The SWNT densities in the pulsed web material produced in the 10 and 24 kHz experiments closely approach the densities found in the c.w. web material. The SWNTs are much purer in the web components because they easily stick to one another while growing and adhere to the tube walls. Therefore we intuitively expect the SWNT content in the web material to be similar in both c.w. and pulsed experiments. The SWNTs in the soot fractions are not purified in the same manner. Since the web material is a small percentage ($\leq$ 30%) of the total material collected, the data in Figure 1b is more representative of the overall SWNT densities.

Figure 2 a) is a typical TEM image of the soot collected for 6 kHz pulsed laser irradiation. Only a few SWNTs are observed spanning the dense agglomerations of carbon coated cobalt/nickel nano-particles. For comparison, Fig. 2 b) and c) display TEM images of soot collected from the 10 kHz pulsed experiment and the c.w. experiment performed at the corresponding average power of 24 W. The SWNT densities for these operating conditions were ~26% and ~51%, respectively. Finally, the high purity SWNTs (~78%) present in the web component of the material generated with 30 W c.w. laser radiation is shown in Fig. 2 d). Here the material consists primarily of long bundles of SWNTs with only a small amount of amorphous carbon or nano-crystalline graphite found coating the metal particles. Closer inspection of the strands of SWNTs in the images of Fig.

2 revealed bundles of crystalline nanotubes similar to those initially reported for laser synthesis[12, 13].

Clearly the results displayed in Figs. 1 and 2 show that c.w. laser radiation is more effective than pulsed radiation in the production of SWNTs at a given average power. Clues to the underlying reason for this can be found in the experiments using a dense target (without any PEG binder) at room temperature. Here continuous wave experiments (30 W) resulted in a glowing orange spot on the target with no carbon evolution. In contrast, similar conditions for the porous target resulted in the production of a brilliant white light and the evolution of carbon vapor. Apparently the surface temperature never reached the necessary vaporization threshold in the case of the dense target due to the very high thermal conductivity. Pulsed experiments on the dense target at a peak power of ~30 kW (table 1) resulted in the slow removal of particulate matter, but no SWNTs were found. In this case the material was likely removed by ablation rather than vaporization processes. Here, the term "ablation" encompasses a broad scope of processes dealing with a more aggressive ejection of relatively large pieces of the target material. Thus, the energy incident onto the target can be dissipated in either an evaporative or ablative mechanism depending on the target porosity and the time scale in which the energy is delivered. In order to produce SWNTs efficiently it is necessary to remain dominantly in a vaporization regime.

Single-wall carbon nanotubes are highly stable graphitic structures and are therefore favored thermodynamically for formation. It is thus probable that optimal SWNT formation will occur for thermal or near-thermal processes with appropriate nucleation centers. The present study confirms the hypothesis that for the efficient laser-generation of SWNTs, it is necessary to operate primarily in a vaporization regime. In fact, if vaporization mechanisms are exclusively in operation, it may be possible to acquire material which contains only single-wall nanotubes and transition metal nano-particles. We have achieved a dominantly vaporization regime and high yield production of SWNTs at room temperature using a c.w. Nd:Yag laser process.

HNO_3 Purification of SWNTs

Single-wall carbon nanotube materials produced in gram quantities with the Molectron MY35 pulsed Nd:Yag laser vaporization methods were purified by a combination of refluxing and sonicating in nitric acid. Figure 3 a) displays a TEM image of an initial relatively low-quality laser-generated SWNT material. Long bundles of SWNTs are clearly visible in Fig. 3 a), however, the image also reveals a high concentration of amorphous carbon or nanocrystalline graphite as well as cobalt and nickel nanoparticles with diameters between 50-100 nm. Fig. 3 b) displays the same material following the nitric acid purification treatment outlined here. Note that all of the metal nanoparticles and the majority of the other non-nanotube carbon materials have been removed. A slight non-graphitic carbon coating does still remain on the bundles of SWNTs in Fig. 3 b). However, it is likely that the removal of this carbon coating may be achieved by the addition of an HNO_3 sonication step where the acid is decanted away rather than removed by filtration. This purification scheme is simpler and more effective than those previously reported in the literature [14, 15].

Cutting / Opening of Laser-generated SWNTs

The high purity laser generated SWNTs do not enable the adsorption of large quantities of hydrogen as previously anticipated. The 10-15 Å diameter SWNTs produced at high yield by the methods of laser vaporization may be 100's of microns in length. The poor hydrogen uptake by these materials may be attributed to very slow hydrogen diffusion down the long nanotube walls resulting in an effective blockage at the ends of the tubes. Since so few tube ends are present in the laser-generated materials, the overall hydrogen uptake is low. We have explored methods for

cutting these long bundles into segments to produce short opened tubes for effective hydrogen uptake.

The nanotube materials were sonicated in the following solutions known to damage graphitic structures: concentrated H_2SO_4, HCl, Aqua Regia (4:1 HCl:HNO_3), 3:1 H_2SO_4:HNO_3, 5:18:1 HCl:H_2SO_4:HNO_3, and 5% bromine and iodine in methanol. Of these strong oxidizers the concentrated HCl and the mixture containing 5:18:1 HCl:H_2SO_4:HNO_3 were the most effective for the cutting of the long SWNT bundles. Little or no damage was observed to the nanotube structures following treatments with the 5% bromine and iodine in methanol mixtures.

Figure 4 a) displays a TEM image of laser-generated SWNT material sonicated in 5:18:1 HCl:H_2SO_4:HNO_3. Individual nanotubes with lengths between ~0.25 - 1 μ are clearly visible in the image. Figure 4 b) displays a high resolution TEM image of the same initial material following sonication in HCl. A very high density of SWNT ends is apparent. In the untreated samples a clear image of nanotube ends could not be found following hours of TEM analysis. Applying the successful methods of cutting to highly purified SWNT materials and improving methods for the collection of the cut nanotubes should result in a material with very high H_2 adsorption capabilities.

Temperature Programmed Desorption with Electric-Arc Material

High purity carbon nanotube materials which were produced by electric arc at the Universite de Montpellier II by Patrick Bernier's research group were investigated with TPD spectroscopy. Materials produced by the electric-arc method can have diameter distributions different from the diameter distributions found for tubes produced by laser vaporization. Figure 5 shows the TPD spectrum obtained from 1 mg of the Bernier material after the sample was heated in vacuum at 1 K/s to 970 K. The hydrogen exposure was performed at 300 Torr for 10 min. at room temperature. The sample was cooled to ~ 130 K prior to the evacuation of the hydrogen gas.

The TPD signal from the electric arc-material has two peaks in addition to the 145 K peak which is produced by pumping out the hydrogen dose while holding the sample at 130 K. The spectrum differs significantly from those which we typically observe in NREL electric-arc materials. Fig 5. displays peaks at ~205 and 310 K. NREL arc-discharge materials typically display only one peak at ~285K. The Bernier materials are produced with catalytic elements such as lanthanum and yttrium [16] and therefore can contain nanotubes of differing diameters than the tubes we have produced with Ni and Co catalysts in our arc-discharge apparatus. We have not yet performed Raman spectroscopy to characterize the diameter distribution in the Bernier sample, but the TPD spectroscopy suggests a bi-modal distribution of tube diameters in the Bernier sample with one type of tube being larger than (9,9), and the other being smaller. If this interpretation is correct, then improved control over the synthetic process to produce specific diameters will result in the tailoring of SWNTs for adsorption/desorption over specific temperature and pressure conditions.

Production of SWNTs with Specific Diameters

Theoretical calculations predict that the Raman frequencies of the radial breathing modes for SWNTs are diameter dependent. Calculated frequencies include 206, 183, 165 and 150 cm^{-1} for (8,8), (9,9), (10,10) and (11,11) SWNTs where the diameters are 1.08 1.22, 1.35 and 1.49 nm, respectively. Figure 6 displays Raman spectra of the radial breathing modes of SWNT materials formed using the Molectron MY35 Nd:Yag laser. For the top spectrum in Fig. 6 the material was produced using 10 Hz pulses at ~ 800 mJ/pulse at 1000°C. The middle spectrum corresponds to material produced under the same conditions with the target at 1200°C. The spectrum observed for the 1000°C material indicates the production of SWNTs with a fairly wide distribution in size. In the spectrum of the 1200°C material, very little intensity is observed at frequencies > 165 cm^{-1} indicating the production of predominantly larger diameter SWNTs. The bottom spectrum in Fig.

6 is of material produced at 1000°C employing the Q-switched mode of operation with the laser. Here very little intensity is observed for frequencies < 165 cm^{-1} indicating the production of predominantly smaller diameter SWNTs. These results suggest the ability to selectively tune the SWNT diameters by varying the synthesis conditions. These results may prove very crucial to the development of an effective hydrogen storage material as a specific diameter nanotube may be the most effective for the high uptake of hydrogen.

Seivert Apparatus for Pressure-Composition-Temperature Measurements

As noted previously [17], the behavior of SWNTs in real-world hydrogen storage applications will be governed by their charge/discharge capabilities while in the presence of over-pressures of hydrogen. Our work has been focused on the TPD behavior of hydrogen desorbing from these materials into an UHV environment since the TPD technique is very sensitive, and only small quantities of SWNTs could be synthesized until recently. Since we are now able to fabricate gram quantities, we are in a position to evaluate the pressure-composition-temperature phase diagrams for H_2 interacting with carbon nanotubes.

A Sievert apparatus has been constructed to measure the absorption of hydrogen in nanotubes as a function of pressure, temperature, and nanotube processing. Its operating principle is based on introducing a known amount of a gas into a known volume containing an absorption sample and measuring the pressure. By assuming an equation of state (usually the ideal gas law), the amount of absorbed gas can be calculated. To accurately determine the absorbed amount requires measuring the temperature, volume, and pressure of both the reference and sample chambers to high accuracy. Careful calibration procedures must be observed to determine the reference and sample chamber volumes. There are numerous subtle considerations, such as the volume displaced by the sample itself and the effect of temperature and pressure on the volumes, that must be factored into the calibration and absorption calculations.

The apparatus built at NREL consists of several components and the block diagram of the Sievert apparatus is given in Figure 7. The maximum pressure rating for the setup is 5000 psi; however, our maximum pressure source is currently 2500 psi. There is a vacuum system to initially evacuate all volumes of the system as well as to assist in the initial degassing of the sample. The experiment can then proceed with the pressures being recorded and pneumatic valves operating under computer control. At the present time, the apparatus operates at room temperature; however, we are working on extending the operating temperature range to 75 - 775 K. The system currently is undergoing verification tests and trial runs. It is expected that we will be able to readily detect the absorption of ~10^{-3} moles of gas which corresponds to 0.2 wt. % of hydrogen in a 1 gram sample of nanotubes.

Conclusions / Future Work

This year we have made significant advances in the synthesis and characterization of SWNT materials so that their potential may be realized in hydrogen storage applications. We can now prepare gram quantities of high-purity SWNT samples and measure and control the diameter distribution of the tubes by varying key parameters during synthesis. We have also developed methods which purify nanotubes and cut nanotubes into shorter segments. These capabilities provide a means for opening the (10,10) tubes which were unreactive to the oxidation methods that successfully opened (9,9) tubes, and offer a path towards organizing nanotube segments to enable high volumetric hydrogen storage densities. Further work in this area will be focused on improving yield and selectivity of the purifying and cutting procedures. We also performed temperature programmed desorption spectroscopy on high purity carbon nanotubes material obtained from our collaborator Prof. Patrick Bernier. The difference in the hydrogen storage capabilities of these materials will be investigated in more detail in the future to allow further

control and improvement in the H_2 storage behavior of SWNT materials. We have finished construction of a high precision Seivert's apparatus which will allow the hydrogen pressure-temperature-composition phase diagrams to be evaluated for SWNT materials, and detailed work in this area will be a main focus during the upcoming year.

References

1. Cannon, J.S., *Harnessing Hydrogen.* 1995, New York: INFORM, Inc.

2. N.E.S., *National Energy Strategy.* 1991/1992. .

3. Flavin, C. and N. Lessen, *Power Surge.* 1994, New York: W.W. Norton & Co.

4. Dillon, A.C., *et al. Carbon Nanotube Materials for Hydrogen Storage.* in *Proceedings of the U.S. DOE Hydrogen Program Review.* 1995. Coral Gables, FL:

5. Carpetis, C. and W. Peschka, *A Study of Hydrogen Storage by Use of Cryoadsorbents.* Int. J. Hydrogen Energy, 1980. **5**: p. 539-554.

6. Schwarz, J.A. *Activated Carbon Based Storage System.* in *Proceedings of the 1993 DOE/NREL Hydrogen Program Review.* 1993. Cocoa Beach, FL.:

7. Schwarz, J.A. *Modification Assisted Cold Storage (MACS).* in *contract report to Brookhaven National Laboratories, contract # 186193-S.* 1.

8. Gregg, S.J. and K.S.W. Sing, *Adsorption, Surface Area and Porosity.* 2nd. ed. 1982, London: Academic Press.

9. Breck, D.W., *Zeolite Molecular Sieves: Structure, Chemistry and Use.* 1974, New York: Wiley.

10. Pederson, M.R. and J.Q. Broughton, *Nanocapillarity in Fullerene Tubules.* Physical Review Letters, 1992. **69**: p. 2689.

11. Krajnovich, D.J., J.E. Vazquez, and R.J. Savoy, *Impurity-Driven Cone Formation During Laser Sputtering of Graphite.* Science, 1993. **259**: p. 1590.

12. A.Thess, *et al., Cryastalline Ropes of Metallic Carbon Nanotubes.* Science, 1996. **273**: p. 483-487.

13. Guo, T., *et al., Catalytic growth of single-walled nanotubes by laser vaporization.* Chem. Phys. Lett., 1995. **243**: p. 49-54.

14. Bandow, S., *et al., Purification of single-wall carbon nanotubes by microfiltration.* Journal of Physical Chemistry B, 1998. **101**(44): p. 8839-42.

15. Jie Liu, *et al., Fullerene Pipes and Capsules.* Nature, 1997. **(in the press)**.

16. Journet, C., *et al., Large-scale production of single-walled carbon nanotubes by the electric-arc technique.* Nature (London), 1997. **388**(6644): p. 756-758.

17. Dillon, A.C., *et al., Storage of Hydrogen in Single-Wall Carbon Nanotubes.* Nature, 1997. **386**: p. 377-379.

Acknowledgments

We are grateful for the assistance of J.D. Perkins and M.D. Landry for assistance with experimental set-up, and the research group of P. Bernier for providing SWNT samples prepared by electric-arc.

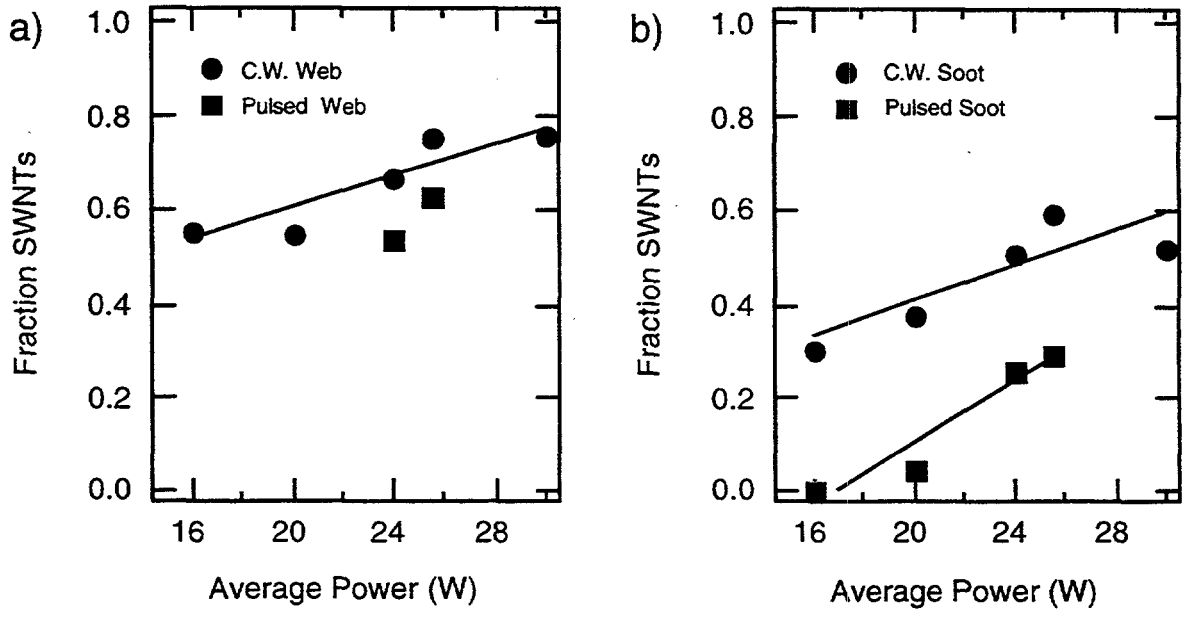

Figure 1: SWNT densities observed for pulsed and c.w. laser production in a) collected web and b) collected soot components. The c.w. experiments were performed at the average power which was measured for each of the 3, 6, 10 and 24 kHz pulsed experiments (see Table 1). SWNT fractions are given versus average laser power for both c.w. and pulsed modes of operation.

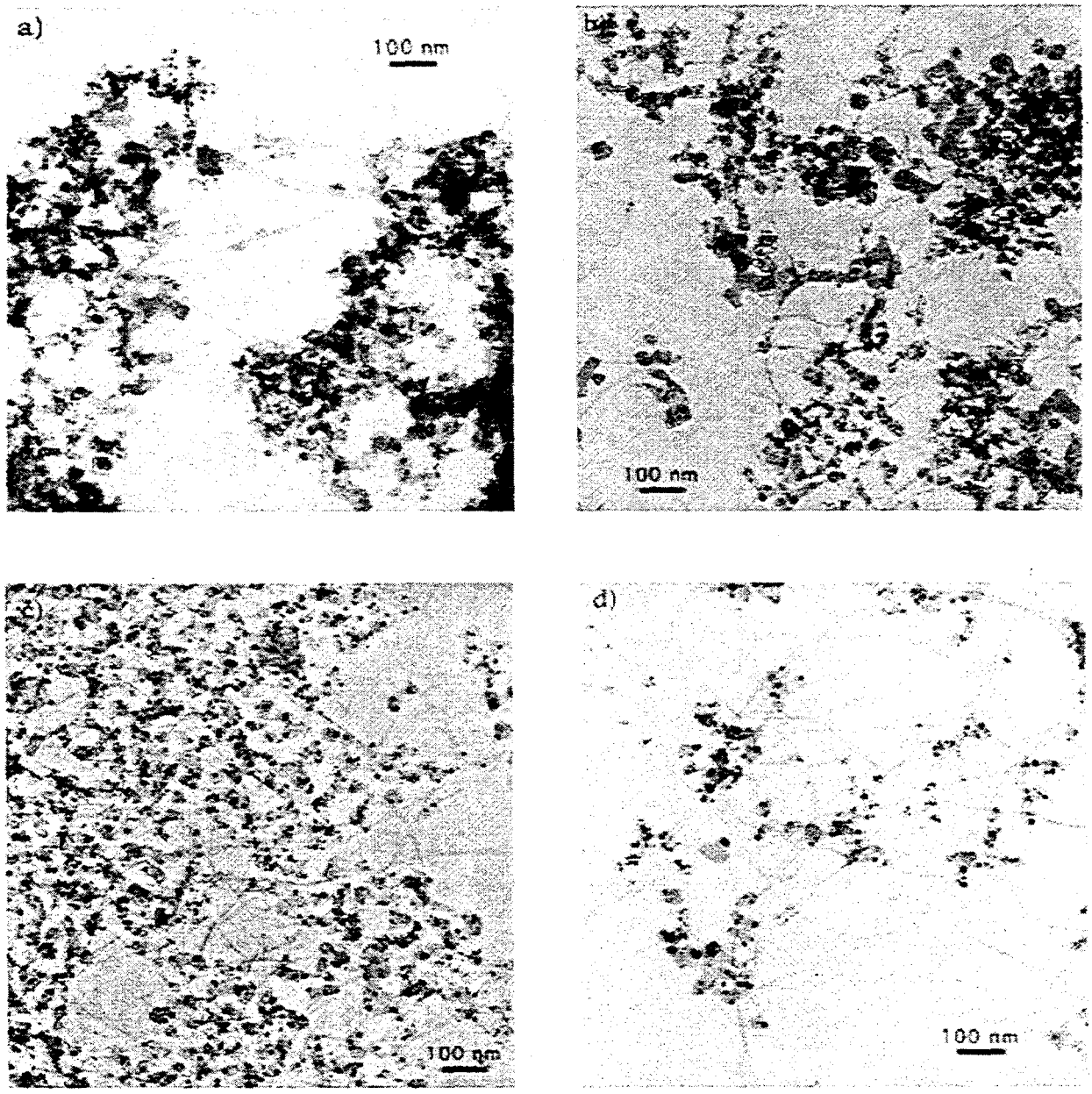

Figure 2: Characteristic TEM images of the material collected following laser irradiation of porous nickel-cobalt /graphite targets. a) soot produced by 6 kHz pulses, ~4% SWNTs, b) soot produced by 10 kHz pulses, ~26% SWNTs, c) soot produced by 24 W c.w. laser light, ~51% SWNTs, and d) web produced by 30W c.w. laser light, ~78% SWNTs.

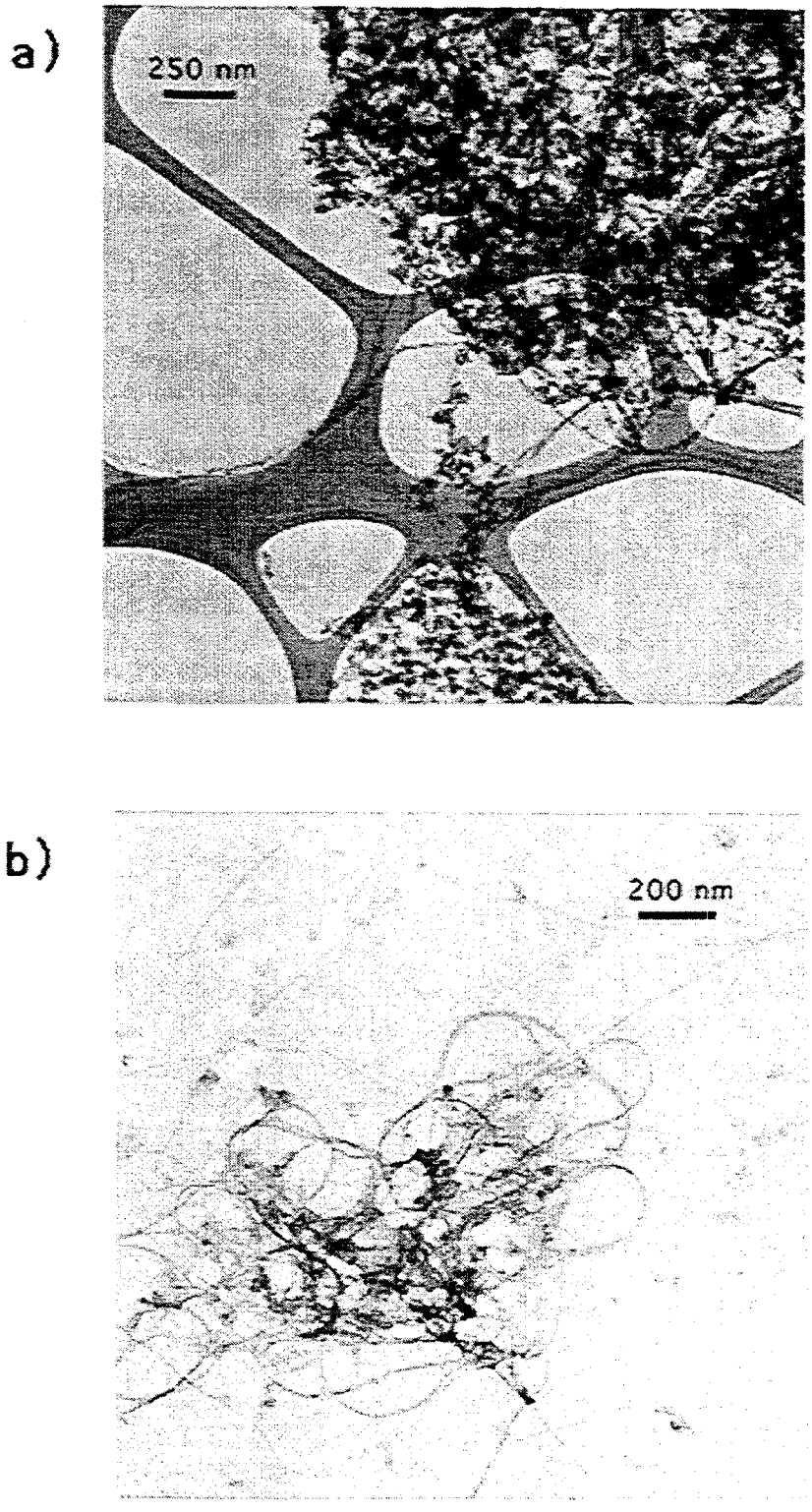

Figure 3: TEM images of a) initial relatively low quality pulsed laser generated SWNT material and b) the same material following nitric acid purification.

a)

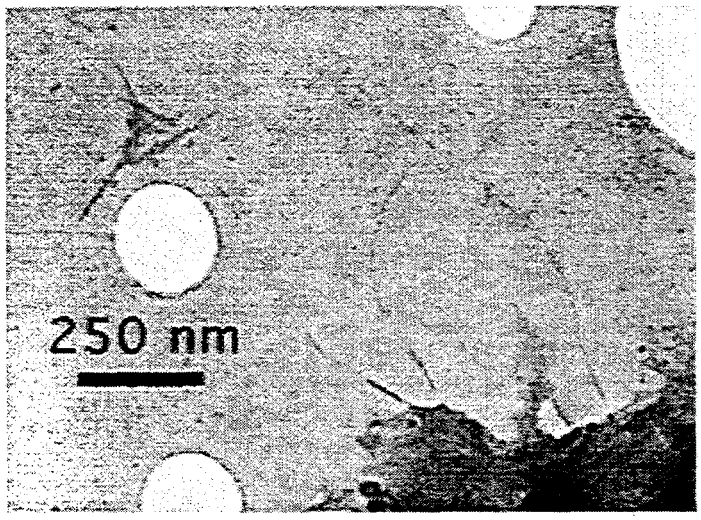

b)

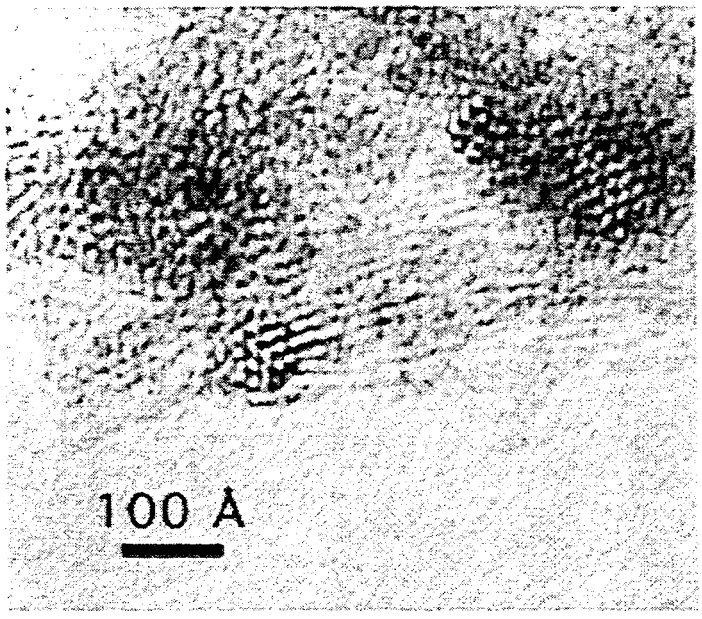

Figure 4: TEM images of laser produced SWNT materials following a) sonication in 5:18:1 $HCl:H_2SO_4:HNO_3$ where SWNTs with ~0.25-1μ lengths are observed and b) sonication in HCl revealing a high density of nanotube ends.

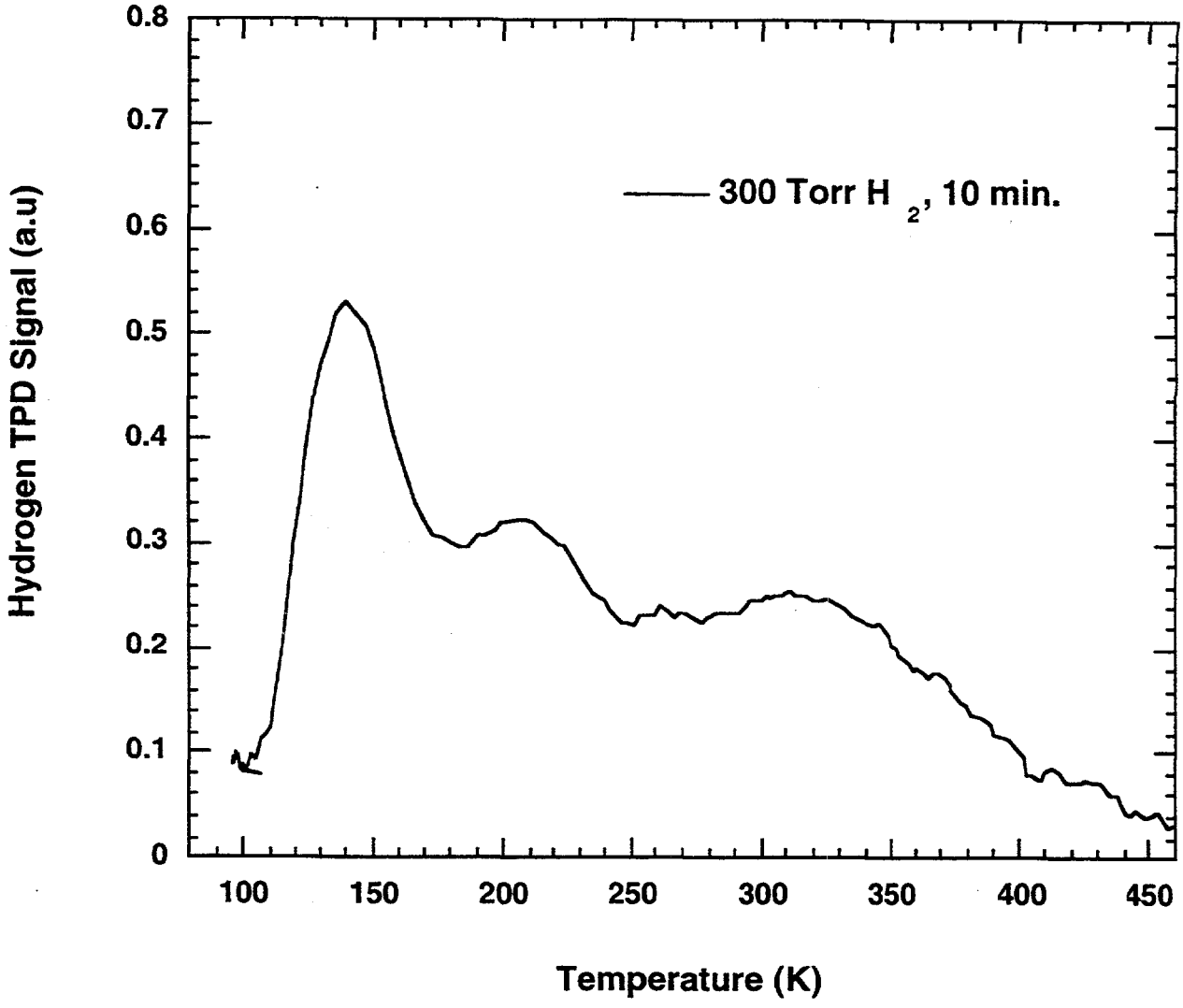

Figure 5: Temperature programmed desorption spectrum of material produced by electric-arc and supplied by P. Bernier.

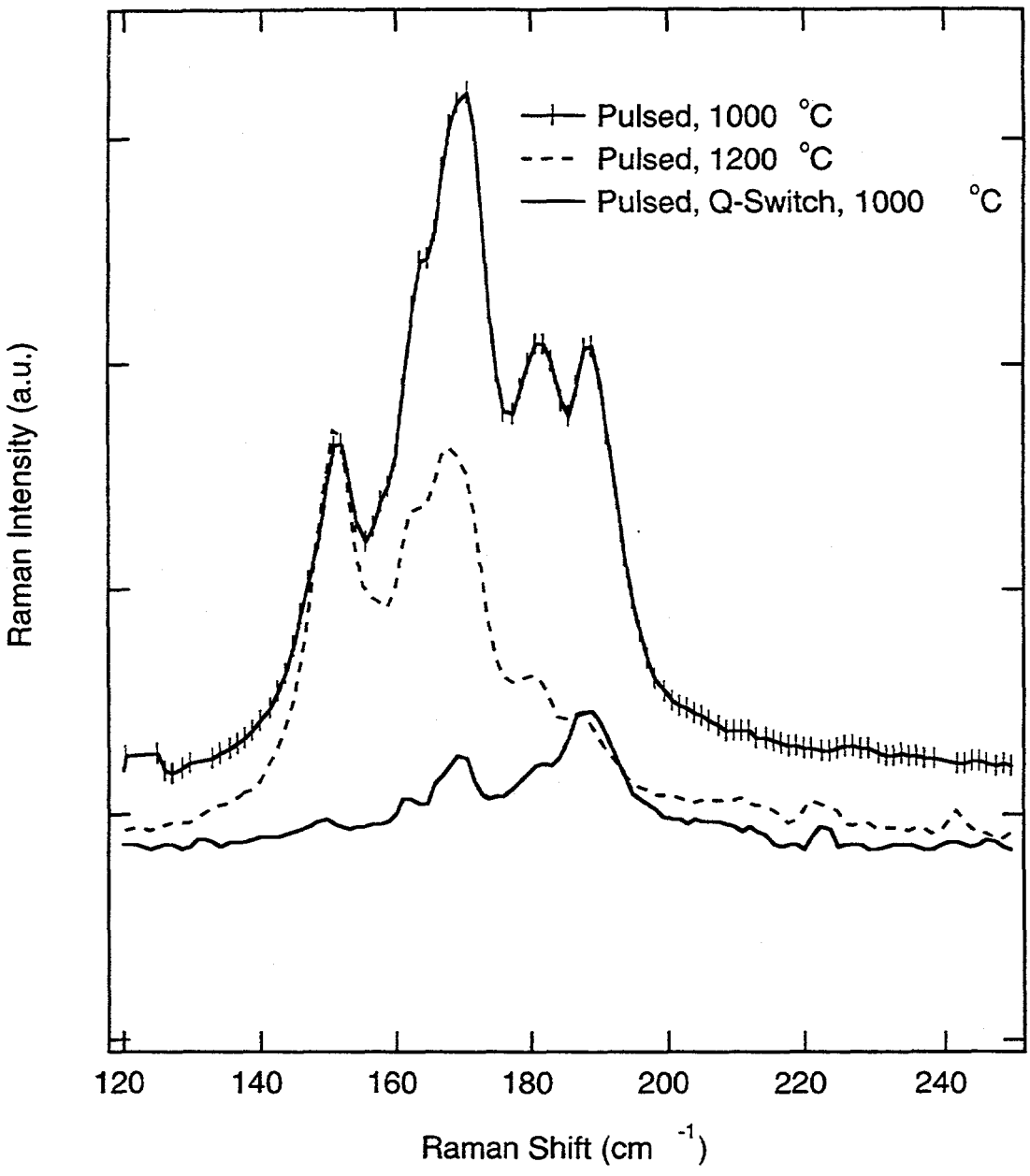

Figure 6: Raman spectra in the region of the radial breathing mode for various laser generated SWNT materials indicating the ability to produce nanotubes with differing diameters by varying synthesis parameters.

Sievert Apparatus

for measurement of hydrogen absorption in nanotubes

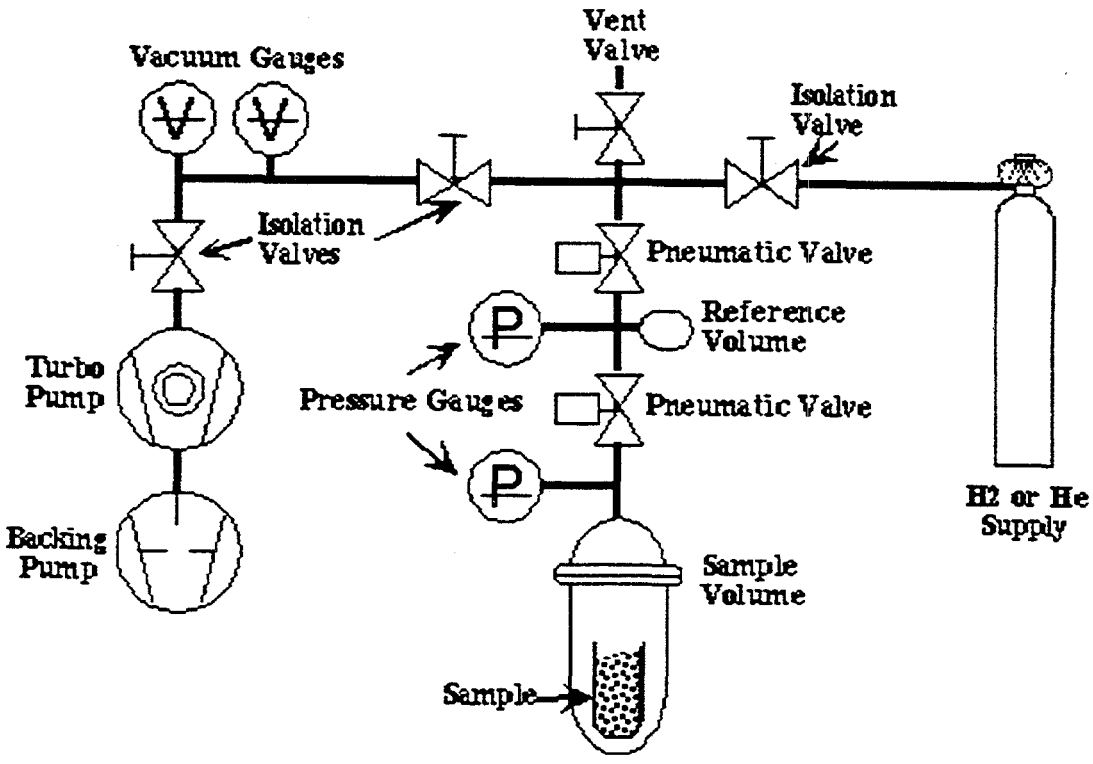

Figure 7

Production of Hydrogen from Biomass by Catalytic Steam Reforming of Fast Pyrolysis Oil

Stefan Czernik, Dingneng Wang, and Esteban Chornet

Center for Renewable Chemical Technologies and Materials

National Renewable Energy Laboratory, Golden, Colorado, USA 80401

Abstract

Hydrogen is the prototype of the environmentally cleanest fuel of interest for power generation using fuel cells and for transportation. The thermochemical conversion of biomass to hydrogen can be carried out through two distinct strategies: (a) gasification followed by water-gas shift conversion, and (b) catalytic steam reforming of specific fractions derived from fast pyrolysis and aqueous/steam processes of biomass. This paper presents the latter route that begins with fast pyrolysis of biomass to produce bio-oil. This oil (as a whole or its selected fractions) can be converted to hydrogen via catalytic steam reforming followed by a water-gas shift conversion step. Such a process has been demonstrated at the bench scale using model compounds, poplar oil aqueous fraction, and the whole pyrolysis oil with commercial Ni-based steam reforming catalysts. Hydrogen yields as high as 85% have been obtained. Catalyst initial activity can be recovered through regeneration cycles by steam or CO_2 gasification of carbonaceous deposits.

Introduction

Renewable lignocellulosic biomass has been considered as a potential feedstock for gasification to produce syngas (a mixture of hydrogen and carbon monoxide) for the last few decades. However, the economics of current syngas production processes favor the use of hydrocarbons (natural gas, C_2-C_5, and naphtha) and inexpensive coal. An alternative approach to the production of hydrogen

from biomass is fast pyrolysis of biomass to generate a liquid product (also known as bio-oil) and catalytic steam reforming of the whole oil or its fractions. This latter approach has potential to be cost competitive with the current commercial processes for hydrogen production. The objective pursued in this work is to prove the feasibility of a process strategy based on the use of biomass, of either agricultural or forest origin, as a feedstock to small and medium size (< 250 tonnes/d biomass input, dry basis) regional pyrolysis plants to produce bio-oil, that would be subsequently converted to hydrogen via catalytic steam reforming. The second step of the process could be carried out at a different location (bio-oil is easily transportable), with the existing infrastructure for hydrogen use or distribution. The above process strategy is conceptually possible thanks to the significant advances in fast pyrolysis technology made in the 80's and 90's,[1-4] the improved understanding of the composition of the bio-oils and their fractionation,[5] and the knowledge-base accumulated in the past few years of how to steam reform oxygenates derived from carbohydrates and lignin.[6-8]

Fast pyrolysis technologies have reached near commercial status. Circulating fluid bed processes have been installed in the USA (50 tonnes/d) and in Italy (15 tonnes/d), while a bubbling fluid bed pilot process is under development in Spain (3 tonnes/d).[9-10] The basis of these technologies is the understanding of pyrolytic mechanisms. When biomass is rapidly heated its constitutive macromolecules depolymerize and dehydrate.[11-12] Volatile intermediates are formed and exit the reaction zone when appropriate fluid-dynamics are applied.[1,3] Since these intermediates undergo subsequent cracking in the vapor phase when exposed to high temperatures, the yield and nature of the bio-oil is a function of the secondary cracking severity.[12-13]

It is well documented that yields of bio-oil can reach 75 wt%.[5] The bio-oil produced from fast pyrolysis of biomass contains 75-85 wt% organics and 15-25 wt% water. The latter is the result of the moisture content in the biomass feed and dehydration reactions which proceed in parallel with the thermal depolymerization reactions. The organics are predominantly a mixture of aldehydes, alcohols and acids derived from the carbohydrate fraction of biomass and phenolics from lignin.[5,8] Thermal depolymerization reactions can be conducted in such a way that the

hemicellulose and cellulose yield volatile compounds which are predominantly monomeric with small amounts of oligomers. However, lignin depolymerization invariably produces more oligomers than monomers. The oligomers, both from the carbohydrate and the lignin are found in the vapor phase due to their carry over as aerosols. By an appropriate choice of the condensation sequence we can separate the bio-oil into an oligomer-rich fraction and a monomer-rich fraction, the latter being water-soluble. Alternatively, the whole bio-oil can be split into two fractions via a simple addition of water (a water/bio-oil weight ratio of 2 is normally used). Fast pyrolysis thus produces two bio-oil fractions: a monomer-rich aqueous fraction (containing typically 20 wt% organics that can be concentrated by evaporation or nanofiltration) and a hydrophobic fraction composed mainly of oligomers derived from lignin.[5,8]

Steam reforming can be conceivably conducted with the entire bio-oil or with each of its fractions. Figure 1 shows the schematic diagram of the proposed process. The solid line specifies the route leading to co-products hydrogen and "depolymerized lignin". Lignin-derived oligomer-rich fraction can be used as a feedstock for the production of resins with formaldehyde.[14] Such resins can become a valuable co-product (a substitute for phenol-formaldehyde) which will lower the production costs of hydrogen from the aqueous fraction as demonstrated in related technoeconomic studies.[8,15] Another viable application of the lignin-derived fraction is the production of cyclohexyletheres, a new class of high octane fuel additives, which is under development.[16]

The economics of the whole bio-oil reforming are less favorable than for the co-product strategy. However, the hydrogen yields obtained from the whole oil are higher than when only the aqueous, carbohydrate-derived fraction is processed. In addition, since hydrogen is the only product, this option is independent of co-product markets.

We have also shown (Figure 1) the approach of stabilizing (via controlled depolymerization of the oligomers, selective dehydration and, probably, esterification/ etherification) the aqueous fraction of the bio-oil to yield a biomass-derived oxygenates that could be stored, transported and converted very much like any other hydrocarbon or alcohol. We are not reporting on this effort in the context

of this paper but we want to emphasize the significance of this bio-oxygenate as a "potential new biofuel".

Because biomass fast pyrolysis has almost reached the commercial status, this work has focused on the catalytic steam reforming of bio-oil, its fractions, and representative components. At this stage of the work we have concentrated our efforts in the reforming of the aqueous fraction and the whole bio-oil.

Experimental Section

Tests were carried out in two systems: a bench-scale fixed-bed unit and a 2 inch diameter fluidized bed reactor.

The schematic of the bench-scale system is shown in Figure 2. The reactor is a stainless steel tube (1.65 cm id x 42.6 cm length) housed in a tubular furnace equipped with three independently controlled heating zones. The reactor was packed with about 100 g of a commercial, nickel-based catalyst (particle size: 2.4-4.0 mm). Most studies were carried out using the UCI G-90C catalyst and a dual-catalyst bed of 46-1 and 46-4 from ICI Katalco. Steam was generated in a boiler and superheated. The organic feed from a diaphragm metering pump was sprayed using N_2 and mixed with superheated steam in a triple nozzle injector. Products exiting the reactor were passed through a condenser. The condensate (just water in most cases) weight, as well as the volume and compositions of the permanent gas output were recorded periodically. An on-line IR gas analyzer was used to monitor CO/CO_2 concentrations and a MTI-QUAD GC was used to measure concentrations of H_2, N_2, O_2, CO, CO_2, CH_4, and other light hydrocarbons. The reformer system was interfaced with a computer to monitor temperatures and other important parameters.

The schematic of the fluidized bed system is shown in Figure 3. The two-inch-diameter inconel reactor is heated by a three-zone furnace. 150-200g of commercial nickel-based catalysts from UCI ground to the particle size of 150-250μ are fluidized using superheated steam which is also a reactant in the reforming process. Liquids are fed using a diaphragm pump and a specially designed oil injection nozzle supplied with a cooling jacket. The oil temperature in the injector is

maintained below boiling point to prevent deposition of nonvolatile components. The product collection line includes a cyclone that captures fine catalyst particles and, possibly, char generated in the process, and two heat exchangers to condense excess steam. The outlet gas flow rate is measured by a flowmeter and a dry test meter. The gas composition is analyzed by a MTI gas chromatograph. The unit is connected to the G2/OPTO control and data acquisition system.

The bio-oil and its aqueous fraction were prepared at NREL. A poplar oil[17] generated by fast pyrolysis in the NREL vortex reactor system was separated into aqueous (carbohydrate-derived) and organic (lignin-derived) fractions by simply adding water to the oil with a weight ratio of water:oil = 2:1. The aqueous fraction (55% of the whole oil) contained ca. 20% organics ($CH_{1.5-1.9}O_{0.6-0.8}$) and 80% water.

Results and Discussion

The overall steam reforming reaction of bio-oil (or any oxygenate with a chemical formula of $C_nH_mO_k$), is given by:

$$C_nH_mO_k + (2n\text{-}k)\,H_2O = n\,CO_2 + (2n + m/2\text{-}k)\,H_2 \quad (1)$$

The stoichiometric yield of hydrogen is 2+m/2n-k/n moles per mole of carbon in the feed, and k/n for the aromatic phenolics from lignin is less than for most carbohydrate-derived products such as sugars.

Our initial work focused on demonstrating high efficiency of catalytic steam reforming as a method for conversion of bio-oil to hydrogen. The findings obtained from rapid screening experiments carried out using a microreactor interfaced with a molecular beam mass spectrometer, have been discussed in details elsewhere.[7-8] It was concluded that steam reforming of oxygenated organic compounds faces a serious competition from gas-phase thermal decomposition prior to entering the catalyst bed and the acid-catalyzed reactions at the acidic sites of the catalyst support. These competing thermal cracking reactions may result in the formation of carbonaceous materials (coke), which could block the reactor and even deactivate the catalyst. However, a complete conversion of both the oxygenate feed and its decomposition products to hydrogen can be achieved with

commercial Ni-based catalysts under reasonable operating conditions, if char formation prior to reaching the catalyst bed and coking on the catalyst can be eliminated, or at least controlled. Therefore, a special emphasis during bench-scale experiments was placed on how to feed bio-oil or its fractions into the reactor.

Tests were carried out using the bench-scale fixed-bed system to obtain the global and elemental mass balances, yield of hydrogen, and the carbon-to-gas conversion. We quantified the distribution of gas products under conditions of complete conversion of the pyrolysis oil feedstock, and studied the catalyst lifetime and the efficiency of its regeneration. Initially, we used model compounds (methanol, acetic acid, syringol and *m*-cresol, both separately and in mixtures) then real bio-oil (and its aqueous fraction). Representative results are listed in Tables 1 and 2. Profiles of the output gas composition are shown for the 3-component mixture in Figure 4 and for the poplar oil aqueous fraction in Figure 5.

During the processing of the three-component mixture of 67% acetic acid, 16% *m*-cresol, and 16% syringol we observed *some coke deposits* on the top portion of the UCI G-90C catalyst bed. The overall mass balance (carbon, hydrogen, and oxygen) was 99% and the carbon conversion to gas was 96% (Table 1). The other catalyst tested for steam reforming of the 3-component mixture was the 46-series from ICI Katalco (46-1/46-4). This dual catalyst bed is used in commercial naphtha reforming plants to reduce coke formation and extend catalyst lifetime. It showed an excellent and steady performance *without any coke deposition* on the catalyst. The gas composition (Figure 5) remained constant throughout the whole run. The overall mass balance (including carbon, hydrogen, and oxygen) was 104%, and for carbon 105%, indicating that there may be a systematic error in our measurement. An excellent hydrogen yield of 86% of the stoichiometric amount was obtained, and the total hydrogen potential may be as high as 98% with a second water-gas shift reactor. These results confirm that both the UCI G-90C and especially the ICI 46-series catalysts can efficiently convert oxygenates to hydrogen.

Steam reforming of bio-oil or its fractions was found to be more difficult than that of model compounds. The main problem that needed to be solved was feeding the oil to the reactor. Bio-oil

cannot be totally vaporized; significant amounts of residual solids are often formed that block the feeding line and the reactor. Thus, the simple injection system used for model compounds had to be modified to allow spraying bio-oil and its fractions in to the catalytic reactor without prior char formation.

The aqueous fraction of NREL-made poplar oil was successfully fed to the reactor using a triple-nozzle spraying system with minimal accumulation of char in the reactor inlet. A large excess of steam (S/C = 20-30) was used, together with a high flow rate of nitrogen, to allow for proper oil dispersion and heat transfer required to maintain a sufficiently high temperature (>500°C) at the reactor entrance. A portion of water and other volatiles in the sprayed droplets evaporate during mixing with the superheated steam and the remaining nonvolatiles will contact the catalyst surface directly. The ICI 46-series catalysts performed satisfactorily with no coke formation. We observed a stable gas production rate and composition throughout the whole 4-hour-long experiment (Figure 5).

The carbon conversion of the aqueous fraction to gas products was almost quantitative in both runs that used the same catalyst bed (Table 2). We observed similar levels of mass balance closures as in the experiments using model compounds: global 99%, carbon 105%, and hydrogen 97%. The methane concentration (with N_2 excluded) increased from 0.56% in the first run (2 h, t=0.03 s) to 2.2% in the second run (4 h, t=0.02 s), and both values were much higher than that (0.01%) obtained from the 3-component model compound mixture (17 h, t=0.09 s). This was likely caused by the shorter residence time forced by the large flow rate of steam and nitrogen used in the experiment.

Lowering steam-to-carbon ratio did not change much the overall H_2 yield, but only caused an increase in CO yield due to the WGS reaction. We also observed some thermal decomposition of the bio-oil fraction, which resulted in the accumulation of carbonaceous deposits in the region between the injection nozzle and the catalyst bed. There was a progressive formation of carbonaceous deposits in the catalyst bed. As a result, the hydrogen yield gradually decreased, as shown in Figures 6 and 7. Therefore, it seems necessary to regenerate the catalyst in order to

achieve high performance over a long period of time. This can be effectively achieved by gasification with either CO_2 (a co-product of the process) or steam. Experiments using both model compounds (e.g., acetic acid) and the poplar oil aqueous fraction proved validity of this regeneration. The H_2 yield profiles before and after regeneration by steam are also shown in Figures 6 and 7, indicating the recovery of H_2 yield after a 12 h treatment at 800°C and ambient pressure.

The steam reforming of the whole bio-oil in the fixed-bed reactor was much less successful than in the case of model compounds or the carbohydrate-derived oil fraction. Thermal decomposition of the oil resulted in fast accumulation of carbonaceous deposits on the catalyst and in the freeboard (above the bed). Therefore, only a very small fraction of the catalyst (top layer) was effectively used in the process while the most of it was not accessible to contact the oil. In addition, this caused a pressure buildup in the reactor and forced termination of the tests after 30-40 minutes. Figure 8 shows how the concentration of hydrogen and carbon dioxide in the product gas decreased with time, especially after 20 minutes on stream. The total mass balance closure was in this case 92%, however, only 62% of bio-oil were converted to gases and the hydrogen yield was only 41% of the stoichiometric, that corresponds to 4 kg of hydrogen from 100 kg biomass. Additional amounts of hydrogen could be produced from methane and carbon monoxide present in the gas that would increase the final yield to 65%, which is still significantly less than obtained from the carbohydrate-derived oil fraction.

The carbon/coke deposits could be efficiently removed from the reactor freeboard and from the catalyst surface by steam gasification carried out at 800°C. However, the time required for this process was almost four hours, much longer than that available for reforming. Because of these reasons we concluded that the fixed-bed configuration was not appropriate for steam reforming of the whole bio-oil. We believe that the application of the fluidized bed reactor will eliminate, or at least lessen most of the problems encountered in the fixed-bed unit. Even if we are not able to prevent partial carbonization of the oil, the bulk of the fluidizing catalyst will remain in contact with

the oil droplets in the reactor, which will greatly increase the reforming efficiency and extend the catalyst time-on-stream.

Preliminary tests of the whole oil reforming that were performed in the fluidized bed unit are encouraging: the oil can be injected into the bed using an appropriately designed nozzle and the cracking/reforming reactions proceed well while the catalyst can conceivably be continuously regenerated in a second reactor. Complete results will be presented within the next few months.

Summary and Conclusion

1. Biomass can be converted to bio-oil using a fast pyrolysis technology. The yield of bio-oil for a fluidized bed process is on the order of 75% biomass weight.
2. Bio-oil or its aqueous fraction can be reformed to generate hydrogen by a thermocatalytic process using commercial, nickel-based catalysts. The hydrogen yield obtained in a fixed-bed reactor from the aqueous fraction was up to 85% of the stoichiometric value which corresponds to almost 6 kg of hydrogen from 100 kg of wood.
3. Catalysts are easy to regenerate by steam or CO_2 gasification of carbonaceous deposits.
4. Fixed-bed is not the right reactor choice for reforming whole bio-oil. We believe, based on initial results, that fluidized bed will significantly improve the process efficiency.
5. The proposed strategy can be applied to any lignocellulosic biomass, either from agriculture or from forest operations. Residues as well as plantations and agricultural crops are equally suited as feedstocks to the process. The concept of using biomass via a regionalized system of production of bio-oils is entirely compatible with our strategy.

References

1. Scott, D. S.; Piskorz, J.; Radlein, D. *Ind. Eng. Chem. Process Des. Dev.* **1985**, *24*, 581-586.

2. Graham, R. G.; Freel, B. A.; Bergougnou, M. A. In *Research in Thermochemical Biomass Conversion*; Bridgwater, A. V.; Kuester, J. L., Eds.; Elsevier Applied Science: London, 1988; pp 629-641.
3. Diebold, J.; Scahill, J. In *Pyrolysis Oils from Biomass: Producing, Analyzing and Upgrading*; Soltes, E. J.; Milne, T. A., Eds.; ACS Symposium Series 376, American Chemical Society: Washington, D.C., 1988; pp 31-40.
4. Roy, C.; de Caumia, B.; Plante, P. In *5th European Conference on Biomass for Energy and Industry*; Grassi, G.; Goose, G.; dos Santos, G., Eds.; Elsevier Applied Science: London, 1990; p 2595ff.
5. Piskorz, J.; Scott, D. S.; Radlein, D. In *Pyrolysis Oils from Biomass: Producing, Analyzing and Upgrading*; Soltes, E. J.; Milne, T. A., Eds.; ACS Symposium Series 376, American Chemical Society: Washington, D.C., 1988; pp 167-178.
6. Wang, D.; Czernik, S.; Montané, D.; Mann, M.; Chornet, E. *Ind. Eng. Chem. Res.* **1997**, *36*, 1507-1518.
7. Wang, D.; Montané, D.; Chornet, E. *J. Appl. Catal. A* **1996**, *143*, 245-270.
8. Czernik, S.; Wang, D.; Montané, D.; Chornet, E. In *Developments in Thermochemical Biomass Conversion*, Bridgwater, A.V. and Boocock, D.G.B., Eds.; Blackie Academic & Professional, 1996; pp. 672-686.
9. Freel, B. A.; Graham, R. E.; Huffman, D. R. In *Development in Thermochemical Biomass Conversion*, Bridgwater, A.V. and Boocock, D.G.B., Eds.; Blackie Academic & Professional, 1996; pp. 86-95.
10. Cuevas, A.; Rebollo, L.; Reinoso, C. ; Scott, D. S. In *Bio-Oil Production and Utilization*, Bridgwater, A. V. and Hogan, E. N., Eds.; CPL Scientific Information Services, Ltd., Newbury, UK, 1996; pp 82-85.
11. Antal, M. J. In *Advances in Solar Energy*; Boer, K. W., Duffield, J. A., Eds.; Solar Energy Soc.: New York, 1982; pp 61-111.

12. Elliott, D. C. In *Pyrolysis Oils from Biomass: Producing, Analyzing and Upgrading*, Soltes, E. J.; Milne, T. A., Eds.; ACS Symposium Series 376, American Chemical Society: Washington, D.C., 1988; pp 55-65.

13. Czernik, S.; Scahill, J.; Diebold, J. *Journal of Solar Energy Engineering* **1995**, *117*, 2-6.

14. Kelley, S. S.; Wang, X.-M.; Myers, M. D.; Johnson, D. K.; Scahill, J. W. In *Development in Thermochemical Biomass Conversion*, Bridgwater, A.V. and Boocock, D.G.B., Eds.; Blackie Academic & Professional, 1996; pp. 557-572.

15. Mann, M.; Spath, P.; Kadam, K. In *Proceedings of the 1996 U.S. DOE Hydrogen Program Review*. NREL/CP-430-21968, National Renewable Energy Laboratory: Golden, CO, 1996; pp 249-272.

16. Shabtai, J.S. and Zmierczak, W.; in *Proceedings of the Third Biomass Conference of the Americas, Overend, R.P. and Chornet, E., Eds.*;Elsevier Science Inc.; pp. 1037-1040.

17. Scahill, J. W.; Diebold, J. P.; Feik, C. J. In *Developments in Thermochemical Biomass Conversion*, Bridgwater, A.V. and Boocock, D.G.B., Eds.; Blackie Academic & Professional, 1996; pp. 253-266.

Table 1. Fixed-Bed Bench-Scale Results with Model Compounds

Feed	S/C[a]	$G_{C_1}HSV$[b]	% C-to-gas conversion	% st. yield of H_2 (+WGS)[e]	Time on stream (h)
acetic acid	4.7	1973[c]	101	73 (98)	6
	12.8	777[c]	104	86 (100)	8
syringol/	6.3	2454[c]	100	75 (96)	4
MeOH	7.4	1985[c]	101	76 (97)	4
3-comp.	6.5	1053[c]	96	78 (91)	11
mixture	4.9	1053[d]	105	86 (98)	17

[a] Molar ratio of steam to carbon. [b] Gas hourly space velocity on C_1 basis (h^{-1}). [c] UCI G-90C catalyst. [d] ICI 46-1/4 catalysts. [e] Assuming all CO being converted to H_2 in a down stream WGS unit.

Table 2. Fixed-Bed Bench-Scale Results with Poplar Oil Aqueous Fraction

S/C[a]	$G_{C_1}HSV$[b]	% C-to-gas conversion	% st. yield of H_2 (+WGS) [f]	Time on stream (h)
19	1110[c]	97	103 (108)	2
30	1000[d]	102	103 (108)	4
35	860[c]	99	86 (88)	1
24	850[d]	100	89 (92)	1
12	860[d]	97	82 (88)	1
7	860[d]	98	79 (90)	1
5	1010[c]	92	75 (85)	6
10	1230[d]	102	78 (86)	6
23	870[e]	92	73 (76)	1
15	850[e]	89	71 (75)	1
10	760[e]	86	71 (76)	4

[a] Molar ratio of steam to carbon. [b] Gas hourly space velocity on C_1 basis (h^{-1}) with ICI 46-1/4 catalysts. [c] Fresh catalyst used. [d] Used the same catalyst as the previous run above it. [e] UCI G-91 catalyst. [f] Assuming all CO being converted to H_2 in a down stream WGS unit.

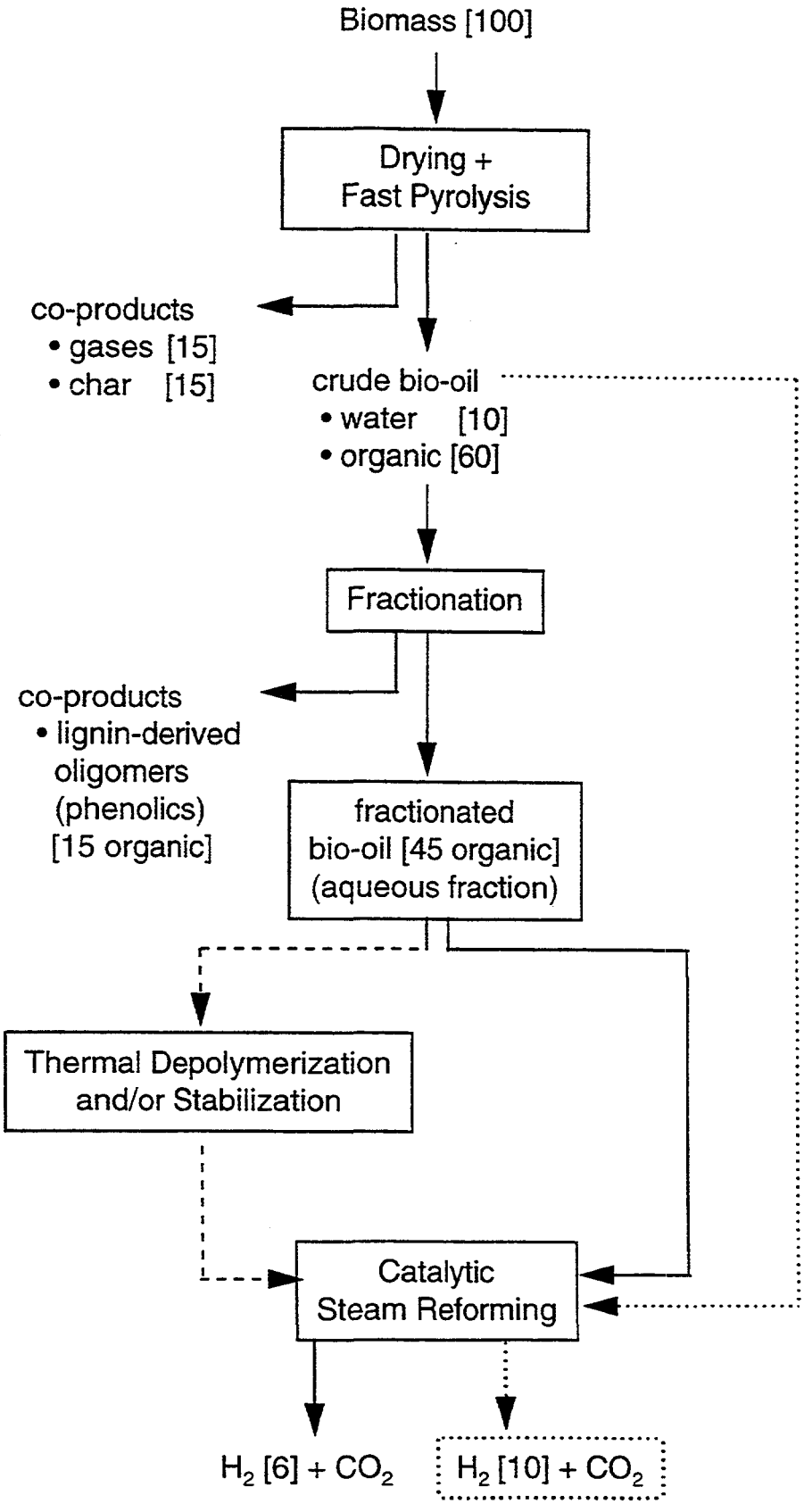

Figure 1. Process diagram for the production of hydrogen fro biomass via fast pyrolysis and catalytic steam reforming

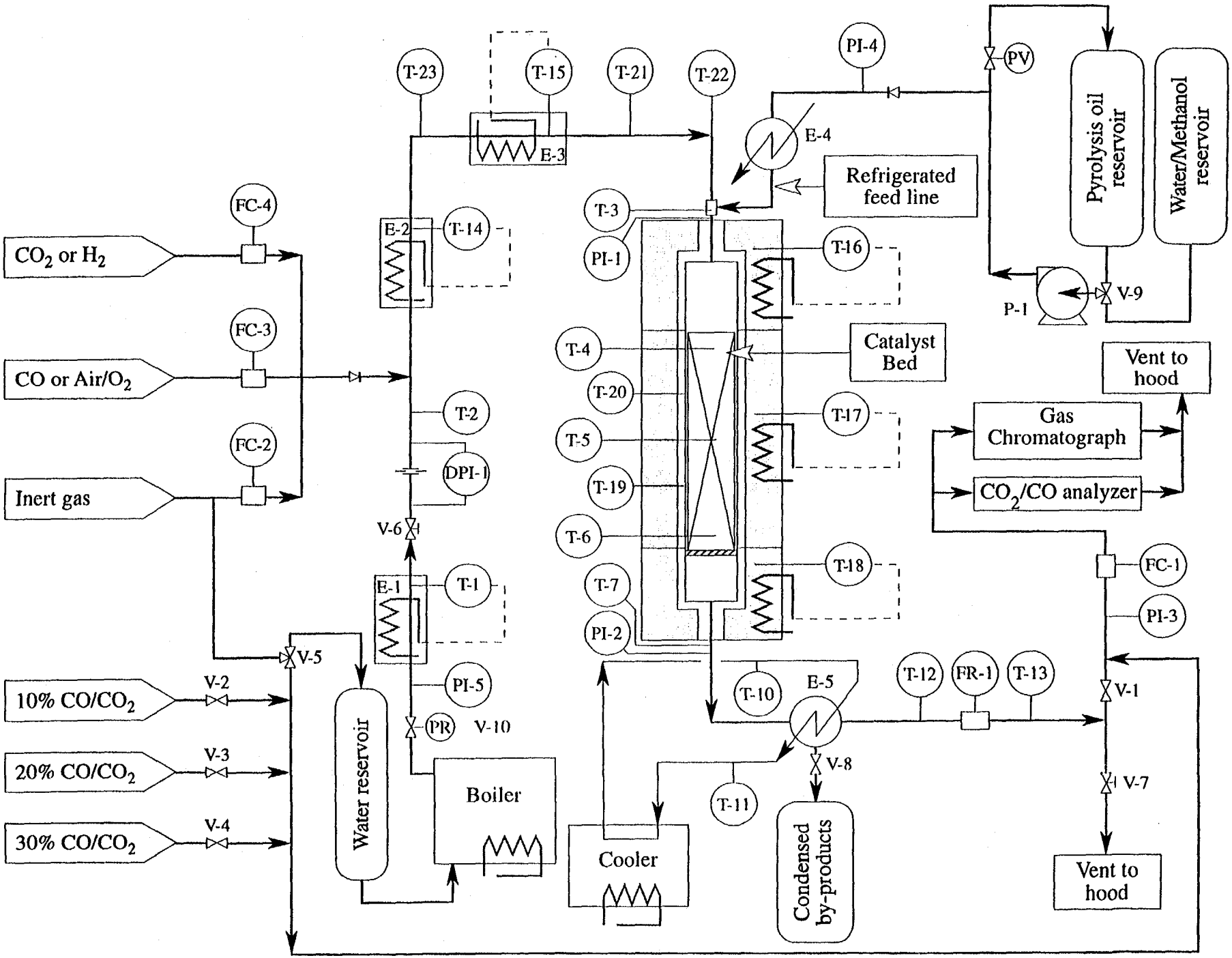

gure 2. Schematic of the fixed-bed reformer system

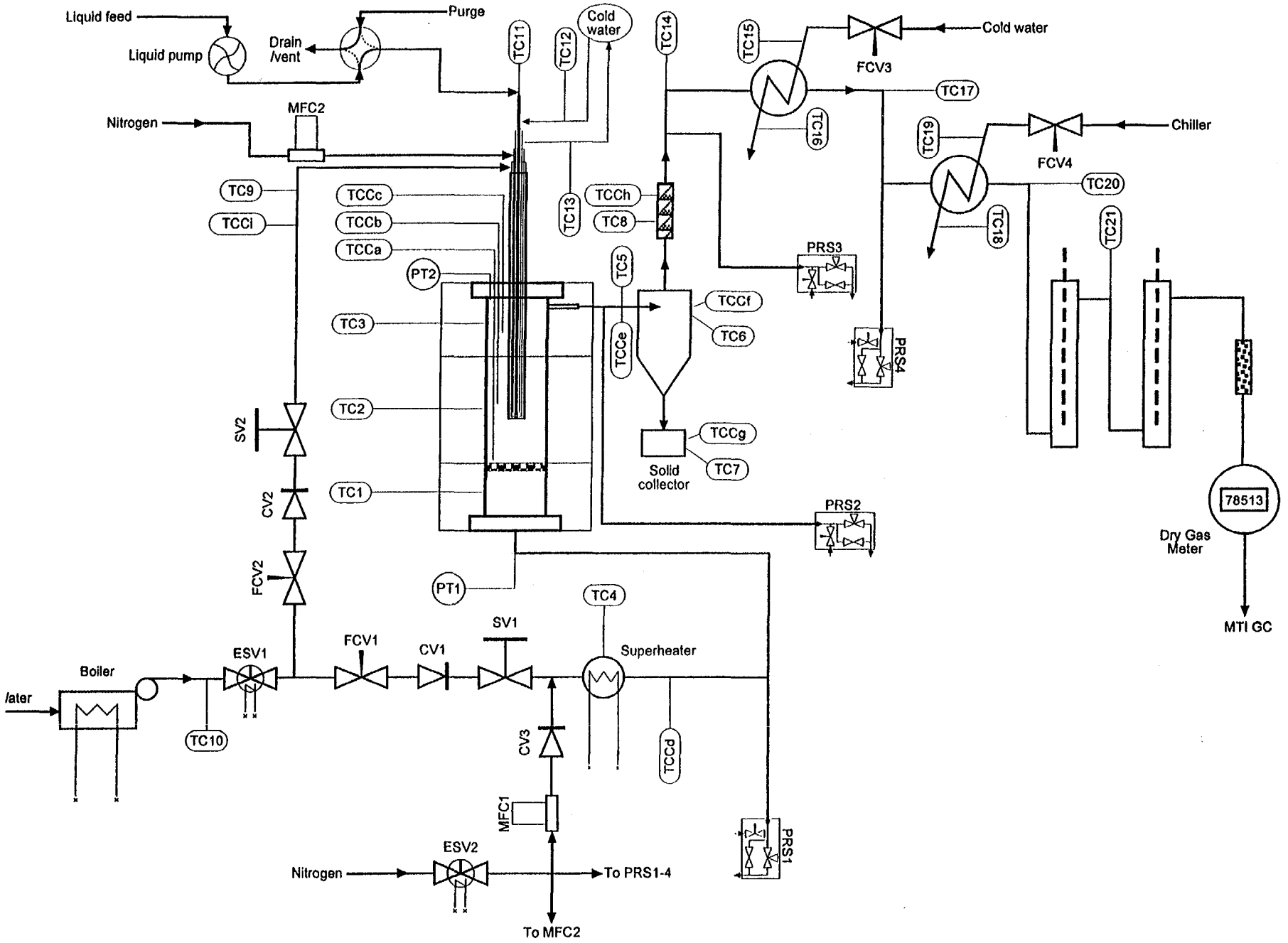

Figure 3. Schematic of the fluidized bed reformer

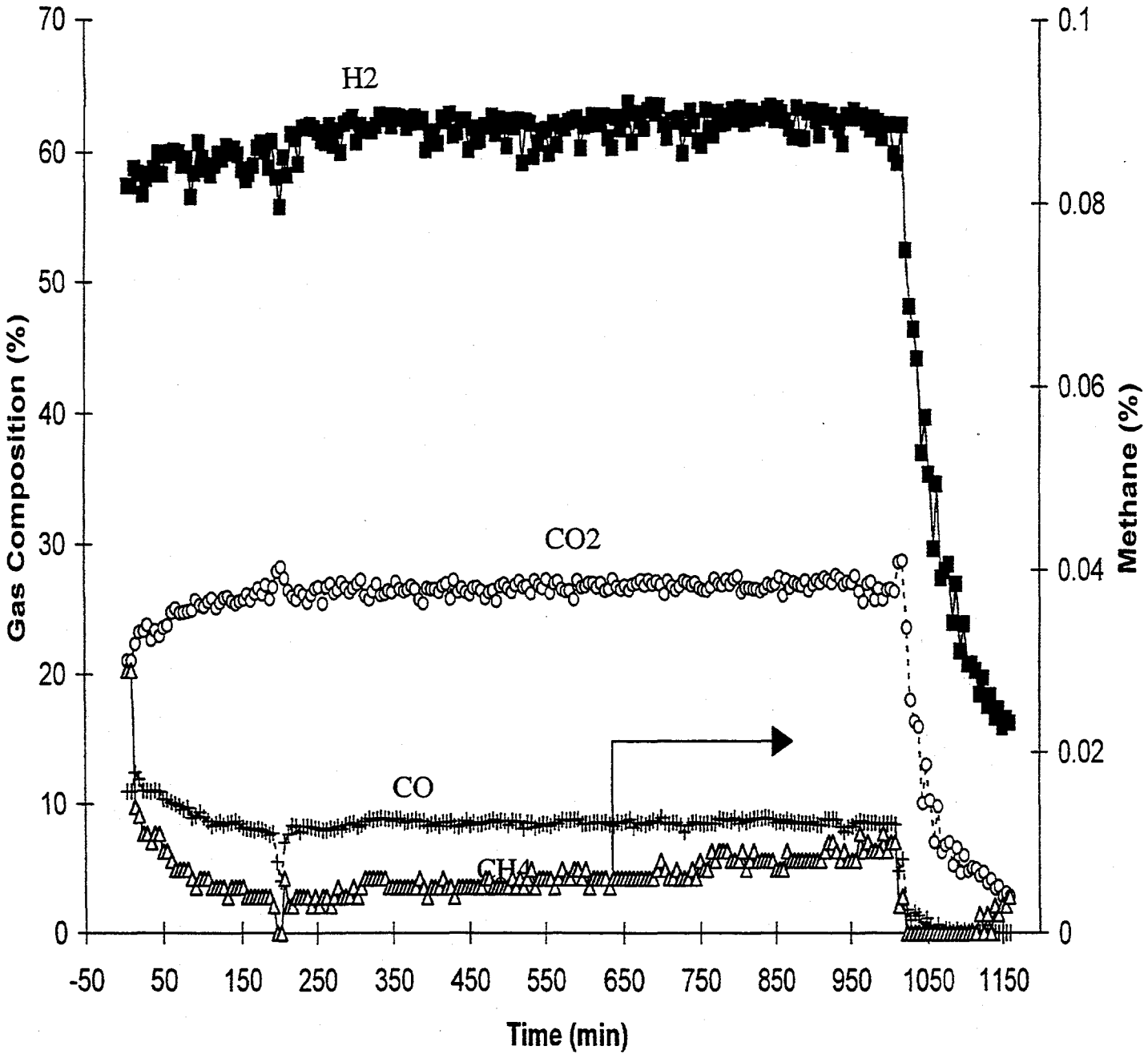

Figure 4. Product gas composition from reforming of a three-component mixture of acetic acid, m-cresol, and syringol

Figure 5. Product gas composition from reforming aqueous oil fraction

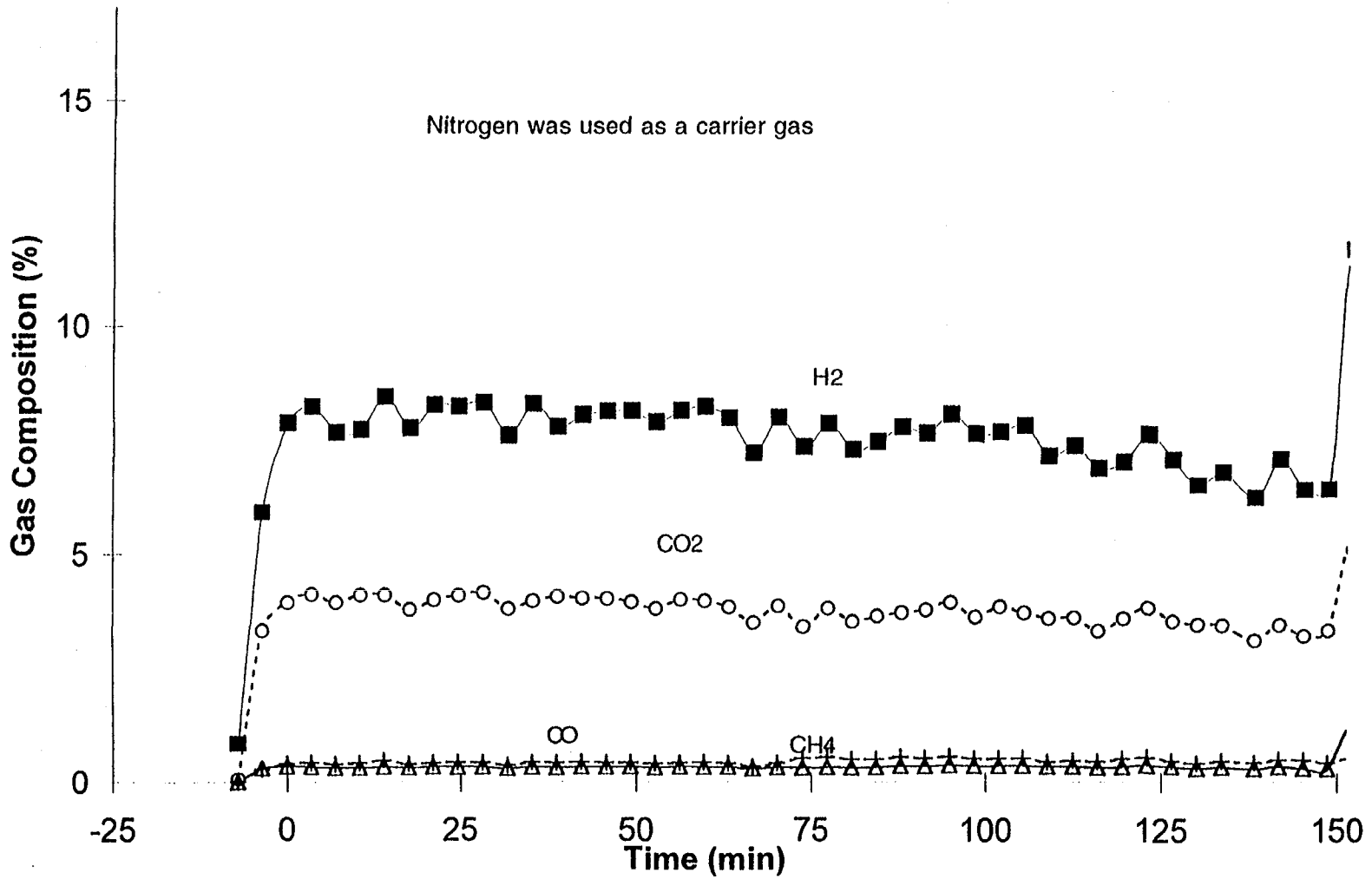

Figure 6. Hydrogen yield from aqueous fraction of poplar oil

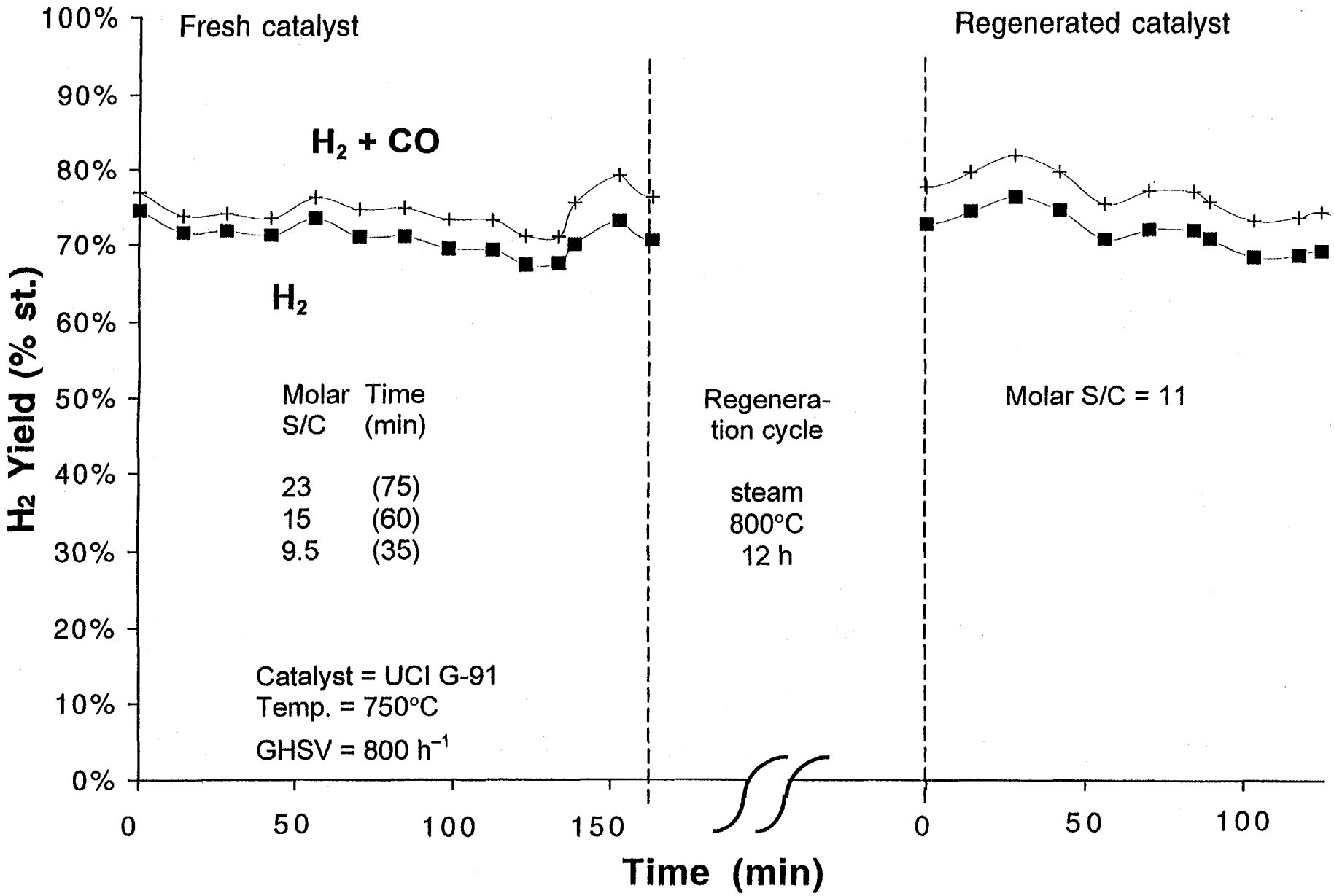

Figure 7. Product gas composition from reforming whole bio-oil

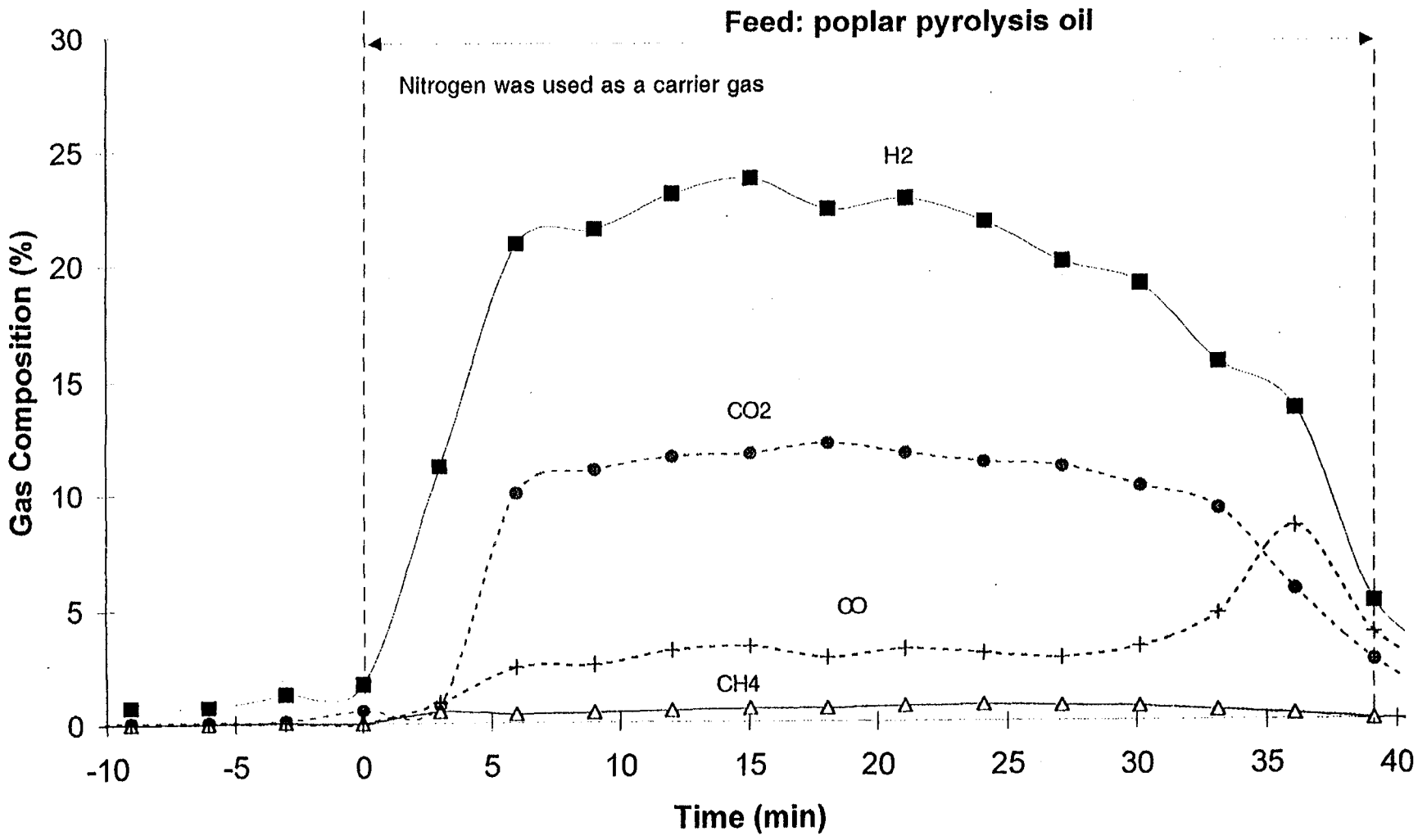

NUMERICAL SIMULATION OF VORTEX PYROLYSIS REACTORS FOR CONDENSABLE TAR PRODUCTION FROM BIOMASS

R.S Miller and J. Bellan
Jet Propulsion Laboratory
California Institute of Technology
Pasadena, CA 91109-8099

A numerical study is performed in order to evaluate the performance and optimal operating conditions of vortex pyrolysis reactors used for condensable tar production from biomass. A detailed mathematical model of porous biomass particle pyrolysis is coupled with a compressible Reynolds stress transport model for the turbulent reactor swirling flow. An initial evaluation of particle dimensionality effects is made through comparisons of single- (1D) and multi-dimensional particle simulations and reveals that the 1D particle model results in conservative estimates for total pyrolysis conversion times and tar collection. The observed deviations are due predominantly to geometry effects while directional effects from thermal conductivity and permeability variations are relatively small. Rapid ablative particle heating rates are attributed to a mechanical fragmentation of the biomass particles that is modeled using a critical porosity for matrix breakup. Optimal thermal conditions for tar production are observed for $900K$. Effects of biomass identity, particle size distribution, and reactor geometry and scale are discussed.

1 Introduction

Among the pyrolysis reactor designs investigated for commercial production of condensable tars from biomass, the vortex reactor is a potentially efficient configuration due to the rapid particle heating rates achieved through direct-contact ablation (Diebold and Power 1988). The vortex reactor is characterized by a strongly swirling flow of superheated steam through a cylindrical reactor that creates a centrifugal acceleration which results in the injected biomass

particles maintaining direct-contact with a high temperature outer wall. Biomass tars and gases resulting from the pyrolysis are then removed from the reactor through a central exit pipe whereas partially pyrolyzed material is re-entrained using a separate recycle loop resulting in complete reaction of the particles. To prevent the degradation of product tars within the reactor, it is important to achieve small residence times for the gaseous pyrolysis products. The condensed high molecular weight tars are collected and quenched, and are later used in a variety of applications including hydrogen fuel production (Chornet *et. al.* 1994). In spite of the attractive nature of the design, there are no thorough analyses of vortex pyrolysis reactors addressing the crucial issues of efficiency, optimal operating conditions and scale up for commercial use.

Previous investigations of vortex biomass pyrolysis reactors have been confined primarily to small scale experiments and limited global modeling. Such investigations have been performed by Diebold and Power (1988) utilizing a reactor $\sim 1m$ in length with a wall temperature of approximately $900K$ and measured mass feed rates up to $30kg/hr$. The reactor efficiency was observed to be enhanced by inserting a narrow pitch groove on the inside wall of the reactor in order to increase the particle residence times. Despite the fact that no quantitative experimental measurements were reported, their analysis suggests that the configuration is capable of efficiently pyrolyzing biomass for conversion to condensable tars. Quantitative measurements, parameter studies and mathematical optimization are the next necessary step before commercial use can be considered.

Although the literature addressing the vortex reactor is limited, previous investigations of different types of ablative reactor designs exist lending support to the potential of fast pyrolysis. While most reactors have been utilized in bench scale experiments, few have been shown to be viable for scale up to commercial sizes. These reactors generally employ a combination of direct-contact between the biomass particles and the heated surface in conjunction with mechanical breakup or grinding of the particles to further increase heating rates. The 'rotating cone' flash pyrolysis reactor is similar in design to the vortex reactor and was considered by Wagenaar *et. al.* (1994); however, only for 'cold flow' conditions. Peacocke and Bridgwater (1994) recently proposed an as yet untested ablative reactor design in which a four blade arrangement is used to apply the biomass particles directly to a hot surface under high relative velocity and pressure. Currently, published work for all of the above reactor types is relatively limited and many questions remain before actual commercial applications are viable. In particular, further research is needed to determine the efficiency of direct-contact pyrolysis, effects of ablative pyrolysis, optimal reactor temperatures, effects of the turbulent gas flow field, and range of particle sizes which can be economically pyrolyzed.

In this paper we present quantitative results from numerical simulations of full scale vortex reactors under viable operating conditions obtained from detailed mathematical models including a realistic formulation for the turbulent carrier gas flow field. The reactor design under investigation is based on the experimental facility at the National Renewable Energy Laboratory (NREL). Of particular interest are the identification and elucidation of pertinent physical processes as well as a quantitative assessment of parameter effects, optimal conditions and scaling potential. The full reactor simulations are obtained by coupling detailed sub-models used to describe the individual physical processes including: the individual particle pyrolysis, the turbulent carrier gas flow and the particle trajectories through the reactor. As will be discussed below, there is presently no complete documented set of data from the NREL reactor

that can be used to validate our simulations. The current validation philosophy is therefore based upon comparing the individual sub-models with experimental results from the literature that were obtained under appropriate conditions. Thus, the kinetics model and porous particle model composing the individual particle pyrolysis description were validated in Miller and Bellan (1997a). The turbulent carrier gas flow model will be validated here by comparison with swirling jet flow data (Nikjooy and Mongia 1991). Favorable comparisons for the sub-models lends support to the overall model validation when self-consistent sub-model couplings are instituted. Furthermore, consistency of the predictions with known aspects of the vortex reactor operation was checked as well.

The paper is arranged as follows. Specifics of the vortex reactor and its sub-models are addressed in Section 2. Single particle simulation results are presented in Section 3. Here we address the issues of particle dimensionality, wall heating, the response of the particle behavior to temporal oscillations in the free stream boundary conditions, and the introduction of a new fragmentation model needed to describe the mechanical break up of particles. Section 4 describes the coupling of sub-models and contains the reactor simulation results and parametric studies; the parameters being the wall temperature, feed rate, feed stock, particle size distribution and reactor scaling. Conclusions and further discussions are provided in Section 5.

2 Vortex Reactor and Sub-Model Formulation

Figure 1 provides a schematic illustration of the modeled vortex reactor. The design is an approximation of the experimental facility at NREL (note that the NREL reactor has been modified but not yet documented, since the publication of Diebold and Power 1988). A high temperature steam carrier gas is mixed with a biomass feed upstream of the inflow pipe. The mixture is then introduced tangentially into the reactor at high velocity creating a strongly swirling flow whereby the particles are centrifuged against the wall and remain primarily in direct sliding contact with the heated constant temperature surface (Diebold and Power 1988). Steam and resulting gaseous pyrolysis products then exit the reactor through an outflow of specified diameter whereas partially pyrolyzed particles are re-entrained through a small tangential recycle loop (not shown). The present investigation aims at modeling the steady state reactor operation. The modeling is accomplished through the coupling of sub-models for the individual particle pyrolysis, the turbulent swirling flow and the particle trajectories along the outer ($r = R_R$) heated wall.

2.1 Particle Pyrolysis Model

The individual macro-particle pyrolysis is based on the detailed model of Miller and Bellan (1997a) with a modification to incorporate particle fragmentation (described below). The kinetics scheme for the model is based on superimposed cellulose, hemicellulose and lignin reactions (Miller and Bellan 1997a). In this manner, any biomass feedstock can be simulated through the knowledge of its initial mass composition with respect to these three primary components. Each of the virgin components undergoes the same generic competitive reaction scheme:

$$\text{Virgin} \; - K_1 \rightarrow \text{Active}, \tag{1}$$

$$\text{Active} \; - K_2 \rightarrow \; \text{Tar}, \tag{2}$$

$$\text{Active} \; - K_3 \rightarrow \; X \text{ Char} \; + (1 - X) \text{ Gas}, \tag{3}$$

$$\text{Tar} \; - K_4 \rightarrow \; \text{Gas}. \tag{4}$$

Throughout the paper, the term 'tar' is used to refer to the primary high molecular weight pyrolysis condensable sometimes called 'bio-oil' or 'bio-crude' and includes any enriched oxygen and water vapor content. The virgin components, 'active' intermediates and char are solid phase species, while tar and 'gas' are vapor products; all the species represent groups of compounds rather than pure chemical species. All reactions are modeled with first order Arrhenius kinetics. The frequency factors and activation energies for reactions K_1, K_2, K_3, and the mass ratio X are all dependent on the particular biomass component, whereas all heats of reaction and secondary tar decomposition parameters are independent of the source component. Reaction K_1 has $\Delta h_1 = 0$, reaction K_2 is endothermic with $\Delta h_2 = 255 \; kJ/kg$, and both the char formation and secondary tar reactions are exothermic with $\Delta h_3 = -20 \; kJ/kg$ and $\Delta h_4 = -42 \; kJ/kg$. All remaining parameter values are provided in Miller and Bellan (1997a)

The porous particle model incorporates all property variations, is valid both inside and outside the particle, and employs a fully transient momentum equation in contrast to the traditional use of the empirical Darcy's Law. The derivation of the model has been addressed previously in Miller and Bellan (1997a) and only the final general form of the equations is presented here. The governing equations for apparent densities (ρ), gas velocity (u), mass fraction of species ξ (Y_ξ), total specific internal energy (e_t) and the equation of state relating gas density, pressure (p) and temperature (T) are:

$$\frac{\partial \rho_{s,\xi}}{\partial t} = \dot{S}_{s,\xi}, \tag{5}$$

$$\frac{\partial \rho_g}{\partial t} + \frac{\partial}{\partial x_j}\left(\rho_g u_j\right) = \dot{S}_g, \tag{6}$$

$$\frac{\partial \rho_g Y_\xi}{\partial t} + \frac{\partial}{\partial x_j}\left(\rho_g Y_\xi u_j - \rho_g D_{eff}^{(\xi)} \frac{\partial Y_\xi}{\partial x_j}\right) = \dot{S}_{g,\xi}, \tag{7}$$

$$\frac{\partial \rho_g u}{\partial t} + \varepsilon\left[\frac{\partial}{\partial x_j}\left(\rho_g u_i u_j\right)\right] = -\frac{\partial p}{\partial x_i} + \frac{\partial}{\partial x_j}\left[\mu_{eff}\left(\frac{\partial u_i}{\partial x_j} + \frac{\partial u_j}{\partial x_i} - \frac{2}{3}\frac{\partial u_j}{\partial x_j}\,\delta_{ij}\right)\right], \tag{8}$$

$$\frac{\partial e_t}{\partial t} + \frac{\partial}{\partial x_j}\left[e_g u_j - \lambda_{ji}^{eff}\frac{\partial T}{\partial x_i}\right] = p\frac{\partial u_j}{\partial x_j} + \sum \dot{S}_\xi \, \Delta h_\xi, \tag{9}$$

$$p = \frac{\rho_g}{\varepsilon}\left(\sum^{g} Y_\xi / M_\xi\right)\overline{R}T, \tag{10}$$

where

$$\rho_g = \varepsilon\widehat{\rho}_g, \qquad \rho_{s,\xi} = (1-\varepsilon)\widehat{\rho}_{s,\xi}, \qquad \varepsilon = 1 - \sum^{s} \rho_{s,\xi}/\widehat{\rho}_{s,\xi}, \tag{11}$$

$$D_{eff}^{(\xi)} = \varepsilon D^{(\xi)}, \qquad \mu_{eff} = \varepsilon \sum^{g} Y_\xi \mu^{(\xi)}, \tag{12}$$

$$\lambda_{ij}^{eff} = (1-\varepsilon)\left\{\frac{\sum^{s} \rho_\xi \lambda_{ij}^{(\xi)}}{\sum^{s} \rho_\xi} + \frac{\sigma d T^3}{\omega}\delta_{ij}\right\} + \varepsilon \sum^{g} Y_\xi \lambda_{ij}^{(\xi)}, \tag{13}$$

and

$$e_g = \rho_g \left(\sum^{g} C_v^{(\xi)} \right) T, \qquad e_s = \left(\sum^{s} \rho_{s,\xi} C^{(\xi)} \right) T, \qquad e_t = e_g + e_s, \tag{14}$$

where indices i, j correspond to coordinate directions (Einstein summation notation), ξ denotes species ξ (no summation over Greek indices) and δ_{ij} is the Kronecker delta function. In the above formulation, subscripts s, g and eff denote solid phase, gaseous phase and effective property values, respectively. Source terms due to reactions are represented by $\dot{S}$, the porosity is ε, the molecular weight is M, the true density is $\widehat{\rho}$, the universal gas constant is $\overline{R}$ and summations are over all species of indicated phase. Additionally, σ is the Stefan Boltzmann constant, ω is the biomass emissivity and d is a characteristic pore dimension; constant volume and solid phase heat capacities are C_v and C, and properties μ, D, λ are the viscosity, species diffusivity and thermal conductivity (tensor), respectively.

While the momentum equation (8) will be used in all reactor studies, for the purpose of obtaining qualitative understanding of some multi-dimensional particle effects it is convenient to also consider the more traditional Darcy's Law which is valid only within the particle. Darcy's Law states that the velocity is proportional to the local pressure gradient and the permeability (Γ):

$$u_i = -\frac{\Gamma_{ij}}{\mu_g} \frac{\partial p}{\partial x_j}, \tag{15}$$

where μ_g is the gas viscosity. Both forms of momentum equations are investigated in the following section for the purpose of comparing 1D and 2D Cartesian geometry simulation results. Several property values and initial conditions (subscript 0) used for biomass woods are given in Table 1 while remaining properties are provided in Miller and Bellan (1997a) The models for both the pyrolysis kinetics and porous particle transport have been tested extensively by Miller and Bellan (1997a) and shown to agree well with a large number of experimental results from a variety of investigators. Note that in the above set of equations both the thermal conductivity and the permeability are presented in full tensor format in order to account for spatial variations as addressed below.

Table 1: Property and initial parameter values for wood (across grain) and char.

Property	Value
$\rho_{s,0}$	$650 \frac{kg}{m^3}$
ε_0	0.67
C	$2.3 \frac{kJ}{kg \cdot K}$
λ	$1.256 \times 10^{-4} \frac{kJ}{m \cdot s \cdot K}$
Γ	$0.05\ Darcys$
λ_{char}	$8.37 \times 10^{-5} \frac{kJ}{m \cdot s \cdot K}$

Boundary conditions are defined based on the geometry under consideration and the particular choice of momentum equation as explained below. Particle shapes are assumed to be parallelepipeds based on elongated wood 'splinters.' These shapes have been observed in cold

flow visualizations in the bench scale vortex reactor at the National Renewable Energy Laboratory (NREL) (e.g. Diebold and Power 1988). Throughout the present work only Cartesian geometries are considered for both 1D and 2D particle analyses. Boundary conditions on the wall side of the particle are independent of the momentum equation: the temperature at the solid surface is matched to the wall condition ($T = T_w$), the velocity is set to zero, and all other fluxes are nulled (zero first derivative). Darcy's Law being qualitatively valid only within the particle, the model domain extends only to the outer edge of the particle; thus, the thermal boundary condition in direction i is based on a modeled surface condition (see e.g. Di Blasi 1993):

$$-\lambda_{nj}^{eff}\frac{\partial T}{\partial x_j} = \sigma\left(T^4 - T_\infty^4\right) + h'(T - T_\infty), \tag{16}$$

where n is the coordinate direction normal to the surface. Eq.(16) states that the heat flux entering the particle is due to both radiative and convective exchange with the far field temperature T_∞. In the present work, the coefficient of convection is assumed to be constant with $h' = 20W/K$. The pressure is assumed constant and equal to the far field condition. With the momentum equation derived from first principles (Miller and Bellan 1996), the solution domain includes regions outside of the particle, thereby accounting for the effects of exothermic tar reactions within the mass boundary layer immediately adjacent to the particle. Then, boundary conditions are provided by directly matching temperature and pressure values to the flow conditions at the particle location ($T = T^*$, $p = p^*$, where the superscript indicates local flow values), while velocity conditions are calculated through mass conservation constraints, and mass fractions are assumed to have zero first derivatives at the boundary. The use of both momentum equations and the dimensionality of the simulations are considered in the following section.

2.2 Turbulent Carrier Gas Model

The present vortex reactor is characterized by strongly swirling and recirculating flow regions. Such flows are poorly modeled using $k-\epsilon$ and all other turbulence models which invoke the gradient diffusion hypothesis relating turbulent viscosity and mean strain rate. For complex flows of the type addressed here, full Reynolds stress closures are recommended (Jones and Pascau 1989) in which modeled transport equations are solved for each of the individual components of the Reynolds stress tensor. The particular model chosen for this work is the fully compressible (to account for strong density variations) single species model of Zha and Knight (1996) with a modified model for the stress component diffusion terms (based on Launder *et. al.* 1975). Furthermore, the model has been extended to include species transport and chemical reaction. The tensorial form of the final model for the transport of the 'long time' Favre averaged (density weighted) variables is:

$$\frac{\partial \overline{\rho}}{\partial t} + \frac{\partial}{\partial x_j}(\overline{\rho}\widetilde{u}_j) = 0, \tag{17}$$

$$\frac{\partial \overline{\rho}\widetilde{u}_i}{\partial t} + \frac{\partial}{\partial x_j}(\overline{\rho}\widetilde{u}_i\widetilde{u}_j) = -\frac{\partial \overline{p}}{\partial x_i} + \frac{\partial}{\partial x_j}(\overline{\tau}_{ij} - \overline{\rho u_i'' u_j''}) + \overline{\rho} g_i, \tag{18}$$

$$\frac{\partial \overline{\rho e}}{\partial t} + \frac{\partial}{\partial x_j}(\overline{\rho e} + \overline{p})\widetilde{u}_j = \frac{\partial}{\partial x_j}\left[(\lambda + C_p\overline{\rho}C_h\frac{k^2}{\epsilon})\frac{\partial \overline{T}}{\partial x_j} + \widetilde{u}_i\overline{\tau}_{ij} - \overline{\rho u_i'' u_j''}\widetilde{u}_i\right] + \sum \dot{S}_\xi \, \Delta h_\xi, \tag{19}$$

$$\frac{\partial \overline{\rho}\widetilde{Y}_\xi}{\partial t} + \frac{\partial}{\partial x_j}(\overline{\rho}\widetilde{u}_j\widetilde{Y}_\xi) = \frac{\partial}{\partial x_j}\left[\overline{\rho}(D + C_h\frac{k^2}{\epsilon})\frac{\partial \widetilde{Y}_\xi}{\partial x_j}\right] + \dot{S}_\xi, \tag{20}$$

$$\frac{\partial}{\partial t}(\overline{\rho u_i'' u_j''}) + \frac{\partial}{\partial x_k}(\overline{\rho u_i'' u_j''}\widetilde{u}_k) = A_{ij} + B_{ij} + C_{ij} + D_{ij}, \tag{21}$$

$$\frac{\partial \overline{\rho}\epsilon}{\partial t} + \frac{\partial}{\partial x_j}(\overline{\rho}\epsilon\ \widetilde{u}_j) = -C_{\epsilon,1}\frac{\epsilon}{k}\overline{\rho u_i'' u_j''}\frac{\partial \widetilde{u}_i}{\partial x_j} - C_{\epsilon,2}\overline{\rho}\frac{\epsilon^2}{k} + \frac{\partial}{\partial x_j}\left[(\mu + C_{\epsilon,3}\frac{k^2}{\epsilon})\frac{\partial \epsilon}{\partial x_j}\right], \tag{22}$$

$$\overline{p} = \overline{\rho}\left(\sum \overline{R}\widetilde{Y}_\xi/M_\xi\right)\overline{T}, \tag{23}$$

where the shear stress tensor is,

$$\tau_{ij} = \mu\left[(\frac{\partial \widetilde{u}_i}{\partial x_j} + \frac{\partial \widetilde{u}_j}{\partial x_i}) - \frac{2}{3}\frac{\partial \widetilde{u}_k}{\partial x_k}\delta_{ij}\right], \tag{24}$$

the kinetic and internal energies are,

$$k = \frac{1}{2}\overline{\rho u_k'' u_k''}/\overline{\rho}, \qquad \widetilde{e} = C_v\overline{T} + \frac{1}{2}\widetilde{u}_k\widetilde{u}_k + k, \tag{25}$$

and the Reynolds stress production, diffusion, pressure rate of strain and dissipation term models are:

$$A_{ij} = -\overline{\rho u_i'' u_k''}\frac{\partial \widetilde{u}_j}{\partial x_k} - \overline{\rho u_j'' u_k''}\frac{\partial \widetilde{u}_i}{\partial x_k}, \tag{26}$$

$$B_{ij} = \frac{\partial}{\partial x_k}\left[\frac{C_s k}{\overline{\rho}\epsilon}\overline{\rho u_k'' u_l''}\frac{\partial}{\partial x_l}(\overline{\rho u_i'' u_j''})\right], \tag{27}$$

$$C_{ij} = -C_{p,1}\frac{\epsilon}{k}\left[\overline{\rho u_i'' u_j''} - \frac{2}{3}\overline{\rho}k\delta_{ij}\right] + C_{p,2}\overline{\rho}k(\frac{\partial \widetilde{u}_i}{\partial x_j} + \frac{\partial \widetilde{u}_j}{\partial x_i}), \tag{28}$$

$$D_{ij} = -\frac{2}{3}\overline{\rho}\epsilon\delta_{ij}, \tag{29}$$

respectively. In the above equations, subscripts i, j, k, l take values corresponding to the three orthogonal coordinate directions, the over bar corresponds to a time averaging, the tilde is used to denote Favre averages and the double prime superscripts represent fluctuations with respect to the Favre average. In addition, C_p is the heat capacity at constant pressure, g_i is the gravitational acceleration vector, ϵ is the turbulence dissipation, $\overline{\rho u_i'' u_j''}$ is the symmetric Reynolds stress tensor with six independent components, the subscript ξ corresponds to the gas phase species (steam, tar and gas); all remaining variables have been defined previously and properties are taken to be those of steam. Fluctuation contributions to the reaction terms are neglected due to the first order nature of the reactions and the relatively small heats of combustion involved. The turbulence model constants are provided in Table 2.

Since the full three dimensional solution of Eqs.(17)-(29) is prohibitively expensive, it is assumed that the vortex reactor flow (see Fig.1) is nearly axisymmetric, the assumption being valid when azimuthal variations are small compared to changes in the axial and radial directions; i.e. $\partial/\partial\theta \ll \partial/\partial x$, $\partial/\partial r$. This assumption is commonly used in confined swirling flow simulations (e.g. Jones and Pascau 1989; Sharif and Wong 1995; Sloan *et. al.* 1986; Nallasamy 1987), its validity being ensured within a short distance downstream of the entrance pipe. The 'reduced' equations are derived by expanding Eqs.(17)-(29) into three dimensional

cylindrical polar form and then dropping all terms involving derivatives with respect to the θ direction (while retaining the azimuthal velocity). This results in a set of 15 coupled transport equations along with the equation of state which are integrated to steady state from 'best guess' initial conditions. The integration uses a second order accurate in space and time explicit McCormack finite difference scheme. Inflow conditions are generally obtained from experimental measurements and will be discussed in more detail below, whereas outflow conditions are specified through zero first derivative approximations for all variables except the axial velocity component which is found through mass conservation constraints. Boundary conditions along solid walls are based on a combination of wall functions (following Sharif and Wong 1995) used to treat the turbulent boundary layer, constant outer wall temperature and zero first derivatives for remaining variables. Furthermore, the two end walls at $x = 0$, and at $x = L_R$ are assumed to be thermally insulating for reasons to be discussed below. Boundary conditions at the outer wall (where the particles reside) are used to couple the turbulent flow equations to the remaining sub-models in a manner described below. The turbulent flow code has been rigorously tested and validated both through agreement between results of our simulation with the data from measurements of a confined swirling jet flow (Nikjooy and Mongia 1991), and through comparison with the Reynolds stress model simulation of Nikjooy and Mongia (1991) (isothermal and incompressible) that used well documented initial and downstream conditions. Comparisons showed good agreement between the current code and the cited results (not shown).

Table 2: Turbulence model constants.

Constant	Value
C_s	0.22
C_h	0.0857
$C_{p,1}$	4.325
$C_{p,2}$	0.179
$C_{\epsilon,1}$	1.01
$C_{\epsilon,2}$	1.80
$C_{\epsilon,3}$	0.10

2.3 Particle Trajectory Model

The cold flow visualizations of Diebold and Power (1988) suggest that the majority of wood particles in the vortex reactor remain in flat contact with the wall, are parallelepiped in shape and in general convect with major axis (along the grain) parallel to the flow direction. In the present model, the particles are assumed to remain in sliding contact with the wall. In addition, it is assumed that the particle's relative dimension in the transverse direction is constant and equal to the particle height normal to the wall, H_p. Therefore, the particle dimensions are specified by the choice of the height and the aspect ratio $\Theta = L_p/H_p$ (where L_p is the particle length parallel to the grain). Lacking a complete resolution of the flow field around a real three dimensional wood particle, including the wake region, it is reasonable to assume that the drag experienced by the particle can be modeled as that over an elongated (prolate) spheroid

having the minor axis equal to H_p and the same aspect ratio. Under these assumptions, the trajectory of a single particle is governed by both drag resulting from slip velocities with the exterior flow and by a friction force at the wall which impedes forward acceleration. The modeled equations for position and velocity (in the x direction along the outer wall) are:

$$\frac{dx_p}{dt} = u_p, \tag{30}$$

$$\frac{du_p}{dt} = f\left[\frac{18V_p\mu}{m_p H_p^2}\right](\widetilde{u}_x^* - u_p) - f_\mu \frac{(\widetilde{u}_\theta^*)^2}{R_R} + g, \tag{31}$$

where x_p and u_p are the instantaneous particle position and velocity, V_p and m_p are the particle volume and mass, f_μ is the coefficient of sliding friction (assumed constant and equal to 0.1), g is the gravitational acceleration, the superscript $*$ denotes carrier gas variables evaluated at the particle location, and the modeled coefficient f is:

$$f = 1 + \frac{3\Delta Re_p}{16} + \frac{9\Delta^2 Re_p^2}{160}\ln(\Theta Re_p/2), \tag{32}$$

where,

$$Re_p = \frac{\overline{\rho}^* \left|\widetilde{u}_x^* - u_p\right| H_p}{\mu}, \tag{33}$$

and

$$\Delta = \frac{8(\Theta^2 - 1)/6}{\left[(2\Theta^2 - 1)\ln(\Theta + \sqrt{\Theta^2 - 1})/\sqrt{\Theta^2 - 1}\right] - \Theta}. \tag{34}$$

The bracketed term in [31] corresponds to Stokes drag over a sphere, whereas the factor f includes corrections for prolate spheroid aspect ratio at moderate particle Reynolds numbers (Clift *et. al.* 1978). The above equation set is Lagrangian and requires the specification of initial conditions for the particle position and velocity, in addition to the exterior turbulence flow field ($\overline{\rho}^*$, $\widetilde{u}_x^*$, $\widetilde{u}_\theta^*$) evaluated at the particle location ($r = R_R - 0.5H_p$) as indicated by the superscript $*$ (Favre fluctuations neglected).

3 Single Particle Results

Before discussing the coupling of the individual sub-models, it is necessary to first analyze the behavior of the single stationary particle model and seek possible simplifications. This section is devoted to such analysis and includes discussions of the numerical solution procedure and range of parameters for the model, along with further useful evaluations. In particular, although the particle model has been derived in general tensor coordinates, full multi-dimensional simulations are prohibitively intensive computationally. A comparison of 1D and 2D simulation results is made in this section in order to quantify the conditions under which the 1D approximation is justifiable. The extent of individual particle response to external flow conditions is then investigated in order to simply the outer edge particle boundary conditions as described below. Finally, a new fragmentation model is introduced in order to describe physical breakup processes occurring for ablative pyrolysis.

3.1 Multi-Dimensional Particle Evaluation

In order to assess the effects of dimensional and directional effects for wood particles, the particle equations (1)-(15) are solved numerically on both 1D and 2D grids. Darcy's Law is used instead of the full momentum equation for several reasons. First, Darcy's Law is computationally less intensive than the full momentum equation (8) due to both the numerical treatment of the pressure solution, and also because the domain extends only to the edges of the particle, thus requiring fewer computational grid points than the full equation solution which extends to exterior regions. Second, the full momentum equation was developed for 1D solutions applied to relatively large permeability porous particles; as such, it does not explicitly include the effects of varying parallel and cross grain permeability. Miller and Bellan (1996) showed that the use of Darcy's Law can result in substantial over predictions of the surface temperature and pyrolysis rate. Therefore, it will be desirable to use the full equation for the final reactor calculations. However, for the present purposes of directional analysis, Darcy's Law is sufficient.

The numerical solution to the particle equations uses finite difference approximations to the governing equations. The solution procedure is essentially the same as applied in Miller and Bellan (1996) with the exception that Darcy's Law is combined with the continuity equation to provide an equation for pressure in order to filter acoustic waves while retaining density variations. The resulting Poisson type equation is:

$$\frac{\partial}{\partial x_j}\left(\frac{\rho_g}{\mu_g}\Gamma_{ji}\frac{\partial p}{\partial x_i}\right) = -\left(\dot{S}_g - \frac{\partial \rho_g}{\partial t}\right). \tag{35}$$

Directional effects for both the permeability and the thermal conductivity of the wood are considered; however, mixed directional property variations are not considered, *i.e.* $\Gamma_{ij} = \lambda_{ij} = 0$, when $i \neq j$. Equation (35) is solved through a Jacobi iteration procedure at each numerical time step.

The geometry for the particle simulations is that of an elongated rectangular particle in flat contact with a hot constant temperature wall. Coordinates for the rectangular particle are defined with x_1 parallel to both the grain and the wall), and x_2 in the normal direction (the wall is then located at $x_2 = 0$). Calculations are made with identical particle size in the x_2 direction, $H_p = 5mm$, and 24 numerical grid points are used to partition the x_2 dimension, with equal grid spacing used for the parallel grain dimension ($L_p = \Theta H_p$). The single particle is assumed to be stationary in initially quiescent vapor phase steam. The symmetry in the x_1 direction at the particle mid-point allows for the solution of only one half the entire domain. Values for the wood conductivity and permeability are also fixed in this direction as listed in Table 1 and correspond to approximate cross grain values for typical Maple wood (SERI 1979); the results for all 1D simulations correspond to these cross grain property values. The kinetics scheme used for Maple wood follows the method of Miller and Bellan (1997a) by prescribing initial cellulose, hemicellulose and lignin content. The particle, wall and free stream temperatures are initially uniform at $400K$ and the pressure is $p = 100kPa$. During each simulation, the wall and free stream temperatures are both raised over a duration of $30s$ from $400K$ to their final values of $T_w = T_\infty = 900K$. The linear heating of the surface conditions is necessary for numerical resolution and does not affect the value of the results because the mass loss relative to the particle's initial mass is always $< 10\%$ at the final heatup time. All simulations discussed in this section are terminated when 90% of the virgin wood mass is consumed.

For comparison, an entire 2D calculation utilizing 24×24 numerical grid points ($\Theta = 2$) requires approximately $6300s$ of central processor time on a Cray J90 supercomputer whereas the corresponding 1D simulation requires approximately $300s$.

An example of directional property effects in a 2D particle simulation is illustrated in Fig.2. The figure depicts instantaneous velocity vectors for the internal flow field for three different simulations of particles with aspect ratio $\Theta = 2$. The wall is located at the surface $x_2 = 0$ and the surface at $x_1 = 0$ is a plane of symmetry located at the actual center of the particle. In all cases, the vector snap shots are taken at a time corresponding to 40% reduction in the wood mass (virgin plus active). Particle initial conditions and properties are identical for all these simulations including $\lambda_{11} = \lambda_{22} = \lambda$, except the permeability which is varied in the parallel grain direction (Γ_{11}). In general wood samples, the permeability in the parallel grain direction can exceed the cross grain permeability by several orders of magnitude (SERI 1979). The present results correspond to cases in which $\Gamma_{11}/\Gamma_{22} = 1$, 10, and 100, for parts (a), (b) and (c) of the figure, respectively. The vectors suggest that tar and gas produced by pyrolysis exit all surfaces of the particle nearly uniformly when there are no preferential permeability effects (Fig.2a). However, when the permeability is increased parallel to the wood grain, the exiting gas flow is redirected nearly completely through the surfaces defined by $x_1 = \pm H_p$.

The preferential permeability effects illustrated in Fig.2 can be quantified by examining the relative mass of tar collected from the particle as a function of time:

$$\beta = \frac{1}{m_{p,0}} \int_0^t \oint_A \rho_g Y_{tar} \, \vec{u} \cdot \vec{dA} \, dt, \tag{36}$$

where $m_{p,0}$ is the initial particle mass and the inner integral is over all surfaces. Tar collection for single isolated spherical biomass particles has been examined by Miller and Bellan (1997b) who studied the effects of reactor temperature, tar quenching and parameter sensitivity. The mass of gas, or the combined masses could also be examined; however, it is the tar which is ultimately of interest for the present purposes (in particular for hydrogen production). Figure 3 shows the temporal evolution of β for each of the three 2D simulations in Fig.2. Results from a 1D simulation are also included for comparison. The simulations suggest that there is virtually no deviation in the temporal mass loss due to preferential permeability effects. Only a very small increase in conversion time, with negligible change in final tar collection, is observed as the parallel grain permeability is increased by two orders of magnitude. This result is similar to a previous observation made by Di Blasi (1993) who found nearly no change in final char masses upon altering both the char and wood permeabilities in 1D simulations using Darcy's Law. The 1D particle approximation is observed to slightly over predict conversion times and under predict all of the 2D tar collection results for all times. However, the final magnitude of β is only slightly lower than the maximum observed value from the 2D calculations.

In order to highlight the effects, and limitations, of the 1D approximation it is instructive to compare simulation results for various values of the particle aspect ratio. Figure 4 depicts the tar collection as a function of time for both 1D and 2D simulations with particle aspect ratios of 1, 2 and 4. The simulation parameters are identical to those discussed above, and both the permeability and the conductivity have constant uniform values in order to isolate geometric effects. The 1D case corresponds by definition to an infinite aspect ratio particle; however, the results show that the approximation becomes reasonable for realistic finite aspect ratios. Again, results for the 1D geometry produce conservative estimates for β at all times and all

aspect ratios. The primary effect of particle geometry is observed in the total conversion time which decreases with decreasing aspect ratio. This effect is directly related to the surface area exposed to heating and pyrolysis relative to the total particle volume. On the other hand, the final values for β are much less influenced by the aspect ratio. In fact, the deviation in this value between the 1D approximation and a square particle is less than 5% of the initial particle mass. For $\Theta = 2$ this deviation is reduced to approximately 2.5%.

Biomass wood samples also have directional variations in thermal conductivity: a review of the literature shows that the conductivity is generally larger in the cross grain direction for both hard and soft woods. For example, measured ratios of $\lambda_{11}/\lambda_{22}$ for white pine, oak and balsa are approximately 0.75, 0.80 and 0.88, respectively (SERI 1979). These ratios are dramatically smaller in magnitude than those observed for permeability. The effects of these deviations are illustrated in Fig.5 which shows β as a function of time for both the 1D and 2D simulations with three conductivity ratios. The aspect ratio is fixed at $\Theta = 2$ and $\Gamma_{11}/\Gamma_{22} = 1$ in all cases in order to isolate conductivity effects. As with the permeability, only relatively small effects of conductivity are observed for either the conversion time or the final tar mass. The 1D approximation again results in conservative estimates for tar production with time; however, the final tar conversion is well predicted. Further simulations were conducted with conductivity ratios as large as 10 (not shown) which resulted in very large deviations from the behavior exhibited in Fig.5. Although such ratios are unrealistically large, they explain the permeability and aspect ratio behavior discussed when examining Figs.3 and 4. Both conductivity and aspect ratio affect pyrolysis in a direct manner, *i.e.* the particle heating rate is a direct function of the ability to heat large portions of the wood to pyrolysis temperatures. The majority of heat transfer into the particle occurs through conduction. As such, the conductivity plays a strong role in pyrolysis (even though realistic directional variations are relatively small as shown in Fig.5). The particle's aspect ratio also plays a strong role by dictating the surface to volume ratio of the particle which is exposed to heating. However, permeability primarily determines the path of the pyrolysis gaseous products upon being formed, resulting in only minor and secondary effects on the pyrolysis evolution even when large directional variations are present.

The above results suggest that the 1D particle geometry represents a valid approximation to the more complex multi-dimensional pyrolysis behavior for relatively large aspect ratio particles; in particular it produces conservative estimates of both tar collection and conversion time. The validity is not significantly affected by directional variations in the permeability, or for realistic values of the thermal conductivity. The approximation can also be considered justified for small aspect ratios ($\Theta \geq 1$) when only the final product yields are of interest. When the time evolution of pyrolysis products is needed, the 1D approximation results in over predictions of the conversion time. However, the deviations in total conversion time become negligible in the context of the vortex reactor due to a large number of passes (recycle loops) made by each particle through the reactor (discussed below), and the 1D approximation will, therefore be considered hereinafter. Furthermore, all simulations discussed hereinafter utilize the full momentum equation (8) in order to resolve the thermal and mass boundary layers adjacent to the particle surface, and the computational domain is extended to include the range $0 \leq x_2 \leq 1.5H_p$ for all simulations using a 32 grid point discretization. The value $1.5H_p$ is somewhat arbitrary; however, it is sufficiently large to resolve the region adjacent to the particle, while being small enough to allow for accurate sampling when the temperature

and pressure boundary conditions are later matched to the boundary layer flow conditions. All further simulations are continued until 99% decomposition of the virgin wood is completed and with a thermal boundary condition heatup time equal to one second per millimeter thickness H_p unless otherwise specified. Test cases comparing the results from single isolated 1D particle simulations with identical conditions (*i.e.* $0 \leq x_2 \leq H_p$) using the two momentum equations reveal essentially identical evolutions (not shown).

3.2 Direct-Contact Particle Heating

To further the discussions of isolated particle simulations, it is useful to analyze the efficiency of direct-contact particle pyrolysis. This is accomplished by performing two 1D simulations under the conditions previously discussed, *i.e.* $H_p = 5mm$, $T_w = 900K$, $\overline{T}^* = 900K$, where $\overline{T}^*$ now corresponds to the local exterior flow temperature condition at $x_2 = 1.5H_p$. In the first simulation, heating is only performed at the wall while the thermal flux is null in the free stream. The opposite conditions are employed for the second simulation; in this case heating is exclusively from the free stream and the wall is insulating. Both the tar collection and mass averaged particle temperature,

$$< T > = \frac{\int_0^{H_p} \rho_s' T \cdot dx_2}{\int_0^{H_p} \rho_s' \cdot dx_2}, \tag{37}$$

evolutions are presented in Fig.6. The superscript $'$ in the above equation denotes that solid phase char is excluded (Miller and Bellan 1996; Miller and Bellan 1997a; Miller and Bellan 1997b). Clearly, the direct-contact wall heating provides a dramatically improved pyrolysis and heating rates as compared to the flow heating case. The total conversion time is decreased by approximately 65% by direct-contact conduction heat transfer. For free stream heating, although thermal transfer occurs both through convection and conduction, the thermal conductivity of the gases is nearly an order of magnitude smaller than for the solid phases. Mass averaged heating rates are observed to be as large as $\sim 10K/s$ for the wall heating case and can exceed the calculated values by small percentages for realistic multi-dimensional particles. Furthermore, larger heat transfer rates result in higher effective pyrolysis temperatures which yield significantly larger final tar collection values from direct conduction pyrolysis. These results suggest that direct-contact reactors offer a significant potential for improvement in pyrolysis yields for tar production when compared to non-contact reactors.

3.3 Particle Response to Carrier Gas Flow

The governing equations for an individual particle's trajectory (30)-(34) are Lagrangian and solved numerically through forward time differences. These equations describe both the position and velocity of each biomass 'test particle' as it convects through the reactor (a test particle is a representative particle whose behavior is assumed to be the same as that of its surrounding neighbor particles). In general, a particle will make many passes through the reactor during its lifetime due to the recycle loop. As such, boundary conditions on the flow side of the particle ($\overline{\rho}^*$, $\overline{T}^*$, $\overline{p}^*$, $\widetilde{u}_x^*$, $\widetilde{u}_\theta^*$ at $x_2 = 1.5H_p$) are functions of the particle position, and hence of time. In addition, each recycle loop corresponds to a discontinuity in these boundary conditions as the particle is reset to $x_p = 0$, resulting in a difficult numerical resolution. In this section, we describe the conditions under which the time average values of the boundary

conditions (denoted by the double brackets << >>) can be used:

$$<< \phi^* >> = \frac{1}{t_c} \int_0^{t_c} \phi^*(t') \cdot dt', \tag{38}$$

instead of the instantaneous time values for any boundary condition variable ϕ^*.

An analysis of the relative time scales is useful in predicting the particle response to the boundary conditions. The majority of heat transfer to the particle from the free stream occurs through thermal diffusion (convective heat transfer is away from the particle due to the venting of pyrolysis gases). The ratio of the time scale for thermal diffusion ($t_\lambda \sim \rho C H_p^2/\lambda$) through the gas to the particle residence time during one loop through the reactor ($t_R \sim L_R/\tilde{u}_{x,in}$) is:

$$\frac{t_\lambda}{t_R} = \frac{\rho C/\lambda}{L_R/\tilde{u}_{x,in}} H_p^2, \tag{39}$$

where $\tilde{u}_{x,in}$ is the particle injection velocity into the reactor. In order to consider the particle pyrolysis evolution independent of temporal oscillations (and therefore well modeled using average boundary values), this ratio must be significantly larger than unity ($t_\lambda \gg t_R$); *i.e.* the particle passes through the domain much faster than the thermal diffusion response time. Using properties for wood and an assumed injection velocity $\tilde{u}_{x,in} = 10m/s$ with $L_R = 1m$ suggests that particles with H_p larger than approximately $0.3mm$ ($t_\lambda/t_r \approx 10$) can be justifiably assumed to respond only to average values for free stream boundary conditions.

To further illustrate the influence of boundary condition temporal oscillations on the particle, we calculate the particle response to a specified temporal disturbance in the free stream temperature boundary condition. This calculation is performed for a $1mm$ particle using a boundary temperature equal to $\overline{T}^*(t) = 850 + 25\sin(\omega' t)$. The amplitude of $\pm 25K$ is approximately the root mean square fluctuation calculated from actual reactor simulation results (not shown) and $T_w = 900K$. The temporal evolutions of tar collection produced from such simulations are presented in Fig.7 for various values of the oscillation frequency. The value $\omega' t = 0$ corresponds to no temperature fluctuations (*i.e.* using $<< \overline{T}^* >>$), while $\omega' t_c = 30$ results in 30 periods and corresponds approximately to the maximum number of re-entrainment loops for an experimental vortex reactor as estimated in Diebold and Power (1988) As it is clearly observed, there is no effect on pyrolysis due to thermal disturbances. The physical reason for this behavior is provided through the graphical illustration of char apparent density profile evolution displayed in Fig.8 for the $\omega' t_c = 0$ particle. The figure shows that even though there is a high temperature free stream boundary condition at $x_2 = 1.5H_p$, the direct conduction heat transfer from the $900K$ wall located at $x_2 = 0$ is significantly stronger. The char profiles reveal that the pyrolysis occurs almost entirely on the wall side which results in a pyrolysis wave moving outward, towards the free stream. Only a small fraction of the pyrolysis occurs on the free stream side as indicated by a small bulge in the char profiles near $x_2 = H_p$ for intermediate times. These results suggest that time averaged values for free stream temperature and pressure boundary conditions result in no loss of information, as the pyrolysis is effectively decoupled from the free stream disturbances. In addition, these results provide further justification for the use of a particle pyrolysis model with quiescent adjacent flow (neglected cross flow), since effects from the flow side of the particle are minimal. This can be understood by considering that a co-flow can affect the tar collection (36) in one of two primary manners: 1) by changing the pyrolysis evolution and hence the mass of tar production,

or 2) by affecting the ejection velocity at the particle surface (u_2 only, for 1D simulations). The above discussions have already highlighted how the thermal pyrolysis evolution is controlled mostly by the wall conditions; hence co-flow effects on pyrolysis are negligible. In addition, there is a velocity boundary layer due to no slip conditions such that $u_1 \rightarrow 0$ at the particle surface. This indicates that the ejection velocity is determined primarily by the internal particle pyrolysis, and the co-flow can only dictate the direction of the pyrolysis gases upon exiting the particle, not the tar collection parameter, β. Therefore, a quiescent particle model can be used for the present flow with no significant loss of information.

3.4 Particle Fragmentation

The single particle model was originally derived to describe the pyrolysis of large stationary biomass particles in initially quiescent steam or nitrogen environments and under controlled experimental conditions. In the case of stationary direct surface contact, the particle is in direct thermal contact with a hot surface and heat transfer to the particle proceeds almost entirely from the contact edge of the particle. As the pyrolysis wave progresses, an insulating layer of char is left behind which substantially diminishes the effective heating rate (Miller and Bellan 1996). In contrast, heating rates and conversion times are much more rapid in real reactors where the biomass particles convect at high velocities and pressures along the heated surface. Although no experimental measurements of such conversion times and pyrolysis yields are known to the authors, Esteban Chornet (Chornet 1997) of NREL suggests that large particles ($\sim 1cm$) have pyrolysis conversion times of $\sim 1s$ for reactor wall temperatures of $900K$. This value is approximately two orders of magnitude smaller than for stationary particles of similar sizes and at similar temperatures and under the above mentioned conditions (see e.g. Figs.3-6). This large difference in conversion times must be reconciled by identifying the pertinent physical causes which are unique to ablation pyrolysis.

One yet unproved explanation for the increase in pyrolysis rates under ablative conditions that has received renewed attention recently by Lede *et. al.* (1997) is based on the possible existence of a liquid intermediate pyrolysis product ('active' in Eqs.(1) and (2)). The explanation speculates that such an intermediate, which remains liquid at the high temperature reactor conditions, forms a thin lubricating and highly conductive layer between the biomass particle and the hot reactor wall, thus increasing heat transfer rates to the particle. This layer is stated to be of negligible influence for lower temperature TGA conditions but becomes significant at the higher temperatures associated with ablation processes. However, such an argument appears inconsistent with the results of many isothermal, non-ablative experiments at similar temperatures (with up to $1000K/s$ heating to final temperature) which have been well described without liquid layer effects by a model which also agrees with experimental results obtained in the TGA regime (Miller and Bellan 1997a). Furthermore, no direct observations have ever been made of such a liquid and its existence is hypothesized primarily on indirect evidence such as observed similarities between the pyrolysis and actual solid phase melting, whereby pyrolysis is restricted to a relatively narrow band of temperatures. In this section we provide supporting evidence that rejects the liquid layer postulate and also present a new and self-consistent explanation for increased ablative heating rates.

Within the present context, it is useful to address at least the following three considerations related to the existence of an intermediate liquid layer of the type described above: (1) The limited range of temperatures over which pyrolysis is observed to occur has already been well

explained in terms of the endothermicity of biomass reactions by several researchers (Miller and Bellan 1996; Narayan and Antal 1996). (2) A liquid layer inserted between the particle and hot wall, regardless of thickness, cannot decrease the conversion times for direct wall contact particle pyrolysis. This is due to the fact that it is the insulating char layer that is the limiting factor in heat transfer from the wall (see Table 1). (3) It is well understood that the production of char from a non-fluid state results in a 'non-graphitizing', disordered carbon (i.e. hard carbon; see e.g. Fitzer *et. al.* 1971), in contrast to the smoother fine scale structure that would be observed had the char been produced directly from a fluid intermediate. The actual chars produced through pyrolysis of cellulose and other biomass stocks are indeed observed to be of the disordered (amorphous) carbon form (Fitzer *et. al.* 1971; Wornat *et. al.* 1995). Therefore, chars produced during biomass pyrolysis are direct products of solid phase *media* and are not produced from a liquid 'active' intermediate.

In light of the above arguments, the observed discrepancy in heating rates can only be attributed to a mechanical breakup of the insulating char region formed between the heated wall and the un-pyrolyzed particle matrix; *i.e.* as the particle slides along the wall, this char layer is 'smashed' or scraped off due to large shearing and stress forces. This is evidenced by the fact that the chars collected from the NREL reactor are powder size ($\sim 50\mu m$) in contrast to the large ($\sim 1cm$) input wood chips (Diebold and Power 1988). In order to model these breakup processes it is useful to consider past work in the field of particle fragmentation. Kerstein and Niksa (1984) used the results of both deterministic and statistical models based on percolation theory (geometric theory of the connectedness of irregular objects) to describe the fragmentation of carbon chars undergoing combustion. In their model, a homogeneous and stationary sample fragments due to a loss of structural integrity when the porosity reaches ≈ 0.7; a value found to be in good agreement with experiments. For the present situation, we hypothesize that there exists a similar critical value of the biomass porosity at which fragmentation of the char occurs. When this critical porosity is reached, the particle collapses upon the insulating char layer, thus bringing the un-pyrolyzed portion of the particle closer to the wall and increasing the effective heating rate. Unfortunately, percolation theory cannot be directly applied to the current more complex problem as the critical porosity is expected to depend on many unknown factors including the biomass feed stock, the particle velocity and the contact pressure.

In order to illustrate the possible effects of such a critical porosity (denoted ε_c), a series of simulations of the porous biomass particle equations (Eqs.(5)-(14)) are performed incorporating a simple model for critical porosity effects. Fragmentation modeling is implemented by assuming that as the porosity reaches the specified critical value on the wall side of the particle, the particular location comes into direct thermal contact with the wall due to the removal of all fragmented chars. In practice this is accomplished by setting the temperature to be $T = T_{wall}$ for all $\varepsilon \geq \varepsilon_c$ within the wall side of the particle. This model has the additional feature that all un-pyrolyzed mass in the region $\varepsilon \geq \varepsilon_c$ continues to react at the wall temperature as though it had fragmented into many small (kinetically controlled) pieces, each piece remaining in thermal contact with the wall. Consider a single Maple particle of initial thickness $H_p = 5mm$ and temperature $T_0 = 450K$, that is exposed at time $t = 0$ to a heated wall located at $x_2 = 0$ on one side and a high temperature steam having the same temperature on the opposite side. The outer boundary for the solution of Eqs.(5)-(14) is located at $x_2 = 1.5H_p$ in order to accurately capture all mass and species boundary layer phenomena. The one dimensional domain is

discretized using 48 grid points and the proceeding simulations require between approximately $600s$ and $7200s$ of processor time on a Cray J90 supercomputer. Additional details of the solution procedure and boundary conditions can be found in Miller and Bellan (1996); Miller and Bellan (1997a); Miller and Bellan (1997b) Figure 9 shows both the tar collection variable β and the 99% conversion time (t_c) as a function of the critical porosity and for various values of the wall temperature. Fragmentation is observed to result in substantial variations in tar collection and several orders of magnitude decreases in conversion times. As the critical porosity approaches the initial matrix porosity, $\varepsilon_0 = 0.67$, the solutions approach the kinetic pyrolysis limits. Note that the maximal tar collections are consistent with the upper bounds measured for nearly kinetically controlled Maple particles by Scott *et. al.* (1988). The wide range of values for the conversion time and tar collection are evidence of the model's robustness in portraying a broad degree of ablation without resorting to a hypothetical liquid layer. Currently, there are no available quantitative experimental measurements under related conditions to guide the choice of a specific value of ε_c, or to determine its dependence and sensitivity to velocity and pressure. In the absence of such information, a constant value $\varepsilon_c = 0.75$ is selected in order to match suggested (Chornet 1997) values of $t_c \sim 1s$ at $T_{wall} \approx 900K$. This value for ε_c is used hereinafter throughout the paper.

4 Reactor Results

The above sets of governing equations for the particle pyrolysis, turbulent reactor flow and particle trajectories are coupled through appropriate conservation constraints in order to provide a complete description of the final reactor operation. Under steady state operation, the contribution of all injected biomass particles can be simulated by obtaining numerical solutions for a single 'test' particle for each injected size class and each biomass type contained within the reactor feed. As each test particle convects along the reactor outer wall, its free stream boundary conditions for temperature and pressure correspond to the same conditions for the turbulent reactor flow field at a position corresponding to $r = R_R - 1.5H_p$ (averaged as in Eq.(38)). On the other hand, complementary boundary conditions for the turbulent reactor flow equations must account for the presence of particles through a mild 'wall blowing' (tar and gas evolving from the pyrolyzing particles) whereby an inward directed radial velocity component enters the reactor through the outer wall. This wall inflow has appropriate contributions for the tar and gas being generated by the pyrolysis of a single test particle multiplied by the local particle number density (N is the number of particles per unit wall area specific to each test particle group):

$$N = \frac{\dot{m}_{feed}}{m_{p,0}\ 2\pi R_R\ u_{p,in}}, \tag{40}$$

where $\dot{m}_{feed}$ is the specified mass feed rate of particles, and $u_{p,in}$ is the particle injection velocity. Such a coupling is valid as long as $H_p \ll R_R$. It is assumed that the local number density N corresponding to each injected test particle remains constant throughout the particle's evolution (divergence free spread velocity along the wall) and that the particles are in direct sliding contact with the wall and maintain a tight helical path through the reactor such that their downstream axial paths can be described by a continuous $u_p(x)$ in the axisymmetric coordinates (see Fig.1). Re-entrainment is performed by re-introducing all particles that reach the down

stream edge of the reactor, $x = L_R$, and the tar and gas generated from each recycle loop, size class and biomass type are superimposed. The actual mass of flow entering the real recycle loop is assumed to be much smaller than that passing through the exit pipe. In this case, the recycle loop is not included in the reactor simulation as its practical implementation is of questionable validity due to the axisymmetric geometry. For conditions in which each test particle makes many passes through the reactor (satisfied in this work), the particle contributions are essentially equal to the total tar and gas yields from each test particle multiplied by the total number of particles within the reactor and then distributed uniformly over the entire outer wall surface area. This results in a near uniform value for $\overline{\rho}\widetilde{u}_r(r = R_R)$ corresponding to the rate of gaseous mass generation from all particles. Boundary conditions for the tar and gas mass fractions at the reactor wall are derived to include the diffusion (molecular plus turbulent) velocity:

$$(\Psi_\xi\ \overline{\rho}\widetilde{u}_r)\ |_{r=R_R} = \left(\widetilde{Y}_\xi \overline{\rho}\widetilde{u}_r\right)|_{r=R_R} - \left[\overline{\rho}(D + C_h\frac{k^2}{\epsilon})\frac{\partial \widetilde{Y}_\xi}{\partial r}\right]|_{r=R_R}, \tag{41}$$

where Ψ_ξ is the relative fraction of the generated gaseous mass $(\overline{\rho}\widetilde{u}_r\ |_{r=R_R})$ for species ξ. Equation (41) ensures that the proper mass of tar and gas enter the domain: it is an implicit relation for the outer wall boundary conditions, $\widetilde{Y}_\xi\ |_{r=R_R}$, and is solved at each numerical time step and axial wall node. In practice, the test particle, particle trajectory and turbulent reactor flow equations are first solved independently using guessed coupling conditions, and then successive iterations are performed until a converged steady state solution is obtained.

Table 3: Base case reactor geometry and inflow conditions.

Parameter	Value
L_R	$1.0m$
R_R	$0.125m$
D_{in}	$0.4R_R$
D_{out}	R_R
$\overline{T}_{in}$	$450K$
$\overline{p}_{in}$	$100kPa$
$\widetilde{u}_\theta$	$200m/s$
k	$0.2\widetilde{u}_\theta^2$
ϵ	$k^{3/2}/0.4D_{in}$
H_p	$5mm$
Θ	2
$\dot{m}_{feed}$	$50kg/hr$ Maple

Simulation of the current NREL vortex reactor requires the specification of the reactor geometry, wall temperature and all pertinent inflow conditions; however, these parameters have not been documented (note that the reactor has been renovated since the publication of Diebold and Power 1988) and these values must therefore be estimated. Table 3 contains a list of all 'base case' geometry and inflow conditions used hereinafter in the reactor simulations. The inflow profiles (i.e. at $x = 0$) are uniform in the region $R_R - D_{in} \leq r \leq R_R$ and

slightly smoothed near the boundaries for numerical stability. The turbulent inflow is pure steam whose mean turbulence kinetic energy is assumed to be equally divided among each of the three diagonal components of the Reynolds stress tensor. However, the off-diagonal terms at the inflow have a zero first derivative allowing the development of a more natural measure of anisotropy. The radial injection velocity is null and the turbulence dissipation rate ϵ is modeled using a commonly used function of k and the inflow pipe diameter, D_{in} (Nikjooy and Mongia 1991). In addition, an axial velocity component must be defined such that the correct mass flow rate ($\rho \widetilde{u}_{\theta,in} \pi (D_{in}/2)^2$) of steam entering the numerical domain is obtained. The axial velocity is calculated using the ratio of the true entrance pipe area to the numerical axisymmetric inflow area:

$$\widetilde{u}_{x,in} = \widetilde{u}_{\theta,in} \left[\frac{\pi (D_{in}/2)^2}{\pi \left[R_R^2 - (R_R - D_{in})^2 \right]} \right] = \widetilde{u}_{\theta,in} \left[\frac{1}{4} \left(\frac{\Phi_1}{2 - \Phi_1} \right) \right], \tag{42}$$

where $\Phi_1 = D_{in}/R_R$. Note that if the pipe diameter has its maximum value, $D_{in} = R_R$, then the inflow remains predominantly swirling with $\widetilde{u}_{x,in} = 0.25\ \widetilde{u}_{\theta,in}$. In addition, the injected particles are assumed to be in dynamic and thermal equilibrium with the steam flow (zero slip and zero temperature difference, i.e. $u_{p,in} = \widetilde{u}_{x,in}$ and $T_{p,0} = \overline{T}_{in}$, respectively). All reactor flow simulations incorporate a numerical grid having 192×48 grid points in the (x, r) plane and require approximately $7200s$ of processor time on a Cray J90 supercomputer for convergence to steady state mean reactor flow. Generally, two or three iterations between the test particle, particle trajectory and reactor flow equations are needed for final convergence.

Figure 10 depicts various steady state (x, r) reactor flow profiles of the steady state solution from the base case simulation with $T_{wall} = 900K$ ($r = 0$ is the axis of symmetry). The velocity vectors in Fig.10a reveal a region of strongly recirculating core flow near the entrance region of the reactor as it is expected for strongly swirling confined flows (e.g. Sloan *et. al.* 1986; Nallasamy 1987). The temperature contours in Fig.10b show that this recirculation zone consists primarily of low temperature material entrained from the inflow. However, further downstream the core flow is rapidly heated due to turbulent convective heat transfer from the walls. Had heated wall conditions been used for the end walls at $x = 0$ and $x = L_R$, both the recirculation region and the reactor core temperature would be significantly larger than the current values. Such high temperature conditions would enhance tar decomposition (through Eq.(4)) within the reactor, thus decreasing its efficiency for tar collection from the exit pipe flow; thus, heated-end-wall reactor operation is not recommended. Tar and gas mass fraction contours are presented in Figs.10c and 10d, respectively. Although the mass addition of these species generated by the biomass pyrolysis is nearly uniform along the $r = R_R$ wall, the actual boundary condition values increase monotonically with x due to the effects of the turbulent diffusion term in Eq.(41). However, for all axial locations, both the tar and gas profiles have maximal values at the wall and decrease monotonically towards the central reactor core region.

4.1 Reactor Efficiency and Wall Temperature Effects

Regardless of the particulars of the interior reactor flow profiles, the 'true' measure of the reactor efficiency for tar production can be determined quantitatively by comparing the actual mass rate of tar exiting the reactor (Ω_R) and the mass rate of tar exiting the particles (Ω_p):

$$\Omega_R = \int_0^{0.5 D_{out}} 2\pi r \left(\overline{\rho} \widetilde{Y}_{tar} \widetilde{u}_x \right) |_{x=L_R} \cdot dr, \tag{43}$$

$$\Omega_p = \sum \left\{ 2\pi R_R N \int_0^{t_c} (\rho_g Y_{tar} u) \mid_{n=H_p} \cdot dt \right\}, \tag{44}$$

where the summation is over all particle size classes and biomass types (i.e. all different test particles injected). With these definitions two unique measures of the reactor performance are the reactor efficiency (η) and the % tar reduction (γ):

$$\eta = \Omega_R / \dot{m}_{feed}, \qquad \gamma = (\Omega_p - \Omega_R)/\Omega_p, \tag{45}$$

which quantify the relative efficiency of reactor tar production normalized by the mass feed rate of biomass and the relative proportion of tar produced in the reactor which is decomposed to gas before exiting the reactor, respectively.

A brief evaluation of the above relations and the following model aspects yields an interesting feature of the reactor efficiency parameters η and γ: (1) The results of Figs.7 and 8 showed that the mass of tar produced by the particles (Ω_p) is dependent almost exclusively on the wall temperature due to the dominance of pyrolysis on the wall side of the particle relative to the flow side heating. (2) The species mass fraction equations (Eq.(20)) are linear in $\overline{Y}_\xi$. (3) The exothermicity of tar reactions is essentially negligible due to its relatively small heat of combustion and the very dilute fractions of tar observed (see Fig. 10c). (4) Under the assumptions of the model, any increase (decrease) in mass injection rate results in a corresponding linearly proportional increase (decrease) in the tar and gas mass fraction values along the outer wall due to particles. (5) The mass rate of generation of tar and gas by the particles is much smaller than the inflow pipe mass flow rate of steam. The ensemble of these characteristics leads to the following conclusion: both of the efficiency parameters η and γ are essentially independent of the biomass feed rate, $\dot{m}_{feed}$. In addition, considerations (2) and (3) indicate that for fixed reactor geometry, the parameter γ is essentially a function of the wall temperature only. These conclusions have been tested using actual results from a variety of simulations (not shown).

Figure 11 shows the steady state efficiency parameters for the base case reactor flow as a function of both the wall temperature and the corresponding minimum heating energy:

$$E_{\min} = \int_0^{L_R} 2\pi R_R \left[(\lambda + C_p \overline{\rho} C_h \frac{k^2}{\epsilon}) \frac{\partial \overline{T}}{\partial r} \right]_{r=R_R} \cdot dx + \dot{m}_{feed}\, C\, (T_{wall} - T_{p,0}), \tag{46}$$

which is given by the summation of the integrated thermal flux rate through the outer wall and the estimated energy needed to raise the particle mass feed from its initial temperature to the wall temperature. This minimum energy corresponds to a perfectly insulating reactor with no heat loss to the surroundings, and both the steam and pyrolysis gases are assumed to be transparent to radiation heat transfer from the reactor walls. For the present conditions, the contribution from the second term on the right hand side of Eq.(46) due to particle heating is in all cases less than 5% of the total $E_{\min}$; therefore, the majority of input energy is used to heat the steam. Although $E_{\min}$ could be reduced by increasing the inflow steam temperature, similar power would still be required for the necessary steam pre-heat. The results of Fig.11 show an optimal wall temperature of approximately $900K$ for which tar harvest is maximized at slightly more than 80% of the feed mass. The vortex reactor is characterized by competing influences of Ω_p and γ which both increase linearly over the range of temperature considered. These two effects result in the optimal wall temperature observed which corresponds to a minimum input energy of approximately $355kW$ required to heat both the steam carrier gas and the Maple particles.

4.2 Particle Size, Biomass Type and Size Distribution

Miller and Bellan (1997b) observed that relative tar yields are significantly increased as the initial particle size decreases. This effect was attributed to the relative residence time of tar within the particle and its adjacent boundary layer. The longer residence times associated with large particles allow for more substantial tar decomposition to gas through Eq.(4). Using similar reasoning, tar yields are maximized for very small particles which approach the kinetic limits of pyrolysis (provided that tar can be rapidly quenched upon exiting the particle). However, these trends due to particle size are not observed in the present simulations as illustrated by Fig.12 which shows the reactor efficiency as a function of wall temperature for the base case conditions and for two particle sizes. Note that the curves are nearly identical for temperatures $T_{wall} > 800K$. This new behavior is due to the introduction of the critical porosity for fragmentation. As $\varepsilon_c \rightarrow \varepsilon_0$ the pyrolysis occurs very rapidly and approaches the kinetic limits regardless of the initial particle size. All gaseous pyrolysis products are forced at increasingly large velocities out of the particle before significant decomposition can occur. Therefore, as $\varepsilon_c \rightarrow \varepsilon_0$ the pyrolysis becomes independent of the initial particle size. For the present case of $\varepsilon_c = 0.75$, the results show only negligible differences in behavior between $H_p = 1mm$ and $H_p = 5mm$ particles, except at very low wall temperatures. When $T_{wall} < 800K$ the pyrolysis rate is relatively slow as compared to the tar reaction rate and the particle size becomes more significant.

Effects of different biomass feedstocks and polydisperse particle injection distributions can also be investigated with the model. Table 4 shows various steady state reactor efficiency values calculated for the base case conditions with the optimal $T_{wall} = 900K$ together with the biomass contributions of cellulose, hemicellulose and lignin (Miller and Bellan 1997a). Tar harvest is observed to be strongly dependent on the lignin content of the biomass which is known to be the primary source of char (Miller and Bellan 1997a). In general, the representative Bagasse grass, Maple and Oak woods all result in very similar tar collections from the reactor due to their similar compositions. It is only for the relatively extreme samples of pure cellulose and high lignin content Olive Husk that large deviations in tar yield are observed.

Table 4: Compositions and reactor efficiencies for base case conditions and various biomass with $T_w = 900K$.

Biomass	Cellulose	Hemicellulose	Lignin	η
Cellulose	1	0	0	0.903
Bagasse	0.36	0.47	0.17	0.824
Maple	0.40	0.38	0.22	0.814
Oak	0.35	0.40	0.25	0.824
Olive husk	0.22	0.33	0.45	0.749

Due to the primary influence of the wall heating on the particle pyrolysis and corresponding lack of particle-flow and particle-particle interactions, the model predicts that polydisperse particle injections will result in essentially mass weighted linear superpositions of the contributions from each individual test particle. Consider a bimodal injection of Maple particles

with $H_p = 1mm$ (denoted group I) and Olive Husk particles with $H_p = 5mm$ (denoted group II). In this case a dispersity variable (α) can be defined based on the relative injection rate of Maple particles:

$$\alpha = \frac{\dot{m}_{feed}\,(I)}{\dot{m}_{feed}\,(I) + \dot{m}_{feed}\,(II)}, \tag{47}$$

which takes continuous values between 0 (pure group II) and 1 (pure group I). The superposition effect is illustrated for this bimodal distribution in Fig.13. Therefore, within the range of conditions for which the current model is applicable, results for any polydisperse mixture injection can be deduced through knowledge of the individual pure component/pure initial particle size behaviors.

4.3 Reactor Scaling

As discussed above, the mass of tar produced by particles (Ω_p) can be optimized through appropriate choices of the reactor wall temperature and biomass species. The reactor configuration and inflow steam parameters therefore primarily affect only the relative decomposition of the tar once it exits the particles and proceeds through the reactor. In this section, the effects of the reactor geometry and scaling are investigated in order to suggest optimal conditions for minimizing tar conversion to gas within the reactor. A mathematical estimate for the extent of such reactions is obtained by examining the ratio of the tar residence time within the reactor ($t_R \sim L_R/\widetilde{u}_{x,in}$) relative to the characteristic time scale for tar decomposition ($t_{tar} \sim K_{tar}^{-1}$, where K_{tar} is the Arrhenius reaction rate from Eq.(4)):

$$\frac{t_R}{t_{tar}} \sim \left(\frac{L_R}{\widetilde{u}_{x,in}}\right) K_{tar} = 16 \left[\frac{R_R \Phi_2}{\widetilde{u}_{\theta,in}} \left(\frac{1}{\Phi_1} - \frac{1}{2}\right)\right] \times \left[A_{tar} \exp\left(\frac{-E_{tar}}{\overline{R} T_{wall}}\right)\right], \tag{48}$$

$$0 < \Phi_1 \leq 1, \qquad \Phi_2 > 0, \tag{49}$$

where $A_{tar} = 4.28 \times 10^6 s^{-1}$ is the tar reaction frequency constant, $E_{tar} = 108 kJ/mol$ is the corresponding activation energy, $\Phi_2 = L_R/2R_R$ is the overall reactor aspect ratio and Eq.(42) has been invoked. The first term in brackets on the right hand side of Eq.(48) is due to reactor geometry and inflow steam mass rate, whereas the second bracketed term is due entirely to the wall temperature. Note that the above estimate does not reveal any dependence on the exit pipe diameter as the tar residence time is primarily only dependent on the axial injection velocity and the reactor length. Optimal reduction of tar decomposition occurs when $t_R/t_{tar} \ll 1$ in which case the tar is removed from the reactor much faster than it can react to form gas. Note that the use of T_{wall} as a characteristic reaction temperature results in generating an upper bound for t_R/t_{tar} as the majority of tar is located away from the walls where the temperature is in reality always less than T_{wall} (see Fig.10b).

An evaluation of the above time scale ratio for the base case reactor parameters as a function of wall temperature is depicted in Fig.14 for three different reactor scales. The scale factor (M) in this case represents a direct multiplication of the reactor length and radius by the particular M factor (e.g. $M = 3$ is a reactor having $L_R = 3m$ and $R_R = 0.375m$); all remaining dimensions and parameters are determined by the relations in Table 3 and previous discussions. The time scales clearly illustrate how tar decomposition is increased with both increasing wall temperature (due to higher reaction rates) and increasing reactor scales (due to longer tar residence times). In fact, the curve for $M = 1$ shows clearly that these reactions

should become significant ($t_R/t_{tar} \sim 0.1$) for wall temperatures of $\approx 900K$, which is also the optimal reactor temperature found previously from the simulation results of Fig.11.

The accuracy of the time scale estimate, t_R/t_{tar}, in predicting reactor performance can be further confirmed by comparing the results of complete simulations. Figure 15 shows the reactor efficiency and % tar reduction parameters calculated from base case simulations with $T_{wall} = 850K$ as a function of the reactor scale. The relative extent of tar decomposition reactions appears to increase linearly with M exactly as predicted by Eq.(48) which is linear in R_R (with Φ_2 fixed). A comparison of Figs.14 and 15 along with the above discussions appears to indicate that 'good' reactor designs which minimize tar decomposition are characterized by $t_R/t_{tar} < 0.1$. This would indicate that a large reactor needs to operate at low temperatures. Unfortunately, low temperatures do not promote large tar generation from the particles indicating that large reactor sizes are undesirable.

5 Conclusions

A detailed mathematical model of vortex pyrolysis reactors used for harvesting tar from biomass has been presented. The model is based on detailed sub-models for the porous particle pyrolysis, turbulent reactor flow and test particle trajectories. The sub-models were chosen for their ability to capture the pertinent physics and were based on the requirements of each subsystem. The kinetics and porous particle model of Miller and Bellan (1997a) were chosen to simulate the individual particle pyrolysis. Both one dimensional (1D) and two dimensional (2D) Cartesian coordinate simulations were performed in order to assess the effects of geometry and spatial property variations for single particles. The results showed that the 1D model based on cross grain properties yields correct qualitative pyrolysis behavior while providing slightly conservative estimates for the quantitative particle conversion times. However, the total tar and gas products predicted by the 1D approximation are in good agreement with the multi-dimensional simulations. Further results were obtained exclusively with the 1D model. The individual particle trajectories were then modeled based on a prolate spheroid particle drag coefficient and on contact friction with the wall. Extensive studies of these equations showed that the individual particle pyrolysis evolution is effectively de-coupled from temporal disturbances of the temperature and pressure boundary conditions on the flow side of the particle. This means that the particle responds to only time averaged values of the flow properties, and greatly simplifies the solution procedure. A new fragmentation model was then introduced into the particle equations to account for mechanical breakup of the insulating char layers which occurs during ablative pyrolysis. Large ablative heating rates were shown to be well described by the fragmentation model without resorting to the artificial introduction of a liquid 'active' lubricating layer. In order to properly simulate the complex reactor flow, a compressible form of the full Reynolds stress transport model for swirling axisymmetric flow was used. All sub-models were then coupled using appropriate conservation laws to provide complete solutions to the steady state vortex reactor problem.

The simulation results elucidated many of the important physical processes and characteristics of the vortex reactor for tar collection from biomass pyrolysis. An optimal reactor wall temperature was identified as $T_{wall} \approx 900K$ for which tar yields are maximized. This value was found to be practically independent of the initial particle size for H_p as large as $5mm$ due to relatively severe char fragmentation. It was additionally observed that tar yields can be

increased by using low lignin content feed stocks, and that they are independent of the initial particle aspect ratio if the assumptions necessary for the one dimensional particle equation approximation are satisfied ($\Theta \geq 2$). Polydispersity of the injected biomass was shown to be well modeled using mass weighted superpositions of the pure substance/single particle size distribution contributions. Under the base case reactor conditions with biomass injection having $\dot{m}_{feed}$= $50kg/hr$ of $5mm$ Maple particles and $T_{wall} = 900K$, it was found that more than 80% of the mass feed can be harvested in the form of tar. This optimal case requires a minimum of $355kW$ of operational input power to heat both the carrier gas and the biomass. Note that the tar yields measured in this work depend to a significant extent on the proper choice of the critical porosity (ε_c) for the fragmentation model. The critical porosity was only estimated and it is recommended that experimental measurements should be performed to determine its value.

Evaluation of simulated results and a simple model indicate that the time scale ratio (t_R/t_{tar}) is directly proportional to the reactor size (both its radius and overall aspect ratio). In contrast, t_R/t_{tar} is inversely proportional to both the entrance flow velocity and the entrance pipe diameter. Therefore, tar reactions within the reactor can be reduced by: (1) small reactors in both size and length to diameter ratio, (2) large steam inflow velocity and mass flow rate, (3) low reactor wall temperatures which reduce the tar reaction rate. Note that criterion (2) must be balanced with a corresponding increase in the energy needed to heat the inflow steam ($E_{\min}$) while (3) must be balanced with its adverse relation on the total tar produced by the biomass particles. It is therefore recommended that vortex reactors used to harvest tar from biomass pyrolysis operate with $T_{wall} \approx 900K$ with large inflow velocity and flow rate, and have relatively small length and aspect ratio similar to the base case geometry investigated here. Insulated end-walls should be used to further reduce the tar decomposition reactions which occur within the reactor. For commercial applications using large mass feed rates, we recommend the utilization of multiple small reactors operating in parallel rather than a single scaled up reactor.

Acknowledgments

This research was conducted at the Jet Propulsion Laboratory (JPL) and sponsored by the U.S. Department of Energy (DOE), with Mr. Neil Rossmeissl (DOE Headquarters) and Mr. D. Hooker (DOE Golden Center) serving as contract monitors, under an agreement with the National Aeronautics and Space Administration. Computational resources are provided by the super computing facility at JPL.

References

Chornet, E. 1997. Personal communication.

Chornet, E., Wang, D., Montane, D. and Czernik, S. 1994. Hydrogen production by fast pyrolysis of biomass and catalytic steam reforming of pyrolysis oil. In A.V. Bridgwater, editor, *Advances in Thermochemical Biomass Conversion*, volume 1, pages 246–262. Blackie Academic and Professional, New York, New York.

Clift, R., Grace, J.R. and Weber, M.E. 1978. *Bubbles, Drops and Particles*. Academic Press, New York, New York.

Di Blasi, C. 1993. Analysis of convection and secondary reaction effects within porous solid fuels undergoing pyrolysis. *Combust. Sci. and Tech.*, 90:315–340.

Diebold, J.P. and Power, A. 1988. Engineering aspects of the vortex pyrolysis reactor to produce primary pyrolysis oil vapors for use in resins and adhesives. In A. V. Bridgwater and J. L. Kuester, editors, *Research in Thermochemical Biomass Conversion*, pages 609–628. Elsevier Applied Science, New York, New York.

Fitzer, E., Mueller, K. and Schaefer, W. 1971. The chemistry of the pyrolytic conversion of organic compounds to carbon. In M. Dekker, editor, *The Chemistry and Physics of Carbon*, volume 7, pages 237–377. M. Dekker, New York.

Jones, W.P. and Pascau, A. 1989. Calculation of confined swirling flows with a second order moment closure. *Trans. ASME*, 111:248–255.

Kerstein, A.R. and Niksa, S. 1984. Fragmentation during carbon conversion: Predictions and measurements. In *Proceedings of the Twentieth Symposium (International) on Combustion*, pages 941–949.

Launder, B.E., Reece, G.J. and Rodi, W. 1975. Progress in the development of a Reynolds-stress turbulence closure. *J. Fluid Mech.*, 68(3):537–566.

Lede, L., Diebold, J.P., Peacocke, G.V.C. and Piskorz, J. 1997. The nature and properties of intermediate and unvaporized biomass pyrolysis materials. In A.V. Bridgwater and D.G.B. Boocock, editors, *Developments in Thermochemical Biomass Conversion*, volume 1, pages 27–42. Blackie Academic and Professional, New York, New York.

Miller, R.S. and Bellan, J. 1996. Analysis of reaction products and conversion time in the pyrolysis of cellulose and wood particles. *Comb. Sci. Tech.*, 119:331–373.

Miller, R.S. and Bellan, J. 1997a. A generalized biomass pyrolysis model based on superimposed cellulose, hemicellulose and lignin kinetics. *Comb. Sci. Tech.*, 126(1-6):97–138.

Miller, R.S. and Bellan, J. 1997b. Tar yield and collection from the pyrolysis of large biomass particles. *Comb. Sci. Tech.*, 127(1-6):97–118.

Nallasamy, M. 1987. Turbulence models and their applications to the prediction of internal flows: A review. *Comp. and Fluids*, 15(2):151–194.

Narayan, R. and Antal, M.J. 1996. Thermal lag, fusion, and the compensation effect during biomass pyrolysis. *Ind. Eng. Chem. Res.*, 35(5):1711–1721.

Nikjooy, M. and Mongia, H.C. 1991. A second-order modeling study of confined swirling flow. *Int. J. Heat and Fluid Flow*, 12(1):12–19.

Peacocke, G.V.C. and Bridgwater, A.V. 1994. Design of a novel ablative pyrolysis reactor. In A.V. Bridgwater, editor, *Advances in Thermochemical Biomass Conversion*, volume 2, pages 1134–1150. Blackie Academic and Professional, New York, New York.

Scott, D.S., Piskorz, J., Bergougnou, M.A., Graham, R. and Overend, R.P. 1988. The role of temperature in the fast pyrolysis of cellulose and wood. *Ind. Eng. Chem. Res.*, 27:8–15.

SERI. 1979. A survey of biomass gasification: Volume II - Principles of gasification. Technical Report TR-33-239, Solar Energy Research Institute, Golden, Colorado, July.

Sharif, M.A. and Wong, Y.K.E. 1995. Evaluation of the performance of three turbulence closure models in the prediction of confined swirling flows. *Comps. and Fluids*, 24(1):81–100.

Sloan, D.G., Smith, P.J. and Smoot, L.D. 1986. Modeling of swirl in turbulent flow systems. *Prog. Energy Comb. Sci.*, 12:163–250.

Wagenaar, B.M., Kuipers, J.A.M., Prins, W. and Van Swaaij, W.P.M. 1994. The rotating cone flash pyrolysis reactor. In A.V. Bridgwater, editor, *Advances in Thermochemical Biomass Conversion*, volume 2, pages 1122–1133. Blackie Academic and Professional, New York, New York.

Womat, M.J., Hurt, R.H., Yang, N.Y.C. and Headley, T.J. 1995. Structure and compositional transformations of biomass chars during combustion. *Comb. and Flame*, 100(1):131–143.

Zha, G. and Knight, D. 1996. Three-dimensional shock/boundary-layer interaction using Reynolds stress equation turbulence model. *AIAA J.*, 34(7):1313–1320.

Figure Captions

Figure 1: Schematic of the vortex reactor.

Figure 2: Velocity vectors for a 2D wood particle with aspect ratio $\Theta = 2$ ($x_1 = 0$ is a plane of symmetry) at a time corresponding to 40% reduction of the virgin wood mass; (a) $\Gamma_{11}/\Gamma_{22} = 1$, (b) $\Gamma_{11}/\Gamma_{22} = 10$, (c) $\Gamma_{11}/\Gamma_{22} = 100$. The particle height is $H_p = 5mm$, and the heating conditions are $T_w = T_\infty = 900K$.

Figure 3: Comparison of 1D and 2D particle pyrolysis simulation tar collections for various ratios of the parallel to cross grain permeability. The particle height is $H_p = 5mm$, with $\Theta = 2$, and the heating conditions are $T_w = T_\infty = 900K$.

Figure 4: Comparison of 1D and 2D particle pyrolysis simulation tar collections for various particle aspect ratios. The particle height is $H_p = 5mm$, and the heating conditions are; $T_w = T_\infty = 900K$.

Figure 5: Comparison of 1D and 2D particle pyrolysis simulation tar collections for various ratios of the parallel to cross grain thermal conductivity. The particle height is $H_p = 5mm$, with $\Theta = 2$, and the heating conditions are $T_w = T_\infty = 900K$.

Figure 6: Comparison of (a) tar collections and (b) mass averaged particle temperature obtained through exclusive heating at either the wall or the flow boundary for 1D particle pyrolysis employing the complete momentum equation (Eq.(8)) with $H_p = 5mm$ and $T_w, T^* = 900K$.

Figure 7: Temporal evolution of the tar collection for a 1D particle simulation having $T^* = 850 + 50\sin(\omega' t)$. The simulation conditions are $H_p = 1mm$ and $T_w = 900K$.

Figure 8: Temporal development of apparent char density profiles during a 1D particle simulation. The simulation conditions are $H_p = 1mm$, $T_w = 900K$, $\overline{T^*} = 850K$ and the profiles correspond to times; $t/t_c = 0.25,\ 0.5,\ 0.75,\ 1.0$ and $t_c = 12.9s$.

Figure 9: Single particle pyrolysis behavior for $5mm$ Maple sample as a function of the critical porosity for fragmentation; (a) tar collection, (b) 99% conversion time. The value $\varepsilon_c = \varepsilon_0 = 0.67$ is the kinetic limit.

Figure 10: Steady state vectors and contours from a reactor simulation for base case conditions with $T_{wall} = 900K$; (a) velocity vectors, (b) temperature, (c) tar mass fraction $\times 100$, (d) gas mass fraction $\times 100$.

Figure 11: Reactor efficiency and % tar reduction for base case conditions as a function of (a) wall temperature and (b) minimum input energy.

Figure 12: Reactor efficiency as a function of wall temperature for two initial particle sizes.

Figure 13: Reactor efficiency for base case conditions as a function of dispersity for biomass feed mixtures of $1mm$ Maple and $5mm$ Olive Husk particles.

Figure 14: Ratio of reactor residence time scale to tar decomposition reaction time scale as a function wall temperature for various values of the reactor scale factor (M).

Figure 15: Reactor efficiency and % tar reduction as a function of the reactor scale factor for base case conditions with $T_{wall} = 850K$.

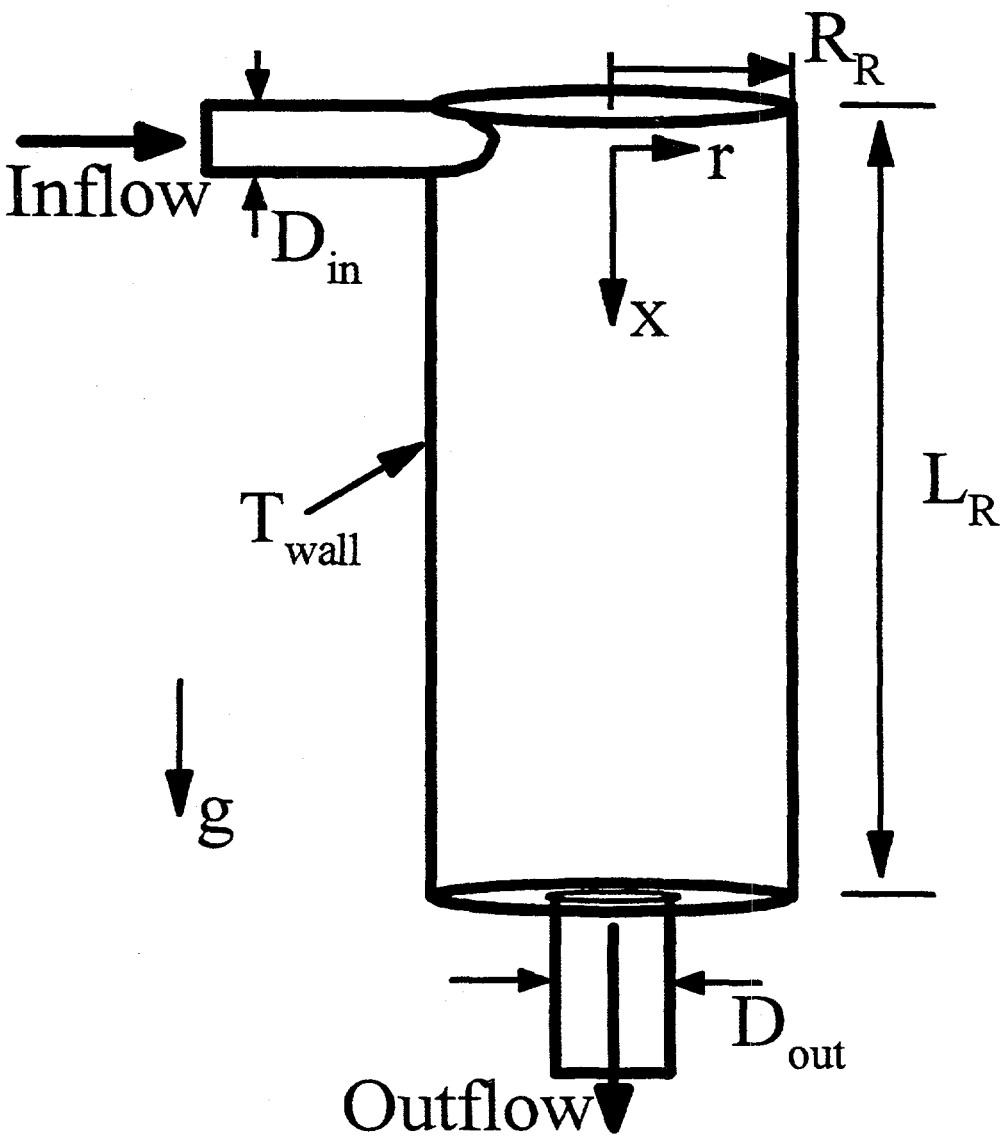

Figure 1

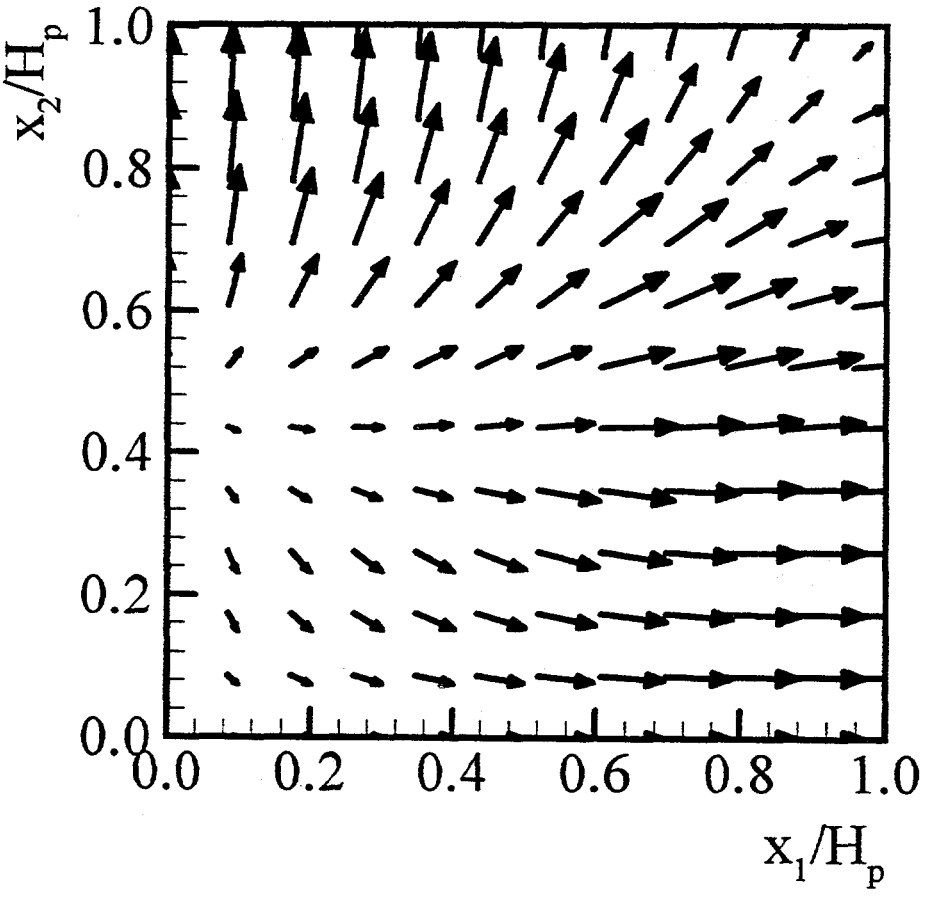

Figure 2 (a)

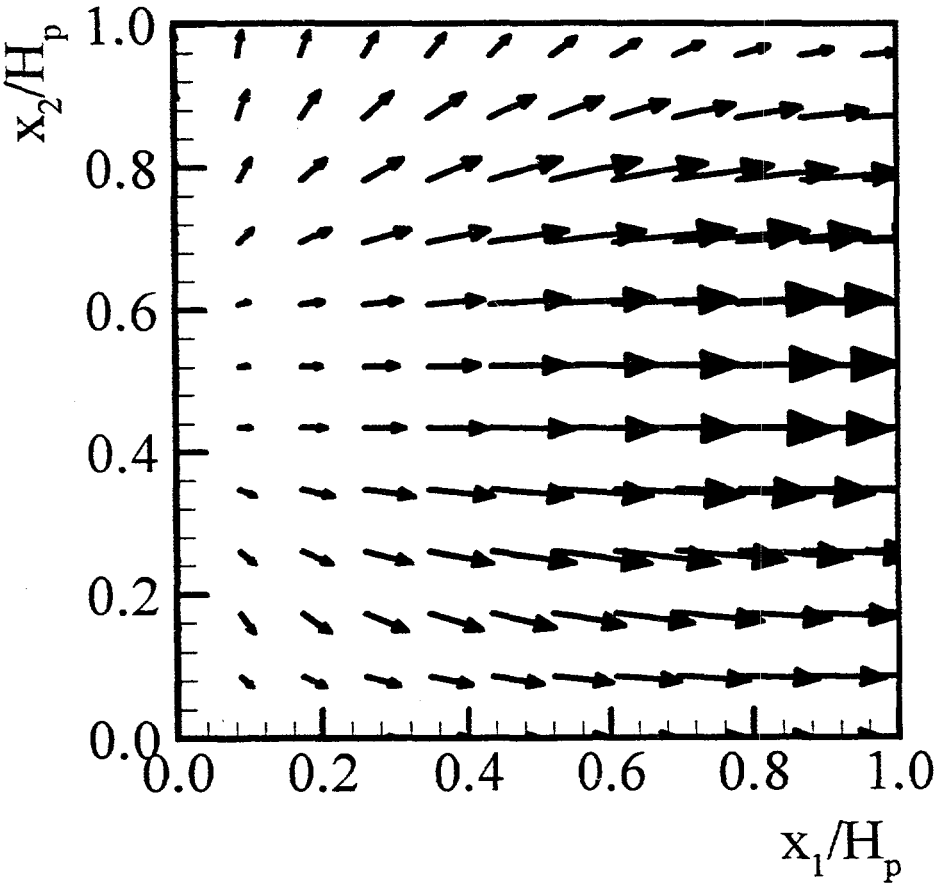

Figure 2 (b)

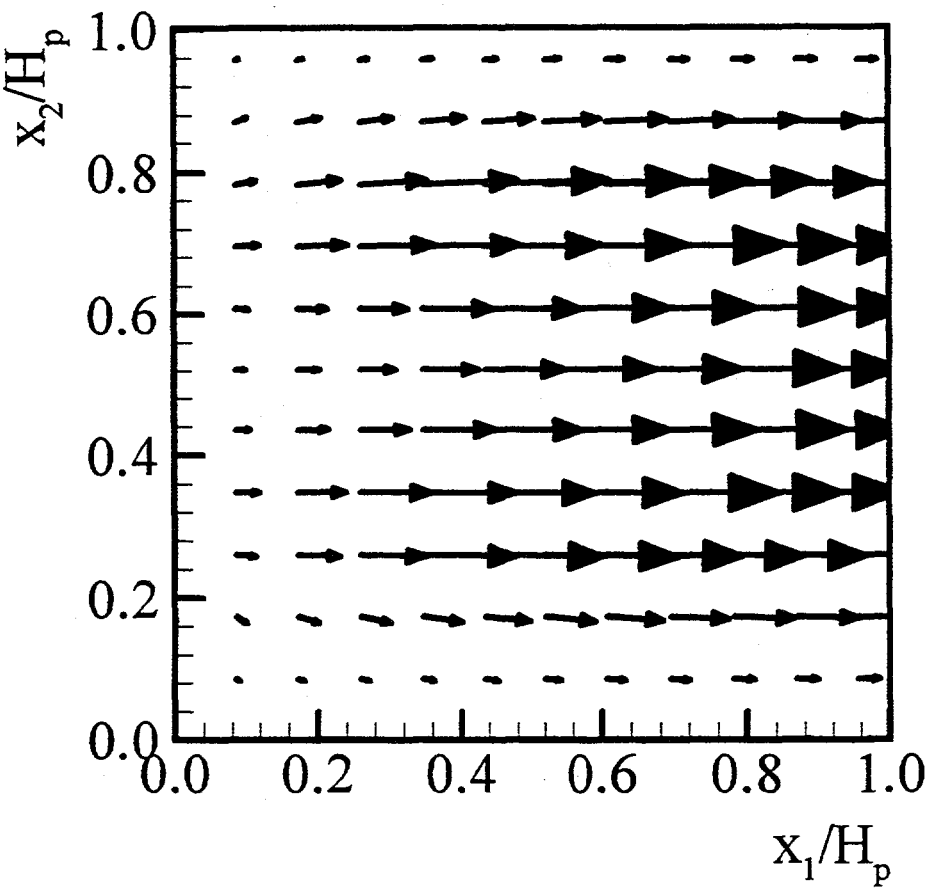

Figure 2 (c)

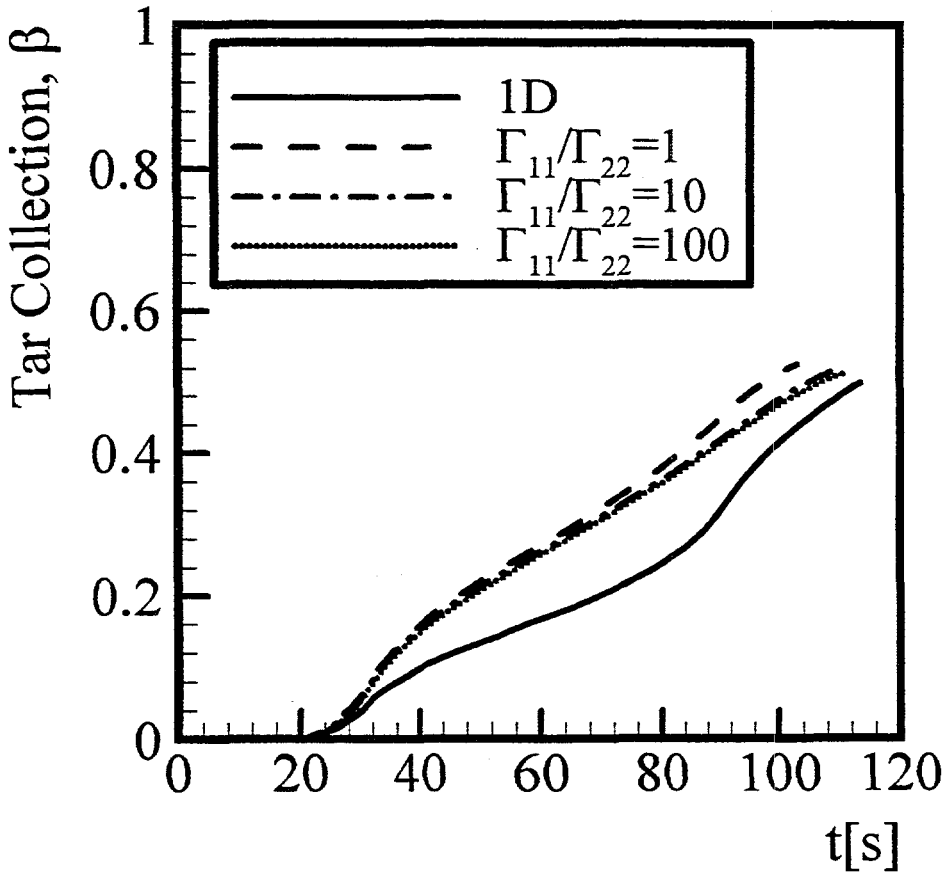
Tar Collection, β
1
0.8
0.6
0.4
0.2
0
0
20
40
60
80
100
120
t[s]
1D
Γ11/Γ22=1
Γ11/Γ22=10
Γ11/Γ22=100

Figure 3

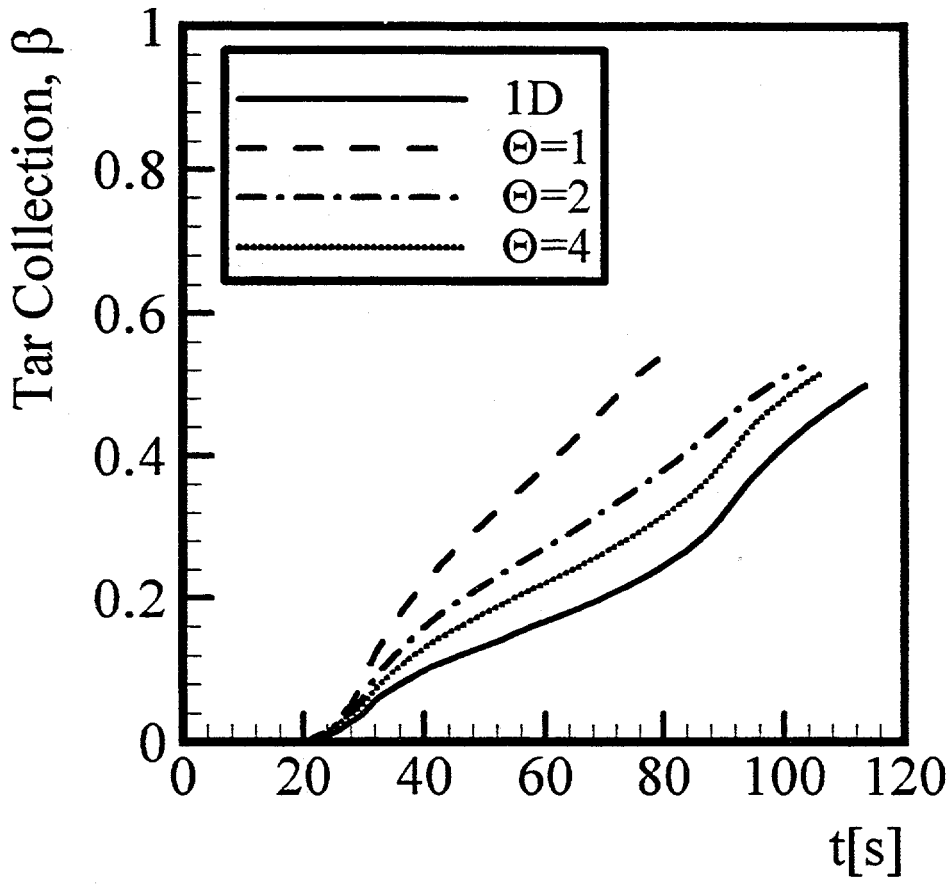

Figure 4

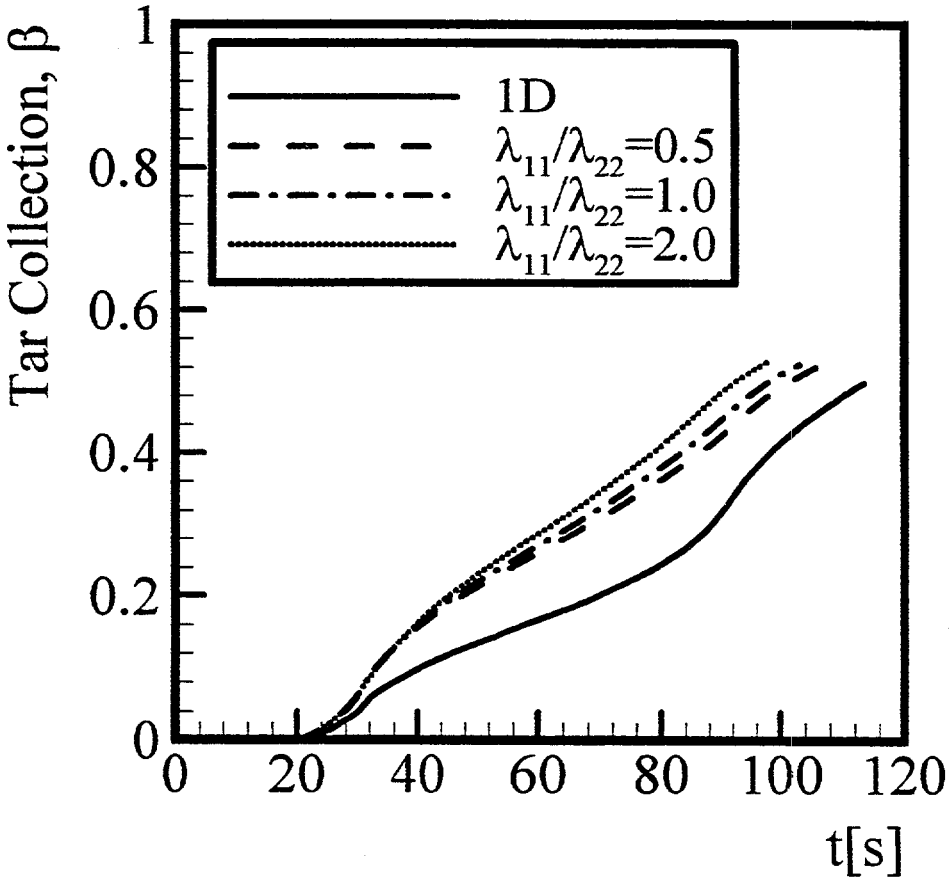
Tar Collection, β
1
0.8
0.6
0.4
0.2
0
0
20
40
60
80
100
120
t[s]
1D
λ11/λ22=0.5
λ11/λ22=1.0
λ11/λ22=2.0

Figure 5

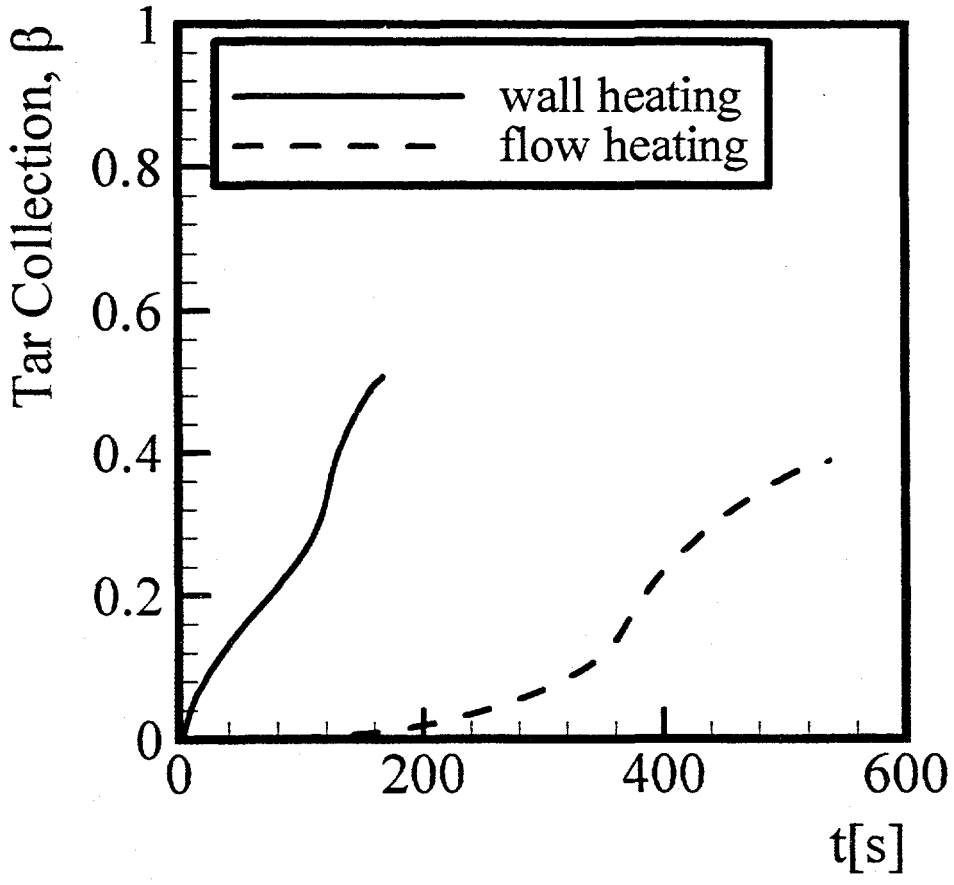
Tar Collection, β
1
0.8
0.6
0.4
0.2
0
0
200
400
600
t[s]
wall heating
flow heating

Figure 6 (a)

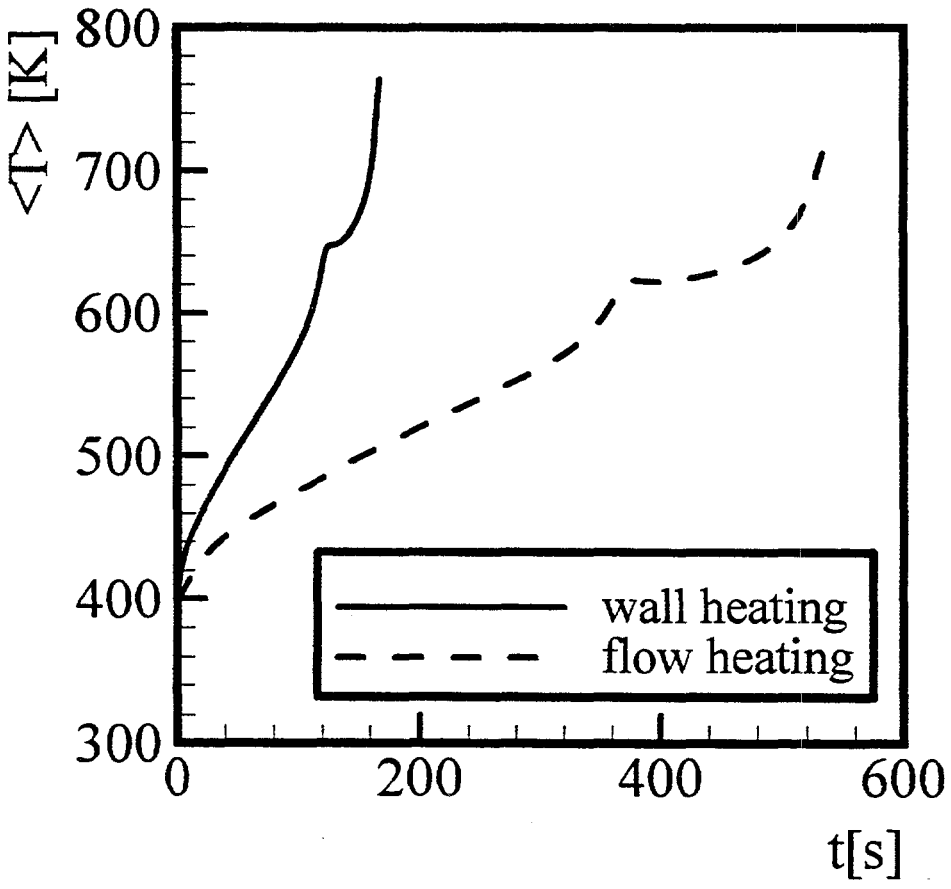
<T> [K]
800
700
600
500
400
300
0
200
400
600
t[s]
wall heating
flow heating

Figure 6 (b)

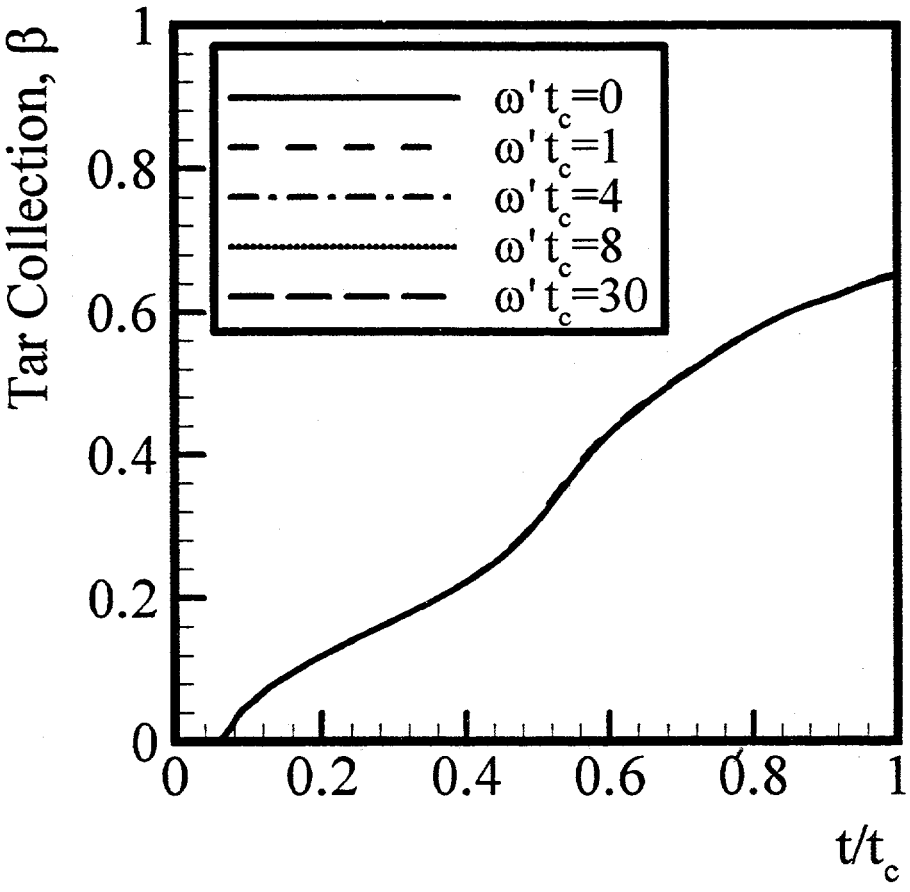
Tar Collection, β
1
0.8
0.6
0.4
0.2
0
0
0.2
0.4
0.6
0.8
1
t/t_c
ω' t_c=0
ω' t_c=1
ω' t_c=4
ω' t_c=8
ω' t_c=30

Figure 7

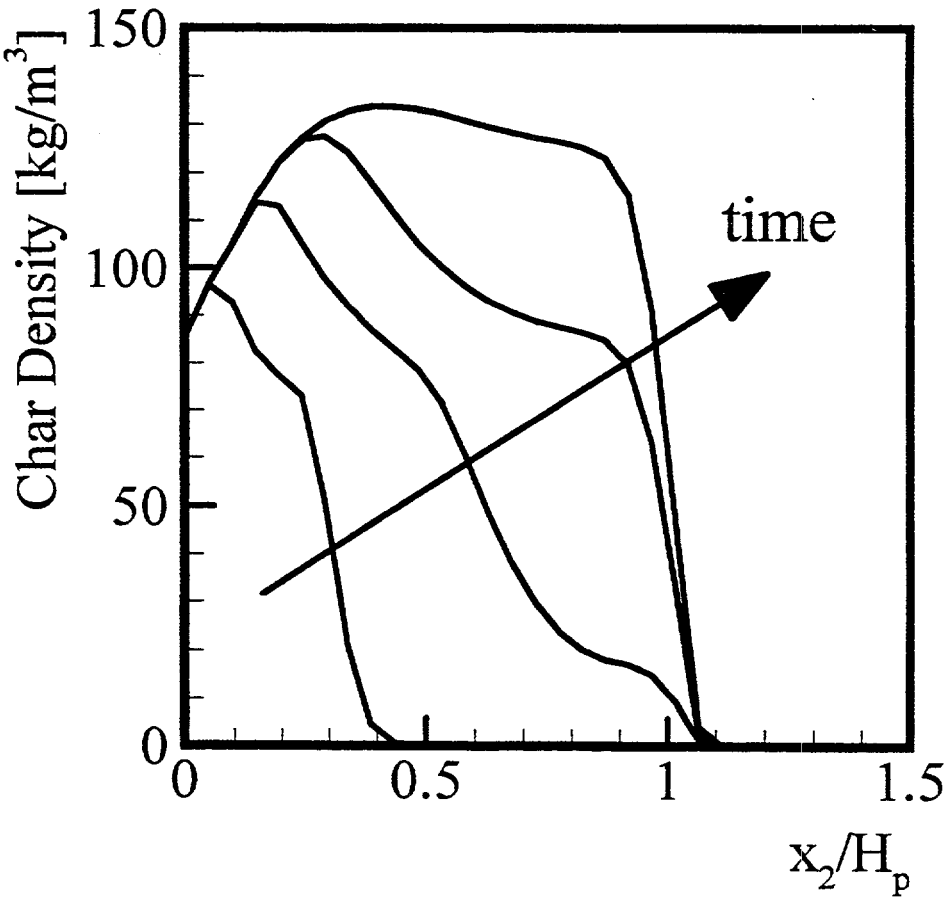

Figure 8

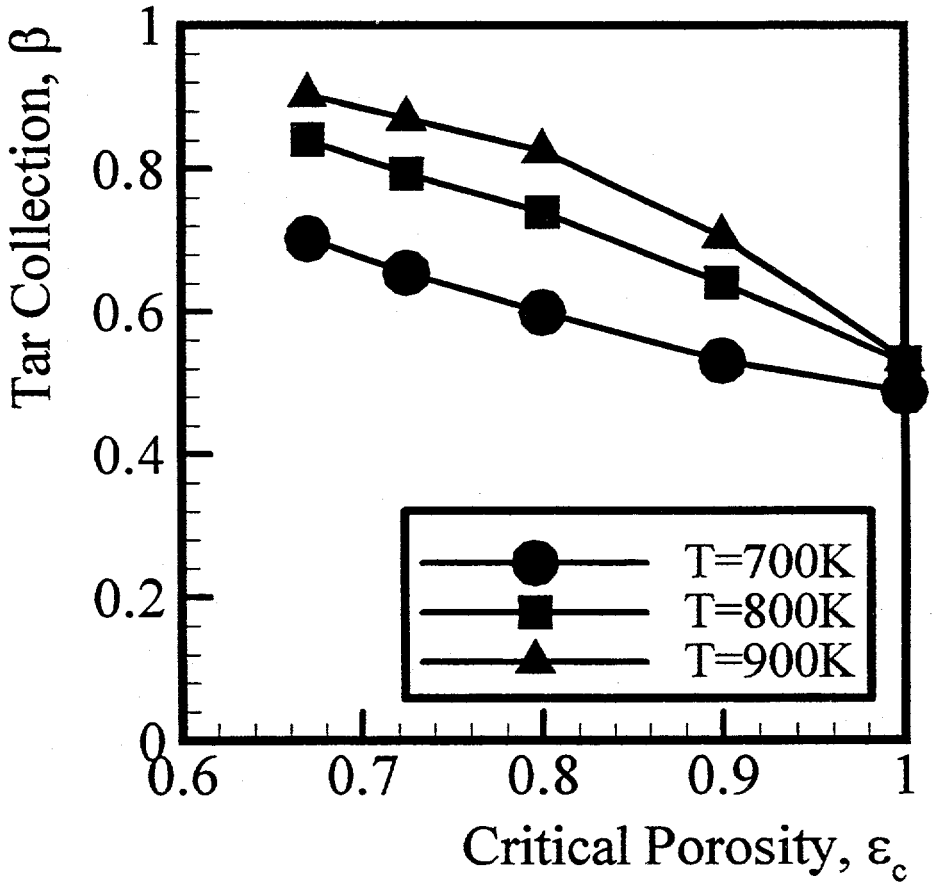
Tar Collection, β
1
0.8
0.6
0.4
0.2
0
0.6
0.7
0.8
0.9
1
Critical Porosity, ε_c
T=700K
T=800K
T=900K

Figure 9 (a)

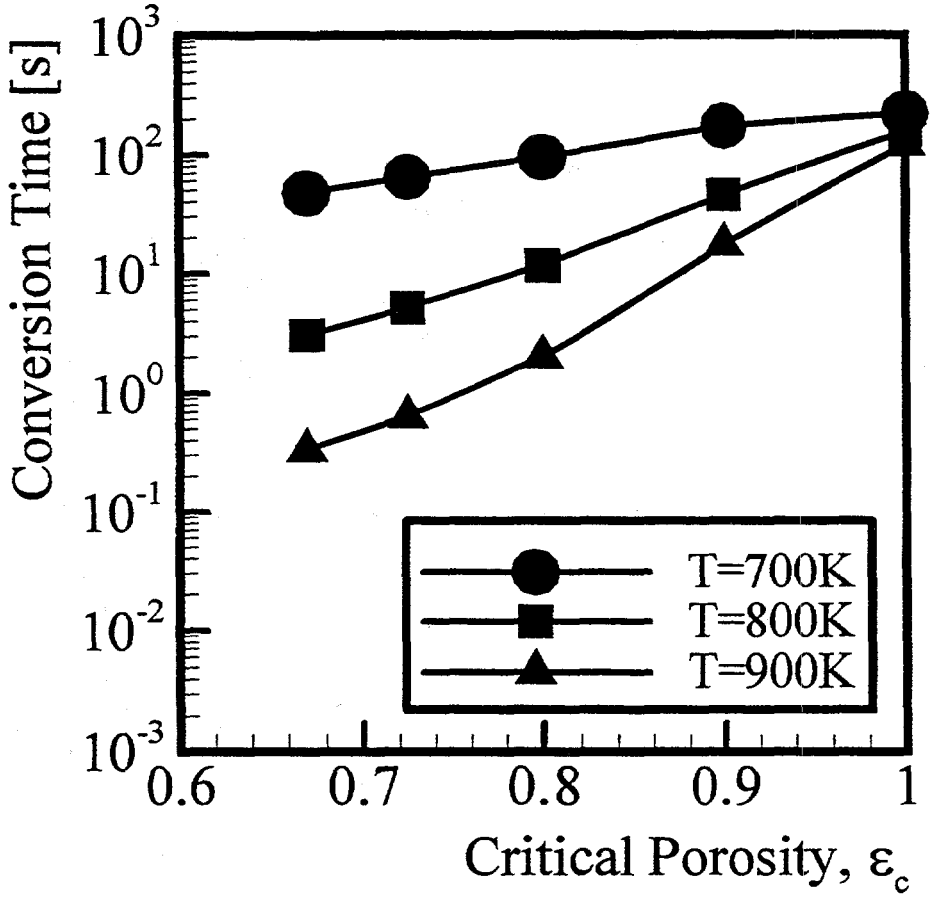
Conversion Time [s]
10^3
10^2
10^1
10^0
10^{-1}
10^{-2}
10^{-3}
0.6
0.7
0.8
0.9
1
Critical Porosity, ε_c
T=700K
T=800K
T=900K

Figure 9 (b)

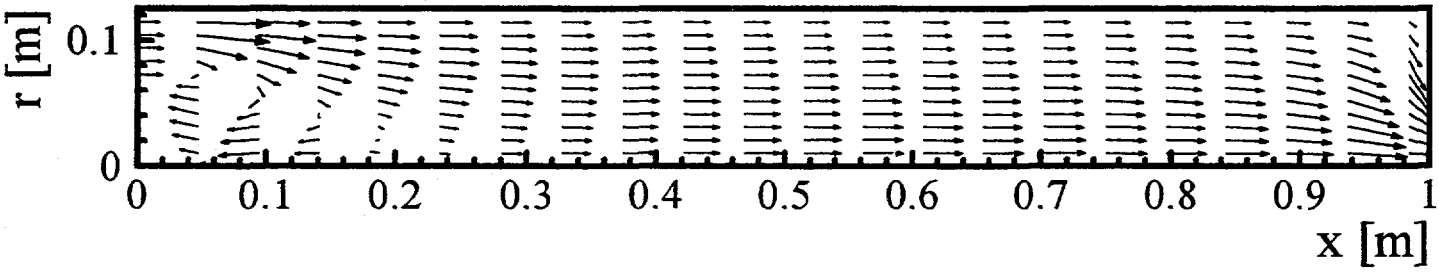

Figure 10 (a)

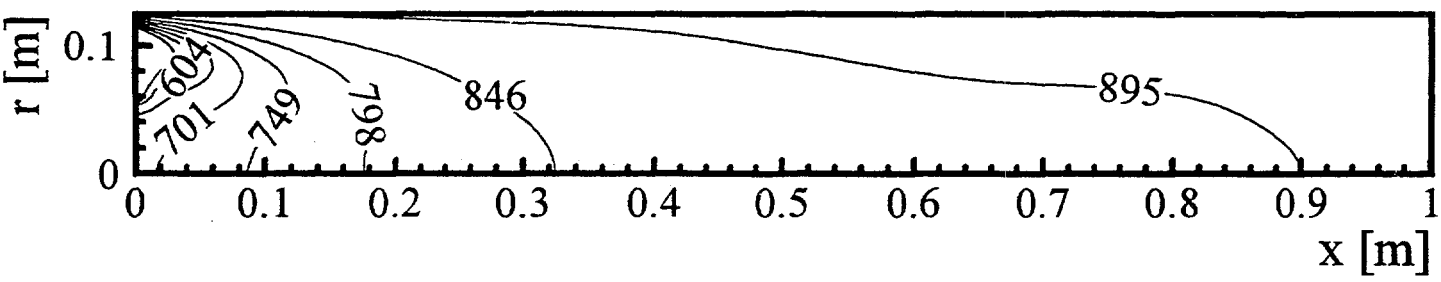

Figure 10 (b)

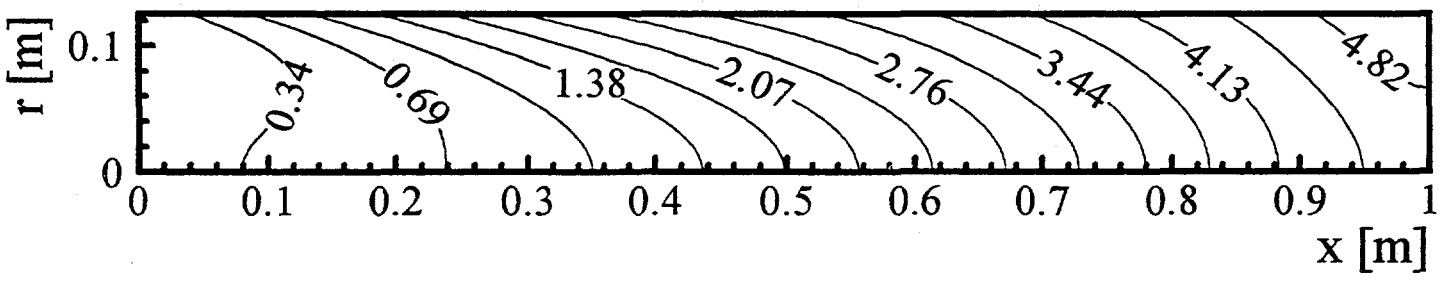
r [m]
0.1
0
0.34
0.69
1.38
2.07
2.76
3.44
4.13
4.82
0
0.1
0.2
0.3
0.4
0.5
0.6
0.7
0.8
0.9
1
x [m]

Figure 10 (c)

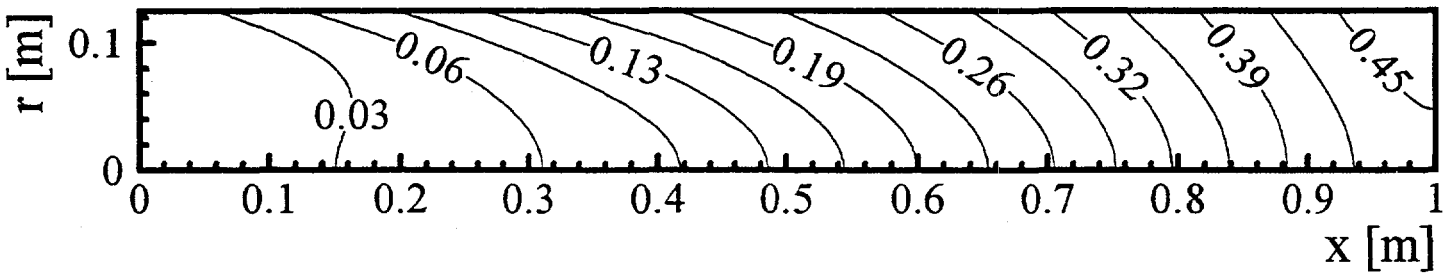
r [m]
0.1
0
0.03
0.06
0.13
0.19
0.26
0.32
0.39
0.45
0
0.1
0.2
0.3
0.4
0.5
0.6
0.7
0.8
0.9
1
x [m]

Figure 10 (d)

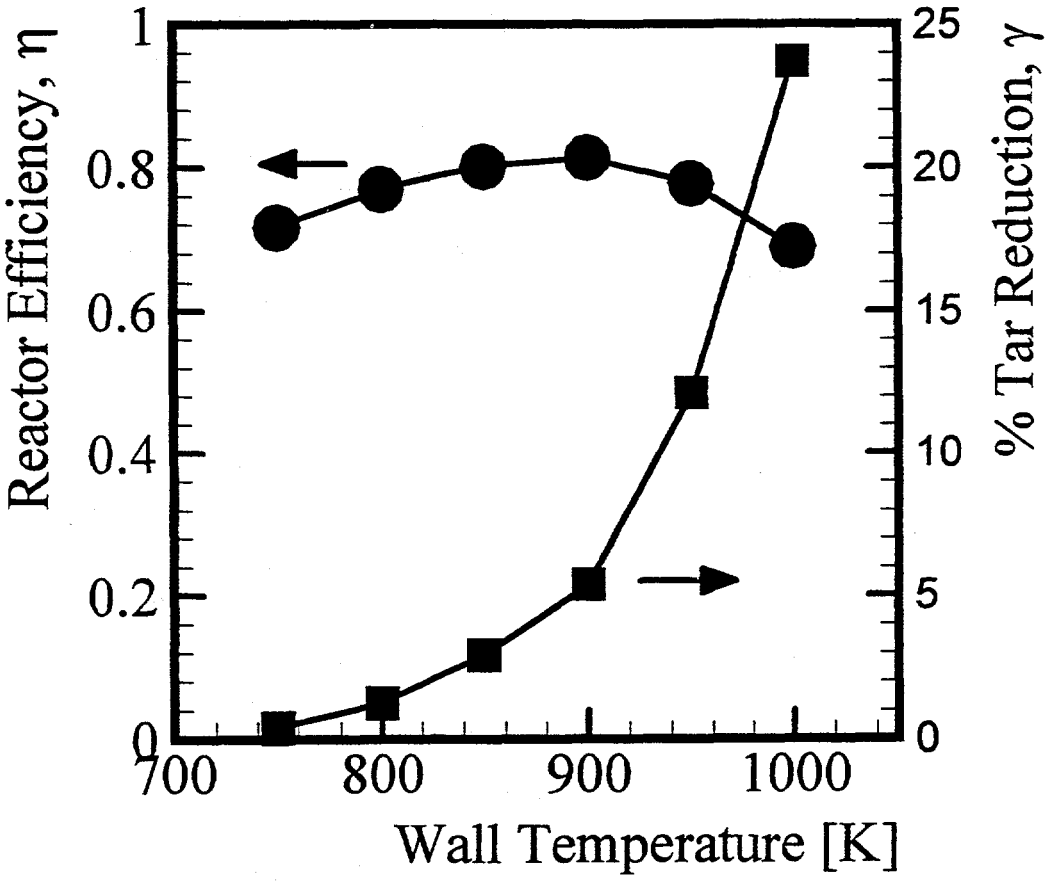
Reactor Efficiency, η
% Tar Reduction, γ
Wall Temperature [K]
1
0.8
0.6
0.4
0.2
0
25
20
15
10
5
0
700
800
900
1000

Figure 11 (a)

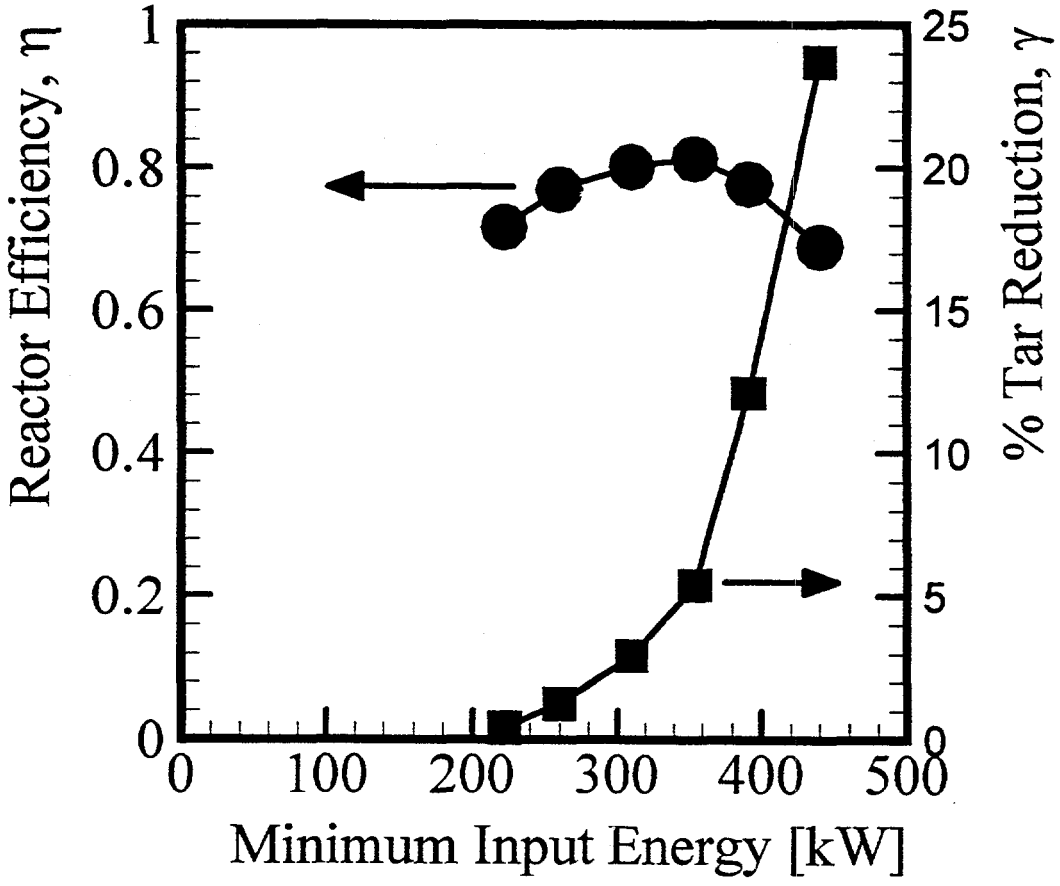
Reactor Efficiency, η
% Tar Reduction, γ
Minimum Input Energy [kW]
1
0.8
0.6
0.4
0.2
0
25
20
15
10
5
0
0
100
200
300
400
500

Figure 11 (b)

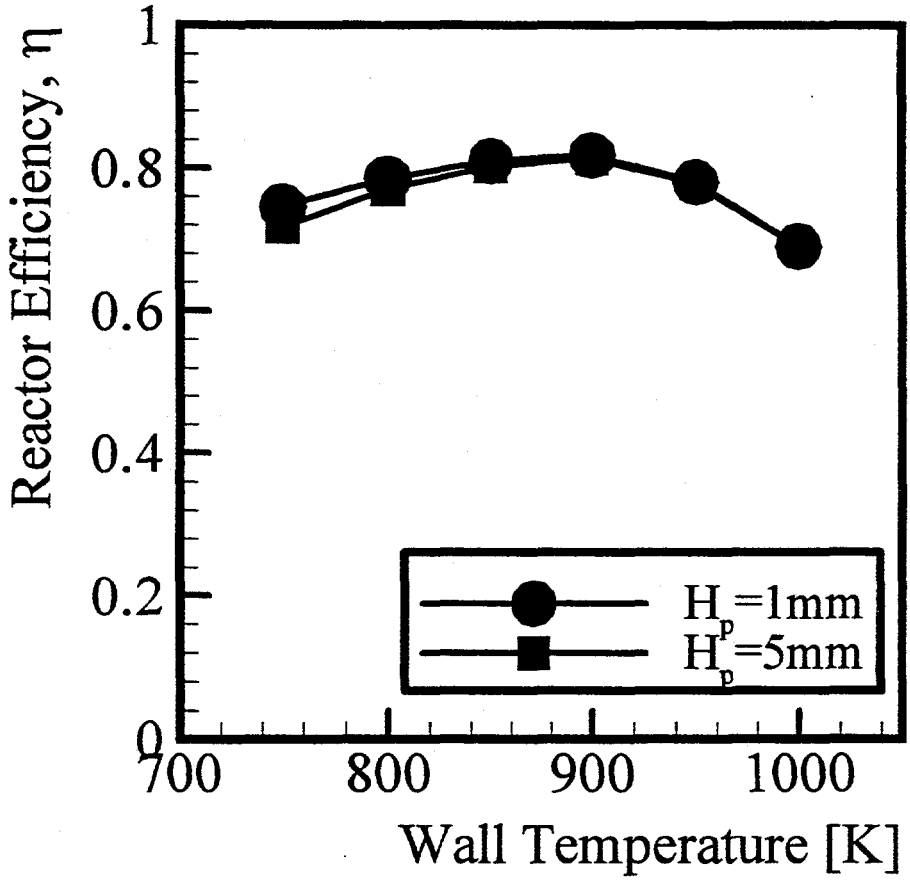
Reactor Efficiency, η
1
0.8
0.6
0.4
0.2
0
700
800
900
1000
Wall Temperature [K]
H_p=1mm
H_p=5mm

Figure 12

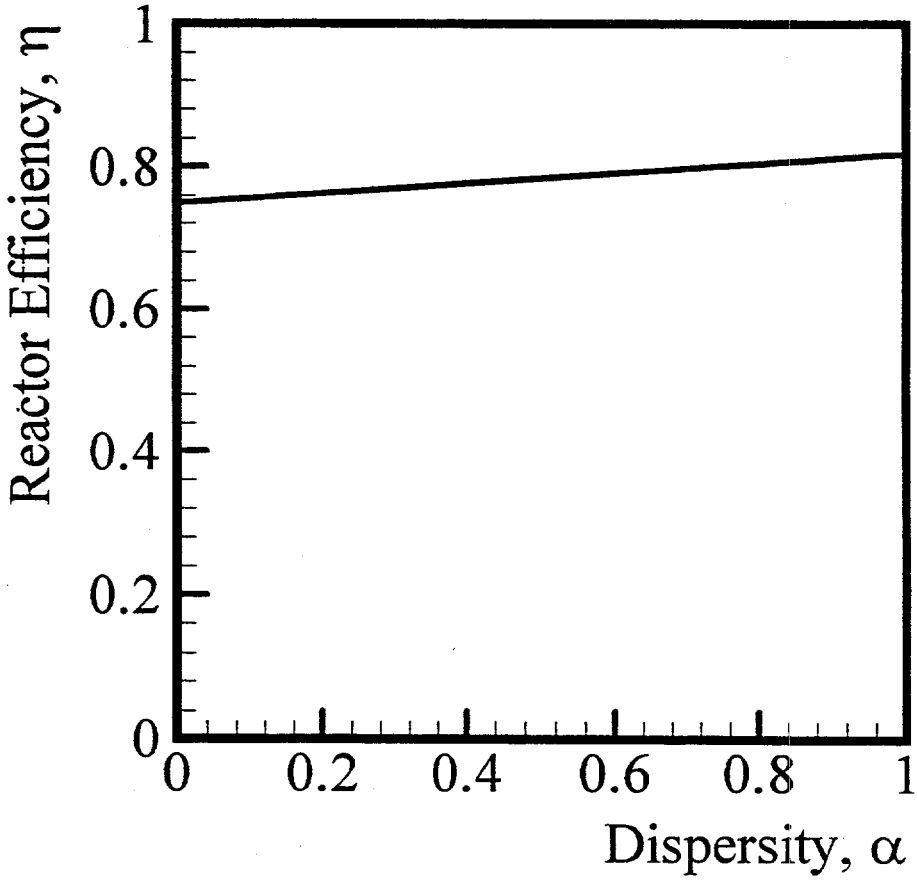

Figure 13

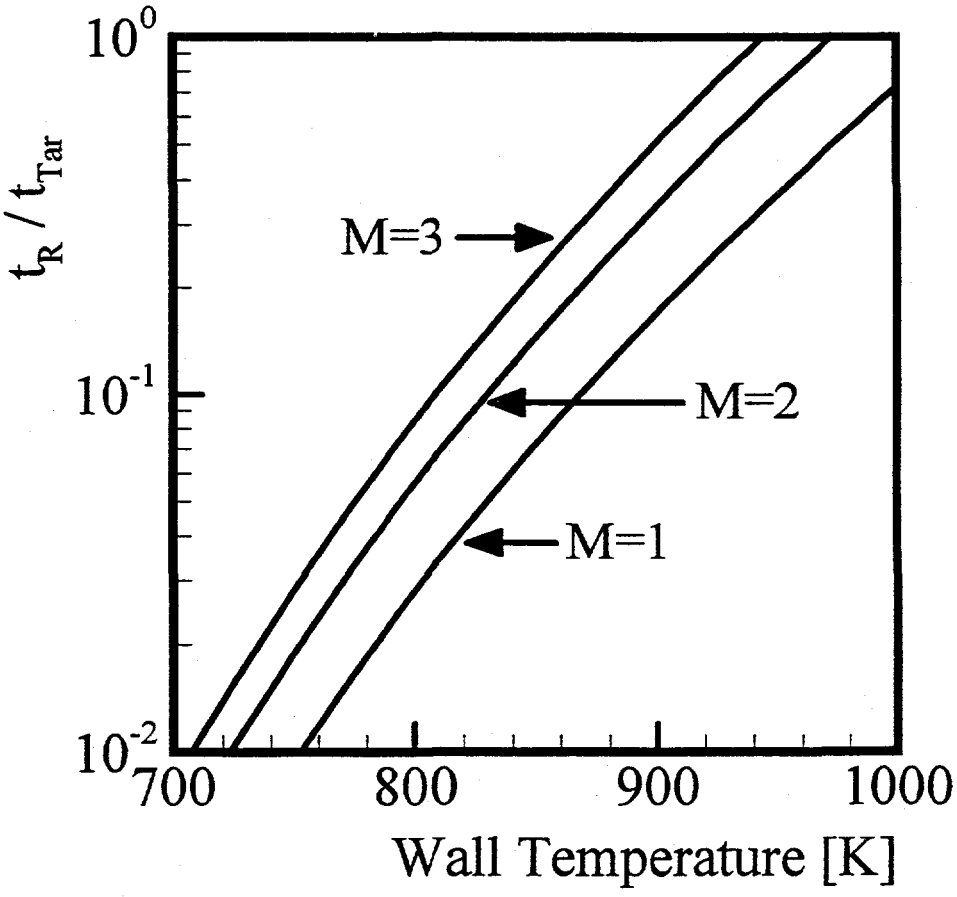
10^0
10^{-1}
10^{-2}
t_R / t_{Tar}
M=3
M=2
M=1
700
800
900
1000
Wall Temperature [K]

Figure 14

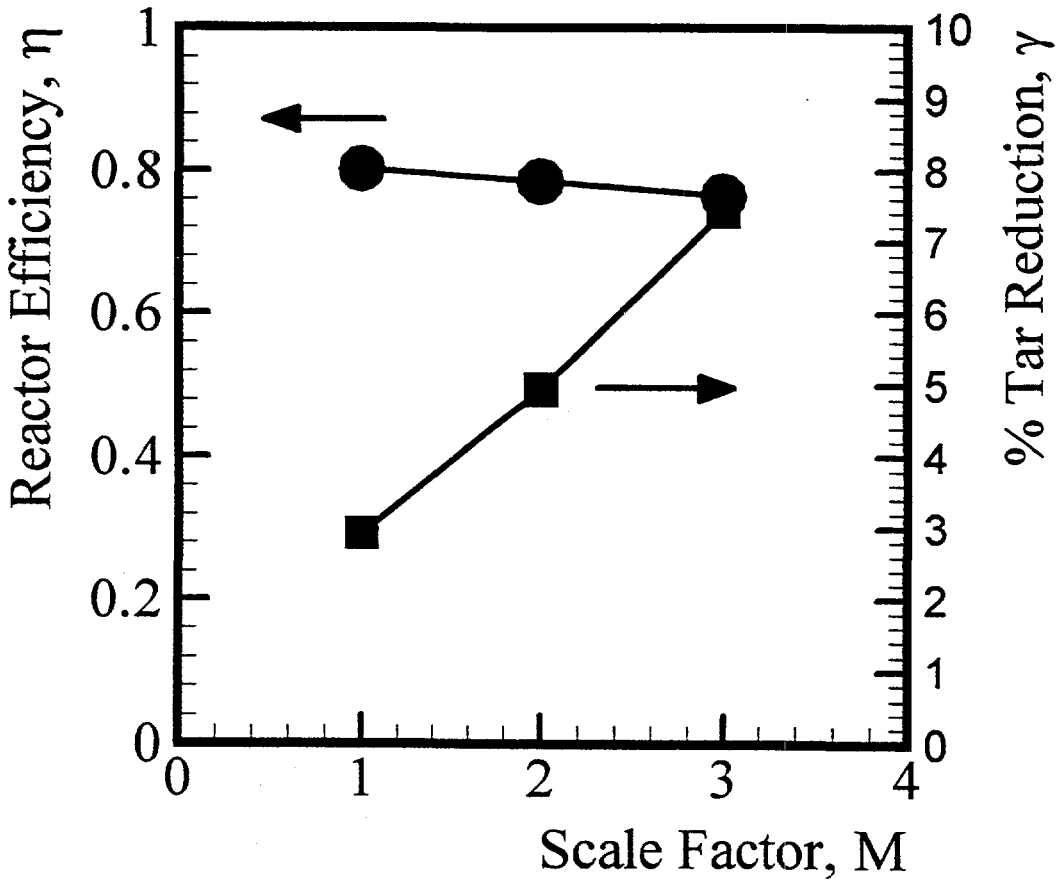
Reactor Efficiency, η
% Tar Reduction, γ
Scale Factor, M
0
0.2
0.4
0.6
0.8
1
0
1
2
3
4
0
1
2
3
4
5
6
7
8
9
10

Figure 15

Plasma Catalytic Reforming of Methane

L. Bromberg, D.R. Cohn, A. Rabinovich
MIT Plasma Science and Fusion Center
Cambridge, MA 02139

and

N. Alexeev
Baikov Institute of Metallurgy
Russian Academy of Sciences
Moscow, Russian Federation

ABSTRACT

Thermal plasma technology can be efficiently used in the production of hydrogen and hydrogen-rich gases from methane and a variety of fuels. This paper describes progress in plasma reforming experiments and calculations of high temperature conversion of methane using heterogeneous processes. The thermal plasma is a highly energetic state of matter that is characterized by extremely high temperatures (several thousand degrees Celsius) and high degree of disociation and substantial degree of ionization. The high temperatures accelerate the reactions involved in the reforming process. Hydrogen-rich gas (50% H_2, 17% CO and 33%N_2, for partial oxidation/water shifting) can be efficiently made in compact plasma reformers. Experiments have been carried out in a small device (2-3 kW) and without the use of efficient heat regeneration. For partial oxidation/water shifting, it was determined that the specific energy consumption in the plasma reforming processes is 16 MJ/kg H_2 with high conversion efficiencies. Larger plasmatrons, better reactor thermal insulation, efficient heat regeneration and improved plasma catalysis could also play a major role in specific energy consumption reduction and increasing the methane conversion. A system has been demonstrated for hydrogen production with low CO content (~1.5%) with power densities of ~30 kW (H_2 HHV)/liter of reactor, or ~10 m^3/hr H_2 per liter of reactor. Power density should further increase with increased power and improved design.

I. Introduction

Manufacturing of hydrogen from hydrocarbon fuels is needed for a variety of applications. These applications include fuel cells used in stationary electric power production and in vehicular propulsion. Hydrogen manufacturing is also needed for industrial applications and could be used in refueling stations for hydrogen powered vehicles. There is a wide range of requirements on the capacity of the hydrogen manufacturing system, the purity of the hydrogen fuel, and capability for rapid response.

Plasma technology has potential advantages over conventional means of manufacturing hydrogen. The shortcomings of the conventional reformers include the need of large scale plants, cost and deterioration of catalysts; size and weight requirements; limitations on rapid response; and limitations on hydrogen production from heavy hydrocarbons.

The main disadvantages of plasma reforming are the dependence on electrical energy and the difficulty of high-pressure operation (required for processes that require high pressure, such as ammonia production). Dependence on electrical energy results in energetics that are less favorable than purely thermal processes, specially for endothermic reforming reactions such as steam reforming. High pressure, while achievable, increases electrode erosion and decreases electrode lifetime.

Plasma devices referred to as plasmatrons can generate very high temperatures (>2000 C) with a high degree of control, using electricity. The heat generation is independent of reaction chemistry, and optimum operating conditions can be maintained over a wide range of feed rates and gas composition. Compactness of the plasma reformer is ensured by high energy density associated with the plasma itself and by the reduced reaction times, resulting in short residence time. Hydrogen-rich gas can be efficiently produced in plasma reformers with a variety of hydrocarbon fuels (gasoline, diesel, oil, biomass, natural gas, jet fuel, etc.) with conversion efficiencies into hydrogen-rich gas close to 100% (1,2).

The plasma conditions (high temperatures and a high degree of dissociation and substantial degree of ionization) can be used to accelerate thermodynamically favorable chemical reactions without a catalyst or provide the energy required for endothermic reforming processes. Plasma reformers can provide a number of advantages:

- compactness and low weight (due to high power density)
- high conversion efficiencies
- minimal cost (simple metallic or carbon electrodes and simple power supplies)
- fast response time (fraction of a second)
- operation with a broad range of fuels, including heavy hydrocarbons and with "dirty" hydrocarbons

The technology could be used to manufacture hydrogen for a variety of stationary applications e.g., distributed, low pollution electricity generation from fuel cells [1]. It could also be used for mobile applications (e.g., on-board generation of hydrogen for fuel cell powered vehicles) and for refueling applications (stationary sources of hydrogen for vehicles).

A previous paper [2] presented results of plasma conversion of methane, using partial oxidation (air as the oxidizer), steam reforming (water) and pyrolytic reforming (no oxidizer). Results for homogeneous operation, and preliminary results of plasma catalysis were reported in that paper.

In this paper, further optimization of plasma catalysis is described as a means to decrease the electrical requirements. The energy requirement, the hydrogen conversion, and the use of a one-step reforming/water shift reactor are investigated as a function of the plasma parameters. Section II briefly describes calculations of the homogeneous process using the method of non-equilibrium thermodynamics. Section III briefly describes the experimental results with methane. Preliminary costs projection are described in Section IV. Finally, the conclusions are summarized in section V.

II. Computer Simulation by methods of non-equilibrium thermodynamics

In this section, the process of partial oxidation of methane is investigated using the method of non-equilibrium thermodynamics [3]. The method is based on the *extreme principle* that assumes that the entropy increases at the maximum rate. Together with the laws of non-equilibrium thermodynamics, it allows to determine quantitatively a trajectory of chemical process and changes of reactants concentrations in any gaseous systems. This new technique of chemical kinetics simulation has been used to determine the reaction trajectory of methane high temperature partial oxidation in an adiabatic reactor.

The partial oxidation/water shifting reagents are mixed according to the ratio

$$CH_4 + 0.5\ O_2 + 1.88\ N_2 + H_2O$$

Figures 1-3 show results of the calculations for initial temperatures of 500 K, 1500 K and 2000 K.. It was found that:

- reaction trajectory may be divided into two stages
    - during the first stage, complete combustion of part of methane occurs, producing mainly CO_2 and H_2O and substantially increasing the temperature of the system;
    - during the second stage, reactions of the remaining methane with CO_2 and H_2O occur providing H_2 and CO production and decreasing the temperature of the system;
- at low initial temperatures (500 K), the "length" of the trajectory of combustion (first stage) is very small compared with methane reactions with H_2O and CO_2;

- an increase of the initial temperature decreases the difference between length of the trajectory of combustion (first stage) and reforming reactions (second stage).

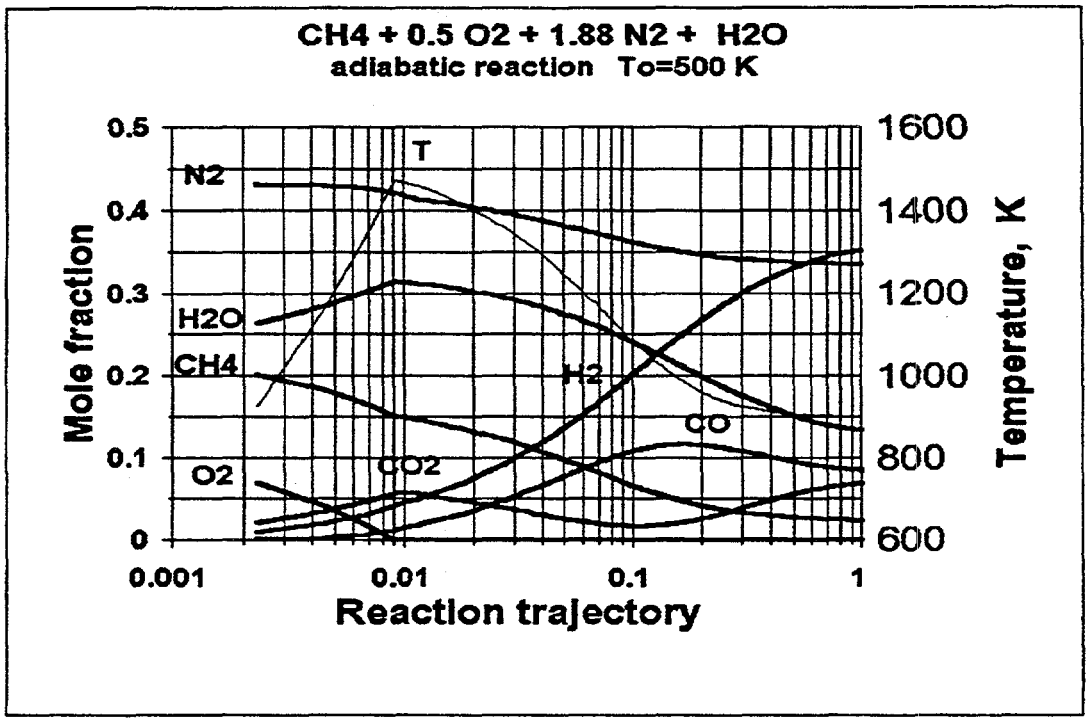

Figure 1. Reaction path for methane reforming, with initial mixture $CH_4/O_2/N_2/H_2O$ or 1/.5/1.88/1. Initial temperature of mixture is 500 K

These results of the simulation correspond to the well known *two-step kinetic* model of hydrocarbon partial oxidation process. However, these results have been obtained without the use of kinetic data.

The use of the plasma in plasma catalysis affects both stages. The plasma process accelerates the reactions, preparing the hydrocarbon-air mixture for the catalytic phase. In addition, although not considered in this paper, this process should be very efficient for heavier hydrocarbons. The heavier hydrocarbons are converted in the plasma phase into lighter hydrocarbons that are easily processed by the catalytic phase.

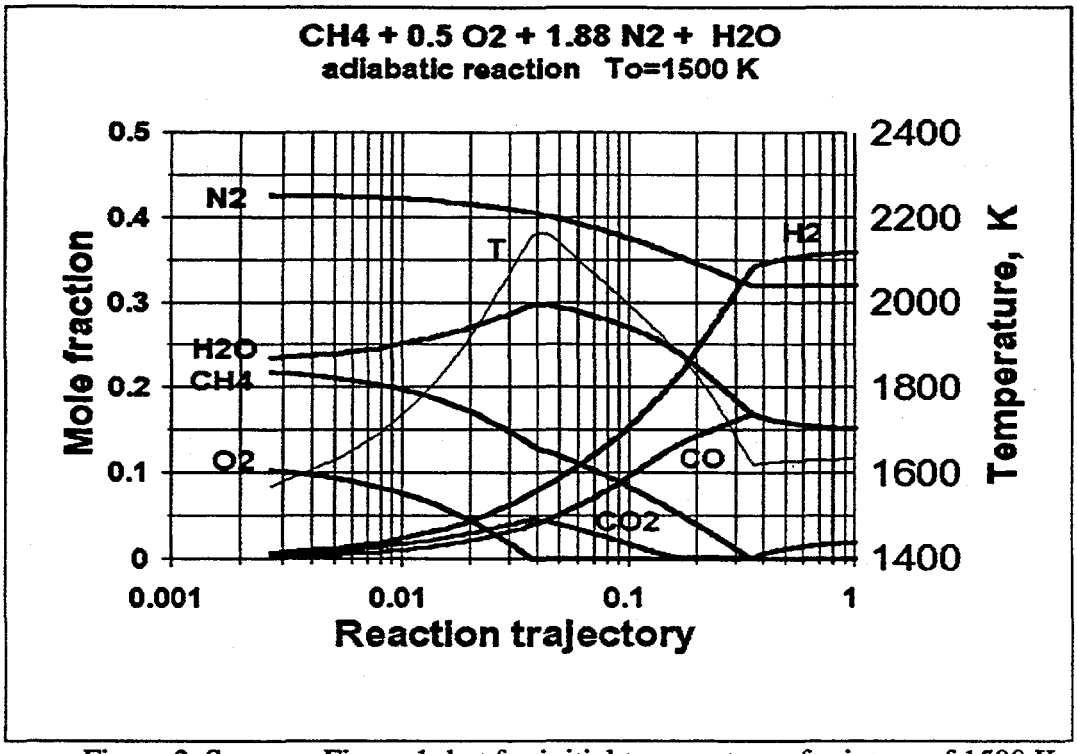

Figure 2 Same as Figure 1, but for initial temperature of mixture of 1500 K

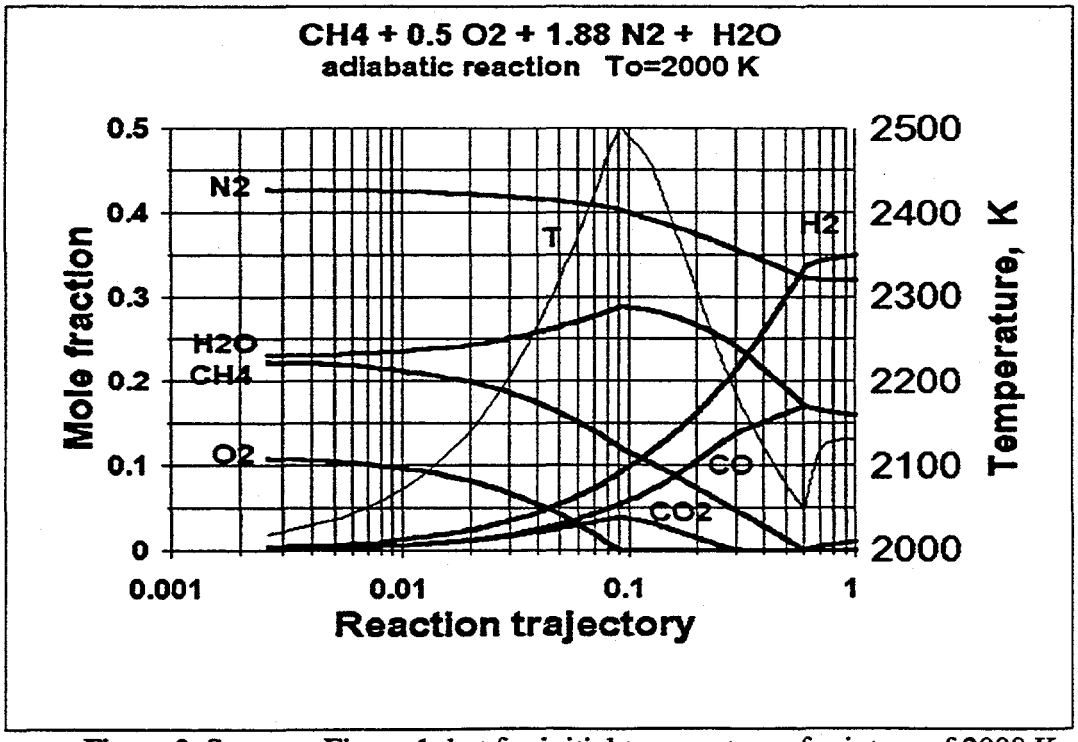

Figure 3 Same as Figure 1, but for initial temperature of mixture of 2000 K

III. Experimental investigations

The experiments with methane were carried out with a system similar to that described in [2]. Both gas phase reactions as well as catalytic reactions were studied for air and air/water vapor mixtures injection into an air plasma. In the heterogeneous experiments, nickel based catalyst on alumina support was used.

The plasmatron operated on conventional building compressed air. Bottled methane was used for the experiments. Drinking water was the source of the steam. The gas analysis was performed using a HP M200D GC, with two columns and with two thermal conductivity detectors. Calibration gases were provided by Matheson Gas. No NOx is expected because of the highly reducing product gas. Similarly, no HCN or CN's are expected because of the presence of an oxidizer, which binds the carbon as CO or CO_2, instead as CN.

The following basic process parameters are varied in experiments:

- power input (plasma enthalpy);
- air/CH_4 and H_2O/CH_4 ratios;
- total throughput

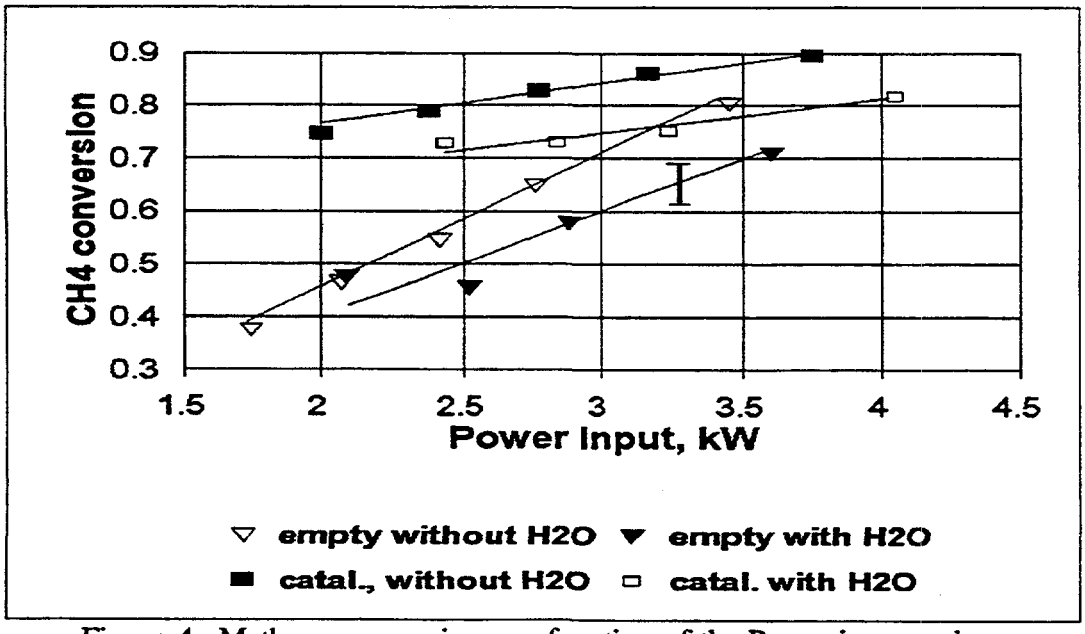

Figure 4. Methane conversion as a function of the Power input to the reactor for constant methane flow rate.

Figure 4 shows the hydrogen yield as a function of the power input. Methane conversion depends strongly on power input, especially for homogeneous reaction. Under low value of power input homogeneous plasma process provides low

conversion of methane about 40%. The use of stationary catalyst bed makes possible to increase methane conversion up to 75 % even at the lowest values of input power.

In principle, a homogeneous reactor may provide conversion of methane more than 80%, but the power input is high (more than 100 MJ/kg H_2).

The downstream addition of water vapor into the methane-air mixture decreases the methane conversion and the hydrogen yield.. Hydrogen yield is maximized, and the specific energy consumption is minimized when the water is added together with the methane and the non-plasma air.

A feature of plasma catalytic reactions is the low CO content in the products with a one-stage process. CO content in reaction product is about 1.5-3 vol.%, with hydrogen content ~40%. Water vapor excess in the initial gas mixture is required to obtain low CO concentration in the products. However, injection of water vapor downstream from the plasma, in the of catalyst bed, has little effect on the hydrogen yield.

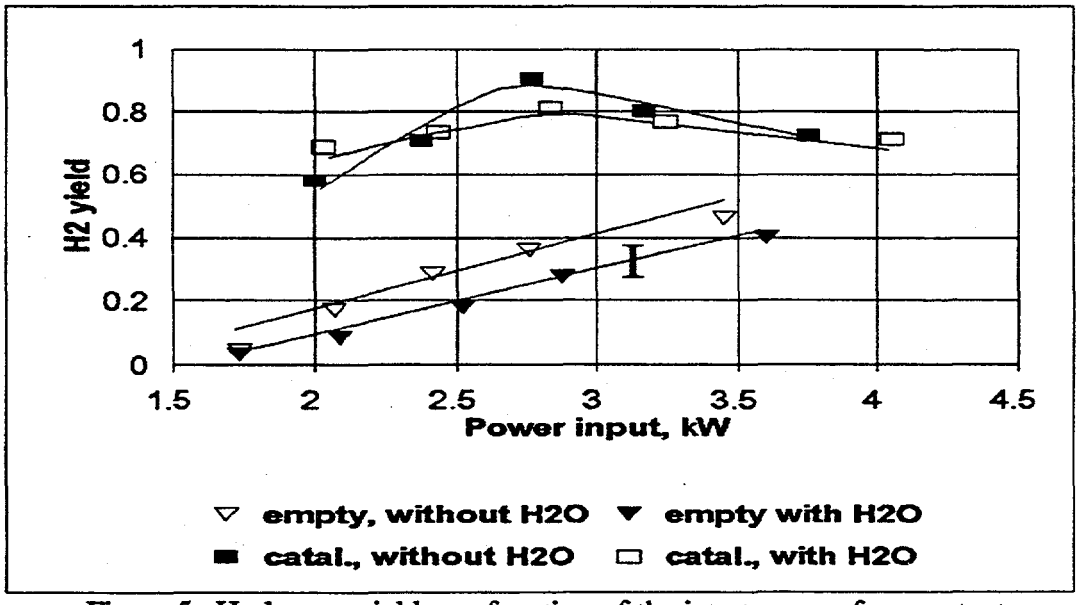

Figure 5. Hydrogen yield as a function of the input power, for constant methane flow rate.

Figure 5 shows the corresponding values of the hydrogen yield (Hydrogen released to hydrogen content in methane). The hydrogen yield in the homogeneous process increases monotonically with power input. The hydrogen yield in the case of the heterogeneous reaction is more complex. The hydrogen yield has a broad maximum for given power input, as shown in Fig.5. The presence of this maximum may be explained by an increase in the of reaction temperature at the higher input powers. This shifts the reaction $CO+H_2O \Leftrightarrow CO_2+H_2$ to the production of CO and H_2O.

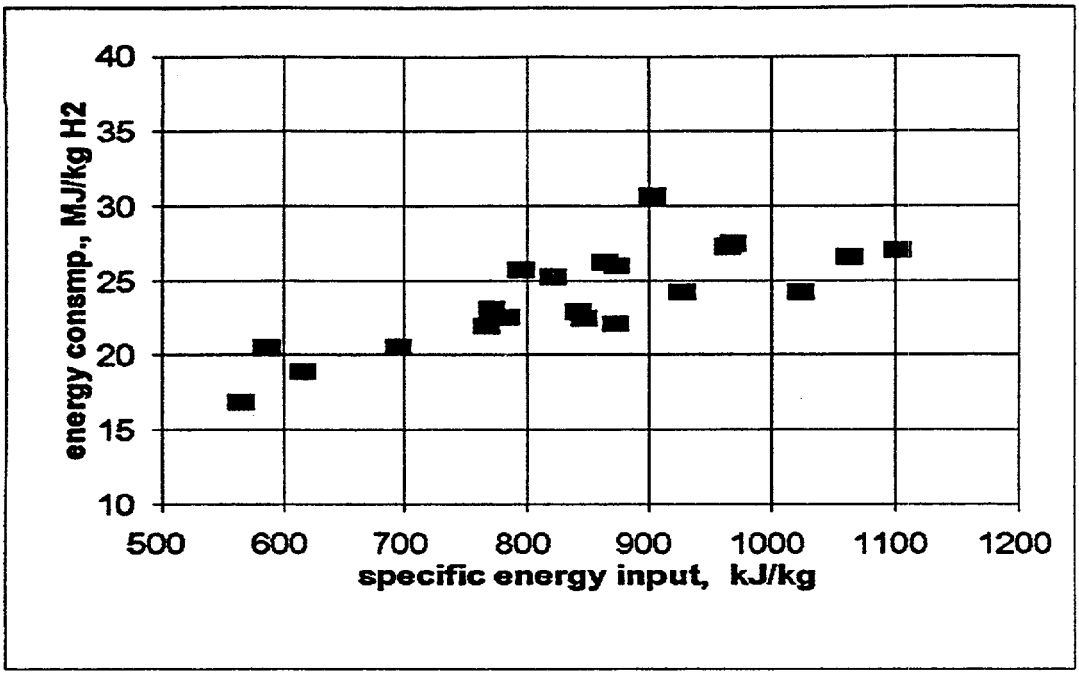

Figure 6. Hydrogen specific energy consumption as a function of the specific energy input

Figure 6 shows the specific energy consumption as a function of the specific energy input. The specific energy consumption is defined as the ratio of the electrical power to the hydrogen throughput of the product gas. The specific energy input is the ratio of the electrical power to the total mass throughput. Plasma catalytic process decreases the required specific energy consumption to less than 17 MJ/kg H_2. Under such conditions, the calculated mean temperature of the unreacted methane/air/water mixture is about 750 - 800 K. This temperature corresponds to the required initial temperature for the autothermal conversion of methane in conventional catalytic reformers. The specific energy consumption can be readily compared with the heating value of the produced hydrogen, 120 MJ/kg H_2 (LHV).

The presently achieved composition and specific energy requirement of catalytic plasma reforming are shown in Table 1.

Table 1. Composition, yield and specific energy consumption for methane reforming using plasma catalysis.

H2		35%
CH4		5%
CO		3.7%
CO2		15%
N2		41%
Methane conversion		70%
Specific energy consumption	(MJ/kg H2)	16

Further decrement of the specific energy consumption may be achieved through the use of a heat exchanger to preheat the input reagents using the enthalpy of the product gases, as well as with reactor design and process parameters optimization. The reactor design can be further optimized by the use of improved heat insulator in conjunction with new types of catalysts. Optimization of the process parameters involves the increase of methane conversion excluding increase of power input by variation of initial mixture composition and methane space velocity.

Figure 7 shows the corresponding hydrogen yield. The hydrogen yield increased by a factor of 2 from those of the homogeneous reactions, as reported in 1997 [2]. Decreasing the specific energy consumption has not decreased the hydrogen yields from those reported in 1997 [2]. The hydrogen yield is shown in Figure 7 as a function of the total energy consumption, for a large number of experiments at different powers and different throughputs.

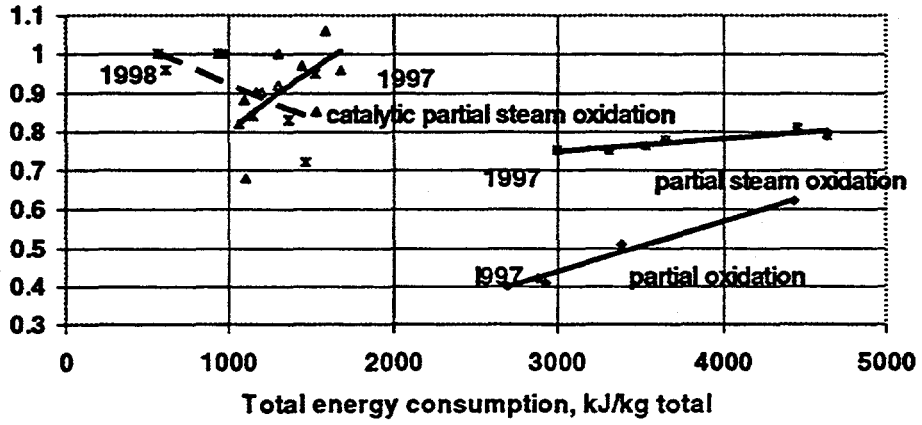

Figure 7. Hydrogen yield for plasma reforming of methane, as a function of the total energy consumption.

The progress in minimization of specific energy consumption is demonstrated in Fig 8. The specific energy consumption is shown in the figure as a function of the total energy consumption. The specific energy consumption decreased by a factor of 3 from those of homogeneous reactions, as reported in 1997 [2]. Since then, the specific energy consumption has decreased by another factor of 3 since, to less than 17 MJ/kg H_2.

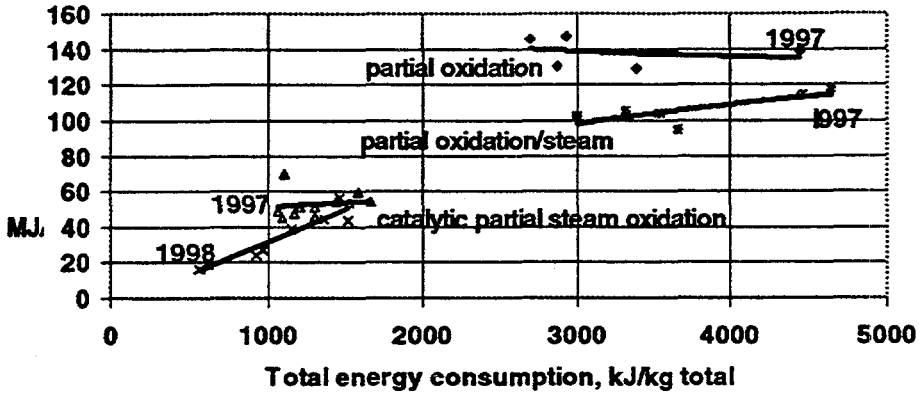

Figure 8. Specific energy consumption for hydrogen manufacturing from methane, as a function of the total energy consumption.

IV. Hydrogen costs

Although preliminary, it is useful to determine the costs of hydrogen manufacturing using a plasma reformer.

There are three major costs in the manufacturing of hydrogen-rich gas. There is the cost of the natural gas, the cost of the electricity, and the capital costs of the plasmatron reactor system. In addition, there is the need of gas cleanup, reducing the CO, CO_2 and N_2 contents. In this section, the costs of producing the clean gas are presented, and only rough costs of the gas cleanup process are described.

For the calculations, it is assumed that the optimized process can produce hydrogen at an specific energy consumption of 8 MJ/kg H_2.

This number is a factor of two lower than the one that has already been achieved. It is expected that the process can be improved through the use of a heat exchanger and through further optimization of the process, as described in the previous section.

It is estimated that the cost of the plasmatron system in about \$0.5 per W of electrical power. This includes the cost of the power supply and the plasmatron. Spare parts are additional, with a lifetime of 1000 hours. The cost of the system is actually not linear with power, but less than linear. Thus larger systems will produce hydrogen at lower costs than what is presented here.

The methane cost is assumed to be \$0.1/m^3 (\$2.6/MMBTU). Finally, the cost of the electricity is assumed to be \$0.05/kWhr.

It is assumed that the capital equipment is depreciated over a three year period, a conservative assumption since the power supply and ancilliary systems will last substantially longer.

The capital and operating costs of hydrogen-rich gas manufacturing are shown in Figure 9 as a function of the specific energy consumption. For a specific energy consumption less than ~20 MJ/kg H_2, the cost of the electricity and plasma/reactor equipment is substantially lower than the cost of the natural gas, and further decreases in the specific energy consumption do not decrease substantially the cost of the hydrogen-rich gas.

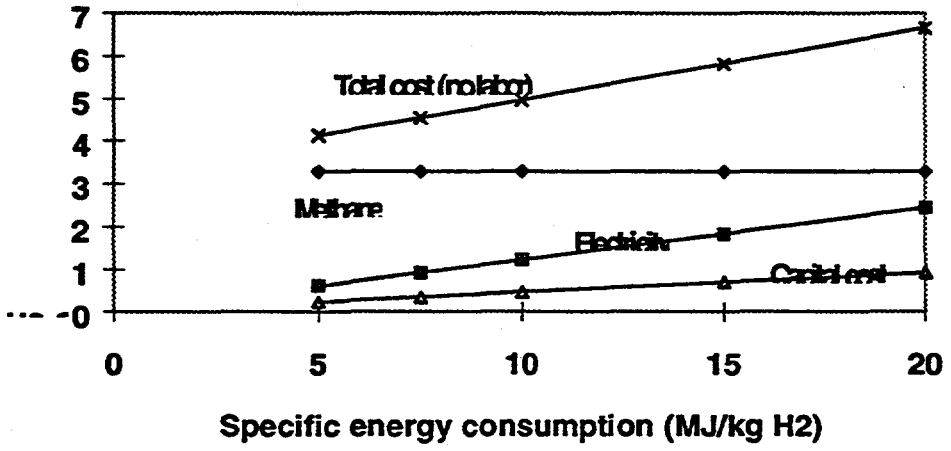

Figure 9 Contributors to cost of manufacturing hydrogen as a function of the specific energy consumption.

Table 2 shows the items associated with the cost of generating hydrogen-rich gas, assuming 8 MJ/kg H_2. If the cost of gas cleanup is less then \$5/MMBTU, then the cost of generating hydrogen, even at the low production rates assumed, is less than \$10/MMBTU.

Table 2. Distribution of costs of manufacturing hydrogen rich gas from methane using plasma catalysis, in \$/MMBTU H_2

Methane cost	\$3.28
Electricity cost	\$0.92
Depreciation cost of equipment	\$0.35
Total	\$4.55

V. Conclusions

Plasma reforming of methane, specially plasma catalysis, has been demonstrated with sufficiently low energy consumption and with high hydrogen yields to be economically interesting for energy applications.

The obtained results with plasma catalysis indicate hydrogen yields of about 100% (corresponding to about 80% methane conversion) and minimal specific energy consumption. Substantial improvements should be obtained through the use of heat regeneration, improved reactor and optimized residence time.

With water injection, it was possible to combine reforming and water shift reactions in a single stage with no soot buildup on the catalyst or on the surfaces of reactor. The device is very compact, with power densities of ~30 kW (H_2 HHV)/liter of reactor, or ~10 m^3/hr H_2 per liter of reactor.

Plasmatron generation of hydrogen could be used for decentralized energy production with fuel cells. Another one possible applications of this technology is for onboard reforming for the manufacturing of hydrogen rich gases. The compactness of the reformer, with high power densities, makes the technology attractive for this application.

Plasma reforming could also find uses for decentralized hydrogen production, such as in transportation refueling systems, either on-demand generation of hydrogen (requiring 200-500 kW plasmatrons) or small 20 kW CW plasmatrons (with stationary storage) for 30-50 vehicle fleets. The technology could also be used for industrial applications. Finally, plasma reformers could be used with hard to use fuels, such as raw biofuels or heavy oils.

Acknowledgments

This work was performed under the auspices of DOE under contract FG04-95AL88002

References.

[1] Bromberg, L., Cohn, D. R., and Rabinovich, A., *Plasma Reformer/ Fuel Cell Systems for Decentralized Power Applications, Int. Journal of Hydrogen Energy.* Vol. 22, pp. 83-94 (1997)

[2] Bromberg, L.; Cohn, D.R.; and Rabinovich; A.; *Plasma Reforming of Methane, Energy and Fuels* **12**, pp. 11-18 (1998)

[3] Trusov B.G. *Application of the Variational Principle for Solving Problems, Chemical Kinetics - Doklady Physical Chemistry*, **.339**, N.4-6, 1994, pp.239-242. Translated from Doklady Akademii Nauk, **339**, No.6, pp.771-775 (1994)

HYDROGEN PRODUCTION FROM HIGH MOISTURE CONTENT BIOMASS IN SUPERCRITICAL WATER

Michael Jerry Antal, Jr. and Xiaodong Xu
Hawaii Natural Energy Institute
University of Hawaii at Manoa, Honolulu, HI 96822

Abstract

By mixing wood sawdust with a corn starch gel, a viscous paste can be produced that is easily delivered to a supercritical flow reactor by means of a cement pump. Mixtures of about 10 wt % wood sawdust with 3.65 wt % starch are employed in this work, which we estimate to cost about $0.043 per lb. Significant reductions in feed cost can be achieved by increasing the wood sawdust loading, but such an increase may require a more complex pump. When this feed is rapidly heated in a tubular flow reactor at pressures above the critical pressure of water (22 MPa), the sawdust paste vaporizes without the formation of char. A packed bed of carbon catalyst in the reactor operating at about 650 °C causes the tarry vapors to react with water, producing hydrogen, carbon dioxide, and some methane with a trace of carbon monoxide. The temperature and history of the reactor's wall influence the hydrogen-methane product equilibrium by catalyzing the methane steam reforming reaction. The water effluent from the reactor is clean. Other biomass feedstocks, such as the waste product of biodiesel production, behave similarly. Unfortunately, sewage sludge does not evidence favorable gasification characteristics and is not a promising feedstock for supercritical water gasification.

Introduction

The goal of this work is to define conditions which enable the steam reforming of biomass (represented below as cellulose $C_6H_{10}O_5$) to produce hydrogen:

$$C_6H_{10}O_5 + 7\ H_2O \rightarrow 6\ CO_2 + 12\ H_2.$$

Earlier work has shown that when biomass is heated quickly in water above its critical pressure, no char is formed. Instead, the biomass decomposes into simple organic molecules dissolved in the water, which further decompose to hydrogen, carbon dioxide, and some methane when exposed to a carbon catalyst at temperatures above 600 °C. In this paper we detail the conditions which evoke the biomass steam reforming chemistry, and we offer insight into the influence of the reactor's wall on the product distribution.

Apparatus and Experimental Procedures

The two flow reactors (see Figures 1 and 2) used in this work are fabricated from Hastelloy C276 tubing with 9.53 mm OD x 6.22 mm ID x 1.016 m length. The reactant flow is quickly heated by an annulus heater (located along the reactor's centerline) and an entrance heater outside the reactor to temperatures as high as 800 °C. The annulus heater (3.18 mm OD x 15.2 cm heated length) delivers all its heat directly to the feed. The entrance heater is made from a split stainless steel tube that is held in good thermal contact with the reactor, and an electrical heater which is coiled around the outer surface of the stainless steel tube. Downstream of the entrance heater, the reactor's temperature is maintained in an isothermal condition by the furnace. The chief purpose of the furnace is to prevent heat loss. In fact, in some experiments the temperature setpoint of the furnace was below the lowest temperature measured along the reactor wall. Carbon catalyst is usually packed in about 60% of the heated zone of the reactor, as well as the downstream cold section of the reactor. The reactor's temperature profile is monitored by 12 fixed, type K thermocouples held in good thermal contact with the reactor along its outer wall. Also, in reactor #1 the reactant temperature is measured by a fixed, internal, annulus thermocouple which is located 5.08 cm upstream of the furnace (see Figure 1). Pressure in the reactor is measured by an Omega PX302 pressure transducer. A Grove Mity-Mite model 91 back-pressure regulator reduces the pressure of the cold, two phase, product effluent from 28 to 0.1 MPa. After leaving the back-pressure regulator, the reaction products pass through a gas-liquid separator. The liquid product is collected over a measured time period to calculate the liquid outlet flow rate. The gas flow rate is measured using a wet test meter.

Five different types of feedstocks are used in this work: glycerol, biodiesel waste (a mixture of methanol and glycerol), corn starch gel, poplar wood sawdust mixed in the corn starch gel, and sewage sludge mixed in the corn starch paste. Both the poplar sawdust and the sewage sludge are ground with a Wiley mill (Thomas Scientific) to 40 mesh before they are mixed with the paste. Table 1 gives elemental analyses of the feedstocks.

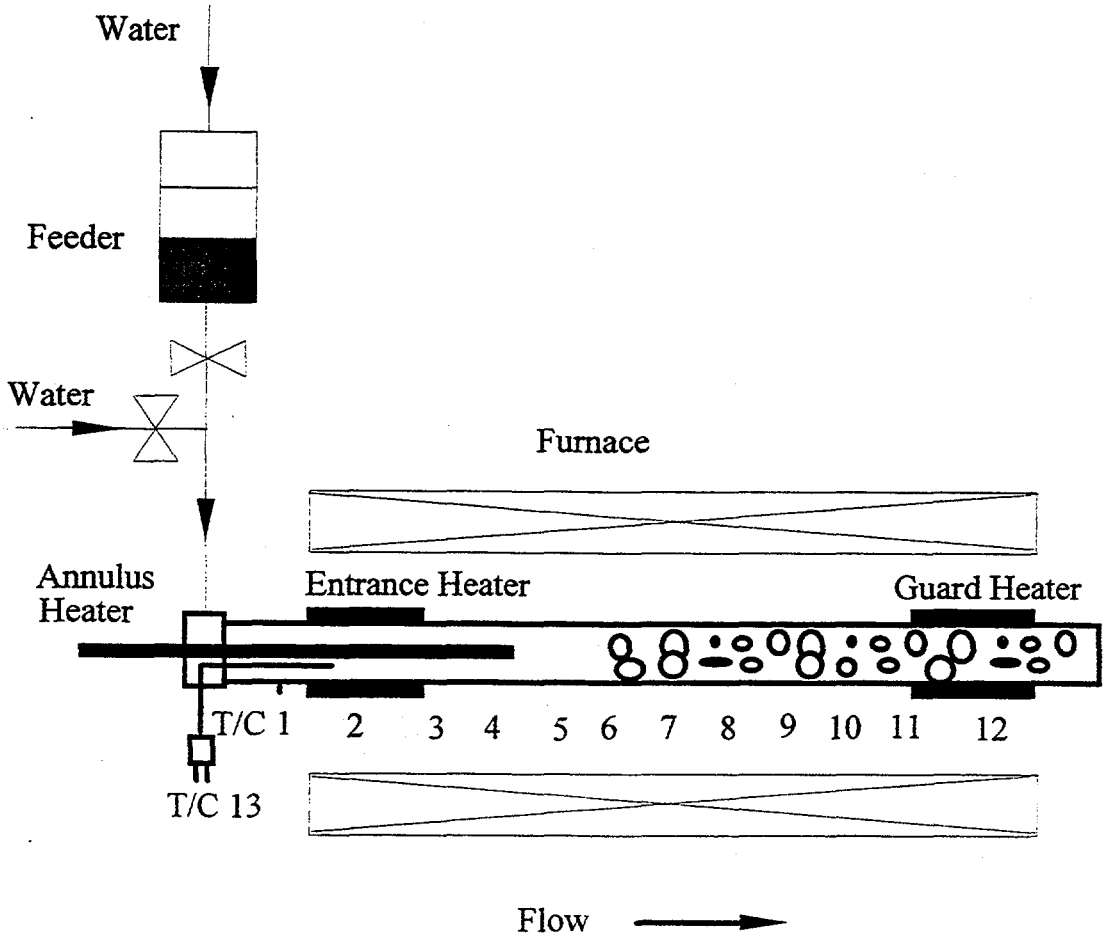

Figure 1. Reactor #1.

The feeder consists of a cylinder, a movable piston, and two end-caps (High Pressure Equipment). The cylinder is first filled with the feedstock, then the piston is placed on top of the feed, and the two end-caps are installed. Both the feeder and the reactor are pressurized separately to 28 MPa at the beginning of a run. During the time that the system is being brought up to temperature, water is pumped into the reactor by a Waters 510 HPLC pump. When the main body of the reactor reaches the desired temperature (usually about 650 °C), the feeder is connected to the reactor. Thereafter, water flow to the reactor is terminated, and water flow to the feeder is initiated, displacing the sawdust paste feedstock into the reactor. Because the thermophysical properties of the paste are considerably different than those of water, and possibly also because of exothermic pyrolysis reactions associated with the decomposition of the paste, the temperature of the feed rises very rapidly in the entrance region of the reactor. To avoid excessively high temperatures, usually it is necessary to reduce the heat input to the feed from the annulus heater and the entrance heater.

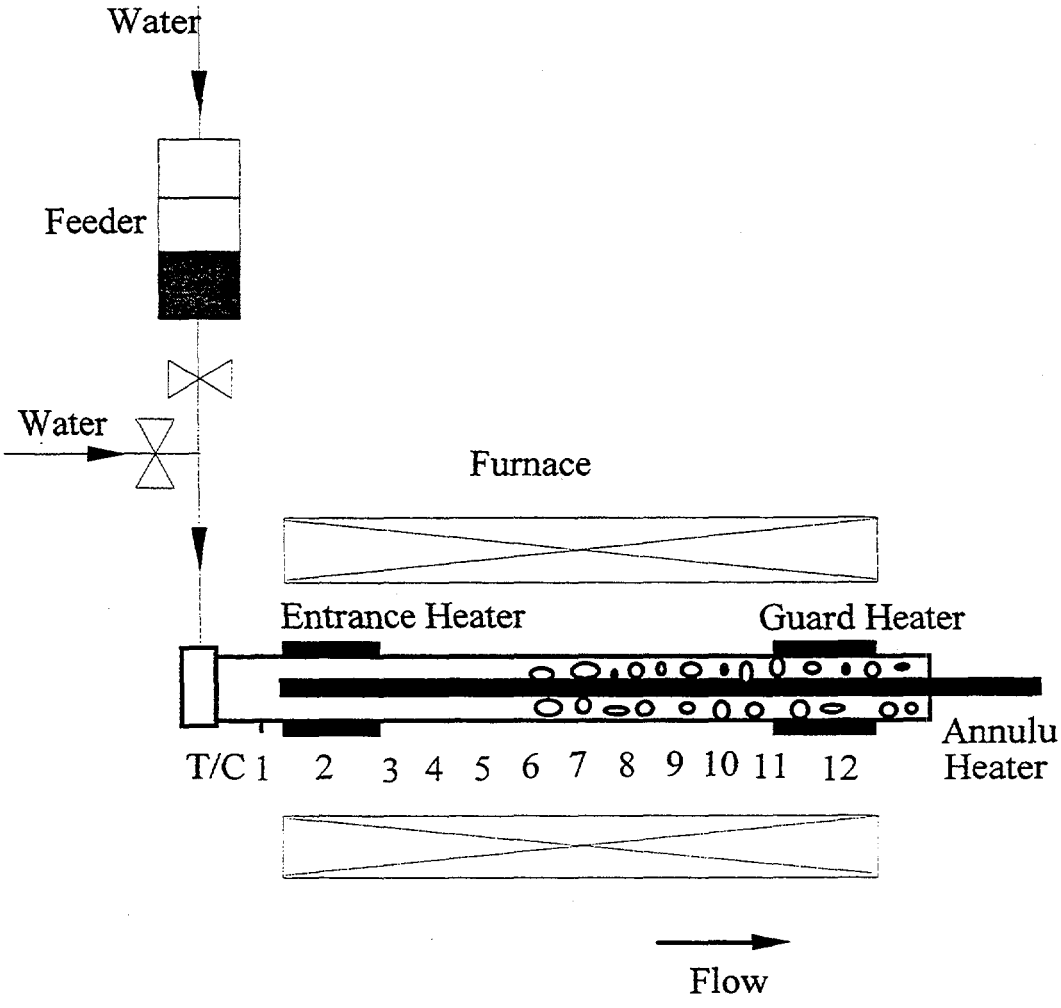

Figure 2. Reactor #2.

Gas samples are taken by gas-tight syringes from the gas sample outlet of the separator. Analysis of the gas is conducted using a Hewlett-Packard model 5890 gas chromatograph equipped with flame ionization and thermal conductivity detectors. A 80/100 mesh carbosphere molecular sieve packed column is used, operating at 35 °C for 4.2 min, followed by a 15 °C/min ramp to 227 °C, another ramp of 70 °C/min to 350 °C, and a 5 min hold at 350 °C. The carrier gas is a mixture of 8% hydrogen in helium. A standard gas mixture is used for day-to-day calibration. The TOC in the liquid effluent is determined by a Shimadzu model TOC-5000 total organic carbon analyzer.

In what follows we report gas yields as liters of gas at NTP (20 °C and 0.1 MPa) per gram of organic matter in the feedstock (L/g), and grams of gas per gram of organic matter in the feed (g/g). The reported carbon efficiency is the mass of carbon in the gas divided by the mass of carbon in the feed. Because the sawdust and sewage sludge pastes were not perfectly homogeneous, and because of variations in the gas flow rate due to unsteady release of gas by the back-pressure relief valve, the carbon efficiency occasionally exceeds 1.0 by a small amount.

The reported global mass balance is based on the flow of water and organics leaving and entering the reactor.

Table 1. Elemental Analysis of Feedstocks

	Corn Starch[1]	Poplar Wood Sawdust[2]	Digested Sewage Sludge[3]
Elemental Analysis (Dry Basis by Weight)			
C	41.1%	49.4%	N/A
H	6.5%	6.0%	N/A
O	52.4%	45.1%	N/A
N	N/A	0.06%	N/A
S	N/A	N/A	N/A
Volatile Matter	N/A	N/A	63.7%
Fixed Carbon	N/A	N/A	11.2%
Ash	N/A	0.16%	25.1%
Moisture Content[4]	12.8%	8.5%	N/A

1. The C, H, and O data were obtained from the Merck Index (5th edition, 1983).
2. The elemental analysis was conducted by Huffman Laboratories, Inc.
3. The digested sewage sludge was provided by Water Technology International Corp., Canada. The volatile matter, fixed carbon, and ash were measured following the ASTM method.
4. Moisture content was measured by placing the samples in an oven at 110°C for 8 hours.

Results

In earlier work we reported the ease of gasification of glycerol in supercritical water. Table 2 confirms the earlier result. In it we see that the hydrogen content of the gas increases from 38% to 51% after 3.45 hr, while the methane content decreases from 20% to 11%. During this time the total gas yield increased from 1.18 to 1.6 L/g and all the carbon in the feedstock was converted to gas. The increasing gas yield is due to the consumption of water and methane by the steam reforming reaction. Evidently this reaction is catalyzed by the reactor's wall and/or the carbon catalyst, which become more active (i.e. "seasoned") as time passes. When the gas yield reached a steady state, the feed was switched and sawdust paste was fed to the reactor for 4 hours. After this, glycerol was again fed to the reactor. Table 2 shows that the sawdust paste causes the reactor's wall and/or the carbon catalyst to lose some activity towards the steam reforming reaction.

The waste product generated by the commercial production of biodiesel fuel contains glycerol and methanol. We prepared a mixture of these two alcohols with a composition identical to that of the industrial waste. The gas produced from this mixture (see Table 3) is very rich in hydrogen, and the yield (2.05 L/g) is high. The water leaving the reactor was clean with a pH of 4-5. Evidently, this waste product is a perfect feedstock for hydrogen production.

As mentioned earlier, we prepare a sawdust paste by mixing wood sawdust into a starch gel, and this paste is easily fed to our reactors. Large quantities of wood sawdust are available at $30 per dry ton, and the quoted price of corn starch in bulk is $0.12 per pound. Using these values, the price of a 10 wt % sawdust, 3.65 wt % starch paste is $0.043 per pound. Similarly, the price of a 20 wt % sawdust, 3.65 wt % starch paste is $0.031 per pound. For comparison, the price of low sulfur coal is about $0.025 per pound.

Table 4 displays results from the gasification of corn starch gel at three different flow rates in reactor #1. Higher peak temperatures in the entrance region of the reactor were required at the higher flow rates to achieve adequate heat transfer to the reactant. In all cases, gasification was complete and the reactor gave no evidence of plugging, even after 6 hours of use. Again, the higher temperatures favorably influenced the steam reforming reaction, leading to high yields (1.7 L/g) of a hydrogen rich (48%) gas. The water leaving the reactor was clean with a pH of 7.

Sawdust paste gasification results from three consecutive runs (no intervening experiments) on different days are displayed in Table 5. In all 3 cases, the effluent water was clean with a pH of 7 to 7.5, but the reactor plugged after 2 to 3 hours on stream. Although the measured temperatures were similar on 3 and 10 July, the gas yield increased from 1.61 to 2.18 L/g, and the hydrogen content of the gas increased from 43 to 57%. Because fresh carbon catalyst was employed with each experiment, we assumed that the increase in gas yield was due to a seasoning effect of the high temperature in the entrance region on the reactor's wall. To see if the seasoned wall would provide a high gas yield at lower temperatures, we employed a lower entrance temperature in the next experiment (21 July). Remarkably, the results were effectively identical to those of the first experiment. This result, and others indicate that high temperatures are requisite to achieve high gas yields with high hydrogen concentrations from wood sawdust.

Table 2. Gas Composition from Glycerol Gasification in Supercritical Water at 28 MPa with Coconut Shell Activated Carbon Catalyst Using Reactor #2 (Exp. Date: 2/19/98)

Feedstock	18.72 wt% Glycerol in Water				
Reactor Peak Temp / Catalyst Bed temp	550°C/ 665°C				725°C/ 665°C
Flow Rate (g/min)	2.0				
Time on Stream (hr)	Before Paste[1]				After Paste[2]
	1.32	2.08	2.55	3.45	5.48
Product	Mole Fraction				
H_2	0.38	0.46	0.51	0.51	0.48
CO	0.02	0.03	0.03	0.03	0.03
CO_2	0.35	0.33	0.31	0.32	0.32
CH_4	0.20	0.13	0.12	0.11	0.16
C_2H_6	0.05	0.04	0.04	0.03	0.01
Total Gas Yield (L gas / g of Organics)	1.18	1.40	1.49	1.60	1.60
(g gas / g of Organics)	1.01	1.11	1.13	1.18	1.17
C Efficiency	0.96	1.00	1.00	1.01	1.01
Global Mass Balance	0.99	1.01	1.01	1.02	1.02

1. Poplar wood sawdust/corn starch paste was fed to the reactor for 4 hours after the gas generation from glycerol reached a steady state.
2. Glycerol was fed to the reactor again after the reactor plugged with the sawdust/corn starch paste.

Table 3. Gas Composition from Gasification of Glycerol/Methanol Mixture in Supercritical Water at 28 MPa with Coconut Shell Activated Carbon Catalyst Using Reactor #2 (Exp. Date: 3/13/98)

Feedstocks	Simulated Biodiesel Waste Product			
Reactor Peak Temp / Catalyst Bed Temp	730°C/ 720°C			
Flow Rate (g/min)	2.0			
Time on Stream (hr)	0.42	0.73	1.25	1.68
Product	Mole Fraction			
H_2	0.64	0.64	0.65	0.64
CO	0.05	0.05	0.05	0.05
CO_2	0.21	0.21	0.21	0.21
CH_4	0.10	0.10	0.10	0.10
Total Gas Yield				
(L Gas / g of Organics)	2.05	2.05	2.05	2.05
(g Gas / g of Organics)	1.25	1.22	1.24	1.20
C Efficiency	1.05	1.03	1.04	1.01
H Efficiency	1.43	1.41	1.44	1.38
O Efficiency	1.36	1.32	1.35	1.31
H Balance	1.04	1.03	1.04	1.03
O Balance	0.99	0.98	0.99	0.98
Global Mass Balance	0.98	0.97	0.98	0.97

Table 4. Gas Composition from Corn Starch (10.4 wt% Dry Basis) Gasification in Supercritical Water at 28 MPa with Coconut Shell Activated Carbon Catalyst Using Reactor #1 (Exp. Date: 2/20/97)

Flow Rate (g/min)	1.0			2.0			4.0		
Reactor Peak Temp / Catalyst Bed Temp	690°C/ 650°C			715°C/ 650°C			805°C/ 650°C		
Time on Stream (hr)	1.33	1.62	2.18	3.52	4.02	4.57	5.12	5.47	5.70
Product	Mole Fraction								
H_2	0.40	0.36	0.38	0.39	0.39	0.38	0.48	0.48	0.47
CO	0.01	0.01	0.01	0.01	0.01	0.01	0.02	0.02	0.02
CO_2	0.41	0.43	0.39	0.41	0.42	0.42	0.36	0.36	0.37
CH_4	0.18	0.20	0.22	0.19	0.18	0.19	0.14	0.14	0.14
Total Gas Yield (L gas/g of organics)		1.28			1.38			1.70	
(g Gas/g of Organics)	1.23	1.22	1.14	1.24	1.27	1.22	1.29	1.33	1.34
C Efficiency	1.0	1.0	0.97	1.02	1.04	1.01	1.0	1.03	1.05
Global Mass Balance	1.01	1.01	1.01	1.01	1.01	1.01	0.99	1.0	1.0

Table 6 displays results similar to Table 5 from reactor #2. In this case, we employed lower entrance temperatures on both days. As a consequence, the hydrogen content of the gas was only 27 – 30%, and the gas yield was lower (1.16 – 1.36 L/g). But in both cases, the water was clean with a pH of 7.

As mentioned earlier, plugging usually occurred with the sawdust paste after 2 – 3 hours on stream. Often we removed the plug by pumping a 1.2 M solution of hydrogen peroxide into the reactor for a short time. Table 7 gives results from the gasification of sawdust paste before and after the reactor was cleaned using hydrogen peroxide. Both the very high gas yield and the high hydrogen content were retained after cleaning. In fact, the cleaning seemed to reduce the presence of hydrocarbons in the gas.

Table 5. Gas Composition from Poplar Wood Sawdust / Corn Starch Gasification in Supercritical Water at 28 MPa with Coconut Shell Activated Carbon Catalyst on Different Dates Using Reactor #1

Experiment Date	7/3/97	7/10/97	7/21/97
Feedstocks (Dry Basis)	10.72 wt% Sawdust/ 4.01 wt% Corn Starch	11.17 wt% Sawdust/ 4.19 wt% Corn Starch	11.1 wt% Sawdust/ 4.15 wt% Corn Starch
Reactor Peak Temp / Catalyst Bed Temp	790°C/ 685°C	790°C/ 690°C	732°C/ 690°C
Flow Rate (g/min)	2.0		
Time on Stream (hr)	1.62	1.52	1.42
Product	Mole Fraction		
H_2	0.43	0.57	0.45
CO	0.03	0.04	0.03
CO_2	0.38	0.33	0.38
CH_4	0.17	0.06	0.15
C_2H_6	0.001	0.001	0.0
Total Gas Yield (L Gas / g of Organics)	1.61	2.18	1.57
(g Gas/ g of Organics)	1.37	1.65	1.48
C Efficiency	0.96	1.01	1.01
Global Mass Balance	1.01	1.00	0.99

Table 6. Gas Composition from Poplar Wood Sawdust / Corn Starch Gasification in Supercritical Water at 28 MPa with Coconut Shell Activated Carbon Catalyst on Different Dates Using Reactor #2

Experiment Date	12/17/97	2/12/98
Feedstocks (Dry Basis)	9.47 wt% Sawdust/ 3.55 wt% Corn Starch	10.04 wt% Sawdust/ 3.65 wt% Corn Starch
Reactor Peak Temp / Catalyst Bed Temp	750°C/ 700°C	725°C/ 700°C
Flow Rate (g/min)	2.0	
Time on Stream (hr)	1.37	1.02
Product	Mole Fraction	
H_2	0.27	0.30
CO	0.02	0.02
CO_2	0.46	0.44
CH_4	0.24	0.23
C_2H_6	0.005	0.009
Total Gas Yield		
(L/g of Organics)	1.36	1.16
(g/ g of Organics)	1.34	1.22
C efficiency	0.98	0.91
Global mass balance	0.95	0.98

Table 7. Effect of H_2O_2 Cleaning on the Gas Composition from Poplar Wood Sawdust / Corn Starch Gasification in Supercritical Water at 28 MPa with Coconut Shell Activated Carbon Catalyst Using Reactor #1 (Exp. Date: 7/10/97)

	Before Plug			After Plug and Pumping H_2O_2	
Time on Stream (hr)	0.78	1.00	1.52	2.92	3.13
Feedstock (Dry Basis)	11.17 wt% Sawdust / 4.19 wt% Corn Starch				
Flow Rate (g/min)	2.0				
Reactor Peak Temp/ Catalyst Bed Temp	790°C /690°C			805°C /690°C	
Product	Mole Fraction				
H_2	0.56	0.58	0.57	0.59	0.56
CO	0.04	0.04	0.04	0.04	0.05
CO_2	0.34	0.32	0.33	0.33	0.34
CH_4	0.06	0.06	0.06	0.04	0.05
C_2H_6	0.001	0.001	0.001	0.0	0.0
Total Gas Yield (L Gas /g of organics)		2.18			2.18
(g Gas/g of Organics)	1.60	1.52	1.65	1.64	1.56
C Efficiency	0.99	0.94	1.01	0.98	0.96
Global Mass Balance	1.00	0.98	1.00	0.99	0.97

To gain further insight into the role of the reactor's wall as a catalyst for the steam reforming reaction, we wrapped the annulus heater with nickel wire. We estimate that the surface area of the wire was 30% of the surface area of the hot region of the reactor. As seen in Table 8, the results indicate that nickel has no special effect on the reaction chemistry with a entrance peak temperature of about 740 °C. Molybdenum is another important component of Hastelloy. To test its effect on the reaction chemistry, we mixed molybdenum powder with the sawdust paste and fed it to the reactor. To our surprise, the metal powder catalyzed char forming reactions which significantly reduced the gas yield, the carbon efficiency, and the global mass balance (see Table 8). The reactor plugged after less than an hour on stream. Evidently, molybdenum is not a catalyst for the gasification reactions at entrance temperatures of about 730 °C.

The results of earlier exploratory experiments led us to believe that the gasification characteristics of sewage sludge over a carbon catalyst in supercritical water would resemble those of wood sawdust. To gain more definitive insight into this matter, we devoted almost two months of effort during the past year to studies of sewage sludge gasification. These tests were frustrating. In addition to the inherent difficulty of handling sewage sludge, we found that mixtures of the sludge with starch gels were not stable unless relatively large amounts of starch were used (about equal to the amount of sludge in the mixture). Results from our most successful tests are given in Table 9. Note that in all the sewage sludge experiments we employed very high entrance temperatures to maximize gasification. Nevertheless, the gas yields from the dried Canadian sewage sludge powder were not high, and the carbon efficiency was low. Because we were unable to learn the exact history of the Canadian sludge sample, we obtained a digested sludge from a local treatment plant for further work. Unfortunately, this sludge was less easily gasified than the Canadian sample: the gas yield was very low and it contained little hydrogen. One consequence of the low gas yield was the fact that the reactor plugged after less than one hour on stream. Some insight into the gasification chemistry can be gained by comparing the sewage sludge results with those of corn starch gel alone (see Table 9). If we imagine the sludge to be an inert additive, we would expect the gas yield to fall from about 1.4 L/g to 0.7 L/g when equal amounts of sludge and starch are fed to the reactor. In Table 9 we see that the Canadian sludge behaves as though it is almost inert. Most of the gas comes from the starch. Remarkably, the Hawaiian sludge not only does not gasify, it even destroys the favorable gasification properties of the starch. This may be due to the presence of sulfur, heavy metals, or other species in the sludge. After the experiments with the sewage sludge, we attempted reproduce some earlier results with the sawdust paste feed. This test failed. Apparently, the sludges altered the properties of the reactor's wall. For this reason, the reactor was retired and a new reactor was fabricated.

Table 8. Gas Composition from Poplar Wood Sawdust / Corn Starch Gasification in Supercritical Water at 28 MPa in a Packed Coconut Shell Activated Carbon Bed with Different Metal Catalysts Using Reactor #1

Experiment Date	2/12/98	2/19/98	12/17/97
Feedstocks (Dry Basis)	10.04 wt% Sawdust/ 3.65 wt% Corn Starch	10.5 wt% Sawdust/ 3.8 wt% Corn Starch	9.47 wt% Sawdust/ 3.55 wt% Corn Starch
Metal Catalyst	Ni Wire Wrapped Around the Annulus Heater	Mo Powder Mixed in the Feedstock	None
Reactor Peak Temp / Catalyst Bed Temp	740°C/ 715°C	730°C/ 680°C	750°C/ 700°C
Flow Rate (g/min)	2.0		
Time on Stream (hr)	1.53	0.60	1.37
Product	Mole Fraction		
H_2	0.31	0.29	0.27
CO	0.02	0.02	0.02
CO_2	0.42	0.46	0.46
CH_4	0.24	0.21	0.24
C_2H_6	0.01	0.02	0.01
Total Gas Yield (L Gas/g of Organics)	1.16	0.90	1.36
(g Gas/g of Organics)	1.22	0.90	1.34
C Efficiency	0.91	0.66	0.98
Global Mass Balance	0.97	0.89	0.95

Table 9. Gas Composition from the Gasification of Different Types of Sewage Sludge/ Corn Starch Feedstocks in Supercritical Water at 28 MPa with Coconut Shell Activated Carbon Catalyst Using Reactor #1

Experiment Date	9/11/97	9/19/97	10/3/97	2/20/97
Feedstocks (Dry Basis)	4.26 wt% Sewage Sludge (Canadian) /5.19 wt% Corn Starch	7.69 wt% Sewage Sludge (Canadian) /7.69 wt% Corn Starch	4.07 wt% Sewage Sludge (Hawaii) /5.06 wt% Corn Starch	10.4 wt% Corn Starch
Reactor Peak Temp / Catalyst Bed Temp	810°C/ 680°C	780°C/ 685°C	820°C/ 685°C	715°C/ 650°C
Flow Rate (g/min)	2.0			
Time on Stream (hr)	1.26	0.57	0.82	3.52
Product	Mole Fraction			
H_2	0.35	0.38	0.20	0.39
CO	0.01	0.02	0.01	0.01
CO_2	0.50	0.37	0.75	0.41
CH_4	0.14	0.22	0.05	0.19
C_2H_6	0.003	0.002	0.0	0.0
Total Gas Yield (L Gas/ g of Organics)	0.75	1.01	0.23	1.38
(g Gas/ g of Organics)	0.81	0.86	0.33	1.24
C Efficiency	0.62	0.73	N/A	1.02
Global Mass Balance	1.02	0.89	0.87	1.01

Conclusion

1. A semi-solid gel can be made from 4 wt % (or less) corn starch in water. Wood sawdust and other particulate biomass can be mixed into this gel and suspended therein, forming a thick paste. This paste is easily delivered to a supercritical flow reactor by a cement pump.
2. Above the critical pressure of water, wood sawdust can be steam reformed over a carbon catalyst to a gas composed entirely of hydrogen, carbon dioxide, methane, and a trace of carbon monoxide. There are effectively no tar or char byproducts. The liquid water effluent from the reactor has a low TOC value, a neutral pH, and no color. This water can be recycled to the reactor.
3. Trace amounts of carbon deposited in the entrance region of the reactor are easily and quickly removed by the delivery of water with some dissolved oxygen (or hydrogen peroxide) to the reactor. Some evidence suggests that this cleaning procedure may improve the performance of the gasifier.
4. The wall affects the gasification chemistry. Products from wood sawdust paste gasification decrease the activity of the wall towards hydrogen production by improving methane yields. These wall effects are strongly temperature dependent. High entrance temperatures strongly favor the methane steam reforming reaction and result in the production of a hydrogen rich gas.
5. Sewage sludge is a very problematic feedstock. Much more work is needed to learn if it is a suitable feedstock for hydrogen production. In light of the availability of biomass feedstocks that are easily gasified, we recommend that further studies of sewage sludge be postponed.

Acknowledgments

This work was supported by NREL/DOE under cooperative agreement DE-FC36-94AL85804, and the Coral Industries Endowment of the University of Hawaii at Manoa. We thank Neil Rosmeissl (DOE), Dr. Patrick Takahashi, and Dr. Richard Rocheleau (UH) for their interest in this work. We also thank Jose Arteiro (UH) for assistance with the experiments, Prof. Don Scott (U. Waterloo), Prof. Esteban Chornet (U. Sherbrooke), Prof. Jefferson Tester (MIT), Dave Nahmias, and William Hauserman, Prof. Angela Garcia (University of Alicante), and Professor Galen J. Suppes (University of Kansas) for useful advice.

MODELING OF BIOMASS TO HYDROGEN VIA THE SUPERCRITICAL WATER PYROLYSIS PROCESS

Robert J. Divilio
Combustion Systems Inc.
Silver Spring, MD 20910

Abstract

A heat transfer model has been developed to predict the temperature profile inside the University of Hawaii's Supercritical Water Reactor. A series of heat transfer tests were conducted on the University of Hawaii's apparatus to calibrate the model. Results of the model simulations are shown for several of the heat transfer tests. Tests with corn starch and wood pastes indicated that there are substantial differences between the thermal properties of the paste compared to pure water, particularly near the pseudo critical temperature. The assumption of constant thermal diffusivity in the temperature range of 250 to 450 °C gave a reasonable prediction of the reactor temperatures when paste is being fed.

A literature review is presented for pyrolysis of biomass in water at elevated temperatures up to the supercritical range. Based on this review, a global reaction mechanism is proposed. Equilibrium calculations were performed on the test results from the University of Hawaii's Supercritical Water Reactor when corn starch and corn starch and wood pastes were being fed. The calculations indicate that the data from the reactor falls both below and above the equilibrium hydrogen concentrations depending on test conditions. The data also indicates that faster heating rates may be beneficial to the hydrogen yield. Equilibrium calculations were also performed to examine the impact of wood concentration on the gas mixtures produced. This calculation showed that increasing wood concentrations favors the formation of methane at the expense of hydrogen.

Introduction

The Department of Energy is currently funding a research project at the University of Hawaii to produce hydrogen gas from high-moisture-content biomass using supercritical water. This work has shown that it is possible to completely gasify a paste composed of water containing 3 to 5% corn starch and 5 to 10% sawdust at supercritical conditions in a flow reactor, when an activated carbon catalyst is present. Combustion Systems Inc. has been contracted by the National Renewable Energy Laboratory (NREL) to develop a comprehensive model of this supercritical gasification process for the Department of Energy under Subcontract Number AXE-8-17103-01. This paper summarizes the status of the first seven months of work on this project.

During this time period, a comprehensive heat transfer model has been developed to calculate the temperature profiles in the University of Hawaii's reactor. A series of heat transfer tests were conducted in March 1998 in the apparatus to calibrate the heat transfer model. A literature review has been performed to identify the major reaction pathways for the pyrolysis of biomass in supercritical water. A preliminary global kinetic model has been developed to model the overall reaction pathways in the reactor. This model attempts to calculate the chemical reactions all the way from the wood feed to the gaseous products, and requires the time temperature profiles predicted by the heat transfer model. Equilibrium calculations were also performed to determine the gas compositions at chemical equilibrium and these results have been compared to the test results from the University of Hawaii's reactor when feeding a variety of materials.

Description of the University of Hawaii's SCW Reactor

The University of Hawaii has tested two configurations of their Supercritical Water Reactor (SCWR) with corn starch and wood pastes. Since the heat transfer tests were conducted using the latest configuration, this configuration will be described here. Where differences exist between the two configurations, the differences will be described using the terminology of "Old Reactor" to describe the previously tested configuration and "New Reactor" to describe the current configuration.

Figure 1 shows the overall configuration of the University of Hawaii's new reactor. The University of Hawaii's Supercritical Water Reactor consists of a Hastelloy tube that is 9.53 mm (0.375 inches) OD by 6.22 mm (0.245 inches) ID which is heated at the inlet by an entrance heater and by a annular heater inside the reactor pipe. Both heaters are electrical heaters that consist of a resistance heating element installed inside of an Inconel 600 sheath. The entire reactor is placed inside of a three-zone tube furnace. During the heat transfer tests, described later, thermocouples were attached to the tube wall at the positions indicated in Figure 1. The thermocouples located both inside the furnace and outside of the furnace were held in place using metal hose clamps. The three thermocouples located in the Entrance Heater block were sandwiched between the block and the tube wall.

Figure 2 shows the entrance region of the new reactor in expanded detail. The Entrance Heater consists of two 63.5 mm (2.5 inches) long steel blocks which fit together to form a round casing that is 25.4 mm (1 inch) OD and 9.53 mm (0.375 inches) ID and fits over the reactor wall at the entrance of the electrically heated furnace. Heat is supplied to this block by a 4.76 mm (3/16 inch) OD by 127 cm (50 inches) long heating element that is coiled around the outside of the Entrance Heater blocks.

In addition to the entrance heater, the SCWR Reactor is also heated by an Annulus Heater that runs down the center of the tube. In the old reactor configuration, the Annulus Heater entered the reactor from the upstream side and extended 15.24 cm (6 inches) inside the furnace. In the new reactor configuration, the Annulus Heater enters from the down stream end of the reactor, forming an annular space for fluid flow along the entire length of the reactor. The Annulus Heater is 3.18 mm (1/8 inch) OD. The heater in the old reactor had a heated length of 15.24 cm (6 inches) which started at the entrance of the Entrance Heater block. The Annulus Heater in the new reactor has a heated length of 25.4 cm (10 inches), and is positioned as shown in Figures 1 and 2.

Both the Entrance Heater and the Annulus Heater are located inside of an electrically heated furnace. The furnace has three zones, shown in Figure 1, which are independently controlled to maintain a constant temperature. Normally, during a test, all three zones are set to maintain the same temperature. Generally, the Entrance Heater and the Annulus Heater supply sufficient heat to heat the reactants flowing in the reactor up to test temperatures, so that the furnace simply prevents heat loss from the reactor walls.

An exit heater is also located at the down stream end of the furnace. The Exit Heater is similar in construction to the Entrance Heater. The primary function of the exit heater is to prevent heat loss from the down stream portion of the furnace.

Heat Transfer Model

The Heat Transfer model involves a differential energy balance around an element of the flowing fluid and a second differential energy balance around an element of the reactor wall. The two differential energy balances are coupled by the boundary conditions at the fluid-wall interface, which state that the heat flux through the wall is equal to the heat flux into the fluid.

Fundamental Equation - Heat Transfer to Fluid

A differential energy balance, in cylindrical coordinates for heat transfer to a fluid flowing in a pipe yields the following differential equation:

$$\left[\frac{\partial^2 t}{\partial r^2}+\frac{1}{r}\frac{\partial t}{\partial r}\right]=\frac{u_x}{\alpha}\frac{\partial t}{\partial x} \qquad (1)$$

Where: t = temperature, °C

r = radius, m

x = distance from the inlet of the pipe, m

u_x = velocity along the length of the pipe, m/sec

$\alpha = \frac{k}{\rho C_p}$, thermal diffusivity, m^2/sec

k = thermal conductivity of fluid Watt/m °C

r = density of fluid, g/m^3

C_p = specific heat of fluid, Joule/g °C

Equation 1 is subject to boundary conditions that specify the location and type of the heating or cooling surfaces. The velocity, u_x, in Equation 1 is also a function of radial position. For a pipe with no internal elements, the velocity profile is generally parabolic, and the velocity is given by:

$$u_x = 2u_b \left[1 - \left(\frac{r}{R_o}\right)^2\right] \tag{2}$$

Where: u_b = the average velocity in the pipe at distance x.

For flow through an annulus, the velocity profile is given by:

$$u_x = \frac{4u_b}{2R_{max}^2 - R_o^2 - R_i^2}\left[r^2 - R_o^2 - R_{max}^2 \ln\left(\frac{r}{R_o}\right)\right] \tag{3}$$

Where: $R_{max} = \sqrt{\frac{R_o^2 - R_i^2}{2\ln(R_o / R_i)}}$

Ro = inside radius of the reactor wall.

Ri = outside radius of the annulus

Equations 1, 2, and 3 were solved using a Crank-Nicholsen Finite Difference method (Chapra 1988).

Fundamental Equation - Heat Conduction to Tube Wall

Because of the high pressures used in the University of Hawaii's SCWR, the tube wall is relatively thick. This results in considerable heat conduction both in the radial direction as well as in the axial direction. To account for this heat conduction, a separate heat balance must be performed for the tube wall. The fundamental equation governing heat transfer and conduction in the tube wall is:

$$\frac{\partial^2 T}{\partial r^2} + \frac{1}{r}\frac{\partial T}{\partial r} + \frac{\partial^2 T}{\partial x^2} = 0 \qquad (4)$$

Equation 4 is also applicable to the heat transfer in the Entrance Heater Block. Note that Equation 4 also accounts for axial heat dispersion with the last term. This term was not included in Equation 1 above, because it was assumed that the flowing fluid makes the axial heat dispersion in the liquid negligible compared to the radial heat transfer. This equation is coupled to Equation 1 by boundary conditions at the inside of the tube wall. This coupling is accomplished in the numerical solution by setting heat flux through the wall equal to the heat flux through the fluid. Solution of Equation 4 was performed using an explicit centered finite difference method with Gausian elimination

Boundary Conditions

Figure 3 shows the boundary conditions applied to the system of equations defined by Equations 1 through 4. The integration is performed from 2 inches upstream of the entrance heater to one inch beyond the end of the annulus heater. No attempt was made to model the heat transfer in the catalyst bed or at the Exit Heater, because the data and the model results showed that the temperature profile was relatively flat and up to the test temperature by the time the fluid enters the catalyst bed.

The fluid enters two inches upstream of the entrance heater at a constant temperature, T_O. Heat is transferred from the ambient air to the wall of the reactor tube via convection. To model the resistance heater that is wrapped around the entrance heater block, a constant temperature, T_B, is applied to the outside edge of the entrance heater block. Because the edge of the Entrance Heater block that faces the outside of the furnace is insulated, a zero heat flux is applied to this face. Inside the furnace, heat transfer is governed by both convection and radiation to both the wall of the reactor and to the inside face of the Entrance Heater block. A constant heat flux is applied to the wall of the heated portion of the Annulus Heater. The unheated portion of the annulus has a zero heat flux, as does the center line of the reactor upstream of the entrance heater.

The heat balance to the Entrance Heater block is coupled to the heat balance to the tube wall by the boundary conditions at the interface between the two pieces of metal. At this interface, the heat flux through the tube wall will be equal to the heat flux through the entrance heater block times a contact factor, α_c, which specifies the contact efficiency between the two pieces of metal ($0 < \alpha_c < 1.0$). This is expressed as:

$$q_m = \alpha_c q_b \qquad (5)$$

or:

$$k_m \frac{T_{(x,zz)} - T_{(x,zz-1)}}{\Delta R_m} = \alpha_c k_b \frac{T_{(x,zz+1)} - T_{(x,zz)}}{\Delta R_b} \qquad (6)$$

Where the subscript "m" refers to the properties of the tube wall, the subscript "b" refers to the properties of the entrance heater block, and zz is the node at the interface between the entrance heater blocks and the tube wall.

At the fluid/metal interface, the heat flux through the metal is equal to the heat flux to the fluid as recommended by Parankar 1980. This couples the temperature distribution of the fluid to the temperature distribution of the metal. This is expressed as:

$$k \frac{T_{(x,M)} - T_{(x,M-1)}}{\Delta R} = k_m \frac{T_{(x,M+1)} - T_{(x,M)}}{\Delta R_m} \qquad (7)$$

Solution of Equations 1 through 7 is accomplished as follows. First the temperature profile is assumed. Equations 1, 2, 3 and 7 are used to solve for the fluid temperatures using the assumed wall temperature profile. Next, Equations 4, and 6 are used to solve for the temperature profile through the reactor wall and in the Entrance Heater block, using the fluid temperature profile that was previously calculated. The calculation then iterates between the solution for the fluid and the solution for the wall temperatures until the calculation converges to a solution. Convergence criteria are set at 0.001 °C for successive iterations for all temperatures in the reactor wall.

Heat Transfer Tests

On March 10 and 11, 1998, a series of tests were conducted to develop the data necessary to calibrate the heat transfer model. Table 1 lists the tests that were conducted.. Tests 1, 2, and 3 consisted of operating each heater element at two different power settings while keeping the other heaters off. The final three tests used combinations of the heaters at power settings typical of the settings used during the gasification tests.

Table 1. Heat Transfer Test Matrix
Test Dates: March 10 and 11, 1998

Test Number	Entrance Heater, %	Annulus Heater, %	Furnace Temp. °C
1A	15	0	Off
1B	30	0	Off
2A	0	10	Off
2B	0	20	Off
3A	0	0	500
3B	0	0	650
4	30	0	650
5	30	20	650
6	30	35	650

Figure 4 shows the temperature profiles obtained for the nine tests listed in Table 1. Also shown in Figure 4 are the relative locations of the Entrance Heater, the heated and unheated portions of the Annulus Heater the catalyst bed, and the exit heater. The data in this figure was used to calibrate the heat transfer coefficients in the Heat Transfer Model.

Model Results

Figures 5 through 9 show the results of the Heat Transfer Model simulations of Tests 3A, 3B, 4, 5, and 6. All four figures contain two graphs which show the axial and the radial temperature profiles calculated by the model. The axial temperature profile graph shows the temperatures along the length of the reactor from 2 inches upstream of the entrance heater block to 11 inches inside the furnace. The data points obtained for the test are plotted on this graph. The heavy solid line on the axial temperature profile graph is the average temperature of the fluid, averaged radially. The heavy dashed line is the average wall temperature of the reactor tube, also averaged radially. The heavy double dashed line is the temperature at the surface of the annulus heater. In addition to those lines, three light dashed lines show the temperature at radii of 2.4 mm, 2.7 mm, and 2.9 mm. The heavy shaded line is the average temperature profile of the Entrance Heater block, averaged radially. The curves on the radial temperature profile graph give the temperature profile in the vicinity of the temperature probes that were attached to the reactor walls. The temperatures are plotted for both the fluid (from 0 to 3.1 mm) and for the reactor tube wall (>3.1 mm). Temperatures of the Entrance Heater block are not shown on this graph.

Figures 5 through 9 show that the model does a reasonable job of predicting the wall temperatures, with the exception of two thermocouples. The first is located outside of the furnace, 1 inch up-stream of the entrance heater. The second is the thermocouple located in the middle of the entrance heater block. We are currently looking at ways to modify the model to improve the temperature predictions in these two areas. However, it is quite likely that these readings are the result of non-ideal geometry's and may not be modeled accurately.

The basic features observed in Figures 5 through 9 can be explained by looking at the quantity of heat necessary to raise the water temperature up to a desired temperature. Figure 10 shows the results of this calculation for the test conditions used during the heat transfer tests. This figure shows that between 375 and 425 °C, there is a dramatic change in the quantity of heat that must be absorbed by the water in order to increase the temperature. The dashed line in Figure 10 shows the quantity of heat that would need to be absorbed, if the heat capacity of the fluid remained constant. The heat absorption in this temperature range is indicative of a phase change, although the water is supercritical and there is no phase change. This "Pseudo Boiling" phenomena is caused by the fact that at 395 °C, the heat capacity of the water at 28 MPa is about 7.5 times the heat capacity at either 200 °C or at 500 °C. Thus, in order for the water to heat above this temperature range, an additional quantity of heat must be absorbed. This causes the axial temperatures around 500 °C to flatten out as the radial temperatures begin to diverge. Figure 9 shows that once this region is passed, the temperatures again rise rapidly as additional heat is applied.

Heat Transfer to Wood-Paste Mixtures

Figure 11 shows the wall temperature profile measured on December 29, 1997. Two wall temperature profiles are shown in this figure. The thin line is the wall temperature profile obtained when feeding water just prior to the wood feed. The second is the wall temperature profile when feeding a mixture of 10.5 wt. % poplar wood and 4 wt. % potato starch in water. This data show that, unlike the water, the wood paste mixture does not experience the axial wall temperature flattening in the region of 500 °C. Instead, the wall temperature rapidly rises to 700 °C and remains relatively flat after that. This indicates that the thermal properties of the wood paste mixture are considerably different than the thermal properties of pure water, particularly in the region of the pseudo critical point.

Figure 12 shows the results of the Heat Transfer Model when the thermal diffusivity is assumed to be constant in the temperature range 250 to 450 °C. The conditions of this figure were the same as the operating conditions of Test 5. This figure shows the same wall temperature trends as observed in the paste data in Figure 11. However, more data will be needed to verify the assumptions made in this calculation.

Figure 13 shows the same data in Figure 12 plotted as a function of time in the reactor, based on the average velocity of the fluid. This plot shows that the fluid takes approximately 40 seconds to enter the heated portion of the furnace. At that point, the average fluid temperature is about 200 °C, while the fluid at the wall is near 400 °C. The fluid takes an additional 20 seconds before it reaches the catalyst bed. Furthermore, it is over 600 °C for almost 12 seconds before reaching the catalyst bed. Fluid temperatures near the annulus can be over 750 °C for as much as eight seconds.

Kinetic Model

The second task of this project was to develop a kinetic model of the supercritical water pyrolysis process. The first step in the development of this model was to perform a literature review of the data on pyrolysis in supercritical water. This review has also been expanded to include supercritical water oxidation (SCWO), as some of the reactions in SCWO are also applicable to the pyrolysis process.

Pyrolysis of biomass in supercritical water is quite rapid. In fact, as the heat transfer model showed, by the time the reaction products are brought up to the test temperature and reach the catalyst bed (about 20 seconds in the new reactor configuration), most of the primary gasification reactions will have been completed. Therefore, a kinetic model of the University of Hawaii's reactor will require a model that is capable of following the chemistry of the reaction from room temperature up to the test temperature. Modeling of the University's apparatus is further complicated by the fact that the only chemical measurements are made on the gas products collected at the exit of the reactor. Critical chemical measurements at the front end of the reactor, where most of the chemical reactions occur, are impossible with this type of reactor.

Literature Review

Supercritical water possesses some unique characteristics that are beneficial to the water-biomass pyrolysis chemistry. Figure 14 shows the hydrogen ion concentration in pure water as a function of temperature and pressure (Marshall 1981). This figure shows the calculated hydrogen ion concentration of water as a function of temperature at pressures of 20.8, 28.0 and 34.6 MPa. This figure shows that the hydrogen ion concentration in water at 250 °C is about 25 times greater than the hydrogen ion concentration at room temperature (10^{-7} mol/L at room temperature). However, above the pseudo critical temperature, the hydrogen ion concentration rapidly drops to several orders of magnitude below the concentration at room temperature. Holgate (1994) concluded that the "... operating conditions of supercritical water oxidation process are not readily able to support ionic chemistry, and that the oxidation process most likely occurs through free radical pathways".

Therefore, reactions that follow a temperature-time profile such as the one shown in Figure 13 will first experience high hydrogen ion concentrations and will be subject to acid catalyzed reactions, such as dehydration of glucose compounds, and will then quickly pass into a reaction regime that favors free radical chemistry. Note that char formation is one such acid catalyzed reaction. Antal (1997) has reported the formation of plugs in the entrance region of their apparatus at the University of Hawaii when feeding wood or sewage sludge. No such plugs were encountered when feeding glucose or corn starch. This would tend to suggest that the plug is a char formation that is caused by acid catalyzed reactions with lignin or lignin decomposition products.

Numerous articles have been published related to the hydrothermal reactions of biomass, particularly at low temperatures (less than 300 °C). An excellent review of the literature on this subject can be found in Bobleter (1994). Hydrothermal processes were generally developed to recover chemicals such as sugars and cellulose fibers from biomass. A variety of processes have been developed to take advantage of the water-biomass chemistry at low temperatures. At these conditions, the basic components of biomass, cellulose, hemicellulose and lignin, behave differently, depending on whether they have been isolated from the wood matrix. As such, this discussion will concentrate on whole biomass experiments.

Bobleter's (1994) discussion of hydrothermal biomass treatment processes can be summarized as follows:

- In the temperature range of 180-220 °C and with short reaction times
  - hemicelluloses (polyoses) can be dissolved in water
  - some lignin will also be extracted
  - the degree of polymerization (DP) of the cellulose decreases with increasing time and temperature.

- In the temperature range 280-300 °C cellulose is also rapidly decomposed to low molecular weight products.

- Cellulose was found to decompose according the following mechanism:

$$\text{Cellulose} \xrightarrow[H_2O]{k_1} \text{glucose} \xrightarrow{k_2} \text{decomposition products}$$

  Over a wide temperature range cotton cellulose follows a first order decomposition with an activation energy E_1 = 129.1 kJ/mol (Schwald 1989). Other cellulose products showed similar activation energies, however the reaction rate constants differed.

- During hydrothermal treatment of biomass, the pH of the water solution increases up to a maximum of about 3.0. However, this pH change does not appear to have a significant effect on the reaction rate.

- The activation energy for the acid hydrolysis of hemicellulose is in the range of 106 to 160 kJ/mol (Bobleter 1994). The activation energy for the thermal hydrolysis of hemicellulose can be expected in this same range.

- Delignification of biomass under hydrothermal conditions is most likely the result of α-aryl ether hydrolysis which has an activation energy of about 80 kJ/mole (Sarakanen 1981).

Insight into the biomass pyrolysis can also be inferred from the literature on glucose pyrolysis in supercritical water. However, it should be stressed that glucose is only one of several sugars that are formed during the thermal hydrolysis of biomass. Furthermore, decomposition of lignins result in compounds, such as monomeric phenols that are expected to behave quite differently than glucose. Holgate (1995) studied the reaction products formed in the temperature range of 425 to 600 °C for the pyrolysis of glucose. Holgate's data is presented in Figure 15 for an initial glucose concentration of 1.02×10^{-3} mol/L and a 6.1 second residence time at a pressure of 246 bar. At 425 °C, the major reaction products were found to be acetic acid, acetonylacetone, 5-hydroxymethylfurfural (5HMF), furfural, and propenoic acid. Above 575 °C, the only reaction products were hydrogen, carbon dioxide, methane, and a small amount of ethane.

The authors of the study indicated that ethylene may also be present at the higher temperatures, and stated that analytical error may be the cause for the disappearance of ethylene at 575 and 600 °C. Xu (1996) also observed ethylene in their gas products even at 600 °C. Xu's data show that the ratio of ethane to ethylene ranged from 4.38 at 500 °C to 10 at 550 °C and increased to 31.25 at 600 °C. Holgate (1995) postulated that the glucose pyrolysis mechanism proceeds via the fast formation of intermediate compounds followed by secondary reactions to form lighter gases, which then degrade to the final reaction products.

The data in Figure 15 show several other interesting features as well. Hydrogen, carbon dioxide and carbon monoxide begin to appear between 425 and 450 °C and are released in equal proportions up to about 500 °C. However above 500 °C, their yields begin to diverge, indicating the start of another reaction mechanism, which the authors of the study termed a "Fast water-gas-shift-type pathway". Methane and ethane both appear to begin forming between 475 and 500 °C and show comparable formation trends

The data in Figure 12 can be explained by two competing intermediate pathways and a third high temperature pathway. One intermediate temperature pathway proceeds through the formation of acetic acid, which ultimately forms CO, CO_2, and H_2, in roughly equal molar amounts and a small amount of methane. The second intermediate temperature pathway proceeds through the formation of propenoic acid, which ultimately forms CO, CO_2, and H_2, again in roughly equal molar proportions and a small amount of ethylene, which reacts with hydrogen to form ethane. The high temperature pathway proceeds via the formation of unstable free radicals which react with water to form CO_2 and H_2 in approximately a molar ratio of 2 moles of H_2 per mole of CO_2 formed.

Comparison of Holgate's (1995) data to Xu's (1996) data also show a concentration effect on the gasification efficiency. Holgate's data showed 100% gasification of 0.001 mol/L glucose at 575 °C and 600 °C after only 6 seconds of residence time. Xu's data indicated only 80% carbon gasification efficiency for 1.2 mol/L glucose at 600 °C after 34 seconds of residence time. Xu needed a carbon catalyst to achieve 100% gasification in their apparatus. It is likely that the higher glucose concentrations in Xu's data resulted in the formation of more light compounds, such as acetic acid, which are quite stable in supercritical water at these conditions. There may also be a pressure effect, as Holgate's data was taken at 24.6 MPa while Xu's data was taken at 34.5 MPa.

The parallel reaction pathways between the formation of propenoic acid and acetic acid will ultimately determine the ratio of methane to ethane from the intermediate temperature reaction pathways. Webley and Tester (1991) indicated that ethane is also formed during supercritical water oxidation conditions by radical recombination of methyl radicals, which will be formed by the high temperature pathway. The ratio of methane to ethane was relatively unaffected by temperature between 500 and 600 °C and averaged 3.6 in Xu's data for a 1.0 mol/L glucose solution, while Holgate's data show higher ratios with considerable scatter. In Holgate's data, the average ratio of methane to ethane over the temperature range of 500 to 600 °C was 10.0 and ranged from a low of 5.7 at 525 °C to a high of 17.5 at 600 °C for the lower concentrations of 0.001 mol/L of glucose (the actual ratios were: 10.0 at 500 °C; 5.7 at 525 °C; 8.0 at 550 °C; 8.75 at 575 °C; and 17.5 at 600 °C, however the authors indicated that there was considerable error in the measurement of ethane for the high temperature tests, which will impact these ratios dramatically, given the low levels of methane and ethane encountered).

One model compound for lignin pyrolysis in supercritical water that has been studied is *1,3*-Butanediol (West 1987). West studied the pyrolysis of *1,3*-Butanediol at 425 °C both with and

without the presence of water. She found that the reaction in supercritical water altered the selectivity of the reactions to give mainly propene and formaldehyde. Significant amounts of hydrogen were not formed at this temperature, which is consistent with Holgate's findings for glucose. However, CO2 was formed in significant quantities, unlike Holgate's data for glucose. West also found that the role of trace quantities of oxygen in the supercritical reaction mixture was to serve as an inhibitor to the overall conversion of *1,3*-Butanediol. She also concluded that the dielectric constant and low hydrogen ion concentration of the supercritical water suppressed the formation of char by reducing dehydration and subsequent condensation or polymerization reactions.

Proposed Reaction Mechanism

While it is not possible to identify all of the reaction mechanisms that occur during the supercritical water pyrolysis of biomass, the literature suggests the following overall reaction pathways. As the reactants begin to heat up, the hemicellulose and the lignin fractions of the wood will begin to hydrolyze and dissolve into solution. This reaction begins to occur at a reasonable rate at temperatures as low as 180 °C, which as Figures 12 and 13 show begins outside of the furnace. As long as the temperature is low enough to support ionic mechanisms, the decomposed hemicellulose will begin to react with the lignin fragments to from char. As the temperature increases further, the cellulose will also begin to decompose into glucose fragments, and these will further decompose to lighter compounds. By the time the fluid reaches the pseudo critical temperature (395 °C at 28 MPa) all of the biomass will have been dissolved into compounds of length C5 and C6 along with their decomposition products (secondary reaction products), especially acetic acid and propenoic acid. At this point, the reaction mechanisms shift from ionic reactions to free radical reactions. Hydrogen, carbon dioxide, and carbon monoxide will begin to evolve at this point in roughly equal molar ratios. Methane and ethane begin to appear around 475 °C either from the decomposition of acetic acid and propenoic acid or through radical recombinations of methyl radicals. Around 500 °C, the free radical reactions begin to dominate the chemistry. Carbon monoxide formation decreases and hydrogen and carbon dioxide begins to form in a molar ratio of roughly 2 moles of hydrogen to one mole of carbon dioxide.

The time-temperature history of the reaction products is critical to the proposed mechanism. For example, acetic acid is quite stable in supercritical water. Xu (1996) gasified acetic acid in their apparatus at the University of Hawaii at 600 °C and 34.5 MPa both with and without the carbon catalyst. Without the carbon catalyst, they achieved a gasification efficiency of 51% after 27 seconds of a 0.1 M solution of acetic acid. With the carbon catalyst, they achieved 82% gasification efficiency. Furthermore, the ratio of H_2 to CO_2 in these tests was 1.3 for the test without the catalyst and 1.0 with the catalyst. Thus, if the upstream temperatures favor the formation of acetic acid, by keeping the reaction in the intermediate temperature range longer, then the yield of hydrogen will suffer.

Equilibrium Considerations

Once the gas products of H_2, CO_2, CO, CH_4 and C_2H_6 are formed by the secondary gasification reactions, they will continue to react according to two reversible tertiary reactions. The first is the water-gas shift reaction:

$$CO + H_2O \Leftrightarrow CO_2 + H_2 \tag{8}$$

and the second is the Methane Formation Reaction:

$$CO + 3H_2 \Leftrightarrow CH_4 + H_2O \tag{9}$$

Because Equations 8 and 9 are reversible reactions, they can be driven in either direction, depending on the concentrations of the reacting species. For example, removing CO_2 from the reaction products will cause higher hydrogen yields as the concentrations of the species in Reaction 8 adjust to the equilibrium ratio given by:

$$\frac{[CO^*][H_2O^*]}{[CO_2^*][H_2^*]} = K_{eq}^{WG} = 10^{1.416} e^{-\frac{3432.5}{T}} \tag{10}$$

In fact, this is the basis for the Sorption Enhanced Reaction process for the production of hydrogen (Sircar 1998).

As a first step in the analysis of the data from the University of Hawaii, HYSIM was used to calculate the theoretical equilibrium concentrations of H_2, CO_2, CO, CH_4 and C_2H_6 that would be expected at the conditions of their tests. Figure 16 shows the flow sheet used for the HYSIM simulation. The feed is composed of carbon, hydrogen and oxygen, contained in the wood and corn starch, and water in the proportions of the feed for each test period. This feed stream is fed to a Gibbs reactor, which calculates the equilibrium concentrations at the temperature and pressure of each test by minimizing the Gibbs Free Energy of the mixture. The equilibrium products are then cooled to 25 °C and 1 atmosphere pressure and fed to a gas/liquid separator which performs a flash calculation to determine the quantity and concentrations of the gas stream and liquid stream. Peng-Rboinson equations of state were chosen for the equilibrium calculations.

Figure 17 shows the results of this calculation for the University of Hawaii's tests where corn starch and corn starch/poplar wood sawdust paste mixtures were fed to their reactor. The legend in Figure 17 shows the test conditions reported for these tests (Antal 1997 and Antal 1998). The x-axis contains the equilibrium mole fractions calculated by HYSIM (on a dry basis). The y-axis contains the measurements made at the University of Hawaii. The diamonds are the hydrogen mole fractions, the squares are the carbon dioxide mole fractions, the triangles are the carbon monoxide mole fractions, the circles are the methane mole fractions and the x's are the ethane mole fractions. Note that the equilibrium mole fraction for ethane at these conditions was zero.

The data in Figure 17 show that the hydrogen mole fractions measurements fall on both sides of the equilibrium concentration. Furthermore, the tests where the hydrogen is below the equilibrium concentration are the same tests where the methane is above the equilibrium concentration. Clearly in these tests, methane is being formed at the expense of the hydrogen yield.

Figure 18 shows a plot of the hydrogen yield, in liters/g of solids feed as a function of the peak reactor temperature. Tests 4, 5 and 6 are not shown on this graph because the total gas yield was not reported for these tests. The peak reactor temperature is usually the temperature measured under the middle of the entrance heater block, and would be indicative of the heating rate of the fluid. This figure shows that higher peak temperatures favor the formation of more hydrogen gas. However, there is a considerable amount of scatter in the data. Tests 8 and 11, for example, show essentially the same hydrogen yield at drastically different peak reactor temperatures, while Tests 8 and 10 show drastically different hydrogen yields at the same peak reactor temperature. It is possible that these tests were conducted at different annulus heater power settings, which were not reported. The heat transfer model showed that the annulus heater power would affect the heating rate of the fluid. However, another explanation for these anomalies is that the wall seasoning phenomena that Antal (1987) discusses.

Figure 19 shows a plot of the predicted equilibrium mole fractions as a function of the concentration of wood feed to the reactor at 600 °C. In this simulation, only wood and water were assumed to be in the feed stream (no corn starch). This figure shows that increasing the concentration of biomass in the feed stream will result in less hydrogen and more methane formation, if the reaction is allowed to go to completion. This will be an important consideration in a commercial process, as lower wood concentrations will increase the quantity of energy required to gasify the same amount of biomass.

Conclusions

The Heat Transfer Model provides some valuable insight into the temperature profiles within the University of Hawaii's Supercritical Water Reactor. Data with corn starch and wood/corn starch pastes indicates that there are substantial differences in the fluid properties of the pastes as compared to those of pure water particularly near the pseudo-critical temperature. The assumption of constant thermal diffusivity in the temperature range of 250 to 450 °C gives a reasonable prediction of the reactor temperatures when paste is being fed.

The results of the literature review and an analysis of the University of Hawaii's data indicate that the hydrogen yield will be favored by higher heating rates of the wood, higher reactor temperatures and shorter residence times, assuming that the secondary gasification reactions produce hydrogen concentrations in excess of equilibrium of the tertiary reactions. Furthermore, equilibrium considerations indicate that higher wood concentrations in the feed stream will favor the formation of methane over hydrogen.

At this time, there is insufficient data to develop a comprehensive kinetic model of the supercritical water biomass pyrolysis process. However, a global model based on the pathways described above and calibrated with kinetic data in the literature may be possible. Such a model would, hopefully, lead to a better understanding of the process and might explain some of the observations that are presently not fully understood, such as the wall seasoning effect.

Acknowledgments

This work was funded by the Department of Energy and the National Renewable Energy Laboratory (AXE-8-17103-01). We are particularly grateful to Dr. Michael Antal, Jr. of the University of Hawaii for allowing us to use his data and for his assistance on this project.

References

Antal, M. J. Jr., and X. Xu, 1997, "Total Catalytic Supercritical Steam Reforming of Biomass", 1997 Annual Report for Coop. Agreement DE-FG36-94AL85804.

Antal, M. J. Jr., 1998, "Hydrogen Production from Biomass in Supercritical Water", Quarterly Progress Report for Coop. Agreement DE-FG36-94AL85804, January-March 1998.

Bobleter, O., 1994, "Hydrothermal Degradation of Polymers derived from Plants", in *Prog. Polym. Sci.*, Vol. 19, 797-841.

Chapra, S. C., and R. C. Canale, 1988. *Numerical Methods for Engineers*, Second Edition, McGraw Hill Book Company.

Holgate, H. R. and J. W. Tester, 1994. "Oxidation of Hydrogen and Carbon monoxide in sub-and Supercritical water: Reaction kinetics, Pathways, and Water Density Effects: 2. Elementary Reaction Modeling", *J. Phys. Chem.*, **98** (3), 810.

Holgate, H. R., J. C. Meyer, and J. W. Tester, 1995 "Glucose Hydrolysis and Oxidation in Supercritical Water", *AIChE Journal*, **41**, 3 (March), 637.

Marshall, W. L.; Frank, E. U., 1981, "Ion Product of Water Substance, 0-1000 °C, 1-10,000 Bars New International Formulation and Its Background", *J. Phys. Chem. Ref. Data*, **10**, 295.

Patankar, S. V., 1980. *Numerical Heat Transfer and Fluid Flow*, McGraw Hill Book Company.

Sarakanen, K. V. and L. H. Hoo, 1981, J. Wood Chem. Technol., **1**, 11.

Schwald, W. and O. Bobleter, 1989, *J. Carbohydrate Chem.*, **8**, 565.

Sircar, S. 1998, "Sorption Enhanced Reaction (SER) for Production of Hydrogen", presented at the 1998 Hydrogen Program Annual technical Review meeting, Project Number DE-FC36-956010059.

Webley, P. A.; Tester, J. W., 1991, "Oxidation of Methane in Supercritical Water" *Energy & Fuels*, **5**, 411.

West, M. A. B. and M. R. Gray, 1987, "Pyrolysis of *1,3*-Butanediol as a Model Reaction for Wood Liquefaction in Supercritical Water", Canadian Journal of Chemical Engineering, **65**, August, 645.

Xu, X., Matsumura, Y., Steinberg, J. and Antal, J. A., Jr., 1996, "Carbon Catalyzed Gasification of Organic Feedstocks in Supercritical Water", *Industrial & Engineering Chemistry Research*, Vol. **35**, No. 8, 2522.

Figure Titles

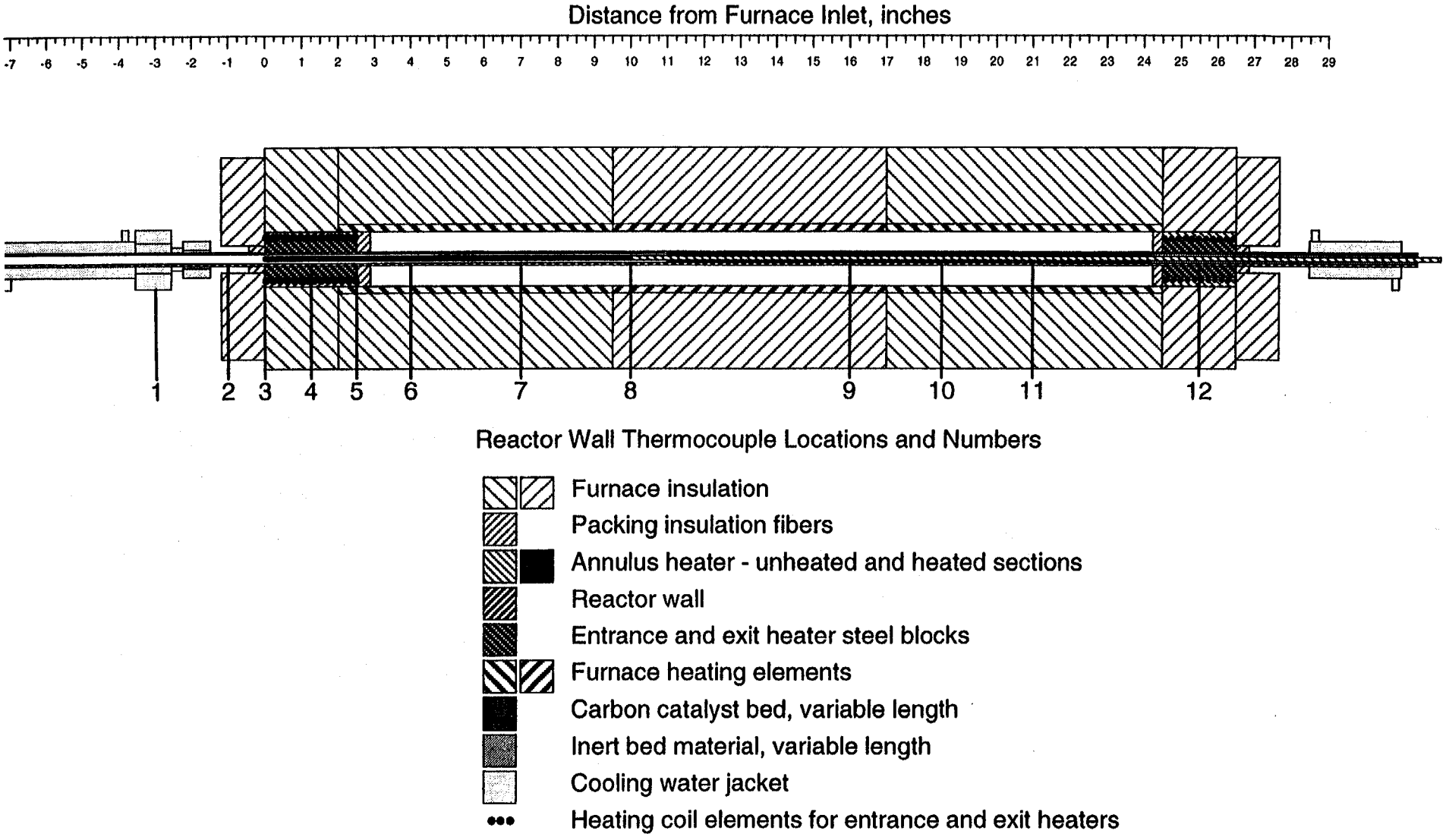

Figure 1. Overall Configuration of the University of Hawaii's SCW Reactor.

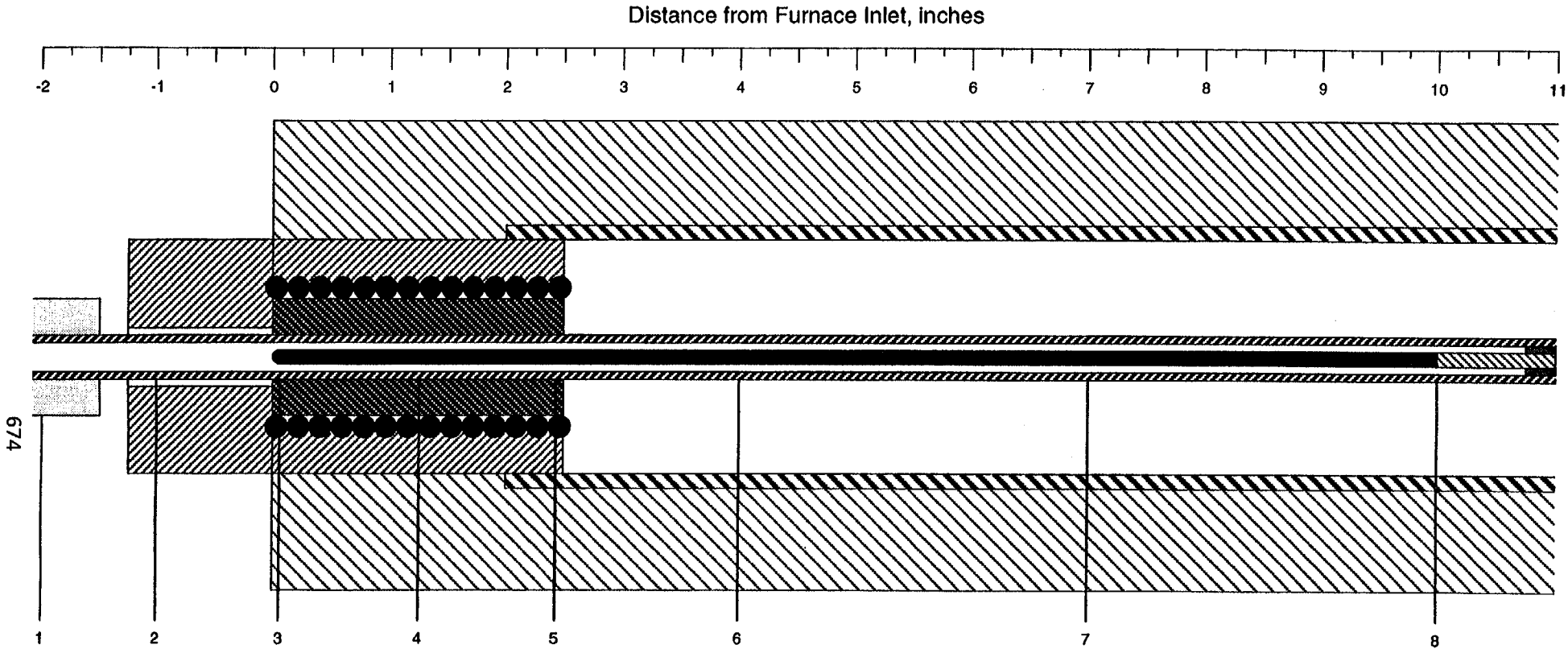

Figure 2. Entrance Heater Details.

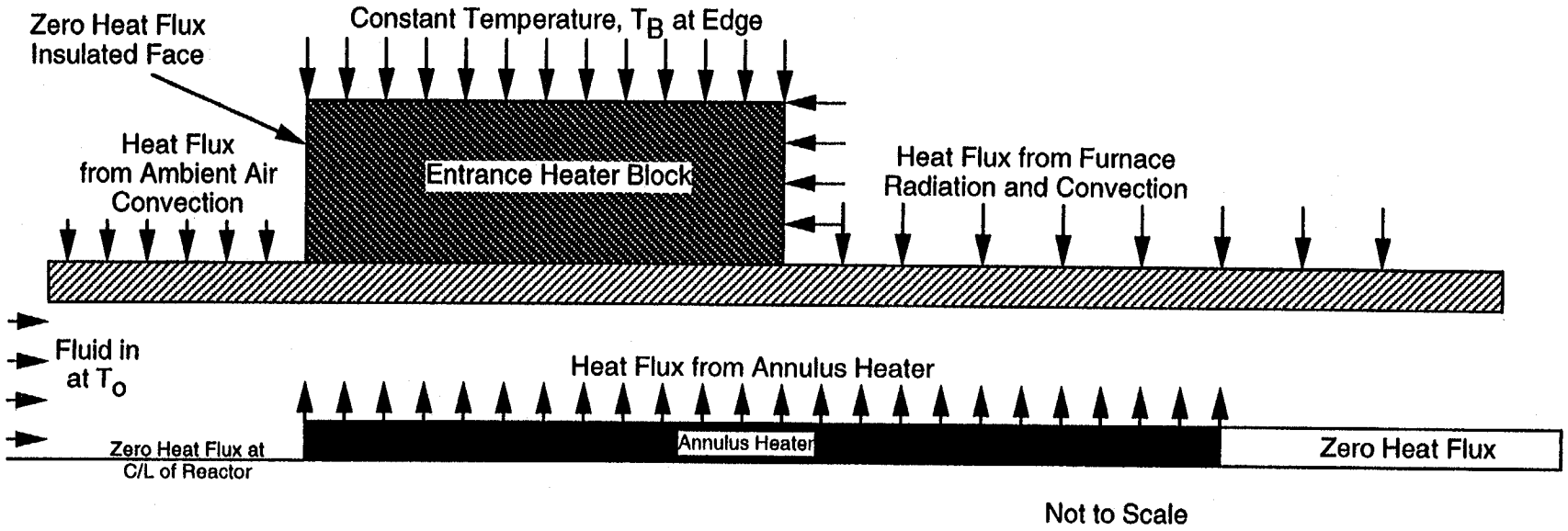

Figure 3. Boundary Conditions for Heat Transfer Model.

Figure 4. Heat Transfer Test Results at the University of Hawaii's SCWR.

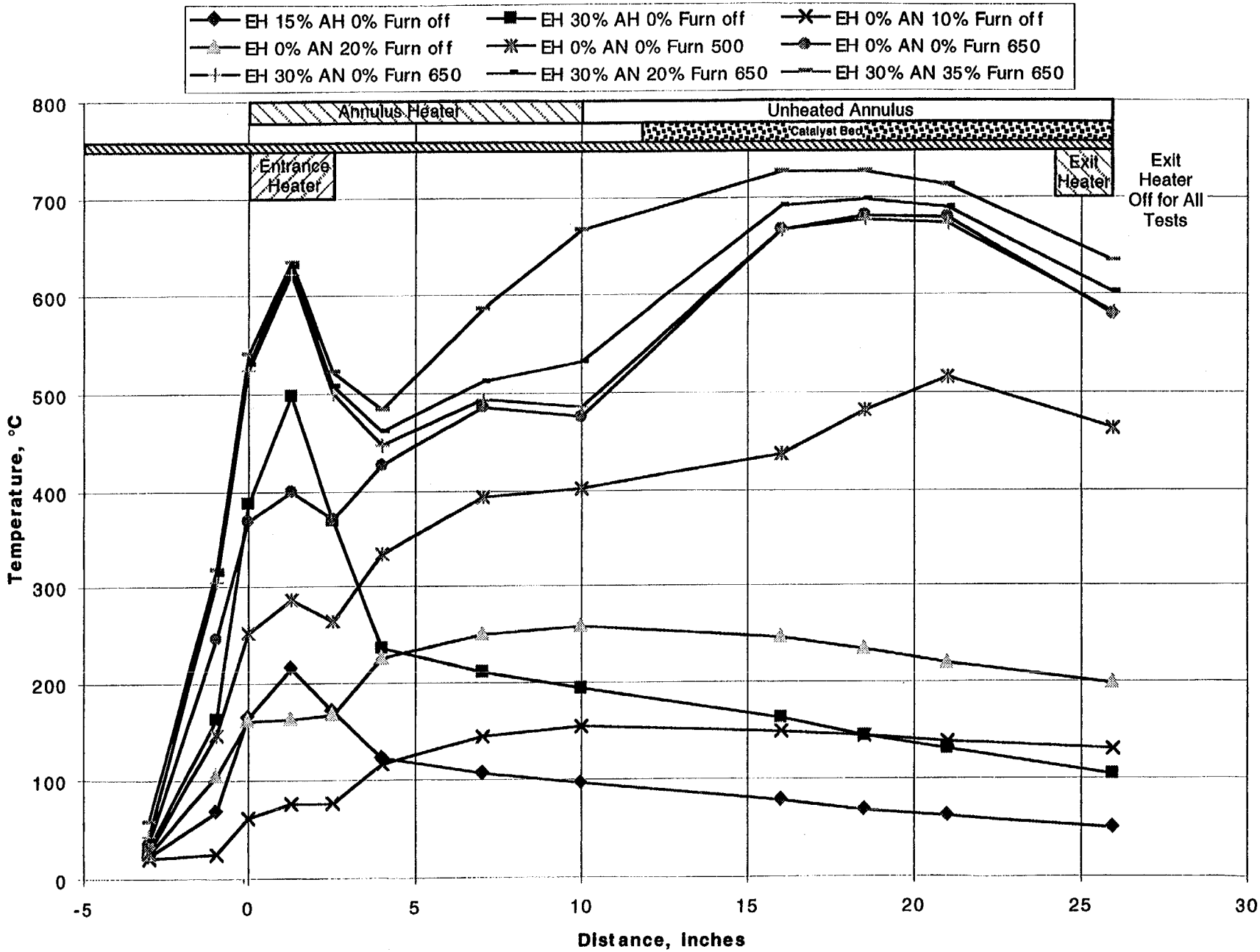

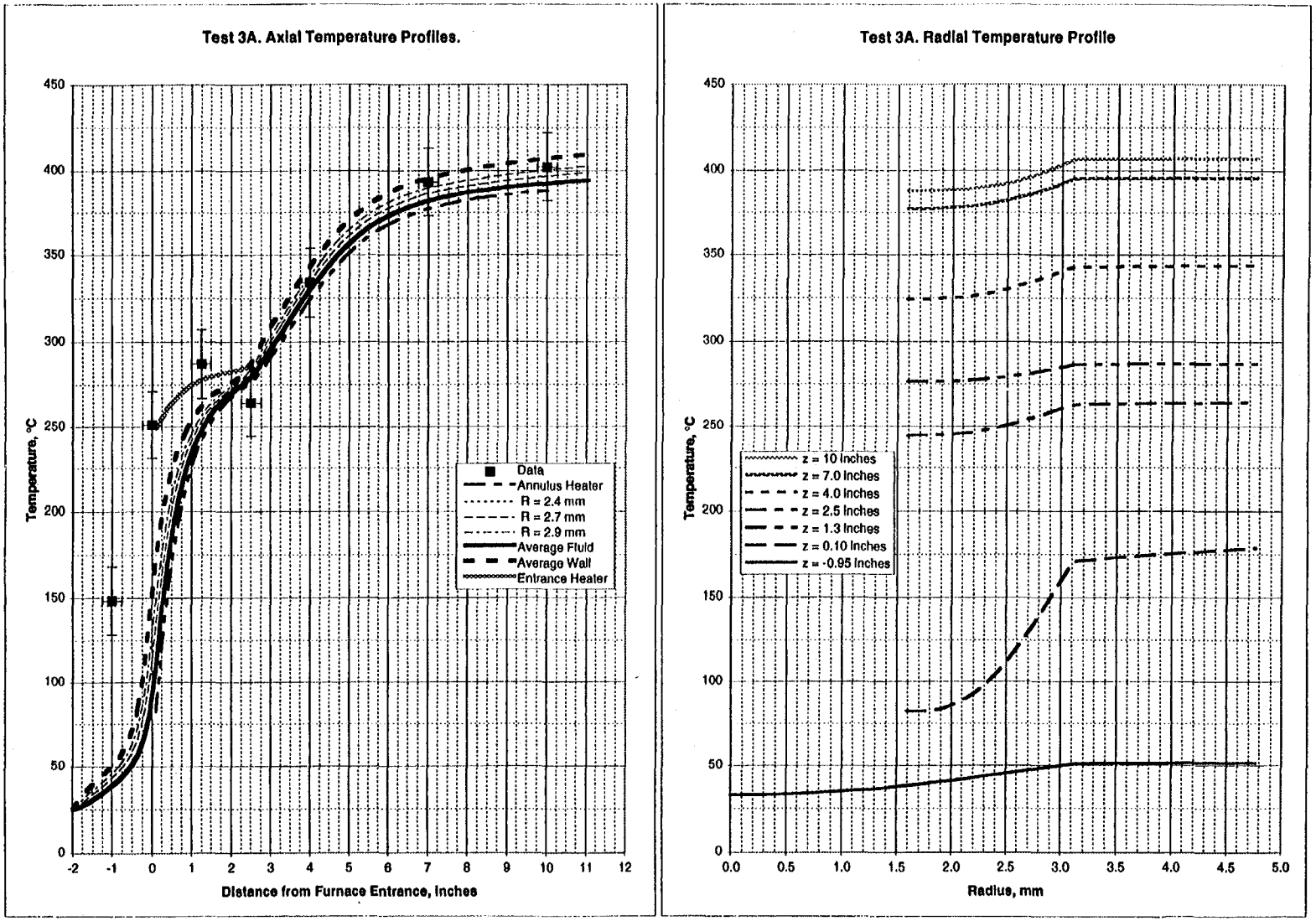

Figure 5. Test 3A Calculated Axial and Radial Temperature Profiles.

Entrance Heater 0% - Annulus Heater 0% - Furnace 500 °C

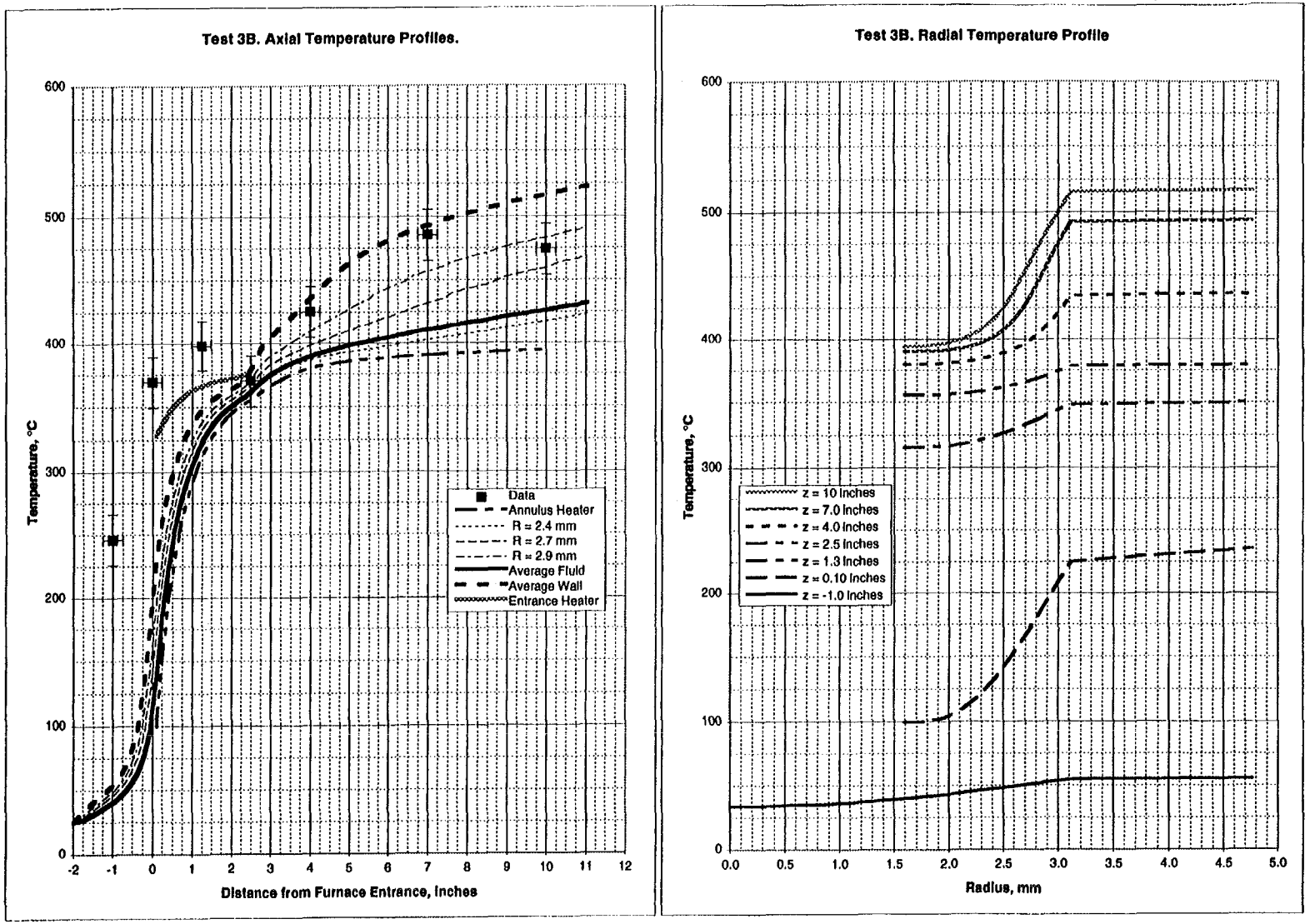

Figure 6. Test 3B Calculated Axial and Radial Temperature Profiles.

Entrance Heater 0% - Annulus Heater 0% - Furnace 650 °C

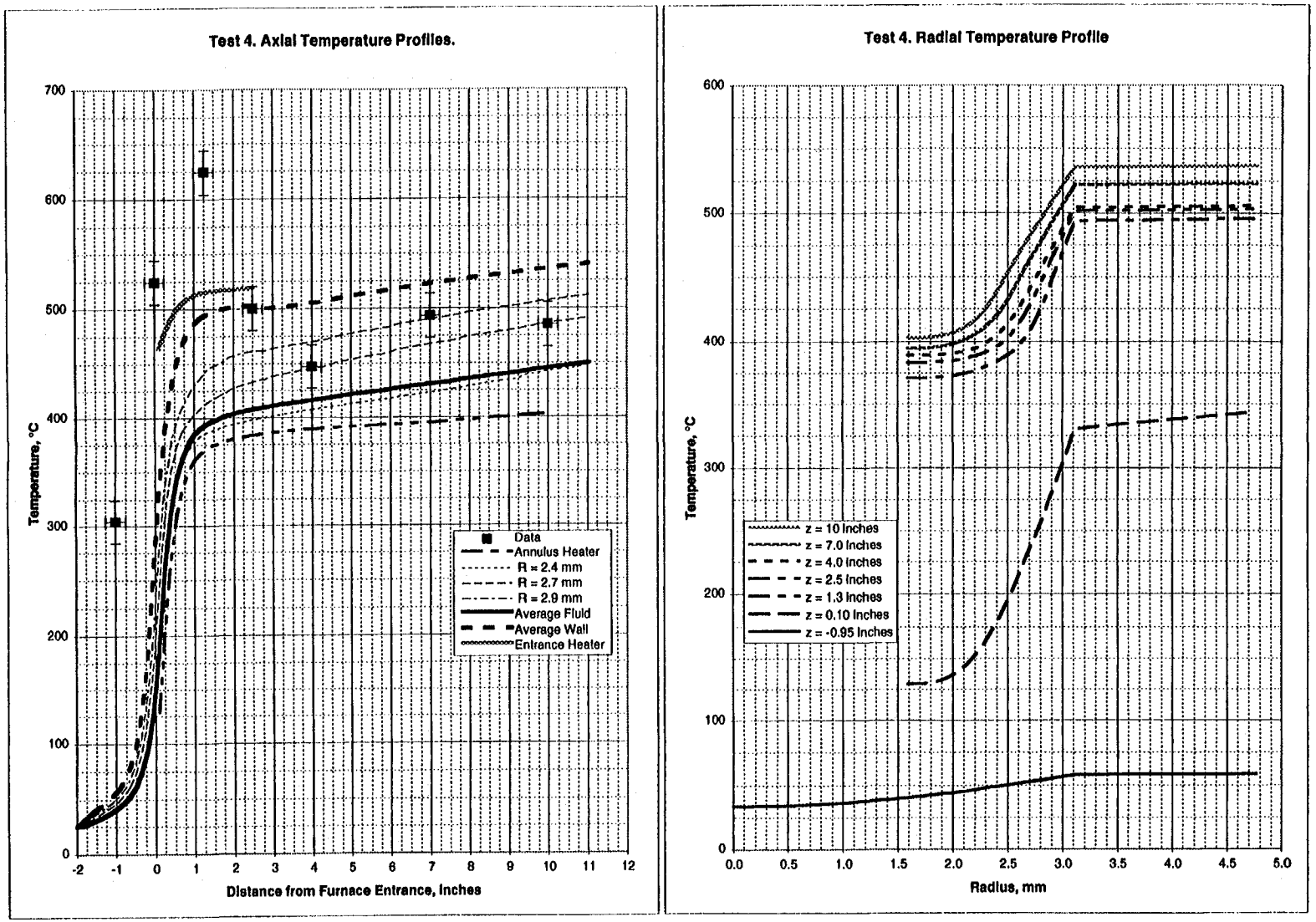

Figure 7. Test 4 Calculated Axial and Radial Temperature Profiles.

Entrance Heater 30% - Annulus Heater 0% - Furnace 650 °C

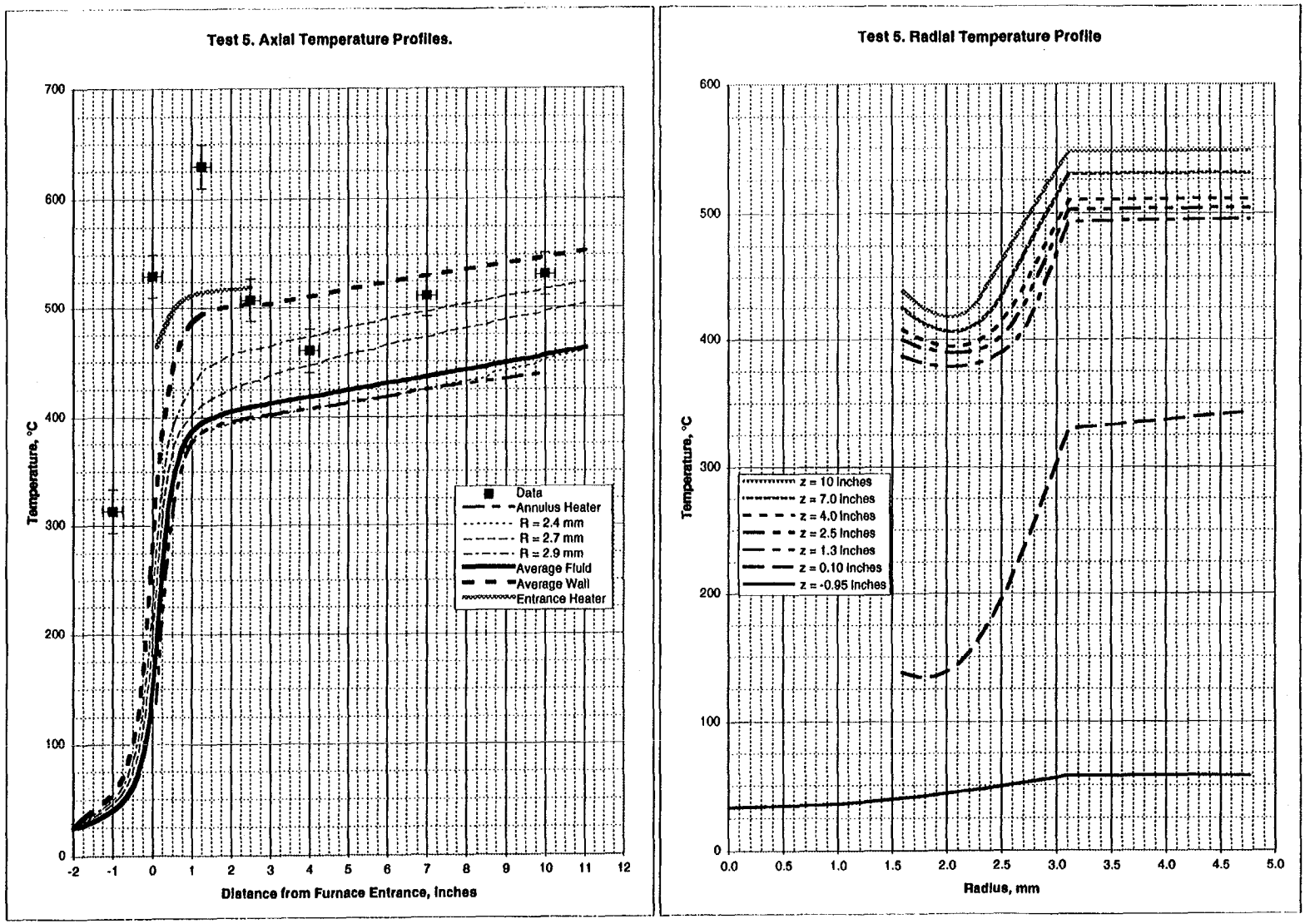

Figure 8. Test 5 Calculated Axial and Radial Temperature Profiles.

Entrance Heater 30% - Annulus Heater 20% - Furnace 650 °C

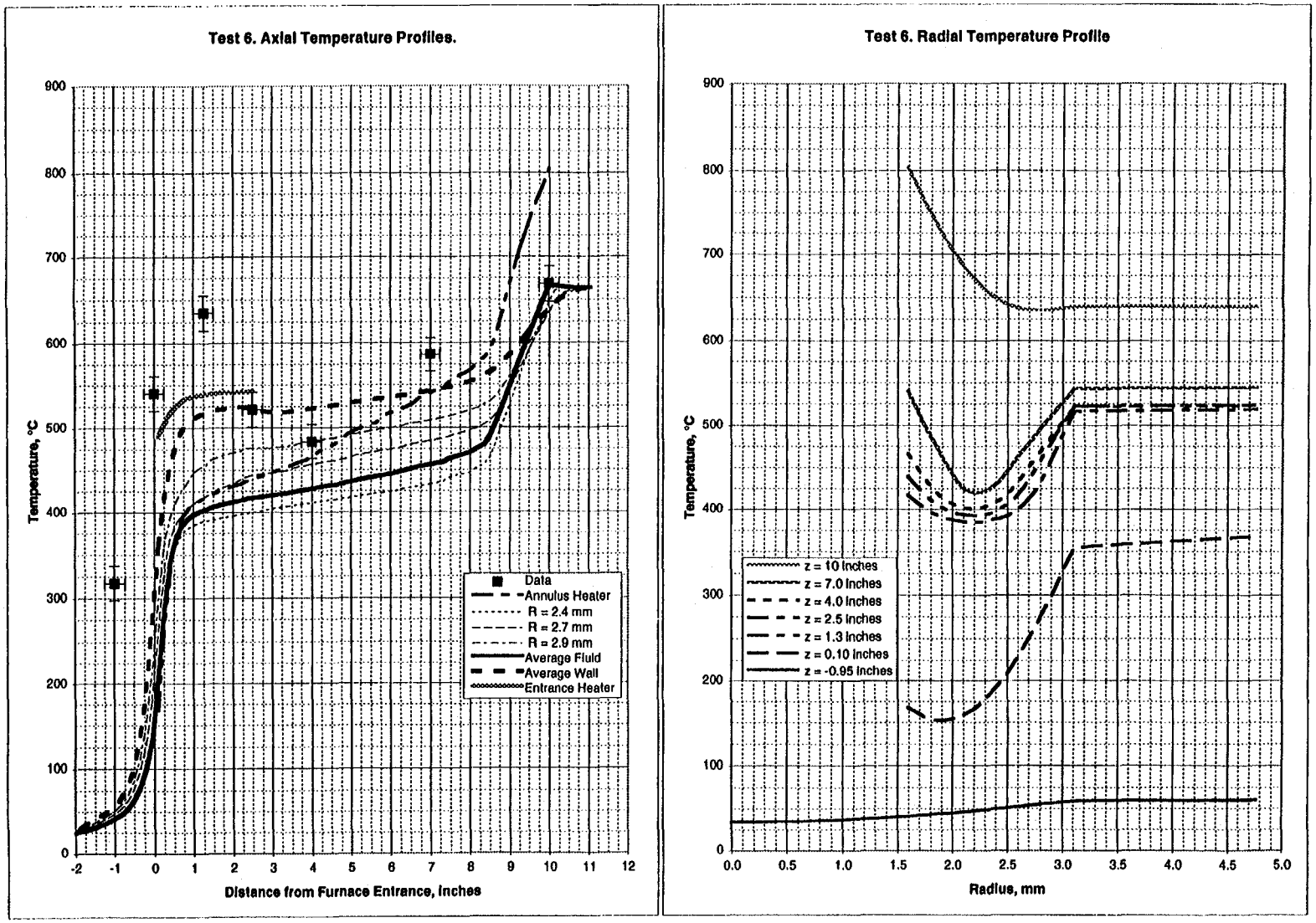

Figure 9. Test 6 Calculated Axial and Radial Temperature Profiles.

Entrance Heater 30% - Annulus Heater 35% - Furnace 650 °C

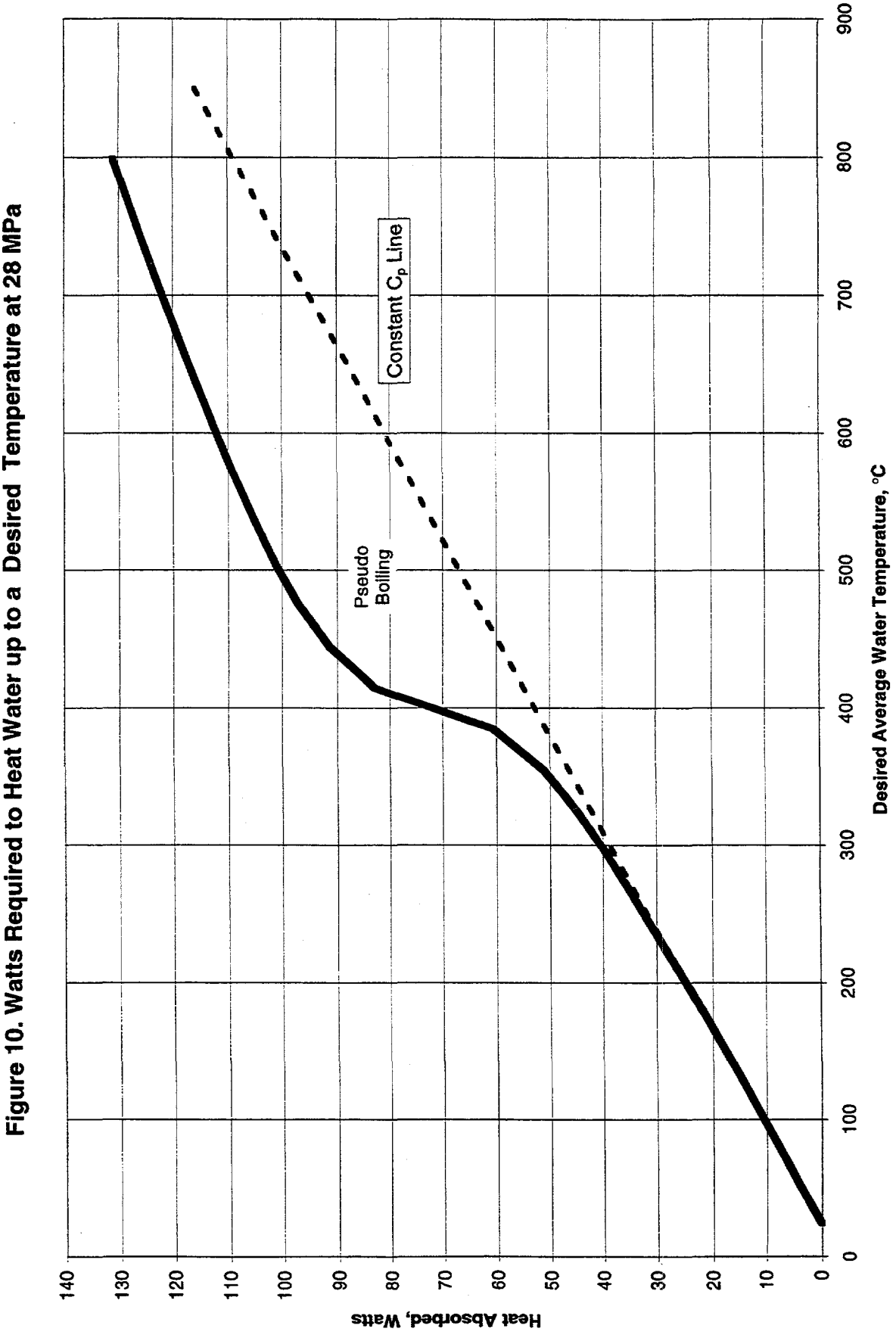

Figure 10. Watts Required to Heat Water up to a Desired Temperature at 28 MPa

Figure 11. Axial Wall Temperature Profiles in New Reactor on 12/29/97

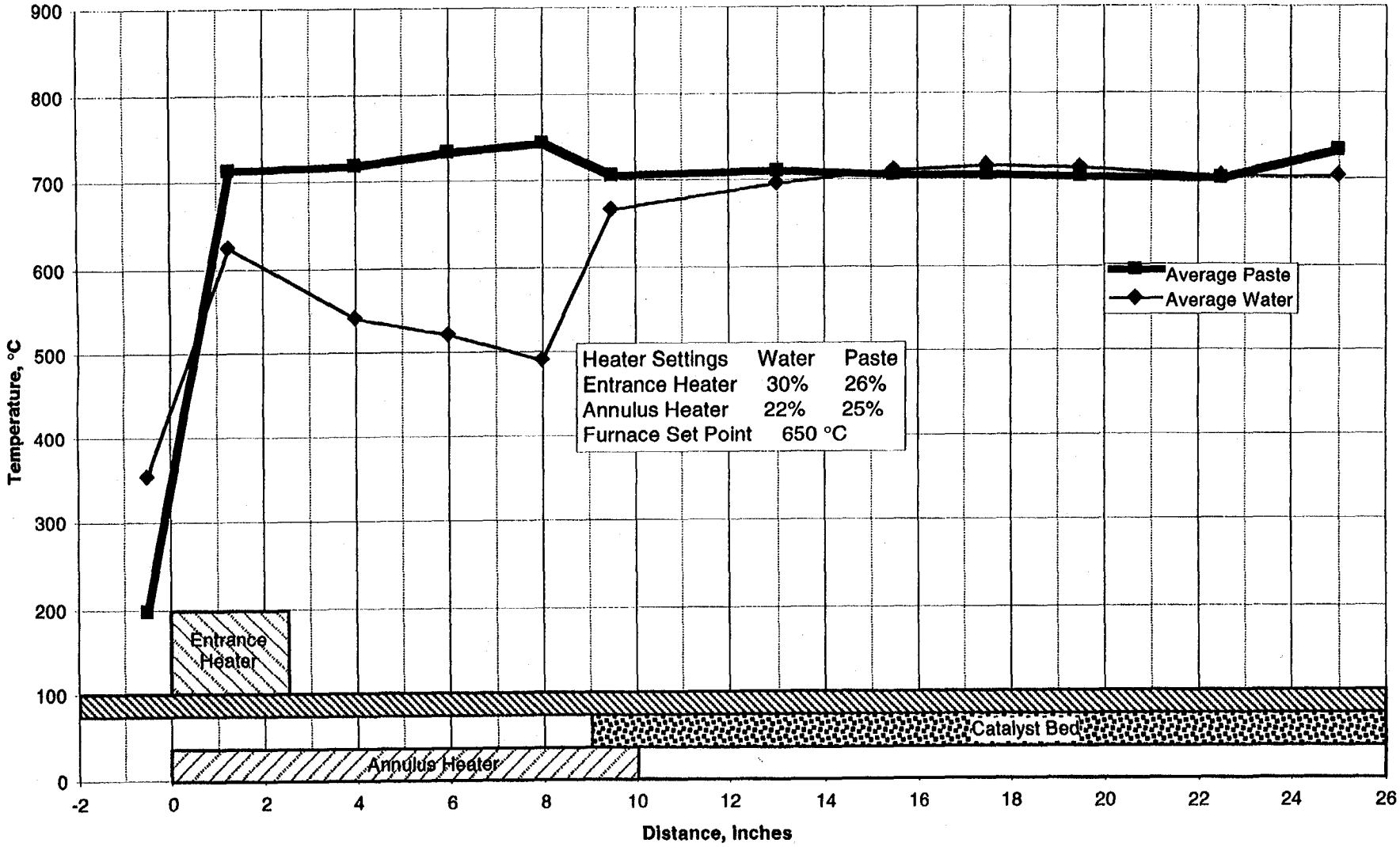

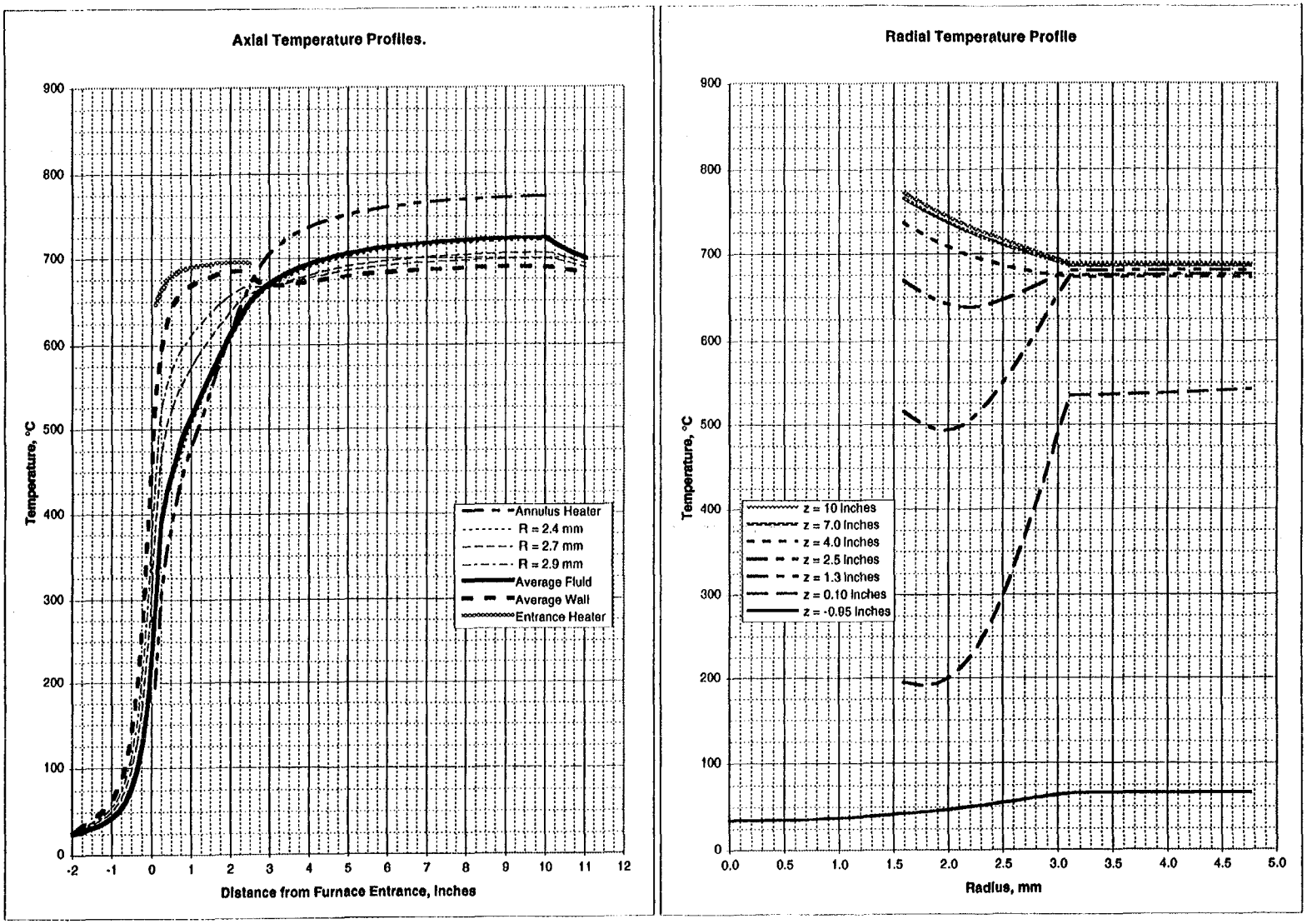

Figure 12. Calculated Axial and Radial Temperature Profiles for Wood Paste.

Entrance Heater 30% - Annulus Heater 20% - Furnace 650 °C

Figure 13. Predicted Temperature versus Time for Wood Paste
Entrance Heater 30% - Annulus Heater 35% - Furnace 650 °C

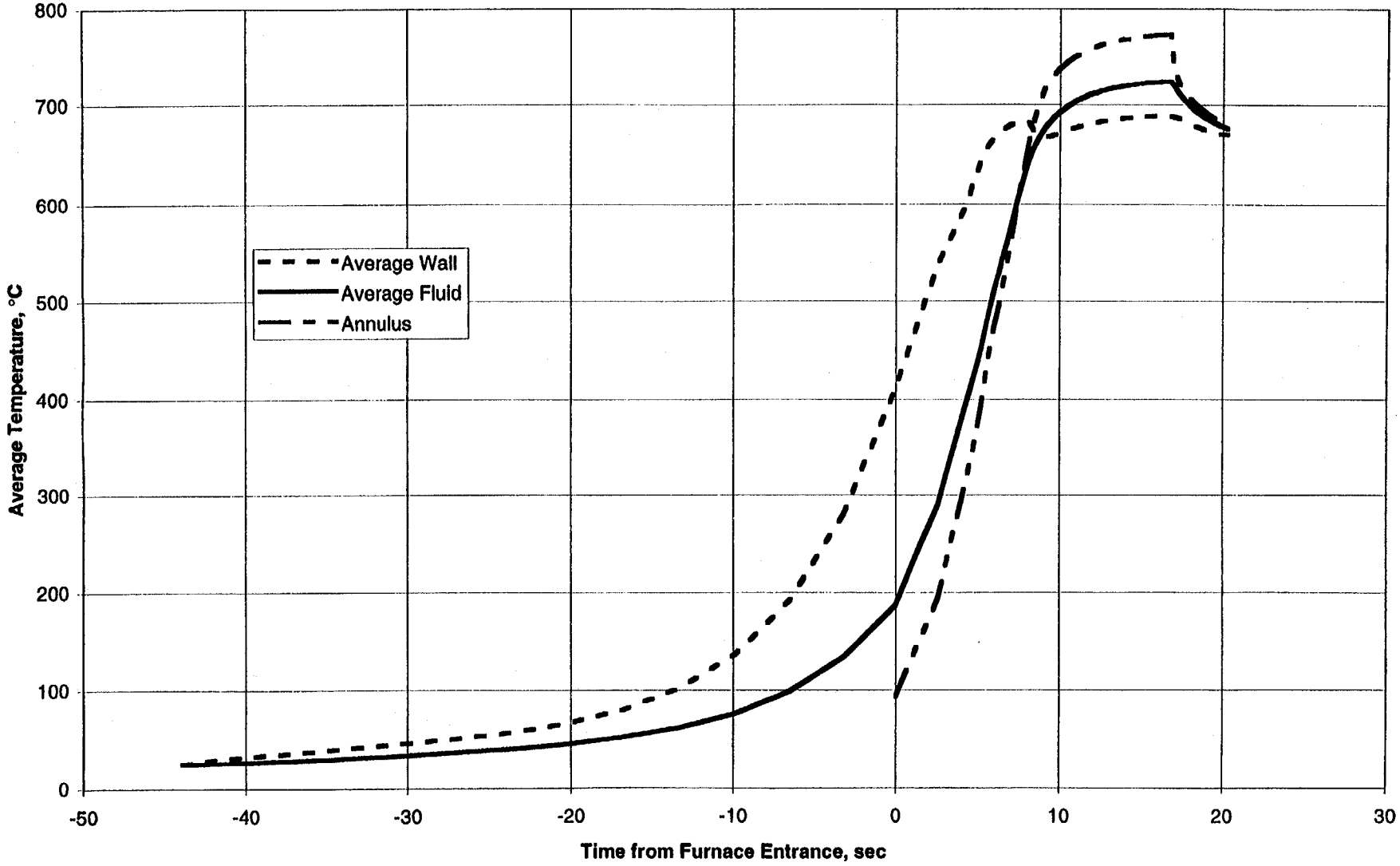

Figure 14. Hydrogen Ion Concentration in Pure Water versus Temperature

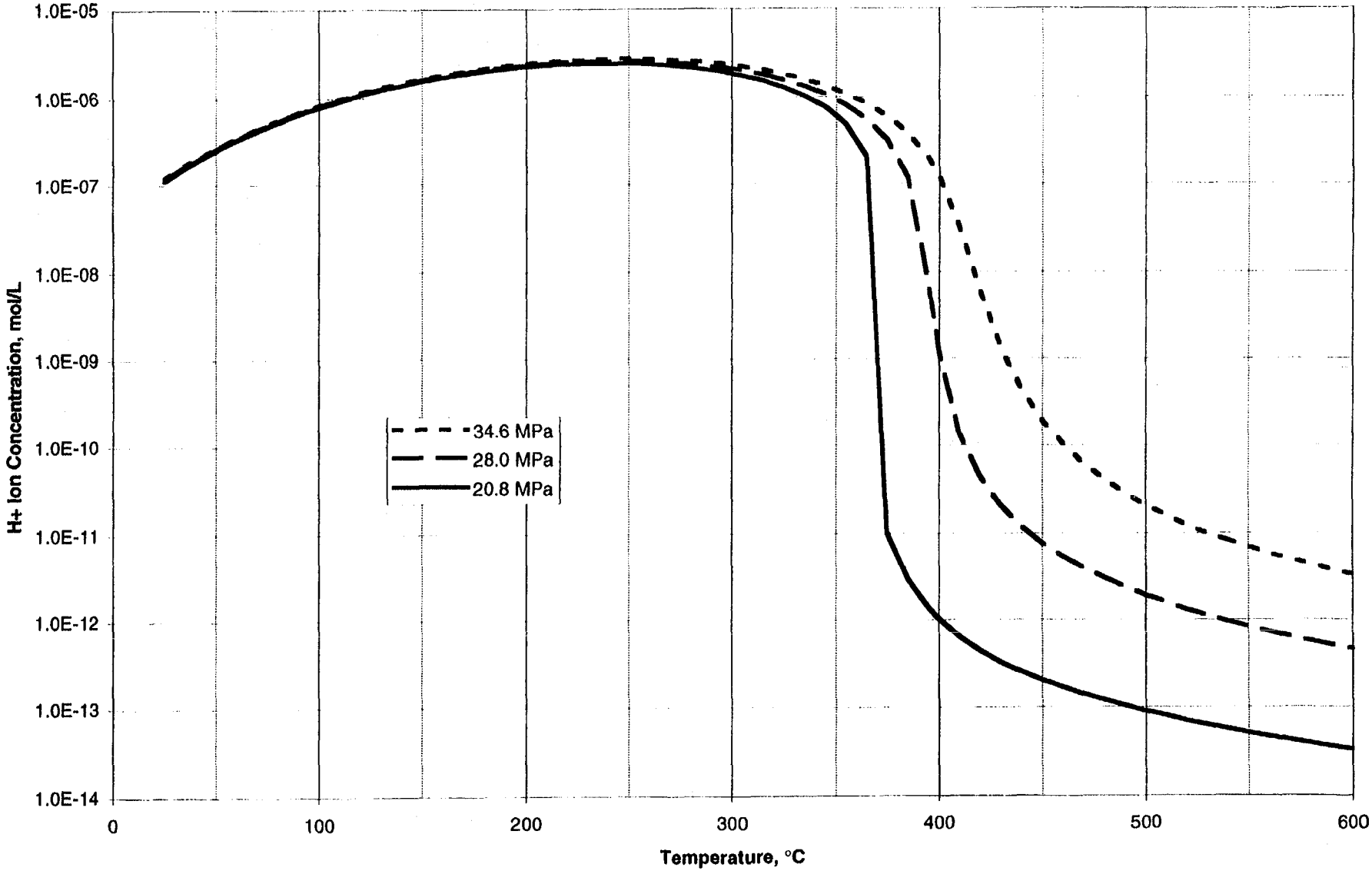

Source: Marshall and Frank, J. Phys. Chem. Ref. Data, Vol 10, No. 2, 1981, P 295-304.

Figure 15. Holgate & Tester (1995) Data Major Pyrolysis Products of 0.001M Glucose in SCW.

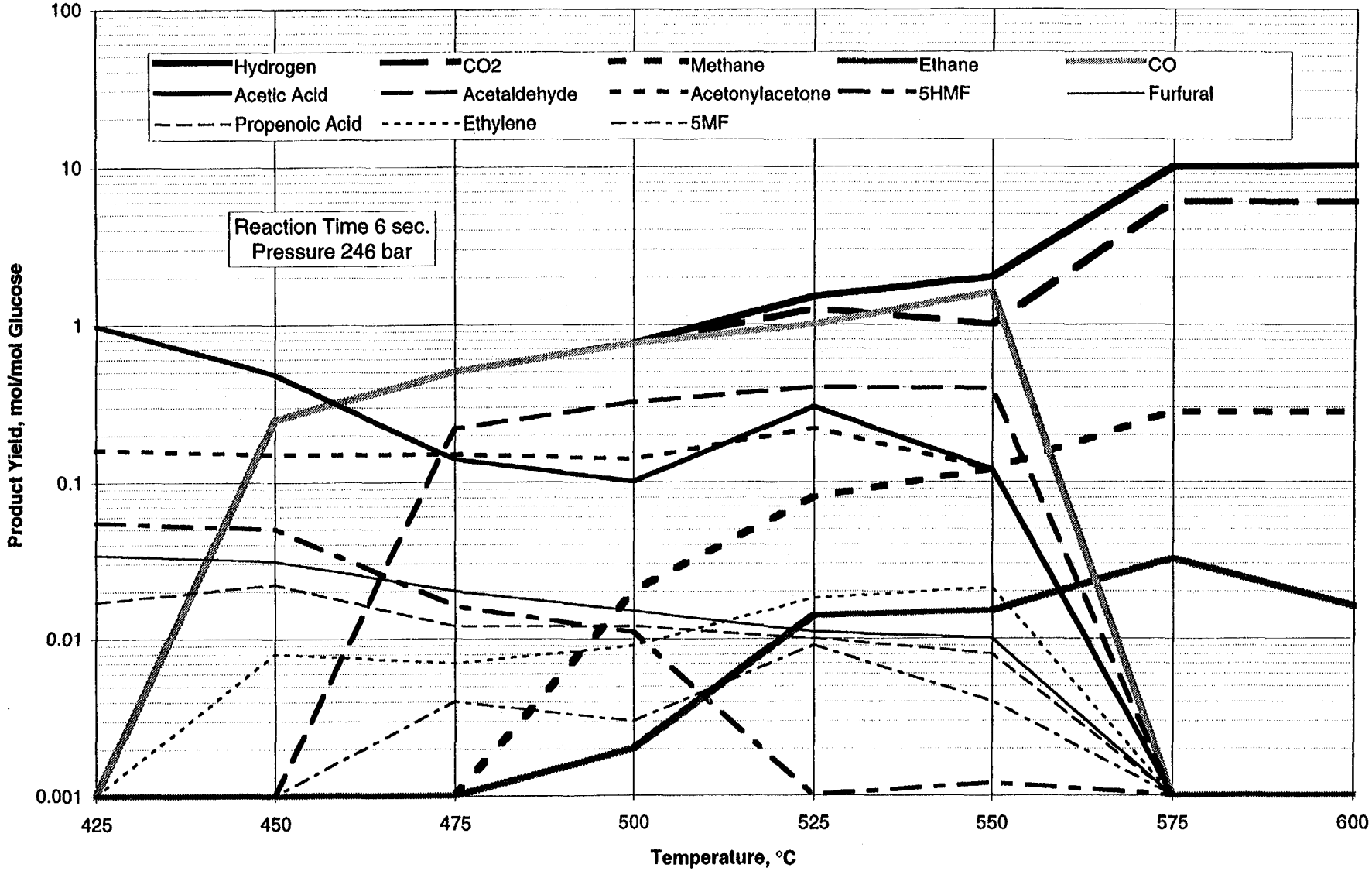

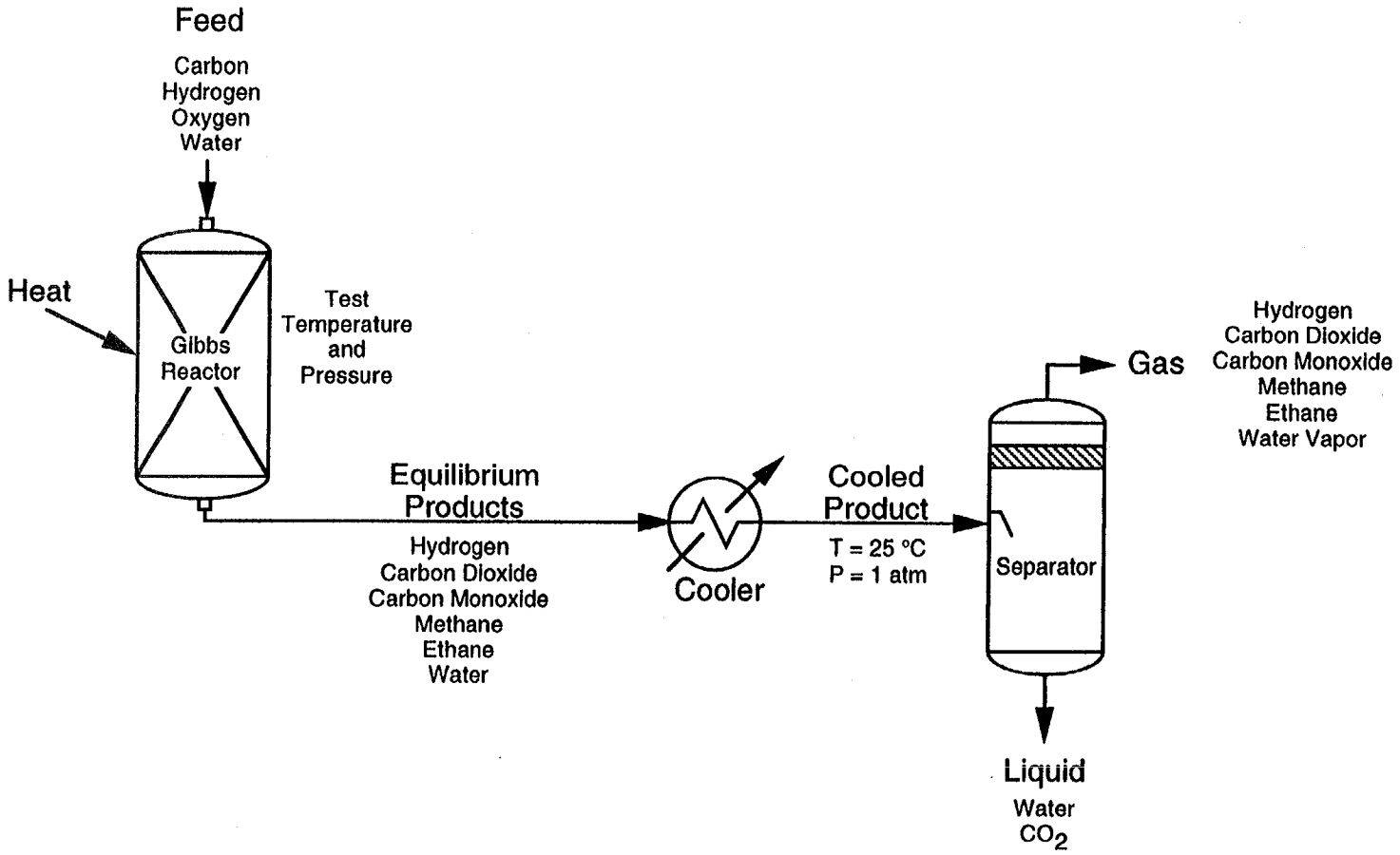

Figure 16. HYSIM Simulation of the University of Hawaii's SCW Reactor.

Figure 17. Comparison of Test Measurements to Equilibrium at Catalyst Temperature.

Point No.	Test Date	Flow Rate, g/min	Wt.% Corn Starch	Wt. % Poplar Wood	Catalyst Temp. °C	Peak Temp. °C
1	20-Feb-97	1.0	10.40	0.00	650	690
2	20-Feb-97	2.0	10.40	0.00	650	715
3	20-Feb-97	4.0	10.40	0.00	650	805
4	25-Mar-97	2.0	5.50	5.00	640	890
5	25-Mar-97	2.5	5.50	5.00	640	900
6	23-Apr-97	2.0	5.55	5.00	650	785
7	1-May-97	2.0	6.09	5.05	630	700
8	3-Jul-97	2.0	4.01	10.72	685	790
9	10-Jul-97	2.0	4.19	11.17	700	790
10	10-Jul-97	2.0	4.19	11.17	700	790
11	21-Jul-97	2.0	4.15	11.10	690	732
12*	21-Aug-97	2.0	4.13	11.08	690	730
13	29-Aug-97	2.0	4.11	11.35	685	770
14	5-Sep-97	2.0	4.19	11.76	690	800
15**	17-Dec-97	2.0	3.55	9.47	700	750
16**	12-Feb-98	2.0	3.65	10.04	700	725

* 1/16" OD annulus used for this test.
** New Reactor Configuration

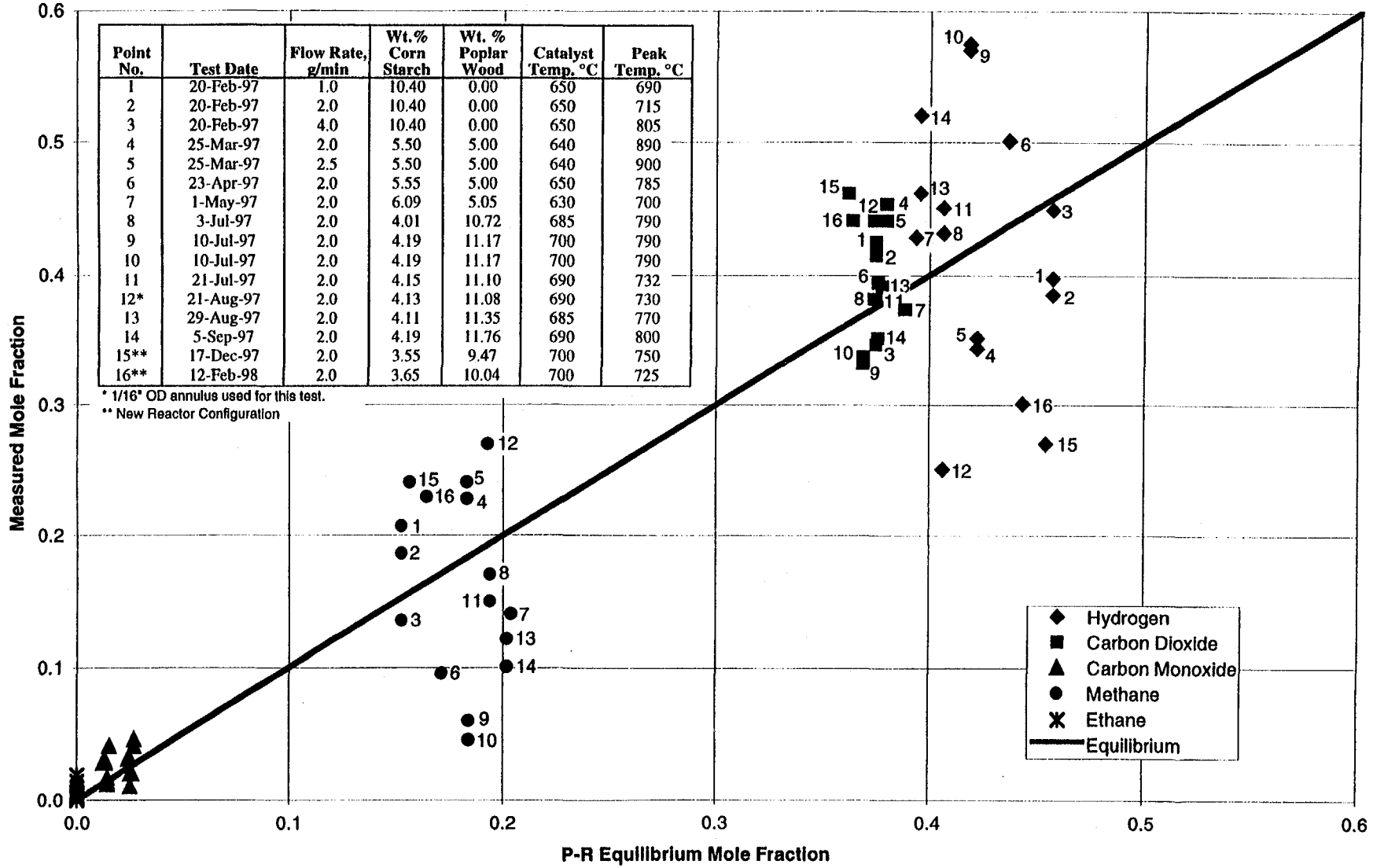

Basis: HYSIM Equilibrium Calculation using Peng-Robinson Equations of State

Figure 18. Hydrogen Yield versus Peak Temperature for Wood Paste Tests

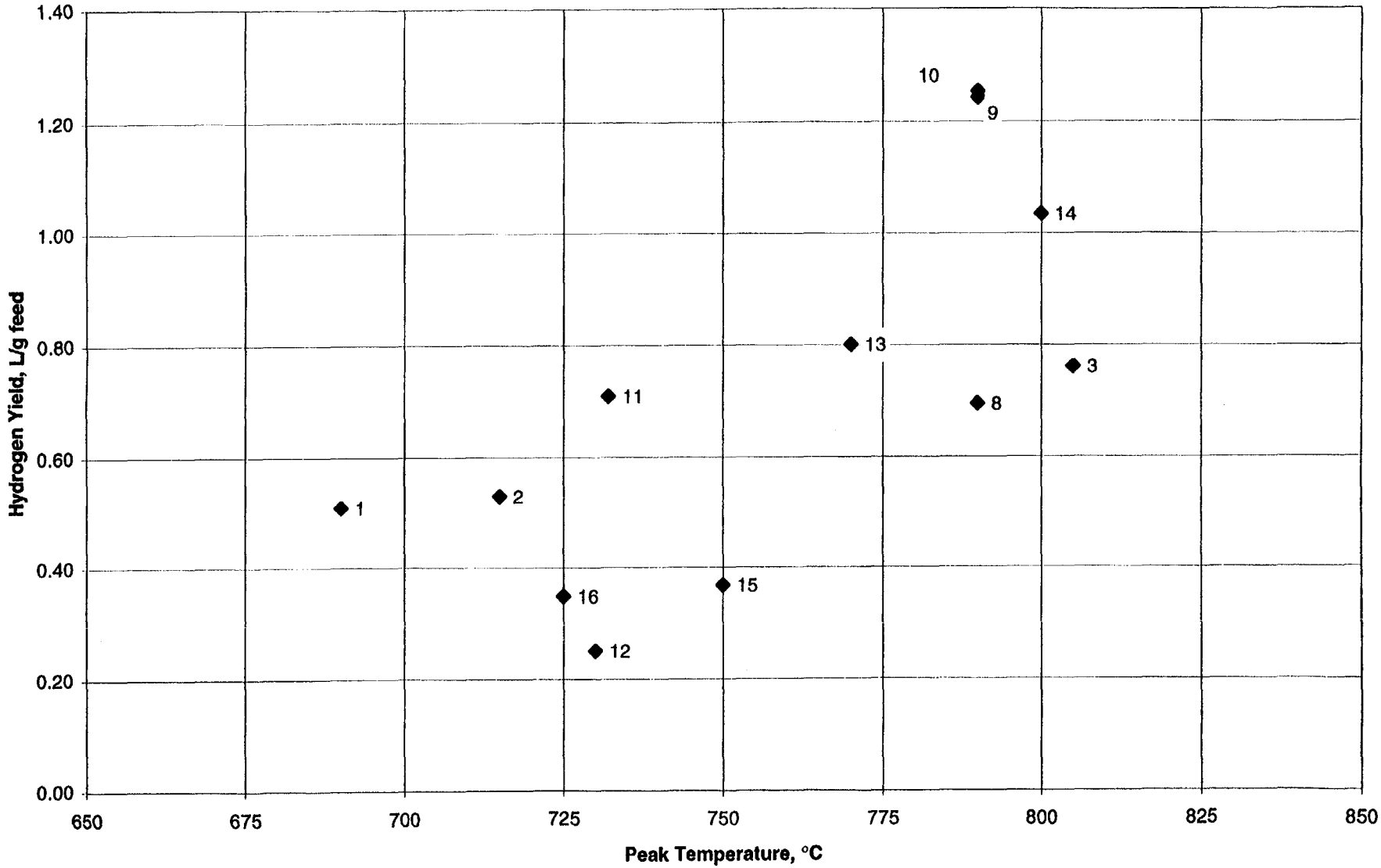

Figure 19. Equilibrium Mole Fractions versus Percent Wood in the Feed at 600 °C.

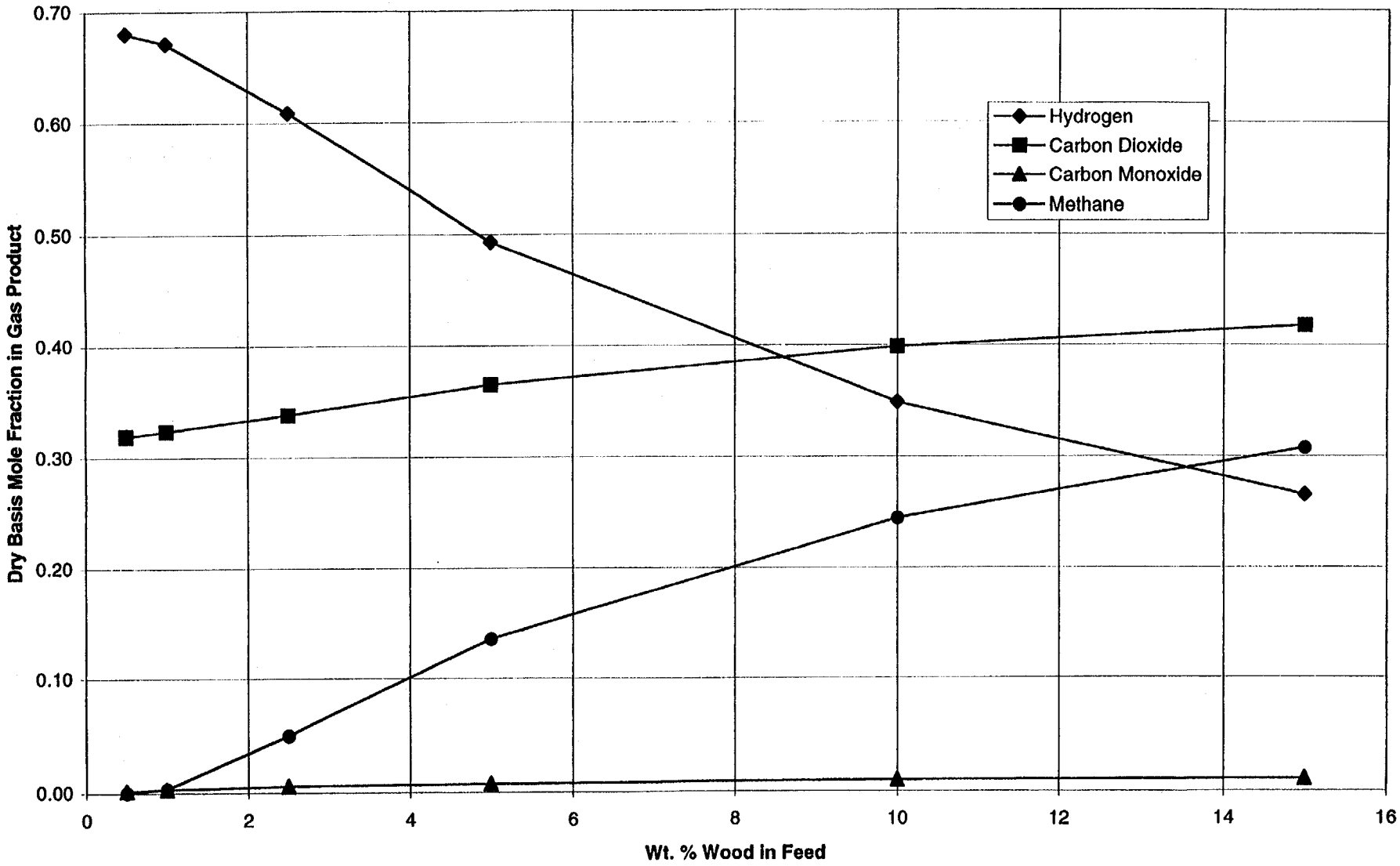

Basis: HYSIM Equilibrium Calculation using Peng-Robinson Equations of State

SORPTION ENHANCED REACTION PROCESS (SERP) FOR THE PRODUCTION OF HYDROGEN

J. Hufton, S. Mayorga, T. Gaffney, S. Nataraj, M. Rao, S. Sircar
Air Products and Chemicals, Inc.
Allentown, PA 18195

Abstract

The novel Sorption Enhanced Reaction Process has the potential to decrease the cost of hydrogen production by steam methane reforming. Current effort for development of this technology has focused on adsorbent development, experimental process concept testing, and process development and design. A preferred CO_2 adsorbent, K_2CO_3 promoted hydrotalcite, satisfies all of the performance targets and it has been scaled up for process testing. A separate class of adsorbents has been identified which could potentially improve the performance of the H_2-SER process. Although this material exhibits improved CO_2 adsorption capacity compared to the HTC adsorbent, its hydrothermal stability must be improved.

Single-step process experiments (not cyclic) indicate that the H_2-SER reactor performance during the reaction step improves with decreasing pressure and increasing temperature and steam to methane ratio in the feed. Methane conversion in the H_2-SER reactor is higher than for a conventional catalyst-only reactor operated at similar temperature and pressure. The reactor effluent gas consists of 90+% H_2, balance CH_4, with only trace levels (<50 ppm) of carbon oxides.

A best-case process design (2.5 MMSCFD of 99.9+% H_2)based on the HTC adsorbent properties and a revised SER process cycle has been generated. Economic analysis of this design indicates the process has the potential to reduce the H_2 product cost by 25-31% compared to conventional steam methane reforming.

A second experimental process test unit has been designed which will permit investigation of the fully cyclic H_2-SER process in FY99.

Novel Sorption Enhanced Reaction Process

The goal of this work is to develop a novel, more efficient steam-methane reformation (SMR) process for the production of hydrogen. The overall SMR reaction is given by:

$$CH_4 + 2\,H_2O \Leftrightarrow CO_2 + 4\,H_2$$

The novel concept is called the Sorption Enhanced Reaction Process (SERP). The reactants, steam and methane, are fed at 300-500°C and 50-300 psig into a tubular reactor containing an admixture of commercial reforming catalyst and an adsorbent for removing carbon dioxide from the reaction zone. A reactor effluent consisting of relatively pure hydrogen (90-98+%) is produced during this step. The primary impurity is methane with traces of carbon oxides. Once the adsorbent is saturated with CO_2, it is regenerated in situ by using the principles of pressure swing adsorption (PSA) at the reaction temperature.

The key benefits of producing H_2 by the SERP concept are: (i) reformation at a significantly lower temperature (300-500°C) than conventional SMR process (800-1000°C), while achieving the same conversion of methane to hydrogen, (ii) significantly lower capital cost, (iii) production of hydrogen at feed gas pressure (200-400 psig) and at relatively high purity directly from the reactor, (iv) significant reduction or even elimination of downstream hydrogen purification steps, (v) elimination of CO in the hydrogen product, (vi) minimization of side reactions, e.g., coking, and (vii) reduction of the excess steam used in conventional SMR.

APCI/DOE Program Goals for FY98

The key program goals and milestones for the cooperative APCI/DOE SER Project during the current year are listed below:

(1) Evaluate sensitivity of H_2-SER process steps to process variables.
(2) Refine the initial H_2-SER design/economic analysis based on experimental data.
(3) Design and begin construction of a cyclic SER process test unit.
(4) Identify and demonstrate improved CO_2 adsorbents for H_2-SER process.

Experimental

Experimental equipment used to characterize the performance of various CO_2 adsorbents and for investigating the H_2-SER process steps have been constructed and described by Hufton et al. (1997). Adsorbent screening is performed with a thermal gravimetric adsorption unit (for measurement of dry CO_2 working capacity), a binary desorption unit (to determine CO_2 capacity

in steam environments), and a hydrothermal stability unit (to assess physical and chemical stability of adsorbents in steam/CO_2 mixtures at elevated temperatures). Procedures and equipment have also been developed for the production of pelletized forms of the synthesized adsorbents. Process experiments have been carried out in an electrically-heated fixed bed tubular reactor (SER#1). These experiments have focused on individual steps of the process, rather than the fully cyclic operation of an industrial SER process unit.

Results and Discussion

High Temperature Sorbents for CO_2

The following criteria were developed for an acceptable CO_2 sorbent for performing steam-methane reforming by the SER concept:

(a) CO_2 working capacity > 0.3 mmole/g at 300-500°C in the presence of steam at high partial pressure and at low partial pressures of CO_2 (P_{CO2}, 0.1 to 1 atm ; $(P_{H2O})/(P_{CO2}) > 20$);
(b) Adequate ad(de)sorption kinetics for CO_2 at reaction and regeneration conditions;
(c) Stable CO_2 sorption capacity after repeated sorption/desorption cycles;
(d) Adequate mechanical strength of adsorbent particles after cyclic exposure to high pressure steam.

Previous efforts have identified a preferred adsorbent, potassium carbonate-promoted hydrotalcite (referred to as HTC), which satisfies the above requirements. It exhibits a stable CO_2 working capacity of ~0.45 mmole/g in the presence of 0.3 atm CO_2 and 10 atm steam at 400°C. The adsorption/desorption kinetics were measured in fixed bed experiments and found to be relatively fast. The active ingredient was found to be non-leachable in steam, and the CO_2 capacity was not negatively influenced by combination with the SMR catalyst. Production of this material was scaled up to the kilogram range for process testing.

A second class of materials, referred to as the 'H' family of adsorbents, was also identified last year. These adsorbents were characterized by much higher CO_2 working capacities than the HTC. Modification of the processing procedures was found to change the shape of the CO_2 isotherm of the 'H' adsorbents to a more linear shape (preferred) at low partial pressures of CO_2. This class of materials held promise as an improved second generation adsorbent for the H_2-SER process.

Current year efforts in the adsorbent development area has been focused on improving the properties of the HTC adsorbent, understanding methods to manipulate the properties of the 'H' family of adsorbents, and developing methods for the production of larger batches of the desired adsorbent for process development study.

An additional experimental screening capability was developed to qualitatively asses the apparent desorption kinetics of small (mg) samples of adsorbents. The technique was based on the thermal gravimetric adsorption (TGA) approach and could be used to benchmark apparent CO_2 desorption kinetics against the promoted HTC material.

A series of K_2CO_3 promoted HTC adsorbents was examined for working CO_2 capacity (dry) at 400°C as a function of the carbonate loading. As illustrated in Figure 1, the data indicate that the CO_2 working capacity does not appreciably change when the HTC is impregnated with a solution containing 2.0-4.0 M K_2CO_3. All of the materials tested in the process test unit, described later in this report, were prepared using 2.0 M solution.

Approximately five kilograms of 20% K_2CO_3/HTC was prepared for continuing engineering evaluation. Each 1 kg batch was produced by promoting the base HTC with carbonate solution, and the CO_2 capacities of each batch were checked with the TGA unit. Plans were made with an external vendor to produce larger batches (100 lbs) of 1/8" HTC pellets with larger scale extrusion equipment. Initial samples prepared with this equipment have adequate crush strength. Additional work is required to further reduce the pellet aspect ratio to our target of 1:1. Fifty to one hundred pounds of adsorbent will be needed for process testing experiments planned for the later part of this year.

Even though the 'H' series of adsorbents exhibited higher CO_2 working capacity in the presence of steam than the HTC, these adsorbents are not very stable in continuous contact with steam. A number of characterization techniques were employed to understand how the variables for synthesis of 'H' series adsorbents affect the chemical, physical and adsorptive properties of these adsorbents. Systematic changes were found to occur in the composition, surface area, porosity, CO_2 adsorption isotherm shape and CO_2 desorption rate as the 'H' adsorbents were post-treated. Transmission electron microscopy analysis of the post-treated adsorbents indicated the presence of extremely small grains of 'active ingredient' in the adsorbent matrix. This unique morphology was not observed in the untreated samples. The presence of these small domains was postulated to be the key to the high reversible CO_2 sorption capacity of the post-treated material, and perhaps also to the adverse effects of steam, which tend to sinter the smaller domains into larger clusters with less effective adsorptive properties.

Several different material compositions and synthesis routes for 'H' adsorbents were pursued in order to improve their steam stability. The general idea was to fix the grains of 'active ingredient' into a substrate which will stabilize the grains and prevent them from sintering. Samples of bound, extruded pellets derived from 'H' material were prepared using 5, 10 and 20 wt.% HTC, bentonite and atapulgite binders. The sorbent bound with 20% atapulgite showed the best performance with a crush strength of over 2 lbs/mm and a reversible CO_2 capacity of 1.33 mmol/g at 375°C. The samples bound with 10-20 wt.% bentonite and attapulgite showed substantially improved resistance to degradation with respect to CO_2 working capacity after one week of exposure to hydrothermal aging conditions relative to the unbound sample. After 4 weeks of steam testing, however, all of the bound H adsorbents had inferior CO_2 capacity/kinetic combinations relative to the promoted HTC.

H_2-SER Process Experiments

The goal of this work was to experimentally investigate the effect of various process variables on the performance of the H_2-SER process steps. Initial experimental efforts were focused on

performing the reaction step with a reactor initially cleaned of both CO_2 and H_2O, and filled to reaction pressure with pure hydrogen. Table 1 contains detailed descriptions of the SERP process steps.

During the last year, reaction step experiments with hydrogen pressurization were carried out at various conditions (temperature ranging from 350 to 450°C, pressure ranging between 55 and 250 psig, adsorbent/catalyst ratio ranging between 1:3 and 3:1, and H_2O/CH_4 ratio in the feed gas ranging between 3:1 to 8:1). In all cases, the SER reactor produced higher purity hydrogen (a mixture of hydrogen and methane, with only trace levels of carbon oxides) at significantly higher methane conversion than a catalyst-only system operating under the same temperature and pressure. The results also indicate that both the hydrogen purity of the effluent gas and the methane conversion increase as the reactor pressure is decreased and the reactor temperature and H_2O/CH_4 ratio are increased. These are exactly the same trends one would expect based on the thermodynamics of the SMR reaction.

The impact of variations of the original H_2-SER process steps (Table 1) have been evaluated by process design analysis, and the most attractive approaches have been tested in the laboratory. These include the utilization of different pressurization gases and different purge conditions, while varying the reaction pressure, temperature, feed gas composition, and adsorbent to catalyst ratio. Figure 2 shows some of the promising SERP reactor performance obtained from these studies. It reports the net average H_2 purity (%) in the reactor effluent (product) and the CH_4 conversion to H_2 as a function of the specific H_2 product (mmole/g of catalyst and adsorbent). The experiment was carried out with 6:1 H_2O/CH_4 in the feed gas, 1:1 adsorbent (HTC) / catalyst in the reactor, 55 psig reactor pressure, and reactor temperatures of 400-450°C.

Table 2 reports examples of the H_2 product purity and CH_4 to H_2 conversion at two levels of H_2 production (0.4 and 0.8 mmole H_2/g adsorbent and catalyst) at 400 and 450°C as measured in our 3.5' long SER#1 reactor. The table also compares the corresponding properties for the catalyst-only SMR reactor operated under identical conditions. The superiority of the SERP concept is obvious. The table also shows that the operation of SERP at 450°C is significantly better than at 400°C.

Figure 3 shows the experimental analysis of reactor effluent gas of Figure 2. It is very important to note that the average carbon oxide (CO_2 and CO) concentration levels in the H_2 product gas is negligible (<50 ppm). Thus, the SERP reactor effluent (H_2 product) mainly consists of bulk H_2 (>90% average) and CH4 (<10% average), which can be very easily separated to produce pure H_2 by using a simple 3-4 column PSA system. This is a key advantage of the SERP which can lead to significantly lower PSA separation costs (less adsorbent inventory and H_2 losses) compared to a conventional SMR-PSA system (which requires removal of ~20% CO_2 and 1% CO from H_2/CH_4 mixture) using 8-12 adsorption columns.

Carbon analysis of used catalyst and adsorbent indicated that no carbon was formed during the H_2-SER experiments.

In summary, the above reaction-step data indicate that relatively high-purity hydrogen (90+%) can be produced directly from the SER reactor at high conversion and much lower reaction temperature than a conventional reformer. The product is essentially a mixture of H_2 and CH_4, with only trace levels of CO_2 and CO. The above results have been obtained with a relatively short reactor operated in a non-cyclic fashion. It is expected that the performance of the system will improve as the reactor length is increased since then the equilibrium zone will represent a larger fraction of the reactor volume.

Industrial-Scale SER Reactor Design

Heat must be supplied to the reaction zone during the reaction and regeneration steps of the SERP process. Previous reports have described a 'condensing heat transfer fluid' approach where a high temperature organic fluid is vaporized and passed on the shell-side of a shell and tube reactor. Catalyst and adsorbent are packed on the tube side, and condensation of the heat transfer fluid in the shell-side provides energy for the reaction. This approach is characterized by a high shell-side heat transfer coefficient and nearly isothermal temperatures along the length of the reactor. Unfortunately, it is also limited to ~400°C by the stability characteristics of the commercial heat transfer fluids.

The experimental data presented above clearly indicate that the lab-scale reactor performance improves with increasing temperature. An alternative reactor design has been developed based on indirect gas heating which has the potential to increase the operating temperature range to 450-500°C.

Preliminary H_2-SER Process Design and Economic Analysis

A best-case industrial H_2-SER process design (2.5 MMSCFD of 99.9+% H_2) was developed based on the experimental process data, SMR thermodynamics, and judicious engineering assumptions. This design was substantially different from that presented last year (Hufton et al., 1997) since it was based on a different adsorbent and process cycle. The process design utilized the condensing heat transfer fluid system operating at 400°C, and the adsorbent properties were those of K_2CO_3/HTC. The system consists of three shell and tube reactors operated in parallel, along with a number of heat exchangers, condensers, and vacuum equipment for subatmospheric regeneration. A H_2-PSA unit was included in the system for final purification of the product gas (H_2-CH_4 separation). Economic analysis of this design indicates that the system has the potential to reduce hydrogen production costs by 25% compared to the conventional SMR route. Savings could increase to 31% if the CO_2 adsorbent capacity is increased by a factor of three (consistent with CO_2 capacities of the H-series adsorbents). It was also found that elimination of the H_2-PSA unit will yield similar savings. This approach would produce a product consisting of 95-98% H_2, balance CH_4, and only trace CO/CO_2. Table 3 provides a breakdown of the relative capital and operating costs associated with the above processes. It is clear that the cost advantages of the H_2-SER processes are due to substantial capital cost reductions (H_2-SER capital 50 to 60% less costly than conventional SMR).

Development of the Cyclic Process Unit

The APCI technical and management teams have decided that demonstration of the cyclic H_2-SER process using a continuous process test unit (SER#2) is needed before the technical and financial risk of a full-scale process development unit are undertaken. This will allow for more reliable development of a process design and definition of cost advantages. Significant effort has been directed towards the design of this experimental unit. It will consist of two reactors in parallel, each 20 ft long and 1 inch in diameter. Both the heat transfer fluid and indirect gas heating schemes will be tested. Valve operations will be completely automated, and the unit will be capable of regenerating the reactors under atmospheric or subatmospheric conditions. Reaction step flow rates will be similar to those envisioned for the industrial-scale process. A detailed process and instrumentation diagram has been developed, along with an initial cost estimate.

The addition of this equipment to the program will require a change in the project schedule. A no-cost extension of the Phase II efforts to the end of October 98 has been accepted by DOE. Completion of the SER#2 unit design and construction of the unit are planned during this time. Phase III efforts will also be adjusted so that the first year will be used for evaluation of the SER#2 unit, while the last two years will be identical to the original project plan (PDU design and operation). This approach will add one year to the overall project lifetime (extending it to six years), but the total cost to the DOE will remain the same.

Future Work

The laboratory data, process design, and economic analysis described above indicate that the H_2-SER process offers very high potential for developing a more cost-effective SMR process for the production of hydrogen. The next phase of effort will largely be directed towards the operation of the cyclic SER#2 unit so that a more refined design of this new process can be developed. The unit will be used to characterize the effects of various operating parameters (e.g., reaction pressure, temperature, regeneration conditions, purge to feed gas ratio, adsorbent/catalyst ratio, type of reactor heating system, etc.) on the cyclic steady-state performance of the SER process. In particular, evaluation of the average hydrogen product purity, methane conversion, and reactor productivity at cyclic steady-state will be assessed.

Concurrent process testing efforts will continue with the present laboratory-scale unit (SER#1) to further investigate the effect of various process parameters on the reactor performance, and to characterize the performance of current and next-generation CO_2 adsorbents. The data obtained from this unit will also help define the range of parameters to be investigated with the SER#2 unit.

The process data generated by these two units will be implemented into revised process designs on a continuous basis, and the economics of H_2 production will be assessed. This will then allow us to develop a commercialization strategy with the APCI Hydrogen business group.

Materials research efforts will be focused on the scale up of production of K_2CO_3/HTC for use in SER#2 (50-100 lbs). Plans for adsorbent scale-up to the PDU level (~1000lbs) will also be considered, and commercial adsorbent vendors will be included in these discussions. The development of an improved second-generation adsorbent will also be pursued, initially by continuing efforts to improve the steam stability of the 'H' material by modifying the synthesis and/or the treatment processes.

Acknowledgments

The authors wish to thank J. Zenon and J. Brzozowski for performing most of the experiments described in this report. Thanks are also due to R. Moore for carrying out the economic analysis.

References

Anand, M., J.R. Hufton, S.G. Mayorga, S. Nataraj, S. Sircar and T.R. Gaffney, "Sorption Enhanced Reaction Process (SERP) for Production of Hydrogen", *Proceedings of the 1996 U.S. DOE Hydrogen Program Review*, **1**, 537 (1996).

Anand, M., S. Sircar, and B.T. Carvill, "Processes for Operating Equilibrium Controlled Reactions," U.S. Patent Pending.

Carvill, B.T., J.R. Hufton, M. Anand, and S. Sircar, "Sorption Enhanced Reaction Process," *AICHE J.*, **42**, 2765 (1996).

Hufton, J.R., S. Sircar, W.F. Baade, J.M. Abrardo and M. Anand, "Integrated Steam Methane Reforming Process for Producing Carbon Monoxide," U.S. Patent Pending.

Hufton, J.R., S. Sircar, W.F. Baade, J.M. Abrardo and M. Anand, "Integrated Steam Methane Reforming Process for Producing Carbon Monoxide and Hydrogen," U.S. Patent Pending.

Hufton, J.R., S.G. Mayorga, S. Nataraj, T.R. Gaffney and S. Sircar, "Sorption Enhanced Reaction Process (SERP) for Production of Hydrogen", *Proceedings of the 1997 U.S. DOE Hydrogen Program Review*, **1**, 179 (1997).

Mayorga, S.G., T.C. Golden, T.R. Gaffney, J.R. Brzozowski and F.W. Taylor, " Carbon Dioxide Pressure Swing Adsorption Process Using Modified Alumina Adsorbents," U. S. Patent Pending.

Nataraj, S.N., B.T. Carvill, J.R. Hufton, S.G. Mayorga, T.R. Gaffney and J.R. Brzozowski, "Process for Operating Equilibrium Controlled Reactions," U.S. Patent Pending.

Sircar, S., M. Anand, B.T. Carvill, J.R. Hufton, S.G. Mayorga and R.N. Miller, "Sorption Enhanced Reaction Process for Production of Hydrogen," *Proceedings of the1995 U.S. DOE Hydrogen Program Review*, **1**, 815 (1995).

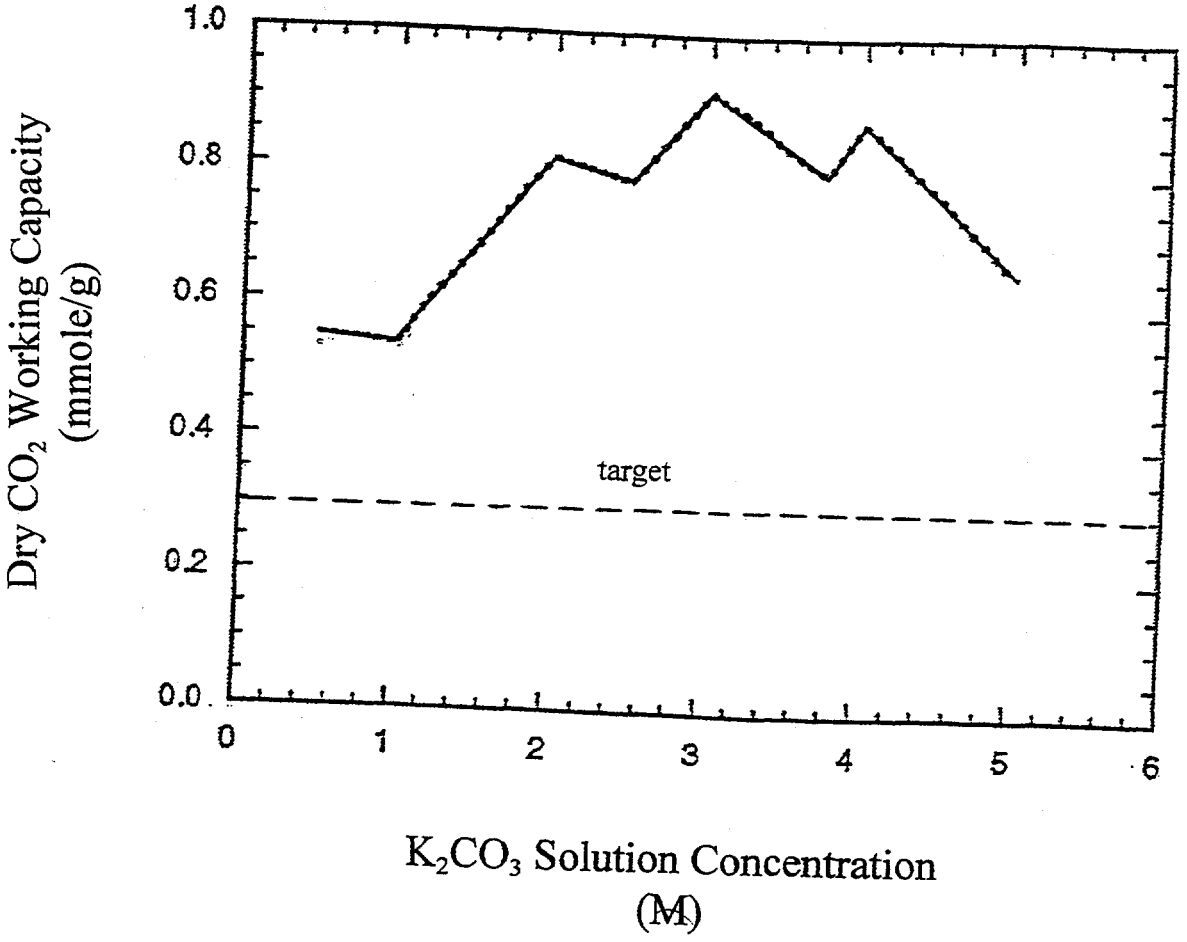

Figure 1. The Effect of K_2CO_3 Loading on CO_2 Adsorption Capacity for Promoted HTC at 400°C.

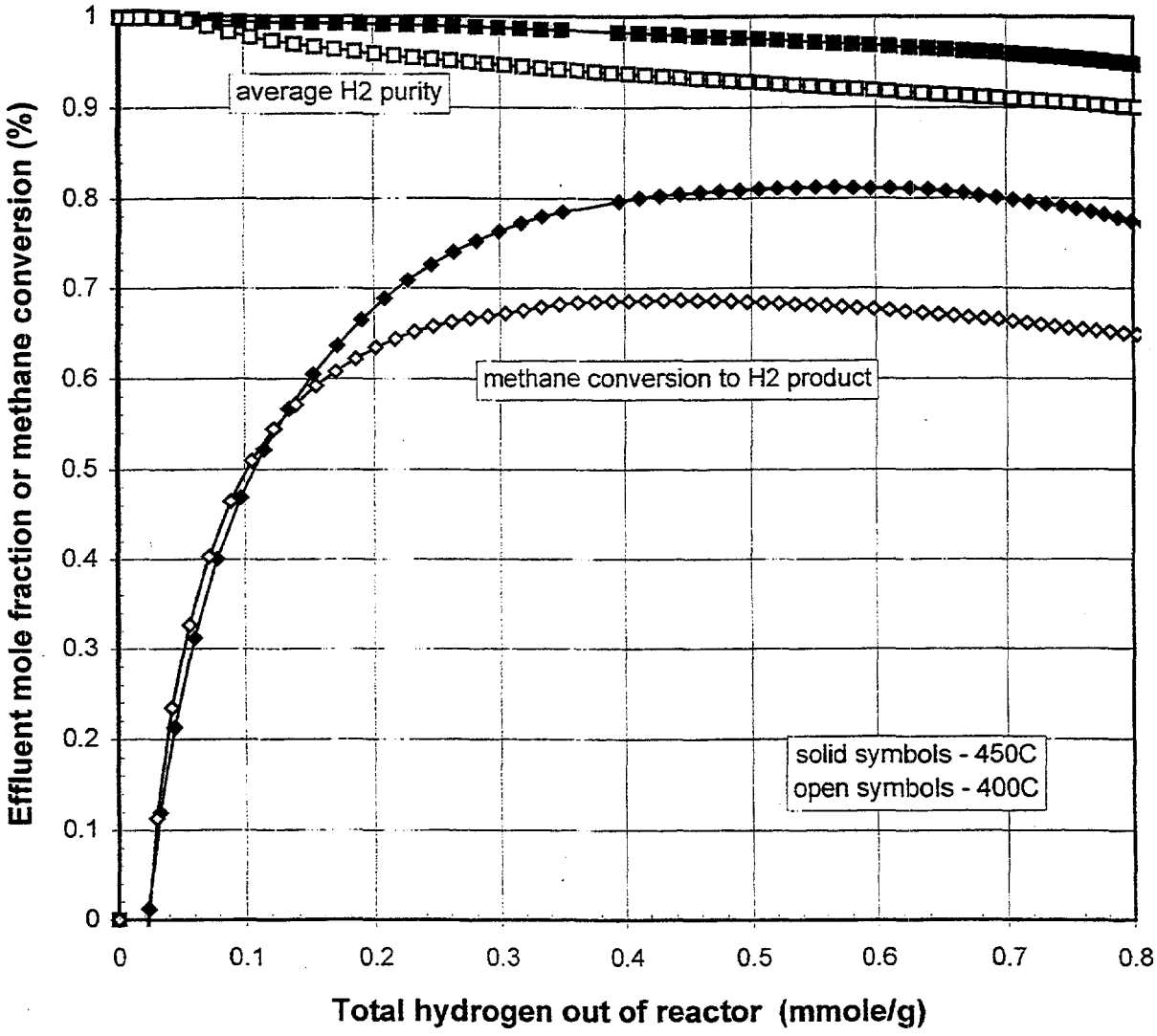

Figure 2. Average Hydrogen Purity and Methane Conversion to Product Hydrogen as Measured on Lab-Scale SER#1 Unit; 6:1 steam/carbon feed, 1:1 adsorbent (HTC)/catalyst, 55 psig.

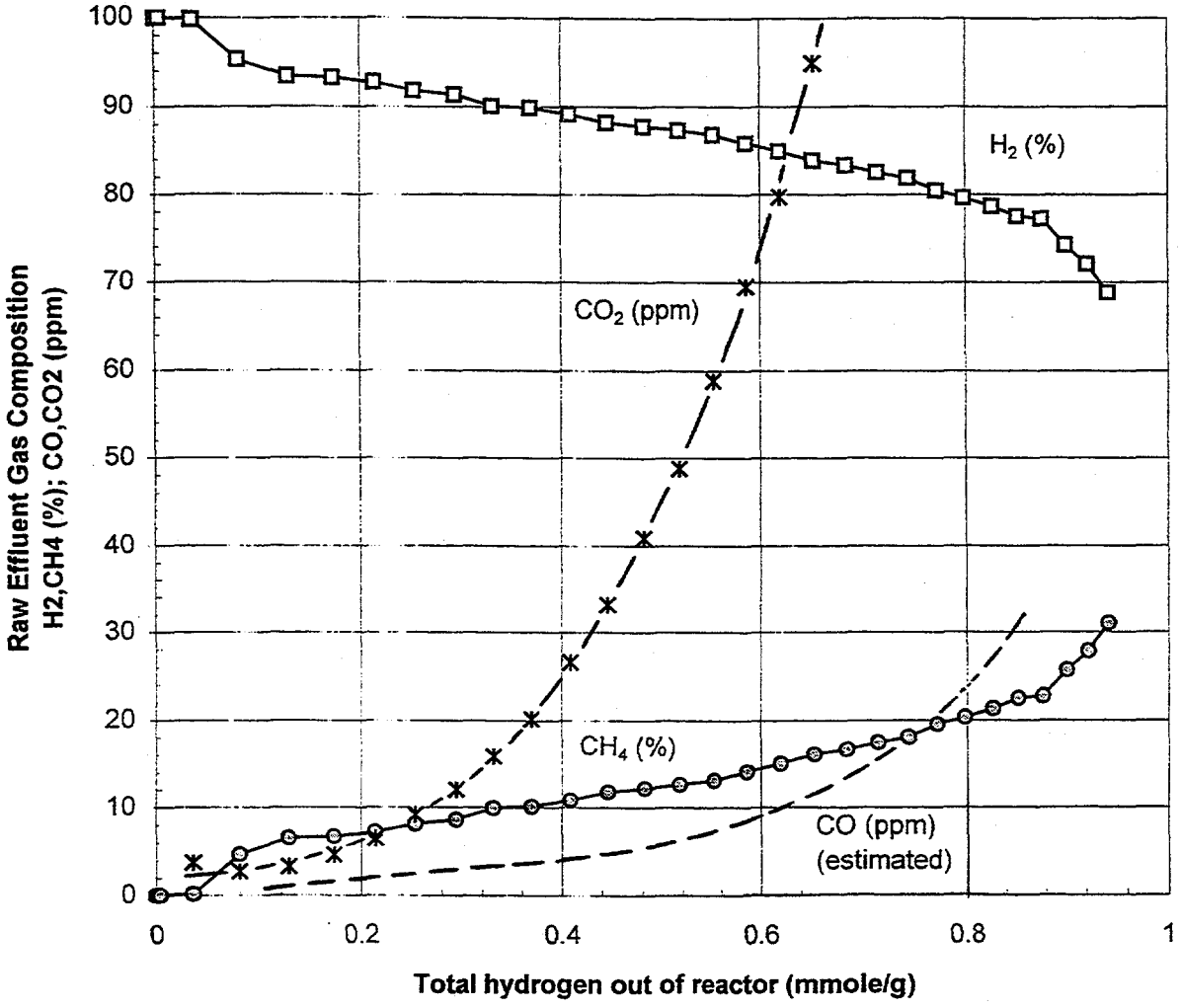

Figure 3. Reactor Effluent Gas Phase Compositions for Typical H_2-SER Reaction Experiment; 6:1 steam/carbon feed, 1:1 adsorbent (HTC)/catalyst, 55 psig.

Table 1. H_2-SER Process Steps.

1. **Sorption-Reaction Step**: The reactor is initially presaturated with a portion of the product H_2 at the desired reaction temperature and pressure. Steam and methane at a prescribed ratio (e.g., 2:1) are fed to the reactor and an essentially pure H_2 product (>98% purity) is collected as the reactor effluent. The reaction step is continued up to the point when the H_2 purity in the product decreases to a preset level. The feed is then diverted to a second identical reactor.

2. **Depressurization Step**: The reactor is countercurrently depressurized. The effluent gas can be recycled as feed to another reactor or used as fuel.

3. **Purge Step**: The reactor is countercurrently purged with a weakly adsorbing gas such as methane to desorb the CO_2. The desorption pressure may range between 0.2 and 1.1 atmospheres. The desorbed gas consists of CH_4, CO_2, H_2 and H_2O and is either separated for recycle of the CH_4 purge gas or used as fuel.

4. **Product Purge Step**: The weakly adsorbing purge gas (CH_4) is countercurrently displaced from the reactor with product H_2. The displaced CH_4 is recycled as purge gas or used as fuel.

5. **Product Pressurization**: The reactor is countercurrently pressurized to the reaction pressure with pure H_2. At this point, the regeneration of the reactor is complete and it is ready to undergo a new cycle.

Table 2. Experimental SER Performance Data; 55 psig, 6:1 H_2O/CH_4 feed, 1:1 adsorbent (HTC) / catalyst.

	Effluent Product (dry basis)	Methane conversion (%)	Productivity (mmole H_2/g)
SER @ 400°C	90% H_2, 10% CH_4 95% H_2, 5% CH_4	68	0.8 0.4
No adsorbent, 400°C	42% H_2, 47% CH_4, 10% CO/CO_2	18	
SER @ 450°C	96% H_2, 4% CH_4 98% H_2, 2% CH_4	82	0.8 0.4
No adsorbent, 450°C	53% H_2, 34% CH_4, 13% CO/CO_2	28	

Table 3. Economic Performance of H_2-SER and Conventional SMR Processes; Relative Cost based on Conventional SMR, 2.5 MMSCFD 99.9+% H_2, $2.5/MMBtu natural gas.

	Conventional SMR	H_2-SER	H_2-SER with improved adsorbent	H_2-SER without H_2-PSA
capital cost	0.54	0.28	0.25	0.21
operating cost	0.46	0.47	0.44	0.48
H_2 product cost	1.0	0.75	0.69	0.69

THE PALM DESERT RENEWABLE TRANSPORTATION SYSTEM

Charles E. Chamberlin and Peter Lehman
Schatz Energy Research Center
Humboldt State University
Arcata, CA 95521

Abstract

This paper describes the Schatz Energy Research Center (SERC) progress on the Palm Desert Renewable Hydrogen Transportation System Project for the period June 1997 through May 1998. The project began in March 1996.

The goal of the Palm Desert Project is to develop a clean and sustainable transportation system for a community. The project demonstrates the practical utility of hydrogen as a transportation fuel and the proton exchange membrane (PEM) fuel cell as a vehicle power system. The project includes designing and building 4 fuel cell powered vehicles, a solar hydrogen generating and refueling station, and a fuel cell vehicle diagnostic center.

Over this last year, SERC has built a fuel cell powered neighborhood electric vehicle and delivered it to the City of Palm Desert. The design of the hydrogen refueling station is near completion and it is anticipated that construction will be complete in the fall of 1998. The vehicles are currently being refueled at a temporary refueling station. The diagnostic center is being designed and maintenance procedures as well as computer diagnostic programs for the fuel cell vehicles are being developed.

City employees are driving the vehicles daily and monitoring data are being collected. The drivers are pleased with the performance of the vehicles.

Objective

The objective of this project is to develop a clean and sustainable transportation system for the City of Palm Desert in Southern California and to demonstrate the practical utility of hydrogen as a transportation fuel and proton exchange membrane (PEM) fuel cells as vehicle power plants.

The outcome of this project will be a complete, operating model transportation system based on hydrogen and fuel cell powered vehicles. This is the first time that solar derived hydrogen will be produced and used in fuel cells to power motor vehicles. The project provides the opportunity to collect data to help understand how differences in system components can influence overall performance, thus gaining information directly relevant to the nation's future transportation system.

Technical Goals

In order to achieve the project objective, the following specific technical objectives must be met:

- Design and construct 3 personal utility vehicles (PUVs) and 1 neighborhood electric vehicle (NEV) and deliver them to the City of Palm Desert. These fuel cell powered vehicles will be driven around the City for normal day-to-day activities and their performance will be recorded and evaluated.

- Design and construct a solar hydrogen generation facility and a hydrogen dispensing station in the City. The generation facility will use photovoltaic electrolysis to produce the hydrogen, which will be compressed and stored. Fuel dispensing to the vehicles will occur at a refueling island in the City and will be convenient and safe.

- Equip a fuel cell vehicle maintenance facility which will have diagnostic capability; personnel will be trained to maintain and service the vehicles.

Major Barriers to Meeting Technical Goals

Several technical and societal barriers have slowed progress in achieving the technical goals of this project:

- Permitting - A conditional use permit and a building permit will be required for the solar hydrogen generation facility. The generation building and gas dispenser will have to meet building, electric, plumbing, and fire codes. The demands on employee time and the length of this process are largely unknown and could delay the delivery of the station.

- Insurance - SERC PUVs are covered under the Humboldt State University Foundation's general policy, even though they use an unconventional power source. Currently the NEV is insured with a conventional insurance agent. Coverage is very expensive.

- Hindenburg Syndrome and Ignorance about Hydrogen - A percentage of the public holds irrational fears about hydrogen and is not knowledgeable of the properties of hydrogen. At a civic meeting, one representative of the College of the Desert responded to a transparency of 5th graders at SERC's solar hydrogen facility with: "How can you even think about having children involved in this technology in light of the Hindenburg accident?" In another situation, an insurance agent asked for indemnification against the possibility of a "toxic hydrogen spill."

- Availability of appropriate and certified system components - Many of the components for the NEV and solar hydrogen station will be integrated in such systems for the first time. Off-the-shelf items sometimes have lead times exceeding 6 weeks while other items have to be modified or custom-made and extensively tested. Certification is another issue; finding components certified for hydrogen use is sometimes difficult, costly, and/or time consuming.

Approach/Background

The creation of this project was motivated by several social, technical and environmental conditions:

- Smoggy air lowers the quality of life of the over 75% of Americans who live in large cities. A 1993 study using Harvard and American Cancer Society research and linking deaths to air pollution showed that the Riverside-San Bernardino region topped the nation in the death rate per capita blamed on particulates. The study linked 17% of cardiopulmonary deaths in the greater Los Angeles area to pollution. This number exceeds the number of people who died from auto accidents.

  In the District, smoggy air is also responsible for millions of dollars of agricultural losses, as well as damage to forests, range, and pastureland in addition to the human health effects.

  In the South Coast Air Quality Management District (SCAQMD), poor air quality is primarily linked to motor vehicles. Development of a clean, sustainable transportation system would eliminate criteria pollutants, decrease reliance on imported petroleum, and improve public health.

- Zero emission vehicles (ZEVs) are currently required in New York and will in the near future be required in California. Massachusetts and other states could soon follow suit. The research and development on fuel cell technology and its integration into a user ready, street safe vehicle will aid in producing ZEVs to meet these mandates.

- In order for this technology to be integrated into our society, people must overcome their fear of hydrogen (see Hindenburg Syndrome above) and learn its benefits. A complete hydrogen fuel cell powered transportation system operating in a community will go far to dispel these fears and educate citizens.

Past Results

In the 1990-1995 period prior to the start of the Palm Desert Renewable Hydrogen Transportation System Project, the Schatz Energy Research Center (SERC) designed and built an automatic solar hydrogen-fuel cell energy system which powers an air compressor at the Humboldt State University Telonicher Marine Laboratory. The first system of its kind in the U.S., it continues to operate today. In addition, SERC developed a fully equipped fuel cell laboratory and production facility and built its first fuel cells, as well as a proof-of-concept fuel cell powered PUV. The proof-of-concept PUV was completed on schedule and debuted on November 5, 1995 at the Palm Desert Golf Cart Parade. The cart performed well and met our initial goals.

SERC began the three-year, $3.9M Palm Desert Renewable Hydrogen Transportation System Project in January of 1996. By May 1997, SERC had:

- completed the design and assembly of the first PUV, including: writing new software, designing new electronic controls, completing a hazards analysis, assembling fuel storage/delivery/refueling, water circulation, and air delivery systems, and installing and testing of the 5 kW fuel cell stack. The PUV was delivered in early September 1996 and remains in day-to-day use in the City.

- designed and installed a temporary hydrogen refueling station at the College of the Desert (COD) and trained the station operators.

- assembled, tested, and delivered two additional fuel cell powered PUVs that incorporate numerous engineering and safety improvements over the first PUV. These PUVs are equipped with pickup beds so they can be used by City personnel for gardening and maintenance work.

- begun negotiations with COD and City officials and their attorneys to secure a site for the solar hydrogen generation facility and the hydrogen dispensing station in Palm Desert.

- begun the design of the solar hydrogen generating facility and hydrogen dispensing station. This included completion of a PV system simulation and sizing of the array, a hazards analysis, a site plan, a floor plan of the generation building, preliminary landscaping plan, and architectural rough sketches.

- acquired, instrumented, and tested an NEV, begun the design of a fuel cell power system appropriate to the NEV, and initiated fuel cell testing necessary to determine the configuration of the NEV stack.

- coordinated activities with Sandia National Laboratory to develop an on-board metal hydride storage system for a PUV and conducted tests on a possible hydride module.

Current Year Accomplishments/Status

During the past year, SERC has:

- completed the design, assembly, testing, and delivery of the first fuel cell powered Neighborhood Electric Vehicle (NEV) which incorporated numerous engineering and safety improvements over the PUVs, including higher cruising speed (35 mph), greater range (30 miles), and greater fuel cell power (9 kW fuel cell stack utilizing Gore PRIMEA membrane electrode assemblies (MEAs)). The NEV was delivered in April 1998 and debuted at the 1998 Palm Desert Clean Cities Celebration and is now in day-to-day use in the City.

- monitored, refueled, and maintained the three fuel cell vehicles in Palm Desert. For more than a year, the PUVs have been in day-to-day use by City employees for gardening, maintenance work, and other activities. The temporary hydrogen refueling station was relocated to City property and a new refueling and maintenance technician was trained.

- secured a site for the solar hydrogen generation facility on the property of SunLine Transit and a site for the hydrogen dispensing station near Palm Desert City Hall. This followed a lengthy and involved negotiation with COD and City officials and their attorneys that ultimately proved unproductive.

- completed the site plans and the architectural plans for the generation and dispensing facilities and submitted review packages to County planning and fire departments to begin the permitting process. Completed the sizing and specification of the grid-connected photovoltaic system and negotiated power purchase agreements with Southern California Edison. Completed the design of the hydrogen plumbing and control system and the development of the schematics, parts lists, and systems descriptions. Begun the development of the control software for the generation facility.

- acquired major components for the solar hydrogen generating and refueling facilities, including an electrolyzer, diaphragm compressor, and computer control system for the generation facility.

- begun the design of a fuel cell vehicle service and diagnostic center.

Design and Production of the Neighborhood Electric Vehicle (NEV)

The design and production of the neighborhood electric vehicle (NEV) began in May 1997, immediately following delivery of PUV2 and PUV3.

Prior to that date, SERC had purchased the original, battery powered Kewet El-Jet 3 that would be the vehicle to be retrofitted with the SERC fuel cell system. The Kewet was selected because it could be purchased in the U.S. and licensed for use on California roads. The retofit was executed in the following discrete steps:

- The original Kewet with its 48 V lead-acid battery pack was instrumented to permit monitoring and recording battery voltage and current over time. The Kewet was then road tested to determine the voltage, current , and power input to the motor controller under highway cruising and city use conditions. The maximum speed and range were verified to be 35 mph and 25 miles.

- Individual subsystems were designed and tested. These subsystems included the fuel cell, hydrogen storage and delivery, air delivery, water circulation and cooling, the high current electrical system for the traction bus, the sensor and actuator system, and the on-board computer hardware and software. The air blower motor was modified to run at the 48 V traction bus voltage and the water pump was retrofitted with a more efficient motor.

- The fuel cell parts were fabricated and the stack was assembled and tested on a test bench fitted with a programmable load to mimic driving cycles developed from Kewet testing data.

- Other separate components were also assembled and tested on the test bench independently and in conjunction with the fuel cell and other components. In response to test results, the control algorithm was iteratively modified to correct bugs and improve system performance.

- Alternative layouts of system components in the Kewet were developed and evaluated and the component layout was finalized.

- The Kewet was structurally augmented to provide adequate protection for the hydrogen storage and delivery system and appropriate heat exchanger area. The dashboard was rebuilt and the seats were replaced.

- The subsystems were installed, including the hydrogen storage and delivery system, air delivery system, water circulation and cooling system, the high current traction bus electrical system, the sensor and actuator system, and the on-board computer hardware and software. Following testing of these subsystems, the fuel cell was installed and tested.

- The NEV was first operated on a static test stand and was then road tested and final adjustments were made.

- The NEV was delivered to Palm Desert on April 22, 1998 (Earth Day) and debuted at the 1998 Palm Desert Clean Cities Celebration.

Figure 1 shows the completed NEV just before shipment to Palm Desert. A rear view of the NEV is presented in Figure 2 and shows the fuel cell compartment with the cover removed.

Table 1 lists the specifications of the NEV. The maximum speed of the NEV is 35 mph and the cruising range of the vehicle is 30 miles. The NEV fuel cell contains 96 Gore PRIMEA MEAs and can produce 9 kW at 600 mV/cell.

Table 1. Specifications of the SERC Neighborhood Electric Vehicle (NEV)

Item	Specification
Fuel Cell Type	Proton Exchange Membrane
Fuel Cell Power	9 kW @ 600 mV/cell (12.2 hp)
Number of Cells	96
Fuel Cell Operating Temperature	50-65°C (120-150°F)
Body and Chassis	Kewet El-Jet 3 (Denmark)
Traction Bus Voltage	48 Volts (nominal)
Electric Motor Size	7.5 kW (10 hp)
Hybrid Battery Size	80 Amp-hrs
Cruising Speed	35 mph
Range (on Full Tank)	30 miles
Hydrogen Tank Volume	31.1 liters
Hydrogen Gas Storage Pressure	3000 psig
Refueling Time	2 minutes

Performance of Personal Utility Vehicles (PUVs)

The three SERC fuel cell personal utility vehicles (PUVs) have been in day-to-day use in Palm Desert for more than a year. Each vehicle is capable of recording operational data for later analysis. PUV1 records data on a lap-top computer while PUV2 and PUV3 store the recorded data on-board until it can be downloaded to a lap-top computer later.

Table 2 summarizes the accumulated performance data for the three PUVs.

Table 2. Summary of PUV Performance in Palm Desert

Vehicle	Delivery Date	Total Miles	Total Run Hours	Maximum Speed (mph)	Mileage (mpg equivalent) City	Mileage (mpg equivalent) Highway
PUV1	Sept. 1996	350	70	13	65	110
PUV2	May 1997	300	120	15	95	120
PUV3	May 1997	300	120	15	90	120

Plans for Future Work

In the coming and final year of the Palm Desert Project, SERC intends to:

- construct, test, and operate the solar hydrogen generation facility on the property of SunLine Transit and the hydrogen dispensing station near Palm Desert City Hall.
- continue monitoring, refueling, and maintaining the four fuel cell vehicles in Palm Desert.
- design and outfit the fuel cell vehicle service and diagnostic center.

Status of Economic Evaluation

This is a research and demonstration project. An economic evaluation is not appropriate for our prototype vehicles and solar hydrogen generating system.

Acknowledgments

The authors gratefully acknowledge generous grant funding from Mr. L.W. Schatz of General Plastics Manufacturing Co., Tacoma, WA, USA, and the assistance of SERC's staff: G. Chapman*, A. Cohen*, S. Cohen*, J. Glandt*, R. Glover, R. Herick, A. Jacobson*, M. Marshall*, S. Ornelas, C. Parra, M. Rocheleau, S. Rommel, L. Reid, R. Reid, M. Winkler*, and J. Zoellick.

There are seven students (one graduate and six undergraduate) involved with this project. All are studying Environmental Resources Engineering at Humboldt State University. They are indicated with an asterisk in the list above.

SERC has contacts in the following companies, which are partners in the project:

Teledyne /Brown Engineering - Energy Systems
DuPont
W. L. Gore & Associates
ASE Americas
SunLine Transit

Publications/Awards/Events

At the request of DOE, PUV3 was exhibited in Las Vegas at Preview 98 in January 1998.

Videos about the project have appeared on:

Tomorrow's World (produced by the BBC, the most watched science program in the world), May 1996

Understanding Cars, The Learning Channel, May 1997

Articles about the project have appeared in:

CNN – OnLine, http://cnn.com/EARTH/9804/29/fuel.cell.car, April 29, 1998

Positive Alternatives, Winter 1998

H_2 Digest, January/February 1998

Motorland Magazine (publication of the northern California AAA), November/December 1996

NHA Advocate, Fall 1996.

Popular Science, September 1996 and October 1996

Scientific American, December 1995

Peter Lehman and Charles Chamberlin made the following project related presentations in 1996, 1997, and 1998:

- Lehman, P.A., "Recent Progress in the Palm Desert Project," 9th Annual National Hydrogen Association Meeting, Alexandria, VA, March 1998.

- Lehman, P.A., "The Palm Desert Project," Symposium at South Coast Air Quality Management District, December 1997

- Lehman, P.A., "The Palm Desert Project," DOE Annual Review Meeting, Alexandria, VA, May 1997.

- Lehman, P.A., "The Palm Desert Project," Meeting at the City of Palm Springs to discuss clean transportation in the Coachella Valley, April 1997.

- Lehman, P.A., "Fuel Cell Powered Electric Vehicles," Monthly Meeting of the HSU Society of Sigma Xi, April 1997.

- Lehman, P.A., "The Palm Desert Project," 8th Annual National Hydrogen Association Meeting, Alexandria, VA, March 1997.

- Lehman, P.A., "Fuel Cell Powered Electric Vehicles," Monthly Meeting of the California Section of the American Chemical Society, February 1997

- Lehman, P.A., "Fuel Cell Basics," South Coast Air Quality Management District, February 1997

- Lehman, P.A., "Recent Progress in the Palm Desert Project," World Car Conference, Riverside, CA, January 1997. Also session chairman for "Fuel Cells and Infrastructure I and II."

- Lehman, P.A. and Chamberlin, C.E., "Design and Performance of SERC's Prototype Fuel Cell Powered Vehicle," Fuel Cell Seminar, Orlando, November 1996.

- Lehman, P.A., "Using Hydrogen Technology: Codes and Standards, Safety, and Common Practice," City of Palm Desert, November 1996.

- Lehman, P.A., "Design and Performance of SERC's Prototype Fuel Cell Powered Vehicle," Commercializing Fuel Cell Vehicles Conference, Chicago, September 1996.

- Lehman, P.A., "The Palm Desert Project," DOE Annual Review Meeting, Miami Beach, May 1996.

- Chamberlin, C.E. and Lehman, P.A., "Design and Performance of SERC's Prototype Fuel Cell Vehicle," 7th Annual National Hydrogen Association Meeting, Alexandria, VA, April 1996.

- Lehman, P.A., "Design and Performance of SERC's Fuel Cell Powered Vehicle," World Car Conference, Riverside, CA, January 1996.

SERC personnel also gave lectures, talks, and tours in our facilities and on campus to university students, secondary school students, emeritus faculty, business people, and community organizations.

Figure Titles

Figure 1: **The SERC Neighborhood Electric Vehicle (NEV)**

Figure 2: **Rear View of NEV Showing the Fuel Cell (Compartment Cover Removed)**

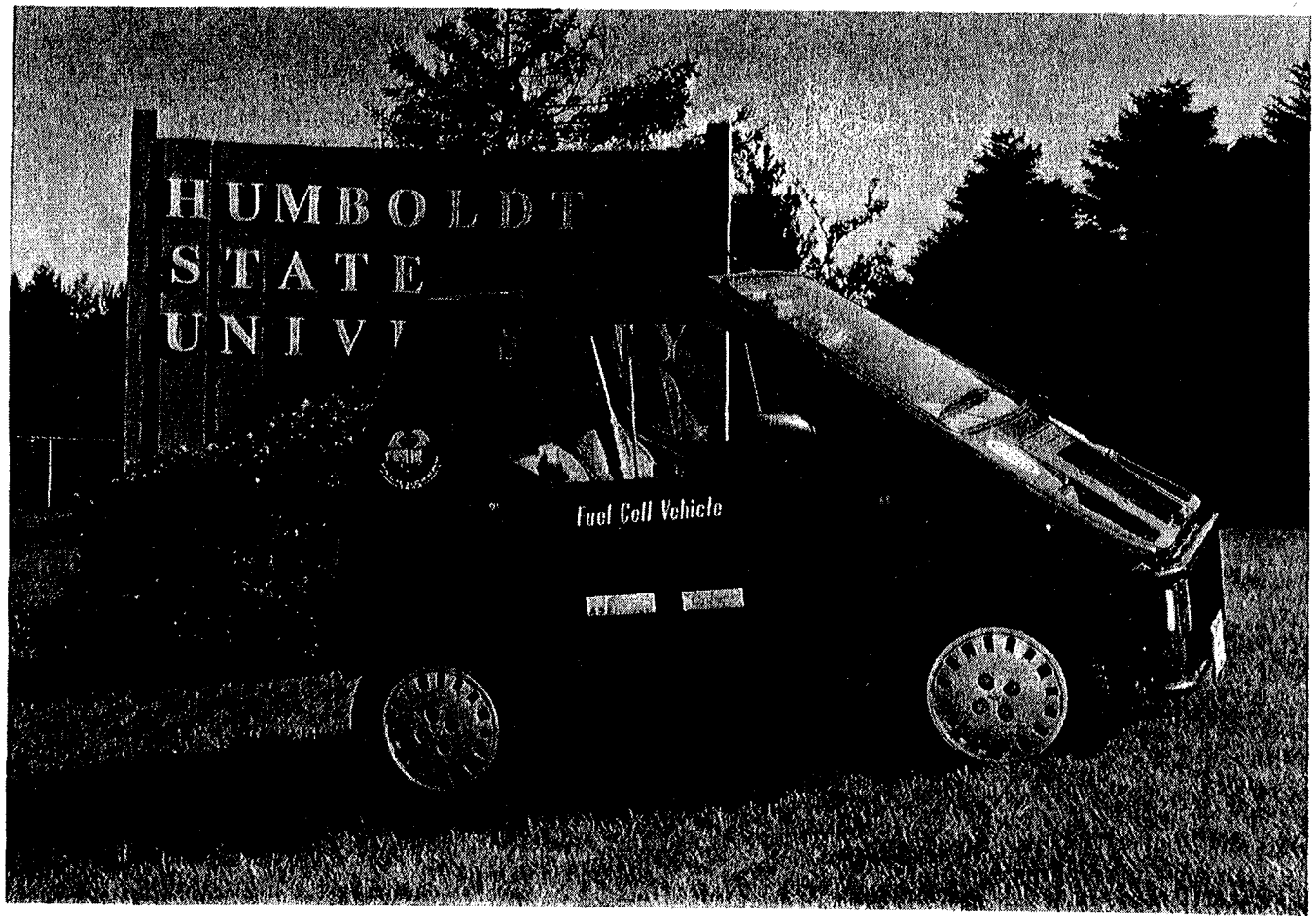

Figure 1

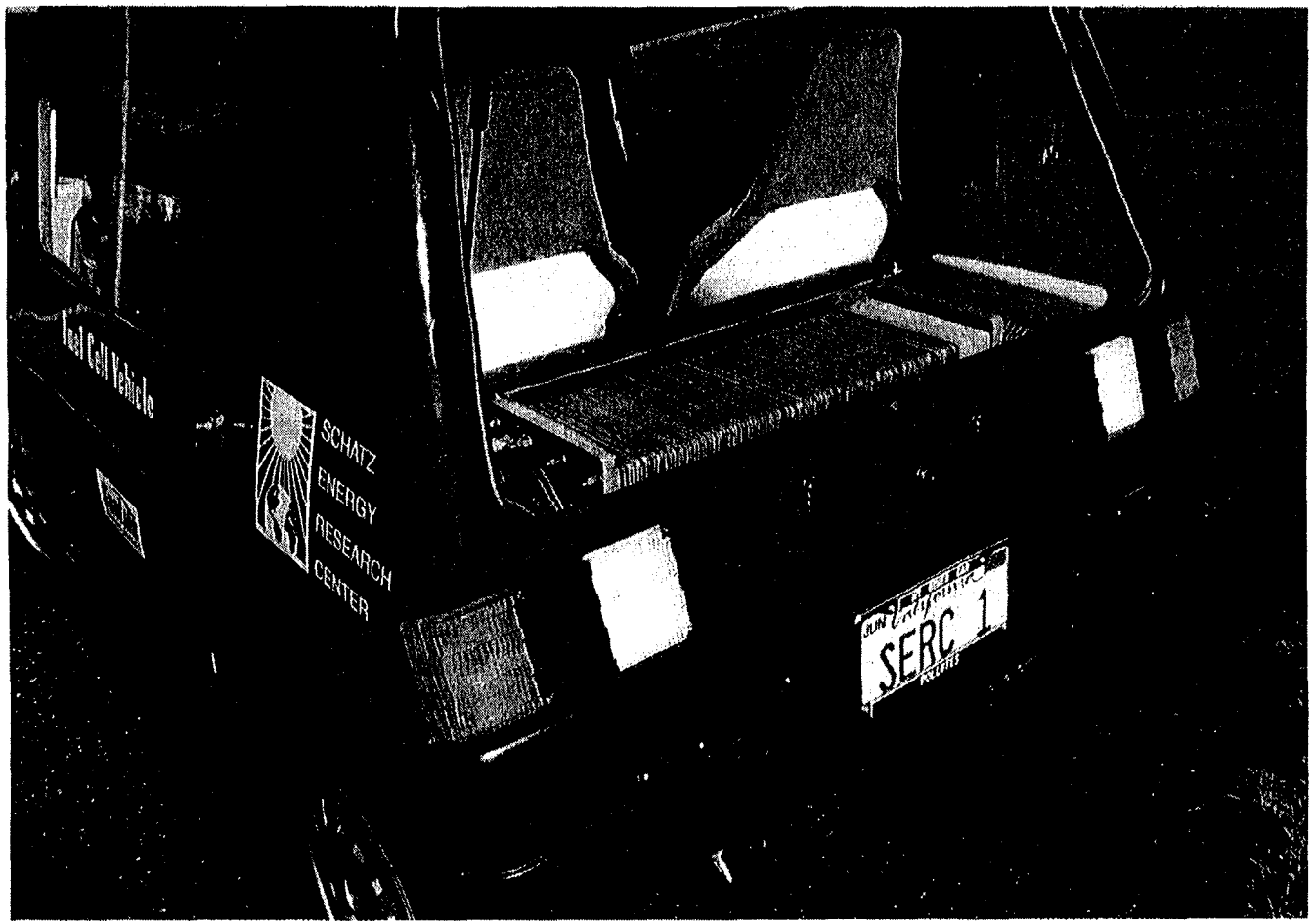

Figure 2

Internal Combustion Engine Report:
Spark Ignited ICE GenSet Optimization
And
Novel Concept Development

1998 Hydrogen Technical Review

by

Jay Keller and Peter Van Blarigan
Sandia National Laboratories
Livermore, CA

Abstract

In this manuscript we report on two projects each of which the goal is to produce cost effective hydrogen utilization technologies. These projects are: 1) the development of an electrical generation system using a conventional four-stroke spark-ignited internal combustion engine generator combination (SI-GenSet) optimized for maximum efficiency and minimum emissions, and 2) the development of a novel internal combustion engine concept. The SI-GenSet will be optimized to run on either hydrogen or hydrogen-blends. The novel concept seeks to develop an engine that optimizes the Otto cycle in a free piston configuration while minimizing all emissions. To this end we are developing a rapid combustion homogeneous charge compression ignition (HCCI) engine using a linear alternator for both power take-off and engine control.

This year our SI-GenSet program shifted from a research and development activity to a technology illustration and deployment activity. The goal of our redirected effort is to produce an optimized internal combustion engine generator set (SI-GenSet) using our current knowledge of hydrogen combustion in an engine. Because of this shift in emphasis, the fluid dynamic reacting flow modeling and the chemical kinetic modeling activities, previously associated with this program, were not funded. A secondary goal is to develop alliances with automobile OEM's (Original Equipment Manufacturing) to promote the utilization of this technology.

The target design for the optimized, spark-ignited internal combustion engine is an indicated thermal efficiency (ITE) of 47% with emissions below 5 PPM of NO_x. It is estimated that with this target the SI-ICE will yield an overall brake efficiency of 40% and emissions of NO_x below the Super Ultra-Low Emission Vehicle (SULEV) or the Equivalent Zero Emission Vehicle (EZEV) proposed legislation by the California Air Resources Board (CARB). Indeed, combining our engine out values with standard NO_x reduction technologies it is shown that this technology will produce emissions in the 0.13 PPM range (below ambient conditions in some cities).

In helping to achieve the goal of technology transfer, we have established alliances with two domestic OEMs. Both of these organizations have expressed interest in developing hydrogen-fueled ICE's based on our work.

Our rapid combustion homogeneous charge compression ignition (HCCI) free piston project has demonstrated indicated thermal efficiencies of 56% with a estimated overall efficiency of 50% while maintaining NO_x in the few PPM level. One side benefit from this HCCI technology is fuel flexibility. Fuel flexibility can have a significant beneficial impact facilitating the transition from hydrocarbon fuels to hydrogen.

Introduction

In this manuscript we report on two projects: 1) the development of a conventional four-stroke internal combustion engine generator set (SI-GenSet) optimized for maximum efficiency and minimum emissions, and 2) the development of a novel internal combustion engine concept. The SI-GenSet can be configured to run on either hydrogen or hydrogen-blends. The novel concept seeks to develop an engine that optimizes the Otto cycle in a free piston configuration while minimizing all emissions. To this end we are developing a rapid combustion homogeneous charge compression ignition (HCCI) engine using a linear alternator for both power take off and engine control.

This year our SI-GenSet program shifted from a research and development activity to a technology illustration and deployment activity. The fluid dynamic reacting flow modeling and the chemical kinetic modeling activities previously associated with this program were not funded this year. We were directed to take a snapshot in time and produce an optimized spark ignited internal combustion engine generator set (SI-GenSet) utilizing our knowledge to date. In addition, we were to develop alliances with automobile original equipment manufactures (OEM's) to promote the utilization of this technology.

Our rapid combustion homogeneous charge compression ignition (HCCI) program is supported by internal Laboratory Directed Research and Development (LDRD) funds and is leveraged with funds from the alternative fuels program from the Office of Advanced Automobile Technologies (OAAT). As such, we will discuss progress in this project as it relates to both hydrogen and alternative fuels.

This report describes the motivation, approach, progress to date, and the parameters that will be employed in the design of our SI-GenSet. This report will also describe the progress made with our rapid combustion HCCI project and future plans.

Motivation

The objective of this program is to develop cost effective highly efficient and ultra-low emission hydrogen fueled end-use technologies for the immediate utilization. Targeted applications include stationary electrical power generation, stationary shaft power generation, hybrid vehicles, and nearly any other application now being accomplished with internal combustion engines.

It is interesting to note that hydrogen use can't be motivated by energy security and pollution concerns. For example, shifting to natural gas as an energy source solves our energy security problem (at least for the near term) and solves all of our current criterion gas emission problems. (Note: Honda has a commercially available natural gas vehicle that satisfies the proposed SULEV and EZEV emission levels in California.) The use of hydrogen as an energy carrier can actually increase the emission of CO_2 (a global climate change gas) over a conventional solution if attention to CO_2 is not given over the entire fuel cycle (cradle to grave). For example, a diesel fueled hybrid vehicle will emit less CO_2 than a hydrogen fueled hybrid vehicle if the hydrogen is made from electrolysis from electrical power made from fossil fuels (coal and/or natural gas fueled turbines) and the resulting CO_2 is not sequestered in a suitable fashion. (S. Thomas, Directed Technologies Inc., private communication May 1998).

Two motivators for the use of hydrogen as an energy carrier today are: 1) to provide a transition strategy from hydrocarbon fuels to a carbonless society and 2) to enable renewable energy resources. The first motivation requires a little discussion while the second one is self-evident. The most common and cost effective way to produce hydrogen today is the reformation of hydrocarbon fuels, specifically natural gas. Robert Williams [1] discusses the cost and viability of natural gas reformation with CO_2 sequestration as a cost-effective way to reduce our annual CO_2 emission levels. He argues that if a hydrogen economy was in place then the additional cost of natural gas reformation and subsequent CO_2 sequestration is minimal [1]. Decabonization of fossil fuels with subsequent CO_2 sequestration to reduce or eliminate our CO_2

atmospheric emissions provides a transition strategy to a renewable, sustainable, carbonless society. However, this requires hydrogen as an energy carrier.

If hydrogen is to make it into the market place the end-use technologies must satisfy a set of suitable boundary conditions while providing the market place a sound, cost-effective technology for end-use. The boundary conditions applied to this problem are:

1. Cost effective capital equipment.
2. The technology must be energy efficient to offset the cost of hydrogen production.
3. For transportation applications the power density must be high to be packaged in a vehicle (transportation is the most stringent application).
4. For transportation applications the specific power must be sufficiently high to keep the mass of the vehicle to a minimum (transportation is the most stringent application)
5. The technology must be environmentally benign (near zero (or below ambient) or zero emissions)
6. There must be compatibility with existing overall infrastructure including parts distribution, service and maintenance personnel. Infrastructure compatibility makes the introduction of a new technology easier.
7. The technologies must be implemented in a way to enable market penetration in the easiest way possible.
8. We need to implement technologies and transition strategies to grow the hydrogen infrastructure that will enable emerging technologies market penetration in the easiest way possible.

Figure 1 shows a comparison of the characteristics of different end-use technologies. The numbers presented are for the overall system needed to employ a particular technology. The fuel cell systems includes the stack, fluid handling equipment, necessary cooling hardware, etc. These numbers exclude any fuel processing equipment since that will be common to all hydrogen end-use technologies and is system dependent (i.e., reformation on or off site). We do consider the transportation market not because it represents the best opportunity for hydrogen use but because it represents the most technically challenging solution.

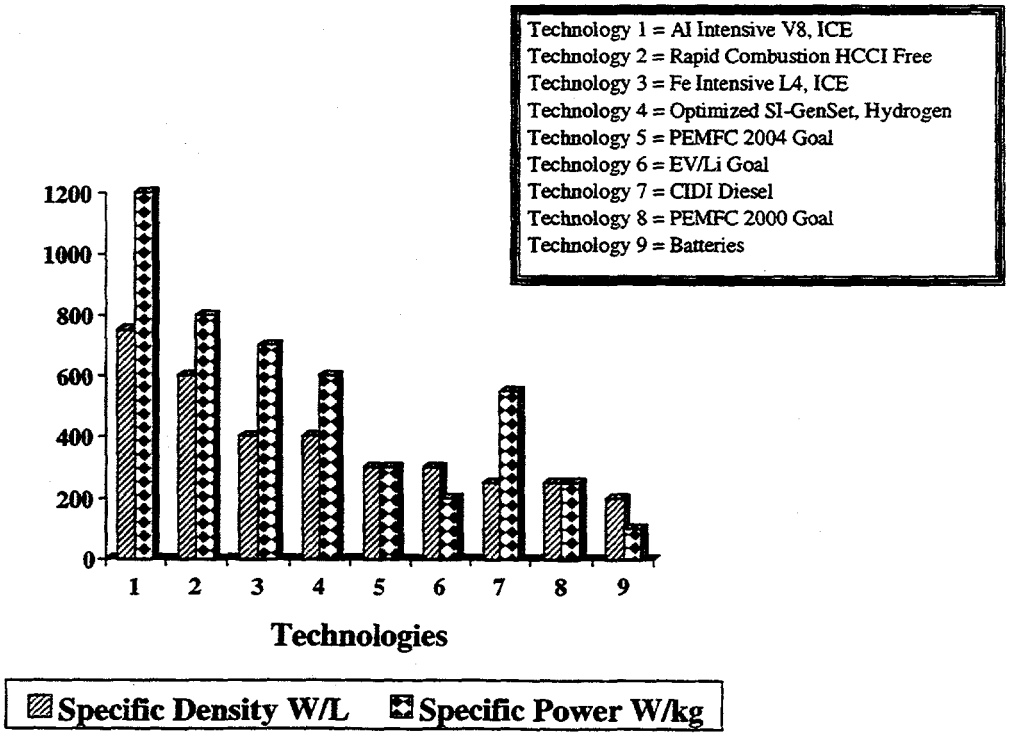

Figure 1. Power densities and specific power for selected energy conversion devices.

A conclusion from the data in Figure 1 is that an optimized ICE exceeds the power density and specific power DOE PEM system goals for the year 2004. Figure 1 compares only the power density and specific power, the system efficiencies need to be compared as well. Simply comparing system efficiencies between technologies without considering an appropriate driving cycle can be very misleading; a thorough analysis is beyond the scope of this work. However, a first order analysis was performed to determine appropriate efficiency targets for the SI-GenSet. Shown in Figure 2 are two vehicle schematics showing the power routing and the relevant efficiencies of each major component. A driving cycle was assumed so that 50% of the drive power goes through the base load system, 30% goes through the peaking system, and 20% is attributed to the regenerative breaking. The results of this first order analysis is given in Fig. 3. Fig. 3 shows that with an efficiency of ~40%, a contemporary optimized SI-GenSet powered hybrid vehicle is within 80% of the hybrid vehicle powered by a PEM fuel cell operating at the DOE Year 2004 goal. It should be noted that a much more sophisticated analysis of the same vehicle types analyzed here was performed by S. Thomas (private communication, May 1998). Thomas predicts 52.9 m/g for a vehicle with a gross vehicle weight (GVW) of 1247 kg for a hydrogen fueled SI-GenSet operated in the same parallel configuration as above and 66 for a vehicle with a GVW of 1291 kg for the fuel cell hybrid vehicle. A comparison using S. Thomas' results yields 52.9/66 = 80% which is the same as in our analysis. Thus the SI-GenSet system addressed in this work provides an attractive technology that satisfies all of the boundary conditions necessary to use hydrogen in a cost effective way today. Implementing optimized conventional technologies as is demonstrated here will pave the way for emerging technologies to enter the market as they mature, such as the emerging PEM fuel cell systems.

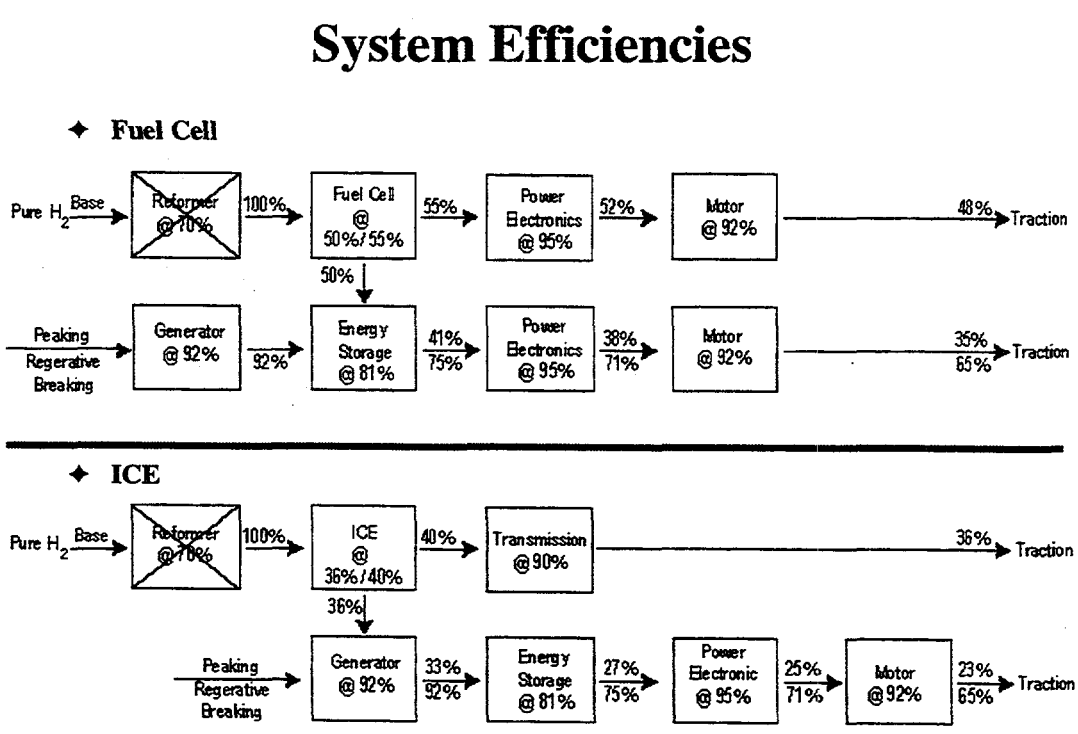

Figure 2. Vehicle system efficiency map.

Vehicle System Efficiencies - Score Card

- **DOE Fuel Cell System Goals**
  - 50% @ 100% load, 57% @ 25% load
    - Straight line gives
      - 50 % @ 100% load, 55% @ 50% load
- **ICE Goal**
  - 36% @ 100% load, 40% @ 50% load

Vehicle System Performance Estimate

	Fuel Cell	ICE	Why wait? (η_{ICE}/η_{FC})
Pure H_2	49 %	39 %	80 %

Figure 3. Comparison between a fuel cell powered hybrid vehicle and an optimized ICE powered hybrid vehicle

Development Progress to Date

In previous work we established the ability to successfully control the combustion process in an SI ICE yielding extremely low emissions (<5 PPM). Shown in Figure 4 are data taken from our research engine that shows a wide range of operating conditions all with engine-out NO_x levels sufficiently low to meet the California proposed EZEV regulation (< 0.02 gm/mile). Controlling the emissions in this way results in a system that does not rely on any post clean up technologies (i.e. a catalytic converter) and can not degrade with time.

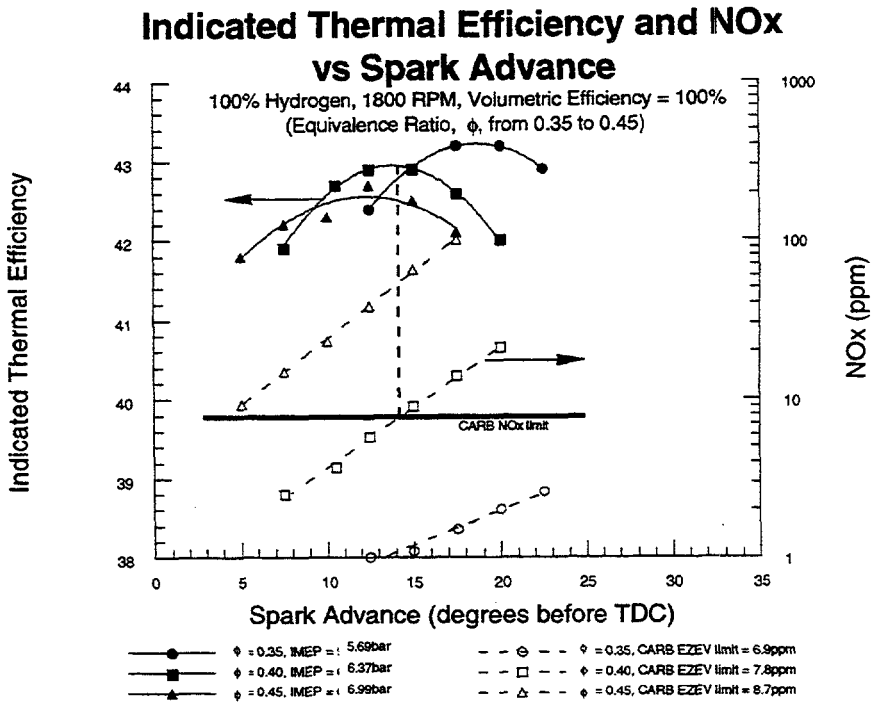

Fig 4. NO_x versus engine performance from our research engine

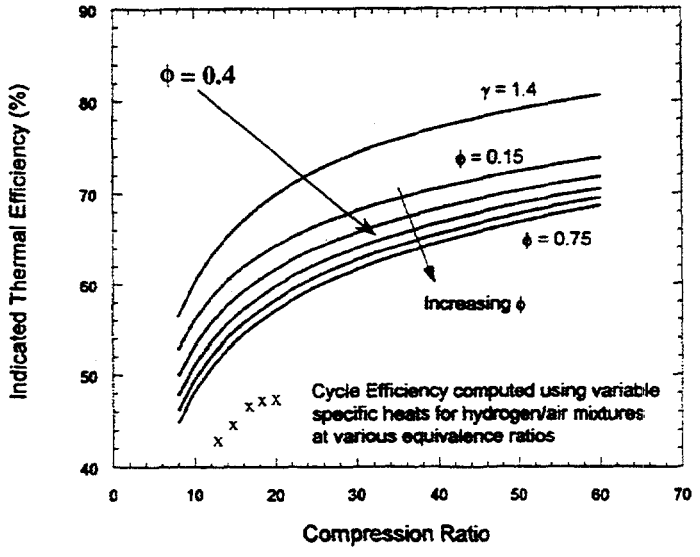

Figure 5. Measured indicated thermal efficiency (x) and theoretical indicated thermal efficiency (lines) as a funtion of compression ratio for several equivalence ratios.

Figure 5 shows the indicated thermal efficiency as a function of compression ratio compared to the theoretical maximum. The lines show the theoretical calculations and the points represent data from our current research engine. Like other researchers (Caris and Nelson (4)) we expect that with increased

compression ratio the performance of our system will start to fall off and deviate from the shape of the theoretical values. While more work needs to be done to accurately predict the efficiency of our system the peak in efficiency most likely occurs at compression ratios of 18:1 to 20:1. We are in the process of obtaining data at 22:1 to further characterize the efficiency curve. For the current configuration, as shown in Figure 5, we have achieved an indicated efficiency of 47%, a value which is 80% of the theoretical maximum. Assuming parasitic losses of 15% (conventional wisdom for Ice's is 10% at full load (Heywood) yields a break efficiency of 40% which is our goal. Our previous work has shown that this particular combustion chamber configuration is not optimized for efficiency, so further improvements can be made by reducing the swirl and fine scale turbulence, and reducing the friction losses. Recall that because we operate lean premixed the emissions from this engine are controlled to be sufficiently low (or lower) to meet the current regulations (10% of ULEV or the proposed EZEV regulations in this case). Indeed, applying the same emission control physics but using exhaust gas recirculation instead of operating lean premixed one can obtain the same engine out NO_x values and can further reduce NO_x by adding a NO_x reduction three way catalysis to the exhaust system. Other researchers have demonstrated this approach and obtain similar engine out values to the work reported on here, but they further reduce their tailpipe emissions to about of 0.13 PPM in some cases. Recall that NO_x values in some of our cities on bad days exceeds this value (Riverside California on a bad day will reach values on the order of 0.3 PPM). Even though with this approach the NO_x levels are extremely attractive recent results suggest that N_2O is formed by the catalyst resulting in elevated levels out of the tailpipe. N_2O is a known global climate change gas that is about 355 times worst than is CO_2.

Operating a lean homogenous charge is our operating condition of choice. Operating lean provides a thermodynamically favorable condition resulting in increased efficiency and provides control over the engine out NO_x values. NO_x emissions can be controlled to sufficiently low values to satisfy the most stringent emission proposed regulation without any emission post clean up technologies thus eliminating a source of N_2O.

SI-GenSet Summary

This project is primed to move on to the next phase of development. We have successfully demonstrated sufficient control over the combustion process to guarantee engine-out NO_x concentrations sufficiently low to satisfy the most stringent of proposed regulations. Our engine out NO_x values would qualify a hybrid vehicle obtaining an equivalent 60 miles/gal to meet the proposed Equivalent Zero Emission Vehicle (EZEV). This can be compared to the Toyota Prius, which is reported to achieve 61 miles / gallon of gasoline. We have also demonstrated a sufficiently high indicated thermal efficiency that our estimated brake efficiency is at 40%. This value puts an ICE powered hybrid within 80% of the DOE PNGV goal for a PEM fuel cell system. We are now in the process of purchasing a multi-cylinder engine generator set that will yield ~50kW of peak output with an optimized base output of 25 kW. Based on our current knowledge base we expect to configure this engine to operate with the following characteristics:

1. 25 kW base load with a 50kW peaking capability. This allows us to optimize the engine for base load and take a minor degradation in efficiency under peak requirements. Note that this engine will operate at peak load only for the "infinite hill climb." All other peaking requirements will be met by the on-board energy storage device, of which batteries are the most likely choice.
2. Heat transfer losses will be minimized by configuring the engine with as large a volume to surface area ratio as is reasonably possible, and as such we will use a 3.2 liter, 4 cylinder engine block as our starting point.
3. The piston and head will be designed to minimize swirl and fine scale turbulence to keep the heat transfer losses to a minimum.
4. The valve timing will be determined in the final configuration to maximize the trade off between increasing the efficiency by turboboost or maximizing the energy extracted by the expansion stroke. This is necessary because of the trade off that occurs between extracting as much energy as possible during the expansion stroke versus leaving enough energy in the exhaust system for use by a turbo charger.

5. This engine will be set up to operate at a compression ratio of about 20:1. The exact value will depend on the outcome of our current measurements
6. At these very high compression ratios, and high diluent loading the burn duration becomes a limiting factor. To maximize the efficiency it is crucial to minimize the burn duration (to better approximate the theoretical maximum efficiency from the Otto Cycle). As such this engine will be equipped with a dual spark plug configuration.
7. The engine will be designed to operate at the nominal power output of ~25kW unthrottled, and at a RPM of about 1800 to 2400 depending on the SI-GenSet match. The high power output (only for the infinite hill climb) condition will be obtained by increasing the engine RPM and the pressure boost from the turbocharger as needed to match the load requirements. This will result in a slight loss in efficiency but it will result in no degradation in the emission performance. Since the duty cycle under these conditions is very low the overall performance of the vehicle will not suffer.
8. The key to guaranteeing the emission performance is to operate the combustion in a lean premixed (homogenous charge) configuration. At equivalence ratios of 0.35 to 0.40 we are well below the knee in the NO_x curve and our measured results are well below the values needed to satisfy the proposed EZEV regulations by CARB. The lean operating limit for these engines under similar conditions is about an equivalence ratio of 0.25. This provides a significant range in equivalence ratio to provide control over the combustion temperature due to weak changes as a result of changing RPM and/or pressure boost.
9. Fuel injection will be done in the port by conventional high pressure injection systems as perfected by the work of Scott, and Heffel at the University of California at Riverside College of Engineering Center for Environmental Research and Technology (CE-CERT) (private communication, P. Scott 1998). The injection will be timed for open valve conditions to provide a fluid dynamic mixing environment to ensure a premixed charge entering into the combustion chamber. This timing and the dilute operation will ensure that preignition does not occur.

Rapid Combustion HCCI Electrical Generator

The advanced generator concept being developed by Sandia utilizes a free piston engine configuration where the piston's oscillating motion directly generates electrical power. A linear alternator component is integrated into the device such that the varying magnetic flux of permanent magnets attached to the piston is harnessed. A schematic of the design is presented in Figure 6.

Within the free piston engine, combustion occurs alternately at each end of the cylinder, thus driving the piston motion. The operating compression ratio is controlled by the linear alternator which precisely manages the piston's kinetic energy through its stroke. A homogeneous charge compression ignition (HCCI) combustion process is employed where the cylinder's premixed fuel-air charge is compressed to the point of autoignition. Compression is achieved quickly, and rapid combustion occurs at nearly top dead center. A two-stroke cycle scavenging process is used to recharge the engine's cylinder.

Several advantages ensue from this unconventional engine design. First, the HCCI combustion process can be extremely fast; ensuring that most of the fuel energy is converted to heat at maximum compression. The Otto cycle's constant-volume combustion condition is more closely approached in this configuration, and thus the efficiency can be maximized. As a result, the engine's achievable thermal efficiency is not restricted by finite combustion processes such as flame propagation or mixing/diffusion times, as it is in conventional IC engines.

A second important attribute of the engine is that the free piston's compression ratio is variable, and potentially greater than in crankshaft-driven configurations. This characteristic allows very lean fuel-air mixtures (equivalence ratios near 0.3) to be successfully ignited at high compression ratio using the HCCI process and it enables operation on a variety of different fuels without significant hardware modifications. Lean operation dramatically reduces the formation of NO_x, and can improve the engine's thermal efficiency. High compression ratios (greater than 20:1) increase the efficiency of the engine cycle.

Finally, the unique dynamics of the free piston aid in minimizing the time that the cylinder gases spend at elevated combustion temperatures. Thus, the free piston configuration enables the heat losses from the cylinder charge to be reduced, and NO_x emissions to be controlled.

Integration of the linear alternator into the free piston geometry provides further benefits to the generator design. In this arrangement mechanical losses in the system are dramatically reduced since there is essentially one moving part, and this allows engine operation at a more or less constant piston speed. These points aid in the generator design, and further improve the fuel-to-electricity generation efficiency of the device.

Benefits of the Rapid Combustion Electrical Generator

The rapid combustion electrical generator represents a revolution in IC engine-generator technology as the efficiency of the device is significantly improved relative to current technologies, while the emissions can be satisfactorily controlled. It is expected that the fuel energy conversion efficiencies will represent an improvement of 20-50% over conventional IC engine-generators (including the class of micro-turbines) with the manufacturing costs comparable to today's piston engines. Additionally, the emissions controls, using only an oxidation catalyst when utilizing hydrocarbon or hydrocarbon / hydrogen blends should enable a small generator of this type to have emissions comparable to large stationary generating plants. Finally, the advanced generator would be able to operate on a multitude of fuels without significant reconfiguration. The capabilities of fuel diversity could allow for greater customer choice, an easy integration of renewables into the electrical system, and the flexibility of fuel substitution based on market considerations.

Technical Feasibility

As with any proposed revolution in technology, the feasibility of achieving the expected advances with the generator concept must be satisfactorily established. Through various background studies, as well as recent experimental and computational investigations, this task has been conducted.

Recent advances in the areas of IC engine combustion and gas transfer, electrical power generation, and modern control theory have addressed critical components necessary for the generator's development. Each of these individual components are established. The integration of the HCCI combustion system, the scavenging cycle, linear alternator, and control dynamics is the purpose of the ongoing project. The following discussion details the work to date, and fully establishes the motivation for future development.

Combustion System - Internal combustion engine systems operating on the Otto cycle ideally represent very high conversion efficiency machines. Thermodynamically, there does not appear to be any fundamental limit to the potential of these devices. Edison (3) analytically investigated the efficiency of the ideal Otto cycle at compression ratios of up to 300:1, including the effects of chemical dissociation, working fluid thermodynamic properties, and chemical species concentrations. It was determined that even at 300:1 the thermal efficiency of the cycle is still increasing for the multitude of hydrocarbon fuels investigated. At this point, for example, the efficiency with isooctane fuel was over 80%.

However, there are many engineering challenges involved in approaching the efficiency potential of ideal Otto cycle operation in real systems, specifically

1. The combustion process must be very rapid such that there is negligible piston motion through the process (this precludes diffusion controlled and flame propagation combustion);
2. The combustible mixture must be compressed to high levels before the burning process begins;
3. Heat loss from the combustion chamber must be minimized;
4. Fuel losses through the gas exchange process must be negligible.

Caris and Nelson (4) experimentally investigated the effect of high compression ratios on the thermal efficiency of homogeneous charge spark-ignition engines. By utilizing strong anti-knock additives, compression ratios of up to 24:1 were achieved. Their investigations revealed however, that the problems of finite burn duration (i.e. flame propagation), and thus non-constant-volume conditions limited the maximum efficiency point to a compression ratio of about 17:1.

Van Blarigan (5) experimentally investigated the potential of HCCI combustion operation to eliminate the problems of finite burn duration from the design considerations. By utilizing lean hydrogen-air mixtures (equivalence ratio = 0.3) under high compression (35:1) in a single-stroke combustion experiment, near constant-volume combustion conditions were achieved. It was concluded that under the proper conditions (based on the fuel, gas temperature, mixture strength, etc.) the compression ratio could be substantially increased and thus the thermal efficiency of the engine cycle improved.

Further experimental work at Sandia this year has continued to verify the potential of the HCCI combustion process for a number of fuels. The results have shown that the achievable compression ratio of the engine cycle is only a function of the autoignition characteristics of the fuel-air mixture. Very lean mixtures can be successfully ignited and burned, where this is impossible in conventional spark ignition hydrocarbon combustion systems. The NO_x emissions from the engine can be sufficiently reduced at these low equivalence ratios to the extent that only oxidation catalysts are required to control CO and HC emissions.

Further, the heat transfer losses from such low strength mixtures are reduced relative to stoichiometric operation since the maximum gas temperatures are lower. Finally, the free piston characteristics of the engine allow the compression ratio to be maximized for specific fuels, as the ignition delay time can be matched to the rate of compression at top dead center.

Figure 7 illustrates the differences in the free piston and crankshaft-driven piston dynamics near top dead center. It is obvious that much faster rates of compression are possible at the end of the stroke, and that the time spent at maximum compression is substantially decreased. The benefits of these characteristics are stated above.

Experimental Results.

Following are selected results of some of the experimental combustion studies completed this year. In these investigations a single-stroke rapid compression-expansion machine has been used to compression ignite homogeneous fuel-air mixtures of propane, natural gas, hydrogen, methanol, hexane, heptane and isooctane. Experimental details can be found in (5).

Figure 8 gives the efficiency and NO_x levels as a function of compression ratio for propane. Under these conditions, autoignition first occurs at a compression ratio of about 34:1. Figure 9 shows the hydrocarbon and carbon monoxide emissions for propane. Note that the hydrocarbon emissions are reported as parts per million of C_3H_y here and throughout this paper. The initial temperature and compression ratio have a large effect on the final emissions.

Results for the remaining fuels are presented in the same format. Figures 10, 11 and 12 are for natural gas. Note that for an initial temperature of 25C combustion does not occur until a compression ratio of 44:1 is reached. This natural gas was a made-up blend of 93.12% methane, 3.2% ethane, 0.7% propane, 0.4% butane, 1.2% carbon dioxide and 1.37% nitrogen. Figures 13 and 14 show results for hydrogen, the fastest burning fuel. No hydrocarbon or carbon monoxide emissions are included.

The methanol test data is found in Figures 15, 16 and 17. The value of not taking too much data is seen here. Following methanol is pentane data in Figures 18, 19 and 20. The pentane tests were run late in our testing and show the consistency of later tests. Also shown in Figure 18 is an early energy release of a small fraction of the fuel, identified as the first ignition point.

The results for hexane shown in Figures 21, 22 and 23 are interesting in that the main reaction compression ratio is only 19:1 at an initial temperature of 25C. There also appears to be some reaction prior to the main combustion event as seen in Figure 21, where this reaction occurs at a compression ratio of about 16:1. This accounts for some of the poor showing in efficiency, but the hydrocarbon emissions are also large indicating not all of the fuel is reacting. The results for heptane shown in Figures 24, 25, 26 and 27 show a fuel that undergoes what appear to be three reaction points. Figures 24 and 25 show this in some detail. The final data set is for isooctane, shown in Figures 28, 29 and 30. A considerable amount of testing was done with this fuel due to the reduced performance at an initial temperature of 25C. The fuel reacted quickly, with no early reaction but did not seem to react completely. At 70C things were much better, although efficiency is still down from propane and emissions are higher.

Discussion

The data presented here were acquired to determine if rapid combustion at high compression ratio would produce high efficiency. Previous work in homogeneous charge spark ignition engines has consistently shown that indicated thermal efficiency does not increase with increasing compression ratio once 17:1 or so is reached, with some researchers reporting considerably lower rollover levels (6,7). To our knowledge, no investigators have measured performance contrary to this trend.

Our data certainly shows that it is possible to do better. From an ideal cycle with real gas effects perspective the potential improvement of a 30:1 compression ratio cycle with lean mixtures relative to a stoichiometric 12:1 compression ratio (about the limit of today's technology with a three way catalyst) cycle is 40% (9). Our experiments show a similar improvement relative to contemporary engine performance (7) with fuels such as propane, hydrogen and natural gas. Indicated efficiency of 56% has been measured with these fuels.

While we have presented all of the data, some of the tests are suspect. For example, we believe the efficiencies considerably above 56% are due to the combustion of seal lubricant from tests conducted immediately following new seal installation. We learned not to lubricate these parts. Similarly, some of the lower (and higher) results are from early tests before we were coating the pressure transducers to reduce thermal shock.

These tests, however, do not represent an engine. Intake/exhaust processes are not included, and the air/fuel mixture is completely quiescent before compression. Therefore, comparison to engine data must be done with great caution. Still, the data have shown the following trends:

1. High compression ratio at the time of combustion can be achieved. While initial temperature and fuel type have a strong effect on the compression ratio at reaction, ratios above 30:1 are possible at practical conditions. However, the data are not clear regarding efficiency improvement with increasing compression ratio. The relationship is confounded with the changes in starting temperature and fuels required to vary the reaction compression ratio.
2. The high combustion rate does approach constant volume combustion. Figure 13 shows a typical logarithmic P / V diagram for hydrogen combustion at top dead center at 33:1 compression ratio. The piston has, for all practical purposes, not moved during the combustion event, which figure 31 shows to take about 40 microseconds. In the free piston configuration high pressure-rise rates can be handled without difficulty since there are no load bearing linkages, as in crankshaft-driven engines. Additionally, operation at equivalence ratios less than 0.5 eliminates the need to consider piston erosion, or other physical damage (8).
3. Compressing the fuel/air mixture to higher levels after combustion occurs does not reduce thermal efficiency significantly. None of the data show a significant drop off in efficiency as the compression ratio is increased beyond that necessary to initiate combustion for constant initial conditions. However, the NO_x emissions do increase, a clear indication of increasing temperature or time at temperature. While it is possible that greater heat loss is compensated by more of the fuel reacting, this effect cannot be large (due to most of the fuel being reacted already) with the conclusion that heat loss does not increase significantly with higher compression ratio. A

contributor to this insensitivity is the coating of both the piston top and cylinder head with 0.25 mm of Silastic J to reduce the thermal conductivity of the surfaces. Figure 32 shows the uncoated cylinder head surface temperature during a combustion cycle. Coating of the head eliminates any measurable head surface temperature increase during this cycle. While all of the data presented were acquired under coated conditions, operation without the coating only reduced the efficiency by 5%.

4. NO_x emissions can be controlled by equivalence ratio to the desired level. C_3H_y and CO emissions are present in varying degree, but increasing the initial temperature generally reduces these emissions. We intend to investigate oxidation catalyst performance on these emissions. An interesting possibility for emissions control would be to utilize 50% internal EGR (i.e. leave 50% of the combustion products in the cylinder) and add a stoichiometric fresh charge of 50% of the cylinder volume. We performed such a test series and measured emissions after 4 cycles. NO_x was 130 PPM, CO was 1720 PPM and C_3H_y was 360 PPM. Efficiency was 50%. Such an operating strategy with a 3-way catalyst could be very attractive.
5. All fuels are not created equal. As the data show some fuels do not react completely or react in two steps. Generally, higher initial temperature and higher compression ratio reacted more of the fuel. All of the tests were conducted at the same compression/expansion rate (40 Hz oscillation rate). This is an interesting variable we intend to investigate in the future.

Other researchers are investigating homogeneous charge compression ignition in crankshaft engines (for example 10-14). Christensen et al (13, 14) evaluated isooctane, ethanol and natural gas in a 1.6 liter single cylinder displacement research engine at a fixed 21:1 compression ratio, at a speed of 1000 RPM. Their results are consistent with ours, with peak indicated efficiency (not including the inlet/exhaust strokes) of over 50% at similar equivalence ratio.

This raises the question as to whether the free piston geometry is important to this combustion concept. Certainly the lack of massive kinematic constraints is attractive for such high compression ratios, and the electronic control of compression ratio broadens the operating range. But the increased compression ratio possible with the free piston at the time of combustion may not provide much advantage. We intend to compare crankshaft and free piston performance under identical operating conditions to quantify the performance difference.

Finally, our work as well as Christensen's (13, 14) adds further credibility to the explanation of finite burn duration as the main cause for real cycle departure from ideal cycle performance as compression ratio is increased.

Summary

This section presents the results of an investigation which was conducted to determine the effect that homogeneous charge compression ignition of dilute fuel/air mixtures with a free piston would have on thermal efficiency and emissions. The investigation was conducted in a single stroke gas driven combustion experiment in which a premixed fuel/air charge was compressed to autoignition and expanded. Efficiency was calculated from measurements of pressure and piston displacement, and emissions were measured on the combustion gasses.

The results of this study have shown that indicated thermal efficiency significantly higher than is possible in spark ignition engines can be achieved. For example, the indicated thermal efficiency of hydrogen, propane or natural gas is 56%. The primary cause of this high conversion efficiency is nearly constant volume combustion at high compression ratio.

In addition this combustion approach controls NO_x formation by utilizing dilute mixtures, an approach not possible in spark ignition engines utilizing hydrocarbon fuels. Other regulated emissions must be dealt with by aftertreatment.

References

1. Robert H. Williams, "Fuel Decarbonization for Fuel Cell Applications and Sequestration of the Separated CO_2," PU/CEES Report No. 295, January 1996.

2. John B. Heywood, "Internal Combustion Engine Fundamentals," McGraw Hill, Inc. 1988, pp 712.

3. Edson, M. H., "The Influence of Compression Ratio and Dissociation on Ideal Otto Cycle Engine Thermal Efficiency," Digital Calculations of Engine Cycles, SAE Prog. in Technology, **7**, 49-64. 1964.

4. Caris, D. F., and Nelson, N. N., "A New Look at High Compression Engines," SAE Transactions, **67**, 112-124, 1959.

5. Van Blarigan, P., "Advanced Hydrogen Fueled Internal Combustion Engines," Energy & Fuels, **12**, 72-77, 1998.

6. Overington, M. T. and Thring, R. H.: "Gasoline Engine Combustion - Turbulence and the Combustion Chamber," SAE Paper 810017, 1981.

7. Muranaka, Y. T. and Ishida, T.: "Factors Limiting the Improvement in Thermal Efficiency of S.I. Engine at Higher Compression Ratio," SAE Transactions, vol. 96, section 4, pp. 526 - 536, 1987.

8. Maly, R. R., et. al., "Theoretical and Experimental Investigation of Knock Induced Surface Destruction," SAE Transactions, **99**, Section 3, 99-137, 1990.

9. Edson, M. H., and Taylor, C. F.: "The Limits of Engine Performance - Comparison of Actual and Theoretical Cycles," *Digital Calculations of Engine Cycles, SAE Prog. in Technology*, vol. 7, pp.65-81, 1964.

10. Thring, R. H.: "Homogeneous-Charge Compression -Ignition Engines," SAE Paper 892068, 1989.

11. Najt, P. M. and Foster, D. E.: "Compression-Ignited Homogeneous Charge Combustion," SAE Paper 830264, 1983.

12. Karim, G. A. and Watson, H. C.: "Experimental and Computational Considerations of the Compression Ignition of Homogeneous Fuel-Oxidant Mixtures," SAE Paper 710133, 1971.

13. Christensen, M., Johansson, B., Amneus, P. and Mauss, F.: "Supercharged Homogeneous Charge Compression Ignition," SAE Paper 980787, 1998.

14. Christensen, M., Johansson, B. and Einewall, P.: "Homogeneous Charge Compression Ignition (HCCI) Using Isooctane, Ethanol and Natural Gas - A Comparison with Spark Ignition Operation," SAE Paper 972874, 1997.

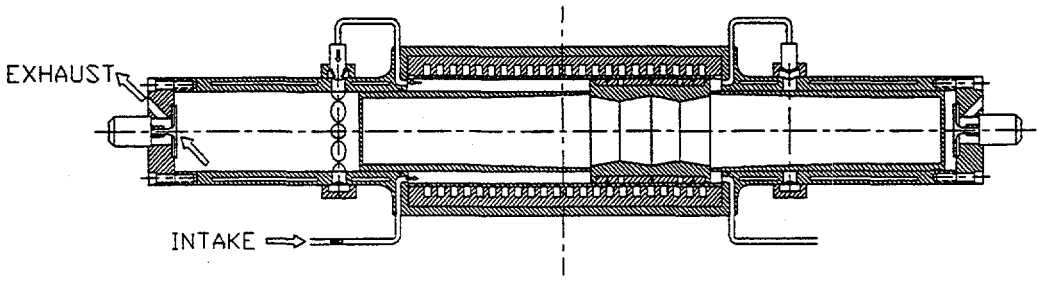

Figure 6 - Rapid Combustion Electrical Generator

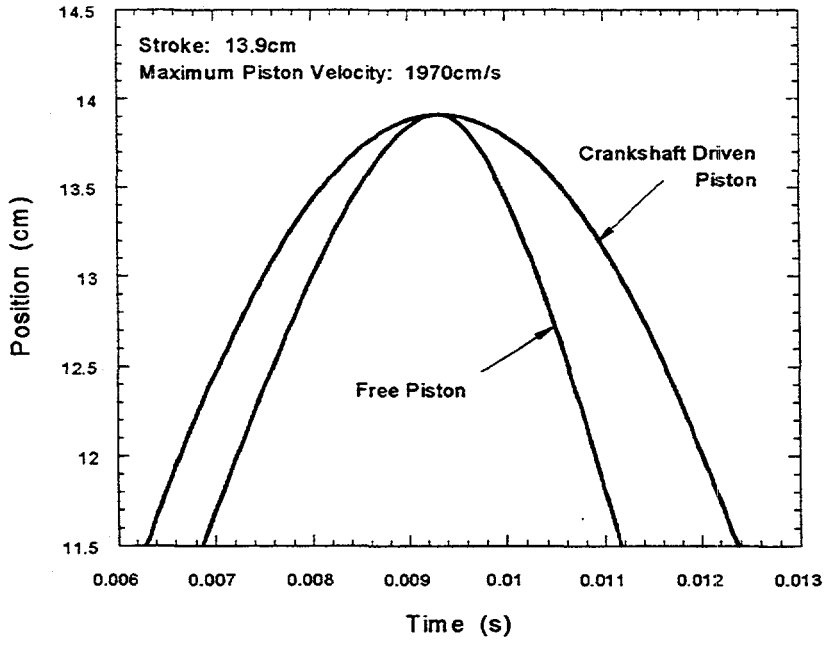

Figure 7 - Free Piston and Crankshaft Driven Piston Profiles

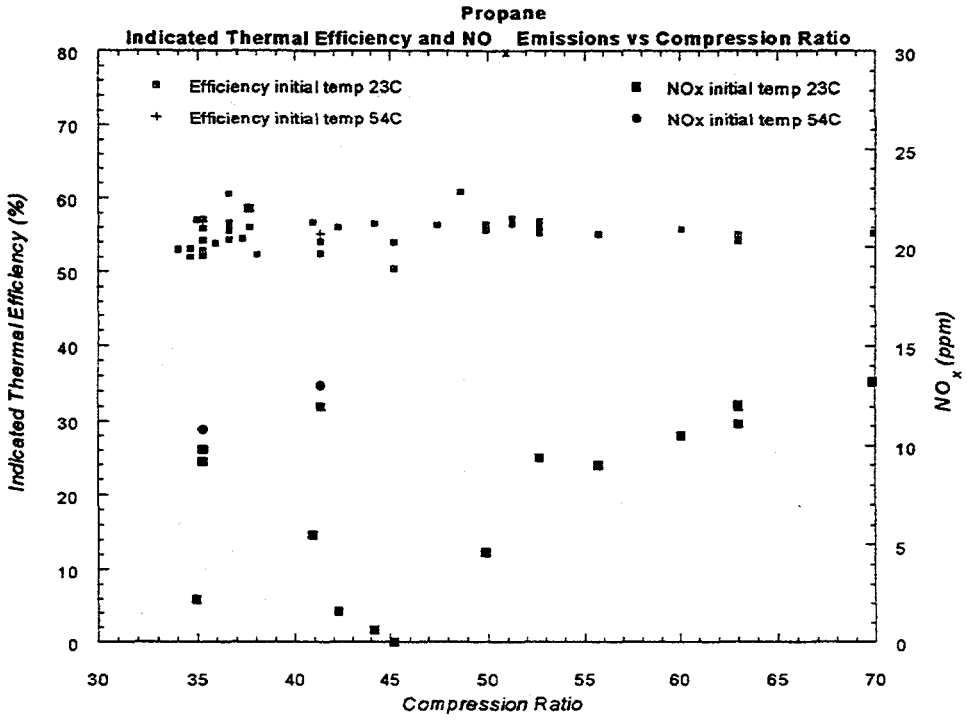

Figure 8

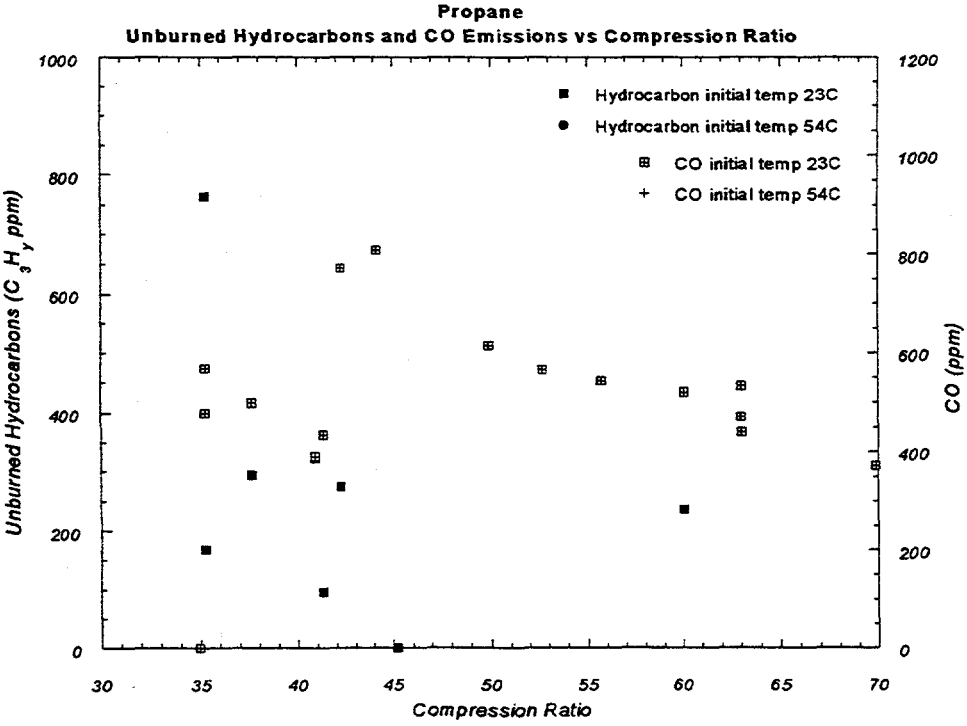

Figure 9

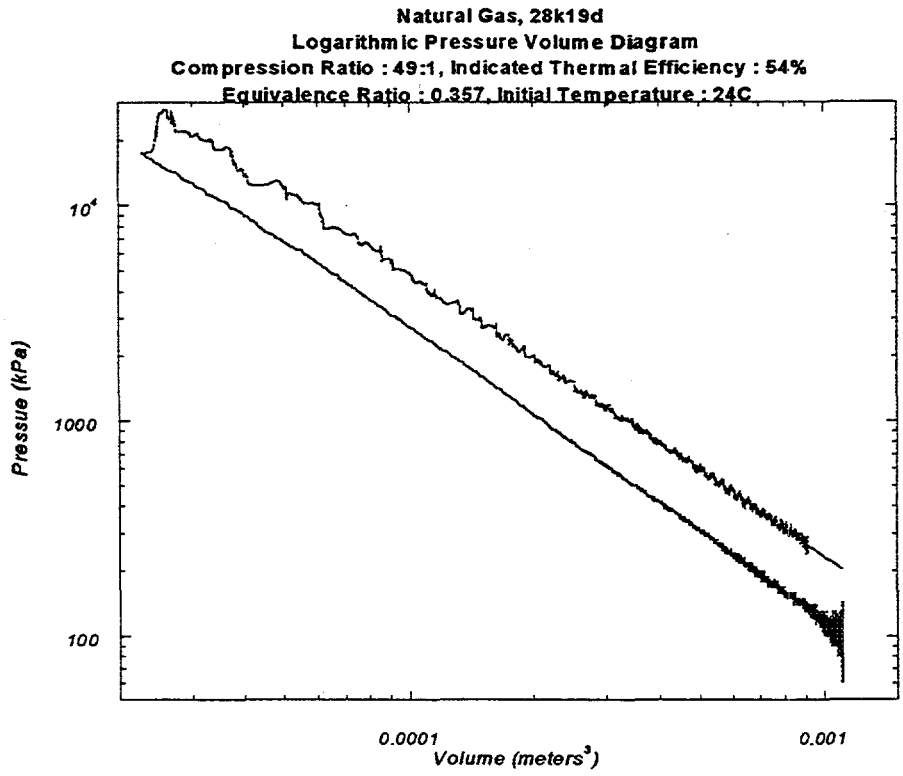

Figure 10

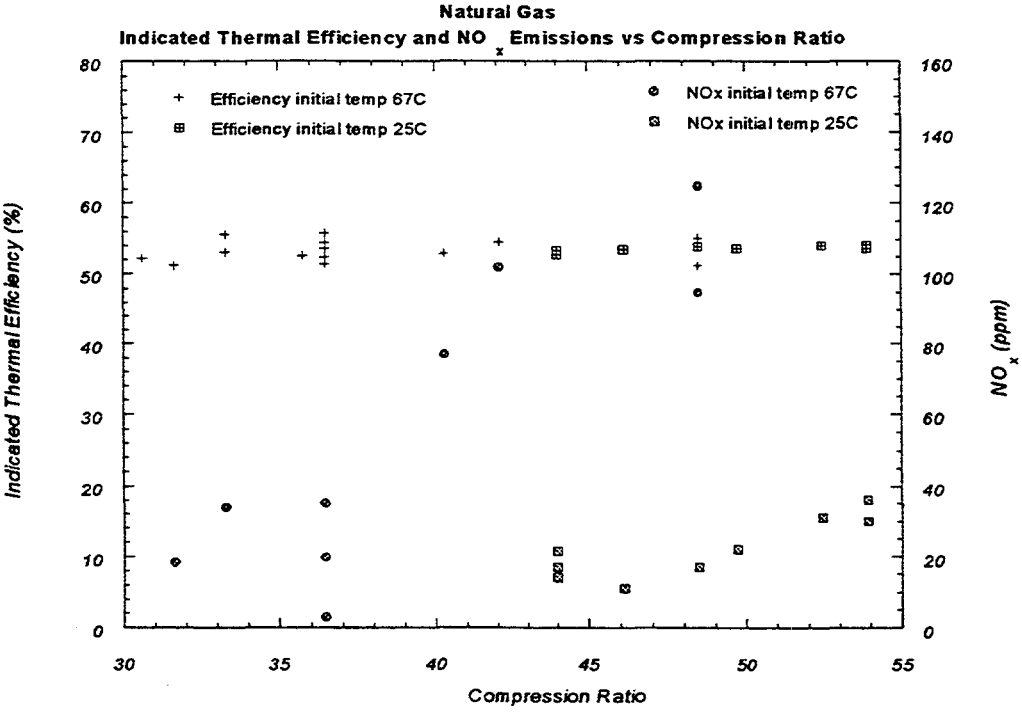

Figure 11

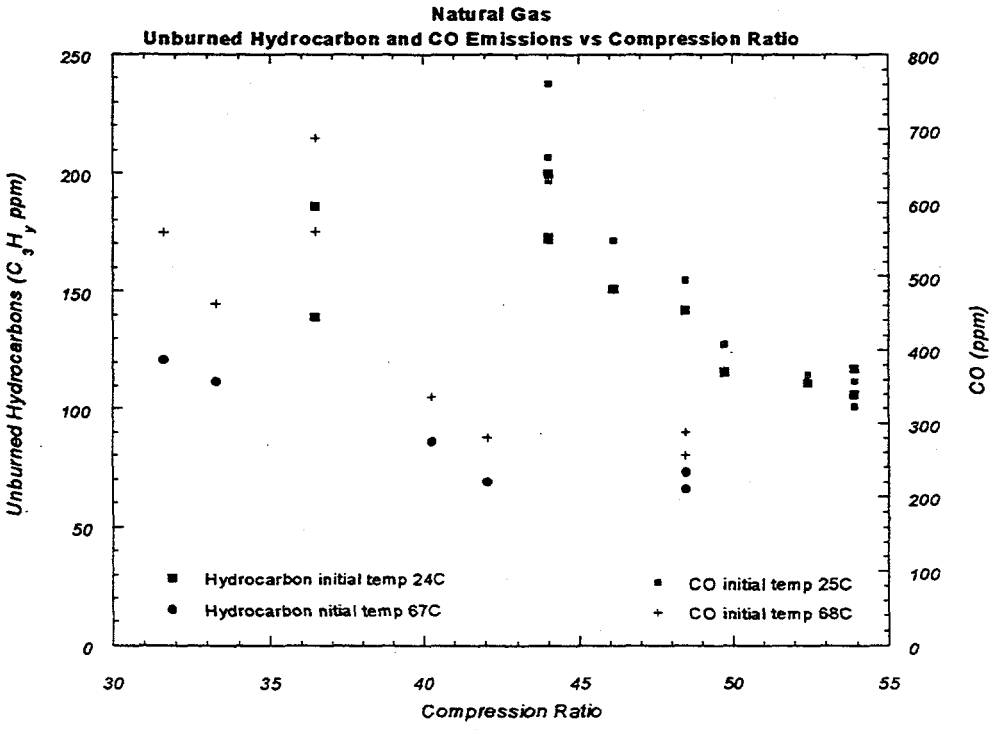

Figure 12

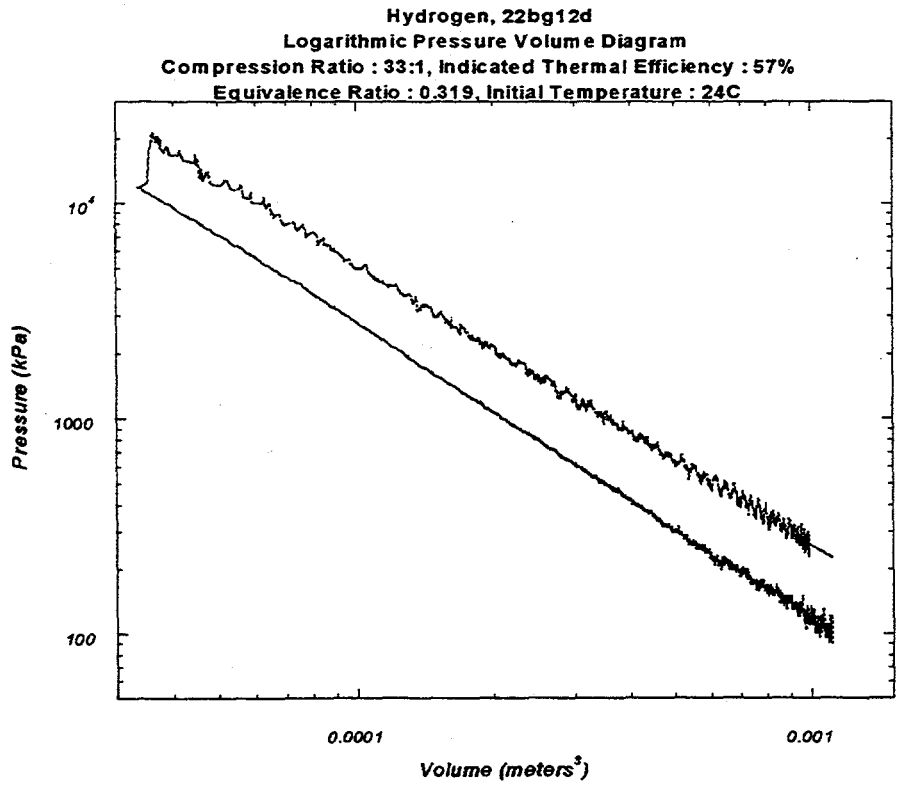

Figure 13

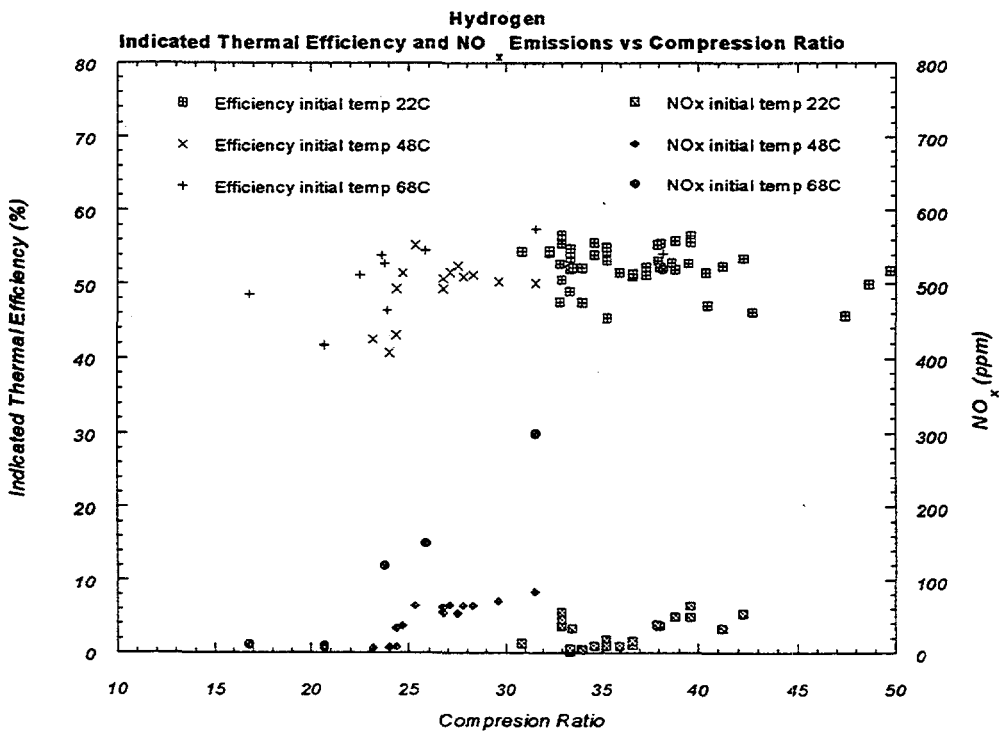

Figure 14

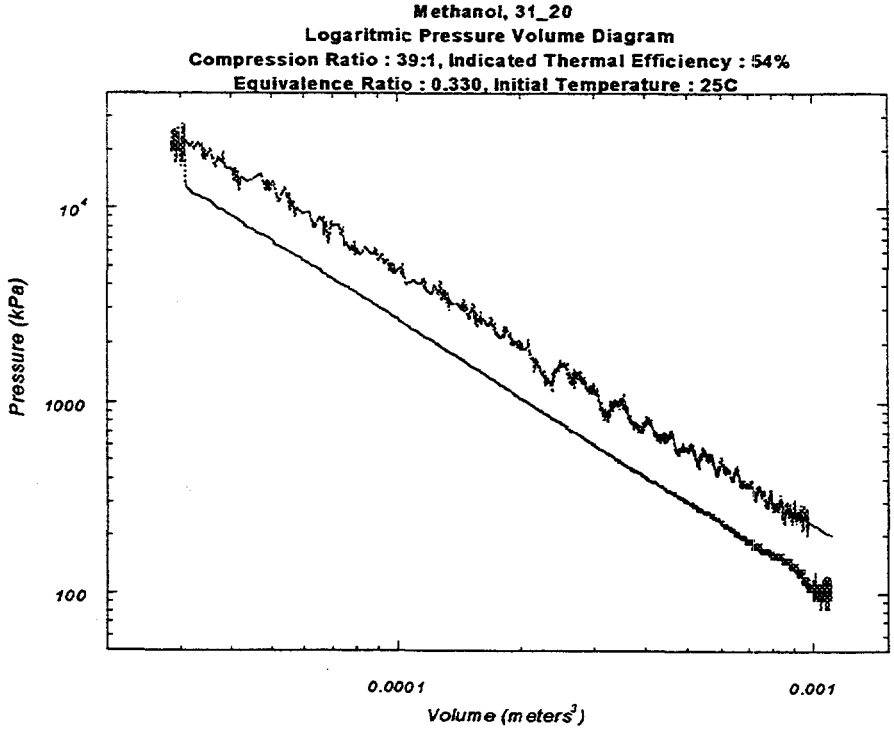

Figure 15

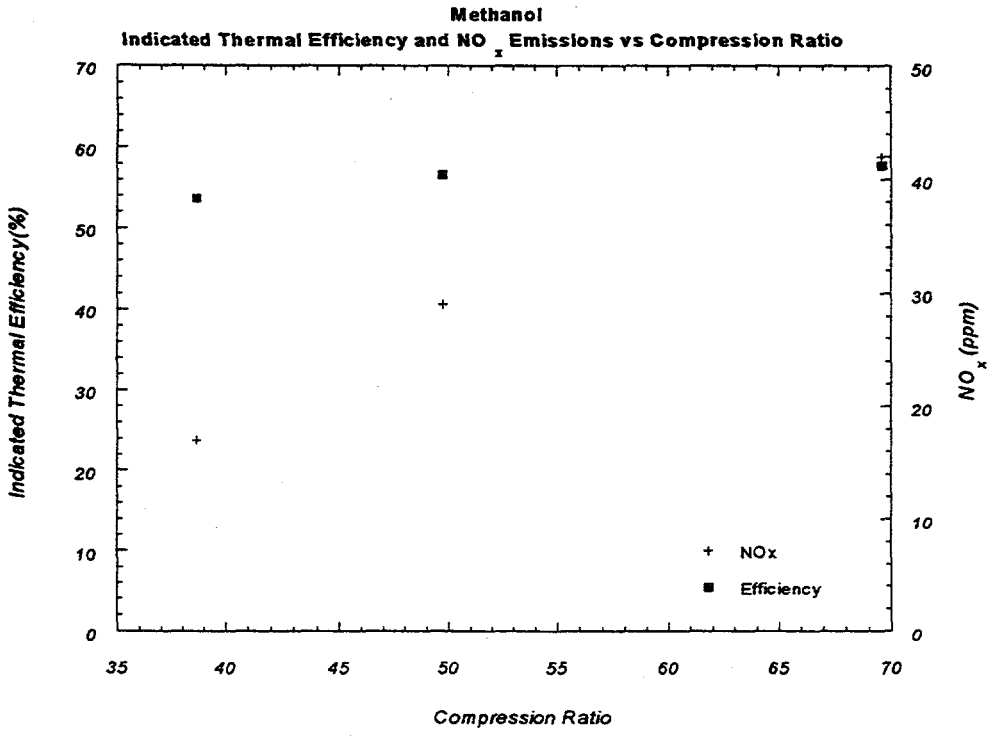

Figure 16

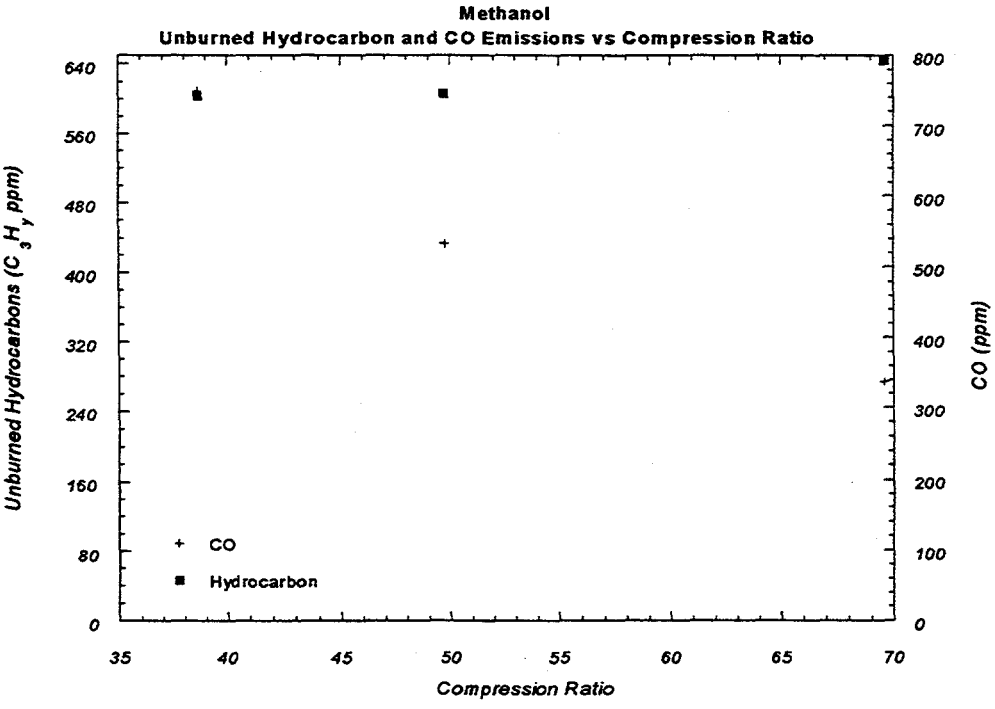

Figure 17

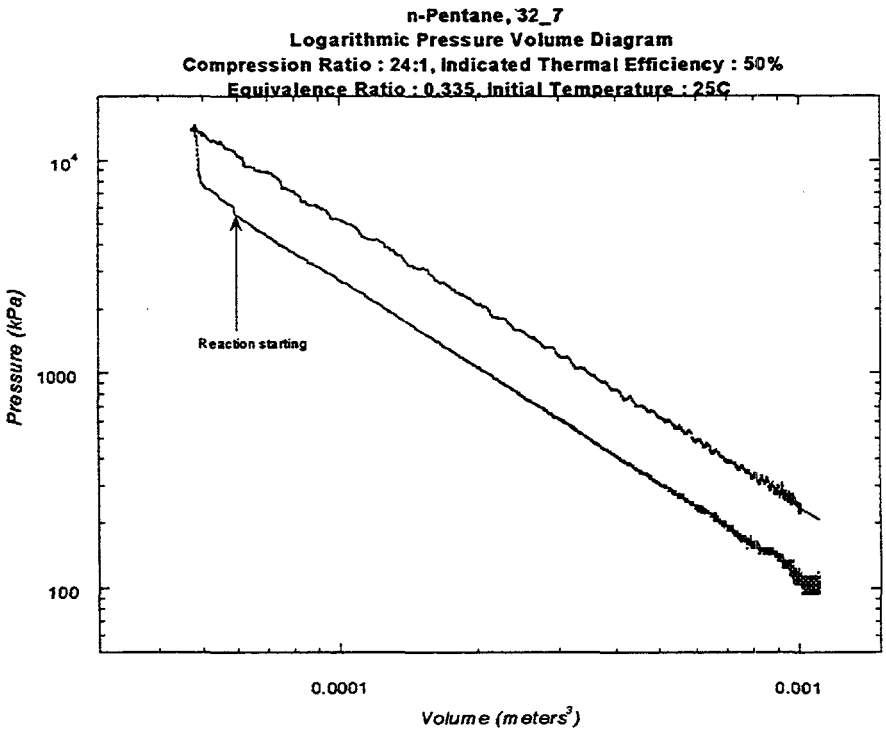

Figure 18

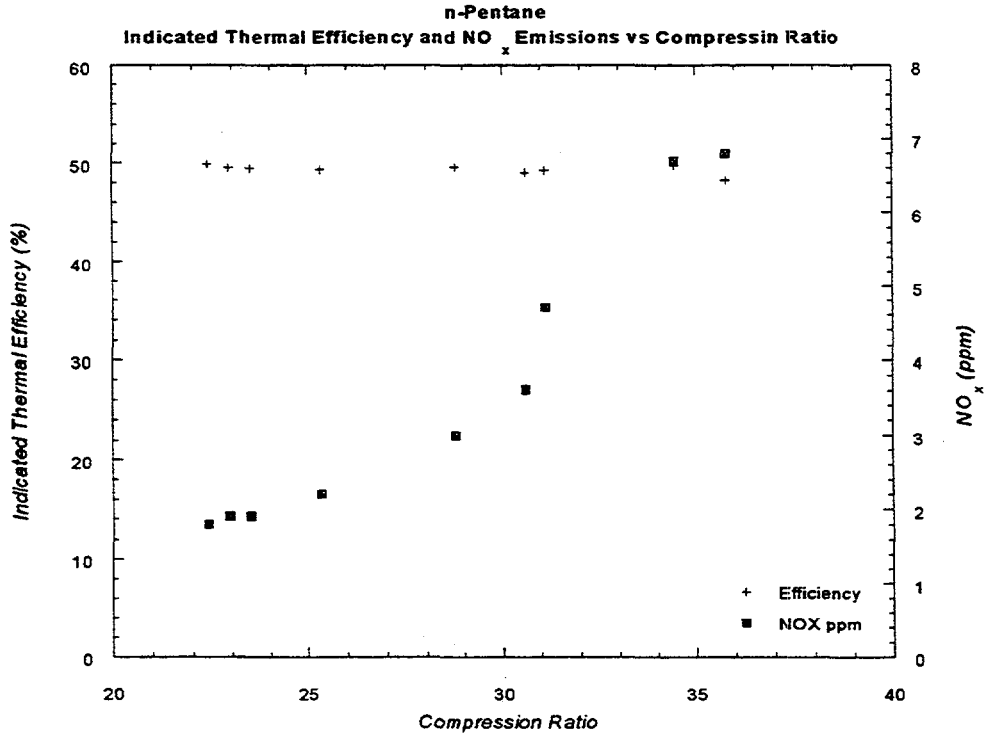

Figure 19

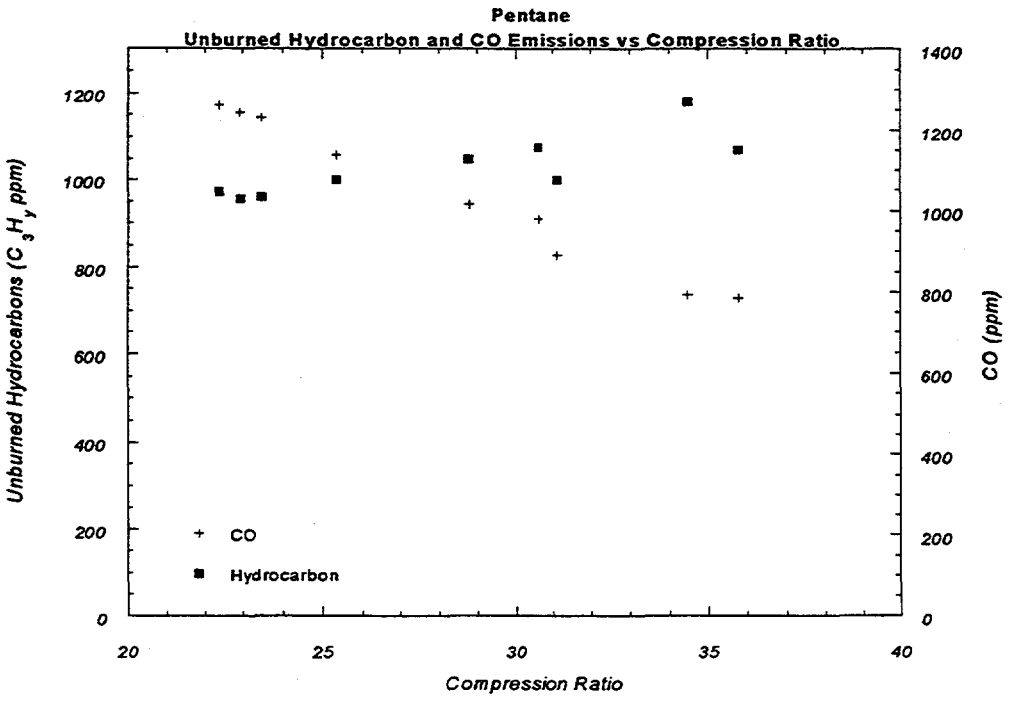

Figure 20

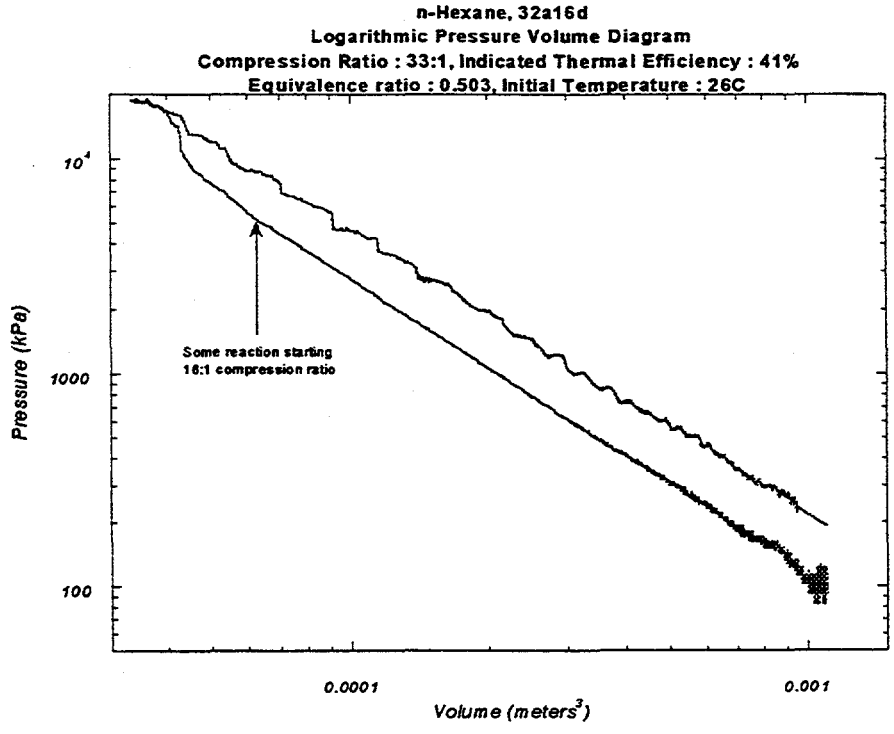

Figure 21

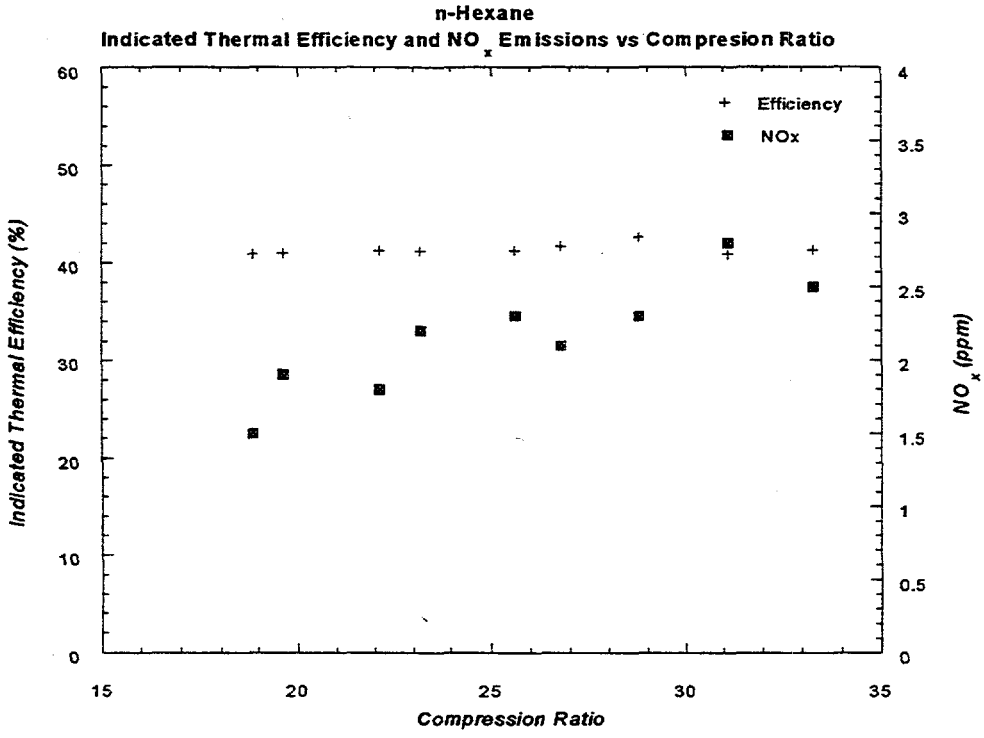

Figure 22

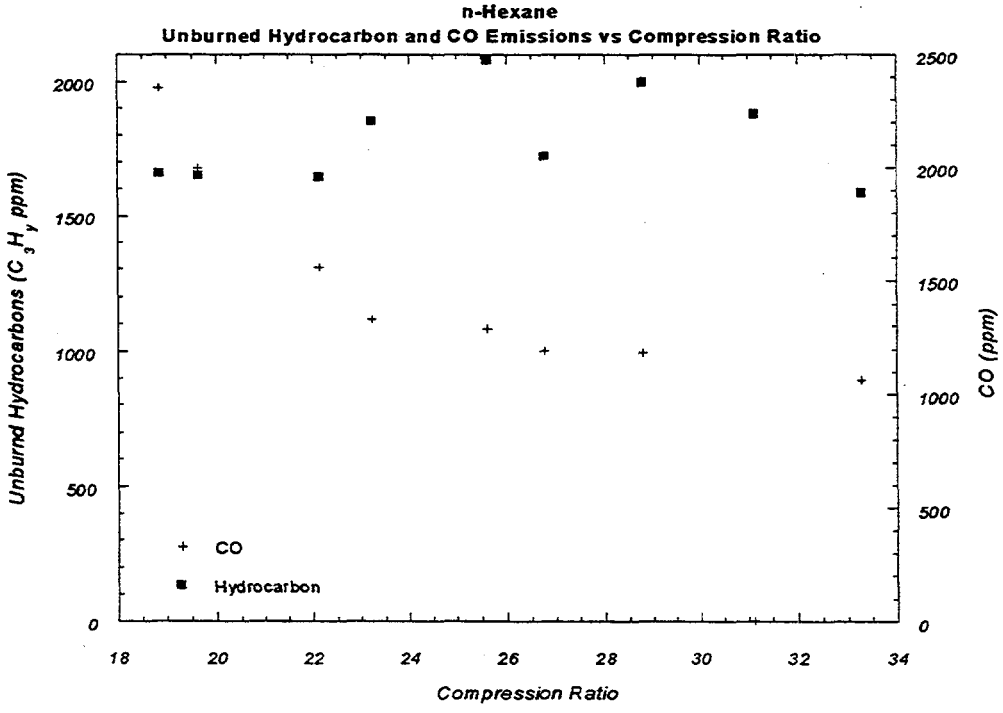

Figure 23

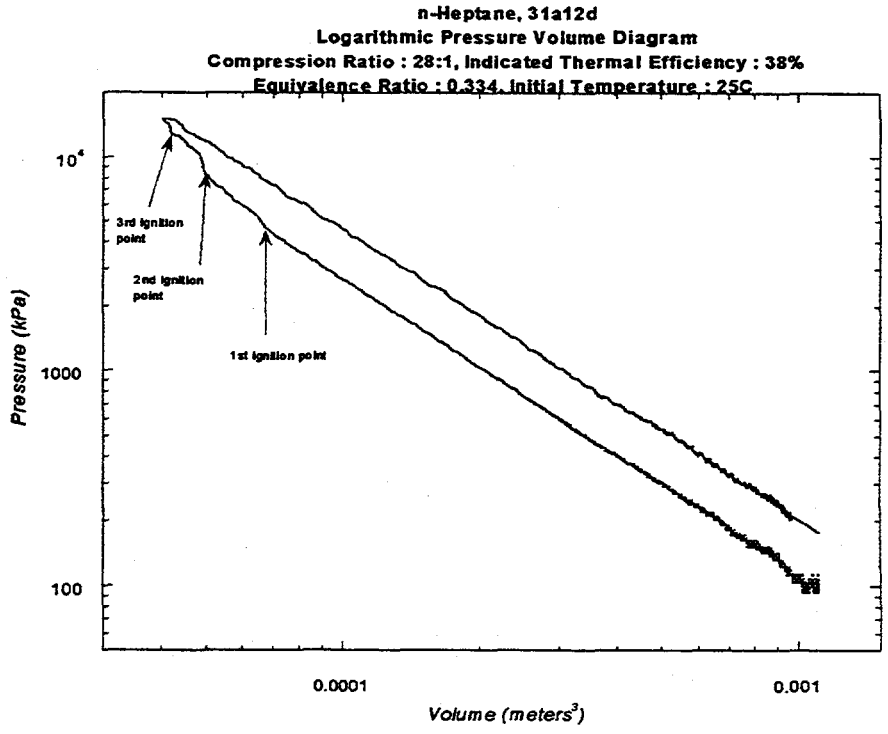

Figure 24

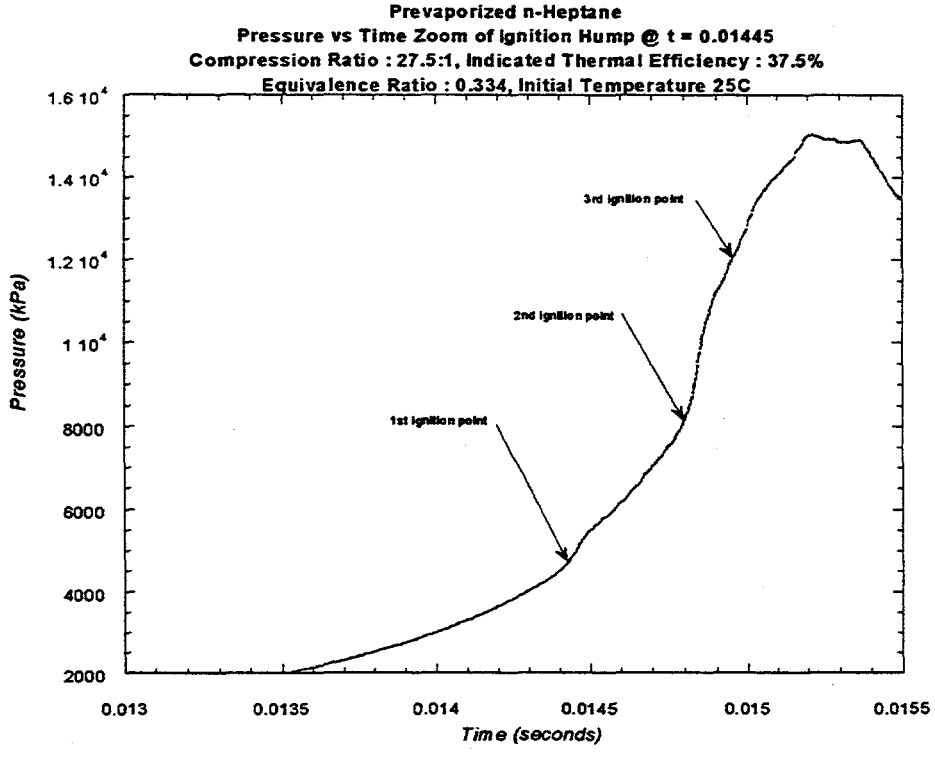

Figure 25

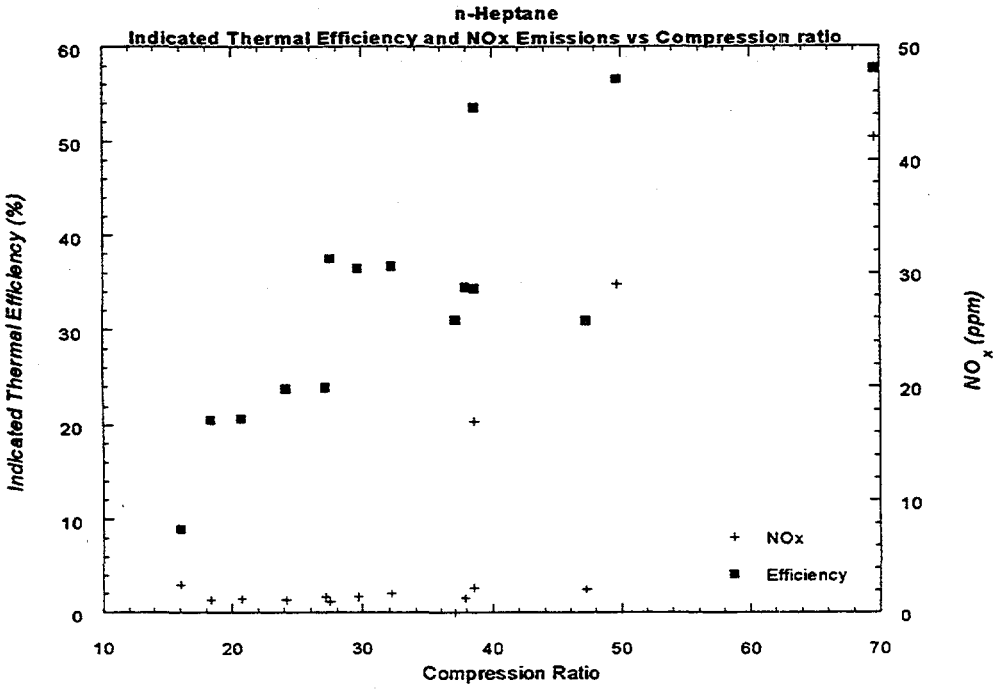

Figure 26

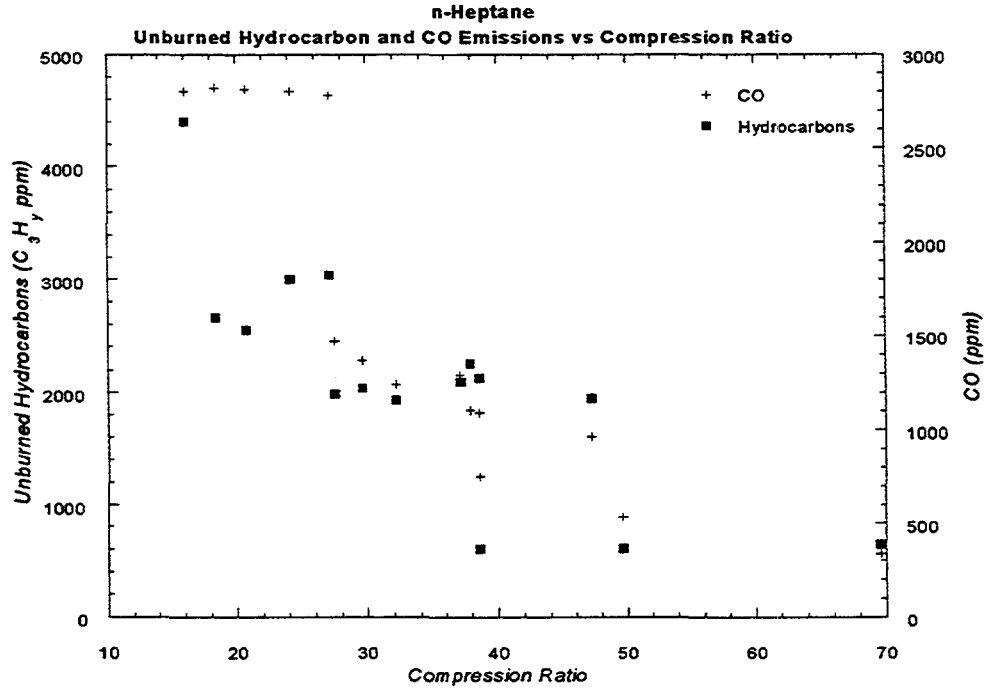

Figure 27

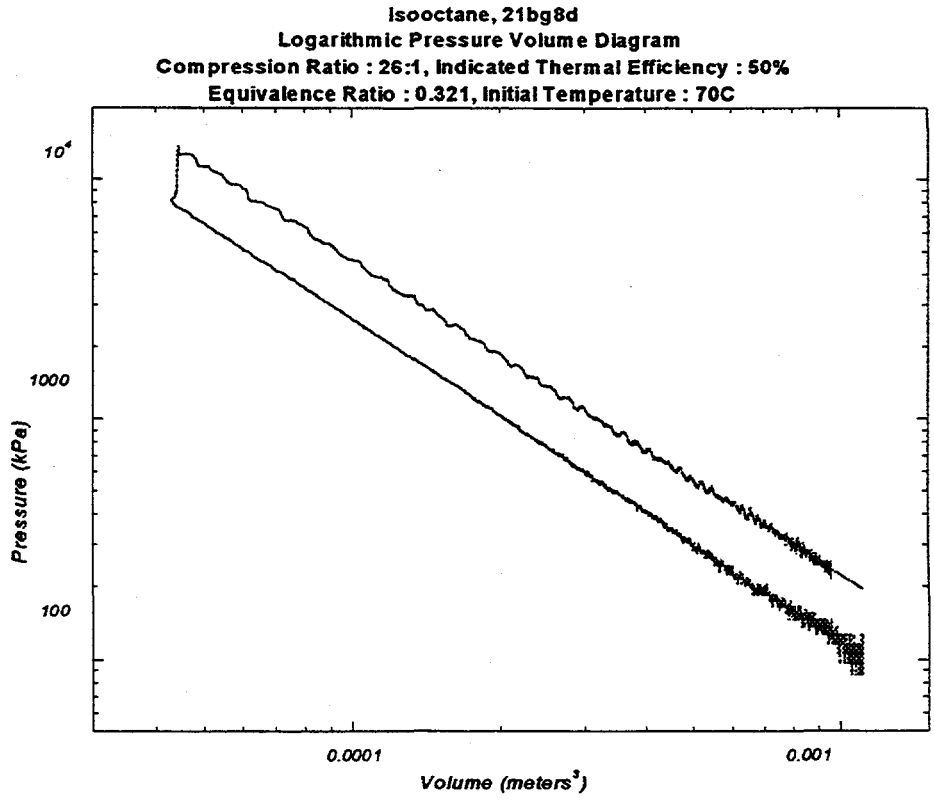

Figure 28

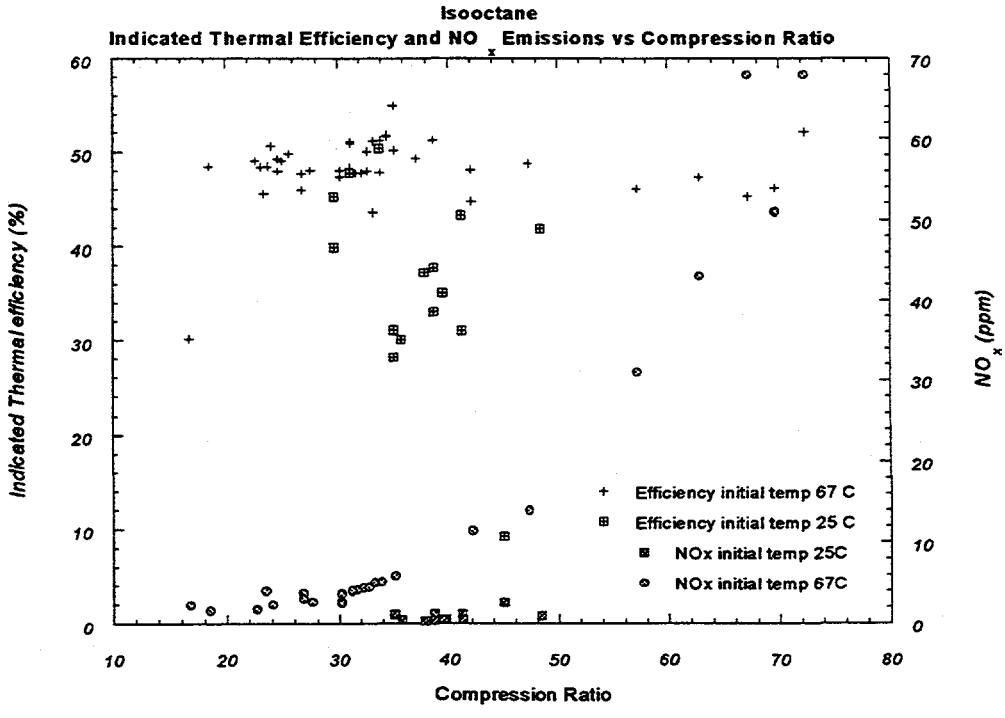

Figure 29

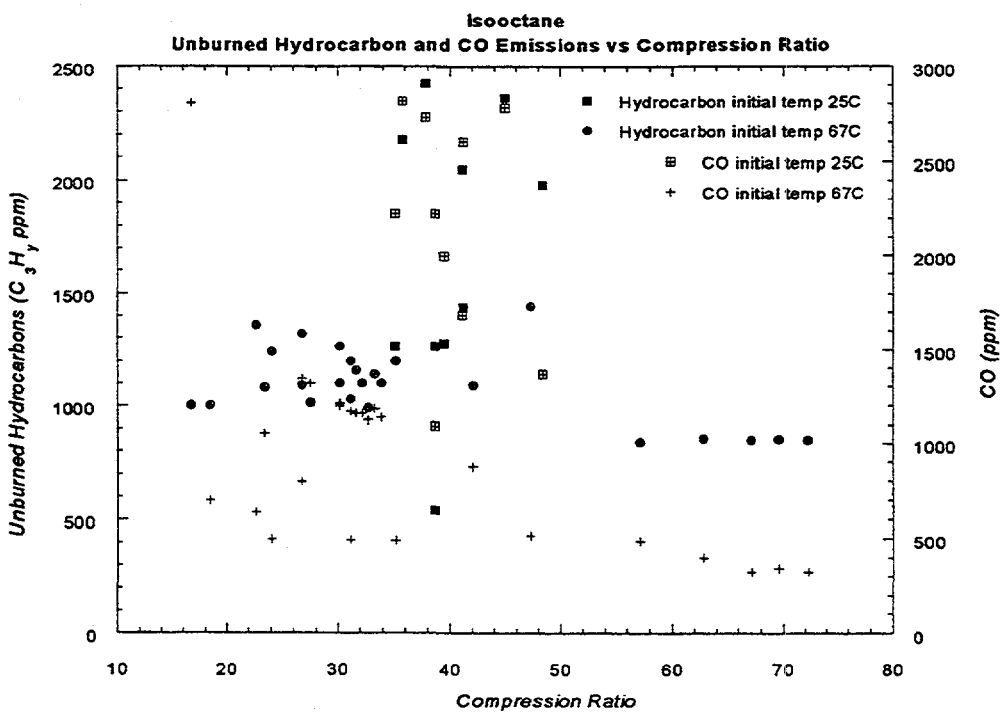

Figure 30

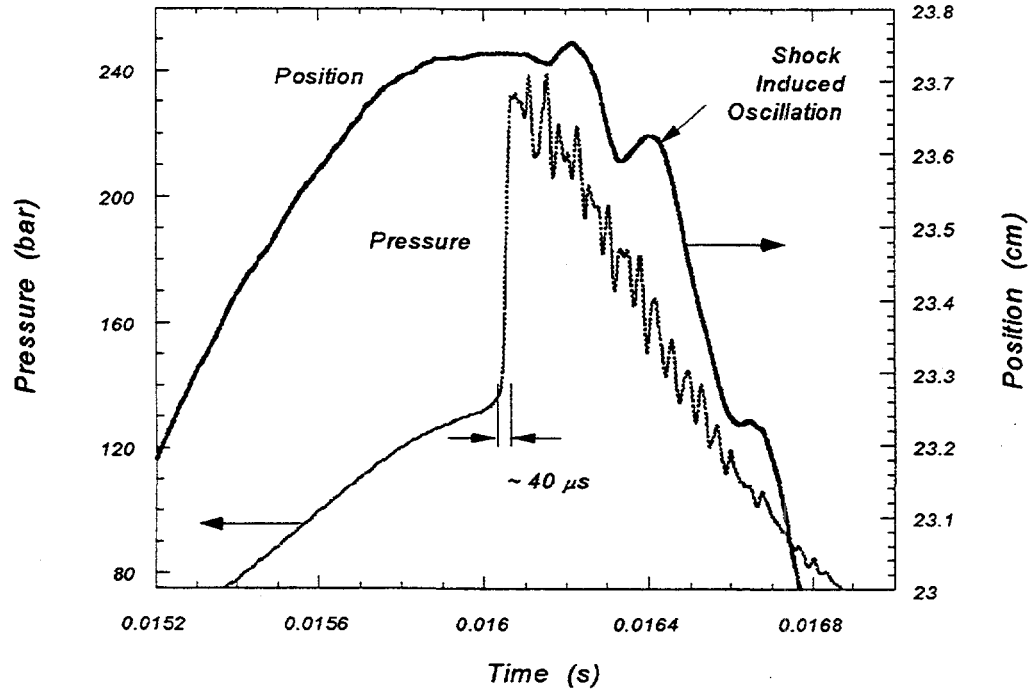

Figure 31

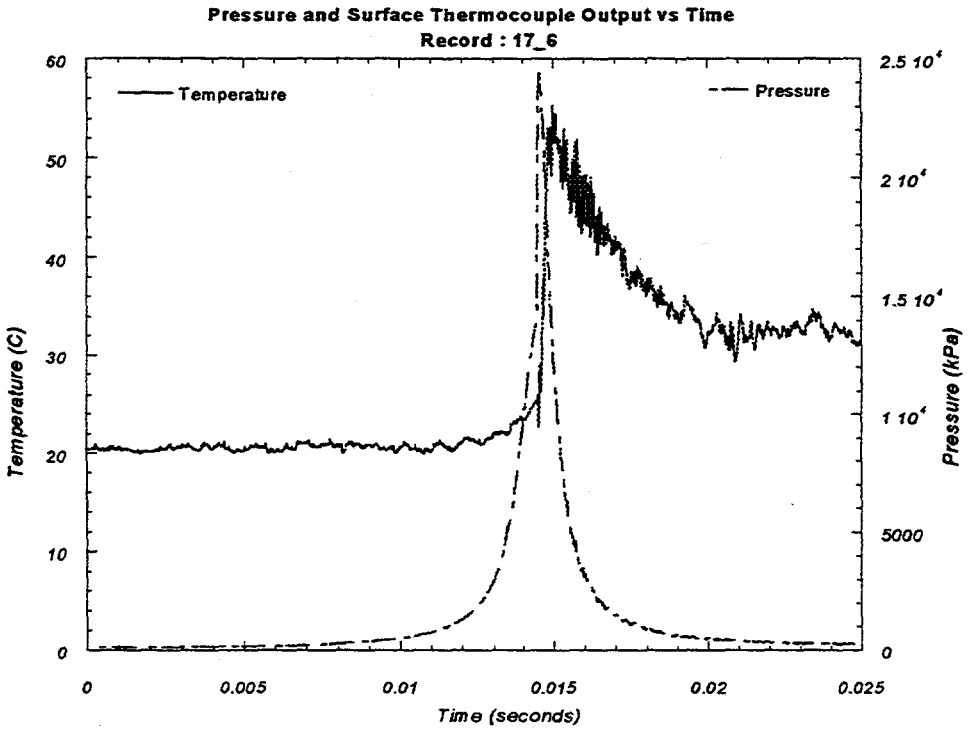
Pressure and Surface Thermocouple Output vs Time
Record : 17_6
Temperature
Pressure
Temperature (C)
Pressure (kPa)
Time (seconds)
60
50
40
30
20
10
0
2.5 10^4
2 10^4
1.5 10^4
1 10^4
5000
0
0.005
0.01
0.015
0.02
0.025

Figure 32

HYDROGEN-ENRICHED FUELS

Ranson Roser
NRG Technologies, Inc.
681 Edison Way
Reno, NV 89502

Abstract

NRG Technologies, Inc. is attempting to develop hardware and infrastructure that will allow mixtures of hydrogen and conventional fuels to become viable alternatives to conventional fuels alone. This commercialization can be successful if we are able to achieve exhaust emission levels of less than 0.03 g/kw-hr NOx and CO; and 0.15 g/kw-hr NMHC at full engine power without the use of exhaust catalysts. The major barriers to achieving these goals are that the lean burn regimes required to meet exhaust emissions goals reduce engine output substantially and tend to exhibit higher-than-normal total hydrocarbon emissions. Also, hydrogen addition to conventional fuels increases fuel cost, and reduces both vehicle range and engine output power. Maintaining low emissions during transient driving cycles has not been demonstrated.

Our approach to overcoming these problems will be to investigate the applicability of know concepts and technologies that can overcome the barriers to success. To recuperate lost engine power, super/turbocharging, and increasing volumetric efficiency, compression ratio, engine speed and displacement are options. Combustion chamber design, valve timing and the "optimization" of tradeoffs between engine power and efficiency with spark timing are also important parameters.

A three year test plan has been developed to perform the investigations into the issues described above. During this initial year of funding research has progressed in the following areas: a) a cost effective single-cylinder research platform was constructed; b) exhaust gas speciation was performed to characterize the nature of hydrocarbon emissions from hydrogen-enriched natural gas fuels; c) three H_2/CH_4 fuel compositions were analyzed using spark timing and equivalence ratio sweeping procedures and finally;

d) a full size pick-up truck platform was converted to run on HCNG fuels. The testing performed in year one of the three year plan represents a baseline from which to assess options for overcoming the stated barriers to success.

Background

The purpose of adding hydrogen to conventional fuels is to extend the lean limit of combustion to the point where harmful exhaust emissions are lowered significantly below the level achievable by existing catalyst technology. Figure 1 shows a graphical representation of this principle. Figure 1 shows a region where increases in excess air in a combustible mixture result in a reduction in oxides of nitrogen (NO_x), carbon monoxide (CO), and total hydrocarbons (THC). The reduction in NO_x is a function of a reduction in peak combustion temperature as the excess air increases the specific heat of the combustible mixture. The reduction in CO and THC results from more complete combustion as the fuel easily and more completely reacts with the greater abundance of oxygen. However, a point is reached in which increases in excess air critically weakens the combustible mixture strength. This reduction in mixture strength results in a decline in combustion stability that induces a rapid increase in THC which is known as the lean limit of combustion.

Figure 1. Lean Burn Emissions Trends

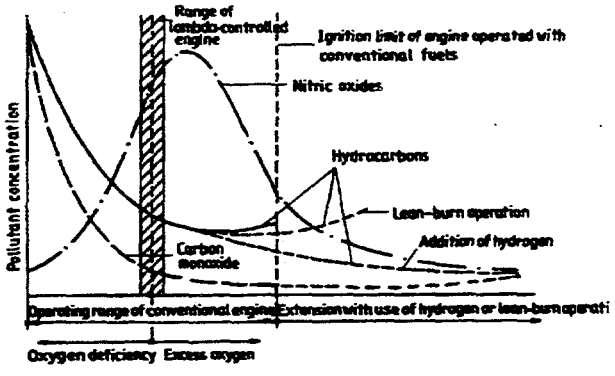

For conventional fuels operating in conventional engines, the emissions of NO_x cannot be reduced sufficiently using lean burn strategies to out-perform commercial catalyst technology. The addition of hydrogen to conventional fuels increases the volatility of the combustible mixture and allows stable combustion to occur in extended lean regimes that would otherwise not be possible. This extension of the lean limit with hydrogen allows an extension of the NO_x reduction trend with increasing amounts of excess air depicted in Figure 1. The question is, "How much hydrogen must be added to achieve desired exhaust emissions?"

Previous work in this area was performed by the NRG Technologies staff while at the Florida Solar Energy Center (Collier, et al 1996). Figure 2 from this work shows the total hydrocarbon emissions as a function of equivalence ratio and percent of the volume of fuel mixture that is hydrogen. The base fuel is natural gas, consisting of 96% methane, and the engine is a Ford 4.6L V8. Notice that as hydrogen is added to the base fuel, the

rapid rise in hydrocarbon emissions occurs at greater amounts of excess air (lower equivalence ratio). An anomaly is apparent in that 10 and 20 percent hydrogen acted similarly, as did 30 and 40 percent. The major extensions of the lean limit occurred between 0 and 10, 20 and 30, and 40 to 50 percent hydrogen. A highlight from that work was the achievement of < 0.05 g/kWh for bmeps up to 500 kPa and rpms above 1700 due to the extension of the lean burn limit with 30% H_2.

Figure 2. THCs As a Function of H_2 and Equivalence (From Collier et. al.)

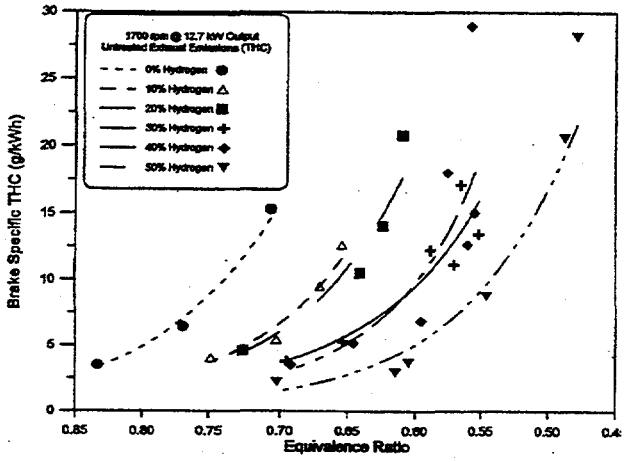

Other research dealing with hydrogen-natural gas mixtures and lean burn has been conducted. The Bartlesville Energy Research Center (Eccleston 1972) and a joint project between Hydrogen Consultants, Inc. and Colorado State University (Fulton 1993) have published results. The BERC project investigated up to 20%, by volume, of hydrogen supplementation of natural gas. They concluded that:

1. The lean limit of combustion is extended by the addition of hydrogen.
2. The lean limit is not extended sufficiently to obtain exhaust emissions lower than that achieved by catalyst systems with only 20% hydrogen.
3. Exhaust gases are generally less reactive with hydrogen addition.

The HCI/CSU work looked at 15 to 30% hydrogen addition. Although that work looked at many other aspects to hydrogen-natural gas mixtures, one lean-burn result is shown in Figure 3. With retarded spark timing, they were able to produce extremely low NOx emissions with 30% hydrogen mixtures and equivalence ratios below 0.65. These data essentially verify the Florida Solar Energy Center work.

Figure 3. Emissions of HCNG, CNG Fuels and Spark Timings (From Fulton et. al.)

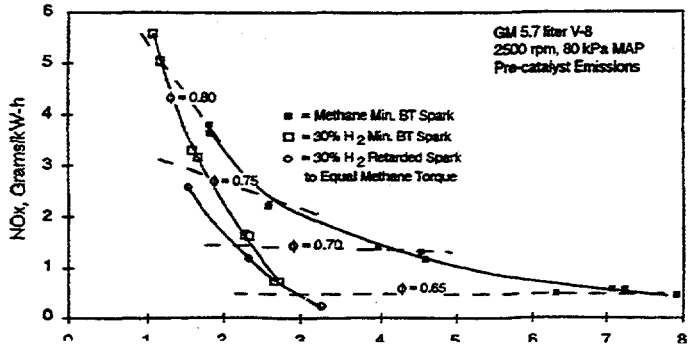

Critical Areas of Interest To Be Investigated During Three Year Project

Relationship Between Hydrogen Content, Spark Timing and Emissions

To be a commercial success, the cost of the fuel must be kept to a minimum. This means that the hydrogen content of the fuel should be minimized. Although the work at FSEC was an important first step, the same degree of thoroughness must be applied to percentages of hydrogen other than 30%.

Photoreactive Hydrocarbon Emissions

Total hydrocarbon emissions are not sufficient to judge the efficacy of the concept. The portion of those emissions that are photoreactive in the atmosphere is the determining factor. At this time, that data is not available, but is critical to the technology.

Recuperating Power Loss

A critical component of any automobile application is driveability. Generally speaking, the amount of power output will be proportional to the amount of fuel burned. Since the air fuel ratio is predetermined to achieve low emissions, the critical factor in determining power output will be the amount of air that can be passed through the engine. For the same amount of air, lean burn engines, will produce less power. To maintain driveability and consumer acceptance, this power loss must be compensated for.

Emissions Verification Under Transient Conditions

Here-to-fore all of the emissions data available for lean bum mixtures of hydrogen and natural gas have been steady state data. Real world driving conditions as well as vehicle certification emissions testing involve transient driving conditions. It is mandatory that low exhaust emissions under transient conditions be demonstrated for the technology.

Engine Design Parameters

Compression ratio, valve timing, piston and cylinder head design, bore-to-stroke ratio, exhaust gas recirculation, and intake air charging strategies are all engine design features that have important effects on engine performance, efficiency, and emissions. The long term potential of any new fuel and emissions control concept cannot be fully assessed until an optimized system is developed. NRG's three year test plan incorporates testing in all of the areas stated above in order to make a fair evaluation of the technology and to use the optimization of these engine design parameters to overcome the barriers to success of lean burn technologies utilizing HCNG fuels.

Summary of Year-One Engine Testing Activities

Test Platform and Instrumentation

This paper reports on the year-one work completion for what is targeted to be a three year program. An initial phase of this work involved the preparation of a cost-effective platform for conducting internal combustion engine research using H_2/CH_4 fuel blends. The platform chosen is a Ford 2.3L engine mounted to a 50 hp eddy-current dynamometer. The 2.3L Ford was chosen because there are a substantial number of aftermarket racing components available for this system. Race components for engines typically involve apparatus for increasing air flow to the engine for the purpose of

increasing power. Therefore, NRG will attempt to use these systems to facilitate lean burn operation while maintaining equivalent power to passenger car systems.

Three of the engine's pistons and rocker arm groups were removed to create a "single-cylinder" arrangement. Intake and exhaust passages were blocked on the three disabled cylinders. Single-cylinder operation was chosen because it is more cost effective in terms of fuel, componentry, and engine modification expenses. It also results in more reliable control of air/fuel ratio parameters which would otherwise be affected by cylinder-to-cylinder distribution inconsistencies common to multi-cylinder engines.

NRG's research revolves around the quantification of an engine's characteristics during varying degrees of lean burn operation. Therefore, much focus was placed on using hardware that would accurately measure air and fuel flow. Air flow is measured by using a laminar flow element system while fuel flow is measured with a Coriolis effect device. The Coriolis device measures gas mass flow directly with no dependency on fuel type, pressure, temperature, or viscosity. Emissions data is taken with nondispersive infrared, chemiluminescent, and flame ionization detectors for CO, NO_x, and THC emissions, respectively.

There are multiple ways of defining the lean limit. While some researches use hydrocarbon emissions as an indication of the lean limit, NRG Technologies uses combustion stability as the determining factor. Therefore, a pressure transducer was mounted in the spark plug and its output was directed into a combustion analysis program. This program calculates the indicated work of individual combustion cycles from PV data and then calculates the average and standard deviation of indicated work for a given series of cycles. The standard deviation in indicated work divided by the average indicated work for a series of cycles calculates the "coefficient of variation" or COV. A COV of 10% is an accepted limit of combustion stability (Heywood year) and has been adopted by NRG as the definition of the lean limit. A COV greater than 10% implies that the engine is running beyond the lean limit and, in an automotive application, that the driver would actually feel the instability.

Engine Testing Methodology

Single-cylinder engine emissions data was taken on 25/75, 30/70, and 35/65 blend ratios of hydrogen and methane, respectively. The testing includes "equivalence sweeps" and "spark maps." Equivalence sweeps were performed by keeping engine load constant and timing at MBT for all points while using air flow as the changing parameter to make sweeps across a range of equivalence ratios. The term MBT is defined as the minimum ignition advance for best brake torque. It essentially represents the ignition timing for optimum thermal efficiency without regards to exhaust emissions. Equivalence sweeps at MBT are useful in that they represent a common baseline by which researches can compare subsequent data. However, commercial automotive engines do not typically have the luxury of operating at MBT because of emissions trade-offs. Therefore, data that illustrates the effects of excess air only is supplemented with ignition mapping data also.

Spark maps were performed by running at designated equivalence ratios using ignition timing as the variable between engine operating points. Adjustments in timing affect emissions, efficiency, and combustion stability. Therefore, the trade-offs among all of these parameters must be assessed before the final "optimal" timing can be determined for any given engine configuration.

Challenge – Hydrogen Not Inherently a Low-NOx Fuel

Hydrogen is often said to be an inherently clean fuel in internal combustion engines because its use eliminates carbon emissions. However, hydrogen burns hotter and faster than conventional fuels which results in higher NO_x emissions when compared at the same equivalence ratios and power output. Figure 4 shows this complication. The two fuels compared are CNG and a 30% hydrogen blend with methane. Both fuels were tested in the single-cylinder research engine at equivalent loads. It can be seen from this case that the HCNG blend can produce more than double the NO_x of CNG at a specific equivalence ratio. Hydrogen's redeeming value, however, is that it allows the HCNG blend to operate far leaner than CNG alone which results in an extension of lean burn's NO_x reducing mechanisms and ultimately a significant reduction in NO_x over CNG.

FIGURE 4. Unoptimized HCNG NO_x Emissions as a Function of Equivalence

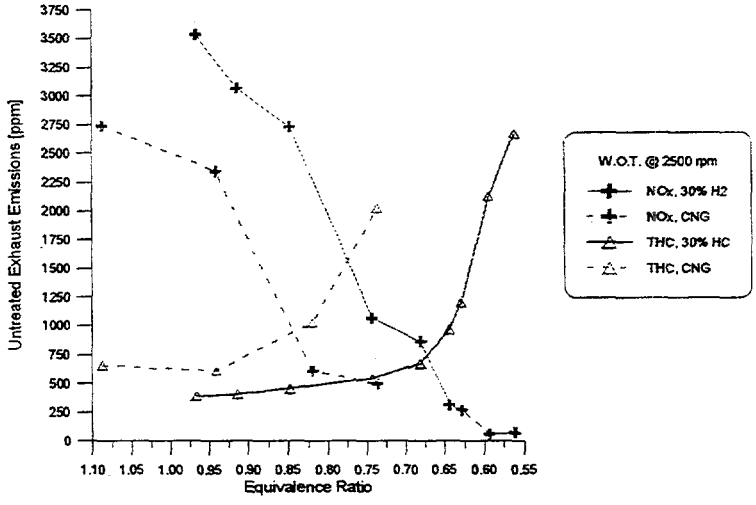

Equivalence (Φ) Sweeps

Equivalence sweeps were performed at 2500 rpm on the single-cylinder engine with 25%, 30%, and 35% H_2 blends. Figures 5 and 6 from these tests show that even the modest H_2 content variations between the three blends tested have quantifiable effects on the lean limit of combustion. Figure 5 indicates that the rapid rise in hydrocarbons associated with the lean limit occur at less excess air when there is less hydrogen in the fuel. Similarly, Figure 6 shows the coefficient of variation plotted against equivalence ratio. At an equivalence = 0.57, the 25% H_2 blend reaches COV = 10% (defined lean limit) whereas the 30% and 35% H_2 fuels are only at COV = 4%. The conclusion that incremental amounts of hydrogen addition have incremental effects on combustion is important. Previous work at FSEC on a Ford 4.6L V8 suggested that a range of H_2 compositions would produce similar results until a H_2 concentration threshold was broken that would produce and observable shift in combustion characteristics.

Figure 5. THC Vs. Equivalence

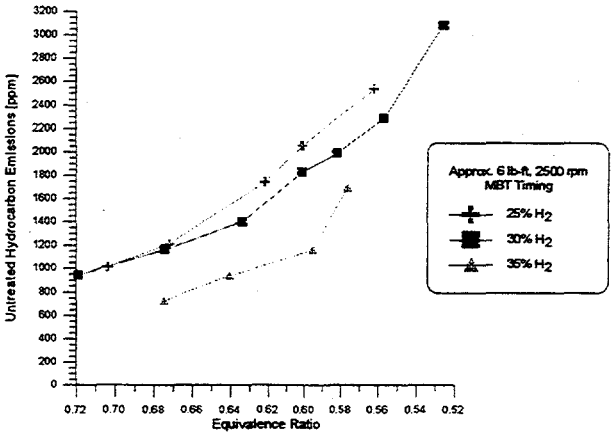

Figure 6. COV Vs. Equivalence

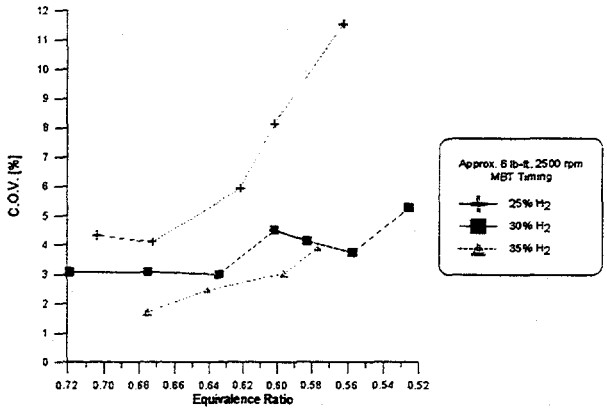

Speed and Load Effects on Combustion

Figure 7 shows the effects of speed and load on combustion stability for 25% and 35% hydrogen blends. Note when comparing equivalent loads that there is always an extension of the lean limit with more hydrogen. Also, increasing the load increases the engine's ability to operate at leaner conditions. This suggests that lean burn power recuperation techniques will aid in the goal of extending lean burn combustion stability. Figure 7 suggests increased engine speed will also be a mechanism to achieve leaner operating points also.

Figure 7. H_2 Content, Speed, and Load Relationships

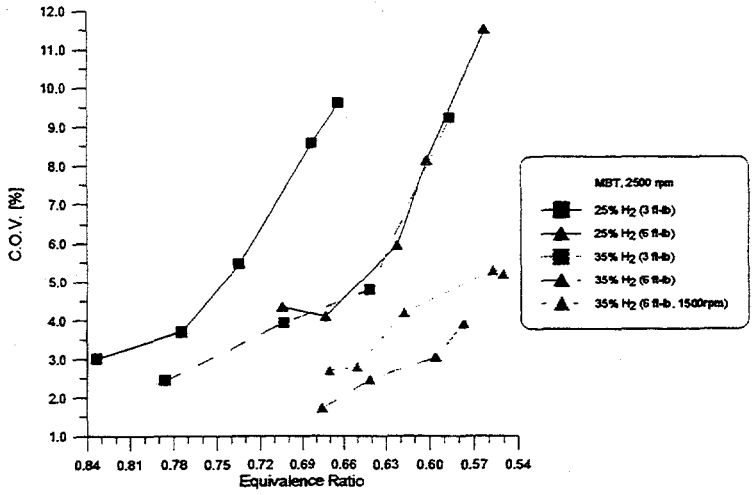

Spark Map Testing

Figure 8 shows the affects of ignition timing on NOx emissions for 25%, 30%, and 35% H_2 fuel blends each run at different equivalence ratios. A very important principle becomes apparent. The tendency for NOx to be reduced by an engine operating at leaner conditions with the aid of increased hydrogen can overcome hydrogen's propensity to increase NOx emissions. For instance, 35% H_2 at $\Phi = 0.61$ produces less NOx than 30%

H_2 at $\Phi = 0.65$ which subsequently produces less NOx than 25% H_2 at $\Phi = 0.70$ over the entire timing sweep range. If equivalence and timing were equal for the three fuels, then more H_2 would equate to more NOx.

Figure 8. NO_x as a Function of H_2, Timing, and Equivalence at 2500 rpm

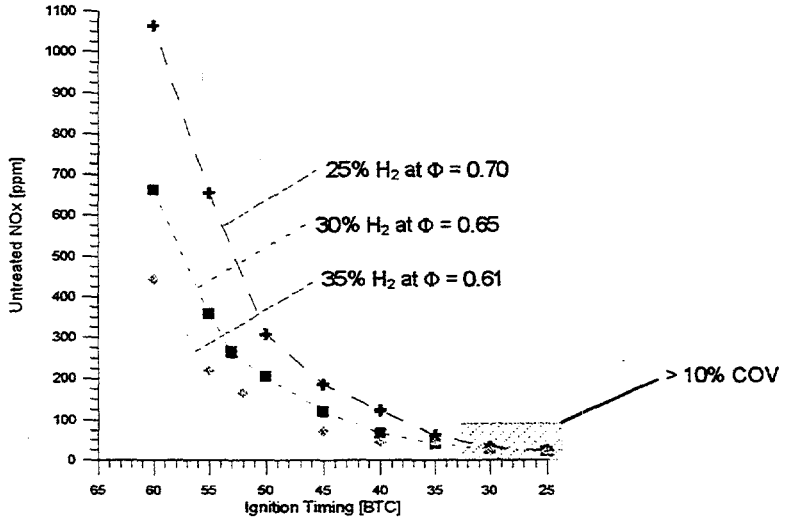

Figure 9 is another spark map set taken at 1500 rpm between 25% and 35% H_2. This data shows another important feature of hydrogen-enriched fuels. If NO_x reductions from hydrogen enrichment are the goal, then the engine must capitalize on incremental lean limit extensions with hydrogen addition in order to make the goal be successful. Even though the 35% H_2 blend was run leaner at $\Phi = 0.615$ than 25% H_2 at $\Phi = 0.64$, it produced no NO_x benefits over the ignition timing range. Note, however, that when 35% H_2 was run at $\Phi = 0.55$ that the NO_x benefits are substantial, especially at the more advanced timing points. This is important because retarding timing to reduce NOx has limitations as efficiency trade-offs are encountered.

Figure 9. NO_x as a Function of H_2, Timing, and Equivalence at 1500 rpm

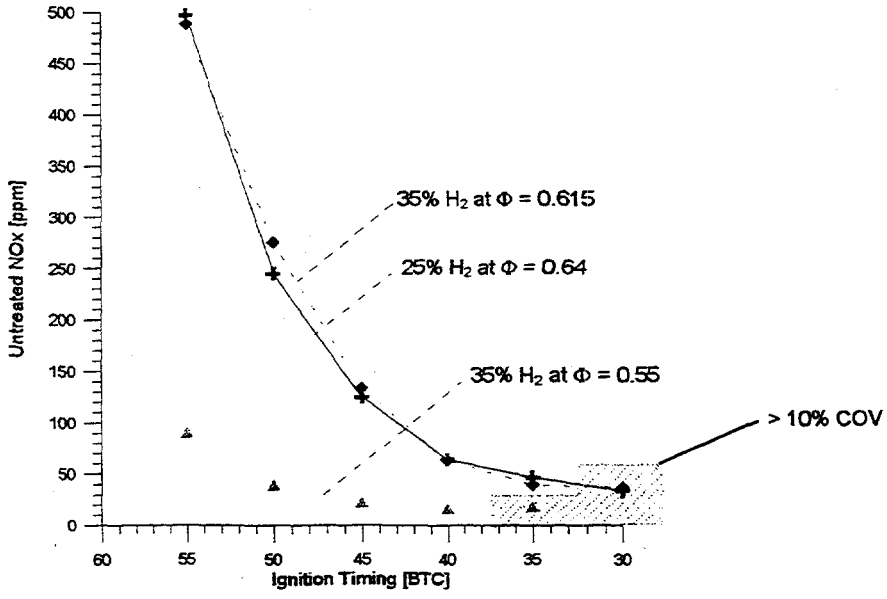

Initial Intake Boost Test

Although testing under intake air boost conditions is not scheduled to be a "year one" task, NRG constructed an external supercharging system shown in Figures 10 and 11. An Eaton supercharger was mounted and powered independent of the engine because of the overwhelming parasitic losses that would occur if a supercharger designed for a multi-cylinder engine were placed on a four cylinder assembly that is actually running only one piston. The supercharger is powered by a 5 hp electric motor. An inverter controls motor speed and hence boost out of the supercharger.

Figure 10. Motor Driven Supercharger

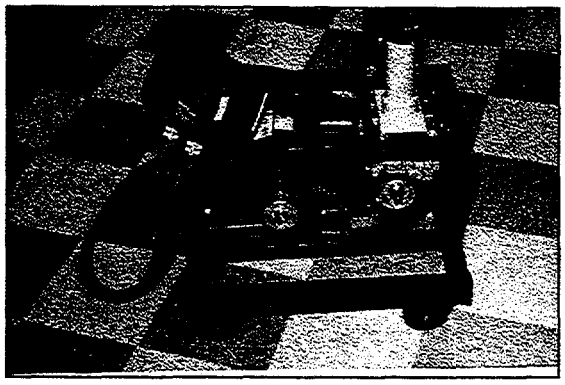

Figure 11. External Supercharger Setup

Only one 25% H_2 emissions test was performed by the time of this report but the initial results shown in Figure 12 demonstrate an important issue to be scrutinized in future power recuperation investigations. The supercharged run with about three times the load produced more NO_x than the naturally aspirated run over the entire spark map even though it was run at a much leaner condition. The higher NO_x emissions at the much leaner condition are believed to be attributable to the fact that an intercooler was not incorporated into the original supercharger setup. Running at steady-state for long periods to stabilize emissions allowed the supercharger to create "runaway" intake air temperature rise conditions because the air was the only heat sink to cool the supercharger's rotors. Higher intake air temperatures before combustion lead to higher NO_x emissions in the exhaust. Therefore, this initial exercise illustrated that laboratory supercharging tests in the future would require intercooling in order to properly assess the impacts of superchargers as power recuperation techniques on NO_x emissions.

Figure 12. Early Intake Boost Test Results

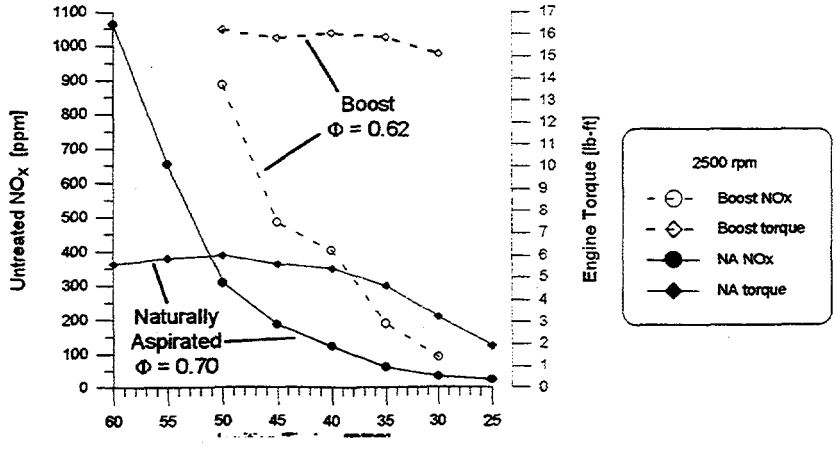

Exhaust Gas Speciation

Natural gas does not consist solely of methane. The other significant hydrocarbon constituents of natural gas are ethane and propane. Because the amounts of these other constituents in natural gas can vary significantly with location and time of year, a series of tests were conducted to speciate hydrocarbon emissions. The purpose of the tests was to determine the relationship between exhaust gas and natural gas hydrocarbon composition and to identify the existence of any new, photoreactive compounds created during the combustion process.

Six gas mixtures, all containing 30% hydrogen, were prepared with varying combinations of propane, ethane, and methane. Each test was conducted with an equivalence ratio such that the total hydrocarbon emissions measured were about 1800 ppm. Gas speciations were performed by Desert Research Institute (DRI) in Stead Nevada using gas chromatograph with FID technology. The fuel gas compositions and a complete tabulation of speciation results are shown in Table 1. The major finding from these data is that ethene emissions are produced without the presence of either ethane or propane and they are increased by the presence of both ethane and propane. Significant propene emissions only occur if propane exists in the fuel. It also appears that ethane emissions are created simply from the combustion of methane. For all tests without ethane in the fuel, ethane exhaust emissions of about 10 ppm were observed.

Table 1. Hydrocarbon Speciation of Six Fuel Compositions

Fuel*	0% propane 0% ethane	8% propane 0% ethane	4% propane 0% ethane	0% propane 8% ethane	0% propane 4% ethane	4% propane 4% ethane
Methane (ppm)	1,226.0	1,264.2	1,238.5	1,612.1	1,459.0	1,821.6
Ethane (ppm)	10.3	11.3	10.2	210.3	89.1	113.6
Ethene (ppm)	13.8	38.1	24.2	51.3	28.9	47.4
Propane (ppm)	0.3	140.6	60.7	0.5	0.3	102.1
Propene (ppm)	1.7	17.2	8.6	1.8	1.5	10.9
Acetylene (ppm)	1.6	3.9	3.0	3.2	2.2	3.7
Isobutane (ppm)	0.0	0.2	0.1	0.0	0.0	0.1
Butane (ppm)	0.0	0.0	0.0	0.0	0.0	0.0
Trans-2-Butene (ppm)	0.1	0.1	0.1	0.1	0.1	0.1
1-Butene (ppm)	0.4	0.8	0.6	0.4	0.4	0.6
Isobutene (ppm)	0.3	0.3	0.3	0.3	0.3	0.3
Cis-2-Butene (ppm)	0.1	0.0	0.0	0.1	0.1	0.0
Isopentane (ppm)	0.0	0.0	0.0	0.0	0.0	0.0
Pentane (ppm)	0.0	0.0	0.0	0.0	0.0	0.0
1,3-Butadiene (ppm)	0.3	0.4	0.2	0.3	0.2	0.3
Hexane (ppm)	0.0	0.0	0.0	0.0	0.0	0.0
* All fuel mixes contained approximately 30% hydrogen and the balance methane.						

Figure 13 shows the relationship between ethane and propane composition of the fuel and their composition in the exhaust gas hydrocarbon emissions. The propane fraction of total hydrocarbon exhaust emissions is very nearly equal to that contained in the fuel.

Ethane emissions are slightly higher. If the ethane emissions due to methane combustion are subtracted from the total, the ethane fractions are also are nearly equal. In either case, the fractional compositions of both ethane and propane, between exhaust and fuel are linear.

Figure 13. Analysis of Propane and Ethane Present In Exhaust

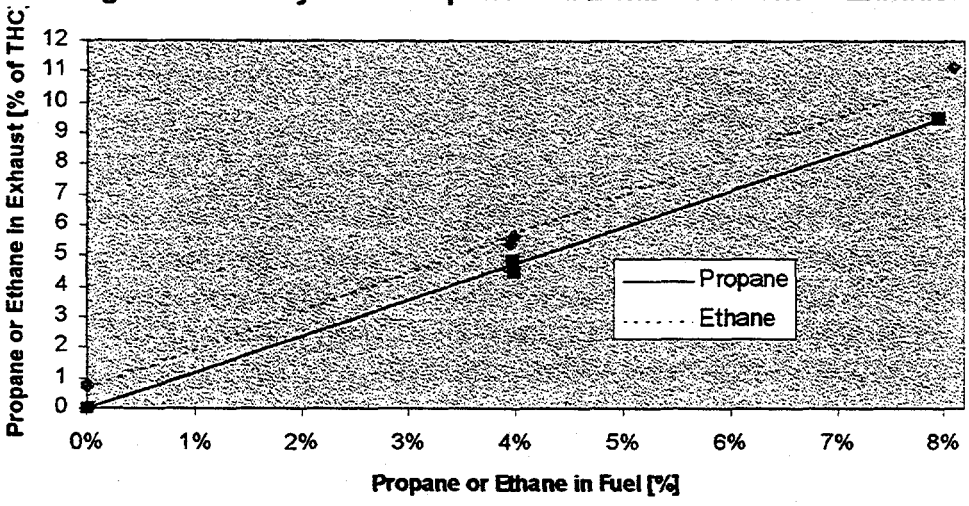

Truck Conversion

NRG was tasked to convert a full-size pickup truck to operate on HCNG fuels for use as a real-world platform to test the HCNG technology advancements expected to be made in the laboratory. NRG has converted a gasoline 1997 Ford F-150 pickup truck to run on gaseous fuels. This truck is currently controlled with an aftermarket engine computer. In October 1997 it was demonstrated at a ride-and-drive event at the Las Vegas Motor Speedway during a Memorandum of Understanding signing between the U.S. Department of Energy and LVMS (Figures 14, 15). Good reviews were received from the participants that drove the truck around the track on 30% hydrogen. As power recuperation techniques are developed on the single-cylinder laboratory engine, they will be incorporated into this platform.

Figure 14. LVMS Ride-&-Drive

Figure 15. MOU Signing With NRG Truck

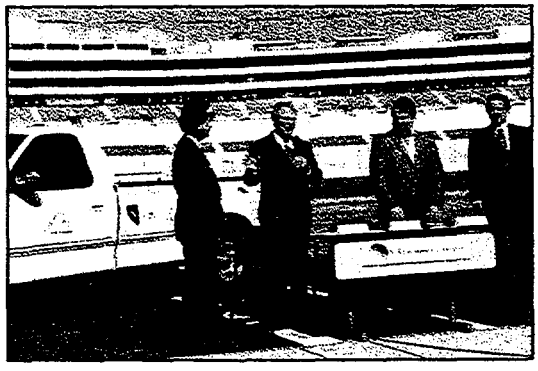

Summary

This report summaries the first year of research activities by NRG Technologies, Inc. in what is outlined to be a three year program developing engine technology for hydrogen-enriched fuels. A single-cylinder engine was created out of a Ford 2.3L four-cylinder platform and mounted to a 50 hp eddy current electric dynamometer. The engine is instrumented to make very accurate air and fuel measurements for quantification of equivalence ratio at all operating points. In-cylinder combustion data is used to quantify combustion stability for determination of the lean limit.

Engine emissions testing was performed at 2500 and 1500 rpm with data representing over 100 individual operating conditions. The effects of varying excess air at constant load and MBT timing with 25%, 30%, and 35% hydrogen supplementation to methane showed that even these 5% variations in hydrogen had observable impacts on combustion stability in lean regimes. Ignition mapping data demonstrates very clearly that adding hydrogen to extend lean burn capabilities reduces NO_x emissions at a greater rate than the tendency of NOx emissions to rise with increases in hydrogen at equivalent excess air ratios. Furthermore, the ignition mapping data suggests that maximum emissions reductions can be gained if engines fully capitalize on the extensions in the lean limit that the added hydrogen can provide.

Exhaust speciation of hydrocarbon emissions from a 30% hydrogen fuel blend was performed by Desert Research Institute in Stead, Nevada. The results showed a linear relationship between both the propane and ethane content in the fuel and the content of these gases in the exhaust hydrocarbons. In addition, the relative methane, ethane, and propane composition in the exhaust gas were almost equal to that of the fuel.

A 1997 Ford F-150 pick-up with a 4.6L V8 was converted by NRG Technologies, Inc. to operate on hydrogen-enriched natural gas mixtures. The truck represents an applications platform for engine development concepts that will be learned from the single-cylinder engine testing during the three year project.

Future Work

NRG's statement of work for year two and three includes continuation of ignition mapping data with multiple fuel compositions. Assessment of alternative engine design work will begin with combustion chamber design, compression ratio, and EGR strategies in year two and will move on to intake air charging and special coatings in year three. Advancements discovered in the single-cylinder development process will be applied to the Ford F-150 throughout the program for real world evaluation.

References

Collier, K., et. al., "Untreated Exhaust Emissions of a Hydrogen-Enriched CNG Production Engine Conversion," SAE Technical Paper Series 960858, International Congress and Exposition, Detroit, Michigan, February 26-29, 1996.

Eccleston, D.B., and R.D. Fleming, "Engine Emissions Using Natural Gas, Hydrogen-Enriched Natural Gas, and Gas Manufactured from Coal (Synthane)," Bureau of Mines Automotive Exhaust Emissions Program, U.S. Department of Interior, Technical Progress Report-48, 1972.

Fulton, J., et. al., "Hydrogen for Reducing Emissions from Alternative Fuel Vehicles," SAE Technical Paper Series 931813, Future Transportation and Technology Conference, San Antonio, Texas, August 9-12, 1993.

ADVANCED CHEMICAL HYDRIDE-BASED HYDROGEN GENERATION/STORAGE SYSTEM FOR FUEL CELL VEHICLES

Ronald W. Breault and Jon Rolfe
Thermo Power Corporation
45 First Avenue
Waltham, MA 02254-9046

Abstract

Because of the inherent advantages of high efficiency, environmental acceptability, and high modularity, fuel cells are potentially attractive power supplies. Worldwide concerns over clean environments have revitalized research efforts on developing fuel cell vehicles (FCV). As a result of intensive research efforts, most of the subsystem technology for FCV's are currently well established. These include: high power density PEM fuel cells, control systems, thermal management technology, and secondary power sources for hybrid operation. For mobile applications, however, supply of hydrogen or fuel for fuel cell operation poses a significant logistic problem.

Currently, various technologies have been considered to provide hydrogen for FCV's. These technologies can be conveniently classified into two categories: (1) onboard fuel processing wherein liquid fuel stored on the vehicle undergoes reformation and subsequent processing to produce hydrogen; and (2) onboard storage of pure hydrogen provided by stationary fuel processing facilities. Onboard liquid hydrocarbon reforming provides an attractive way to supply hydrogen at a high system power density. In high temperature fuel cells, such as solid oxide fuel cells, low molecular weight hydrocarbons may be used directly via direct internal reforming. However, these types of fuel cells are not suitable for fuel cell vehicles, since they may require frequent on/off cycling. Although there has been limited success in direct methanol powered PEM fuel cell technology, the fuel crossover and CO poisoning still pose significant problems, and long term performance is yet to be demonstrated.

Over the last ten years, there have been extensive efforts to develop a reforming process to produce hydrogen from liquid fuels. As a result, numerous hydrocarbon reforming processes have been established. However, the product gas streams usually contain high levels of contaminants, such as CO. The presence of CO in the fuel gas stream is harmful to many fuel cells, especially PEM fuel cells, since the performance of the PEM fuel cell is substantially degraded over a short period of time via the catalyst poisoning. Despite costly efforts, limited success has been achieved to control the CO content in the fuel gas stream. We believe that the conventional approach to reform liquid hydrocarbons to produce hydrogen cannot meet the stringent requirements in fuel quality for the PEM fuel cells.

A great many technologies have also been investigated as candidates for the onboard storage of pure hydrogen for FCV's. These technologies include: (1) compressed hydrogen; (2) liquefied hydrogen; (3) rechargeable metal hydride; (4) carbon adsorption and hybrid systems; and (5) liquid hydrides and other chemical hydrides. However, the volume and/or weight energy densities of these onboard hydrogen storage technologies are significantly lower than those of internal combustion engines or the DOE hydrogen plan. Therefore, development of a high energy density subsystem to supply hydrogen for a fuel cell operation is an urgently needed technology for the successful development of FCV's.

To supply high purity hydrogen for FCV operation, Thermo Power's Advanced Technology Group is developing an advanced hydrogen storage technology. In this approach, a metal hydride/organic slurry is used as the hydrogen carrier and storage media, as shown in Figure 1. At the point of use, high purity hydrogen will be produced by reacting the metal hydride/organic slurry with water. In addition, Thermo Power has conceived the paths for recovery and regeneration of the spent hydride (practically metal hydroxide). The fluid-like nature of the spent hydride/organic slurry will provide us a unique opportunity for pumping, transporting, and storing these materials. The final product of the program will be a user-friendly and relatively high energy storage density hydrogen supply system for fuel cell operation. In addition, the spent hydride can relatively easily be collected at the pumping station and regenerated utilizing renewable sources, such as biomass, natural, or coal, at the central processing plants. Therefore, the entire process will be economically favorable and environmentally friendly.

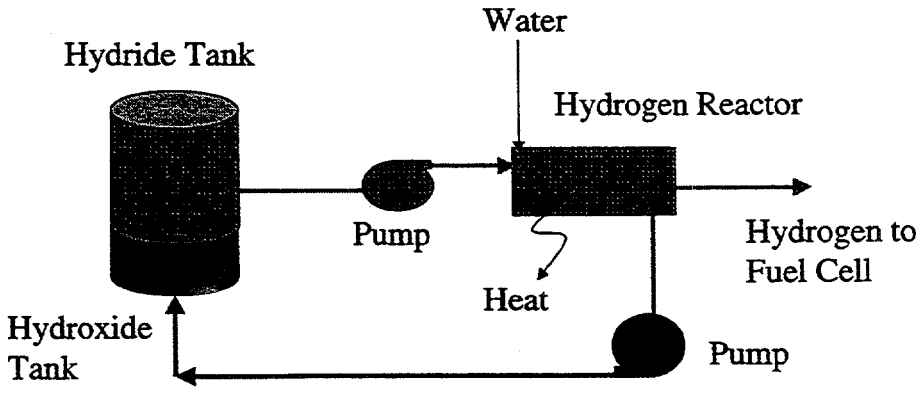

Figure 1. Vehicle Concept

Technology Development Areas

Overall Background and Technical Approach

Hydrogen (H_2) has been suggested as the energy carrier of the future. It is not a primary energy form, but rather serves as an energy carrier through which a primary energy source can be transmitted and utilized. Hydrogen has a number of advantages as an energy carrier, but several problems restricting widespread use of H_2. These include: (1) poor energy storage characteristics; and (2) relatively high production cost compared to fossil fuels. For example, specific weight and specific volume of the most hydrogen storage technologies, currently available and advanced future technologies, are not suitable for transportation applications. Some advanced technologies may satisfy the requirements of the DOE hydrogen plan. However, operational energy loss and infrastructure requirements may not be appropriate for transportation applications in the near future. Pros and cons of the currently available and advanced hydrogen storage technologies, along with expected performance of the proposed technology, are summarized in Table 1. A plot showing how chemically reacting hydrides compare with other fuels is shown in Figure 2.

Table 1. Hydrogen Storage Technology Status

Storage Technology	Specific Weight (HHV)		Specific Volume (HHV)		Remarks
	Wh/kg	$\%H_2$	Wh/L	kg H_2/m^3	
DOE Goal:					
• Liquid/Gas	3963/5323	9.9/13.4	1100/828	28/21	DE-RA02-97EE50443
Liquid H_2:					
• Cryogenic	6350	16.1	1250	32	Not including boil-off loss
Gaseous H_2:					Could be better with new
• 5000 psia	2630	6.7	780	20	high-pressure tanks
Carbon Adsorption:					New materials with better
• 794 psi at 78°K	2858	7.2	1535	39	capacities
Liquid Hydride:					Need more fundamental
• Methylcyclohexane	2070	5.9	1618	46	research
Proposed Chemical Hydride Slurry:					Includes weight and volume of the container, and ancillary components. Does not include reactant water which is assumed to be provided partially from exhaust gas
• CaH_2	2670	6.8	2430	62	
• LiH	5050	12.8	2430	62	
• $LiBH_4$	4760	12.1	2570	65	

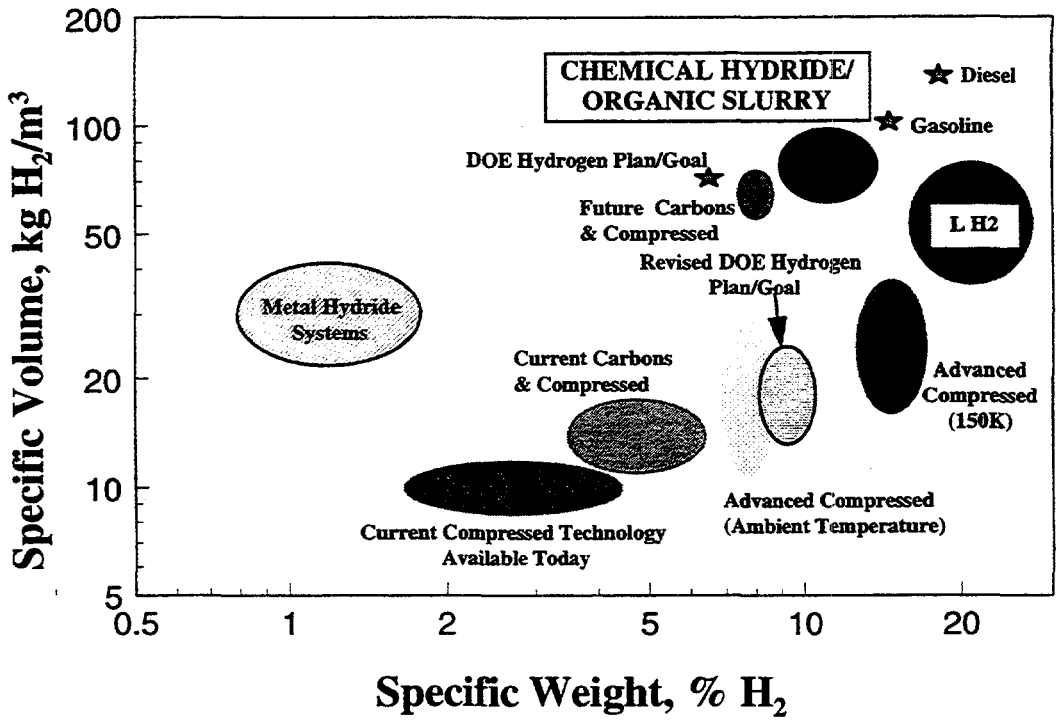

Figure 2. Summary of Current and Future Hydrogen Storage Systems

This new approach greatly improves the energy transmission and storage characteristics of H_2 as a fuel for transportation and industrial applications. An essential feature of the approach is to develop a relatively high energy storage density hydrogen supply system based on exothermic chemical reactions between metal hydrides and water. Hydrogen production via metal hydride and water reactions is a well-established industrial process. In fact, several groups of researchers have investigated the metal hydride/water reaction process to supply hydrogen for fuel cells for mobile power generations. In this research, it has been identified that reaction rate control, frequent on/off operation, and safety of the operation could be significant problems for high energy density operations.

One of the key technical challenges in the program is, therefore, to precisely control the metal hydride and water reaction. In the program, the continuous organic slurry media will act as a path for dissipating heat that is generated from hydride/water reaction. Furthermore, by controlling surface chemistry with the organic media, the water-metal hydride reaction rate can easily be controlled. In addition, Thermo Power has conceived the paths for recovery and regeneration of the spent hydride. Feasibility of the spent hydride regeneration, economical analysis, and engineering design of these processes will be conducted by Thermo Power under different DOE funding.

There are several factors needing consideration in hydride selection and storage system design. As an example, CaH_2 has been selected to illustrate some of the technical aspects and advantages of the concept, even though it does not have the highest volumetric or gravimetric energy density

of the hydrides (Table 1). These advantages include low raw stock (calcium hydroxide) material cost, and ready availability of technical information on properties of materials and process reactions. Regarding safety, CaH_2 is highly ionic and insoluble in all common inert solvents. It can be handled in dry air at room temperature without difficulty. Only when heated to about 900°F will it react with air to form both calcium oxide and calcium nitride. CaH_2 is substantially inert to organic compounds that do not contain acidic hydrogen. CaH_2 reacts vigorously with water to form calcium hydroxide and hydrogen gas. Calcium hydroxide is slaked lime and non-hazardous. It is a component of mortar, plaster, cement, and other building materials, and widely used without difficulty.

One method of using hydride/water reactions as a source of pure hydrogen for vehicular applications is to pump a slurry into the vehicle as shown previously in Figure 1. Use of the slurry would permit refueling similar to current gasoline filling stations. The used reactant slurry containing the LiOH for a lithium hydride-based system is pumped out and returned to the fueling station. By providing a flexible bladder in the tank, the original and the spent hydride will never contact each other. In this way, the tank can easily be topped-off at any time.

Once in place, hydrogen will be generated on demand by water flow rate regulation to the reaction chamber. The pure hydrogen will be used in the fuel cell, producing water. This water will be collected and recycled as produced to use for additional hydrogen generation. Only a small water reservoir is thus required to even out surge demands and provide makeup for water lost and not recycled. The required water does not significantly affect the volumetric and gravimetric energy storage densities.

The used reactant slurry containing LiOH is returned to a central processing plant where the LiOH is recycled to LiH in a large scale chemical process. The LiH is remixed with the slurry fluid and transported back to refueling stations scattered over a large area as needed. The basic energy input to the system is provided at the central plant and can be from a variety of energy sources, including fuels like coal, biomass, natural gas, and petroleum oil. All environmental emissions occur at the central processing plant. The vehicle is zero emission, with no hydrocarbon, CO, or CO_2 emissions. The central plant can include more sophisticated emission cleanup processes than would be possible for an on-board processing system.

An important concept feature that needs to be pointed out, which is not part of this proposal effort, is the recovery and recycle of the spent hydride at centralized processing plants using a low cost fuel, such as coal or biomass. This regeneration effort is reported elsewhere and summarized here. The regeneration process analysis has indicated that recycling can be performed utilizing a carbothermal process with minimum energy input and at a low cost. Compared to current hydrogen costs of about $9.00 to $25.00 per million Btu, this concept should enable hydrogen costs of $4.00 per million Btu to be realized (Breault et al, 1998). Also, because the hydride reaction will liberate only pure hydrogen, fuel cell catalyst life should be maximized, resulting in high system performance and reliability.

Anticipated Results and Commercial Potential

At the completion of the proposed program (30 months), DOE will have a prototype system which can supply 3.0 kg/hr of pure hydrogen for fuel cell operation (50 kW electric power equivalent, assuming 50% fuel cell efficiency). This system will include: (1) ports and pump for hydride/organic slurry charge/discharge, a water addition device, a water/hydride reactor, a pressure/temperature measurements and control unit, and a connecting port to fuel cell stack. A race for the development of zero emission vehicles has already begun across the globe. Developing a reliable hydrogen source for fuel cell operation is the most serious technical challenge in developing fuel cell vehicle technology. Thermo Power's advanced metal hydride-based hydrogen supply system will fully satisfy all the requirements for FCV development.

In addition, Thermo Power has conceived the paths for regeneration of the spent hydride utilizing coal, biomass, or by-product hydrogen from other chemical processing. It will practically expand the range of fuel, which can be used efficiently and economically in fuel cells. Considering the abandoned coal reservoirs in the U.S. and the ever-increasing strategic importance of oil from foreign sources, the development of a reliable and adequate domestic energy supply system is vitally important. Thermo Power's proposed system will provide vital technology to efficiently produce and supply high purity hydrogen from non-petroleum based fuels for fuel cell power generation.

Technical Objectives

Thermo Power is developing a prototype, 50 kW electric power equivalent hydrogen supply system utilizing an innovative chemical hydride/organic slurry technology. The program covers a 30-month period which is comprised of two phases. During the first 15-month phase, we will optimize the hydrogen generation efficiency of the proposed process utilizing a laboratory-scale reactor unit (1 kW-equivalent). In the second phase, we will fabricate and evaluate the performance of a prototype hydrogen supply system for 50 kW fuel cell systems. The specific technical objectives are:

- Investigate and select metal hydride and organic slurry materials to achieve maximum specific energy;
- Develop the means for water and hydride in the minimum weight;
- Establish thermal management design for a prototype system including heat dissipation and use;
- Design and fabricate a 50 kW-equivalent prototype system;
- Evaluate and optimize performance of the prototype system; and
- Complete hydrogen supply system integration into simulated power sources and performance evaluation.

Description of Current Activities

The major objectives of this hydrogen storage system development program are twofold. First, we will use a laboratory-scale system to determine optimum materials and hydrogen generation process conditions to achieve high specific energy for hydrogen supply. The second objective will be the design and fabrication of a prototype hydrogen storage capable of supplying 3.0 Kg of high purity hydrogen for fuel cells.

Although there are numerous metal hydrides and organic carrier candidate materials, only a limited number of metal hydrides and organic carrier materials can be used to satisfy DOE's goals of specific weight and volume. One of the essential considerations for the metal hydride will be its hydrogen generation efficiency which include reaction chemistry between metal hydride and water to complete hydrolysis reactions in a safe and controlled manner. The organic carriers should be chemically inert toward metal hydrides and spent hydrides for storing, transporting, and during hydrolysis reaction. These materials also should be easily separated from spent hydrides, either thermally or mechanically, and be recycled for reuse.

In this task, we will thoroughly analyze, both theoretically and experimentally, the reaction chemistry of a variety of metal hydrides and water, and the chemical stability of the organic carriers in contact with metal hydrides and spent hydrides. Since detailed hydrolysis reaction kinetics of the metal hydride/organic carrier slurry is not known, we will conduct these experiments using a high pressure (2000 psi) and high temperature (232°C) vessel with temperature, pressure, and magnetic stirrer control capabilities (500 cm^3 internal volume).

The first requirement for the organic carrier materials is chemical stability of the materials in contact to metal hydrides and spent hydrides. Most hydrides are chemically reactive with aldehydes, ketones, lower aliphatic alcohols, olefins, etc. But they are relatively stable in saturated hydrocarbons and mineral oils. The selected organic carrier materials should have low molecular weight (to achieve high specific weight density), reasonably low melting point (to prevent freezing) and relatively high boiling point (to prevent vaporizing during hydrolysis reaction). Candidate organic carrier materials and their properties are listed in Table 2.

Table 2. Candidate Organic Carrier Materials and Their Properties

Materials	Molecular Weight (g)	Density	Melting Point (°C)	Boiling Point (°C)
Hexane	86.18	0.659	-95	69
Octane	114.23	0.703	-57	126
Nonane	128.26	0.718	-53	151
Decane	142.29	0.73	-30	174
Dodecane	170.34	0.75	-12	216
Mineral oil	-	0.84-0.88	-	>200

Investigate and Select Metal Hydride and Organic Slurry Materials

Organic Carriers

Initially it was thought that the aliphatic hydrocarbons from C6 to C12 (Hexane, Octane, Nonane, Decane, and Dodecane) were desirable candidates for the organic phase of the slurry. Evaporative losses of the organic media during slurry handling or transfer was considered in their suggestion. Compared to current gasoline fuels, even hexane, the lowest boiling candidate, was not dismissed on this basis. (See Figures 3 and 4.)

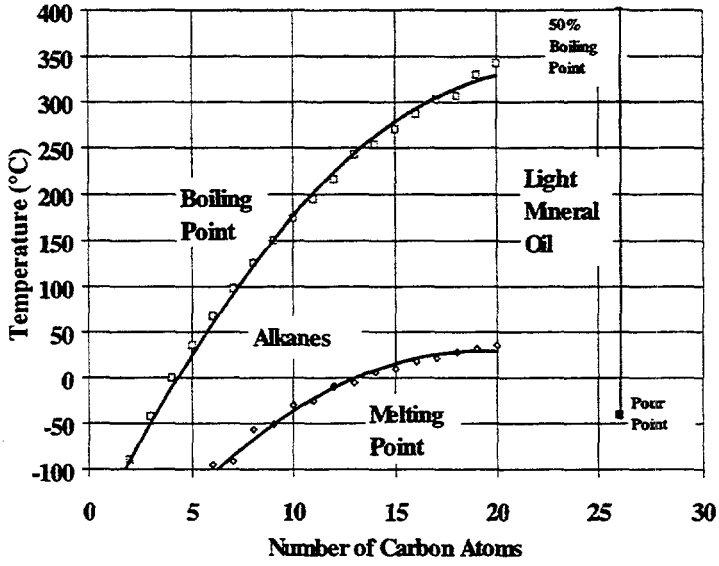

Figure 3. Freezing Point and Boiling Point of Alkanes

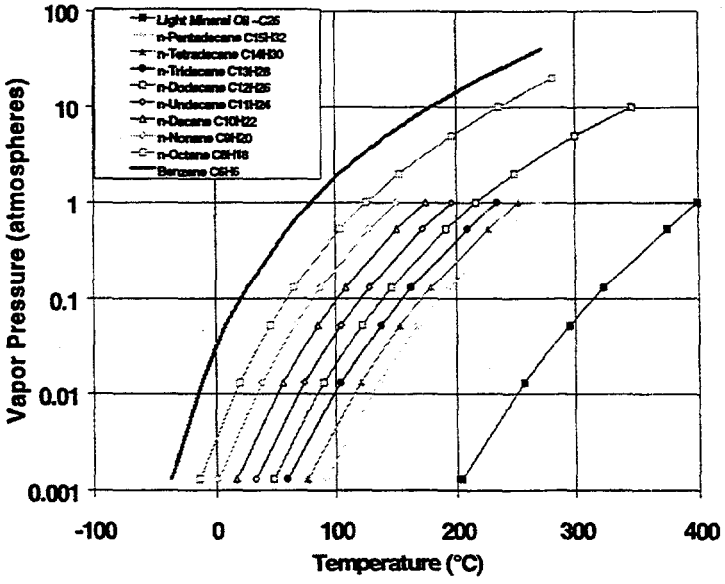

Figure 4. Vapor Pressures of the Alkanes

Experience gained during the testing of many candidate slurry formulations showed that local temperatures within the reaction mass often approach or exceed the boiling points of many of these compounds. More often, it was not the actual boiling, but the increase of vapor pressure of the compounds which presented a risk of hydrocarbon contamination of the hydrogen and subsequent harm to the fuel cell. Early reactions with n-Hexane did boil small amounts of the hydrocarbon.

Therefore, early in the investigation, several mineral oils were used, and the results with these materials were encouraging enough that these materials were pursued for the majority of the slurry tests. At first, some slurries were prepared from heavy mineral oil. Rapid sedimentation of the hydride particles as supplied made the use of the heavier oil necessary. After several appropriate polymeric dispersants were found, it was possible to use the lower viscosity mineral oil as a base for stable slurry formulations. Then, when methods of milling the metal hydrides to obtain finer particle sizes (5-10μ) were applied, experiments to obtain the maximum hydride content for a manageable viscosity were performed.

The mineral oils are generally mixtures of a variety of straight and branched-chain hydrocarbons of a range of molecular weights. Some mineral oils are of napthenic species as well. They are made from the hydrocarbon fractions boiling between 330°C and 390°C . The absence of reactive sites, such as hydroxyls, and stability to high temperatures of short duration are reasons for using these materials. In addition, they have low vapor pressures, so that evaporative losses of the organic carrier or concerns of contamination of the generated hydrogen are nearly nonexistent. In anticipation of future use of the slurry, the nontoxic nature of mineral oils as opposed to some of the lighter paraffins is desirable.

Slurry Physical Stability

The metal hydrides are supplied as a coarse powder, typically 80 Mesh and smaller, with a wide and variable distribution of sizes. Because of differences in polarities and densities, a slurry cannot be successfully prepared by simply mixing the hydride with the oil.

The hydride must be milled to yield smaller particles with higher surface area-to-volume ratios and more predictable size distribution. These particles, ranging from 5-10 microns, may then be sterically stabilized with a polymeric dispersant.

Initially, when slurries were prepared by simply mixing the hydride with the oil, they would sediment in a day or two, into a "Soft Pack". With proper milling in the oil media, slurries are routinely prepared which withstand centrifugation for five minutes at 5,125 G. It requires twenty minutes at this RCF to completely separate the hydride.

Because of the transportation end-use planned, concern had been raised regarding the possibility of continued milling by particle-to-particle attrition caused by sloshing. This effect could result in unmanageably high viscosities after a time. Long-term tests were initiated using a laboratory shaker table, whose sample platform was agitated orbitally in a horizontal plane. The tests have

been ongoing since December 1997, and the table has been operated at 120 cycles per minute at a magnitude of 9 mm.

Slurry Chemical Stability

The organic carrier must be stable, and not contaminate the hydrogen generated by the hydrolysis reaction with organic compounds. Ideally, the organic phase will protect the hydride from degradation from atmospheric moisture.

Metal Hydrides:

Sodium Borohydride:

Despite its high hydrogen content to weight and stability, the borohydrides are not suited to slurry systems for vehicular applications. Sodium borohydride does not spontaneously release its hydrogen upon contact with water, and in fact, has been sold in basic water solutions. The addition of a mineral acid, or the use of a catalyst such as cobalt, is needed to release its hydrogen. Acetic acid cannot be used, as it has been reported to generate boranes in these systems. It is imperative for handling and storage safety that the post-reaction products of hydrolysis have been entirely reacted, and will not continue to release hydrogen after being discharged from the automobile or other system.

Lithium Hydride:

Lithium hydride mills easily to produce physically stable slurries. While not having the energy density of the borohydrides, at 15,500 Btu/Lb (HHV/Mass) as lithium borohydride at 22,5600 Btu/Lb, its hydrolysis is a simple reaction which proceeds to completion.

Sodium Hydride:

While having a better energy density than calcium hydride, sodium hydride presents some difficulties with its pH limited reaction. At the high pH values generated by the production of sodium hydroxide, and the formation of saturated sodium hydroxide solutions as the hydrolysis product, an additional reactant such as aluminum is needed to force the reaction to completion. If aluminum is used, the resulting sodium aluminate is not as dangerous or as corrosive to materials and human tissue as the concentrated sodium hydroxide solutions. Calcium and lithium hydroxides are not as soluble as sodium hydroxide, and these hydroxides precipitate when saturation is reached, thereby allowing the hydrolysis reaction to proceed to completion.

Calcium Hydride:

Less desirable from an energy density at 5,850 Btu/Lb, calcium hydride has some benefits. The end product, calcium hydroxide, is a relatively nontoxic and harmless compound. Further, the hydrolysis of calcium hydride appears to be pressure-limited, stalling at approximately 300 psi at some molar ratios with water. Future safety considerations could make calcium hydride attractive in this sense. Calcium hydride requires three times as long to mill into a 5-10 micron

slurry as does lithium hydride in an alumina ball mill, but the apparently greater hardness of the particles could address concerns with agitation stability.

Selection and Definition of Formulation To Be Used in Subsequent Tasks

It is anticipated that remaining work will be performed with lithium hydride slurries for several reasons:

1) It has a superior energy density per weight.
2) It reacts to completion, producing a fully depleted and relatively safe end product.
3) The end product, lithium hydride, can be regenerated.
4) It mills readily to produce stable slurry suspensions.

Performance Schedule

The tasks are briefly defined in this section.

Task 1: Investigation and selection of metal hydride and organic carrier materials to achieve high specific energy. Reaction chemistry between metal hydride and water to achieve high hydrogen generation efficiency will be the key technical consideration, completed five months after start of work.

Task 2: Optimization of the hydride/organic slurry configuration, completed nine months after start of work.

Task 3: Development of the hydride/water activation process, completed twelve months after start of work.

Task 4: Establishment of the thermal management design for prototype system, completed fifteen months after start of work.

Task 5: Design and fabrication of the prototype system, completed nineteen months after start of work.

Task 6: Evaluation of the prototype performance, completed twenty four months after start of work.

Task 7: Integration of the hydrogen supply system into operating conditions of simulated fuel cell power source, completed twenty six months after start of work.

Task 8: Testing and performance evaluation of the final system, completed twenty nine months after start of work.

Task 9: Final Report preparation, completed thirty months after start of work.

Summary and Future Activities

From the work conducted thus far, the following results and conclusions can drawn, respectively.

Results:

- Best Organic - Light Mineral Oil
- Best Hydrides -LiH & CaH_2
- +95% Hydrogen Release/Recovery
- Stable slurry produced.
- Polymeric dispersants sterically stabilize the suspension.

Conclusions:

- A chemical hydride slurry can be used to generate hydrogen for transportation vehicle applications.
- The system has the potential to be safe and easy to use.
- Chemical hydride based systems can achieve DOE's energy density goals.

During the next year, the following activities will be conducted:

- Continue the optimization of the hydride/organic slurry composition.
- Development of the hydride/water activation process (hydrogen generation reactor).
- Establishment of the thermal management design for prototype system.

References

"Hydrogen Transmission/Storage With A Metal Hydride/Organic Slurry," Breault, R.W., A.W. McClaine, and J. Rolfe, 1998 DOE Hydrogen Program Technical Review, Washington, D.C., April 28-30, 1998.

SAVANNAH RIVER BUS PROJECT

William A. Summers
Westinghouse Savannah River Company
Aiken, SC 29803

Abstract

The H2Fuel Bus is the world's first hybrid hydrogen electric transit bus. It was developed through a public/private partnership involving several leading technology and industrial organizations in the Southeast, with primary funding and program management provided by the Department of Energy. The primary goals of the project are to gain valuable information on the technical readiness and economic viability of hydrogen buses and to enhance the public awareness and acceptance of emerging hydrogen technologies. The bus has been operated by the transit agency in Augusta, Georgia since April, 1997. It employs a hybrid IC engine/battery/electric drive system, with onboard hydrogen fuel storage based on the use of metal hydrides. Initial operating results have demonstrated an overall energy efficiency (miles per Btu) of twice that of a similar diesel-fueled bus and an operating range twice that of an all-battery powered electric bus. Tailpipe emissions are negligible, with NOx less than 0.2 ppm. Permitting, liability and insurance issues were addressed on the basis of extensive risk assessment and safety analyses, with the inherent safety characteristic of metal hydride storage playing a major role in minimizing these concerns. Future plans for the bus include continued transit operation and use as a national testbed, with potential modifications to demonstrate other hydrogen technologies, including fuel cells.

Introduction

The Savannah River Bus Project involves the development, manufacture and testing of the world's first hybrid hydrogen electric transit bus, known as the H2Fuel Bus. The project seeks to successfully transfer technologies developed at the Department of Energy (DOE) Savannah River Site (Aiken, South Carolina) for defense applications to commercial use in a public transit bus. The project is a technology verification activity that seeks to establish the technical feasibility, economic viability, and environmental benefits of hydrogen as a transportation fuel. Solution of hydrogen infrastructure issues (e.g. refueling, liability, safety, etc.) and the public awareness and public acceptance of hydrogen as a vehicular fuel are additional objectives. The H2Fuel Bus was developed through a partnership between federal and local government, universities, non-profits, and industry. The majority of the funding for the project was provided by the DOE Savannah River Operations Office (70%) and the DOE-EE Hydrogen Program Office (15%). The H2Fuel Bus is a 33-foot transit bus which will be operated in regular passenger service in the city of

Augusta/Richmond County, Georgia. The primary goals of the project are to gain valuable information on the technical readiness and economic viability of hydrogen buses and to enhance the public awareness and acceptance of emerging hydrogen technologies.

Discussion

The bus employs a hybrid internal combustion engine/electric drive propulsion system. Fuel is supplied to the engine by using waste heat to release hydrogen from a metal hydride storage system. The use of inherently safe metal hydride storage overcomes public concerns about hydrogen safety. Initial operating results indicate an overall energy efficiency equivalent to 7.5 to 9.0 miles per gallon. This is more than twice that of a similar bus with a diesel engine, and it equals or exceeds projected goals for current hydrogen fuel cell buses, such as those being deployed in Chicago. The tailpipe emission levels of nitrogen oxides (NOx) are some of the lowest ever measured for an internal combustion engine. Preliminary results indicate NOx emissions of less than 0.2 ppm, which is below the Los Angeles ambient air quality standard for a first-level alert.

The bus has undergone extensive testing and is expected to enter regular transit service in the Spring of 1998. Funding from the Department of Energy Office of Energy Efficiency and Renewable Energy during Fiscal Year 1998 provides for test operations and data collection/analysis, including ongoing technical support, specialized maintenance, and hydrogen fuel costs in excess of conventional diesel fuel costs. Continued bus operation provides valuable additional data on the hydrogen system reliability, operating and maintenance requirements, long-term performance, economics and customer acceptance. This information is essential in order to determine the commercial potential of the technology and to attract continued private industry participation. Public transit operation also provides opportunities to inform the general public and to gain broader public acceptance and support for hydrogen as an alternative fuel.

Technical Goals

The Savannah River Bus Project set out to achieve the following technical goals:

- Maintain a Gross Vehicle Weight Rating of 33,000 pounds while integrating a hydrogen engine/generator set and metal hydride storage system into a standard battery-electric transit bus (Note: It was important not to exceed the GVWR to which the electric bus had been certified by the manufacturer).
- Have speed and acceleration characteristics equal to or better than a diesel bus
- Achieve a fuel energy efficiency of two times that of an equivalent diesel-fueled bus
- Achieve an operating range in excess of 100 miles between refuelings (twice that of an equivalent battery-powered bus)
- Achieve negligible tailpipe emissions
- Satisfy all insurance liability, regulatory, safety and licensing requirements
- Operate the bus in regular passenger service
- Demonstrate economic viability based on projected costs for mass produced unit

Major Barriers to Meeting Technical Goals

The H2Fuel Bus is the first hybrid hydrogen electric bus. It also employs the largest mobile metal hydride bed ever installed on a vehicle. Furthermore, the H2Fuel Bus was designed to be operated in regular transit service by normal bus drivers and maintenance personnel. These goals required the project to overcome several major barriers, including the following:

- Weight, physical stability, chemical resistance and thermal conductivity for metal hydride powders
- Compact, durable, and cost-effective metal hydride storage container requirements
- Minimization of NOx emissions from hydrogen internal combustion engine
- Integration of IC engine/gen set with existing battery electric drive system
- Infrastructure issues including refueling, insurance, permitting, public acceptance
- Current high cost of metal hydrides and first-of-a-kind vehicle

Approach/Background:

In order to achieve the stated technical goals and overcome the perceived major barriers, the following design approach was selected:

- Select state-of-the-art electric bus compatible with partial battery replacement (Blue Bird Electric Q-Bus)
- Employ a series hybrid internal combustion engine/electric design arrangement
- Utilize well-tested metal hydride materials based on defense experience (LaNi5)
- Design improved storage device (SRS-patented aluminum foam tubular design)
- Utilize extensive exhaust gas recirculation and constant volume injection engine design to minimize exhaust emissions
- Establish broad-based partnership to address infrastructure and cost issues

The hybrid ICE/electric design approach allowed the bus to be constructed using an architecture that is fully-compatible with future fuel cell power designs, but avoided the near-term developmental and cost issues associated with current fuel cell technology. As fuel cells become commercially available, a power train consisting of a "fuel cell engine" in place of the internal combustion engine could be adapted. The fuel storage, electric drive power train, auxiliary battery system, and many other bus components and systems would remain as demonstrated on the H2Fuel Bus.

Partners and Responsibilities

The H2Fuel Bus project was performed by an extensive public/private partnership involving several leading technology and industrial organizations, mostly located in the Southeastern United States. Partners and their major roles in the project were as follows:

- Department of Energy — Project sponsor
- Westinghouse Savannah River Company — Prime contractor, metal hydride storage system, technical and safety analysis
- Southeastern Technology Center — Project management, public awareness/involvement services
- Georgia Tech Research Institute — Hybrid bus design, integration and testing
- Augusta-Richmond County Public Transit — Electric bus owner, transit operator
- Blue Bird Body Company — Electric bus manufacturer
- Hydrogen Components, Inc. — Hydride vessel construction, engine conversion
- Education, Research and Development Association of Georgia Universities — Contract administration

Other project participants included: Air Products and Chemicals, Inc.; Energy Research and Generation, Inc.; Power Technology Southeast, Inc.; Northrop Grumman Corporation; Air Liquide America Corporation; ElectroSource, Inc.; Neocon Technologies, Inc.

System Description

The H2Fuel Bus is a modified version of a an electric transit bus manufactured by Blue Bird Body Company of Fort Valley, Georgia. A photograph of the bus is shown in Figure 1. The bus is approximately 33-ft long and has a gross vehicle weight rating of 33,000 pounds. Bus features include electric air-conditioning and compatibility with the requirements of the Americans with Disabilities Act, including wheelchair access. There is space for 27 seated passengers plus standees.

The original electric bus was powered by four battery packs containing twenty-eight lead-acid batteries each. Two of the battery packs, weighing approximately 1,000 kg each, were replaced with metal hydride storage vessels. The bus employs a series hybrid electric power system, consisting of a hydrogen-fueled internal combustion engine and a Northrop Grumman electric drive train. The engine-generator set was installed in the rear compartment of the bus and connected to the hydrogen storage system and the electric drive train. The engine is a 7.5 liter V-8 industrial engine modified to operate with hydrogen fuel. A constant volume injection system provided by Hydrogen Components, Inc. is used to introduce hydrogen into the engine. The two remaining lead/acid battery packs provide peaking power capability and permit the hydrogen engine to be operated at peak efficiency and with minimal emissions. The IC engine/generator set produces up to 60 kW AC power, which is directed by a power controller for battery recharging or to help operate the high efficiency 170 kW AC induction electric drive motor. A regenerative

braking system helps increase overall energy efficiency and significantly reduces brake wear. Electric operation provides noticeably quieter transportation, while matching the speed and acceleration performance of its diesel counterparts. The hydrogen hybrid design extends the useful operating range of the bus to over 200 km (nearly twice that of the battery-only version), permitting a full day of transit operation without mid-day refueling.

Hydrogen Storage

Hydrogen is stored onboard the bus at near room temperature and at low pressure in a safe, dry solid form through the use of metal hydride powder. Metal hydrides are intermetallic compounds that undergo reversible chemical reactions with hydrogen. They absorb hydrogen gas when cooled, and release it in a controlled manner when heated. The heating is accomplished onboard the bus by routing the engine cooling water through tubes located in the metal hydride storage vessels. A patented hydrogen storage device was developed by the Savannah River Technology Center (DOE Savannah River Site) to contain the metal hydride powder and to permit efficient hydrogen delivery to the engine. A schematic of a metal hydride storage vessel is shown in Figure 2. The cylindrical hydride vessels are made from thin wall, stainless steel tubes. The components inside each vessel include a porous stainless steel filter, aluminum divider plates, cylindrical aluminum foam pieces and a U-shaped water tube. The filter permits hydrogen to flow freely in and out of the vessel but confines the metal hydride powders in the vessel. The divider plates separate the vessel into short sections to prevent the metal hydride powders from shifting among the sections. The aluminum foam pieces with metal hydride particles in their pores improve the heat transfer between the hydride and the water tube. The engine coolant flows through the water tube to provide heat during desorption and to remove heat during absorption of hydrogen during refueling. The metal hydride vessels are manifolded together and contained inside an air-tight aluminum box. Two metal hydride storage assemblies, consisting of twenty-four individual tubular vessels each, are located under the floor of the bus. A photograph of one of the storage vessel assemblies is shown in Figure 3. These assemblies replace two of the four battery packs normally supplied with a battery-electric version of the bus sold by Blue Bird. The total weight of the two metal hydride storage assemblies is 1900 kilograms, approximately the same as the two packs of batteries they replaced. The hydrogen storage capacity is approximately 15 kilograms.

Lanthanum-nickel-aluminum type material was selected as the storage medium on the bus. This material has been used extensively in defense work at the Savannah River Site for more than 15 years in various applications. It has been shown to have excellent chemical and physical stability, and the hydrogen absorption isotherm can be adjusted to give the desired operating temperature and pressure. In order to operate utilizing waste heat from the engine cooling loop and to recharge the storage beds with normal cooling water, an absorption pressure of 7 atmospheres at 30 degrees Celsius and a desorption pressure of 13 atmospheres at 60 degrees Celsius were selected. The hydrogen capacity on the hydride is approximately 1.27%. Although this weight density was sufficient to meet the design requirements for the H2Fuel transit bus, higher weight density metal hydrides could be utilized for light-duty vehicles and other applications. Satisfying the temperature/pressure limits, cycling lifetime, activation, oxidation/poisoning resistance, and cost requirements are the greatest challenges for selecting lighter weight hydrides.

Engine Design and Exhaust Emissions

The internal combustion engine was extensively modified in order to achieve extremely low nitrogen oxide (NOx) exhaust emissions. Hydrogen Components, Inc. of Littleton, CO performed the engine modifications and designed and built the emission control system. The results to date are based on engine tests prior to installation in the bus. Actual bus emissions data will be collected later this year. NOx levels measured during the engine testes were extremely low, indicating that this may be the cleanest internal combustion engine ever operated.

The engine is a Ford LSG-875 industrial engine. The original 7.5 liter Ford V-8 engine was extensively modified during conversion to hydrogen fuel. New heads and pistons were selected to increase the compression ratio for higher thermal efficiency. The heads have better flow characteristics to improve volumetric efficiency as well. A new intake manifold provides higher flow and accommodates the hydrogen injection ports. Hydrogen fuel is delivered through an HCI-patented Constant Volume Injection (CVI) system, a mechanical timing and metering device in phase with the intake stroke of the engine (i.e. sequential multiport injection). Operating on hydrogen, the engine is rated at 102 hp (76 kW) at 2450 rpm. The brake thermal efficiency of the engine is 31%.

The low NOx emissions were achieved through the use of a novel, high volume exhaust gas recycle system combined with a three-way catalyst. Although the system was designed by HCI, the original EGR/stoichiometric hydrogen engine concept was originally proposed by Dr. Michael Swain of the University of Florida. To achieve stable combustion and low oxides of nitrogen (NOx) emissions, hydrogen engines are typically run ultra lean, with an equivalence ratio of 0.5 or less. However, this results in surplus exhaust oxygen that precludes the use of a three way catalyst for final NOx reduction. The concept employed on the H2Fuel Bus utilizes high volume exhaust gas recycle (consisting primarily of nitrogen and water vapor) to dilute the air/fuel charge to provide slower flame speeds and lower peak flame temperature for stable combustion and lower NOx. This permits the use of a stoichiometric (or slightly rich) fuel mixture, allowing for the further catalytic reduction of NOx by the three way catalyst.

Before installation into the bus, several tests were run in which the exhaust was sampled, dried, and collected during engine operation at full speed (2450 rpm) and at various loads. In its final configuration, the engine's NOx emissions were so low that Hydrogen Consultants, Inc. was unable to detect any NOx in the vehicle exhaust with a 0-1000 ppm instrument. Measurements on bag samples at Honda Motor Company's laboratory in Denver, CO registered less than 1 ppm on their 0-30 ppm scale, as shown below. From the emissions concentration data, the brake specific emissions (BSE) can be calculated from hydrogen flow, engine brake power, and combustion stoichiometry. Tests were conducted at stoichiometric (equiv. ratio = 1.005) and fuel-rich (equiv. ratio = 1.04) conditions. The results are shown in Table 1.

Table 1. Exhaust Emissions for H2Fuel Bus Engine

NOx Emissions for Stoichiometric Operation:

LOAD	NOx (grams/hp-hr)	NOx (ppm)	NOx (grams/mile)*
90%	0.028	11.0	0.056
75%	0.019	7.0	0.038
50%	0.023	7.2	0.046

NOx Emissions for Fuel-Rich Operation (equiv. ratio = 1.04):

LOAD	NOx (grams/hp-hr)	NOx (ppm)	NOx (grams/mile)*
90%	0.0004	0.15	0.0008
75%	0.0005	0.18	0.0010
50%	0.0004	0.13	0.0008

*Note: "grams/mile" estimate based on average energy use of 2.0 hp-hr/mile. This represents total emissions for a fully loaded bus with 27 passengers. Appropriate corrections for passenger vehicles should be made.

Operating Results to Date

The H2Fuel Bus has been operated in a test mode in the City of Augusta since April, 1997. This testing has permitted several refinements and modifications to be performed to improve the bus operation and reliability. Key results to date include:

- Assembly of hybrid hydrogen/electric bus was completed successfully within GVWR limits
- Metal hydride storage vessels were constructed, installed and successfully operated. More than 20 refuelings have been performed.
- Safety analyses, liability insurance, codes & standards issues were resolved
- Refueling capability was established at an existing facility of the hydrogen supplier
- Road testing of approximately 1000 miles has been completed
- Energy efficiency was measured at 67 scf H2/mi or 7.5 mpg (exceeding goal). Energy consumption of 2,800 kcal/km compares to 6,000 kcal/km for diesel equivalent
- Near-zero NOx emissions were measured during engine testing (<0.2 ppm)

Current Year Accomplishments/Status:

During Fiscal Year 1998, the following additional accomplishments were achieved:

- Battery management system installed – significantly improving battery life & performance
- Final modifications completed in order to accept commercial passengers
- Hydrogen storage system modified to meet ASME Pressure Vessel Code requirements

- Engine/battery system operation optimized to permit smoother, more efficient operation
- Bus demonstrated at Eighth Annual U.S. Hydrogen Meeting in Vienna, VA
- Initiation of regular transit service in Augusta, GA planned for Spring, 1998

Conclusions

The H2Fuel Bus establishes the technical readiness of hybrid hydrogen electric buses. The performance, operating range, energy efficiency, and exhaust emissions all meet or exceed expectations. The metal hydride storage system has functioned flawlessly, and the advantages of this method of hydrogen storage have been verified. Insurance liability, licensing, refueling and other infrastructure issues have been successfully addressed.

The major area of difficulty with the technical operation of the bus was associated with the battery system. Hybrid electric vehicles are still in a developmental stage, and the design of charging and operating schemes to optimize battery performance, reliability and lifetime is still evolving.

Future Work

Future plans for the H2Fuel bus include:

- Perform final optimization and checkout testing
- Introduce the bus into regular transit service in Augusta, GA
- Collect and analyze data during transit operations
- Support DOE-EE efforts to transition the bus for continued testing

The H2Fuel Bus is a valuable national resource as a test-bed for hydrogen technologies. Potential future work associated with the bus may involve conversion to fuel cell operation, installation of an improved hydrogen storage system, or other modifications and demonstrations. The assessment of follow-on buses based on the H2Fuel Bus prototype are being discussed with the industry partners.

Acknowledgments

This project was financially supported by the Department of Energy and the contributions of the numerous partners. This support is gratefully acknowledged. We also acknowledge the support and guidance of Mr. Terry Montgomery, DOE Savannah River Operations Office, and Mr. Sig Gronich, DOE-EE Hydrogen Programs.

References and Publications

Awards:

- Federal Laboratory Consortium "1996 Southeast Regional Partnership Award"
- "Keys to City of Augusta" presented by Senator Sam Nunn to Mayor Larry Sconyers

Publications:

- Summers, William A., "Hydrogen-powered Vehicle Holds Promise for Public Transportation Systems," NASA Technology 2005, Chicago, Illinois, October 24, 1995.
- Mosely, w. Clanton, "The H2Fuel Bus Project", Proceedings of the Seventh Annual U.S. Hydrogen Meeting, Alexandria, VA, April 2-4, 1996.
- Summers, William A., "Advancing Hydrogen as a Safe Transportation Fuel," NASA Technology 2006 Seventh National Technology Conference and Exhibition, Anaheim, CA, October 28-30, 1996.
- Coutts, Allan, "Safety Evaluation of a Hydrogen-Fueled Transit Bus, " Proceedings of the Eighth Annual U.S. Hydrogen Meeting, Alexandria, VA, March 11-13, 1997.
- Summers, William A., "The H2Fuel Bus Project," Georgia Spring Municipal Planners Organization Meeting, Augusta, GA, May 23, 1997.
- Heung, L.K., "On-board Hydrogen Storage System Using Metal Hydride," Second HYPOTHESIS Hydrogen Power, Theoretical and Engineering Solutions International Symposium, Grimmstad, Norway, August 22, 1997.
- Heung, L.K.,, "On-Board Hydrogen Storage for a City Transit Bus," Ninth Annual U.S. Hydrogen Meeting, Vienna, VA, March 3-5, 1998.
- Heung, L.K., Summers, W.A, and Motyka, T., "The Savannah River Bus Project", paper submitted to the XII World Hydrogen Energy Conference, Buenos Aires, Argentina, June 21-26, 1998.

Figures

Figure 1. Photograph of H2Fuel Bus in Augusta, Georgia

Figure 2. Schematic of Metal Hydride Storage Vessel

Figure 3. "Hydrogen Fuel Tank" Containing Metal Hydride Storage Vessels

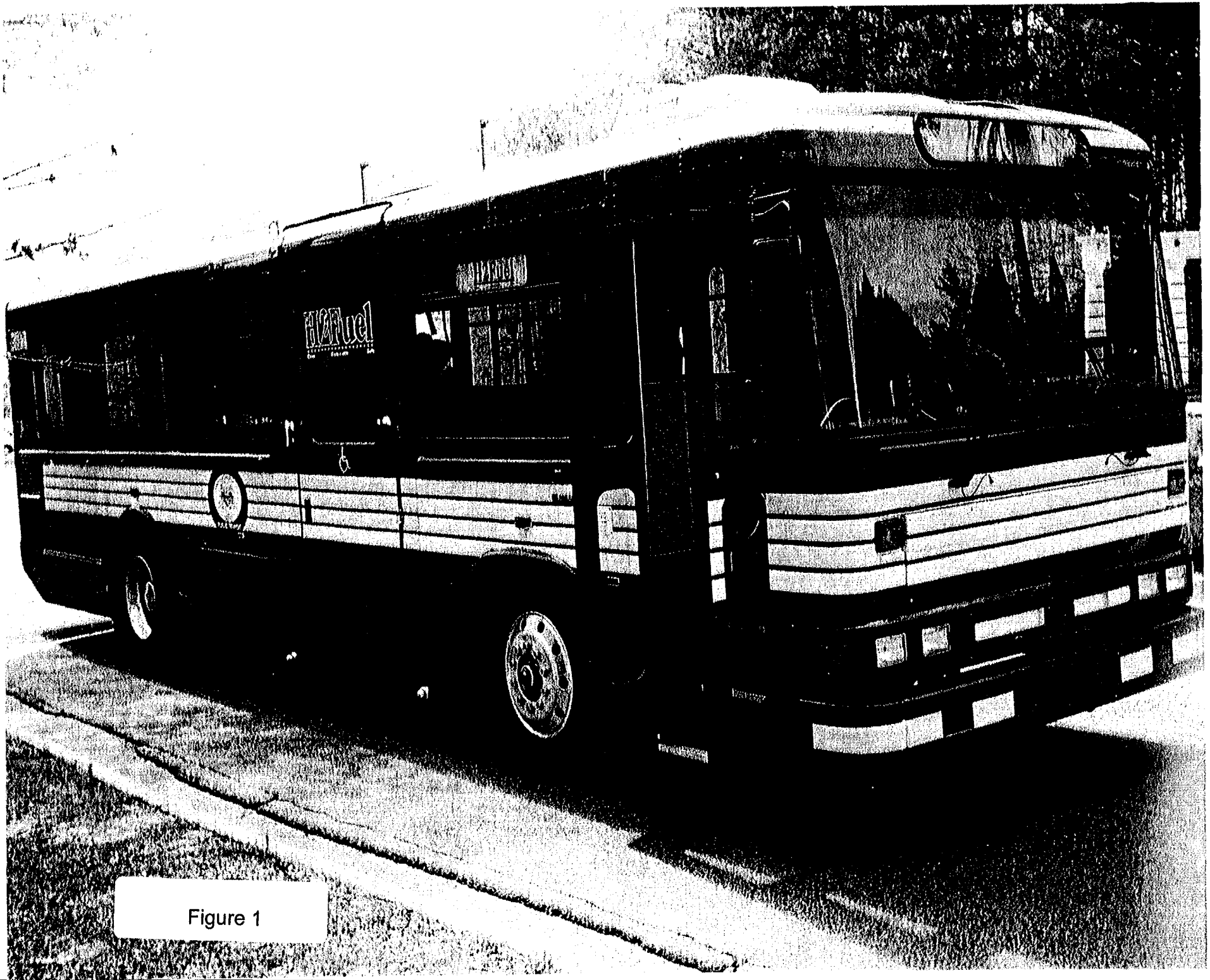

Figure 1

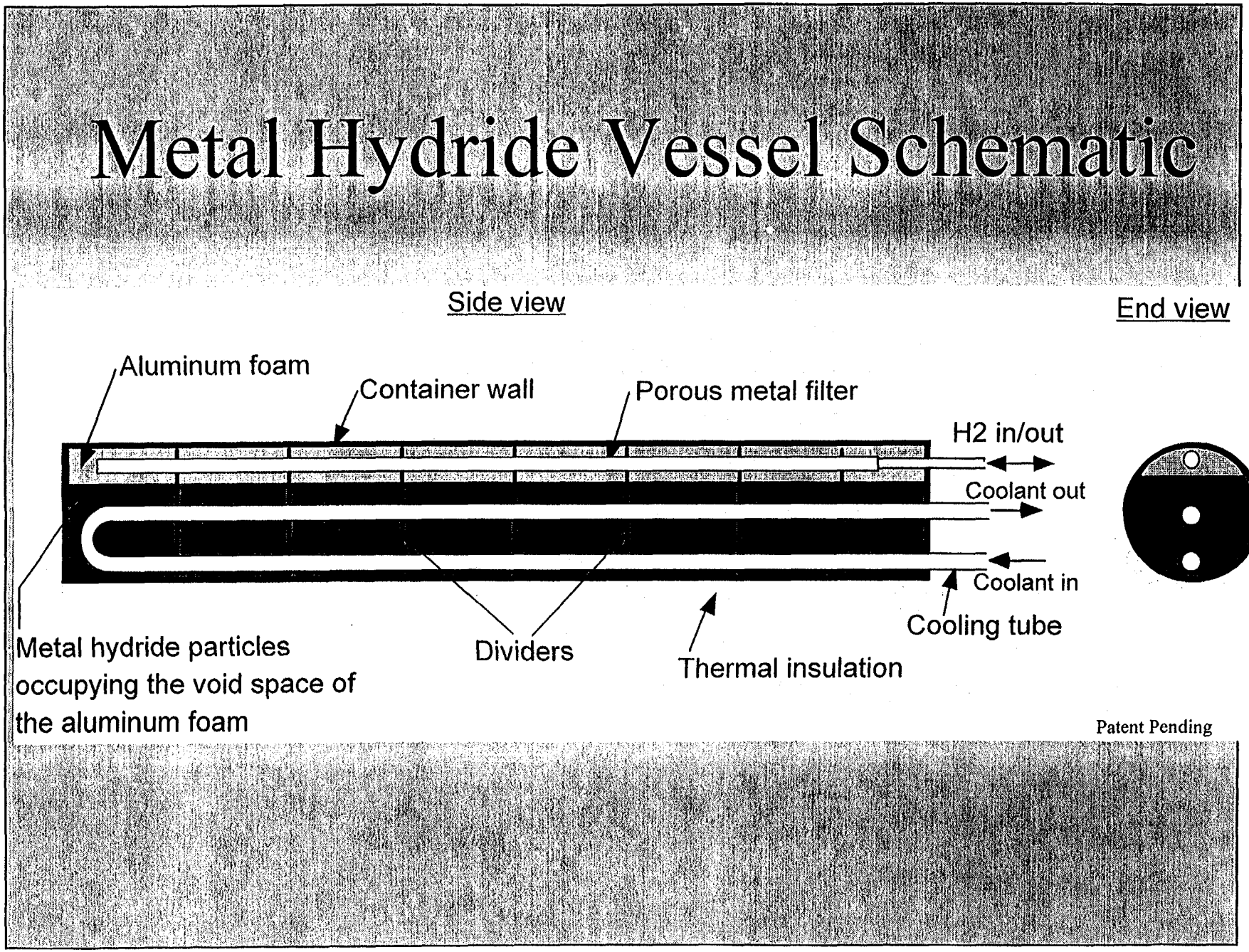
Metal Hydride Vessel Schematic
Side view
End view
Aluminum foam
Container wall
Porous metal filter
H2 in/out
Coolant out
Coolant in
Cooling tube
Metal hydride particles occupying the void space of the aluminum foam
Dividers
Thermal insulation
Patent Pending
Savannah River Bus Project

Figure 2

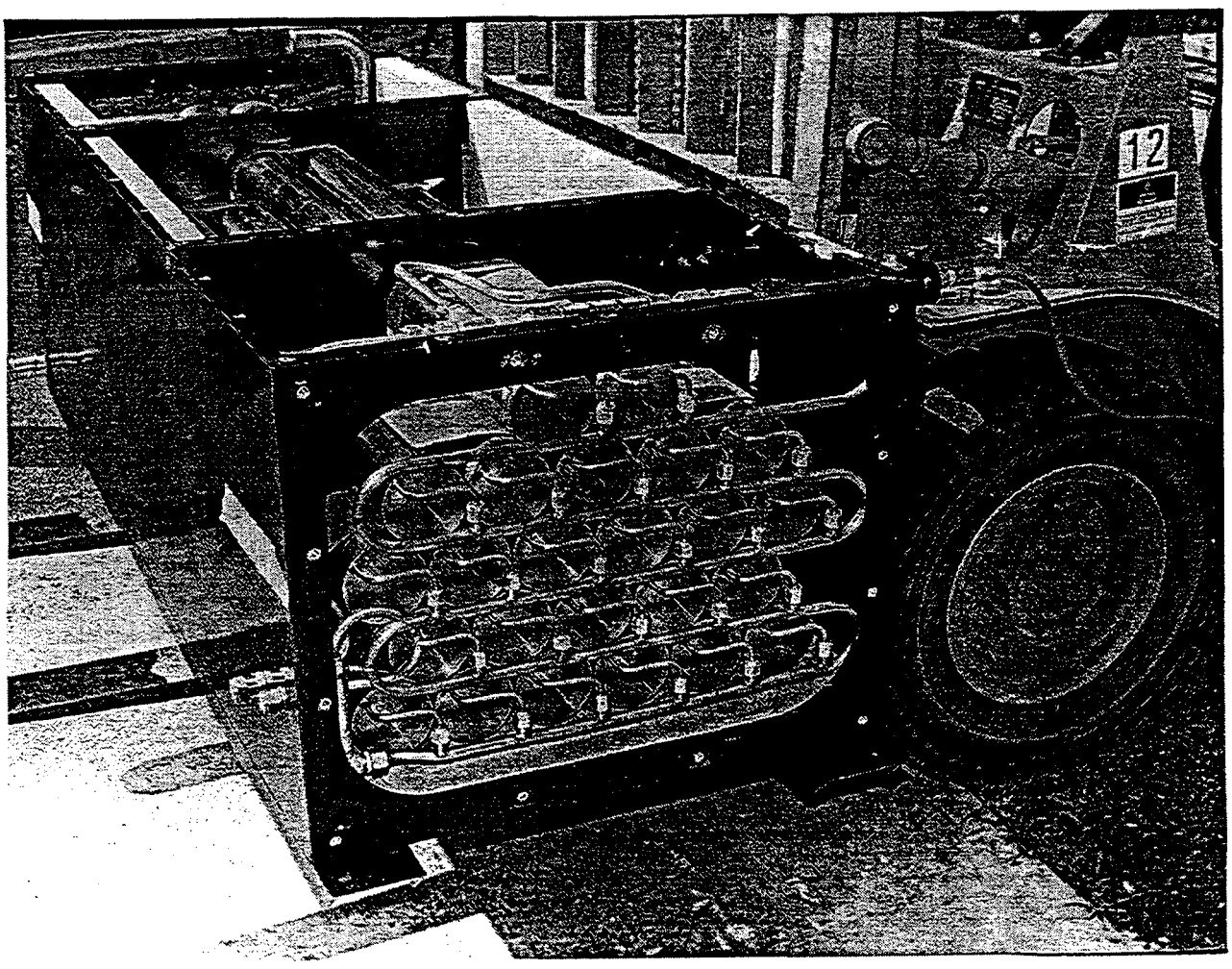

Figure 3

RISKS INCURRED BY HYDROGEN ESCAPING FROM CONTAINERS AND CONDUITS

Michael R. Swain
Eric S. Grilliot
University of Miami
Coral Gables, FL 33124

Matthew N. Swain
Analytical Technologies, Inc.
Miami, FL 33186

Abstract

This paper is a discussion of a method for hydrogen leak classification. Leaks are classified as; gas escapes into enclosed spaces, gas escapes into partially enclosed spaces (vented), and gas escapes into unenclosed spaces. Each of the three enclosure classifications is further divided into two subclasses; total volume of hydrogen escaped and flow rate of escaping hydrogen. A method to aid in risk assessment determination in partially enclosed spaces is proposed and verified for several enclosure geometries. Examples are discussed for additional enclosure geometries.

Introduction

The escape of hydrogen (leak) from a container or conduit produces a risk of combustion. The spatial and temporal distribution of hydrogen produced by the leak is needed to assess the risk of combustion. Depending on the geometry into which the hydrogen is leaking, the flow rate of hydrogen from the leak, the total volume of hydrogen leaked, and any preexisting gas motion, the escaping hydrogen may produce a negligibly small cloud of combustible gases, a large cloud of combustible gases or a cloud of combustible gases in conjunction with a cloud of detonable gases.

Risk Assessment

This paper is a discussion of the clouds formed by escaping hydrogen. Estimates made for worst case accident scenarios often assume hydrogen-air clouds, which could not physically exist. As an example, the following is an accident scenario of hydrogen escaping under a hydrogen powered bus at a flow rate of 50 SCFM (1400 l/min). A "worst case" accident scenario would be to assume a stoichiometric, or somewhat richer, mixture of hydrogen and air evenly distributed under the bus. This produces a large volume of potentially detonable gases. If a detonation is assumed, as a further extension of the "worst case" scenario, a force large enough to raise the bus off the ground is created. In fact, applying these assumptions to any fuel would produce similar results.

In reality, hydrogen's very low density prevents this worst case scenario from occurring. Figure 1 shows the results of a computer model of hydrogen escaping downward from the middle of the underside of an idealized bus. The underside of the idealized bus contained two 24 inch deep cavities, one at each end of the bus (Geometry A). The ground clearance under the bus was 10.5 inches (to the bottom of the bus and bottom of the skirt that formed the walls around the cavities). Figure 1 shows the surface of constant 8% hydrogen concentration at 30 minutes. The flow had essentially reached steady state after 5 minutes of hydrogen leakage. The surface of constant 8% hydrogen concentration shows the basic flow pattern of the escaping hydrogen. The hydrogen spread out evenly in all directions from the leak until it reached the edge of the bus. The hydrogen rose upon reaching the edge of the bus and entrained ambient air. The rising mixture of hydrogen

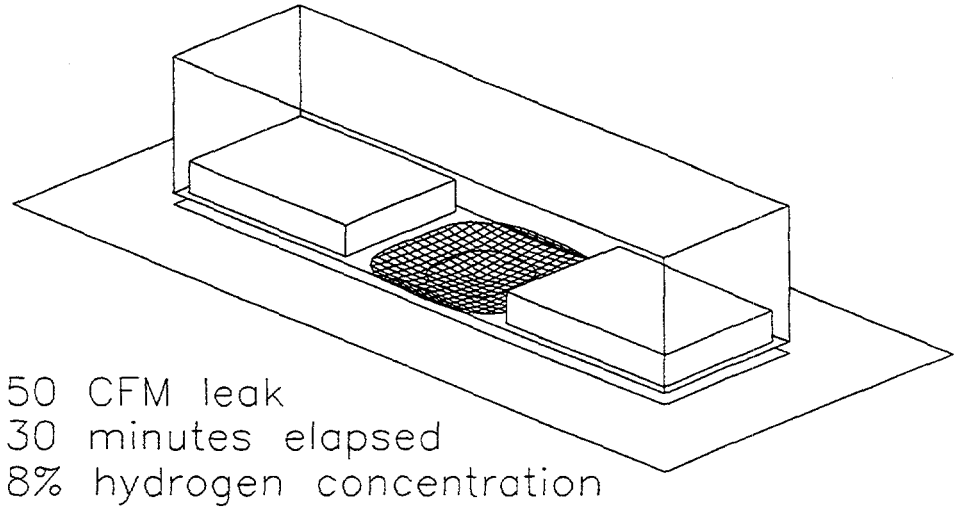

Figure 1 - Geometry A

and air at the sides of the bus drew the flow of hydrogen toward the sides of the bus, the shortest pathway out from under the bus. This flow pattern prevented the hydrogen concentration from exceeding 8% in the cavities.

Figure 2 shows the surface of constant 4.1% hydrogen concentration. 4.1% hydrogen concentration is the upward propagating lean limit of combustion (Coward 1961, Hansel 1993, Lewis 1961) and as such represents the leanest burnable mixture of hydrogen. It can be seen in Figure 2 that the cavities under the front and back of the bus were filled with hydrogen between 8% and 4.1% hydrogen. Hydrogen burns at very low speeds at those concentrations. Experiments with bus wheel wells (Photo 1) containing hydrogen-air mixtures averaging 10% hydrogen have shown flames speeds on the order of 10 to 12 ft/sec.

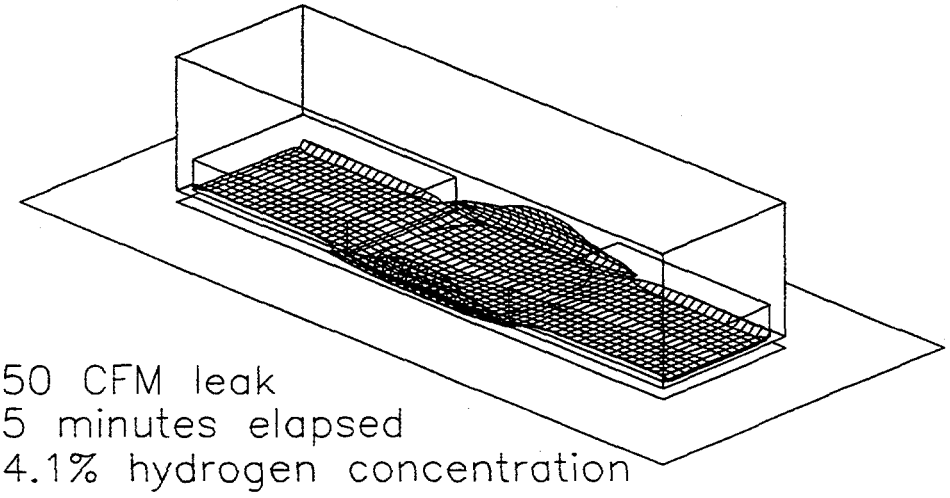

Figure 2 - Geometry A

Photo 1 - Bus wheel well test

Figure 3 shows the surface of constant 18% hydrogen concentration. 18% hydrogen concentration is the accepted value for the lean limit of detonation (Lewis 1961, Ordin 1997). The volume of gases was very small and the likelihood of detonation occurring was very remote.

The accident scenario of hydrogen escaping directly into the cavity under the bus is shown in Figure 4 (Geometry B). It is seen that the cavity fills with hydrogen richer than 18% concentration within 5 minutes. Venting of the cavity was necessary to prevent this dangerous accident scenario. Figure 5 shows the surface of 4.1% hydrogen concentration for a vented cavity (Geometry C). The volume of gases containing more than 4.1% hydrogen was less than the previous case because vents were employed at the top of the cavity. Figure 6 shows the surface of constant 18% hydrogen concentration. Once again, the volume of gases containing more than 18% hydrogen was very small.

All the previously described analyses were without any ambient wind. The presence of wind reduces the size of the hydrogen-air clouds produced.

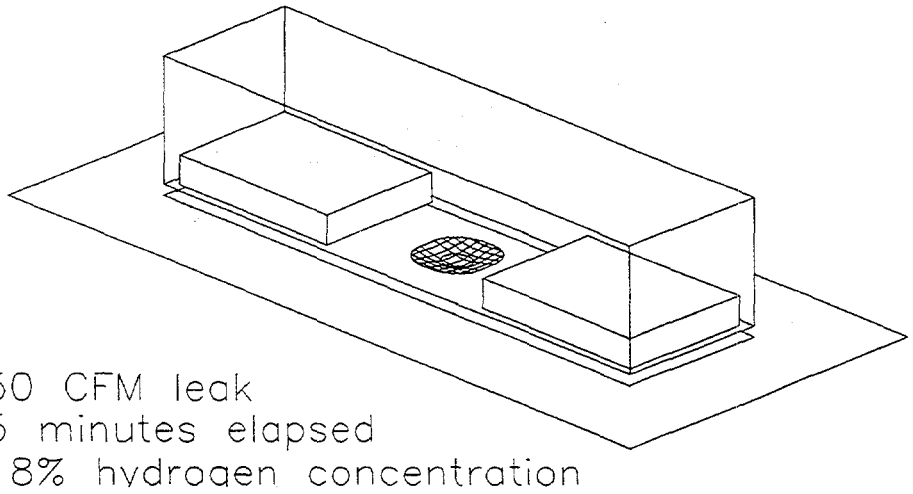

Figure 3 - Geometry A

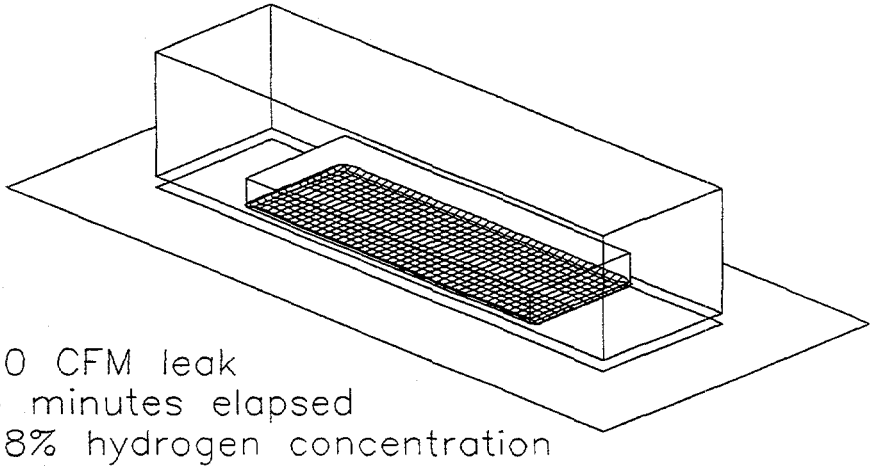

Figure 4 - Geometry B

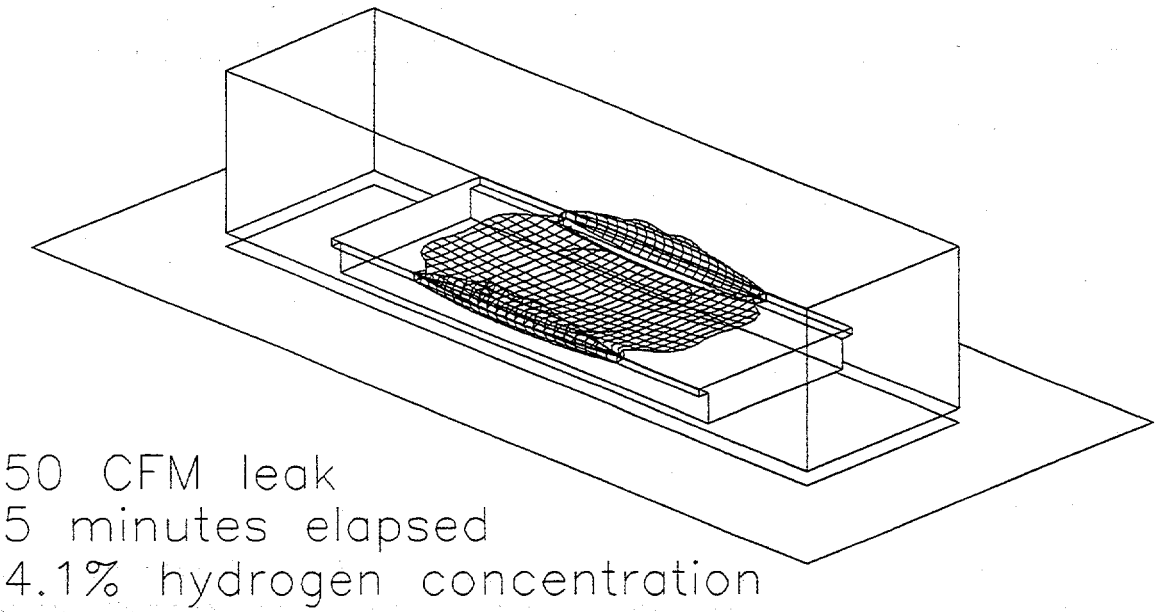

Figure 5 - Geometry C

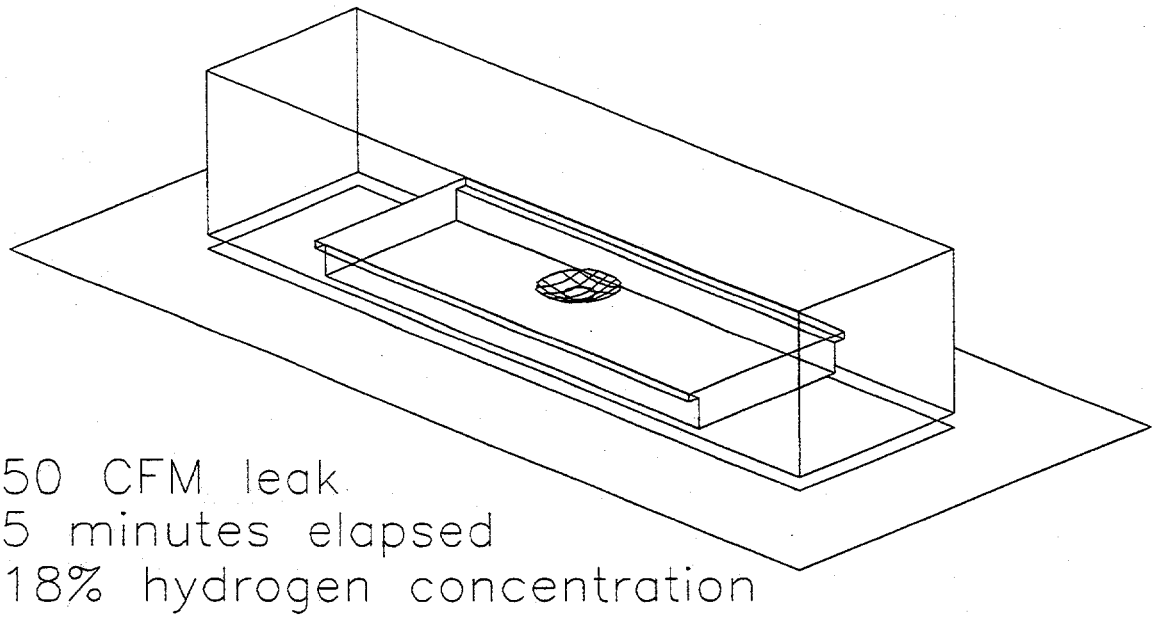

Figure 6 - Geometry C

Leak Classification

The use of "worst case" scenarios can considerably overestimate the risk incurred due to a hydrogen escape. To reduce this potential difficulty it is suggested that gaseous fuel escapes be classified by enclosure geometry and hydrogen flow quantity description. This could be done as follows:

1. **Gas escapes into enclosed spaces**
   a. Total volume of escaped hydrogen.
   b. Flow rate of escaping hydrogen.

2. **Gas escapes into partially enclosed spaces.**
   a. Total volume of escaped hydrogen.
   b. Flow rate of escaping hydrogen.

3. **Gas escapes into unenclosed spaces.**
   a. Total volume of escaped hydrogen.
   b. Flow rate of escaping hydrogen.

Utilizing the above-listed classifications, general descriptions of the type of risks incurred can be made. For leaks into enclosed (non-vented) spaces, the risk incurred is most strongly affected by the total volume of hydrogen escaping rather than the flow rate of hydrogen escaping. This is because ignition can occur soon after the gas escape begins or be delayed. The overpressure created by the delayed ignition of an accumulating combustible mixture typically produces a greater risk than does early ignition resulting in a standing flame.

Ignition early in the escape results in a burning jet or standing flame. The size of the standing flame is dependent on hydrogen flow rate.

If ignition is delayed, the magnitude of the potential overpressure, due to ignition of the accumulating combustible mixture, is a function of the gas motion in the enclosed space. The escaping hydrogen will rise to the ceiling (or any overhead barrier) within seconds and then diffuse back toward the lower section, which takes hours. If the total volume of hydrogen escaping is less than 4.1% of the volume of the enclosure, the resulting risk of combustion will decrease to zero as the hydrogen becomes homogeneously distributed into the enclosure. If the total volume of hydrogen escaping is greater than 4.1% of the volume of the enclosure, the resulting risk of combustion will continue until the enclosure is vented or combustion occurs.

For leaks into unenclosed spaces, the risk incurred is most strongly affected by the flow rate of the hydrogen escape rather than the total volume of hydrogen escaped. Without an enclosure, hydrogen rises and the risk of hydrogen accumulation is removed. For hydrogen escaping into an unenclosed space, steady state combustible gas cloud size is typically reached within 15 seconds. If the hydrogen flow is stopped, combustible mixtures of hydrogen are typically gone in 10 seconds. The risk of large overpressures caused by ignition of the hydrogen-air mixture is small due to the lack of an enclosure to constrain the expanding products of combustion. Additionally, the hydrogen jet produced is very inhomogeneous and the volume of hydrogen-air mixtures that produce high flame

speeds is typically small. It is near stoichiometric and rich mixtures of hydrogen and air that burn rapidly enough to produce appreciable overpressures.

For leaks into partially enclosed spaces (buildings with vents) the risk incurred is affected by the total volume of hydrogen escaping and the flow rate of escaping hydrogen. The relative importance of the total volume and flow rate is dependent on the geometry of the partially enclosed space and the location of the hydrogen escape. Proper design of the partial enclosure reduces the risk incurred due to hydrogen escape.

Hydrogen's low density causes it to rise after escaping from a container or conduit. Vents near the top of the enclosure typically allow hydrogen to exit the enclosure as long as vents are also provided near the bottom of the enclosure. Vents near the bottom of the enclosure allow fresh air to enter and replace the hydrogen enriched mixture exiting from the top vents. If fresh air must enter through the same vent that the hydrogen is exiting, the efficiency of hydrogen removal is substantially reduced.

The design of structures, which might potentially produce partial enclosures for escaping hydrogen, can be facilitated by simulating potential hydrogen escape scenarios with helium escapes. Both hydrogen and helium are low density gases and behave in similar a fashion when released into partial enclosures. Helium concentrations, versus time, can be measured in the partial enclosure during a simulated hydrogen escape scenario. Accurate descriptions of hydrogen behavior can be obtained by creating a verified CFD model using the helium escape data and then using the model to predict hydrogen escape behavior.

Hydrogen Risk Assessment Method

The method of risk assessment utilizes three steps.

1. Simulation of the accident scenario with leaking helium.
2. Verification of a CFD model of the accident scenario (modeling helium) using the helium data.
3. Prediction of the behavior of hydrogen using the CFD model (modeling hydrogen).

The following example is given, together with a comparison of the predicted hydrogen concentrations to experimentally determined values.

The geometry used for this example was a half-scale hallway. The dimensions were 114 inches (2.9 m) by 29 inches (0.74 m) by 48 inches (1.22 m). Figure 7 shows a schematic of the hallway. The hydrogen escaped from the floor at one end of the hallway (left hand side of figure). A roof vent and lower door vent existed at the other end of the hallway (right hand side of figure). Figure 7 shows an example of the velocity vectors predicted by the CFD model. Figure 7 also shows the points at which helium or hydrogen gas concentrations were measured. Figure 8 shows the results of the CFD model compared to the experimentally measured concentrations for helium escaping at 2 SCFM from the floor at the end of the hallway. Figure 9 shows the results of the CFD model compared to the experimentally measured concentrations for hydrogen escaping at 2 SCFM from the floor at the end of the hallway. It can be seen that the CFD model predicted the hydrogen behavior accurately.

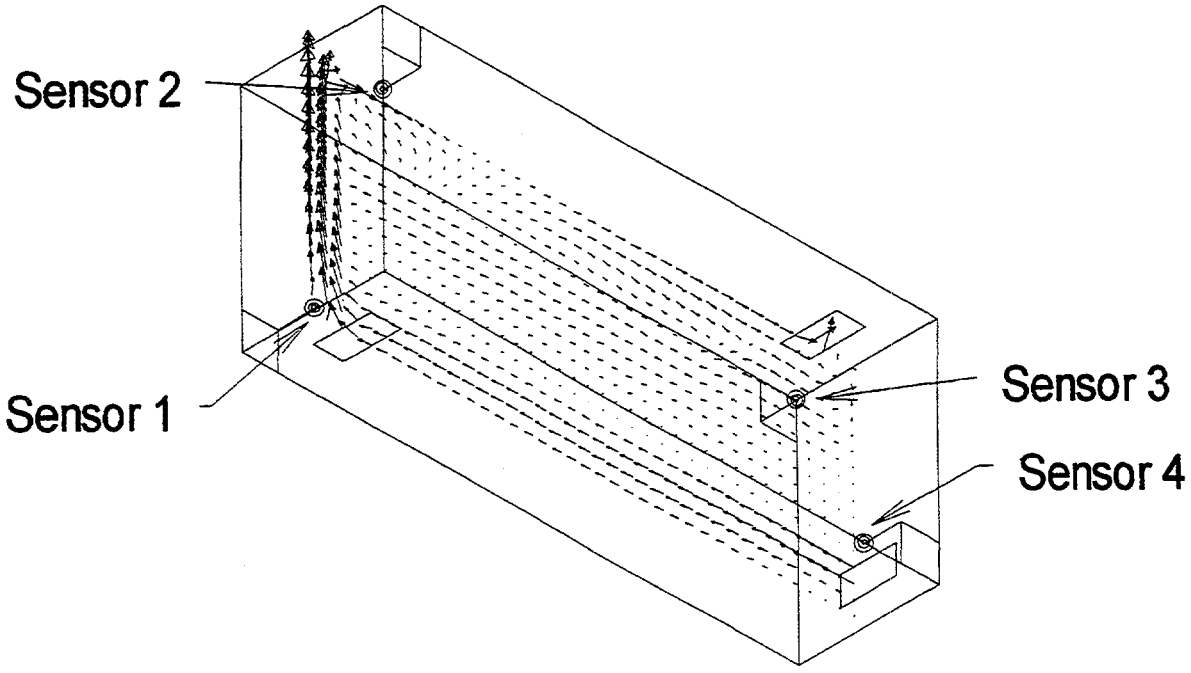

Figure 7 - Hallway with velocity vectors

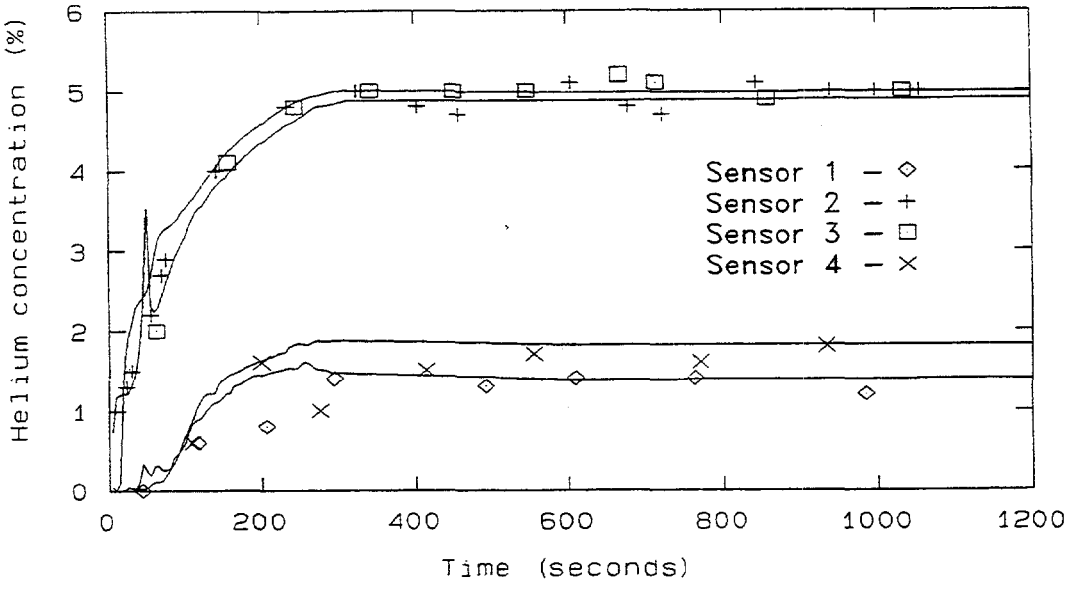

Figure 8 - 2 CFM leak at end of hallway

Figure 10 shows a comparison of the surfaces of constant 3% concentration for both helium and hydrogen. It can be seen that both gases rise from the floor, travel across the ceiling, and leave through the roof vent. The gas leaving the roof vent causes a drop in pressure, which draws air in the lower door vent. The general circulation in the hallway can be seen in Figure 7. All of the gases

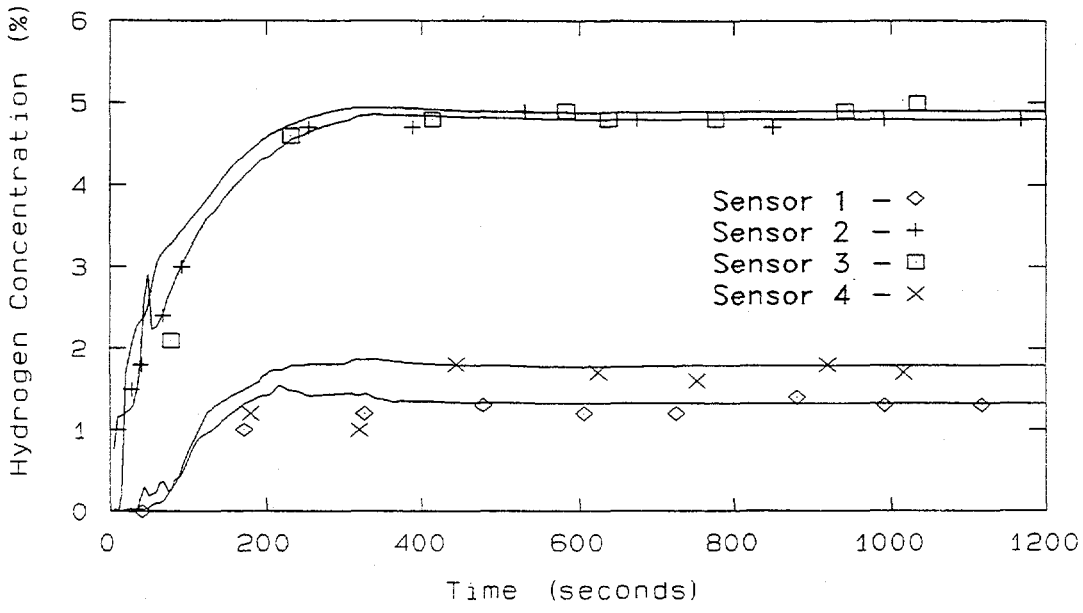

Figure 10 - 2 CFM Hydrogen leak at end of hallway

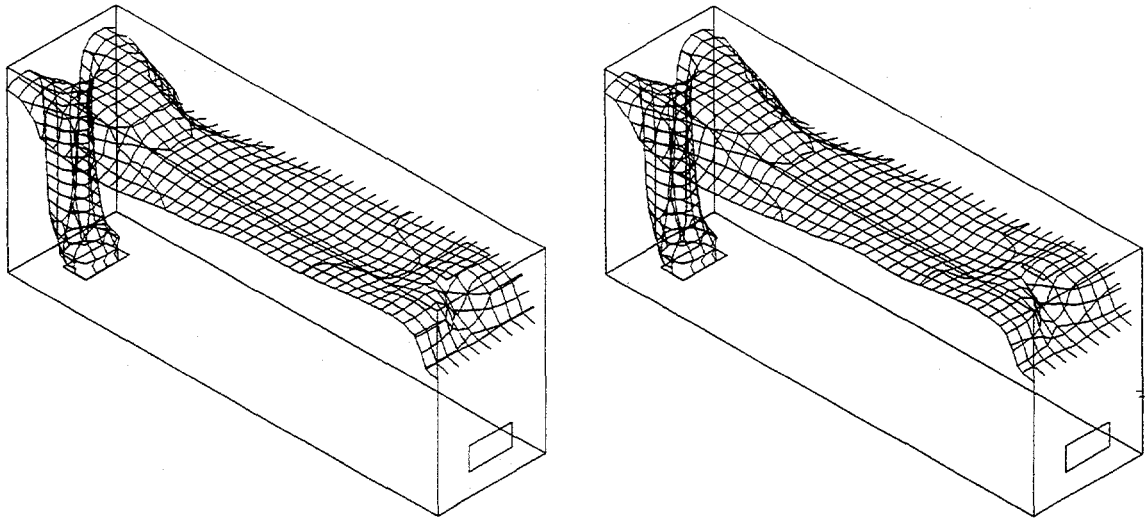

Figure 9 - Helium hydrogen comparison, 2 CFM leak at end of hallway, 1 min elapsed, 3% concentration

inside and above the surface of constant 3% concentration contain more than 3% helium or hydrogen. Those below the surface contain less than 3% concentration.

Figure 11 shows the surfaces of constant 1% concentration for helium and hydrogen. Comparison with Figure 10 gives an indication of the vertical concentration gradient in the hallway.

Figure 12 shows the results of the CFD model compared to the experimentally measured concentrations for hydrogen escaping at 2 SCFM from the middle of the floor in the hallway. Figure 13 shows the results of the CFD model compared to the experimentally measured concentrations for hydrogen escaping at 2 SCFM from the middle of the floor in the hallway. It can be seen that the CFD model predicted the hydrogen behavior accurately.

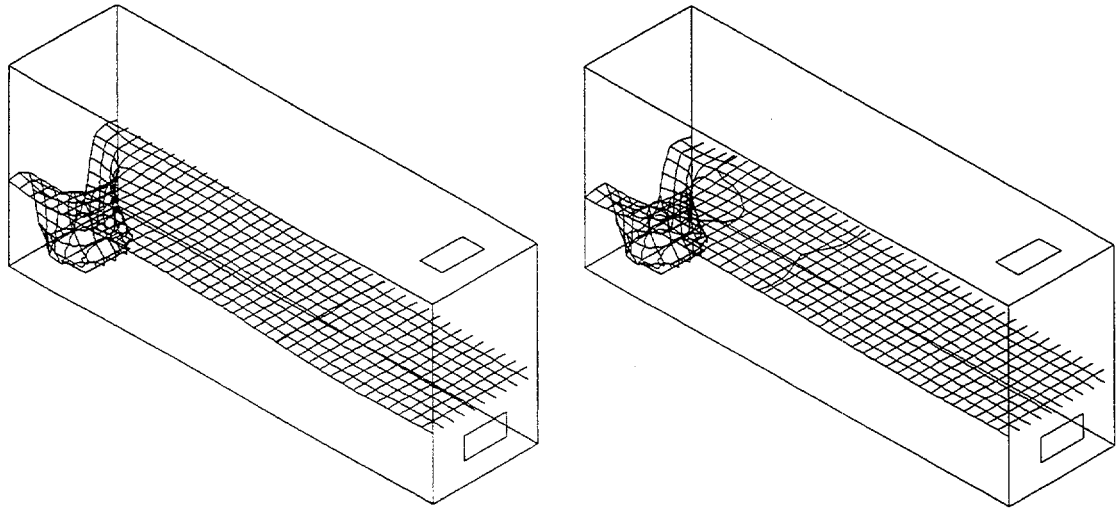

Figure 11 - Helium hydrogen comparison, 2 CFM leak at end of hallway, 1 min elapsed, 1% concentration

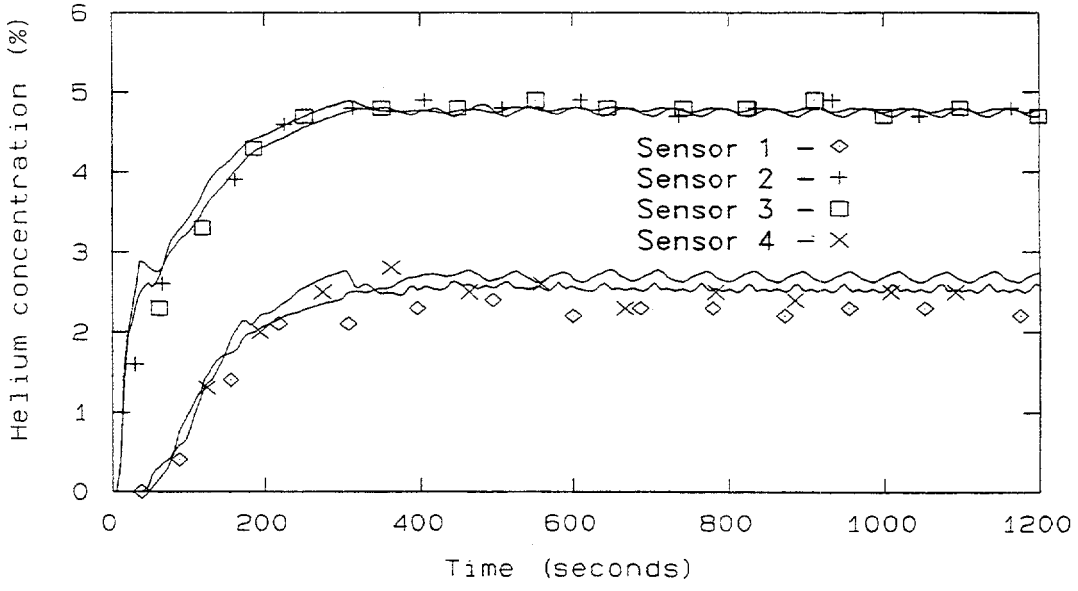

Figure 12 - 2 CFM Helium leak in middle of hallway

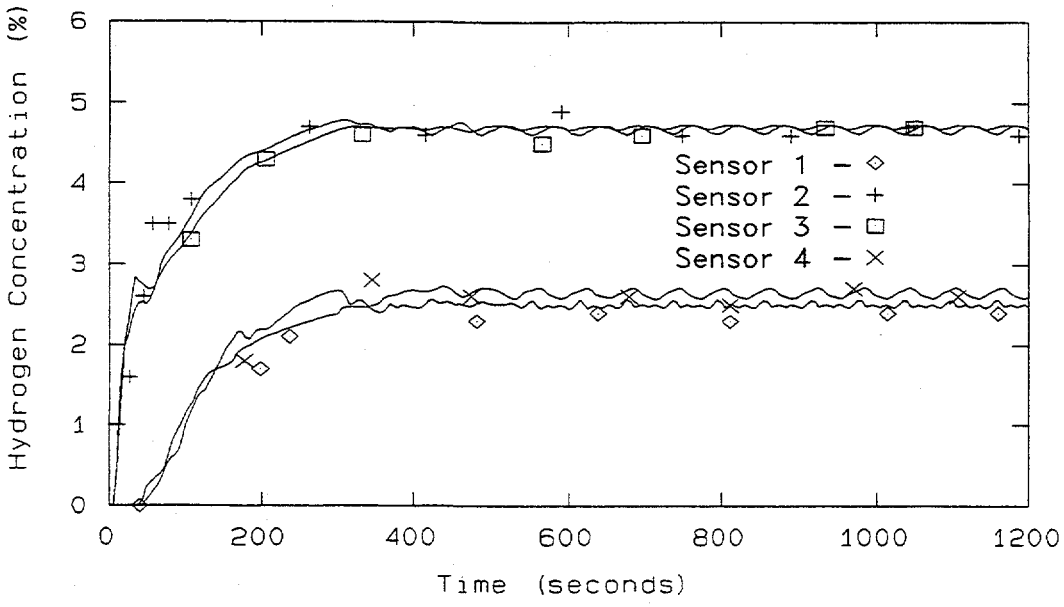

Figure 13 - 2 CFM Hydrogen leak in middle of hallway

The method was tested with an extended vertical vent (chimney). This was done to investigate a geometry that was potentially difficult to model. Figure 14 and 15 show the surfaces of constant 5% concentration versus time for both helium and hydrogen. In both cases the leakage rate was 2700 liters/hr into a 1 ft, by 1 ft, by 6 ft tall, vertical vent. The low density gas (helium or hydrogen) rises, entrains air, and forms a flow that attaches itself to various walls intermittently. The flow pattern fluctuates randomly. The concentration at a specific point was not predictable. It was therefore concluded that a vertical vent should be added to the hallway to test the ability of the CFD model to accurately predict hydrogen concentration.

Figure 16 shows the results of the CFD model compared to the experimentally measured concentrations for helium escaping at 2 SCFM from the floor at the end of the hallway and an extended vertical vent added to the roof vent. The concentration of helium was reduced compared to the hallway without the vertical vent because the vertical vent acted as a chimney, increasing the ventilation rate in the hallway. Figure 17 shows the results of the CFD model compared to the experimentally measured concentrations for hydrogen escaping at 2 SCFM from the floor at the end of the hallway and an extended vertical vent added to the roof vent. It can be seen that the CFD model predicted the hydrogen behavior accurately.

Comparison of Helium and Hydrogen Concentrations

The hydrogen concentration can be greater or less than the helium concentration depending on the enclosure geometry. Hydrogen is 8% more buoyant than helium and tends to rise more rapidly. The increased vertical velocity tends to increase both ventilation rate and gas mixing with air. If the exit vent is near the gas escape the increased gas mixing does not decrease the concentration of hydrogen in the hydrogen-air mixture leaving through the vent enough to overcome the increased ventilation rate, and hydrogen concentration tends to be lower than helium concentration. If the exit vent is far from the escape the increased gas mixing tends to reduce the concentration of hydrogen

in the mixture leaving the enclosure enough to overcome the increased ventilation rate, and hydrogen concentration tends to be higher than helium concentration.

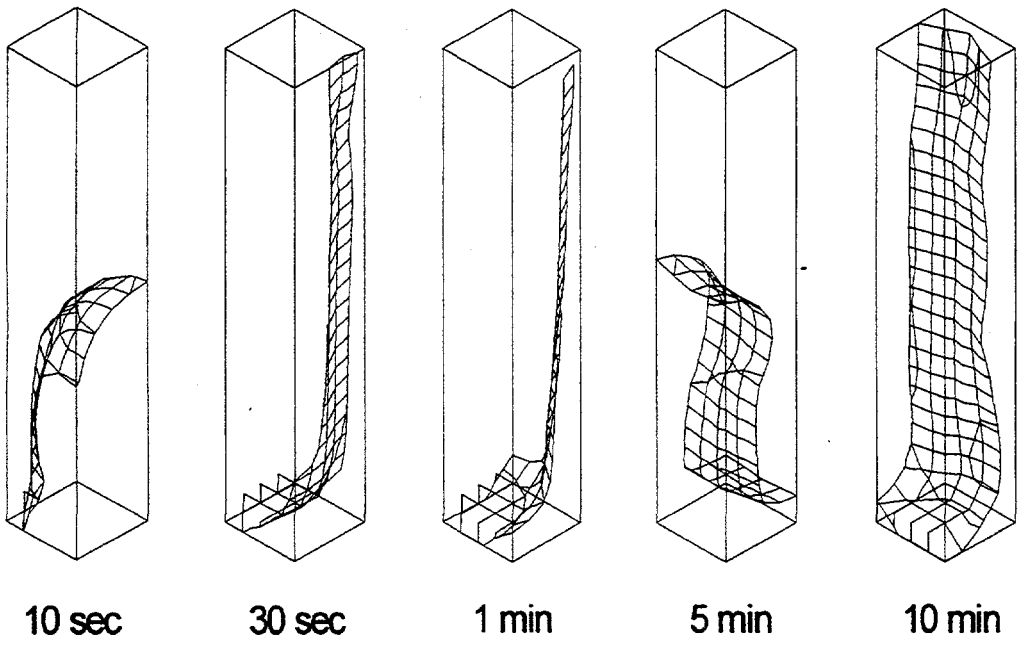

Figure 14 - CFD results for helium in vertical vent

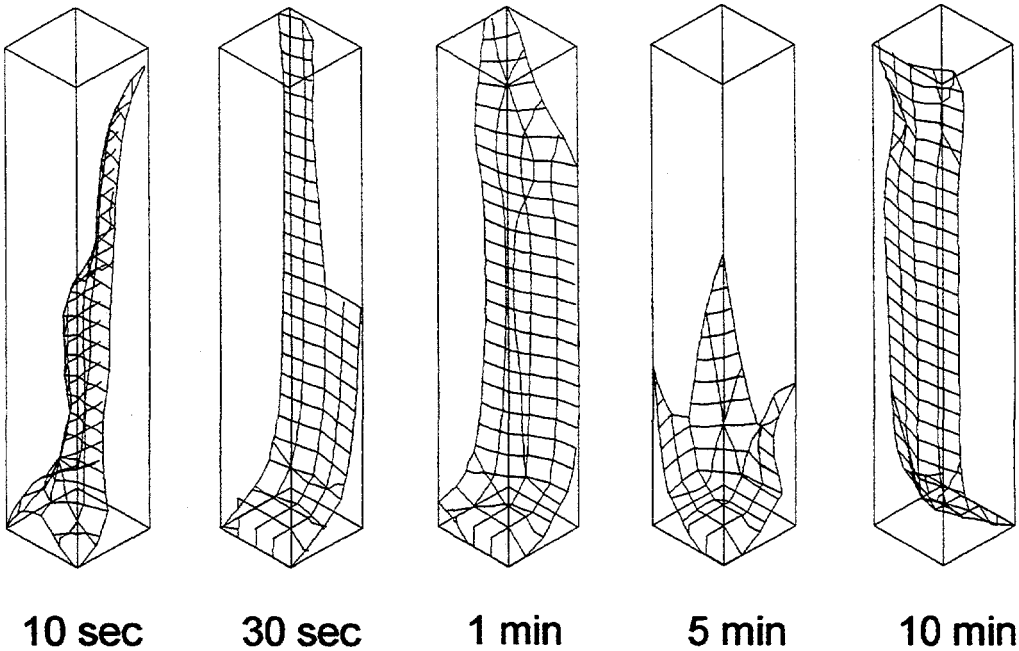

Figure 15 - CFD results for hydrogen in vertical vent

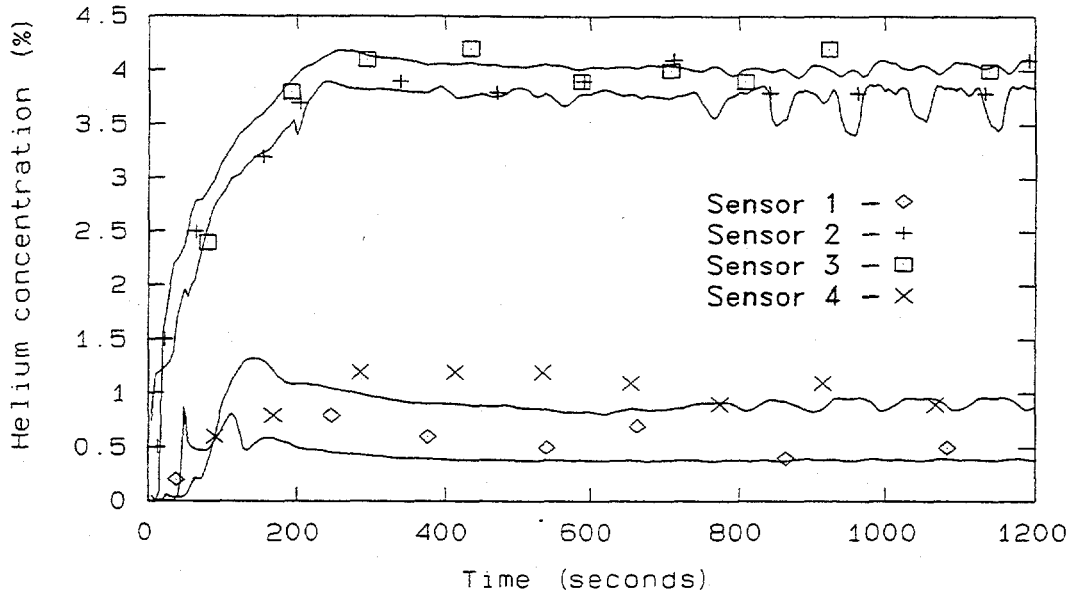

Figure 16 - 2 CFM Helium leak at end of hallway with extended vent

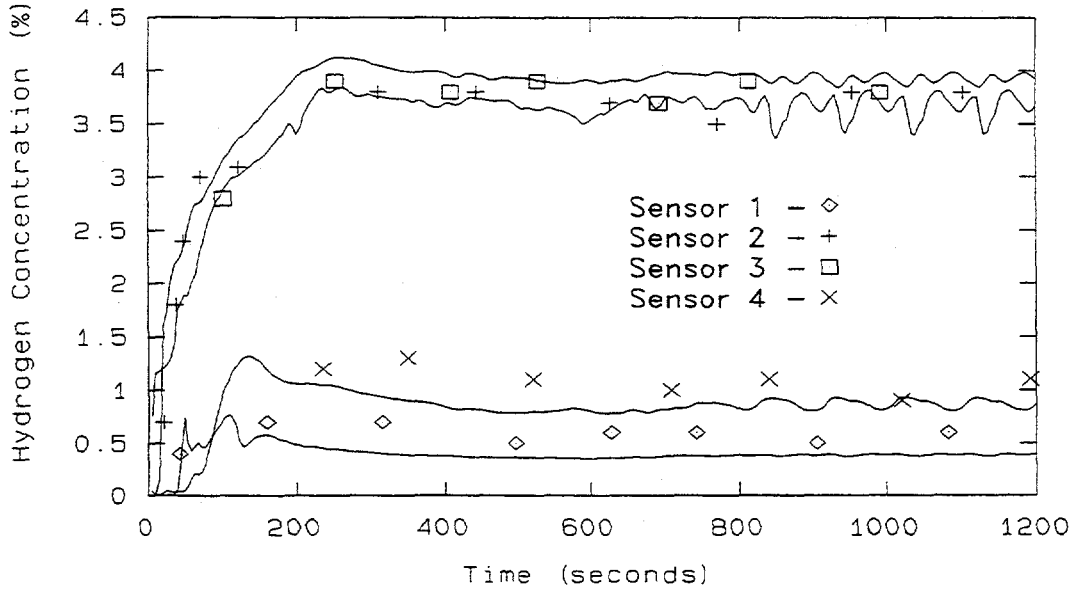

Figure 17 - 2 CFM Hydrogen leak at end of hallway with extended vent

Figure 18 and 19 depict a comparison of helium and hydrogen concentrations in a residential garage with a leaking home vehicle refill unit. Figure 18 is a schematic of the garage. There was a single vent in the garage door and a refill unit leaking 6800 liters/hr in the corner of the garage. The surface of constant 7.5% hydrogen concentration is shown after 20 minutes of leakage. Figure 19 shows a comparison of helium and hydrogen concentrations versus time. In this case, the hydrogen concentrations were higher than the helium concentrations. This was principally due to the use of a single vent from the enclosure. The single vent was very inefficient at removing hydrogen from the enclosure because it produced mixing of the vented gas with the incoming air. Efficiency could be greatly increased by installing both upper and lower vents. Hydrogen concentrations could be held below 2.5% for this accident scenario by utilizing upper and lower vents in the garage door.

Figures 20 and 21 depict a comparison of helium and hydrogen concentrations for a van parked in a garage with a single vent. The accident scenario was hydrogen escaping from under the front of the van. In this case, the presence of the van enhanced mixing to the point that helium and hydrogen concentrations were nearly identical. Again, the hydrogen concentrations could be held below 2.5% for this accident scenario by utilizing upper and lower vents in the garage door.

For the hydrogen escapes into enclosure geometries studied to date, the maximum deviation between helium and hydrogen concentrations was 15%.

Conclusions

1. "Worst Case" accident scenarios can considerably overestimate the risk incurred in hydrogen escapes.

2. A helium data verified CFD computer model can accurately predict the spatial and temporal distribution of hydrogen released in a hydrogen escape.

3. For the hydrogen escapes into enclosure geometries studied to date, the maximum deviation between helium and hydrogen concentrations was 15%.

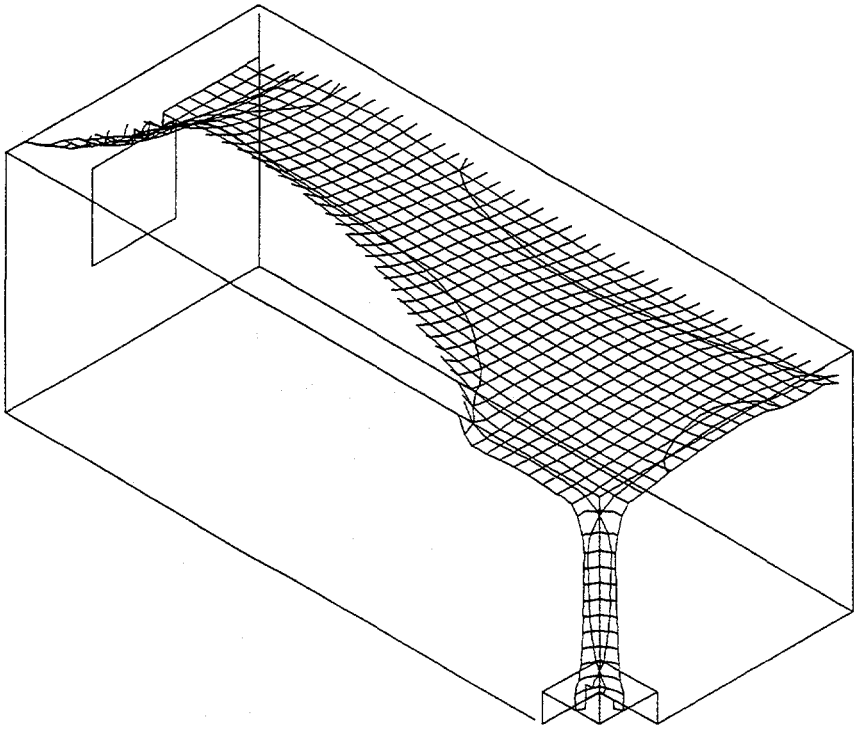

Figure 18 - 7.5% Hydrogen, 6800 l/hr after 20 minutes

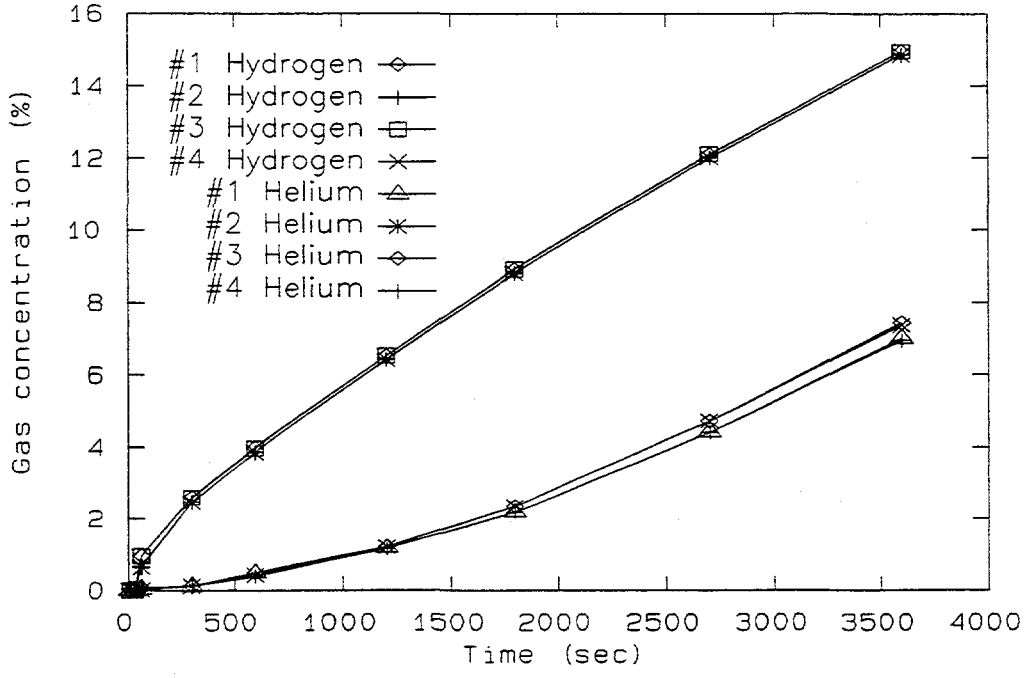

Figure 19 - Home refill scenario 6800 l/hr

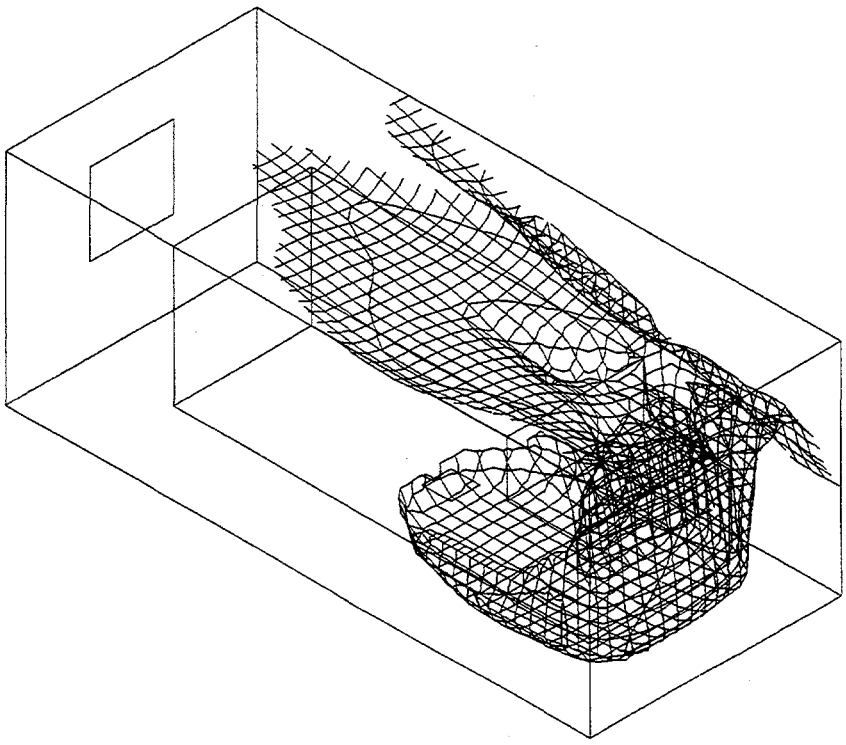

Figure 20- 6.5% Hydrogen, 6800 l/hr after 20 minutes

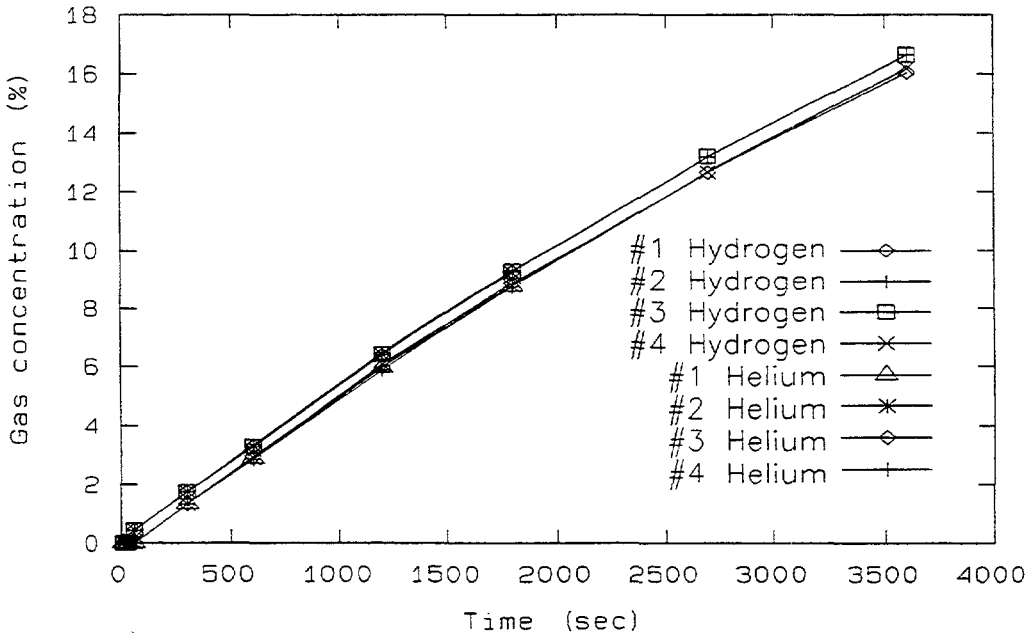

Figure 21- Leaking van scenario 6800 l/hr

REFERENCES

Coward, H.F., and G.W. Jones. 1952. Limits of Flammability of Gases and Vapors, Bureau of Mines Bulletin 503

Hansel, J.G., G.W. Mattern, and R.N. Miller. 1993. "Safety Considerations in the design of Hydrogen Powered Vehicles", Int. J. Hydrogen Energy, Vol. 18, No. 9, pp 790

Lewis, B. and G. VonElbe. 1961. Conbustion, Flames and Explosions of Gases, 2nd Edition New York: Academic Press

Ordin, P.M. 1997. Safety Standards for Hydrogen and Hydrogen Systems, National Aeronautics and Space Administration, NSS 1740.16, Office of Safety and Mission Assurance, Washington D.C.